Quantitative assessment of neurovascular dynamics in ageing, Alzheimer's disease and Huntington's disease

Juliane Bjerkan, MPhys (Hons)

Physics Department

Lancaster University

A thesis submitted for the degree of

Doctor of Philosophy

February, 2025

Quantitative assessment of neurovascular dynamics in ageing, Alzheimer's disease and Huntington's disease

Juliane Bjerkan, MPhys (Hons).

Physics department, Lancaster University

A thesis submitted for the degree of *Doctor of Philosophy*. February, 2025.

Abstract

As individuals age, the risk of neurodegenerative disorders such as Alzheimer's disease increases, largely due to changes in the brain and vasculature. The brain, which consumes about 20% of the body's energy, relies on the cardiovascular system for nutrient transport. This dependence is represented by the neurovascular unit (NVU). Understanding how the functioning of the NVU changes with healthy ageing and neurodegenerative diseases remains insufficiently explored, particularly through *in vivo* measurements in humans. With an ageing population, the prevalence of dementia is expected to rise, highlighting the urgent need for accessible, non-invasive, and cost-effective diagnostic and monitoring tools.

Here, data were collected from younger and older participants, as well as from patients with Alzheimer's and Huntington's diseases, using non-invasive monitoring techniques. Brain oxygenation was measured via functional near-infrared spectroscopy, brain electrical activity via the electroencephalogram, and cardiorespiratory function via the electrocardiogram and a respiration belt. We treat the brain and cardiovascular system as interacting oscillators operating far-from-equilibrium. To analyse their functioning, we apply methods suited to multiscale, time-varying and non-stationary dynamics. The wavelet transform was used to calculate the power of oscillations with logarithmic frequency resolution, and wavelet phase coherence was used to calculate the coordination of oscillations. The efficiency of the NVU was quantified as the wavelet phase coherence between brain electrical activity and oxygenation.

Our findings indicate that NVU efficiency declines with age and is further reduced in patients with Alzheimer's and Huntington's diseases compared to age-matched controls. Specific changes in power and coherence associated with ageing and these neurodegenerative diseases were identified. Previous research on cardiovascular and brain oscillations allows us to link these findings to physiological changes. Thus, the methods presented offer a novel approach for quantitative evaluation of the neurovascular efficiency in ageing and dementia.

Acknowledgements

I would like to begin by expressing my gratitude to my supervisors, Aneta Stefanovska and Trevor J. Crawford. Thank you both for encouraging me to reach my full potential and for providing unwavering support and guidance throughout my PhD journey. Thank you also to the members of the Nonlinear and Biomedical Physics group for making the office a welcoming place. Especially thanks to Sam for all the conversations and pep talks.

I have been fortunate to collaborate with many brilliant co-authors, from whom I have learned so much. This PhD would not have been possible without the foundation you laid with your hard work and your continued support and engagement.

A heartfelt thank you to my friends Tom and Heather for sharing this PhD journey with me, and to Tom for also being an excellent flatmate. You both made lockdown bearable and life in Lancaster enjoyable.

To all my friends from the climbing club, thank you for the laughs, pub trips, and adventures. Starting climbing was the best decision I made during my time in Lancaster. A special thank you to Lorna and Jade—I am so grateful to you both.

To my Norwegian friends—especially Vy, Kristine, Julie, and Madeleine—thank you for always being there for me despite so many years living away. I couldn't have asked for better friends.

Thank you to David Glover for making the last 2 years so much fun, and for being loving, patient and supportive; I look forward to many more adventures together.

To my mum, dad and Svein, thank you for supporting me throughout my academic journey. Life is never too hard knowing I always have a place to come to if needed.

Declaration

I declare that the work presented in this thesis is, to the best of my knowledge and belief, original and my own work. The material has not been submitted, either in whole or in part, for a degree at this, or any other university.

Juliane Bjerkan

February, 2025

Publications

These publications are part of the thesis:

Bjerkan, J., Lancaster, G., Meglič, B., Kobal, J., Crawford, T. J., McClintock, P. V. E. & Stefanovska, A. Aging affects the phase coherence between spontaneous oscillations in brain oxygenation and neural activity. *Brain Res. Bull.* **201,** 110704 (2023)

Bjerkan, J., Kobal, J., Lancaster, G., Šešok, S., Meglič, B., McClintock, P. V. E., Budohoski, K. P., Kirkpatrick, P. J. & Stefanovska, A. The phase coherence of the neurovascular unit is reduced in Huntington's disease. *Brain commun.* **6,** fcae166 (2024)

Barnes, S. J. K., Bjerkan, J., Clemson, P. T., Newman, J. & Stefanovska, A. Phase coherence—A time–localized approach to studying interactions. *Chaos* **34,** 073155 (2024)

Bjerkan, J., Meglič, B., Lancaster, G., Kobal, J., McClintock, P. V. E., Crawford, T. J. & Stefanovska, A. Neurovascular phase coherence is altered in Alzheimer's disease. *Brain Commun.* **7,** fcaf007 (2025)

Conference, symposia and seminar contributions

- Bjerkan J, Lancaster G, Meglič B, et al. Assessment of energy delivery to the ageing brain in the presence of Alzheimer's disease. 2nd SAAgeNet Knowledge Exchange Symposium 2024. Sunway University, Malaysia. (Presentation)

- Bjerkan J, Lancaster G, Meglič B, et al. Assessment of energy delivery to the ageing brain in the presence of Alzheimer's disease. Global Health Technopreneurship 2024. Birmingham, UK. (Presentation)

- Bjerkan J, Lancaster G, Meglič B, et al. Energy supply and the aging brain. Center for ageing research showcase 2023. Lancaster, UK. (Poster)

- Bjerkan J, Lancaster G, Meglič B, et al. The neurovascular unit in ageing and dementia. Data Science Institute lunchtime seminar, December 2023. Lancaster, UK. (Presentation)

- Bjerkan J, Alatawi S, Ugland N, et al. Cardio-respiratory wavelet phase coherence at three ambient temperatures. Workshop on time-series analysis of noisy data 2023. Lancaster, UK. (Presentation)

- Bjerkan J, Lancaster G, Meglič B, et al. Quantitative evaluation of the efficiency of the neurovascular unit in ageing and dementia. Lancaster Biosciences Network Symposium 2023. (Presentation)

- Bjerkan J, Lancaster G, Meglič B, et al. Far from equilibrium approach to complex neurovascular dynamics in healthy ageing and dementia. Physics of Life 2023 conference. Harrogate, UK. (Presentation)

- Bjerkan J, Lancaster G, Meglič B, et al. Neurovascular dynamics is altered in Alzheimer's disease. Alzheimer's Research UK 2023 conference. Aberdeen, UK. (Poster)

- Bjerkan J, Alatawi S, Ugland N, et al. The effect of temperature on the cardiovascular and respiratory system. Workshop on Time Series Analysis 2022. Auckland, NZ. (Invited talk)

- Bjerkan J, Alatawi S, Ugland N, et al. Cardio-respiratory wavelet phase coherence at three ambient temperatures, 12th Conference of the European Study Group on Cardiovascular Oscillations (ESGCO), 2022. Štrbské pleso, Slovakia. (Presentation)

- Bjerkan J, Lancaster G, Meglič B, et al. Neurovascular dynamics is altered in Alzheimer's disease. 35th Global Conference of Alzheimer's Disease International, 2022. London, UK. (Poster)

- Bjerkan J, Lancaster G, Meglič B, et al. Neurovascular dynamics is altered in Alzheimer's disease. Faculty of Science and Technology science week, 2022. Lancaster, UK. (Poster)

- Bjerkan J, Lancaster G, Meglič B, et al. Ageing alters the relationship between blood oxygenation and neuronal dynamics in the brain. British Society of Gerontology 50th Annual Conference, 2021. (Online presentation)

- Bjerkan J. Nonlinear Dynamics of Alzheimer's Dementia. Psychobiology annual scientific meeting, 2019. Windermere, UK. (Poster)

Contents

Chapter 1

Introduction

The brain is the most complex part of the human body. Neurons are considered the fundamental units of the brain, and their number approaches that of the stars in the Milky way. How the brain functions and what leads to its dysfunctions are still captivating questions for a broad range of scientists including psychologists, neuroscientists and physicists. This might be driven by the brain's role in cognition, making the study of the brain synonymous with exploring what makes humans human.

Beyond neurons, the brain comprises vascular cells and glial cells. In fact, combined there is a similar amount of these cells as neurons. Their critical contribution to brain function is starting to be appreciated, which is reflected in concepts such as the neurovascular unit. There is a close link between the cardiovascular system and the brain: the brain, which spends around 20% of the body's energy consumption is naturally dependent on a well-functioning cardiovascular system to transport nutrients and oxygen to the brain cells. Impaired neurovascular interactions might be one path leading to brain dysfunction, and has been linked to several neurodegenerative diseases.

It has proved challenging to uncover how the brain works, both on a microscopic and macroscopic level. Research that would be unethical on humans might be conducted on animals, but there are of course clear differences between human and animal brains (in addition to similarities). *In vitro* studies of human brains give limited information on the dynamic nature of the brain. Fortunately, non-invasive measurement techniques exist that allow scientists to measure *in vivo* brain activity in humans, such as the electroencephalogram (EEG), functional near-infrared spectroscopy (fNIRS) and functional magnetic resonance imaging (fMRI).

Measurements of brain activity can be in the form of a time-series, i.e. a variable (such as voltage from EEG) that is measured at discrete time points. Soon after the EEG was applied in humans, it was clear that brain activity was rhythmic. A clear oscillation with a frequency of around 10 Hz was the first rhythm observed, and was named the alpha rhythm [5]. The study of brain oscillations, or brain waves,

is now fundamental in neuroscience and oscillations are thought to underpin many cognitive processes. Changes in these oscillations are observed in numerous diseases.

The aim of this thesis is to utilise non-invasive techniques to measure brain and cardiovascular activity in humans, with the goal of assessing neurovascular dynamics with age and two neurodegenerative disorders: Alzheimer's disease and Huntington's disease. Age is the biggest risk factor for Alzheimer's disease and the number of people with neurodegenerative diseases rises globally. As such, there is a need for relatively cheap, non-invasive methods to diagnose and monitor disease progression. The measurement techniques used in this work are good candidates for this.

The analysis methods applied are strongly motivated by dynamical systems theory and properties of living systems, emphasising the occurrence of oscillations, time-variability, activity across several time scales and interactions between systems. Due to interactions with the environment, physicists would refer to living systems as being thermodynamically open and operating far from equilibrium. Wavelet analysis offers resolution in time and frequency, with logarithmic frequency resolution, which is ideal for the analysis of time-series from the brain and cardiovascular system.

The structure of this thesis is as follows: given the strong link between the brain and cardiovascular system, the next section of chapter 1 introduces the physiology of these systems. This is followed by a discussion on the "physics of living systems" from a dynamical systems theory perspective. Then, data-driven approaches to dynamical systems will be explored, with an evaluation of time-series analysis techniques to conclude chapter 1. Throughout the chapter, there will be an emphasis on oscillatory processes. Chapter 2 provides an introduction to coherence and examines the benefits of wavelet phase coherence. Chapters 3, 4 and 5 present analyses of real data from participants with ageing, Alzheimer's and Huntington's disease, along with the findings and insights obtained. Chapter 6 will summarise the overall findings and propose future research directions.

1.1 The cardiovascular system

The cardiovascular system is responsible for the transport of nutrients, hormones and immune cells, in addition to the removal of metabolic waste products and temperature regulation [6]. In this work, we are mostly interested in the transport of nutrients, especially to the brain. To better understand the cardiovascular system, let us begin by considering its structure and function.

1.1.1 Structure

The cardiovascular system consists of the heart, the lungs and blood vessels. The circulatory system is broadly divided into two: from the heart to the lungs and back to the heart (pulmonary circulation), and from the heart to the rest of the body and back to the heart (systemic circulation) [6]. The pulmonary circulation ensures the crucial exchange of oxygen and CO_2.

The blood is led to the rest of the body via large vessels, which become smaller as they reach their target destinations. Then, vessels known as venules and veins lead the blood back to the heart. Anatomically, vessels can be classified into elastic arteries, muscular arteries, arterioles, capillaries, post-capillary venules, muscular venules and veins [6]. Capillaries are the smallest vessels and also the type of vessel with by far the largest surface area. Due to the small size red blood cells are deformed when they pass through, and they release oxygen which can then pass into tissue.

Vessel walls are varied in size and composition, as they serve different purposes. Most consist of three main layers: a layer of endothelial cells formed on a basement membrane, a layer of elastic tissue and smooth muscle cells, and a layer of connective tissue (e.g. collagen) where nerves from the autonomic nervous system innervating smooth muscle cells can also be found. Capillaries consist only of the first layer [6].

1.1.2 Function

The heart is the main pump of the cardiovascular system, pumping blood around the circulatory system. The pressure is highest after the blood is ejected from the heart, i.e. in the aorta. The various vessels influence the flow, so that the blood flows through vessels at different speeds and pressures. The elastic and muscular arteries let the blood pass through with low resistance so that it can reach areas of the body far from the heart. Small muscular arteries and arterioles both have many smooth muscle cells, which means they can control the amount of flow to subsequent, smaller vessels through vasodilation or vasoconstriction. This local control of blood flow is therefore due to changes in the resistance to flow. The capillary flow is dependent on the pressure gradient between the arterioles and postcapillary venules, hence the control of arterioles is essential. Before reaching the capillaries, the blood flows through precapillary sphincters that ensure the blood pressure in the capillaries is not too high. These sphincters are found where arterioles split into capillaries. After the blood passes through the capillaries, releasing oxygen and collecting CO_2, the venules and veins lead the blood back to the heart [6]. To ensure the blood flows in the right direction there are valves in the veins.

The vessel sizes are not constant, but rather changing in time due to several different physiological processes. This means that blood flow is dynamic, and the dynamics can tell us much about the cardiovascular system in health and disease. The dynamics stems from systemic influences (the heart and respiration), and local control from the vessels mediated through various means. Previous research based on *in vivo* blood flow recordings has shown that these processes are oscillatory, and manifest in specific frequency bands [7, 8]. We now discuss these processes and frequency ranges, known as the cardiovascular frequency bands.

1.1.2.1 Cardiac

Frequency range 0.6–2 Hz. The heart beats approximately once a second at rest, which corresponds to 1 Hz. However, the heart is not a metronome and the exact timing between each beat varies in time, known as heart rate variability. In some studies the limit of the cardiac frequency range is set below 2 Hz, as healthy, resting humans often have a heart rate well below 2 Hz. However, if one is investigating conditions where the heart rate is expected to be higher one should take this into account.

1.1.2.2 Respiration

Frequency range 0.145–0.6 Hz. Healthy humans at rest breathe at a rate of approximately 0.3 Hz. This oscillation has been observed in recordings of blood flow, as blood flow depends on pressure differences generated by both the heart and lungs [9]. One respiration cycle consists of inhalation and exhalation. During inhalation, oxygen-rich air from the environment enters the lungs, where oxygen diffuses into the bloodstream. Since there is more CO_2 in the blood than in the air, CO_2 diffuses from the bloodstream into the air in the lungs. During exhalation, we breathe out air that is rich in CO_2.

1.1.2.3 Myogenic

Frequency range 0.052–0.145 Hz. The activity of the smooth muscle cells reacting to intravascular pressure is known as myogenic activity. The myogenic hypothesis was first proposed by William Bayliss in 1902 [10]. Performing experiments on dogs, cats, and rabbits he found that smooth muscle cells lining arteries reacted to a stretching force (caused by increased pressure), by contraction. Likewise, when there was a decrease in tension they relaxed. These experiments were performed with cut nerves to be independent of the central nervous system, and so he concluded that the effects detected were myogenic in nature (i.e. initiated by the muscle cell itself, rather than by an outside influence such as a nerve). These reactions, located not

centrally but in the peripheral of the cardiovascular system, could help maintain a constant blood flow through the surrounding tissue as long as they were not overruled by other factors such as the central nervous system. Bayliss' arguments did not gain wide popularity at this point [11], and others argued metabolic factors or nervous mechanisms could cause the changes. It took almost 50 years before the myogenic hypothesis was studied by Björn Folkow who argued in its favour [12–14]. In a study mainly on cats, where effects from vasodilator metabolites and nervous mechanisms were excluded, he still observed vasodilation, which could then be attributed to mechanical factors from changes in blood pressure [12]. This study provided strong support for Baliss' myogenic hypothesis. By the late 20th century the myogenic response was recognized as important for autoregulation, and research into the mechanisms behind the response had started [11, 15]. Exactly which stretch-activated ion channels initiate the response is still not clear [16].

In humans, myogenic oscillations tend to manifest between $0.052-0.145$ Hz [7–9, 17, 18]. These oscillations persist in the presence of neural blockers, which further suggests that the origin is in fact (at least partially) from myogenic activity [9, 19].

Already in 1902, Bayliss pointed out, after reading the work of Hill [20], that the myogenic response was especially interesting in the case of the brain, due to the restriction of the rigid skull. If the arteries were to expand in size they would do so at the expense of capillaries and veins. Due to this many researchers in the 19th century argued that the cerebral blood flow could not be regulated locally, but through systemic blood pressure or cardiac output [21]. However, Bayliss suggested that the myogenic response could instead make vessels more or less rigid, thereby increasing or decreasing blood flow velocity as a means to provide more blood to the active cerebral tissue [10]. That the cerebral blood flow could, in fact, be controlled regionally was shown by Seymour S. Kety and Carl F. Schmidt in 1948 [22]. It has since been observed *in vivo* in human participants [23, 24]. Rayshubskiy et al. [23] utilised multi-spectral optical intrinsic signal imaging (MS-OISI) in an awake participant undergoing brain surgery. Like fNIRS which is used in the research

presented in this thesis, MS-OISI uses light at specific wavelengths and absorption to measure changes in oxygenated and deoxygenated hemoglobin concentration. They observed sinusoidal-like slow oscillations around 0.1 Hz, which was regionally specific and associated with pial arterioles. As the oscillations were localised, it is unlikely they stem from systemic reasons. Noordmans et al. [24] also utilised MS-OISI, in 4 anaesthetised participants undergoing brain surgery. In 3 of the participants, they observed localised slow oscillations ∼0.1 Hz, while for 1 participant the oscillation occurred at a lower frequency.

1.1.2.4 Neurogenic

Frequency range 0.021–0.052 Hz. Nerves from the autonomic nervous system innervate smooth muscle cells, and can therefore influence their activity through discharging. This neurogenic activity from the sympathetic nervous system was shown to manifest in the frequency interval 0.021–0.052 Hz by Soderstrom et al. [9] after measuring skin blood perfusion on skin with and without sympathetic nerve activity. They showed that the normalised power was greatly reduced in this frequency range in the nerve-less skin, which was not the case in higher frequency ranges. A similar finding was obtained by Landsverk et al. [18] when evaluating skin blood perfusion before and after brachial plexus block. Brachial plexus block impairs sympathetic activity, and might also impair endothelial activity. The authors show a decrease in relative power in the 0.0095-0.021 Hz and 0.021-0.052 Hz frequency ranges. The 0.021–0.052 Hz range was associated with sympathetic nervous activity as the lower range has earlier been associated with endothelial activity. The neurogenic activity mostly leads to vasoconstriction, rather than vasodilation.

1.1.2.5 Endothelial

Frequency range 0.005–0.021 Hz. The endothelial cells lining all blood vessels can also influence the vessel tone, through the release of various substances that affect the smooth muscle cells [25]. Hypothesising that the endothelium-dependent

vasomotion might manifest at around 0.01 Hz, Kvernmo et al. [26] assessed skin perfusion by applying an endothelium-dependent vasodilator (acetylcholine (ACh)) and an endothlium-independent vasodilator (sodium nitroprusside (SNP)). The relative power in the 0.0095–0.02 Hz frequency range was significantly higher when using ACh, indicating a contribution of the endothelium in this range. The endothelium releases different molecules, and to investigate which pathway is responsible for the 0.01 Hz oscillation, Kvandal et al. [27] inhibited nitric oxide (NO) and prostaglandins (PGs) synthesis in two different groups. Inhibiting NO resulted in reduced skin perfusion, while inhibiting PGs did not alter the perfusion. Importantly, the difference in the 0.01 Hz oscillation when comparing ACh and SNP reported by Kvernmo et al. was not found when NO was inhibited [27], but still seen when PGs were inhibited. When inhibition of NO was reversed, the difference was seen again. As such, the oscillation around 0.01 Hz is at least to some extent affected by NO, a conclusion that was also reached by Stewart et al. [28].

An oscillation within the 0.005–0.0095 Hz frequency range has also been observed [29–32]. This oscillation is also affected to a greater extent by ACh than SNP, indicating the role of the endothelium. Inhibiting NO did not affect this frequency range [30, 31], but did affect the 0.0095–0.02 Hz frequency range [27, 31]. Inhibiting PGs did not affect either interval. It was therefore concluded that the lowest interval is related to endothelial mechanisms different from NO and PGs, potentially endothelium-derived hyperpolarizing factor (EDHF).

1.1.3 Summary

This section provided an overview of the cardiovascular system, with a key focus on the cardiovascular frequency bands, which define the frequency ranges associated with various physiological processes involved in blood flow regulation. In the following chapters, these frequency bands are used to categorise activity, playing a crucial role in interpreting the results.

1.2 The brain

Together with the spinal cord, the brain makes up the central nervous system. The brain is responsible for cognitive function, movement and also several regulatory processes within the body such as temperature regulation.

1.2.1 Structure

The human brain weighs ∼1100-1700g, or about 2% of the body weight, in adults [33]. It consists of three main parts: the cerebellum, cerebrum and brain stem (figure 1.1A). There are two cerebral hemispheres, which are divided by the interhemispheric fissure (figure 1.1A). The two hemispheres are fairly symmetrical, but there are some asymmetries that are thought to be important for consciousness, speech, language and memory [34]. Fissures are deep sulci, which are grooves between ridges known as gyri (figure 1.1B). Combined, the gyri and sulci give the brain the characteristic walnut-like surface, and this folding gives the brain a large surface area. The pattern of the folding varies between individuals, but larger features tend to be more consistent [33]. White matter is white as it contains many myelinated axons, as opposed to grey matter which contains more cell bodies (figure 1.1B). Axons are fibres along which electrical impulses travel and are important for neuronal communication. Myelin forms around the axons and increases the speed at which electrical impulses can travel.

The cerebral hemispheres can be divided into lobes, based on four major sulci. These lobes are the frontal lobe, temporal lobe, parietal lobe and occipital lobe (figure 1.1C). These lobes are more anatomical than functional, but each lobe can still be associated with certain specific functions. For example, the motor cortex is in the frontal lobe and is responsible for the movement of the body.

The brain consists of brain cells known as neurons, many other cell types known as glial cells and also vascular cells. The cerebellum consists mostly of neurons (∼69 billion neurons, ∼16 billion non-neuronal cells), while the cerebral cortex and white

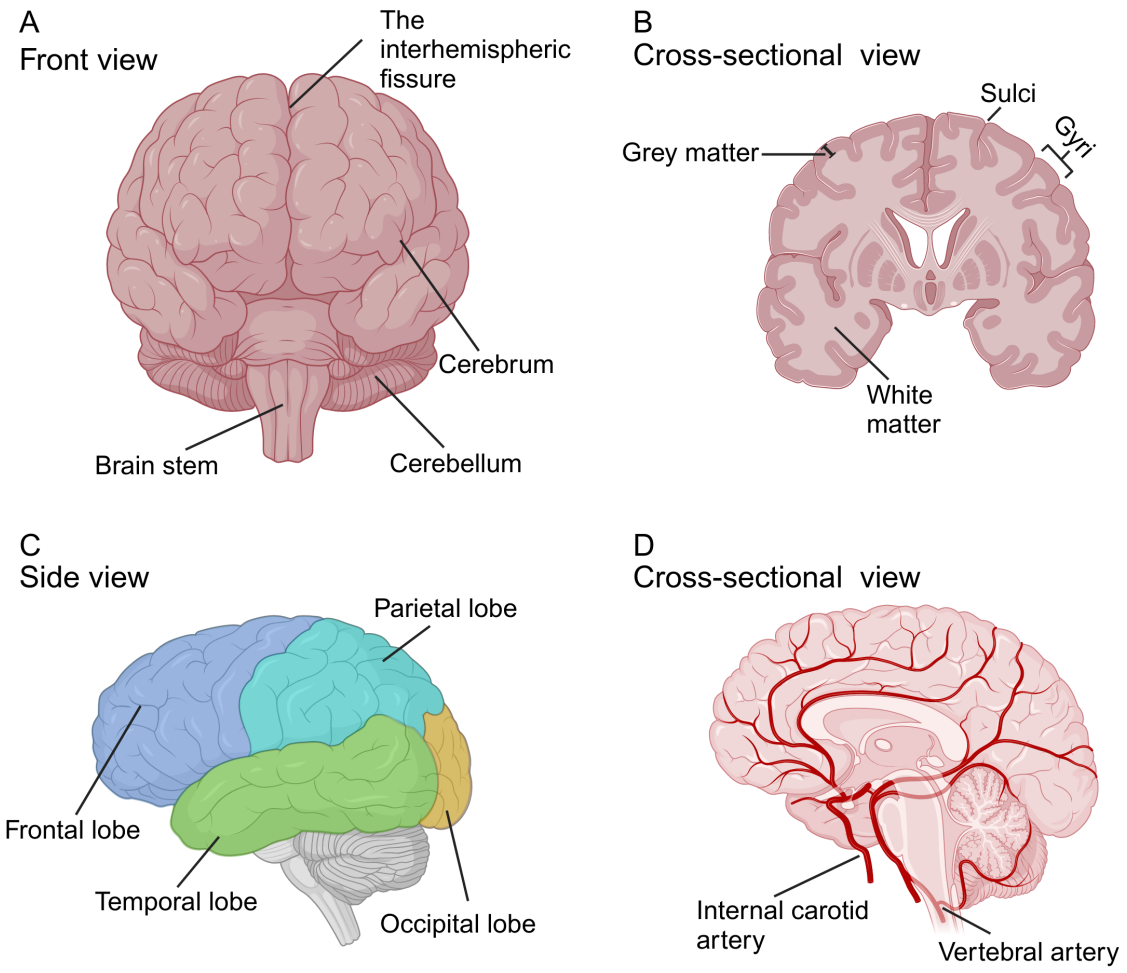

Figure 1.1: Views of the brain. (A) Front view, with the interhemispheric fissure, cerebrum, brain stem and cerebellum indicated. (B) A cross-sectional view of the cerebrum, with grey matter and white matter indicated, as well as sulci and gyri. (C) Side view, with the four main lobes indicated. (D) A cross-sectional view, with the internal carotid artery and vertebral artery indicated. Created with BioRender.com.

matter (part of the cerebrum, figure 1.1B) consist of more non-neuronal cells than neurons (∼16 billion neurons, ∼61 billion non-neuronal cells) [33]. This abundance of non-neuronal cells alludes to their importance, and their function is a major topic of this thesis as we try to uncover the functioning of the neurovascular unit (more details in section 1.3).

There are $\sim$ 100 billion neurons in the brain, and they are connected via synapses. It is estimated to be $\sim$ 200 trillion connections. The number of connections is a lot fewer than the number of possible connections, but despite being sparsely connected

most neurons are not more than a few steps from any other neuron. This is because the brain is thought to be connected in a small-world manner. This means most connections are local and regular, but long-distance connections also occur [35].

1.2.2 Function

The functioning of the brain relies on chemical and electrical signals. The brain activity does not cease unless death occurs. Hence, even without specific stimuli or input from the environment brain activity is ongoing. In fact, compared to the energy usage of the brain 'at rest', the energy usage when engaging in a task is only around 5% higher [36]. For example, in 1955 Sokoloff et al. [37] found that cerebral oxygen consumption was not different when participants were engaging in mental arithmetic compared to during the resting state. Such observations have led to the view that brain function is mostly intrinsic and that the brain process and interprets information so that it can both respond to and *predict* external demands [35, 36]. This is known as top-down processing, where previous experiences are used to predict situations. The alternative to top-down processing is bottom-up processing, where a stimulus is first detected and then the processing follows.

Exactly how the brain processes and stores information is of great interest. In 1949 Donald Hebb published his book, *The organization of behavior*[38], attempting to link behaviour to physiology. His theory on cell assemblies states that persistent or repetitive activity will lead to cellular changes, and as such groups of neurons can become interconnected. In other words, "neurons wire together if they fire together" [39]. Buzsáki has hypothesised that neural syntax [40] is used by the brain. In this case, neuronal assemblies are the fundamental unit of the syntax, and various mechanisms will decide how the assembly activity is organised in time. Both Hebb and Buzsáki's ideas postulate the importance of spatiotemporal patterns of neuronal activity.

On a macroscopic scale, the spatiotemporal patterns of neuronal activity lead to oscillations and neuronal networks [41]. Neuronal oscillations are transient and

time-varying which can make them challenging to study. Macroscopic neuronal oscillations measured by EEG (discussed in section 1.5.2), have frequencies from around 0.05 to 500 Hz [42]. The oscillations are traditionally divided into frequency bands, that are thought to represent independent oscillations. The exact frequency limits are not fully consistent between studies [43]. In the chapters of this thesis we use the frequency limits as specified in [44–46]. Note that beta is then defined up to 22 Hz.

Slower oscillations can recruit larger cortical areas, while quick oscillations are more local in nature [42]. While it can be a simplification to draw a one-to-one association between a certain oscillation and function, there is empirical evidence suggesting the importance of different oscillations in certain tasks and states (discussed in the next subsections). Oscillations of different frequencies can influence each other, by modulating either the amplitude or phase of the other oscillation. An example is theta-gamma coupling, where the amplitude of gamma oscillations depends on the phase of the theta oscillation [47].

1.2.2.1 Infraslow and slow oscillations

Frequency range <0.5 Hz. Oscillations below the delta band are often left out in EEG research due to high pass filters, but there is evidence of slow rhythms both from animal and human studies [48, 49]. The origin and physiological function are still debated. There might be several distinct oscillations below 0.5 Hz, with distinct functions. While EEG is said to measure neuronal activity, electrical activity measured by the electrodes might also stem from non-neuronal sources, which can contribute to these slow oscillations. For example, a potential difference across the blood-brain barrier, or neuron-glial interactions [50–53]. The slow oscillations are associated with cortical excitability and arousal [54–58] and might impact performance [59].

1.2.2.2 Delta δ

Frequency range 0.5–4 Hz. Generators of delta oscillations are found in the hippocampus and a part of the prefrontal cortex [60]. Delta oscillations are associated with sleep, anaesthesia and rest. There is some evidence that delta oscillations are also important during various cognitive processes [61].

1.2.2.3 Theta θ

Frequency range 4–8 Hz. Theta oscillations are observed in the hippocampi of rodents, where they are linked to voluntary, exploratory and orienting movement [62]. As discussed in the previous subsubsection, delta oscillations are observed in the human hippocampus, but an oscillation at $\sim$8 Hz is also seen in the posterior part of the hippocampus [60]. Theta generators are also found in the cortex [60]. Theta are strong during REM sleep and are linked to working memory and demanding cognitive tasks [60].

1.2.2.4 Alpha α

Frequency range 8–13 Hz. Alpha was the first identified rhythm in EEG recordings, observed by Hans Berger himself [5]. In the resting state, sensory and motor systems tend to generate alpha oscillations. For example, when the eyes are closed the alpha rhythm is dominant over the occipital and parietal areas. Capilla et al. [60] observed alpha oscillations generated in the precuneus, which is thought to be the source of posterior alpha oscillations. They also observed alpha generators in the visual, auditory and somatosensory cortices. The different alpha rhythms have different peak frequencies, and the oscillation from the sensorimotor system has been named mu μ, while the oscillation from the auditory system has been named tau τ. One hypothesis on the function of alpha oscillations is that they are a result of inhibition, so they are dominant when an area of the brain is not in use (i.e. the visual cortex when the eyes are closed). However, this hypothesis is based on amplitude measures,

and there is some evidence that the phase of alpha oscillations is important in neuronal processing [63].

1.2.2.5 Beta β

Frequency range 13–30 Hz. Beta oscillations were also identified by Hans Berger, as a quicker oscillation that he observed when participants opened their eyes and the alpha oscillation was no longer dominant. Beta oscillations have been associated with motor control and motor control in response to sensory input, and are observed in the motor and premotor cortexes, the basal ganglia and the cerebellum. Specifically, beta power decreases before and during voluntary movements, and increases in periods without movement and when movement has to be avoided due to a task. Even when participants imagine movement (motor imagery) beta power decreases. It has been suggested that the beta oscillations help maintain the current motor set, or the 'status quo' [64]. Further, stimulating the brain with beta oscillation slows down movement [65].

Beta oscillation generators have been found in the lateral occipito-parietal regions (low beta ∼16 Hz), prefrontal cortex (high beta ∼25 Hz) and motor cortex (high beta ∼20 Hz) [60], and there is evidence of beta oscillations having a role also outside of motor control. In various cognitive processes beta oscillations are stronger if top-down control is required, and can sometimes be observed as transient beta bursts [66].

1.2.2.6 Gamma γ

Frequency range >30 Hz. Gamma oscillations were named by Jasper and Andrews in 1938 [67]. They have since been associated with attention, as stimuli are better detected when gamma is high [68]. It is also hypothesised that gamma is important for unifying perception that is processed in different parts of the brain [41].

1.2.3 Summary

This section provided an overview of the brain, highlighting key concepts such as the abundance of glial and vascular cells, neuronal networks, and the large-scale oscillatory behavior of neuronal populations. These oscillations are split into specific frequency bands, which are utilised in the subsequent chapters for analysis and interpretation.

1.3 The neurovascular unit

To support its ongoing activity, the brain requires around 20% of the body's energy consumption. As the energy demand in the brain varies across space and time, regulation of blood flow is crucial. However, historically many scientists have considered brain cells or cerebral blood vessels separately, not appreciating the close link between them in healthy brains. It was not until 2001 that the Stroke Progress Review Group meeting of the National Institute of Neurological Disorders and Stroke of the NIH popularised the concept of the neurovascular unit (NVU) [69].

Neurons, the microvasculature and various cells known as glial cells make up the NVU. As we remember from section 1.2.1, the cerebral cortex consists of many more non-neuronal cells than neurons. The vascular cells in the NVU are endothelial cells, vascular smooth muscle cells and pericytes. Examples of glial cells in the NVU are astrocytes and microglia.

The endothelial cells play an important role in restricting what molecules can enter the brain from the bloodstream as they are the main component of the blood-brain barrier, and depending on their location they are specialised. The pericytes and vascular smooth muscle cells give structural support to the blood vessels, and as described in section 1.1.2 smooth muscle cells are important for vasomotion. Astrocytes link the neurons to the blood vessels, as their endfeet cover the surface of the blood vessels. As the most numerous glial cell type in the brain, they play an important role in controlling neurotransmitters and the diameter of blood vessels.

Microglia are the primary immune cells of the cerebral nervous system [70].

The vascular response to increased neuronal activity (neurovascular coupling) is initiated by the neurons themselves, and astrocytes act to transmit the message to the local vasculature. It is not just the local vasculature that must respond to the increased neuronal activity. In fact, the response often occurs in the arteries, and the signal can propagate there due to electrical coupling between endothelial cells [69]. Smooth muscle cells act on the signal and alter vasomotion accordingly. The role of pericytes in vasomotion is not clear [69].

In addition to to neurovascular coupling, cerebral blood flow is controlled through autoregulation (response to perfusion pressure), vascular reactivity (response to vasoactive stimuli such as CO_2) and endtohelium dependent responses [71].

1.4 Neurovascular changes with ageing, Alzheimer's disease and Huntington's disease

Dysfunction of the NVU is increasingly considered important in neurodegenerative diseases such as Alzheimer's disease (AD) [72]. However, even healthy ageing affects the various components of the NVU. The endothelial cells release less NO and EDHF with age, which reduces the capacity to initiate vasodilation. Decline in mitochondrial function, and therefore (ATP) availability, might underlie decreased endothelial functioning with age [73]. The blood-brain barrier becomes more permeable with healthy ageing [74], which can be detrimental to brain health. Smooth muscle cells' ability to constrict and dilate vessels reduces with age, further decreasing vasomotion. With age, astrocytes have decreased function in various domains which impacts their ability to support neurons. Both astrocytes and microglia tend to become more proinflammatory with age. In addition to changes in the microvasculature and glial cells, neurons themselves undergo changes, such as mitochondrial dysfunction [73].

Alzheimer's disease and Huntington's disease (HD) have in common that they

involve protein dysfunction. In HD a genetic mutation leads to the production of a mutant huntingtin protein, which has been found in several NVU cells [75]. In AD the protein tau misfolds and can be found inside neurons. In addition, the protein amyloid-beta forms plaques which build up between brain cells. While HD is the result of a genetic mutation, the risk of AD increases with certain genes (such as APOE4). Both of these neurodegenerative diseases have a presymtomatic stage where changes in the brain have developed, but symptoms have yet to appear. Lifestyle factors can influence the onset and development of both diseases [76, 77]. Several risk factors for AD are associated with cardiovascular health [72, 77]. Resting cerebral blood flow is reduced during the presymptomatic stages of AD and the vascular response is not as responsive to increased neuronal demand as for age-matched controls [69]. Vascular changes are not well explored in the presymptomatic stages of Huntington's disease, but there is evidence that reduced blood flow to the striatum is present [78]. In addition, Garcia et al. demonstrated molecular changes in vascular and glial cells in HD [79].

1.4.1 Summary

The previous sections (1.3 and 1.4) introduced the NVU and its role, as well as the neurovascular changes associated with aging, Alzheimer's disease, and Huntington's disease. The key takeaway is the critical importance of the NVU in maintaining a healthy brain. Furthermore, the widespread neurovascular changes highlighted underscore the motivation for studying the cardiovascular system and brain in the mentioned conditions, as explored in the subsequent chapters.

1.5 Non-invasive measurements of the cardiovascular system and the brain

Hemodynamics and neuronal dynamics are closely linked, and so measuring only one does not capture the whole picture. Hemodynamics is usually measured using fMRI or fNIRS, while neuronal dynamics is measured using EEG or magnetoencephalography (MEG). All of these methods have strengths and weaknesses. Due to the portability, non-invasiveness, price and temporal resolution we have combined fNIRS and EEG. In addition, cardiorespiratory function is captured with ECG and a respiration belt. As such, the following subsections introduce the measurement techniques that were used to obtain data that were analysed for chapters 3, 4 and 5.

1.5.1 Functional near-infrared spectroscopy (fNIRS)

1.5.1.1 Technical aspects

fNIRS is a non-invasive, relatively cheap measurement technique that can monitor brain oxygenation. It uses light that is transmitted by a source probe (emitter), often a light-emitting diode (LED). The light propagates through the matter below the probe and is scattered or absorbed depending on this matter. A detector measures the reflected light (figure 1.2). The light is in the near-infrared range (wavelength $\sim$ 690-900nm), as this allows for measuring changes in hemoglobin concentration. Different chromophores (molecules that absorb light at specific wavelengths and then emit light lacking this wavelength) absorb different wavelengths, which is essential for fNIRS. Near-infrared light travels relatively unhindered through skin, tissue and bone, while oxygenated hemoglobin and deoxygenated hemoglobin absorb it. The result is an 'optical window' $\sim$ 690-900nm for monitoring hemoglobin. At wavelengths of 800nm, the absorption is equal for oxygenated and deoxygenated hemoglobin (figure 1.3, isosbestic point). As such, fNIRS devices utilise two

wavelengths within the optical window, but on different sides of the isobestic point to quantify changes in both oxygenated and deoxygenated hemoglobin [80]. For example, the NIRScout from NIRx, the device used in the research presented in this thesis, uses wavelengths of 760nm and 850nm.

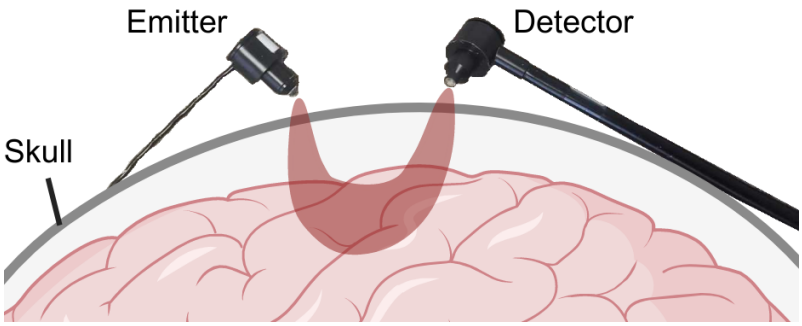

Figure 1.2: Illustration of an emitter and a detector, placed on a head. The light travels from the emitter, reaching the upper parts of the cortex before being reflected and subsequently measured by the detector. Created with BioRender.com.

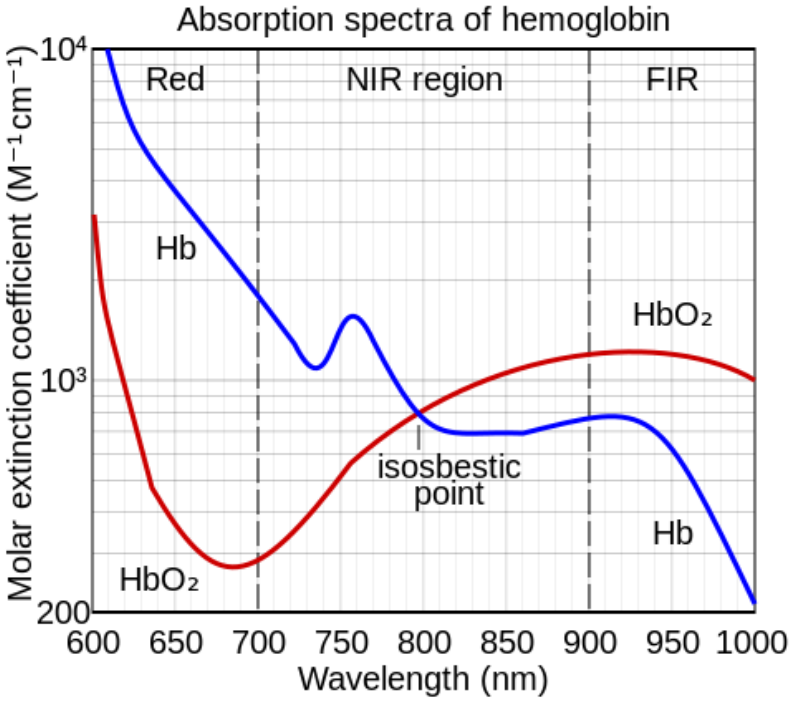

Figure 1.3: Absorption spectra for oxygenated hemoglobin (red) and deoxygenated hemoglobin (blue). The molar extinction coefficient tells how strongly light at a given wavelength is absorbed by a medium per molar concentration. Figure reproduced with changes [81].

Continuous wave fNIRS is most commonly used, meaning that emitted and reflected light intensity is measured. From these measurements the relative concentration changes in oxygenated and deoxygenated hemoglobin are calculated, usually using the modified Beer-Lambert law [82]. As the scattering and absorption coefficients of the tissue are unknown, only relative and not absolute concentration changes can be calculated.

The sampling frequency of fNIRS can be much higher than the sampling frequency of fMRI (often sampled around 0.5-1 Hz [83]). For example, the fNIRS system used for the research presented in this thesis has a sampling frequency of 31.25 Hz. This avoids any aliasing from the heart and respiration activities (see figure 1.4 for illustration of aliasing). These physiological processes are often considered 'physiological noise' if the goal of a study is to measure neuronal activity in response to a task/stimulus. Such studies are based on neurovascular coupling, where increased neuronal activity leads to increased blood flow to the activated area [80]. Other studies are interested in the spontaneous oxygenation dynamics, and so the heart and respiration activities, in addition to other vascular activities, are considered sources of information rather than noise [84].

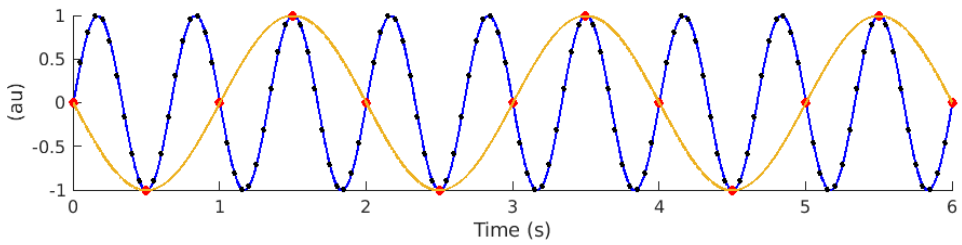

Figure 1.4: A sine wave with frequency 1.5 Hz (blue). The black dots illustrate measurements with a sampling rate of 20 Hz, which is clearly sufficient to capture the sine wave. The red dots illustrate measurements with a sampling rate of 2 Hz. This low sampling rate is not sufficient, and the dynamics might be misinterpreted to represent a sine wave with a frequency of 0.5 Hz (gold).

1.5.1.2 Strengths and weaknesses

As both fNIRS and fMRI measure brain oxygenation, it is natural to compare the two methods. fNIRS has several benefits over fMRI such as reduced costs (3 Tesla MRI scanners can cost 2-3 million US dollars [85], compared to approximately 10000-200000 US dollars for fNIRS), portability and non-invasiveness. As fNIRS is portable, patients might not need to travel for a measurement, and it can also be used for bedside monitoring. fNIRS is suitable for participants with metal implants and is relatively robust against movement artifacts. As it is relatively inexpensive and also easy to use, fNIRS does not have to be in specialist centres only and therefore could be widely applicable [86]. As mentioned above, the high sampling frequency of fNIRS is a benefit. However, fNIRS can only measure oxygenation in the upper parts of the brain with relatively low spatial resolution.

1.5.1.3 Application in research

Since Frans Jöbsis showed that one could monitor concentrations of oxygenated and deoxygenated hemoglobin in the brain non-invasively in 1977, fNIRS has been developed into a popular neuroimaging tool. It has been applied both in studies of healthy ageing [84] and of diseases such as dementia, including Alzheimer's disease [86, 87]. It has also been applied to study brain activity in infants [88]. Further, it has been extensively used in hyperscanning studies [89], i.e. studies that measure the brain activity of two or more participants simultaneously.

As the incidence of Alzheimer's disease is increasing there is a need for low-cost neuroimaging tools to monitor disease progression and to aid in diagnosis. fNIRS is a good candidate for Alzheimer's disease research [90] and was first used for this purpose in 1996 [91]. Since then, the number of articles has increased rapidly [86, 87]. Both resting state studies and task activation are common. Some studies also employ a challenge, like changes to CO_2 concentration in the air the participants were inhaling [92].

Several resting state studies are summarised in table 1.1. Much of the analysis is

done in the time-domain, like calculating the tissue oxygenation index, the standard deviation or average of the time-series, or the Pearson correlation [93–98]. In ageing studies, frequency and time-frequency domain analysis have yielded interesting results, showing the benefit of considering oscillations in the cardiovascular frequency bands [84]. One study considering spectral entropy (entropy of the power spectrum) showed differences between AD and control participants [99].

Most, but not all, studies do find a significant difference between the groups considered. In a recent review paper, it was found that $\sim$ 86% of the 88 published papers (both resting state and task activation) found a significant difference between dementia or mild cognitive impairment (MCI) and controls [86]. This illustrates that fNIRS can be a valuable tool for dementia monitoring and/or diagnosis.

Despite the first fNIRS study on AD having been published in 1996, the field really started to grow in the last decade [86]. As such, clear standards for data collection and analysis methods have yet to be established, and disease-specific markers that can distinguish different dementias are needed.

Table 1.1: Functional near-infrared spectroscopy studies on Alzheimer's disease in the resting state. The methods tell the main analysis method and the length of resting state recording. N = number of participants, AD = Alzheimer's disease, aAD = asymptomatic AD, pAD = prodromal AD C = controls, MCI = mild cognitve impairment, aMCI = amnesic MCI, tissue oxygenation index (TOI) = [Hbo2]/[HbT], Hbo2 = oxygenated hemoglobin, total hemoglobin (Hbt) = oxygenated hemoglobin + deoxygenated hemoglobin, sd = standard deviation.

Paper	N	**Methods**	**Findings**
[100]	10 AD	Baseline values	AD lower oxy-Hb baseline values,
1997	10 C	27s	and higher deoxy-Hb values.
[93]	21 aMCI	TOI	TOI lower in aMCI in frontal
2013	10 C	NA	and parietal channels.
[94]	32 aMCI	TOI	TOI not different
2014	32 C	20min	between groups

Continued on next page

Table 1.1 – continued from previous page

Paper	*N*	**Method**	**Findings**
[101] 2018	27 aMCI 24 AD 21 C	Multiscale entropy (MSE) 11min	Reduced MSE across all scales in AD patients in the frontoparietal, default, dorsal attention and ventral attention networks compared to C
[102] 2019	26 MCI 28 C	Dynamical Bayesian inference coupling (DBIC) 15min	Reduced DBIC in MCI compared to C
[97] 2019	42 MCI 53 C	Pearson correlation 60s	Higher deoxy-Hb correlation in MCI compared to controls
[98] 2019	25 aMCI 23 AD 30 C	Windowed Pearson correlation functional connectivity (FC) 11min	AD and MCI higher variability in FC compared to C.
[103] 2019	51 MCI 64 C	Power spectral density (PSD) with FFT 5min	Mean PSD (0.07-0.11 Hz) reduced in MCI compared to C in parietal areas
[96] 2021	17 AD 18 C	Standard deviation of oxy-Hb 5min	No significant difference in sd, but tendency for lower sd in AD compared to C

Continued on next page

Table 1.1 – continued from previous page

Paper	*N*	**Method**	**Findings**
[104] 2022	53 C 28 aAD 50 pAD 9 AD	Baseline 30s intervals	No difference in oxy-Hb concentrations between C, aAD, pAD and AD
[95] 2022	21 AD 18 C	Standard deviation of oxy-Hb 5min	lower sd in AD compared to C
[99] 2023	8 AD 14 C	Spectral entropy (SE) 5min	Controls higher SE in 0.6-5 Hz range compared to AD. AD higher SE in 0.008-0.1 Hz and 0.1-0.6 Hz ranges compared to C

1.5.2 Electroencephalogram (EEG)

1.5.2.1 Technical aspects

Similarly to fNIRS, EEG is also a non-invasive, relatively cheap measurement technique, but rather than oxygenation it measures brain electrical activity. Electrodes placed on the scalp are usually used for the measurement, but it is possible to use intracranial electrodes too (which would make the recording invasive). Brain electrical activity can refer to Na^+ and Ca^{2+} action potentials, synaptic potentials, oscillatory membrane fluctuations, neuron-glial interactions via gap junctions and glial membrane potentials [105]. However, EEG can only measure electrical fields on the scalp, meaning that for example, action potentials will not contribute to the EEG signal [105]. In fact, the electrical field that can be measured on the scalp is mostly generated by postsynaptic potentials in pyramidal neurons in

the cortex [106]. This is due to the fact that pyramidal neurons are perpendicular to the surface of the cortex [106]. Additionally, EEG does not measure the electrical activity of one neuron, but rather the synchronized activity of neuronal populations.

The soma (main body) of the neuron has synaptic connections. These synapses can be excitatory or inhibitory, leading to excitatory postsynaptic potential (EPSP) (membrane potential increases) or inhibitory postsynaptic potentials (IPSP) (membrane potential decreases). These postsynaptic membrane potentials last longer than the action potentials, which is why they are thought to contribute to the EEG signal [107]. When an EPSP occurs, positive ions enter the cell, meaning the extracellular environment will be relatively negatively charged. At another portion of the cell, current flows out of the cell to complete the closed circuit, resulting in a relatively positively charged extracellular space. The opposite charges occur with an IPSP (figure 1.5). The result is that the pyramidal neuron will appear as a dipole, with a potential field around it. When enough pyramidal cells are synchronized their potential fields will combine to a potential field strong enough to be measured by an EEG electrode on the scalp [106].

Due to the dipoles, extracellular currents will propagate through the brain as a wave, as positive charge repels positive charge and negative charge repels negative charge. This volume conduction is complex because the brain is not homogeneous [108]. When the wave reaches the electrode the electrons in the electrode will be pushed or pulled by the charge. Due to the complex volume conduction, it is hard to pinpoint exactly what location is responsible for the EEG signal, which contributes to a relatively low spatial resolution [108].

Specifically, EEG measures voltage fluctuations. Hence, at least two electrodes are needed as voltage is the difference in electric potential between two points. This means that artifacts affecting all electrodes will be suppressed. There are different methods to define how this difference should be found, and the shape of the EEG signal will vary depending on the choice of method. In the sequential montage, the difference between two adjacent electrodes is used, in the referential montage a

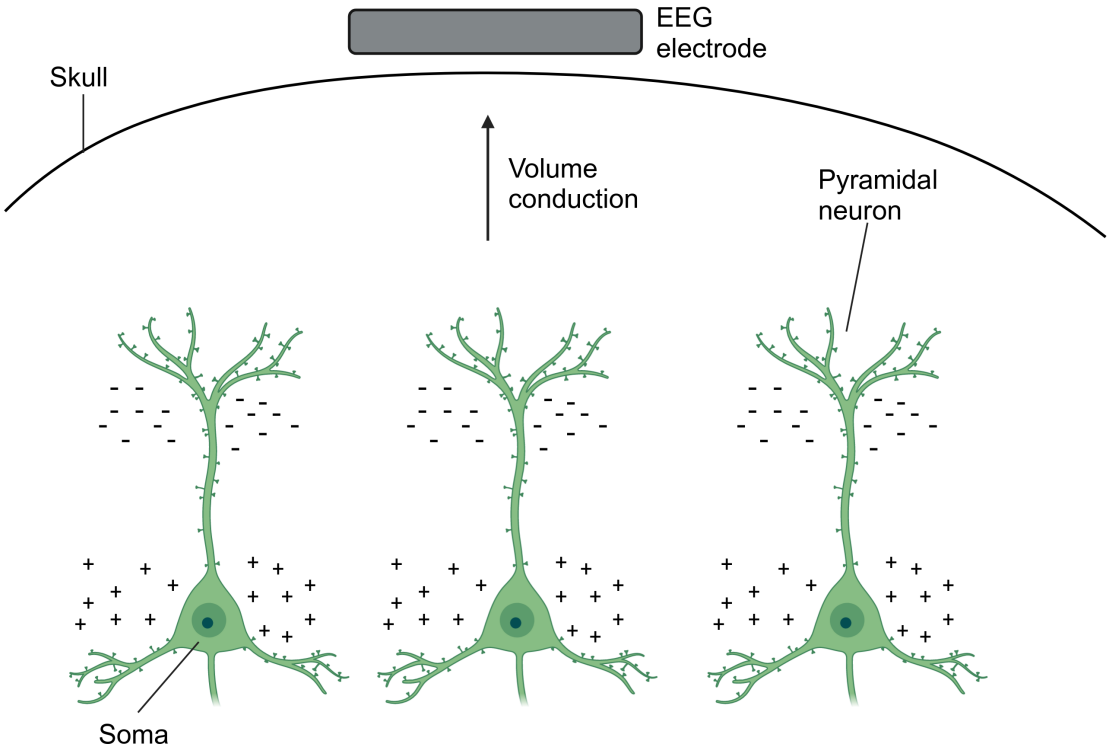

Figure 1.5: Pyramidal neurons where the extracellular space around the soma is positively charged, and around the top of the neuron it is negatively charged. This means that the pyramidal neurons are dipoles. The current wave travels through the brain tissue via volume conduction and can be measured via a scalp electrode. The postsynaptic potentials of pyramidal cells are the strongest contributor to the EEG signal, as pyramidal cells are perpendicular to the cortex surface. Created with BioRender.com.

reference electrode is used and, in the average reference montage, an average signal is used as a common reference [109].

The placement of EEG electrodes is standardised to the international 10-20 system (figure 1.6) [110], so researchers can more easily compare findings. The electrode placement names start with one or two letters, describing which brain region they are placed above: Fp for frontal-polar, F for frontal, C for central sulcus, P for parietal, T for temporal and O for occipital. Electrodes placed on the midline also have a z, such as the electrode Pz [110].

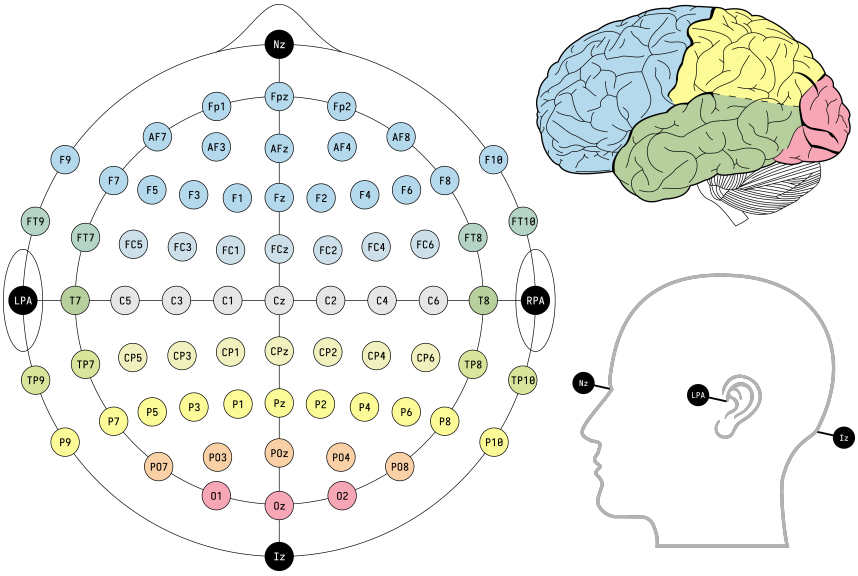

Figure 1.6: The EEG 10 20 international system [111].

1.5.2.2 Strengths and weaknesses

Another method to measure brain electrical activity is MEG. Compared to MEG, EEG is cheaper (around 60000 US dollars compared to a few million US dollars for MEG [85]) and portable, imposes fewer physical constraints on the participants and can therefore be experienced as less stressful. In addition, EEG has excellent temporal resolution and can, like in the work presented in this thesis, be measured at for example 1000 Hz. A weakness of EEG is the poor spatial resolution due to volume conduction, and that it does not only measure electrical signals from the brain. This means that electrical signals generated by muscle and eye movements, and heart activity can also be picked up by the EEG electrodes.

1.5.2.3 Application in research

Hans Berger is considered the inventor of human EEG [85] and since the 1920s EEG research has become very popular. EEG is used in the diagnosis of epilepsy [110] and has been widely used in research on neurodegenerative diseases such as Alzheimer's disease [112] and Huntington's disease [113]. It has also been applied to schizophrenia research [114], ageing research [115] and research on depression [116].

1.5.3 Concurrent fNIRS-EEG studies

As EEG and fNIRS can offer complementary information, combining the methods can yield more information than using only one of the techniques. By August 2021 around 100 studies combining fNIRS and EEG had been published. Most of these studies (∼80) aimed to analyse both fNIRS and EEG in parallel, rather than using one method to inform the analysis of the other [117].

Several studies have employed fNIRS and EEG to quantify neurovascular coupling (NC). For example, in healthy adults at rest, Keles et al. 2016 [118] calculated the delayed cross-correlation between the EEG power time-series and the oxy- and deoxy-hemoglobin time-series. In a study on newborns, Govindan et al. [119] calculated the standard deviation of EEG time-series and the average value of the difference between oxy- and deoxy-hemoglobin time-series in 1 s epochs. The spectral coherence of these new time-series was taken as a measure of NC. Also in a study on newborns, Chalak et al. [120] used fNIRS to measure cerebral tissue oxygen saturation and found the wavelet coherence between this and EEG as a measure of NC. fNIRS and EEG have also been employed to study anaesthesia [121]. Nair et al. calculated NC as the cross-correlation between time-series consisting of the standard deviation of windowed fNIRS and EEG time-series.

NC has also been assessed for patients with Alzheimer's disease. Researching working memory, Perpetuini et al. 2020 [122] calculated conditional entropy between EEG and fNIRS time-series, which was evaluated as indicative of NC. Depending on the task, the entropy was found to be both higher and lower in the AD group. In the resting state, Chiarelli et al. 2021 [96] calculated global NC with a general linear model framework by regressing whole-head EEG power envelopes in three frequency bands (theta, alpha and beta) with average fNIRS oxy- and deoxy-hemoglobin concentration changes in the frontal and prefrontal cortices. They found significantly lower NC in AD patients. Babiloni et al. [123] induced hypercapnia (build-up of CO_2 in the blood) in older participants with and without MCI, by having participants breathe in a relatively high CO_2 concentration. They calculated

NC as the correlation between the change in oxy- or deoxy-hemoglobin before and after CO_2 inhalation, with total EEG coherence during CO_2 inhalation. The MCI and older participants had similar changes in oxy- or deoxy-hemoglobin before and after CO_2 inhalation, which was taken as a measure of vasomotor reactivity.

From the aforementioned studies, and additional ones summarised by Li et al. [117], it is clear that there is not one agreed-upon method to calculate NC using fNIRS and EEG. However, many studies find a relationship between time-series derived from the two methods. Additional research on the physiological underpinnings of the fNIRS-EEG relationships could further improve our understanding of NC.

Aside from NC, Cicalese et al. [124] aimed to classify healthy controls, MCI and, mild and moderate AD patient groups. They found that using both fNIRS and EEG features achieved higher classification accuracy compared to when using only features from one of the methods. Li et al. [125] also combined fNIRS and EEG when researching AD, and used the fNIRS findings as constraints for the EEG source localisation.

1.5.4 Electrocardiogram (ECG)

An electrocardiogram (ECG) measures the electrical activity of the heart over time. As the heart contracts when electrically stimulated, measuring the electrical activity allows one to gather important information across the cardiac cycle. Specifically, electrodes placed on the body measure the voltage, which is the potential difference between two points. The voltage will vary according to the electrical activity of all the cardiac cells. Naturally, where you place the electrodes will impact the measured voltage [126]. A standard clinical ECG is measured using 10 electrodes, while the ECG obtained for the research presented in this thesis used 3 electrodes.

A standard ECG has a characteristic shape (see figure 1.7), with a P wave, QRS complex and a T-wave. The R peak is the most prominent feature of the ECG and is present in each cardiac cycle, meaning it can be used to track the heart rate. The P wave results from atrial depolarization, the QRS complex results from ventricular

depolarization and the T wave results from ventricular repolarization [126]. Various heart problems will cause the ECG trace to have a different appearance. In a research setting, it is common to use the R peak to track the heart rate in time, and then to quantify heart rate variability.

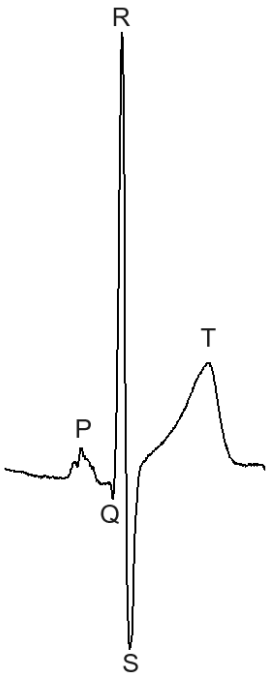

Figure 1.7: Example ECG trace from a healthy participant.

1.5.5 Respiration

Respiration can be measured by a respiratory belt, which measures changes in the circumference of the chest. When inhaling the chest expands, and when exhaling the chest contracts. The belt contains an element that can sense the change in circumference, usually by sensing stretch. A transducer converts the stretch into voltage, which will vary linearly with the stretch. The result is a characteristic inverted U shape per cycle, as seen in figure 1.8, where the peak corresponds to the end of inhalation.

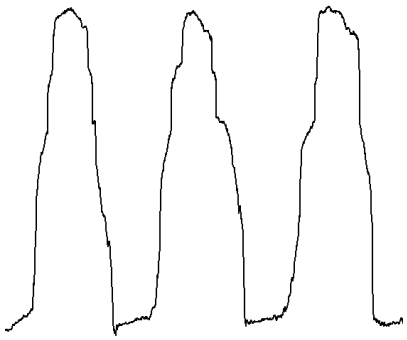

Figure 1.8: Example respiration trace from a healthy participant, showing three cycles of respiration.

1.5.6 Summary

This section introduced the measurement techniques used to obtain data analysed in chapters 3, 4, and 5. The key takeaway is that fNIRS and EEG can be effectively combined to study neurovascular interactions. The techniques are relatively inexpensive, portable, and non-invasive. Additionally, an ECG and a respiration belt can be used simultaneously to measure cardiorespiratory function, enhancing the breadth of physiological data collected.

1.6 Physics of living systems

While the history of biophysics has roots in animal physiology, the field was mostly concerned with the nanoscale and structure (e.g. DNA, proteins) in the twentieth century ([127]). However, understanding the structure of life is not sufficient to understand the function, as "the whole is greater than the sum of its parts" (Aristotle).

Living systems can be described at micro to macro scales, and across multiple time scales: from brain activity on the order of miliseconds to the circadian rhythm ($\sim$ 24 hours) which arises as a consequence of Earth's rotation. From the level of single cells to the level of an entire organism. Understanding how the different

scales work and impact eachother, and understanding the link between structure and function are important questions for the field.

Better understanding living systems and how they behave in time can be attained within the framework of dynamical systems theory, which is discussed in subsection 1.6.2.

1.6.1 Systems far from equilibrium

When physics meets biology it is important to carefully consider how to best apply methods from physics to living systems. Physicists learn to classify systems into thermodynamically isolated, closed and open systems. Isolated systems are completely separated from the environment, in that they cannot exchange matter or energy with the surroundings. Closed systems can exchange energy with the environment, such as dissipation of heat. Lastly, open systems can exchange both energy and matter with the environment. It is clear from these definitions that living systems are open systems. They exchange matter and energy with the environment, an exchange that is vital for life. Plants need light from the sun for photosynthesis, humans need food to survive. Interactions between living systems and the environment result in varied and complex dynamics that are characteristics for life on earth. Potentially due to the great complexity of biological systems, biophysics, or the physics of living systems, is now a large field spanning many research interests.

The concept of equilibrium is also often discussed in physics, and often a physicist assumes a system is in equilibrium to simplify a problem. To achieve thermodynamic equilibrium a system must have no macroscopic change in matter or energy, or change in macroscopic properties such as temperature and pressure. A system in equilibrium can not do work, which is essential for living organisms. A steady-state system has an equal flow of energy or matter in and out of the system, which also does not (in most cases) describe a living system. Rather than assuming unchanging macroscopic variables, out-of-equilibrium approaches can track variables and how

they change in time. These changes can come from interactions between the system and the environment. This topic will be further explored in section 1.7.

1.6.2 Dynamical systems theory

Dynamical systems are systems that evolve with time. The study of such systems was initiated by Isaac Newton, when he studied planetary motion [128]. With differential equations he was able to calculate the position of Earth around the sun. However, adding a third object to the calculation proved very difficult, and is known as the three-body problem. Obtaining the exact motion for the three objects was simply not doable. However, moving from a quantitative to a qualitative approach, Poincaré has left a lasting impact on the field of dynamics. Instead of worrying about the exact position of a planet, one might rather question if the orbit of the planet is stable. Such questions regarding stability and evolution of a system can in many cases be answered, and is considered a geometric approach [128]. Later, Winfree applied dynamical systems theory to biological systems, using nonlinear phase oscillators [129], a direction of thinking that was also pursued by Kuramoto [130]. In the next subsections we will explore dynamical systems and how they might be applied to study living systems.

Dynamical systems are often described using differential equations, for example in the form:

$$\begin{aligned} \frac{dx_1}{dt} &= f_1(x_1, ..., x_n, t) \\ &\vdots \\ \frac{dx_n}{dt} &= f_n(x_1, ..., x_n, t). \end{aligned} \tag{1.1}$$

The change of a variable x_i with time t is thus governed by a function f_i whose exact form will depend on the system one is dealing with. The variable x_i can for example be the position of a planet or the concentration of a molecule in a

chemical reaction. Note that the change in x_i with time can depend on x_i itself. As f is explicitly dependent on time the equation 1.1 describes a nonautonomous dynamical system [131]. In contrast, an autonomous dynamical system does not depend explicitly on time. Equation 1.1 also describes a deterministic dynamical system, as opposed to a random dynamical system who's state is associated with a probability. Hence, a deterministic dynamical system will always evolve to the same state from a set of initial conditions, while in a random dynamical system this is not the case. If we add randomness in the form of noise to the deterministic equation we have a stochastic dynamical system.

The dynamical system is considered linear if the form of f is such that all terms are to the first power only, e.g.:

$$\frac{dx_i}{dt} = Ax_i + B, \tag{1.2}$$

where A and B are constants. For nonlinear systems, the form of f can have nonlinear terms, such as products, powers and functions such as sine and cosine. Nonlinear systems are harder to deal with mathematically, as one cannot simply divide the problem into parts and assume the solution equals the sum of the parts. However, as living systems, and indeed many other systems, are nonlinear we must find methods that that can tackle this.

The geometric approach often employs a phase space to gauge the dynamics, also of nonlinear systems. A phase space consists of all possible states of a system. Starting from an initial condition x_0 and seeing how $f(x)$ evolves in time, a trajectory can be drawn in the phase space. If all qualitatively different trajectories are shown we have a phase portrait. Beginning with a very simple, autonomous system of the form [128]:

$$\frac{dx_i}{dt} = \sin(x), \tag{1.3}$$

figure 1.9A shows an example of the evolution of $x(t)$ from one initial condition.

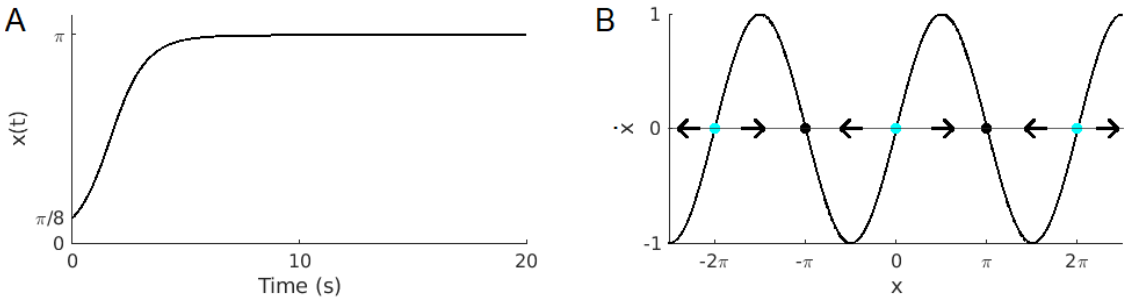

Figure 1.9: (A) Time evolution of $x(t)$, given by equation 1.3. Initial condition $x(0) = \sin(\pi/8)$, time step is 0.01 s, and the integration scheme is the forth order Runge-Kutta method. (B) Phase space for the dynamical system given by equation 1.3. Fixed points, corresponding to constant $x(t)$, are indicated by black circles (stable) or cyan circles (unstable). $\dot{x} = \frac{dx}{dt}$. The arrows indicate the velocity vector (towards a smaller value of $x(t)$ if $\dot{x} < 0$, and towards a greater value of $x(t)$ if $\dot{x} > 0$.)

Figure 1.9B shows the phase space for this system. From different initial conditions of x, one can reason about the evolution of the system by considering this plot, but first we must understand how to read such a plot.

Fixed points are indicated by circles. These are found when $\dot{x} = 0$, as these solutions corresponds to a constant $x(t)$. Fixed points are important when considering how a system will evolve, and they can be stable or unstable. A stable fixed point x^* (also called an attractor) is attracting, as solutions in the vicinity go towards it. Mathematically this can be written as $x(t) \to x^*$ as $t \to \infty$. An unstable fixed point is repellent, as solutions in the vicinity move away from the fixed point.

The arrows indicates the velocity of $x(t)$, in this case if the value of $x(t)$ is increasing or decreasing. Hence, when $\dot{x} < 0$ the arrows points to the left, and then $\dot{x} > 0$ the arrows points to the right.

Consider the initial condition $x = \sin(\pi/8)$. In figure 1.9B we can see that $x(t)$ will be increasing faster and faster, until $x = \pi/2$, where the acceleration $\frac{dx}{dt}$ starts slowing down ($x(t)$ is still increasing, but at a slower rate). When $x(t) = \pi$ the acceleration is zero, and the value of $x(t)$ will stay constant for the rest of time. This is indeed what is depicted in figure 1.9A.

This is an example of a first-order system, and the possible dynamics for such

systems are limited. Solutions go towards a fixed point or head towards infinity. Such solutions do not describe many biological processes sufficiently, and they cannot capture oscillations.

1.6.2.1 Limit cycles

Self-sustained oscillations are common in biological systems, such as the beating of the heart. An oscillation that is self-sustained is not dependent on external periodic forces for sustenance. Self-sustained oscillations can be described by limit cycles. In the phase space, a limit cycle is an isolated, closed trajectory meaning that solutions around the limit cycle either spiral towards or away from it (figure 1.10) [128]. If the surrounding trajectories spiral towards the limit cycle it is stable. Limit cycles describe autonomous self-sustained oscillatory systems, but do not capture nonautonomous oscillations [132]. Oscillations described by limit cycles are easily affected by external perturbations.

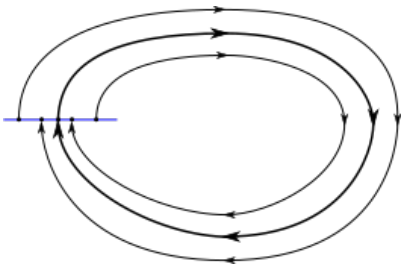

Figure 1.10: Stable limit cycle in phase space [133].

1.6.2.2 Chronotaxic systems

Many oscillators can have time-varying amplitudes and frequencies, that are resistant to perturbations. Again, take for example the human heart. It is well known that heart rate changes throughout time, even at rest. However, there is clearly stability in the heart rate, and the range of frequencies the heart can beat at is narrow. The traditional limit cycle does not describe such dynamics well, as only the amplitude dynamics is stable. The frequencies of oscillations can be easily perturbed.

Therefore, to describe such systems Suprunenko et al. [134] introduced chronotaxic systems, named as such because *chronos* means time and *taxis* means order in Greek. Mathematically, a chronotaxic system, and a nonautonomous systems, can be defined as:

$$\dot{\mathbf{p}} = f(\mathbf{p}) \qquad\qquad \dot{\mathbf{x}} = g(\mathbf{x}, \mathbf{p}), \tag{1.4}$$

where bold indicates that $\mathbf{p}$ and $\mathbf{x}$ are vectors. f and g are functions. This is called a drive and response system, where $\mathbf{p}$ is the driver and $\mathbf{x}$ is the responder [135]. $\mathbf{x}$ is nonautonomous as it depends on $\mathbf{p}$ which is changing in time.

The dynamics of a chronotaxic system is described by a point attractor $\mathbf{x}^A(t)$ which changes position along a nonautonomous limit cycle $\tilde{\Gamma}_0$, hence $\mathbf{x}^A(t) \in \tilde{\Gamma}_0$ [132]. Any initial point on the limit cycle is attracted to the point attractor, and it is not sufficient that the attraction is defined in the infinite time limit. Rather than defining attraction in the limit $t \to \infty$, a pullback attractor is defined in the limit $t \to -\infty$. Any trajectory starting at time t_0 is attracted to $\mathbf{x}^A(t)$ in this limit. Hence, the chronotaxic system satisfies:

$$\lim_{t \to -\infty} |\mathbf{x}(t, t_0, \mathbf{x}_0) - \mathbf{x}^A(t)| = 0. \tag{1.5}$$

In addition, it satisfies:

$$\mathbf{x}(t, t_0, \mathbf{x}_0^A) = \mathbf{x}^A(t). \tag{1.6}$$

Combined, this means that $\mathbf{x}(t)$ approaches the point attractor and then moves along with it. Chronotaxic systems are resistant to external perturbations which can be added to the equation 1.4 as, for example, noise. They are also not sensitive to initial conditions. Hence, chronotaxic systems are deterministic and non-chaotic [132]. It is clear that many biological processes, in addition to the heart rate, are stable and nonautonomous and that they therefore are good candidates for

chronotaxic systems.

1.6.3 Are oscillations beneficial for living systems?

Biological oscillations are abundant in nature [136]. One might ask if such fluctuations serve an intentional purpose, or if they are simply by-products of different mechanisms [137]. An example of such a by-product is the vibration in a bridge due to resonance, which is not a beneficial effect. However, the abundance and persistence of biological oscillators might hint at their importance [136]. For example, vasomotion, which is oscillatory as discussed in subsection 1.1.2, is hypothesised to ensure an efficient delivery of oxygen to the tissue [138]. In the following subsubsections we will explore various benefits of oscillations in living systems.

1.6.3.1 Environment

Living systems are subjected to cycles from the environment, such as the day-night cycle and yearly cycle. This means that living systems can anticipate regular changes in the environment, and adapt their own cycles accordingly. For example, humans tend to sleep during the night, as it is beneficial to be awake when it is light. In fact, the circadian cycle is present in most organisms on earth, so ingrained that there are specific clock genes responsible for maintaining the circadian rhytmn in mammals [139].

1.6.3.2 Time compartmentalization

Two processes might be conflicting, and therefore needing to be separated. One option is to separate them in time, so called time compartmentalization [139]. This allows two incompatible processes to coexist in the same space, and therefore avoids spatial compartmentalization. For example, expiration and inspiration have different purpose (dispose off CO_2 vs resupply oxygen), but the respiratory system is responsible for both. Temporal compartmentalization is also applicable for

metabolic processes [140], and is relevant in the context of the sleep-wake-cycle. The brain is thought to need sleep as a period to "clear out" by-products of the high metabolic activity during the day [140].

1.6.3.3 Regulation and information transfer

Physiological sensors can become de-sensitised when subjected to constant stimuli. Oscillations might therefore be necessary for self-calibration within an organism, with two such examples being heart rate variability and blood pressure [139]. Oscillations can also be preferable for information transfer in the presence of noise. For example, frequency modulation (FM) radio has better sound quality compared to amplitude modulation (AM) radio, as it is less susceptible to interference by noise. The brain appears to use oscillations to consolidate information [41].

1.6.3.4 Interactions

By having time-varying processes, rather than constant ones, processes can interact and synchronize. There are many examples of coupled processes in the human body, such as respiratory sinus arrhythmia; the heart rate varies in synchrony with respiration. During inspiration the heart rate tends to be quicker, and during expiration it tends to be slower. This is thought to save energy for the organism. Interactions might vary depending on states, like the strength of respiratory sinus arrhythmia depends on sleep states [141]. Interactions are also plentiful within brain networks [41, 142].

1.6.4 Homoestasis vs. homeodynamics

Having established that oscillations can be beneficial for living systems, one might assume that oscillations have different properties in health and disease. As an example, a disrupted circadian rhythm is often observed in Alzheimer's disease patients, and sleep disturbances are predictive of the development of the disease [143]. With this in mind, it might be needed to move from homoestasis as a measure

of health to homeodynamics [137]. Rather than assessing constant values, one might assess disease by asking questions about the strength and timings of oscillations, and if different oscillations are synchronized or coherent to the expected level. In chapters 3, 4 and 5 we investigate ageing, Alzheimer's disease and Huntington's disease through the lens of homeodynamics.

1.6.5 Summary

This section established that living systems are thermodynamically open systems and introduced dynamical systems theory as a valuable framework for studying their behavior. Chronotaxic systems were highlighted as effective models for describing time-varying yet stable oscillations, commonly observed in biological systems such as the cardiovascular system and brain. The inherent time variability of these oscillations must be accounted for when analysing data in subsequent chapters. The section concluded with a discussion on the potential benefits of oscillations, particularly their capacity for interactions. In the following chapters, we aim to quantify interactions using wavelet phase coherence.

1.7 Data-driven approach to studying dynamical systems

Dynamical systems can be investigated using modelling, or through measurements of real life dynamical systems. This latter approach means researchers learn directly from the data measured from the system under investigation. Such measurements can be in the form of a "time-series", i.e. measurements of a variable over time. From time-series many properties of a dynamical system can be determined. Here we will discuss methods for investigating the existence and strength of oscillations, as well as the coordination of oscillations. A time-series has a sampling frequency fs, describing the interval between each measurement. We will assume a constant

sampling frequency. A time-series also has a length L, which describes how long the recordings were conducted for. The sampling frequency and length of the time-series limit what oscillations we can observe. Therefore, both the length of recording and the sampling frequency should be determined based on knowledge of the dynamical system under observation.

1.7.1 Presence and strength of oscillations

Time-series from real systems contain the dynamics of the system and measurement noise. The dynamics might consist of several oscillations, with time-varying properties. Hence, when looking at a time-series it can be hard to see the oscillations with the naked eye. Therefore, quantitative measures of oscillations are needed. In this section we will introduce the autocorrelation function, Fourier transform, short-time Fourier transform and wavelet transform, and discuss their strengths and limitations.

1.7.1.1 Autocorrelation

The autocorrelation function is the correlation between a time-series and the same time-series shifted in time [144]. It can be plotted as a function of this time shift. If a time-series contains an oscillation of a certain frequency one would expect a peak in the autocorrelation spectrum at the time shift corresponding to N periods of the oscillation. The autocorrelation function is therefore well suited if a time-series has one dominant oscillation. However, if a time-series contain noise, numerous oscillations, or time-varying oscillations the interpretation of the autocorrelation spectrum is not straight forward. The autocorrelation is calculated as [145]:

$$C_\tau = 1/T \int_0^T f(t)f(t+\tau)dt, \tag{1.7}$$

where τ is the time shift. In figure 1.11B the auto-correlation for a time-series is plotted. There are peaks at 1s, 2s and 4s, so it is not clear that there are two modes.

In addition, there is no information on the time-variability of these modes.

1.7.1.2 Fourier transform

The Fourier transform can be used to investigate the frequency content of a time-series, via the power spectrum. The transform is named after Joseph Fourier, who laid the foundation on which the transform was developed [146]. The raw time-series is presented in the time domain, while the Fourier transform converts it to the frequency domain. For a function $f(t)$ the Fourier transform is given by [147]:

$$A_k = 1/T \int_0^T f(t) e^{-\frac{2\pi i k t}{T}} dt, \tag{1.8}$$

where k is an integer, and the amplitude at each k equals

$$\text{Amplitude}_k = |A_k| \,. \tag{1.9}$$

You can convert from k to frequency like $f_k = k/T$.

The Fourier transform is not limited by the number of oscillations, but they must have sufficiently different frequencies to be separated in the power spectrum. However, the Fourier transform loses all time localisation, and is therefore not suitable for time-series containing time-varying or transient oscillations (i.e. it is only suitable for stationary time-series). In figure 1.11C the Fourier transform for a time-series is plotted. There are peaks around 0.5 Hz and 1 Hz as expected. However, there are several spectral lines around 1 Hz and it would be difficult to tell if this is due to several modes without also having time resolution.

1.7.1.3 Short-time Fourier transform

We can achieve time resolution by performing the Fourier transform on sections of the time-series. This is known as a short-time Fourier transform (STFT) or a windowed Fourier transform. The STFT can be thought of as a Fourier transform of the signal multiplied by the window function. The window function can for example

be rectangular or Gaussian. A STFT with a Gaussian window is also known as the Gabor transform, after Dennis Gabor who first introduced the STFT [148]. However, this windowing greatly impacts the time-frequency resolution. For quick oscillations a shorter window will provide better time resolution. However, this comes as a cost for the slower oscillations, as at least one full oscillation is needed within a window to reason about this oscillation. Hence, if a time-series contain multiscale oscillations (i.e. several oscillations at various frequencies) it is hard to choose an optimal window size. The STFT is calculated as:

$$\tilde{f}(k,t) = \int_0^T g(u-t)f(u)e^{-\frac{2\pi iku}{L}}du, \tag{1.10}$$

where L is the length of the window, and $g(u-t)$ is the window function, which is centred at time t. Similarly to the Fourier transform, the amplitude can be found by taking the absolute value of the transform, and power can be found by squaring the amplitude. In figure 1.11D the short-time Fourier transform for a time-series is plotted. Here we can clearly see two modes around 0.5 Hz and 1 Hz. There is high amplitude from 0.005 Hz to 0.5 Hz, as the resolution is poor for such low frequencies.

1.7.1.4 Wavelet transform

The wavelet transform (WT) has an adaptable window size, depending on the frequency of the oscillation under investigation. In contrast to the sinusoidal waves used in the Fourier transform, wavelets decay quickly and therefore provide time-localisation. In the process of computing the wavelet transform, a wavelet is stretched (to investigate slower oscillations) and squeezed (to investigate quicker oscillations) and slid across the time-series (to investigate different times) [149]. Hence, for slower oscillations a long window is used which results in a good frequency resolution, and for quick oscillations a small window is used resulting in good temporal resolution. The wavelet transform is therefore a good choice for time-series with multiscale oscillations with time-varying properties. The WT is given by:

$$W_T(s,t) = \int_0^T \Phi(s, u-t) f(u) du, \tag{1.11}$$

where Φ is the wavelet function, for example the Morlet wavelet (named after Jean Morlet, who was one of the inventors of the wavelet transform [150]):

$$\Phi(s,u) = \frac{1}{\sqrt[4]{\pi}} (e^{\frac{2\pi i \omega_0 u}{s}} - e^{-\frac{2\pi\omega_0}{2}}) e^{\frac{u^2}{2s^2}}, \tag{1.12}$$

where s is the scale of the wavelet, which is related to frequency like $f_s = \omega_0/s$. Again, amplitude and power can be found from the absolute values. In figure 1.11E the wavelet transform for a time-series is plotted. Both oscillatory modes are clearly resolved, and we can see that they have time-varying frequencies. Due to the logarithmic frequency resolution the lower frequencies do not appear noisy, as in the short-time Fourier transform. However, there is still a limit to the time-frequency resolution, known as the Gabor uncertainty principle. This is further discussed in chapter 2.

The WT has been shown to capture the dynamics of chronotaxic systems [134]. Further, the WT fits within the framework of time-dependent finite-time-dynamics [151]. Rowland-Adams et al. [151] illustrated that this framework is needed to resolve the deterministic dynamics of nonautonomous systems, which can be misinterpreted as noise when using methods such as the autocorrelation function or the Fourier transform. As such, we will apply the wavelet transform when analysing time-series in the future chapters. Due to the amount of data the time-averaged power will be used to compare the different groups. It is calculated as the mean of the power over the length of the time-series, for each frequency. The length was 25 minutes in chapters 3 and 4, and 20 minutes in chapter 5. In chapter 2 time-averaged phase coherence is discussed in detail. In chapters 3, 4 and 5 the coherence is calculated over the whole duration of the signal, shown in the equation of section 2.5 in chapter 3.

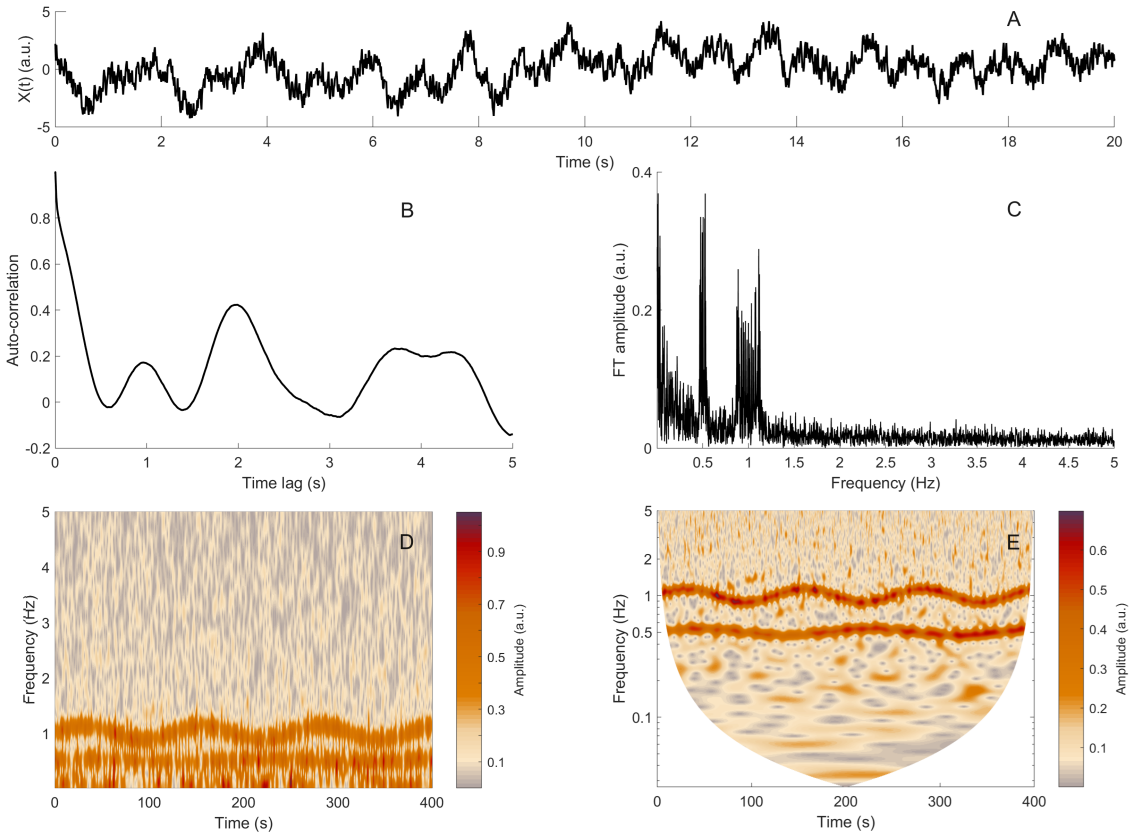

Figure 1.11: (A) Time-series of Poincaré oscillators, defined in chapter 2, with noise. The time-series have two oscillatory modes with time-varying frequencies. The plot shows 20s of the 400s time-series. (B) The auto-correlation of the time-series in (A). Peaks can be seen at time lags 1s, 2s and 4s. (C) The Fourier transform amplitude of the time-series. Peaks can be seen around 0.5 Hz and 1 Hz. (D) Short-time Fourier transform. Two modes can be seen around 0.5 Hz and 1 Hz, in addition to higher amplitude between 0 and 0.5 Hz. (D) The wavelet transform of the time-series in (A). Two modes around 0.5 Hz and 1 Hz can easily be seen.

1.7.2 Phase of oscillations

An oscillation can be characterised by its amplitude and phase. When the phase is estimated it can be used to calculate the phase coherence, phase locking index and other measures based on phase, and so this is an important step for further investigations. There are different ways to estimate the phase of an oscillation when starting from a time-series. If a time-series has only one oscillatory mode, marked events can be used. An example is marking R-peaks (the event) in the ECG time-

series. If assuming that the phase grows uniformly from 0 to 2π in the time between two R-peaks, linear interpolation can be used. This method effectively reduces the sampling frequency to the frequency of event occurrence, and it does not contain any information on the dynamics in-between events. Kluger et al. [152] obtained respiratory phase by identifying peaks and troughs. Linear interpolation was used from troughs to peaks ($-\pi$ to 0), and from peaks to troughs (0 to π). Still, this method has similar limitations as when only considering one marked event per cycle.

Another method is to use the Hilbert Transform (HT) [153]. It can estimate the instantaneous phase of a time-series if the time-series has one narrow-band mode with slowly varying amplitude and frequency [154]. While you can perform the HT on any time-series, the results can only be expected to be sensible if the above is true. If the time-series contain multiple modes then it is possible to first filter or decompose the time-series, for example using a Butterworth filter [155]. It is important that the filtering does not distort the phases of the modes.

Another option is to estimate the phase from the WT, using ridge extraction [156]. From the wavelet coefficients, which are complex numbers on the form $X_{s,t} = a_{s,t} + ib_{s,t}$, the phase can be estimated as

$$\varphi_{s,t} = \arctan(\frac{b_{s,t}}{a_{s,t}}).$$

In this case the phase can be estimated for time-series with multiscale dynamics. Nonlinear mode decomposition can also be used to extract instantaneous phases of physically meaningful oscillations [157].

1.7.3 Interactions

In neuroscience, the terms functional and effective connectivity is used to describe dependencies or interactions between brain regions, while structural connectivity refers to the anatomical connections (nerve fibers, synapses) between brain regions [158, 159]. Functional connectivity refers to the statistical dependencies of brain

activity from different locations. Effective connectivity refers to the influence one neural system has on another, so-called causal model interactions.

Functional connectivity can be quantified using different measures of coordination between time-series of brain activity. For example, the Pearson correlation coefficient can capture a linear relationship between two variables [160]. Several information theoretical approaches such as mutual information are based on entropy and aim to measure shared information [161]. However, if focusing specifically on oscillations, there are several ways oscillations can be coordinated: the phase difference between oscillations of the same frequency can stay constant (phase coherence), cross-frequency coherence with a mutual adjustment of phases, cross-frequency coherence where the amplitude of one oscillation depends on the phase of another, or the amplitude of one oscillation can depend on the amplitude of another oscillation. These are all functional connectivity measures, meaning that the wavelet phase coherence applied in the subsequent chapters is a functional connectivity measure. Chapter 2 explores how coherence as a concept emerged in physics and how it is used today.

Examples of effective connectivity are dynamical inference methods used to infer parameters of models that describe interactions, for example coupling functions [44].

Granger causality evaluates if a time-series Y can help predict the evolution of another time-series X, and if this prediction is better than if using only past values of X [162]. Granger causality can be considered as a lagged functional connectivity measure [159], despite the focus on causality.

1.7.4 Summary

This section explored how properties of a dynamical system can be inferred from data measured directly from the system. It discussed methods for quantifying the amplitude of oscillations and argued that the wavelet transform is particularly well-suited for capturing time-varying oscillations. Details on the application of this method in the subsequent chapters were provided. Beyond amplitude, oscillations

are also characterised by their phase, and the section explained how to extract phase information from a time-series. Additionally, the concepts of functional, effective, and structural connectivity were introduced, along with methods for calculating functional and effective connectivity. Notably, wavelet phase coherence, a functional connectivity measure, is used in the analyses presented in the subsequent chapters.

1.8 Summary and thesis outline

This chapter has provided an introduction to the cardiovascular system and the brain, with particular focus on the oscillatory processes associated with these systems. Further, the cooperation between these two systems was highlighted and the neurovascular unit was presented. This strong link is why including both systems in the methodology is so important, as done in this work. The effects of age, Alzheimer's disease and Huntington's disease on the neurovascular unit were discussed, to motivate the study of the neurovascular unit with both age and these diseases. To do so *in vivo* in human participants, non-invasive measurements of brain electrical activity, brain oxygenation, heart rate and respiration can be utilised. The measurement techniques used to do this, which provides the data on which the work in this thesis is based, were presented: the electroencephalogram, function near-infrared spectroscopy, electrocardiogram and the respiration belt. These methods are relatively inexpensive and also portable, making them suitable for repeated measurements and therefore valuable in a clinical setting.

This chapter also provided a brief introduction to the physics of living systems and dynamical systems theory. Here we highlighted properties of living systems that are essential to consider when analysing data from living systems, such as time-variability. The potential benefits of oscillations in living systems was addressed. Then, based on these considerations we discussed data-driven approaches for the study of dynamical systems, focusing on identifying oscillations in time-series. The wavelet transform was highlighted as a suitable method when analysing multiscale,

time-varying dynamics, due to the resolution in both time and frequency in addition to logarithmic frequency resolution.

The next chapter will build on the content of this latter part of the introduction. Focusing on coordination between oscillations, which can give an indication of interactions, chapter 2 will introduce coherence as a concept, and discuss both amplitude-weighted phase coherence and phase coherence. The chapter highlights the need for time-localisation when analysing non-stationary time-series, such as time-series from living systems. Practical considerations of applying coherence to real data where noise is present are also covered.

The remaining chapters, chapters 3, 4 and 5, apply the knowledge from chapter 2 to real data from participants of different ages, and participants with Alzheimer's disease and Huntington's disease. First, in chapter 3, the effect of ageing on the neurovascular unit, the cardiovascular system and the brain are explored. Then, in chapter 4, these parameters are assessed in people with Alzheimer's disease. Lastly, in chapter 5, they are considered in Huntington's disease. Both Alzheimer's disease and Huntington's disease are neurodegenerative diseases, but with different underlying causes. The last chapter of the thesis will summarise the findings and discuss future directions of this work.

Chapter 2

Phase coherence – A time-localised approach to studying interactions

This research is published in Chaos: An Interdisciplinary Journal of Nonlinear Science.

Barnes, S. J. K., Bjerkan, J., Clemson, P. T., Newman, J. & Stefanovska, A. Phase coherence—A time–localized approach to studying interactions. *Chaos* **34,** 073155 (2024)

Chaos ARTICLE pubs.aip.org/aip/cha

Phase coherence—A time-localized approach to studying interactions

Cite as: Chaos **34**, 0731 55 (2024); doi: 1 0.1 063/5.0202865
Submitted: 7 February 2024 · Accepted: 1 3 June 2024 ·
Published Online: 25 July 2024

View Online Export Citation CrossMark

S. J. K. Barnes,[1] J. Bjerkan,[1] P. T. Clemson,[1] J. Newman,[2] and A. Stefanovska[1,a)]

AFFILIATIONS

[1] Physics Department, Lancaster University, Lancaster LA1 4YB, United Kingdom
[2] Department of Mathematics and Statistics, University of Exeter, Exeter, United Kingdom

Note: This paper is part of the Focus Issue: Data-Driven Models and Analysis of Complex Systems.
[a)] **Author to whom correspondence should be addressed:** aneta@lancaster.ac.uk

ABSTRACT

Coherence measures the similarity of progression of phases between oscillations or waves. When applied to multi-scale, nonstationary dynamics with time-varying amplitudes and frequencies, high values of coherence provide a useful indication of interactions, which might otherwise go unnoticed. However, the choice of analyzing coherence based on phases and amplitudes (amplitude-weighted phase coherence) vs only phases (phase coherence) has long been seen as arbitrary. Here, we review the concept of coherence and focus on time-localized methods of analysis, considering both phase coherence and amplitude-weighted phase coherence. We discuss the importance of using time-localized analysis and illustrate the methods and their practicalities on both numerically modeled and real time-series. The results show that phase coherence is more robust than amplitude-weighted phase coherence to both noise perturbations and movement artifacts. The results also have wider implications for the analysis of real data and the interpretation of physical systems.

Coherence is a universal principle of interactions between oscillations and waves. We explain how coherence has been introduced in physics and review procedures to measure coherence numerically. We expand the current knowledge by establishing the universal importance of measuring coherence not only as a static property but as a property evaluated locally in time. We also compare coherence defined to involve amplitude (the peak-to-peak height) vs purely the phase (the position in the cycle) by applying these different approaches to numerically modeled data. We argue that phase coherence is more robust and less susceptible to noise, particularly in cases where measurements are influenced by movement relative to the sensors. We provide an in-depth guide to the application of methods to measure coherence in data and demonstrate these points using real-world examples, including the interaction between the heart and lungs, noisy measurements of the brain, and the movement of electrons on the surface of liquid helium.

I. INTRODUCTION

Oscillations and waves are ubiquitous in nature. They occur in mechanical and dynamical systems in virtually all areas of science: many physiological processes are oscillatory, such as the beating of the heart, breathing, or neuronal oscillations in the brain; the ecology abounds with seasonal cycles; most dynamical phenomena in astrophysics and space science are oscillatory, as are geological and hydrodynamics phenomena, such as ocean waves or earthquakes; there are business cycles in economy; strings in musical instruments produce vibrations, as do many man-made devices. Most electronic devices, the Internet, TV signals, communication systems, and medical imaging, use electromagnetic waves. The study of oscillations and waves is, therefore, essential for understanding the universe, as stated by Tesla in the quote: "If you want to find the hidden secrets of the universe, you must think in terms of energy, frequency, and vibration."

While the underlying dynamical system may be very different in distinct cases, oscillatory processes share two key time-dependent features: *amplitude* (associated with the energy of the oscillation) and *phase* (associated with the time evolution of the oscillation). To identify interactions between different parts of a system, we can calculate the similarity of these features using the physical property known as *coherence*.

In this paper, we provide a review of coherence, beginning in its conceptualization in physics and subsequently evaluating

relevant numerical methods used to measure coherence. In particular, we improve current understanding by both establishing the fundamental importance of taking a time-localized approach to coherence and comparing a method based on amplitude and phase to one only using phase information.

In Sec. II, we provide an overview of the development of coherence in physics and its adoption in time-series analysis. We also provide a definition of coherence based on the Fourier transform and explain the differences between coherence and the related concept of synchronization.

In Sec. III, we provide a model for a dynamical system, which is used to numerically illustrate the differences between the phase-only and amplitude-weighted methods of measuring coherence when the system is perturbed by different forms of noise.

In Sec. IV, we introduce wavelet-based coherence and explain the consequences of moving to the time–frequency domain that arise from the uncertainty principle. In this section, we also specify the alternate definitions of coherence in amplitude and phase and, based on results found using the illustrative model, argue that phase coherence is more resistant to the effects of noise and particularly movement artifacts.

In Sec. V, we provide an in-depth guide to the application of coherence in time-series analysis, including how to identify significant coherence.

In Sec. VI, we apply this knowledge and evaluate the two methods considered by considering four real-world problems, including the cardio-respiratory interaction, noisy electroencephalography (EEG) and functional near infrared spectroscopy (fNIRS) data, and electron dynamics on the surface of liquid helium.

We conclude in Sec. VII with a discussion of the time-localized approach to coherence and the impact of using methods based on only phase to those that rely also on amplitude information.

II. BACKGROUND

A. Physics of coherence

The theory of waves was initially developed by Young, Huygens, and Fresnel.[1] Along with providing explanations for phenomena, such as diffraction and refraction, they also studied wave interference. In this latter case, multiple waves combine to produce a characteristic pattern of spatially and time-localized maxima and minima. However, this effect is only seen clearly when the change in the phase of the waves is the same. It is this property of the waves that we term coherence.

The study of interference and wave coherence has already led to many well-known discoveries. These include the Michelson–Morley experiment, which disproved the existence of the luminiferous ether.[2] Variations of Young's double-slit experiment have also played an important role in the understanding of wave–particle duality.[3–5] In addition, the drive to develop a coherent source of light led to the invention of the laser.[6] Subsequent to the development of lasers, larger-scale interference experiments have been possible, which resulted in the discovery of gravitational waves.[7] Coherence is now studied across a broad spectrum of domains. This includes solid state and quantum physics,[8–11] remote sensing,[12] electrophysiology,[13–15] communications,[16] and space science.[17]

B. Coherence in time-series analysis

With the advent of computers, the study of coherence is no longer restricted to physical experiments. Numerical methods allow for the analysis of oscillations in recorded data. Using this recorded data, coherence can be investigated.[18] Coherence between different parts of a dynamical system can result from either synchronization or from modulation by a common process. While one can separately analyze two variables and qualitatively assess the common features present in each, interactions are often nonlinear in nature and, hence, difficult to discern. Coherence, therefore, provides a useful quantitative measure to identify these interactions.

An important aspect of coherence is that it is a time-localized phenomenon. This makes it particularly useful for analyzing dynamics comprised of oscillations with time-dependent quantitative characteristics. Such dynamics has been modeled using chaotic, stochastic, and non-autonomous systems.[19,20] Time-series analysis methods that give a non-time-dependent representation of a time-series, such as its histogram or Fourier transform, may yield some insight into the amplitudes of oscillations present. However, these methods will generally provide little understanding of phase dynamics if the quantitative characteristics of the oscillations, or of their interactions with each other, are being modulated over time. In contrast to this, the time evolution of phases carries a great wealth of information about the underlying system when such time modulation exists.[21]

Time-evolving time-localized analysis is typically performed in the time–frequency domain. This type of analysis was originally developed in quantum mechanics, with the distribution proposed by Wigner providing the highest possible frequency resolution that is mathematically possible within the limitations of the uncertainty principle.[22] Ville later applied this function in the context of time–frequency analysis more generally.[23] At the same time, the windowed Fourier transform was also developed,[24] and the field has since been advanced with the introduction of the continuous wavelet transform.[25,26] Time–frequency analysis has been applied most commonly to deal with simple forms of nonstationary data, with applications in communications, radar, sonar, and acoustics.[27] Recently, it has also been invaluable in the analysis problems, such as turbulence,[28] brain signals,[29] blood flow,[30] and excited electron oscillations on liquid helium.[31] These systems involve multiple potentially mutually interacting oscillatory processes that take place simultaneously across a range of timescales; we refer to such systems as *multi-scale* systems.

One specific advantage of the time–frequency methods is that they, to various degrees, allow for the time-localized extraction of instantaneous phases over time (see, e.g., Ref. 32). These phases can be studied further to give insight into the system. This can be seen in phase synchronization methods, which have been applied to the cardiorespiratory system.[33] Phase differences can also be observed and point to delays in coupled networks of oscillators, such as those seen in biology.[34] Beyond this, we can estimate coupling functions and infer the directionality of coupling (see Ref. 35 and the references therein). In the case of weakly coupled oscillator networks, connectivity can be inferred directly from the phases.[36] There are also phase stability methods, which have been used to find stable oscillations in the heart rate variability.[37]

In the case of coherence represented in the time–frequency domain, the initial development of the methods was motivated by applications to biomedical data. Specifically, it has been of great importance to the mapping of functional connectivity and study of synchronization in the brain.[38–45] At the same time, the development of time–frequency coherence has spearheaded investigations into microvasculature dynamics.[46–51] It has since been used in other biomedical studies and found use as a marker for ageing of the cardiorespiratory system,[52] as well as revealing the relation between the width of the subarachnoid space and blood pressure.[53] Moreover, the generality of time–frequency coherence means that it has found applicability elsewhere. In particular, these methods have also been used extensively in the analysis of solar, geophysical, and meteorological time-series to determine the Earth–Sun dynamical relationship.[54–57] Coherence has also found use in the analysis of economic time-series, where it has been used to identify instability and risk in specific markets as well as the relation between the monetary policy and the macroeconomic activity.[58–62] It has also been applied in the case of cyclo-nonstationarity, where it has been used to analyze mechanical systems, such as engines and wind turbines.[63] Further examples include the evaluation of electron dynamics,[31] behavioral rhythms in mice,[64] and social networks.[65]

C. Definition of coherence

The original formulation of coherence was within the field of optics, where it is used to quantify the degree to which two sources of light can interfere. It was developed from a similar measure of the intensity of the interference pattern, or *visibility*,

$$v = \frac{I_{\max} - I_{\min}}{I_{\max} + I_{\min}}, \tag{1}$$

where $I_{\max}$ is the intensity of the light at the peaks and $I_{\min}$ is the intensity at the troughs. The value of v is 1 when the interference is maximized and 0 is the case of no interference (i.e., the intensity curve of the light is smooth). While this definition is useful from an empirical standpoint, it is more difficult to use for the mathematical analysis of waves of arbitrary phase and amplitude. Coherence was, therefore, developed as a similar measure of the degree of interference, but using the phase and amplitude of the interfering waves as parameters.[66]

It is worth noting that while interference was originally investigated in optics, the phenomenon prevails throughout all types of waves. As such, coherence can also be defined for any type of wave. A general analytic framework for the study of waves is provided by the Fourier transform. In this context, we can find a measure of the similarity between the waves in two data series by computing the Fourier cross spectrum,

$$S_{ab}(f) = F_a(f) \times \overline{F_b(f)}, \tag{2}$$

where F_a and F_b are the corresponding Fourier transforms of the two series and $\overline{\ }$ denotes the complex conjugate. However, this similarity measure is still proportional to the amplitude of the Fourier components. This means that if a dominant oscillation appears in one data series but only background fluctuations are present in the other, then the cross spectrum will still have a peak at the frequency of that oscillation as long as there is *some* amplitude at that frequency in the other data series. With this in mind, it is clear that we need to normalize the cross spectrum so that it is not biased by this effect. The way this is achieved is by defining *Fourier coherence* as

$$C(f) = \frac{\left|\langle S_{ab}(f)\rangle\right|}{\left[\langle S_{aa}(f)\rangle \times \langle S_{bb}(f)\rangle\right]^{1/2}}, \tag{3}$$

where the angle brackets $\langle\ \rangle$ denote taking an average value of the Fourier spectra $S_{ab}(f)$, $S_{aa}(f)$, $S_{bb}(f)$ computed for different time-segments of the time-series.[66] This defines coherence on a scale between 0 and 1, making it directly comparable with the interference visibility shown in (1).

D. Coherence and synchronization

It is worth noting that coherence should not be confused with synchronization. In terms of dimensionality, synchronization is defined specifically in the time dimension and, therefore, applies to the dynamics of oscillations in time. In contrast, coherence refers to a more general phenomenon, which extends to waves that are defined across space as well as time.

There are also important differences in the context of time-series generated by dynamical systems. While many types of synchronization exist, they all result from an interaction between two or more oscillations.[33,67] As such, synchronization refers to a process of adjustment of rhythms caused by interactions. In contrast, coherence implies that two oscillations are observed to have the same frequency and frequency modulation, but this does not necessarily imply that they are coupled.

As examples, consider two linear oscillators with the same frequencies or two autonomous nonlinear oscillators with the same parameters and initial conditions. In both of these cases, the oscillations produced by the two systems will be coherent. However, since the state of one oscillator does not depend on the state of the other, they are not coupled.

Despite this difference, there is still a strong connection between coherence and specific types of synchronization. The states of complete 1:1 synchronization or 1:1 phase synchronization are more or less the same as coherence as the strength of the interaction reduces to a small value when two oscillators are completely synchronized. One can also consider indirect synchronization, such as two non-autonomous oscillators becoming synchronized via the same time-dependent modulation. In each of these cases, the effect can be measured directly using coherence.[39]

III. ILLUSTRATIVE MODEL

A. Poincaré oscillators

In order to illustrate the factors affecting the measurement of coherence, we consider a pair of time-series, which contain common oscillations generated by non-autonomous systems with independent perturbations. To ensure that we are not biased toward perturbations in amplitude or phase, we consider a system with a separable amplitude and phase dynamics.

The Poincaré oscillator is a two-dimensional limit cycle oscillator, which can be defined in polar coordinates as

$$\frac{dr}{dt} = -\alpha r(r-a), \quad \frac{d\theta}{dt} = \omega, \tag{4}$$

where r is the amplitude and θ is the phase of the oscillator. A stable limit cycle is defined in state space with radius $r = a$, with α parameterizing the rate at which the trajectory converges to this amplitude. The phase is neutrally stable and changes with a rate defined by the frequency ω. A time-series $x(t)$ of the oscillation can be generated by transforming from polar coordinates by using $x(t) = r(t)\cos(\theta(t))$.

The important feature of this system is that r and θ vary independently. This means that the amplitude of the oscillator can be perturbed without affecting the phase and vice versa. However, comparing the effect of amplitude and phase perturbations this way using the current system would not be a fair comparison since r has a stable point attractor while θ does not. This leads to the perturbations to r being suppressed over time, while perturbations to θ are integrated over time.[37]

To resolve this issue, we modify the Poincaré oscillator so that the form of stability is the same in both amplitude and phase. Unfortunately, we cannot simply copy the function used for $\frac{dr}{dt}$ to $\frac{d\theta}{dt}$ since θ will converge to a. For persistent oscillations, θ needs to change on average monotonically, which is provided by the parameter ω in the current form. However, we cannot use $\frac{d\theta}{dt} = \omega - \alpha\theta(\theta - a)$ either as θ is unbounded and $\lim_{t\to\infty}[\omega - \alpha\theta(\theta - a)] = -\alpha\theta^2$, which results in an unstable trajectory. Instead, we use the following modification:

$$\begin{aligned} \frac{dr}{dt} &= -\alpha(r-a)^3 + \xi_r\eta_r, \\ \frac{d\theta}{dt} &= \omega - \alpha(\theta-\phi)^3 + \xi_\theta\eta_\theta, \\ \frac{d\phi}{dt} &= \omega, \end{aligned} \tag{5}$$

where ϕ is an auxiliary dimension, which is left unperturbed and provides a stable point in phase moving at the same rate ω. The cubic function was chosen because it gives similar scaling of the strength of attraction to the stable point relative to the distance, but is symmetric around the stable point. The terms $\xi_i\eta_i$ are white Gaussian noise with a standard deviation specified by ξ_i.

To generate each time-series, the amplitudes $\{r_1, r_2\}$ and phases $\{\theta_1, \theta_2\}$ of two modified Poincaré oscillators were numerically modeled and summed together in a time-series $X(t) = r_1(t)\cos(\theta_1(t)) + r_2(t)\cos(\theta_2(t))$. However, even with perturbations, this time-series would appear as two noisy sinusoids with approximately stationary dynamics. To simulate more realistic nonstationary time-series, the system was made non-autonomous by modulating the oscillator frequencies with $\omega(t) = 2\pi\omega_0 + A\sin(2\pi\omega_m t)$. To investigate the effect of phase differences, the phase offset of the oscillations was also adjusted by changing the initial value of ϕ.

In the numerically modeled examples used in Sec. IV, we considered a high-frequency mode with $\omega_0 = 1$, $\omega_m = 0.008$, $A = 0.8$ and a low-frequency mode with $\omega_0 = 0.5$, $\omega_m = 0.0055$, $A = 0.2$. For the other oscillator parameters, we used $a = 1$ and $\alpha = 5$ in each case.

B. Noise

Noise plays a significant role in the evaluation of coherence. Consider two time-series with a single, identical sinusoidal oscillation with frequency $f_{\sin}$. By analyzing Eq. (3), we can see that $S_{ab}(f_{\sin}) \equiv S_{aa}(f_{\sin})$ and $S_{aa}(f_{\sin}) \equiv S_{bb}(f_{\sin})$, which results in the expected value $C(f_{\sin}) = 1$. However, since the time-series contain no other oscillations, this relation holds true not just for $f_{\sin}$ but for *all* values of f. This means that we might mistakenly believe that coherent oscillations exist at all frequencies.

Similar behavior is apparent whenever dominant oscillations are present in both time-series. Without independent fluctuations at adjacent frequencies, significant coherence will be observed at values far from the frequencies of the corresponding oscillations.

In most real data, this is not an issue as they are usually influenced by both system noise and measurement noise. We must, therefore, take care to approximate real-world examples in our analysis by including noise in the numerical model.

To investigate the effect of both amplitude and phase perturbations, two cases were considered. In the first case, each of the modes was perturbed only by amplitude noise with $\xi_r = 0.5$, $\xi_\theta = 0$, while in the second case, they were perturbed only by phase noise with $\xi_r = 0$, $\xi_\theta = 0.5$. We also considered a case with additive noise to simulate measurement noise and common artifacts in the time-series. These were generated by adding the same dichotomous noise, with random abrupt transitions between two states, to both time-series. This was defined using the time-dependent transition probabilities,

$$\begin{aligned} p_{0\to d}(t) &= \frac{\lambda_1}{\Lambda} - \frac{\lambda_1}{\Lambda}e^{-\Lambda t}, \\ p_{d\to 0}(t) &= \frac{\lambda_2}{\Lambda} - \frac{\lambda_2}{\Lambda}e^{-\Lambda t}, \end{aligned} \tag{6}$$

where t is the time since the last transition from one state to another and $\Lambda = \lambda_1 + \lambda_2$. The transition rates were chosen as $\lambda_1 = 0.000\,01$ Hz and $\lambda_2 = 0.000\,19$ Hz, causing a series of spike-like features with rare $0 \to d$ transitions followed by quicker $d \to 0$ transitions. The amplitude of the spikes was chosen as $d = 10$. In addition to these spikes, independent $1/f$ noise series were added to each time-series to simulate background fluctuations.

IV. WAVELET COHERENCE

A. Time–frequency analysis

For the analysis of coherence of phases of oscillations in time-series, the Fourier-based definition of coherence is perfectly valid when the time-series are stationary. However, for multi-scale, non-stationary time-series, the dynamics cannot be approximated by assuming a constant time-averaged phase and amplitude, as is assumed in the Fourier transform. As discussed in Rowland Adams *et al.*,[21] such time-series must not be analyzed from the infinite-time, non-time-evolving framework of analysis that is designed for stationary time-series—which is precisely the framework within which Fourier coherence exists—but rather, such time-series need to be analyzed from within the framework of time-evolving time-localized analysis of oscillatory characteristics.

Accordingly, it is natural to seek a way to compute coherence from time–frequency representations of the data. As already mentioned, we can compute a time–frequency representation using an ordinary Fourier transform with a moving window, which is also known as a short-time Fourier transform. However, as soon as we do this, we must ask what size of window? A large window gives us excellent frequency resolution, but then it is more difficult to determine the time at which oscillation frequencies change. Similarly, while a small window enables us to track the change in frequency more precisely, the frequency resolution is lower and makes it difficult to determine the exact frequencies of oscillations. These characteristics of the measurement of waves are well known in quantum mechanics and famously summarized in the Heisenberg uncertainty principle.

The main limiting factor in the choice of window size is the lowest-frequency oscillation that we wish to observe. It is necessary to choose a window that contains enough cycles of this oscillation to determine its frequency to reasonable precision. However, this window size is larger than the window needed to have the same frequency resolution for higher-frequency oscillations. For higher-frequency oscillations, this window size will represent a slower timescale than the timescale of these oscillations, making the analysis effectively equivalent to the kind of long-time-averaging associated with the classical non-time-evolving, long-time-asymptotic-statistics framework designed for stationary time-series described above.

Therefore, to achieve a time-localized analysis of multi-scale time-series, we would need to use an adaptive window size to increase the time resolution at high frequencies while maintaining an optimal frequency resolution overall.

The difference between this time-localized approach and the slow-timescale averaging that takes place in the fixed-window-size approach is illustrated in Fig. 1. Here, time–frequency analysis is performed on a time-series from the illustrative Poincaré oscillator model. In this case, the oscillators were not perturbed with phase noise, and only minimal amplitude noise, $\xi_r = 0.005$, was introduced. In addition, background fluctuations were numerically modeled by adding independent $1/f$ noise to each time-series. In Fig. 1(a), depicting the fixed-window approach, the idea is to characterize all aspects of the dynamics at a given time using the data in a given window. This means that all of the analysis for every frequency is performed within the same window (note that this window is shown as rectangular for illustrative purposes only—a Gaussian window was used in the short-time Fourier transform to enable a fairer comparison of the two approaches).

By contrast, as depicted in Fig. 1(b), the time-localized approach uses a variable-sized window depending on which frequency is being analyzed. For the former approach, where at each time a full-frequency-spectrum Fourier transform is performed inside a pre-specified window, the result is that the time–frequency analysis can be optimized around one frequency only. However, in the time-localized approach, the analysis is centered around each frequency under analysis, much like adjusting an optical focus. This means that the time–frequency plots for this latter approach provide much greater detail across time at high frequencies, as well as much greater detail across frequency at low frequencies. An alternative version, with a Fourier transform presented with a logarithmic scale, is provided in Fig. 1 of the supplementary material. When comparing the two figures, it is obvious that a logarithmic scale is disadvantageous for the Fourier transform, which is calculated with linear frequency resolution.

The time-localized, adaptive window approach is realized by the *continuous wavelet transform*[26] (which we shall sometimes just call the wavelet transform, abbreviated WT). This is defined by

$$W(s,t) = \frac{1}{s}\int_0^T \overline{\Psi\left(\frac{u-t}{s}\right)} x(u)\,du, \tag{7}$$

where $x(t)$ is a time-series of length T; the variable $s > 0$, called the "scale," controls the width of the windowing function, enabling it to be adapted to the frequency under investigation (as described shortly); and Ψ is a complex-valued function called the *mother wavelet*. Using the convolution theorem (or, equivalently, Fourier isometry), the wavelet transform can be computed in the Fourier domain by

$$W(s,t) = \frac{1}{2\pi}\int_{-\infty}^{\infty} \overline{\hat{\Psi}(sw)}\hat{x}(w)e^{iwt}\,dw,$$

where

$$\hat{\Psi}(\omega) = \int_{-\infty}^{\infty} \Psi(\tau)e^{-i\omega\tau}\,d\tau,$$

$$\hat{x}(w) = \int_0^T x(t)e^{-iwt}\,dt.$$

An example of a mother wavelet is the Morlet wavelet, which is approximately a complex exponential function multiplied by a Gaussian envelope, such that the resulting wavelet transform is approximately the adaptive-window-width version of the Gaussian-windowed Fourier transform. Specifically, the Morlet wavelet is given by

$$\Psi(\tau) = \frac{1}{\sqrt{2\pi}}\left(e^{2\pi i f_0\tau} - e^{-\frac{(2\pi f_0)^2}{2}}\right)e^{-\frac{\tau^2}{2}}, \tag{8}$$

where f_0 is a free parameter called the *frequency resolution*: it can be changed to adjust the resolution toward greater frequency precision (higher f_0) or time precision (lower f_0). The Fourier-domain representation of the Morlet wavelet Ψ is given by

$$\hat{\Psi}(\omega) = e^{-\frac{(\omega-2\pi f_0)^2}{2}}\left(1 - e^{-2\pi f_0\omega}\right).$$

Note that $\hat{\Psi}$ is a real-valued function; i.e., the Morlet wavelet Ψ is a Hermitian function.

In the wavelet transform, one can adapt the scale s to the frequency f under investigation in such a manner as to give logarithmic frequency resolution by taking s to be inversely proportional to f. Specifically, when working with the Morlet wavelet, we take

$$s = \frac{\omega_{\max}}{2\pi f},$$

where $\omega_{\max}$ is the value at which the real-valued function $\hat{\Psi}$ is maximized. Provided f_0 is not too small (larger than about 0.5), $\omega_{\max}$ is almost exactly equal to $2\pi f_0$, i.e., $s \approx \frac{f_0}{f}$.

It is worth noting an issue that arises from the fact that the integral in Eq. (7) is bounded between 0 and T. This means that when t is close to one end of $x(t)$, a significant part of the amplitude of the wavelet function extends beyond the bounds of the integral. This bounded integral is also equivalent to an unbounded integral where the ends of $x(t)$ are padded with infinite zeros. This problem is common among methods using a moving window and other strategies include using reflected data or predicted data equal to half the length of the window. However, each of these methods causes boundary effects that result in errors in the time–frequency representation.[68] The other alternative is to not include these regions in the plot. This results in a *cone of influence*, which is larger in size at lower frequencies due to the larger-sized wavelets reaching the ends sooner than smaller wavelets.

From the wavelet transform, one can extract an instantaneous amplitude and phase associated to each frequency f at each time t by expressing $W(s,t) = |W(s,t)|e^{i\theta(s,t)}$ and taking $|W(s,t)|$ as the amplitude and $\theta(s,t)$ as the phase.

B. Definition of wavelet coherence

With an optimal time–frequency representation of the time-series, we can proceed to define the coherence between them. Following from the original definition in Eq. (3), time–frequency

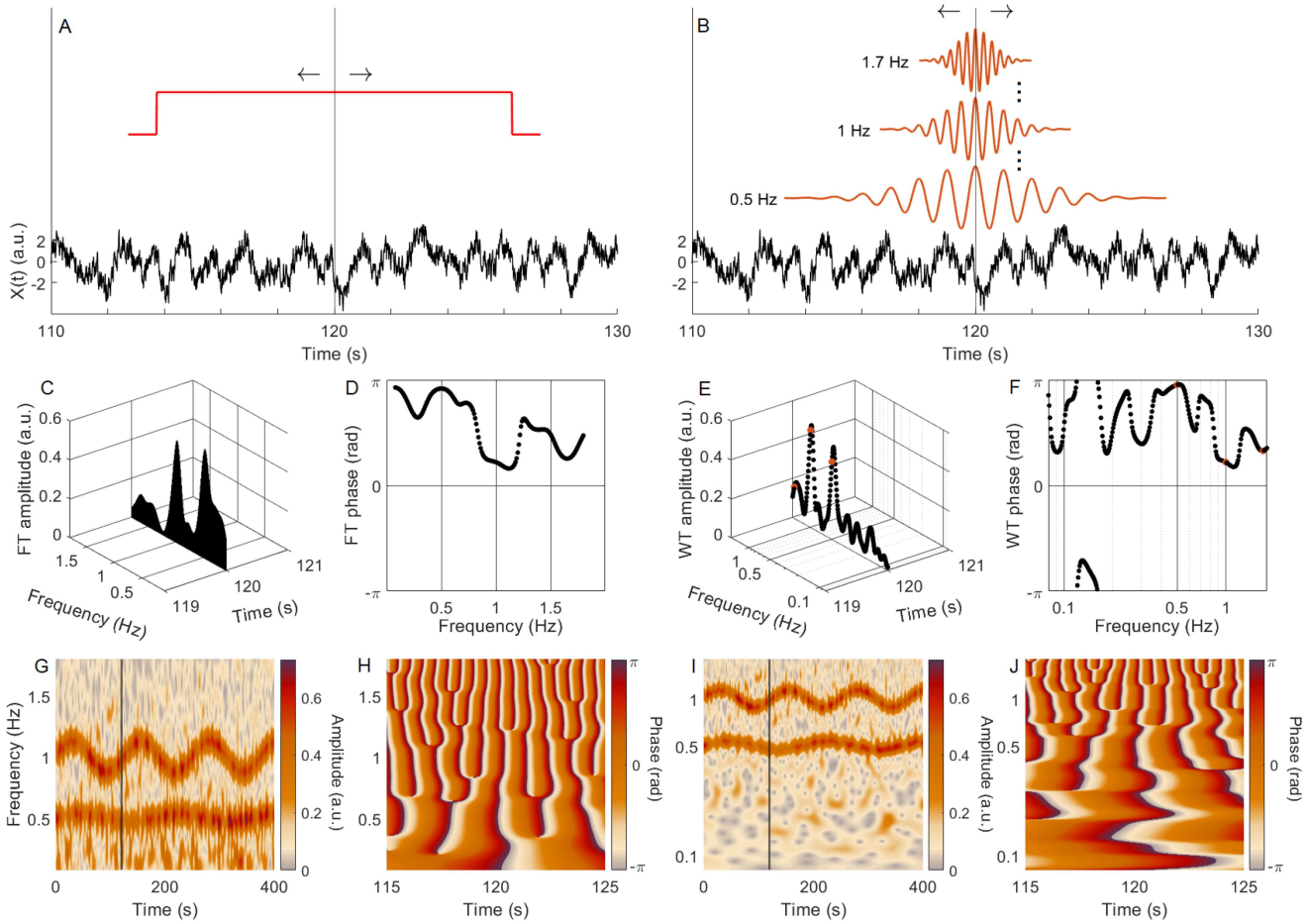

FIG. 1. Time–frequency analysis illustrated for time-localized vs fixed-window approaches. (a) Generated time-series of Poincaré oscillators as defined by Eq. (5), with additive $1/f$ noise and $\xi_r = 0.005$. A window of size 12.6s centered at 120s is drawn above the time-series. The arrows above the window illustrate that the window slides across the time-series when the short-time Fourier transform (STFT) is applied. (b) The same time-series as in (a), with three wavelets with frequency resolution $f_0 = 2$ at different frequencies (0.5, 1, and 1.7 Hz) drawn above the time-series. The wavelets slide across the time-series when the WT is applied. The dots between the wavelets illustrate that there is one wavelet for each frequency, in our case 288 wavelets. (c) The STFT amplitude found at 120s. (d) The STFT phase found at 120s projected onto the frequency-phase plane. (e) The WT amplitude found at 120s. The orange dots correspond to the frequencies of the three wavelets in (b). Note the logarithmic frequency resolution of the WT. (f) The WT phase found at 120s projected onto the frequency-phase plane. (g) The STFT amplitude for the whole 400s time-series. A line is drawn at 120s. (h) The STFT phase for 10s of the time-series. (i) The WT amplitude for the whole 400s time-series. (j) The WT phase for 10s of the time-series.

domain coherence between two time-series $x(t)$ and $y(t)$ was originally popularized by Torrence and Webster[69] and then again by Lachaux *et al.*[38] where it was defined as

$$C_W(f,t) = \frac{|SW_{ab}(f,t)|}{[SW_{aa}(f,t)\cdot SW_{bb}(f,t)]^{1/2}}, \tag{9}$$

where SW_{ab} are the wavelet cross spectra as defined by

$$SW_{ab}(f,t) = \int_{t-\frac{\delta}{2}}^{t+\frac{\delta}{2}} W_a(f,\tau)\cdot W_b^*(f,\tau)d\tau. \tag{10}$$

Here and in the rest of the text * denotes complex conjugate. δ defines the length of a moving window in the time domain over which the cross spectra are averaged. Like wavelets, δ is chosen to be adaptive in order to maintain an optimal resolution over frequency such that $\delta = n_{cy}/f$, where n_{cy} is the number of cycles at any given frequency. Values between 6 and 10 for n_{cy} were originally recommended in the context of data recorded by brain electrodes.[38] However, in other applications of time–frequency analysis, $n_{cy} = 5$ has been used.[70]

The application of a wavelet-based approach vs a Fourier-based approach has a significant effect on the information provided by coherence analysis. This can be seen by comparing the studies of Karavaev *et al.*[71] and Mizeva *et al.*,[72] both of which consider cardiovascular time-series recorded over similar timescales (15 and 20 min, respectively). In the former study, the macroscopic autonomic control is characterized by dividing the Fourier coherence into a "high-frequency" (0.15–0.4 Hz) and "low-frequency" (0.05–0.15 Hz) band. In the latter study, the wavelet coherence is divided into five separate frequency bands with ranges 0.6–2, 0.145–0.6, 0.052–0.145, 0.021–0.052, and 0.0095–0.021 Hz, which allows for the characterization of both the macroscopic and microscopic dynamics. The logarithmic scale provided by the wavelet coherence, therefore, acts much like a telescope or microscope, allowing us to zoom in and out of all frequencies of interest at every moment in time.

C. Phase coherence

If we use a complex wavelet, such as the Morlet wavelet defined in Eq. (8), then the cross spectrum in the numerator of Eq. (9) can be separated into phase and amplitude, with

$$SW_{ab}(f,t) = \int_{t-\frac{\delta}{2}}^{t+\frac{\delta}{2}} |W_a(f,\tau)|\cdot|W_b(f,\tau)|e^{i(\theta_a(f,\tau)-\theta_b(f,\tau))}d\tau. \tag{11}$$

Doing the same for the denominator terms, we find

$$\begin{aligned} SW_{aa}(f,t) &= \int_{t-\frac{\delta}{2}}^{t+\frac{\delta}{2}} |W_a(f,\tau)|\cdot|W_a(f,\tau)|e^{i(\theta_a(f,\tau)-\theta_a(f,\tau))}d\tau \\ &= \int_{t-\frac{\delta}{2}}^{t+\frac{\delta}{2}} |W_a(f,\tau)|^2 d\tau. \end{aligned} \tag{12}$$

Written this way, the coherence defined in Eq. (9) is expressed as a phasor of the phase difference, $e^{i(\theta_a(f,\tau)-\theta_b(f,\tau))}$, multiplied by the normalized amplitudes. We, therefore, term this definition as amplitude-weighted phase coherence (AWPC).

However, we can actually remove the influence of the wavelet amplitude altogether. We can define *phase coherence* (PC) as

$$C_\theta(f,t) = \frac{1}{\delta}\left|\int_{t-\frac{\delta}{2}}^{t+\frac{\delta}{2}} e^{i(\theta_a(f,\tau)-\theta_b(f,\tau))}d\tau\right|. \tag{13}$$

This definition of coherence was developed independently by Lachaux *et al.*[38] (where it was termed single-trial phase coherence) and Bandrivskyy *et al.*[46] While Eq. (13) defines PC for a pair of time-series, it has since been extended to groups of three or more time-series.[73,74]

Like Fourier coherence, both PC and AWPC take values between 0 and 1. Note, however, that for oscillations with time-dependent characteristics, strong coherence will not typically manifest as a coherence value of 1, but often as distinctly less than 1.

In the examples shown in this paper, PC was calculated using MODA—an interactive MATLAB toolbox.[75] We also encourage readers to consult the MODA user guide, which contains practical information for performing PC and other time–frequency analyses.[76]

The differences between PC and AWPC are shown in Figs. 2–4 using the previously defined illustrative Poincaré model. In each case, the two time-series, their corresponding WT, and the PC and AWPC plots are shown. The methods were applied using three different time–frequency resolutions by changing the central frequency f_0 of the Morlet wavelet. The effect of adjusting f_0 can be seen in the WT, where the frequency width of the bands corresponding to the oscillatory modes is decreased with increasing f_0. This effect is also seen for the coherence plots. Here, the darker bands of coherence reveal the common frequency modulation of the two modes, which becomes more localized in frequency as f_0 is increased.

An additional effect seen when increasing the frequency resolution is that the background coherence between the modes also increases. The reason for this effect is due to the fact that larger wavelets average over more cycles, leading to extracted wavelet components that are more stationary in frequency. These components, therefore, appear coherent, but only because the rate of change in frequency converges to the same value (i.e., 0) for all oscillations as f_0 is increased.

Figure 2 shows the effect of amplitude perturbations on the modes following the two coherence measures. The coherence bands associated with the modes are lighter and less well-defined in the case of AWPC, with the effect being greatest for the lowest frequency resolution. The explanation for this can be found in the independent fluctuations seen in the amplitude of the WT. As highlighted in Eq. (11), AWPC is dependent on the wavelet amplitude, which means that the amplitude perturbations result in lower coherence. In contrast, PC is not dependent on the wavelet amplitude and is, therefore, resistant to such perturbations.

As one might expect, the effect is similar for both approaches when the perturbations are instead applied to the phase of oscillations. Figure 3 illustrates the effect of phase perturbations, where PC and AWPC are affected similarly by the noise due to both methods being dependent on the phase of the wavelet components.

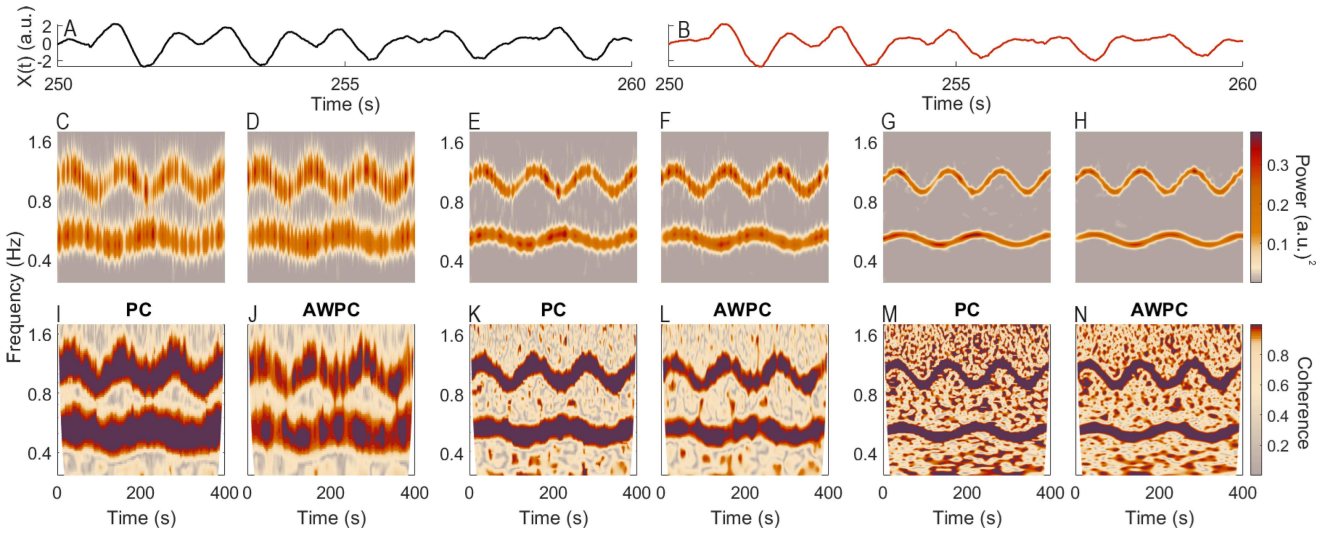

FIG. 2. Comparison between PC and AWPC applied using wavelets of different frequency resolution to modes generated by amplitude-perturbed Poincaré oscillators as defined by Eq. (5). (a) and (b) Ten-second segments of the two time-series containing modes with independent perturbations. The second row (c)–(h) presents the WT plots of the two time-series at different frequency resolutions: $f_0 = 1$ (c) and (d), $f_0 = 2$ (e) and (f), and $f_0 = 5$ (g) and (h). The time-series in (a) was the input for the transforms (c), (e), and (g), while (b) provided the input for (d), (f), and (h). The final row (i)–(n) indicates the time-localized coherence for the PC and AWPC methods using the transforms shown in (c)–(h). For example, (i) and (j) were both generated using the WT plots indicated by (c) and (d).

A significant difference between PC and AWPC can be seen in the additive noise case shown in Fig. 4. Here, the common dichotomous noise results in time-localized spikes in the time domain. These can be seen as large cones of amplitude permeating into the lower frequencies in the WT. In the coherence plots, this effect has the most significant impact on the low frequencies, as larger wavelets have a lower time resolution and span across a greater period. Furthermore, it can be seen that the case for $f_0 = 5$ is most

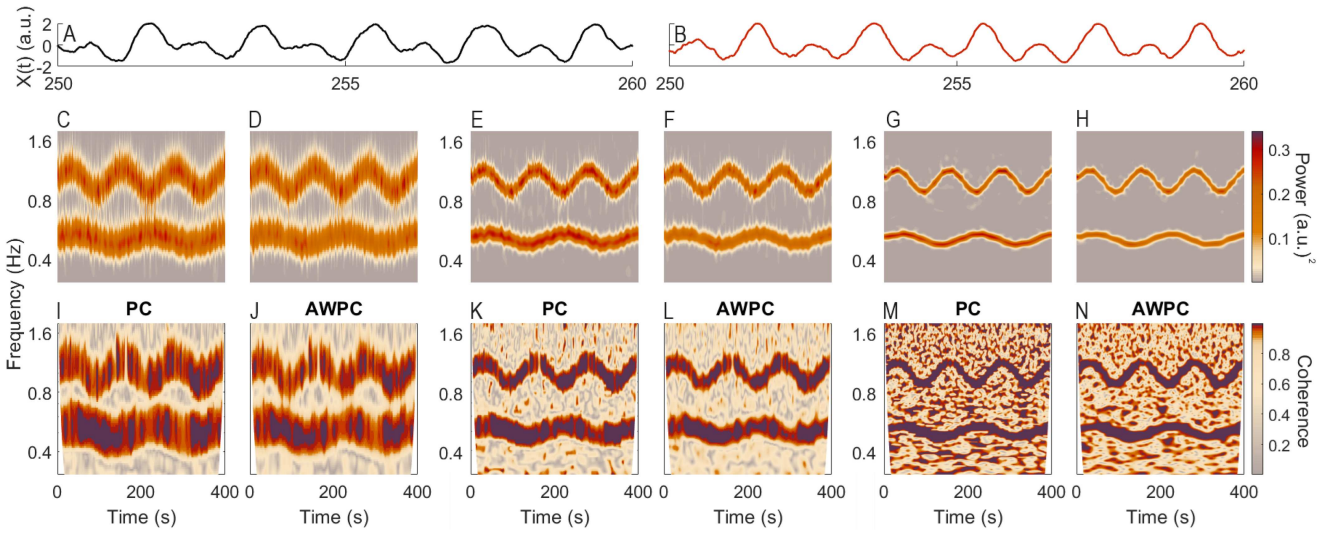

FIG. 3. Comparison between PC and AWPC applied using wavelets of different frequency resolution to modes generated by phase-perturbed Poincaré oscillators as defined by Eq. (5). (a) and (b) Ten-second segments of the two time-series containing modes with independent perturbations. The second row (c)–(h) presents the WT plots of the two time-series at different frequency resolutions: $f_0 = 1$ (c) and (d), $f_0 = 2$ (e) and (f) and $f_0 = 5$ (g) and (h). The time-series in A was the input for the transforms (c),(e) and (g), while (b) provided the input for (d),(f) and (h). The final row (i)–(n) indicates the time-localized coherence for the PC and AWPC approaches using the transforms shown in (c)–(h). For example, (i) and (j) were both generated using the WT plots indicated by (c) and (d).

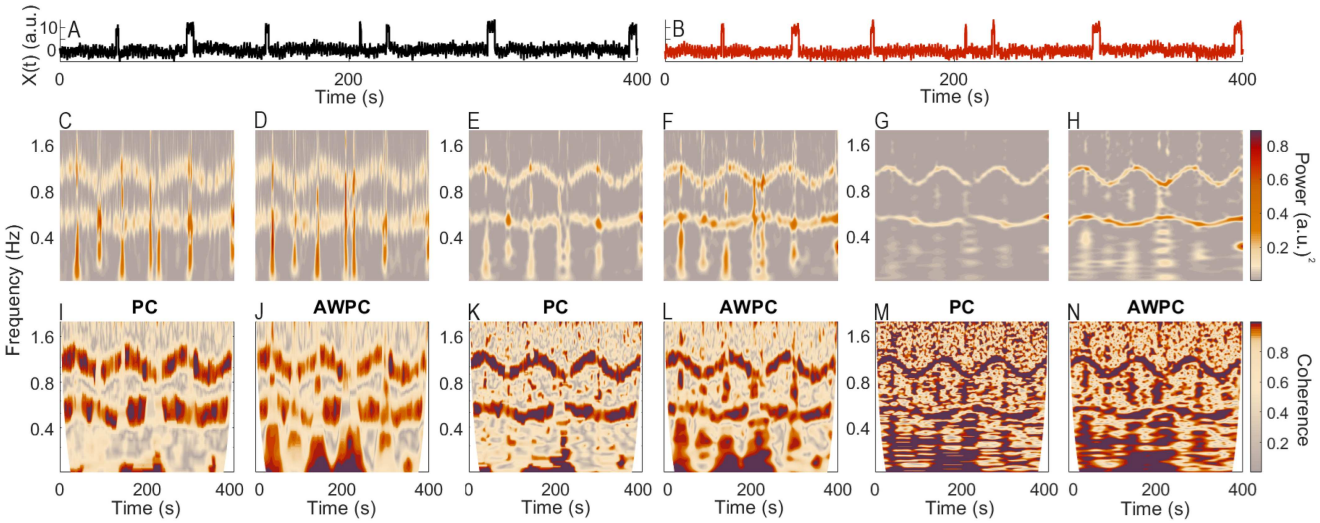

FIG. 4. Comparison between PC and AWPC applied using wavelets of different frequency resolution to modes generated by phase-perturbed Poincaré oscillators as defined by Eq. (5), with the same dichotomous noise and independent realizations of $1/f$ noise added to both time-series. (a) and (b) The independently generated time-series. The second row (c)–(h) presents the WT plots of the two time-series at different frequency resolutions: $f_0 = 1$ (c) and (d), $f_0 = 2$ (e) and (f), and $f_0 = 5$ (g) and (h). The time-series in (a) was the input for the transforms (c), (e), and (g), while (b) provided the input for (d), (f), and (h). The final row (i)–(n) indicates the time-localized coherence for the PC and AWPC approaches using the transforms shown in (c)–(h). For example, (i) and (j) were both generated using the WT plots indicated by (c) and (d).

affected by the amplitude perturbations due to the increased temporal width of the wavelets. Generally speaking, therefore, smaller values of f_0 should be used in cases where extremely time-localized noise features are present, such as movement artifacts in biomedical measurements.

Also worth noting in the additive noise example is that even though the added dichotomous and $1/f$ noise affect both the phase and amplitude of the wavelet components, the coherence bands of the modes are more strongly defined in the PC plots and the low-frequency coherence is reduced. This is caused by the time-localized properties of the dichotomous noise, which only affect a relatively small number of cycles at each wavelet scale. Since the window used to calculate the coherence averages the phase difference over a relatively large number of cycles, the effect on PC is reduced. In contrast, as shown in Eq. (11), the phase difference in AWPC is weighted by the amplitude. This means that even though the noise spikes last only a small number of cycles, the relative weight to the calculation of the coherence is increased due to the large associated amplitude.

D. Phase difference

Beyond coherence, it is often useful to extract the instantaneous wavelet phase difference $(\theta_a(f,t) - \theta_b(f,t))$ and analyze this directly. This has been done in many studies to investigate deterministic phase differences in oscillations from two time-series.[77–80] While phase is technically a time-independent measure, the direction and magnitude of the phase difference are still a valuable measure that can be used to determine time lags, which provide weight to statements of causality.

In the studies cited above, analysis of the phase difference involves extracting individual pairs of instantaneous phases and examining the change in the phase difference over time. However, in time-series containing many modes, it is often useful to analyze the phase differences in the frequency domain. Doing this reveals the phase relationships present across different timescales of the dynamics.

To define the time-averaged phase difference, we use

$$\psi(f) = \arg\left[\int_0^T e^{i(\theta_a(f,t)-\theta_b(f,t))}\,dt\right]. \tag{14}$$

To be able to take the integral in Eq. (14) over the whole duration $[0, T]$ of the signal, it would be necessary to add padding to the signal before time 0 and after time T before computing the WT. If, instead, one just computes the WT within the cone of influence, then the time-interval over which the integral in Eq. (14) is taken is the f-section of the cone of influence—that is, the set of times t over which $W(f, t)$ has been computed; this is a subinterval of $[0, T]$ that depends on f: as f decreases, this subinterval becomes narrower.

Note that while this definition of the time-averaged phase difference correctly identifies the phase differences of the coherent modes, it does not necessarily provide a meaningful value for areas of zero coherence. This is because the result will be the argument of the sum of random phasors. While the amplitude of this sum correctly gives a value of the time-averaged PC at the background level, the argument will be a random angle between 0 and 2π. It is, therefore, important to assess such a measure of the phase difference in conjunction with the actual coherence and only to evaluate its values where the coherence is significant.

In analogy to the difference between PC and AWPC, it is also possible to define an overall phase difference using not the *time*-averaged phase difference as in (14), but rather the *energy*-averaged phase difference,

$$\psi_E(f) = \arg\left[\int_0^T W_a(f,t)\cdot W_b^*(f,t)dt\right] = \arg\left[\int_0^T |W_a(f,t)|\cdot|W_b(f,t)|e^{i\left(\theta_a(f,t)-\theta_b(f,t)\right)}dt\right].$$

In this paper, we use the time-averaged phase difference.

E. Time-averaged coherence

We have defined PC and AWPC as functions of time and frequency since they represent information about the time-localized frequency content of the pair of signals. When we want an overall measure of the coherence at each frequency-value, taken over the whole duration of the signal, there are two approaches that one can take:

One is simply to take the time-average of the time-localized PC or AWPC as already defined in Secs. IV B and IV C.
The other is to compute PC or AWPC not over small time-windows $(t-\frac{\delta}{2}, t+\frac{\delta}{2})$ as in Eqs. (10)–(13), but rather over the whole duration of the signal.

Under the former approach, we have a time-averaged PC given by

$$C_\theta^{\text{average}}(f) = \frac{1}{T-\delta}\int_{\frac{\delta}{2}}^{T-\frac{\delta}{2}} C_\theta(f,t)\,dt \tag{15}$$

and a time-averaged AWPC given by

$$C_W^{\text{average}}(f) = \frac{1}{T-\delta}\int_{\frac{\delta}{2}}^{T-\frac{\delta}{2}} C_W(f,t)\,dt. \tag{16}$$

Let us recall here that δ itself depends on f, as described in Sec. IV B. Under the latter approach, we have an over-all-time PC given by

$$C_\theta^{\text{overall}}(f) = \frac{1}{T}\left|\int_0^T e^{i\left(\theta_a(f,\tau)-\theta_b(f,\tau)\right)}d\tau\right|$$

and an over-all-time AWPC given by

$$C_W^{\text{overall}}(f) = \frac{\left|SW_{ab}^{\text{total}}(f)\right|}{\left[SW_{aa}^{\text{total}}(f)\cdot SW_{bb}^{\text{total}}(f)\right]^{1/2}},$$

where SW_{ab}^{total} are the over-all-time wavelet cross spectra as defined by

$$SW_{ab}^{\text{total}}(f) = \int_0^T W_a(f,t)\cdot W_b^*(f,t)dt = \int_0^T |W_a(f,t)|\cdot|W_b(f,t)|e^{i\left(\theta_a(f,t)-\theta_b(f,t)\right)}dt.$$

In all four cases, we have given formulas according to the assumption that the WT is defined over the whole of $[0,T]$. Once again, this requires that padding has been added to the signal before time 0 and after time T; if, instead, the WT has been computed only over the cone of influence, then the integrals $\int_0^T$ or averages $\frac{1}{T}\int_0^T$ taken over the time-interval $[0,T]$ in the above formulas need to be taken instead over the f-section of the cone of influence.

In this paper, we work with the former of the two approaches, namely, Eqs. (15) and (16).

V. PRACTICAL ASPECTS

Coherence analysis is restricted by the properties of the measured data. Each dataset is likely to contain idiosyncrasies that require specific attention to avoid false representation of the results. By unlocking the temporal dimension with time-resolved analysis methods, one may properly view and assess the type of data under investigation, and once this step is completed, choose and perform the appropriate analysis. The multi-scale nature of the present analysis also enables simultaneous observation of the behavior across a number of frequencies, which in many cases are representative of various independent behaviors in the system. A review of the statistical properties of wavelet coherence is provided in Cohen and Walden.[81] However, here, we focus on the practical implementation and application of these methods.

To demonstrate the nuance required when selecting parameters for analysis, we consider two sets of time-series containing two common modes. As before, the modes are generated using the modified Poincaré system and have independent perturbations. The key difference is that the first set of time-series has modes with frequencies $\omega_0 = 1$ and $\omega_0 = 0.2$ that are stationary in time, with $\omega_m = 0$ (the leftmost set of Fig. 5). In contrast, in the second set of time-series, the frequency of the modes varies with $\omega_m = 0.016\pi$ for the high-frequency mode and $\omega_m = 0.010\pi$ for the low-frequency mode (the rightmost set of Fig. 5).

Importantly, when considering coherence between simultaneously measured time-series, one may use two sets of apparatus with varying sampling frequencies, f_s. For the calculation of coherence, a common f_s must be established. While it is theoretically possible to up-sample the data series with the smaller sampling frequency, this is not recommended as it will not recover information regarding higher-frequency oscillations. Instead, the solution is to downsample the larger time-series so that a common f_s is established.

The value of f_s determines the maximum observable frequency, $f_{\max}$, because we need at least two points in each cycle to capture an oscillation. Consequently, the upper-frequency limit, or the Nyquist frequency, is defined as $f_N = f_s/2$. A low value of $f_{\max}$ can introduce problems when assessing data, as seen in Fig. 5(j). In this case, the system was simulated with $f_s = 4$ Hz, which means that $f_{\max} = 2$ Hz is selected. The coherent mode seemingly passes above $f_{\max}$, illustrating the need for a higher f_s.

The lowest attainable frequency, $f_{\min}$, is determined by the length of the time-series. In the examples demonstrated in this work, AWPC and PC are evaluated across ten cycles of oscillation at a given frequency. It follows that the length of the time-series restricts $f_{\min}$ and that the length must be at least ten times the length of the minimum frequency of interest. If the interaction is time-varying, then more cycles are needed to account for the modulation present, dependent upon the frequency of the modulation. The time-varying

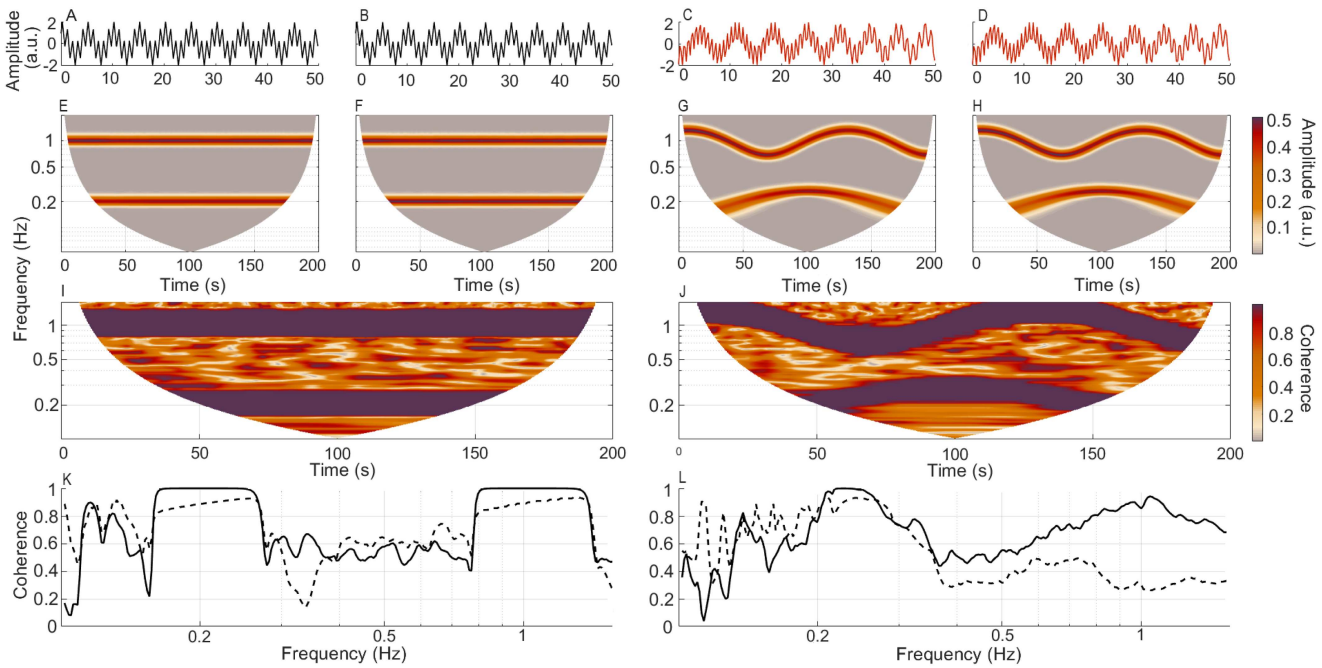

FIG. 5. Practical aspects to consider when applying phase coherence. Time-series generated from a pair of Poincaré oscillators, as defined by Eq. (5). The time-series were obtained numerically with f_s= 4 Hz and minimal amplitude modulation ($\xi_r = 0.005$, $\xi_\theta = 0$). The frequencies of these modes are unchanging in time for (a) and (b) and time-varying in (c) and (d). Their corresponding WT (e)–(h) demonstrate these differences. The time-localized phase coherence plots (i) and (j) are generated from the wavelet transforms (e)–(h). (k) and (l) Time-average values are shown as solid black lines and mismatch surrogate thresholds as dashed lines.

example shown in Figs. 5(c), 5(d), 5(g), 5(h), 5(j), and 5(l) demonstrates a situation where the simulated mode may be interpreted as being centered upon a greater frequency (0.25 Hz) than it really is. Specifically, the mode should be centered upon 0.2 Hz. Due to the shortness of the recording, the cone of influence contains only the upper half of the modulation cycle, resulting in an apparently higher value. In the non-time-varying frequency case, there is no issue, and the peak coherence is centered around 0.2 Hz.

The presence of oscillatory dynamics can be confirmed by first considering the time–frequency representation of the data. In addition, this step will provide information on the frequency range of interest if this is not known beforehand. Limiting the coherence analysis to this range will reduce the burden on computational capacity and save time. The WT will guide the choice of the resolution parameter. However, one must consider that this is always a trade-off, as discussed in Sec. IV C and seen in Figs. 2–4.

A. Testing for significance

The considerations outlined above will help to reduce false conclusions regarding the data. However, to further reduce the chance of falsely representing spurious coherence as significant, a further step must be performed.

Even with the existence of independent fluctuations in both time-series, the interpretation of coherence is not straightforward, as illustrated by Holm.[82] This is because even two completely independent noise time-series will contain fluctuations that appear at the same time and frequency, resulting in a non-zero value of coherence.

We must, therefore, determine whether observed coherence is *significant*. This is necessary both for being able to make physical inferences from the observation of coherence values and for being able to make physical inferences from phase-shift values $\psi(f)$ associated with high coherence. Consideration of significance of coherence values can be divided into two aspects: First, the coherence values themselves need to be statistically significant in terms of exceeding some critical threshold, i.e., some baseline coherence value. Second, when one computes the time-averaged phase difference $\psi(f)$ as a function of f, where there is significant coherence, one should observe a plateau—i.e., an approximately constant phase difference—over the frequency range in which the phase-coherent oscillations manifest in the time–frequency representation. One should only regard coherence as significant if it is found to satisfy both of these aspects of testing for significance.

In regard to the first aspect, defining the baseline coherence value for significance is not trivial, as it is dependent on the nature of the background dynamics generated by the system under investigation. For example, in the system described above, the independent fluctuations generated from perturbations to the phase and amplitude will result in a different level of background coherence to the case of independent $1/f$ additive noise. Furthermore, in real systems, the deterministic dynamics cannot be separated from the

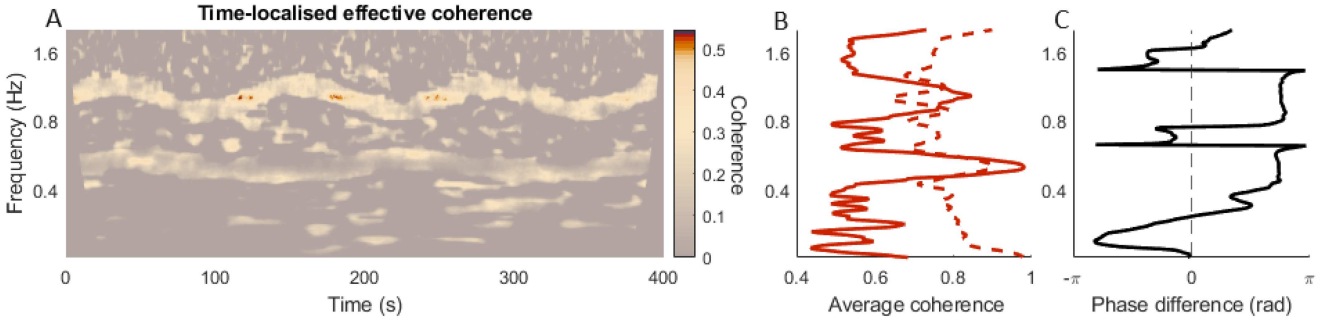

FIG. 6. (a) Time-localized effective phase coherence generated using the Poincaré oscillator example with amplitude noise and a frequency resolution parameter of $f_0 = 2$. The 75th percentile of 99 mismatch surrogates was considered as a zero threshold and was subtracted from the original time-localized coherence. Resulting negative values were set to zero. (b) The time-average of the raw coherence (solid line) and the surrogate threshold (dashed line). (c) The average phase difference across frequency.

noise perturbations, which increases the difficulty of defining a coherence baseline.

A more formulaic approach is to use a hypothesis test. Specifically, we would like to test a null hypothesis that two time-series are not coherent at a specific frequency. Such a hypothesis can be tested through the use of surrogate data.[83] Surrogate data are numerically modeled time-series that are designed to preserve all features of the measured time-series apart from the feature under investigation. In this method, a set of surrogate time-series is first randomly generated. The same analysis that is performed on the real time-series is then performed on the surrogates, with the end result being the discriminating statistic corresponding to the factor of interest. This results in a distribution of values for these statistics, which can then be used to define a specific confidence interval (i.e., the value of a percentile) for discerning significance and rejection of the null hypothesis.

The optimal percentile to use in the test varies from case to case. This can be due to a number of factors. For example, a high intensity of the difference between the noises affecting the two time-series will decrease the coherence between the two time-series to a greater extent than it would decrease the coherence between surrogates, making a lower percentile for the surrogate threshold more appropriate. In this paper, we will adopt a 95th percentile threshold for most cases. However, in some cases, due to factors like the one we have just mentioned, we will use a lower threshold.

One of the most common uses of surrogate data is to test for nonlinearity, where it is possible to apply methods, such as amplitude-adjusted Fourier transform surrogates, that preserve only the linear statistical properties of the time-series (see Ref. 84 for a review of surrogate data methods). However, in testing for significant coherence, we must also preserve the effects of nonlinearity in the surrogate data. Otherwise, even if the surrogates preserve the linear statistical properties, such as the amplitude probability distribution and the frequency spectrum, the null hypothesis may still be spuriously rejected due to increased coherence resulting from nonlinearity.

Mismatched surrogates, also known as intersubject surrogates in the context of biomedical data, are one of the simplest ways to preserve potential nonlinearity in the surrogate data. With this method, pairs of real measurements of the same system (such as the human body, measured across different subjects) are separated and then re-paired with the corresponding time-series from an independent measurement (i.e., another subject). This has the advantage of preserving all properties of the time-series apart from the time-specific information. However, coherence is not preserved as the oscillations are no longer ordered in time.

While mismatched surrogates usually apply only to measured data from real systems, it is still possible to generate time-series approximating mismatched surrogates with the illustrative model defined in Sec. III. In this case, we can simply modify the frequency modulation of the two modes, $\omega(t) = 2\pi\omega_0 + A\sin(2\pi\omega_m t + \psi)$, where ψ is a phase offset of the modulation. Each pair of surrogate time-series is then generated using different values of ψ for each mode, which are uniformly sampled on the interval $[0, 2\pi]$.

It is also worth noting that surrogate testing is not the only method for determining significance thresholds for coherence values. The method proposed by Sheppard *et al.*[85] provide analytically derived significance thresholds based on higher-order statistics, which was shown to give better performance than amplitude-adjusted Fourier transform surrogates.

The effect of time-averaged surrogates is illustrated in Figs. 5(k) and 5(l), which show the 95th percentile of 99 mismatch surrogates. These surrogate thresholds give a much clearer indication of the coherence values that are present in the system vs the spurious coherence. One may also choose to illustrate the time-localized effective coherence. This is demonstrated in Fig. 6, with parameters identical to those in Figs. 2(e), 2(f), 2(k), and 2(l). The threshold here was chosen as the 75th percentile of 99 mismatch surrogates. One can now discriminate the coherence due to the modes vs the background fluctuations in the time-averaged coherence. However, many areas of significant coherence still remain in the time-localized plot distributed away from the modes. This illustrates the fact that it is easier for spurious significant coherence to occur in the time–frequency domain, where the testing area is essentially squared.

The other effect of surrogates can be seen on the effective coherence of the low-frequency mode, which is much reduced

compared to the high-frequency mode. This is due to the fact that spurious coherence between random fluctuations is more likely to be found since the average coherence is calculated over fewer cycles. This essentially reduces the observable frequency range, adding to the effects already caused by the size of the wavelets (parameterized by f_0) and the window size used for the coherence calculation (parameterized by n_{cy}). Taking into account these cumulative effects, we generally recommend that effective coherence can only be assessed if a minimum of 30 cycles can be observed, giving the lowest observable frequency of $30/T$.

Now, to illustrate the second aspect of considering significance of coherence: In the two frequency bands where Fig. 6(b) shows coherence values exceeding the surrogate threshold, Fig. 6(c) shows the phase difference plateauing at about 0.75π. These plateaus in conjunction with the statistical significance of the coherence values suggest that the coherence in these two frequency bands is significant. Moreover, as a consequence, we can conclude that the value 0.75π around which the phase difference plateaus is the amount by which the first time-series leads the second, consistent with the numerically modeled input values.

Therefore, we have seen that the surrogate threshold and the phase difference are invaluable tools when interpreting coherence; this will be demonstrated in Sec. VI via a series of examples.

VI. APPLICATIONS

A. Cardio-respiratory coherence

The heart rate is modulated through several processes, with respiration being an important factor. During inhalation, the heart tends to beat quicker, and during exhalation, it tends to slow down. This interaction is known as respiratory sinus arrhythmia.[86] Cardio-respiratory interactions are perhaps one of the most widely studied interactions. Several methods have been employed,[87,88] including coherence analysis based on the Fourier and wavelet transforms.[89,90] Utilizing PC to study cardio-respiratory interactions has also proven valuable,[50] for example, in the context of ageing,[52] malaria,[91] and hypoxia.[92]

In this example, we evaluate cardio-respiratory interactions based on the simultaneously recorded respiratory effort and the electric activity of the heart. The 1400 s recordings are taken from a 28-year healthy male participating in the study of ageing,[93] where the sensor/electrode placements are described. A time-insert of respiration is shown in Fig. 7(a) and the ECG in Fig. 7(b). The instantaneous frequencies of respiration [IRR, Fig. 7(c)] and beating of the heart [IHR, Fig. 7(d)] are extracted by ridge extraction[32] after the WT was obtained. Two types of interactions are investigated: (a) between the original respiratory time-series and the IHR and (b) between both instantaneous rates, IRR and IHR. The PC and AWPC for both cases are shown in Figs. 7(e), 7(f), 7(i), and 7(j). The surrogate threshold was set to the 95th percentage of 140 intersubject surrogates, as used in the original study.[93] The time-averaged values of PC and AWPC from the entire 1400 s recordings are shown in Figs. 7(g) and 7(k) for the cases (a) and (b), respectively. The phase differences, as a function of frequency, obtained for case (a) and (b), are shown in Figs. 7(h) and 7(l).

It is clear that both PC and AWPC are much higher for the respiration-IHR case, compared to IRR-IHR case, and that the highest values of coherence are at the frequency of respiration (around 0.2–0.3 Hz), consistent with earlier studies. This indicates that, in the resting state, the heart rate is strongly modulated by the amplitude of respiration and to a much lesser extent by the frequency of respiration. In Fig. 7(g), one can see that the PC and AWPC are similar. The phase difference at the respiration frequency is around 0 rad.

B. Phase coherence and movement artifacts

Coherence analysis is often applied to find common oscillatory behavior between brain signals from different locations. This can elucidate the functional connectivity of the brain, which is known to change in various conditions.[94,95] Spontaneous activity in the brain can be measured noninvasively at a relatively low cost using EEG or fNIRS with minimal discomfort to the subjects. However, both methods are susceptible to movement artifacts.[96] Several approaches exist to remove these artifacts from the data, although they often compromise the quality of the data and may additionally remove information of interest.[97,98] As seen in Secs. IV, phase-based approaches may be more resilient against movement artifacts and noise and, as such, can circumvent some of the more draconian preprocessing requirements. In this section, we investigate two examples of movement artifacts, one using EEG and the second using fNIRS.

1. Autism spectrum disorder

Non-invasive brain activity measurements in children are fraught with artifacts due to difficulties in keeping younger subjects still for extended periods. Analysis of signals derived from younger cohorts, therefore, necessitates methods that are robust to movement artifacts. In addition, when considering the presence of interactions between time-series, it can be important to assess how the nature of these interactions changes over time. Time-localized methods can reveal temporal dependencies in this mutual behavior. In a wide array of neurological conditions, it is not only the intensity of interaction between brain regions but the duration of interaction that is altered.[99,100] By observing the time-localized coherence, one may deduce the regularity and strength of time-varying interactions.

We consider a resting-state measurement with eyes open of two simultaneously recorded EEG time-series. These data were measured in a cohort of male children aged 3–5 years old with a diagnosis of autism spectrum disorder (ASD). The time-series were captured using a Nicolet cEEG instrument (Viasys Healthcare, USA) at a sampling rate of 256 Hz. A 20-min recording period was used to collect the data, and a 180-second interval was analyzed, with the central 60 s illustrated in Fig. 8 as it contained a clear artifact. Measurement sites corresponding to F3 and F4 in the international 10–20 system were chosen, as the initial objective of the investigation was to assess reports of reduced frontal connectivity in children with ASD.[101–104]

The effect of the movement artifact is clearly seen in both the time domain, Figs. 8(a) and 8(b), and the WT, Figs. 8(c) and 8(d), where at the instance of the movement, all frequencies are present (around 93 s) in the spectrum. The effect on the coherence is much stronger and can be seen in Figs. 8(e)–8(g) for the AWPC compared

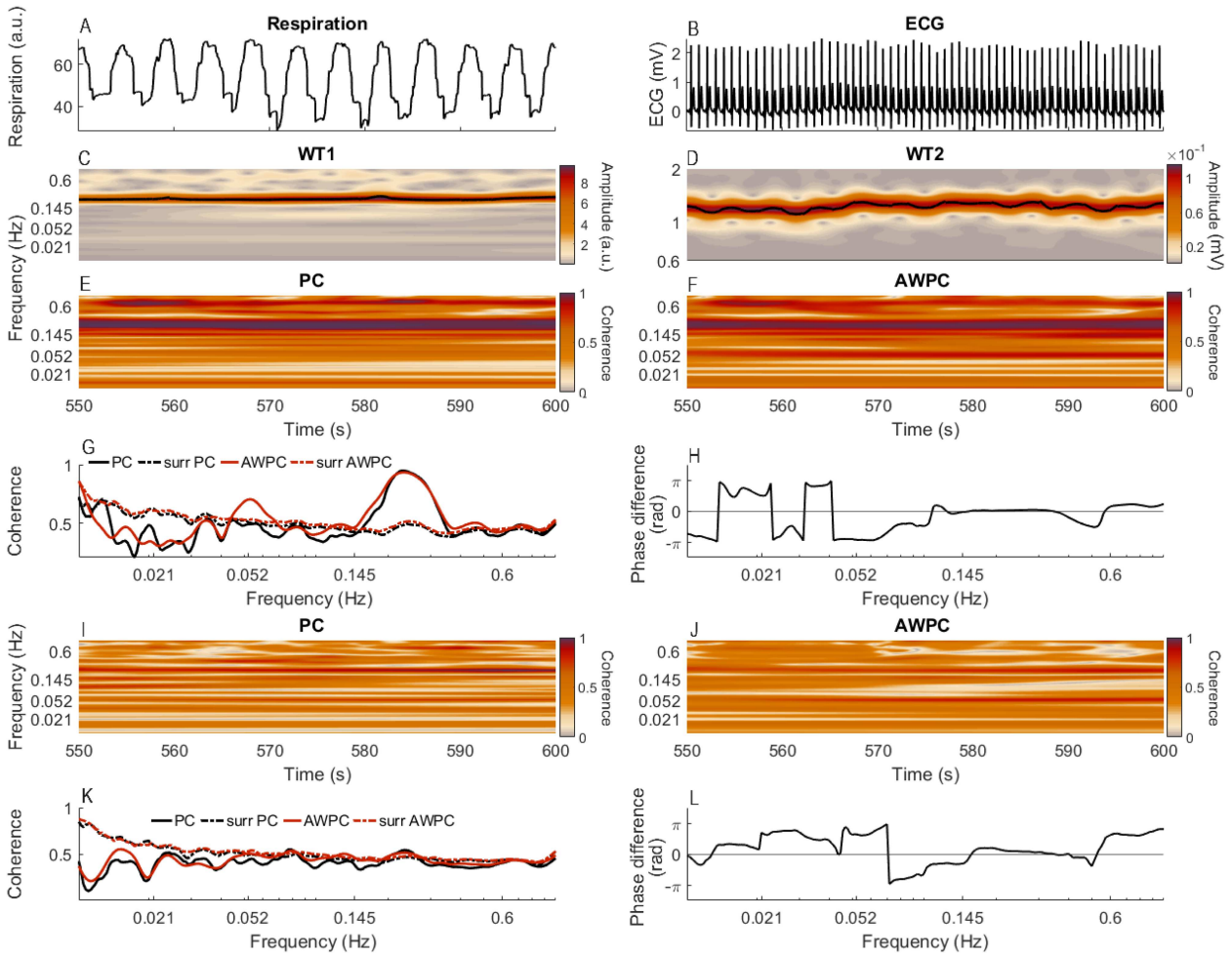

FIG. 7. (a) and (b) Time-series of respiration and ECG from a 28-year-old healthy man, shown for 50 out of the 1400 s of recordings. (c) The WT of the time-series in (a). The solid line is the extracted ridge, giving the instantaneous respiration rate (IRR). (d) The WT of the time-series in (b). The solid line is the extracted ridge, giving the instantaneous heart rate (IHR). (e) The PC between the respiration and IHR. (f) The AWPC between the respiration and IHR. (g) The time-averaged PC (solid black line) and AWPC (solid orange line), with the corresponding surrogate thresholds (dashed lines). (h) The time-averaged phase difference at each frequency. A positive value means that the time-series in (a) is leading. (i) The PC between IHR and IRR. (j) The AWPC between IHR and IRR. (k) The time-averaged PC (solid black line) and AWPC (solid orange line), with the corresponding surrogate thresholds (dashed lines) for IHR and IRR. (l) The time-averaged phase difference at each frequency. A positive value means that the IRR is leading. The time-averaged coherence and the phase difference in (g), (h), (k), and (l) is calculated using the whole time-series (1400 s).

to the PC. A threshold of the 75th percentile of 156 intersubject surrogates was used, leaving only the significant coherence. The time-localized coherence [Fig. 8(e)] shows that the magnitude and presence of the interactions vary over time. Both the time-localized, Figs. 8(e) and 8(f), and the time-average, Fig. 8(g), coherence are elevated for the AWPC compared to the PC.

2. Chorea in Huntington's disease

Now, we consider two time-series recorded from the temporal brain areas, in a study that investigated coherence between neuronal and vascular function.[105] These locations often have artifacts due to movement of the jaw. The data are from a participant with a positive genetic test for Huntington's disease (HD), who has not yet developed the movement disorder known as chorea. Still, as chorea is a hallmark of the disease, HD research would benefit from methods that are resistant to movement artifacts.

We compared PC and AWPC of two resting-state oxygenated hemoglobin (oxyHb) time-series measured using a fNIRS device (NIRScout, NIRx, Germany) with a sampling frequency of 31.25 Hz over 20 min (for further details on measurements, see Ref. 93). The measurement sites correspond to T7 and T8 in the international 10–20 system (left and right temporal locations). The resolution

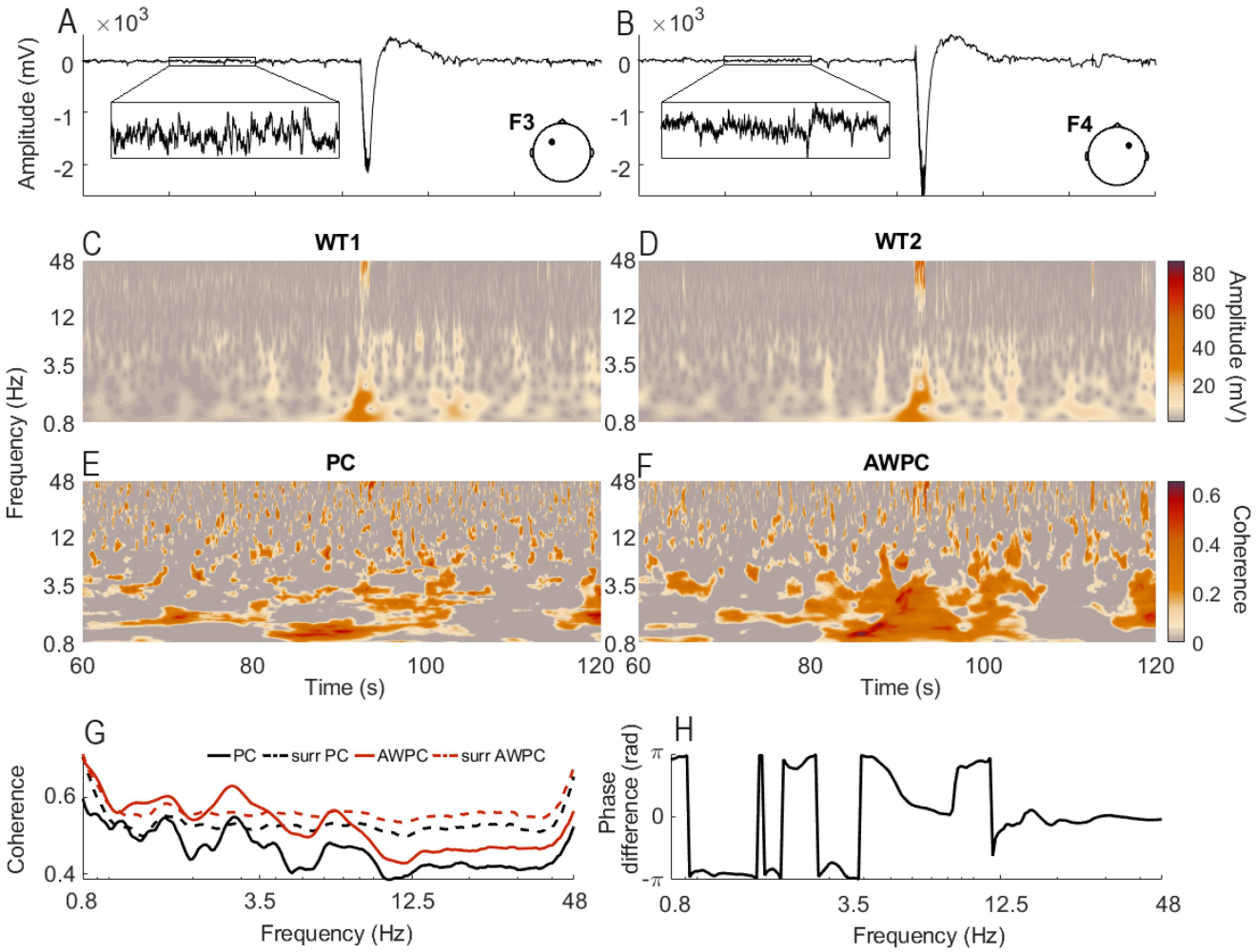

FIG. 8. Movement artifact represented as a downward spike in the time-series recorded simultaneously at two probes: F3 (a) and F4 (b). Their corresponding WTs [(c) and (d), respectively], indicate the amplitude perturbation at around 93 s. The effective phase coherence (e) is resilient against this perturbation, while the amplitude-weighted phase coherence (f) exhibits spurious coherence. In both cases, the surrogate threshold is taken as the 75th percentile of 156 intersubject surrogates. (g) The time-averaged PC (solid black line) and AWPC (solid orange line), with the corresponding surrogate thresholds (dashed lines). (h) The time-averaged phase difference across frequency.

parameter f_0, Eq. (8), was set to 1, as to minimize the spread of an artifact.

The results are shown in Fig. 9. The time-series contain two movement artifacts, which appear as high-amplitude cones in the WT and have the greatest impact at low frequencies. The artifacts have a very significant impact on the AWPC plot and affect an even wider area of time and frequency than is visible in the WT plots. This is a consequence of the moving window used to calculate wavelet coherence. In the plot of PC. the effect of the artifacts is not obvious. This illustrates how any simultaneous increase in amplitude, even if not phase coherent, results in AWPC appearing significant over large areas of the time–frequency domain. This can also be seen in the time-averaged coherence plot, where the AWPC (orange line) is much higher than the PC (black line). The two dashed lines show the 95th percentile of the 136 intersubject surrogates.

This example illustrates that PC is relatively resistant to artifacts, which is beneficial when analyzing time-series from various non-invasive measurement techniques.

C. Electron dynamics on the surface of liquid helium

Time–frequency and coherence analysis can provide valuable information about the dynamics of a system. In addition, the phase difference between oscillations can give information about the direction of influence. We consider the movement of electrons on the surface of liquid helium at very low temperatures, as discussed in Siddiq

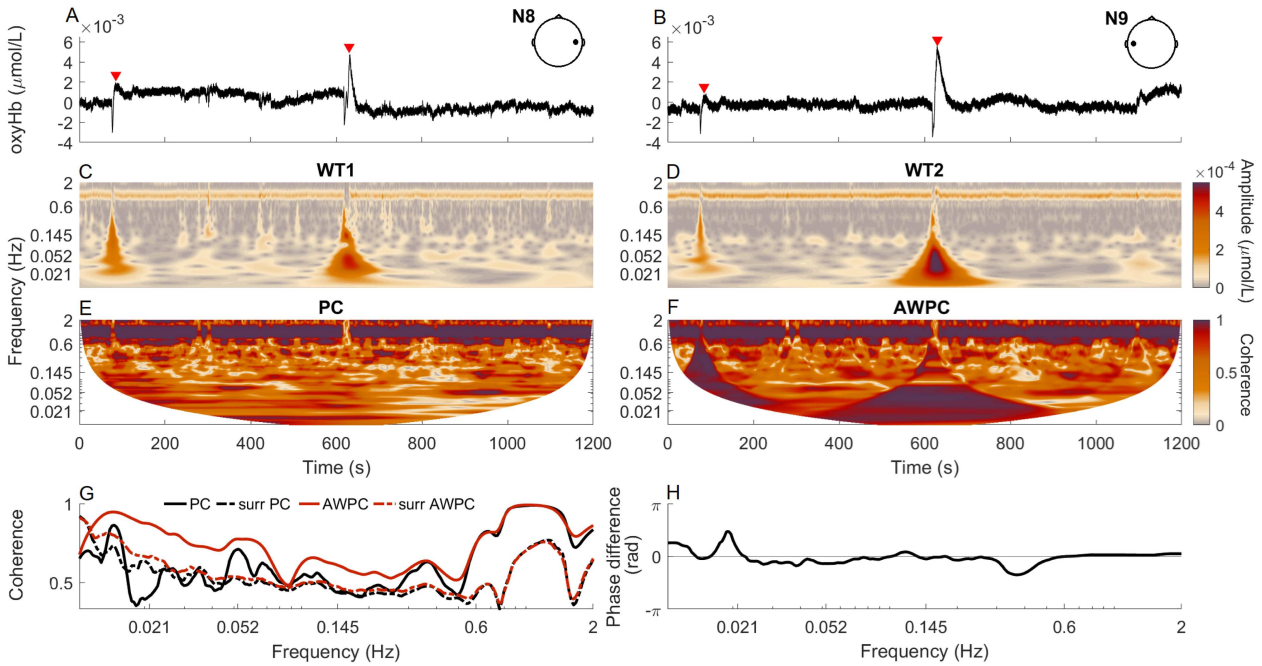

FIG. 9. (a) and (b) Two fNIRS time-series measured from a participant with Huntington's disease. The locations of two artifacts are marked on the time-series using red triangles. (c) The WT of the time-series in (a). (d) The WT of the time-series in (b). (e) The PC of the two time-series. (f) The AWPC plots of the two time-series. (g) The time-averaged PC (solid black line) and AWPC (solid orange line), with the corresponding surrogate thresholds (dashed lines). (h) The time-averaged phase difference at each frequency. A positive value means that the time-series in (a) is leading.

et al.[31] At very low temperatures, the helium will be a superfluid. Since such a system can be used for constructing the qubits that are needed for quantum computers, increasing the understanding of its dynamics is important.

In the experiments, the electrons were just above the liquid helium, trapped between the helium and a vacuum. They were in a perpendicular magnetic field and subjected to microwave radiation and varying pressing voltage. Current oscillations were recorded from five electrodes for 60 s at 100 kHz. The full experimental setup is described in Ref. 31. We chose an example with low electron density and 4.18 V pressing voltage. Currents measured from electrodes E4 and C in the time-interval 30–31.4 s were selected for analysis, and high coherence was obtained as in the original paper.[31]

Figure 10 shows the PC and AWPC between current oscillations at the two electrodes. The current signals were first downsampled to 20 kHz, as in this example, we will focus on oscillations around 0.5 kHz. The resolution parameter was set to 3, in line with the original paper.[31] 100 iterated amplitude-adjusted Fourier transform (IAAFT) surrogates were used to calculate the surrogate thresholds.[84]

Both PC and AWPC methods pick up a time-varying coherence following the dominant mode in the WT plots, which resembles a non-autonomous influence on the system. The time-averaged PC (black line) and AWPC (orange lines) are similar, with the AWPC having a slightly higher value at the higher frequencies. This could indicate that there is some amplitude covariance. The surrogate thresholds are very similar for both methods. The time-averaged phase difference is positive, meaning that the oscillation at E4 is preceding that at C.

The existence of coherence indicates that the electrons are moving, and the phase difference suggests that they are moving toward the C electrode from the E4 electrode. This is consistent with the microwave radiation being applied closer to E4. Furthermore, by studying the time–frequency representations, we see a clear mode with a time-varying frequency. Using ridge extraction,[32] which essentially tracks the maximum amplitude within a frequency range, we can extract a time-series of the instantaneous frequency. The WT of this time-series shows a clear amplitude peak at around 5.2 Hz, indicating modulation of the electron movement at this frequency. This was shown to be caused by slow gravity waves on the liquid helium.[31] It is important to note that in the WT of the original current data, there is also a peak at around 5.2 Hz. However, this peak is relatively weak compared to the rest of the spectrum, and, in particular, compared with the dominant oscillatory component, making it challenging to observe and identify directly from the frequency spectrum. This illustrates that time-localized, time–frequency methods can uncover a great deal of physically meaningful information.

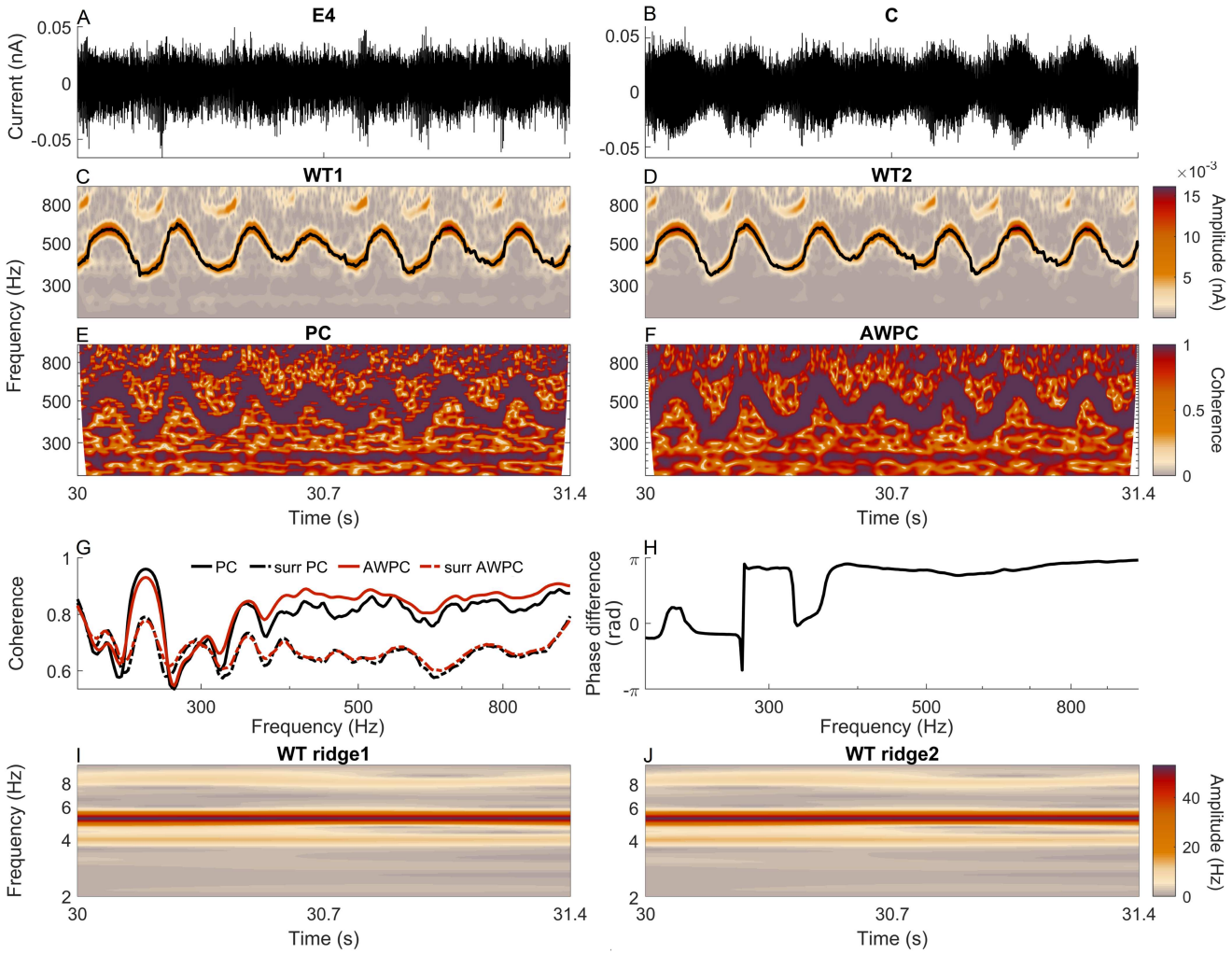

FIG. 10. (a) and (b) Time-series of current oscillations caused by the movement of electrons on the surface of liquid helium. The two electrodes are labeled E4 and C. (c) and (d) The WT of the time-series in (a) and (b), respectively, with the extracted ridge shown by the solid black line. (e) The PC of the two time-series. (f) The AWPC of the two time-series. (g) The time-averaged PC (solid black line) and AWPC (solid orange line), with the corresponding surrogate thresholds (dashed lines). (h) The time-averaged phase difference at each frequency. A positive value means that the time-series in (a) is leading. (i) The WT of the ridge time-series plotted in (c). (j) The WT of the ridge time-series plotted in (d).

VII. DISCUSSION AND SUMMARY

The study of coherence has its foundations in physics, where methods were first developed to measure the coherence between the phases of waves. It has then been extended to considering coherence between the phases of more general oscillatory processes occurring in a wide variety of scientific disciplines; for this, one of the most fundamental issues is the quantification of such coherence from measured data. Accordingly, it is a subject particularly treated by harmonic analysis in mathematics and by signal-processing theory. We have approached this same question again from a physics perspective, but still with this greater generality than the kinds of setup that initiated the study of coherence—namely, from the perspective of multi-scale time-dependent oscillatory dynamics.

We have seen that for time-series data recorded from systems involving interacting oscillations, key information about the interactions is contained in the time evolution of the phases of the oscillations. Moreover, we have seen that for the analysis of systems involving oscillations with temporally modulated quantitative characteristics, such as frequency and amplitude, time-series analysis methods that are fundamentally designed for time-series with stationary statistics are inappropriate. For example, the measure of coherence of phases intended to be revealed by Fourier

coherence will have little meaning for systems with frequency-modulated oscillations. Rather, tools designed to extract time-evolving, time-localized information about systems exhibiting time-dependent far-from-equilibrium dynamics are needed. In particular, phase information needs to be extracted in a suitably time-localized manner.

Such time-localization inherently needs to be understood relative to the timescale of the dynamical process under investigation, and therefore, for multi-scale time-series involving oscillations of a range of frequencies, this time-localization needs to be adaptive to the range of timescales involved. This has been illustrated in Fig. 1.

In the setting of time–frequency analysis, where the Heisenberg uncertainty principle requires a trade-off between precision in measurements of frequency and precision in location in time, this multi-scale adaptivity corresponds to a logarithmic frequency resolution. This is achieved by the continuous wavelet transform, where the scale variable is taken as inversely proportional to the frequency under investigation. Accordingly, we have seen that the wavelet transform is the appropriate tool for extracting phase information from multi-scale nonstationary time-series, and in particular, WT-based coherence analysis is the appropriate approach to investigating coherence of phases manifesting in such time-series.

In this paper, we have provided an introduction to wavelet-based coherence analysis and evaluated several related issues—some already established and others that had not previously been addressed.

Existing discussions of different approaches to quantifying coherence, and more generally of different approaches to time–frequency analysis, have mainly treated the different approaches as if on essentially equal footing, and practical choices, such as the use of WT over STFT, or of PC over AWPC, are often treated merely as a matter of quantitative optimization, without theoretically reasoned or experimentally explored consideration of the qualitative impact of such choices on the resulting analysis.

To address this issue, we have provided a systematic explanation of the practicalities and pitfalls of how to carry out wavelet coherence analysis in practice. In particular, we have provided a detailed review of the methodology for reliably testing for and detecting significant phase coherence from measured data.

Since the wavelet transform provides extractable phases and amplitudes, one can calculate[38,46] a measure of coherence independent of changes in the amplitude, namely, PC, as well as a measure of coherence that is weighted in time by amplitude, namely, AWPC. Prior to this work, an in-depth comparison between AWPC and PC had not been performed. Perhaps counterintuitively, we found a consistent difference in the performance of the two definitions of coherence when applied to noisy time-series. PC is, in general, more robust to noise and particularly to time-localized perturbations, meaning that it is affected to a much lesser degree by phenomena, such as movement artifacts.

Along with the definition of PC, one can also analyze phase differences in the oscillations present in the pair of time-series under investigation. This is first needed as one of the aspects of determining significance of coherence, along with statistical significance of the coherence values themselves: the time-averaged phase difference as a function of frequency needs to have a plateau in the frequency band where coherent oscillations manifest in time–frequency representation. Second, where there is significant coherence, the phase difference can provide indications of which oscillation is leading.[106] However, it is important to note that causality (i.e., which process is the origin of the common oscillations) is not always possible to infer from the phase shift. This can be because the phase shift is wrapped on the interval $[-\pi, \pi]$ or because of the existence of higher degree interactions, such as node triples.[107]

This investigation of coherence has revealed the wealth of information provided by the phase. Part of the utility of phase over amplitude comes from the fact that phase dynamics is constrained by the frequency interval within which an oscillation lies. For example, each wavelet has a defined frequency response, which limits the rate at which the phase can change. However, in contrast to the phase, the amplitude is not bounded to frequency in such a manner, making the separation of amplitude dynamics from noise harder to satisfactorily achieve. This is analogous to the advantages of frequency modulation over amplitude modulation in radio communications.[108]

The practical implications of the main points highlighted by our work are effectively illustrated in our analyses of real data in Sec. VI. In the examples shown in Sec. VI B, the presence of movement artifacts has a significant effect on the results of any analysis. Such artifacts usually need to be removed prior to analysis, which often requires subjective identification. The techniques used to remove identified artifacts may also introduce artificial manipulations in the data.[109] The resistance of amplitude-independent phase-based methods to these sorts of artifacts allows for the analysis of noisy data without the need for preprocessing or constraints on the measurement setup, leading to better research into conditions, such as HD and ASD.

In the example of electron dynamics on the surface of liquid helium, using phase coherence analysis, we identified the existence of gravity waves. Without the time-localized approach, these waves might not have been detected. This illustrates how the application of coherence methods and time–frequency analysis can be used to identify specific properties of a physical system. Thus, we see the importance of using a time-localized approach instead of an asymptotic approach, i.e., infinite-time, non-time-evolving approach. The wider adoption of explicitly finite-time and time-localized methods should, therefore, lead to similar discoveries in systems characterized by non-autonomous dynamics involving nonstationary amplitudes and frequencies.

VIII. CONCLUSION

We review the current understanding of coherence, a universal phenomenon that can appear between oscillations or waves, irrespective of their origin. We start from its definition in physics and review numerical methods for analyzing coherence from modeled or real data. We focus particularly on coherence between non-autonomous oscillatory processes whose oscillations have deterministically time-varying frequencies. For this reason, we apply wavelet-based, time-resolved coherence analysis. We discuss differences between amplitude-weighted phase coherence and phase coherence. In the former case, time-resolved information includes both the amplitude and the phase; in the latter case, only the information about phase is considered. We illustrate that the amplitudes

are more readily perturbed than phases by noise or movement artifacts, and consequently, that phase coherence provides more robust information about interacting oscillatory systems. We illustrate this in relation to several real-world examples.

SUPPLEMENTARY MATERIAL

An alternative to Fig. 1 in the main paper is presented in the supplementary material. It shows the Fourier transform in a logarithmic scale. By comparing Figs. 1(c), 1(d), 1(g), and 1(h) in the main text and supplementary Figs. 1(c), 1(d), 1(g), and 1(h), it is clear that the logarithmic scale is disadvantageous to the short-time Fourier transform, which is obtained with linear frequency resolution.

ACKNOWLEDGMENTS

We are grateful to Peter McClintock and Kostya Nasyedkin for useful comments on the paper. The work of P.T.C. and A.S. is funded through the Sony Research Award Program. A.S. is also funded by the Engineering and Physical Sciences Research Council, UK (Grant No. EP/X004597/1). J.B. is supported by the Sir John Fisher Foundation. S.J.K.B. is jointly supported by the EPSRC, UK and the MyMind GmbH—Brain Hero, Vienna, Austria (Grant No. EP/T518037/1). The High End Computing facility at Lancaster University was used for some of the computations. The experimental part of the ASD study was supported by the Action Medical Research (UK) MASDA Project (GN1963) and partly by the Slovenian Research Agency (Program No. P20232). The HD and ageing studies were funded by the Engineering and Physical Sciences Research Council, UK (Grant No. EP/M006298/1) and the Slovenian Research Agency (ARRS) (Program No. P20232). The experimental data used for the example on electron dynamics on the surface of liquid helium were obtained by Kostyantyn Nasyedkin in the Quantum Condensed Phases Research Team, RIKEN CEMS, Japan, headed by Kimitoshi Kono. The development of the MODA toolbox used for analyses has been supported by the Engineering and Physical Sciences Research Council, UK (Grant Nos. EP/100999X1 and EP/M006298/1), the EU projects BRACCIA (517133) and COSMOS (642563), the Action Medical Research (UK) MASDA Project (GN1963), and the Slovene Research Agency (Program No. P20232).

AUTHOR DECLARATIONS

Conflict of Interest

The authors have no conflicts to disclose.

Author Contributions

The authors have been listed alphabetically due to their approximately equal contributions.

S. J. K. Barnes: Conceptualization (supporting); Data curation (equal); Formal analysis (equal); Investigation (equal); Software (equal); Validation (equal); Visualization (equal); Writing – review & editing (equal). **J. Bjerkan:** Conceptualization (equal); Data curation (equal); Formal analysis (equal); Investigation (equal); Software (equal); Validation (equal); Visualization (equal); Writing – review & editing (equal). **P. T. Clemson:** Conceptualization (equal); Data curation (equal); Formal analysis (equal); Investigation (equal); Methodology (equal); Software (equal); Supervision (equal); Validation (equal); Visualization (equal); Writing – original draft (equal); Writing – review & editing (equal). **J. Newman:** Conceptualization (supporting); Data curation (supporting); Formal analysis (supporting); Funding acquisition (supporting); Investigation (equal); Methodology (supporting); Validation (supporting); Visualization (supporting); Writing – review & editing (equal). **A. Stefanovska:** Conceptualization (equal); Data curation (equal); Formal analysis (equal); Funding acquisition (equal); Investigation (equal); Methodology (equal); Project administration (equal); Resources (equal); Supervision (equal); Validation (equal); Visualization (equal); Writing – review & editing (equal).

DATA AVAILABILITY

The data used in this work are available in the Publications and Research (Pure) portal on Lancaster University's research information management system. The data used in the cardio-respiratory example can be found at doi.org/10.17635/lancaster/researchdata/630. The data used in the ASD example can be found at doi.org/10.17635/lancaster/researchdata/604. The data used in the HD example can be found at doi.org/10.17635/lancaster/researchdata/631. The data used for the electron dynamics on the surface of a liquid helium example can be found at doi.org/10.17635/lancaster/researchdata/655.

REFERENCES

[1] H. Crewe, C. Huygens, T. Young, A. J. Fresnel, and F. Arago, *The Wave Theory of Light; Memoirs of Huygens, Young and Fresnel* (Cincinnati American Book Company, New York, 1900).
[2] A. Michelson and E. W. Morley, Am. J. Sci. **s3–34**, 333 (1887).
[3] C. Jönsson, Z. Phys. **161**, 454 (1961).
[4] P. G. Merli, G. F. Missiroli, and G. Pozzi, Am. J. Phys. **44**, 306 (1976).
[5] A. Ananthaswamy, *Through Two Doors at Once: The Elegant Experiment That Captures the Enigma of Our Quantum Reality* (Penguin Publishing Group, 2018).
[6] T. H. Maiman, Nature **187**, 493 (1960).
[7] B. P. Abbot *et al.*, (LIGO Scientific Collaboration and Virgo Collaboration), Phys. Rev. Lett. **116**, 061102 (2016).
[8] P. Ilzhöfer, M. Sohmen, G. Durastante, C. Politi, A. Trautmann, G. Natale, G. Morpurgo, T. Giamarchi, L. Chomaz, M. J. Mark, and F. Ferlaino, Nat. Phys. **17**, 356 (2021).
[9] D. Huang and Y. Yang, Phys. Rev. B **104**, L081115 (2021).
[10] S. Ye, C. Zou, H. Yan, Y. Ji, M. Xu, Z. Dong, Y. Chen, X. Zhou, and Y. Wang, Nat. Phys. **19**, 1301 (2023).
[11] A. E. Miroshnichenko, S. Flach, and Y. S. Kivshar, Rev. Mod. Phys. **82**, 2257 (2010).
[12] J. R. Kim, C. W. Lin, and S. Y. Lin, Remote Sens. **13**, 2240 (2021).
[13] A. Delorme and S. Makeig, J. Neurosci. Methods **134**, 9 (2004).
[14] M. Jensen, R. Hyder, B. U. Westner, A. Højlund, and Y. Shtyrov, Neuropsychologia **188**, 108602 (2023).
[15] A. Sauer, T. Grent-'t-Jong, M. Zeev-Wolf, W. Singer, A. Goldstein, and P. J. Uhlhaas, Schizophr. Res. **261**, 60 (2023).
[16] T. Gänsler, M. Hansson, C.-J. Ivarsson, and G. Salomonsson, IEEE Trans. Commun. **44**, 1421 (1996).
[17] T. Hada, D. Koga, and E. Yamamoto, Space Sci. Rev. **107**, 463 (2003).
[18] P. C. Liu, in *Wavelets in Geophysics*, edited by P. Kumar and E. Foufoula-Georgiou (Elsevier, 1994), Vol. 4, pp. 151–166.
[19] J. P. Eckmann and D. Ruelle, Rev. Mod. Phys. **57**, 617 (1983).
[20] P. T. Clemson and A. Stefanovska, Phys. Rep. **542**, 297 (2014).

[21] J. Rowland Adams, J. Newman, and A. Stefanovska, Eur. Phys. J. Spec. Top. **232**, 3435–3457 (2023).
[22] E. P. Wigner, Phys. Rev. **40**, 749 (1932).
[23] J. Ville, Cables Transm. **2A**, 61 (1948).
[24] D. Gabor, J. IEEE **93**, 429 (1946).
[25] J. Morlet, in *Issues on Acoustic Signal/Image Processing and Recognition*, Vol. I, NATO ASI series, edited by C. H. Chen (Springer, Berlin, 1983).
[26] G. Kaiser, *A Friendly Guide to Wavelets* (Birkhäuser, Boston, MA, 1994).
[27] B. Boashash, *Time Frequency Signal Analysis and Processing: A Comprehensive Reference* (Academic Press, Boston, MA, 2016).
[28] M. Farge, Annu. Rev. Fluid Mech. **24**, 395 (1992).
[29] S. L. Bressler, R. Coppola, and R. Nakamura, Nature **366**, 153 (1993).
[30] M. Bračič and A. Stefanovska, Bull. Math. Biol. **60**, 919 (1998).
[31] H. Siddiq, K. Nasyedkin, K. Kono, D. E. Zmeev, P. V. E. McClintock, Y. A. Pashkin, and A. Stefanovska, Phys. Rev. B **107**, 104501 (2023).
[32] D. Iatsenko, P. V. E. McClintock, and A. Stefanovska, Signal Process. **125**, 290 (2016).
[33] C. Schäfer, M. G. Rosenblum, H. H. Abel, and J. Kurths, Phys. Rev. E **60**, 857 (1999).
[34] P. Kvandal, L. Sheppard, S. A. Landsverk, A. Stefanovska, and K. A. Kirkebøen, J. Clin. Monit. Comput. **27**, 375 (2013).
[35] T. Stankovski, T. Pereira, P. V. E. McClintock, and A. Stefanovska, Rev. Mod. Phys. **89**, 045001 (2017).
[36] M. Rosenblum and A. Pikovsky, Front. Netw. Physiol. **3**, 1298228 (2023).
[37] P. T. Clemson, Y. F. Suprunenko, and A. Stefanovska, Phys. Rev. E **89**, 032904 (2014).
[38] J.-P. Lachaux, E. Rodriguez, M. Le Van Quyen, A. Lutz, J. Martinerie, and F. J. Varela, Int. J. Bifurcat. Chaos **10**, 2429 (2000).
[39] F. Mormann, K. Lehnertz, P. David, and C. E. Elger, Physica D **144**, 358 (2000).
[40] B. J. Roach and D. H. Mathalon, Schizophr. Bull. **34**, 907 (2008).
[41] C. Chang and G. H. Glover, NeuroImage **50**, 81 (2010).
[42] C. M. Sweeney-Reed, P. M. Riddell, J. A. Ellis, J. E. Freeman, and S. J. Nasuto, PLoS One **7**, e48357 (2012).
[43] E. Angelopoulos, E. Koutsoukos, A. Maillis, G. N. Papadimitriou, and C. Stefanis, Schizophr. Res. **153**, 109 (2014).
[44] L. Bu, C. Huo, G. Xu, Y. Liu, Z. Li, Y. Fan, and J. Li, Front. Physiol. **9**, 669 (2018).
[45] L. Xu, B. Wang, G. Xu, W. Wang, Z. Liu, and Z. Li, Neurosci. Lett. **640**, 21 (2017).
[46] A. Bandrivskyy, A. Bernjak, P. V. E. McClintock, and A. Stefanovska, Cardiovasc. Eng. **4**, 89 (2004).
[47] L. W. Sheppard, V. Vuksanović, P. V. E. McClintock, and A. Stefanovska, Phys. Med. Biol. **56**, 3583 (2011).
[48] V. Ticcinelli, T. Stankovski, D. Iatsenko, A. Bernjak, A. E. Bradbury, A. R. Gallagher, P. B. M. Clarkson, P. V. E. McClintock, and A. Stefanovska, Front. Comput. Physiol. **8**, 749 (2017).
[49] S. Smirni, A. D. McNeilly, M. P. MacDonald, R. J. McCrimmon, and F. Khan, Sci. Rep. **9**, 186 (2019).
[50] I. V. Tikhonova, A. A. Grinevich, and A. V. Tankanag, Biomed. Signal Process. Control **71**, 103091 (2022).
[51] I. V. Tikhonova, A. V. Tankanag, I. E. Guseva, and A. A. Grinevich, Biomed. Signal Process. Control **79**, 104222 (2023).
[52] D. Iatsenko, A. Bernjak, T. Stankovski, Y. Shiogai, P. J. Owen-Lynch, P. B. Clarkson, A. Stefanovska, and P. V. E. McClintock, Phil. Trans. R. Soc. Lond. A **371**, 20110622 (2013).
[53] M. Gruszecki, G. Lancaster, A. Stefanovska, J. P. Neary, R. T. Dech, W. Guminski, A. F. Frydrychowski, J. Kot, and P. J. Winklewski, Sci. Rep. **8**, 3057 (2018).
[54] A. Grinsted, J. C. Moore, and S. Jevrejeva, Nonlin. Process Geophys. **11**, 561 (2004).
[55] D. S. Bloomfield, R. T. J. McAteer, B. W. Lites, P. G. Judge, M. Mathioudakis, and F. P. Keenan, Astrophys. J. **617**, 623 (2004).
[56] R. Donner and M. Thiel, Astron. Astrophys. **475**, L33 (2007).
[57] A. Volvach, G. Kurbasova, and L. Volvach, Heliyon **10**, e23237 (2024).
[58] L. Aguiar-Conraria, N. Azevedo, and M. J. Soares, Physica A **387**, 2863 (2008).
[59] L. Aguiar-Conraria and M. J. Soares, Empir. Econ. **40**, 645 (2011).
[60] L. Vacha and J. Barunik, Energy Econ. **34**, 241 (2012).
[61] C. Aloui and B. Hkiri, Econ. Model. **36**, 421 (2014).
[62] J. C. Reboredo, M. A. Rivera-Castro, and A. Ugolini, Energy Econ. **61**, 241 (2017).
[63] D. Abboud, S. Baudin, J. Antoni, D. Rémond, M. Eltabach, and O. Sauvage, Mech. Syst. Signal Process. **75**, 280 (2016).
[64] M. Morris, S. Yamazaki, and A. Stefanovska, J. Biol. Rhythms **37**, 310 (2022).
[65] A. Monterde, A. Calleja-López, M. Aguilera, X. E. Barandiaran, and J. Postill, Inf. Commun. Soc. **18**, 930 (2015).
[66] F. Zernike, Physica **5**, 785 (1938).
[67] A. Pikovsky, M. Rosenblum, and J. Kurths, *Synchronization—A Universal Concept in Nonlinear Sciences* (Cambridge University Press, Cambridge, 2001).
[68] D. Iatsenko, P. V. E. McClintock, and A. Stefanovska, Digit. Signal Process. **42**, 1 (2015).
[69] C. Torrence and P. J. Webster, J. Clim. **12**, 2679 (1999).
[70] L. Keselbrener and S. Akselrod, IEEE Trans. Biomed. Eng. **43**, 789 (1996).
[71] A. S. Karavaev, A. S. Borovik, E. I. Borovkova, E. A. Orlova, M. A. Simonyan, V. I. Ponomarenko, V. V. Skazkina, V. I. Gridnev, B. P. Bezruchko, M. D. Prokhorov, and A. R. Kiselev, Biophys. J. **120**, 2657 (2021).
[72] I. Mizeva, C. D. Maria, P. Frick, S. Podtaev, and J. Allen, J. Biomed. Opt. **20**, 037007 (2015).
[73] L. W. Sheppard, J. R. Bell, R. Harrington, and D. C. Reuman, Nat. Clim. Change **6**, 610 (2016).
[74] J. Rowland-Adams and A. Stefanovska, Front. Physiol. **11**, 613183 (2021).
[75] D. Iatsenko, G. Lancaster, S. McCormack, J. Newman, G. V. Policharla, V. Ticcinelli, T. Stankovski, and A. Stefanovska, Lancaster University; see https://doi.org/10.5281/zenodo.3470856 (2019).
[76] J. Newman, G. Lancaster, and A. Stefanovska, Lancaster University; see https://doi.org/10.5281/zenodo.3470856 (2018).
[77] R. W. Thatcher, D. M. North, and C. J. Biver, NeuroImage **42**, 1639 (2008).
[78] D. J. DeShazer, R. Breban, E. Ott, and R. Roy, Phys. Rev. Lett. **87**, 044101 (2001).
[79] O. V. Sosnovtseva, A. N. Pavlov, E. Mosekilde, K. Yip, N. Holstein-Rathlou, and D. J. Marsh, Am. J. Physiol. Renal Physiol. **293**, F1545–F1555 (2007).
[80] G. Carl, D. Doktor, D. Koslowsky, and I. Kühn, Stoch. Environ. Res. Risk Assess. **27**, 1221–1230 (2013).
[81] E. A. K. Cohen and A. T. Walden, IEEE Trans. Signal Process. **58**, 2964 (2010).
[82] S. Holm, Astrophys. Space Sci. **357**, 106 (2015).
[83] T. Schreiber and A. Schmitz, Physica D **142**, 346 (2000).
[84] G. Lancaster, D. Iatsenko, A. Pidde, V. Ticcinelli, and A. Stefanovska, Phys. Rep. **748**, 1 (2018).
[85] L. W. Sheppard, A. Stefanovska, and P. V. E. McClintock, Phys. Rev. E **85**, 046205 (2012).
[86] F. Yasuma and J. Hayano, Chest **125**, 683 (2004).
[87] M. Bračič Lotrič and A. Stefanovska, Physica A **283**, 451 (2000).
[88] Y. Shiogai, A. Stefanovska, and P. V. E. McClintock, Phys. Rep. **488**, 51 (2010).
[89] G. Stanley, D. Verotta, N. Craft, R. A. Siegel, and J. B. Schwartz, Am. J. Physiol. Heart Circ. Physiol. **270**, H1833 (1996).
[90] K. Keissar, L. R. Davrath, and S. Akselrod, Phil. Trans. R. Soc. A **367**, 1393 (2009).
[91] Y. A. Abdulhameed, A. G. Habib, P. V. E. McClintock, and A. Stefanovska, "Phase coherence between cardiovascular oscillations in malaria: The basis for a possible diagnostic test," in *Physics of Biological Oscillators: New Insights into Non-Equilibrium and Non-Autonomous Systems*, edited by A. Stefanovska and P. V. E. McClintock (Springer International Publishing, Cham, 2021), pp. 401–419.
[92] G. Lancaster, T. Debevec, G. P. Millet, M. Poussel, S. J. Willis, M. Mramor, K. Goričar, D. Osredkar, V. Dolžan, and A. Stefanovska, J. Physiol. **598**, 2001–2019 (2020).
[93] J. Bjerkan, G. Lancaster, B. Meglič, J. Kobal, T. J. Crawford, P. V. E. McClintock, and A. Stefanovska, Brain Res. Bull. **201**, 110704 (2023).
[94] P. Van Mierlo, M. Papadopoulou, E. Carrette, P. Boon, S. Vandenberghe, K. Vonck, and D. Marinazzo, Prog. Neurobiol. **121**, 19 (2014).
[95] A. J. Mackintosh, R. de Bock, Z. Lim, V.-N. Trulley, A. Schmidt, S. Borgwardt, and C. Andreou, Neurosci. Biobehav. Rev. **120**, 354 (2021).
[96] T. D. Satterthwaite, R. Ciric, D. R. Roalf, C. Davatzikos, D. S. Bassett, and D. H. Wolf, Hum. Brain Mapp. **40**, 2033 (2019).

[97]A. Delorme, Sci. Rep. **13**, 2372 (2023).
[98]E. Arad, R. P. Bartsch, J. W. Kantelhardt, and M. Plotnik, PLoS One **13**, e0197153 (2018).
[99]E. T. Rolls, W. Cheng, and J. Feng, Transl. Psychiatry **11**, 70 (2021).
[100]S. Petkoski, P. Ritter, and V. K. Jirsa, Cereb. Cortex **33**, 6241 (2023).
[101]D. Liloia, J. Manuello, T. Costa, R. Keller, A. Nani, and F. Cauda, Eur. Arch. Psychiatry Clin. Neurosci. **274**, 3 (2023).
[102]R. Coben, A. R. Clarke, W. Hudspeth, and R. J. Barry, Clin. Neurophysiol. **119**, 1002 (2008).
[103]A. Dickinson, M. Daniel, A. Marin, B. Gaonkar, M. Dapretto, N. M. McDonald, and S. Jeste, Biol. Psychiatry Cogn. Neurosci. Neuroimaging **6**, 59 (2021).
[104]M. M. Chan, M.-C. Chan, O. L.-H. Lai, K. Krishnamurthy, and Y. M. Han, Biomedicines **10**, 1132 (2022).
[105]J. Bjerkan, J. Kobal, G. Lancaster, S. Šešok, B. Meglič, P. V. E. McClintock, K. Budohoski, P. Kirkpatrick, and A. Stefanovska, Brain Commun. **6** (2024).
[106]A. Arinyo-i-Prats, V. J. López-Madrona, and M. Paluš, NeuroImage **292**, 120610 (2024).
[107]M. Günther, J. W. Kantelhardt, and R. P. Bartsch, Front. Netw. Physiol. **2**, 893743 (2022).
[108]M. G. Crosby, Proc. IRE **25**, 472 (1937).
[109]W. Mumtaz, S. Rasheed, and A. Irfan, Biomed. Signal Process. Control **68**, 102741 (2021).

Chapter 3

Aging affects the phase coherence between spontaneous oscillations in brain oxygenation and neural activity

This research is published in Brain Research Bulletin.

Bjerkan, J., Lancaster, G., Meglič, B., Kobal, J., Crawford, T. J., McClintock, P. V. E. & Stefanovska, A. Aging affects the phase coherence between spontaneous oscillations in brain oxygenation and neural activity. *Brain Res. Bull.* **201,** 110704 (2023)

Brain Research Bulletin 201 (2023) 110704

Contents lists available at ScienceDirect

Brain Research Bulletin

journal homepage: www.elsevier.com/locate/brainresbull

Research report

Aging affects the phase coherence between spontaneous oscillations in brain oxygenation and neural activity

Juliane Bjerkan [a], Gemma Lancaster [a], Bernard Meglič [b], Jan Kobal [b], Trevor J. Crawford [c], Peter V.E. McClintock [a], Aneta Stefanovska [a,*]

[a] Lancaster University, Department of Physics, LA1 4YB, Lancaster, United Kingdom
[b] University of Ljubljana Medical Centre, Department of Neurology, 1525, Ljubljana, Slovenia
[c] Lancaster University, Department of Psychology, LA1 4YF, Lancaster, United Kingdom

ARTICLE INFO

Keywords:
Neurovascular unit
Aging
Neurovascular dynamics
EEG
FNIRS
Wavelet analysis

ABSTRACT

The risk of neurodegenerative disorders increases with age, due to reduced vascular nutrition and impaired neural function. However, the interactions between cardiovascular dynamics and neural activity, and how these interactions evolve in healthy aging, are not well understood. Here, the interactions are studied by assessment of the phase coherence between spontaneous oscillations in cerebral oxygenation measured by fNIRS, the electrical activity of the brain measured by EEG, and cardiovascular functions extracted from ECG and respiration effort, all simultaneously recorded. Signals measured at rest in 21 younger participants (31.1 ± 6.9 years) and 24 older participants (64.9 ± 6.9 years) were analysed by wavelet transform, wavelet phase coherence and ridge extraction for frequencies between 0.007 and 4 Hz. Coherence between the neural and oxygenation oscillations at ~ 0.1 Hz is significantly reduced in the older adults in 46/176 fNIRS-EEG probe combinations. This reduction in coherence cannot be accounted for in terms of reduced power, thus indicating that neurovascular interactions change with age. The approach presented promises a noninvasive means of evaluating the efficiency of the neurovascular unit in aging and disease.

1. Introduction

A healthy brain requires sufficient supplies of glucose and oxygen to function properly, and any impairment of the vasculature will affect their delivery to the target cells. The brain and cardiovascular system work closely together in a common endeavour to match energy supply to demand. Their intimate relationship is reflected in the concept of the neurovascular unit (NVU) (Iadecola, 2017), corresponding to consideration of the neurons, astrocytes, microglia, pericytes, endothelial cells and basement membrane as a single functioning entity. In the process of aging, the brain undergoes structural (Cox et al., 2016; Fjell and Walhovd, 2010) and functional changes, and so also does the cardiovascular system. Knowledge of healthy aging can aid understanding of the mechanisms of pathological aging, as age is the biggest risk factor in the etiology of neurodegenerative diseases, such as Alzheimer's disease which appears to include accelerated aging of the brain (Gonneaud et al., 2021).

The neurophysiological changes in the aging brain have been well documented through measures of its electrical and magnetic activities using electroencephalogram (EEG) and magnetoencephalogram (MEG) recordings, respectively (Hashemi et al., 2016; Al Zoubi et al., 2018; Hoshi and Shigihara, 2020; Babiloni et al., 2006; Dustman et al., 1999; Vysata et al., 2014; Scally et al., 2018). Both the power of brain waves, and the functional connectivity patterns in the brain, have been shown to change with age.

The cardiovascular system is a closed system of vessels, where blood circulates, cyclically pumped by the heart and oxygenated by the lungs. It is well known that heart rate variability (Agelink et al., 2001) decreases with aging, whereas the blood pressure (Pinto, 2007; Peters et al., 2015) increases. This has been linked to altered cognition in healthy people below 70 years old (Veldsman et al., 2020), thereby indicating the importance of a well-functioning cardiovascular system for brain health. More local to the brain, changes in cerebral blood oxygenation can be measured non-invasively using functional Near-Infrared Spectroscopy (fNIRS). Several investigations have found differences in oxygenation dynamics between younger and older

* Corresponding author.
E-mail address: aneta@lancaster.ac.uk (A. Stefanovska).

https://doi.org/10.1016/j.brainresbull.2023.110704
Received 25 April 2023; Received in revised form 3 July 2023; Accepted 11 July 2023
Available online 13 July 2023

Table 1
Participants' data. Age, body mass index (BMI), systolic blood pressure (sBP) and diastolic blood pressure (dBP) are given as means ± standard deviations. p is obtained from the Wilcoxon rank-sum test between the two groups.

	N	Age (yrs)	Sex	BMI (kg m^{-2})	sBP (mmHg)	dBP (mmHg)
Younger	21	31.1 ± 6.9	11 F/10 M	23.6 ± 3.6	122 ± 18	79 ± 9.8
Older	24	64.9 ± 6.9	15 F/9 M	26.9 ± 3.0	136 ± 17	83 ± 11
p	–	1.02×10^{-8}	–	0.002	0.004	0.067

subjects, both in the resting state and during task activation (Yeung and Chan, 2021). In elderly subjects, the power and connectivity in the 0.052–0.145 Hz range are reduced compared to younger ones (Li et al., 2013; Wang et al., 2016). This frequency range is associated with vasomotion, the mechanism through which smooth muscle cells modulate the blood flow, by altering the diameter of the blood vessels (Intaglietta, 1990; Salerud et al., 1983; Stefanovska, 2007). However, despite general awareness that all components of the NVU are individually affected by aging (Li et al., 2019), no quantitative method is available for non-invasive assessment of the function of the NVU as a whole. Nor has any study to date investigated directly whether changes with aging occur in the interactions between the dynamics of blood oxygenation and neural activity.

The purpose of the present study is to evaluate the efficiency of interaction between the vascular and neural systems within the brain. We aim to investigate, on a macroscopic scale, the dynamics of oxygen supply and the dynamics of the neurons including the signalling of their needs. We do so by determination of the coherence between spontaneous oscillations in blood oxygenation (measured using fNIRS) and electrical activity (measured simultaneously using EEG). Their coherence quantifies their strength of interaction, which can be taken as a proxy for the efficiency of the NVU. We hypothesise that it will be altered in the aging population due to the structural and functional changes in the brain. Because resting-state networks spanning several brain regions have been observed in both EEG and fNIRS studies (Yeung and Chan, 2021; Mesquita et al., 2010; Custo et al., 2017), and because fNIRS and EEG have previously been found to exhibit long range correlations (Nikulin et al., 2014), we determine the coherence between all signal pairs. As the cerebrovascular system depends on the systemic support of the cardio-respiratory system, we also recorded heart rate and respiration. This allows us to consider the physiological origin of the much-discussed ∼ 0.1 Hz oscillations (Nita et al., 2004; Voipio et al., 2003; Nikulin et al., 2014; Watson, 2018; Rayshubskiy et al., 2014; Noordmans et al., 2018).

To follow the non-linear and time-variable dynamics over many time-scales and to allow for resolution in both time and frequency, we have employed wavelet phase coherence (WPC) (Bandrivskyy et al., 2004) and a novel method of tracing the instantaneous phases of oscillations by ridge extraction (Iatsenko et al., 2016). WPC is more resilient against artifacts than amplitude-based coherence measures and, in addition, provides for logarithmic frequency resolution. Given that frequency and time are inversely related, this makes the method more suitable than those with linear resolution, such as the Fourier transform, and is particularly advantageous when studying low frequency oscillations.

By comparing the analyses of measurements on groups of younger and older participants in the resting state, we seek evidence for changes in the phase interactions between their neural and cardiovascular systems, and thus for age-related changes in the efficiency and health of the NVU.

2. Methods

2.1. Participants

All participants provided written informed consent, and the study was conducted in accordance with the Declaration of Helsinki. The study protocols were approved by the Commission of the Republic of Slovenia for Medical Ethics and/or by the Faculty of Science and Technology Research Ethics Committee (FSTREC) at Lancaster University. The study involved the recording and analysis of data from 45 participants. The younger group consisted of 21 participants between 20 and 39 years. The older group consisted of 24 participants between 56 and 77 years. Participant details are provided in Table 1. The exclusion criteria were neurodegenerative disorders, clinically diagnosed neurological disorders, psychiatric disease and/or diabetes. Three participants were excluded because they fell asleep during the measurements, and one participant was excluded on account of poor probe contact resulting in noisy data.

Based on two groups with 21 and 24 participants, a statistical power of 0.8 and a significance level of 0.05 we expected, at minimum, to reliably detect effects of size 0.92, which were considered large effects (Faul et al., 2007). Effect size was calculated using Cohen's d (Cohen, 1988). Further details are reported in the Supplementary Material (SM) Sec. 2.

2.2. Data acquisition

Data were recorded in quiet rooms at the Neurological Clinic, Ljubljana, Slovenia or in the Nonlinear and Biomedical Physics Lab, Physics Department, Lancaster University, Lancaster, UK (see SM, Sec. 5). The same system was used in both locations. Each participant was seated in a comfortable chair and had their eyes open during the approximately 30 min of measurement. No fixation points were used. An electroencephalogram (EEG) was recorded at 1 kHz using a 16-channel system (V-Amp, Brain Products, Germany). Simultaneously, functional Near-Infrared Spectroscopy (fNIRS) measurements detected changes in oxygenated hemoglobin. Note that we refer to these measurements as "brain oxygenation" although, strictly speaking, we investigate brain oxygenation *dynamics*, because fNIRS does not measure absolute hemoglobin concentrations. An 8-source/8-detector LED system (NIRScout, NIRx, Germany) was used and the recordings were made at 31.25 Hz. The probe layout is shown in Fig. 1B.

The heart rate was evaluated from an electrocardiogram (ECG), obtained with a bipolar precordial lead similar to the standard D2 lead. To maximize R-peak sharpness, electrodes were positioned on the right and left shoulders and over the lower left rib. The respiration rate was evaluated from the respiratory effort recorded using a belt wrapped around the participant's chest, fitted with a Biopac TSD201 Respiratory Effort Transducer (Biopac Systems Inc., CA, USA). Both were sampled at 1.2 kHz using a signal conditioning system (Cardiosignals, Institute Jožef Stefan, Slovenia). Fig. 1A depicts signals from a participant in the younger group.

2.3. Data preparation and preprocessing

Signal processing was done in MATLAB, and the analysis was completed using the toolbox MODA (Newman et al., 2018) to implement the methods illustrated by Clemson et al. (2016). A continuous 25-minute signal, mostly free of movement artifacts, was extracted for each participant. The data were detrended by subtracting a best-fit third-order polynomial, and bandpass filtered in the range 0.007–4 Hz. The preprocessing procedures were as described by Iatsenko et al. (2015a). To reduce computational load, the EEG, ECG and respiration signals

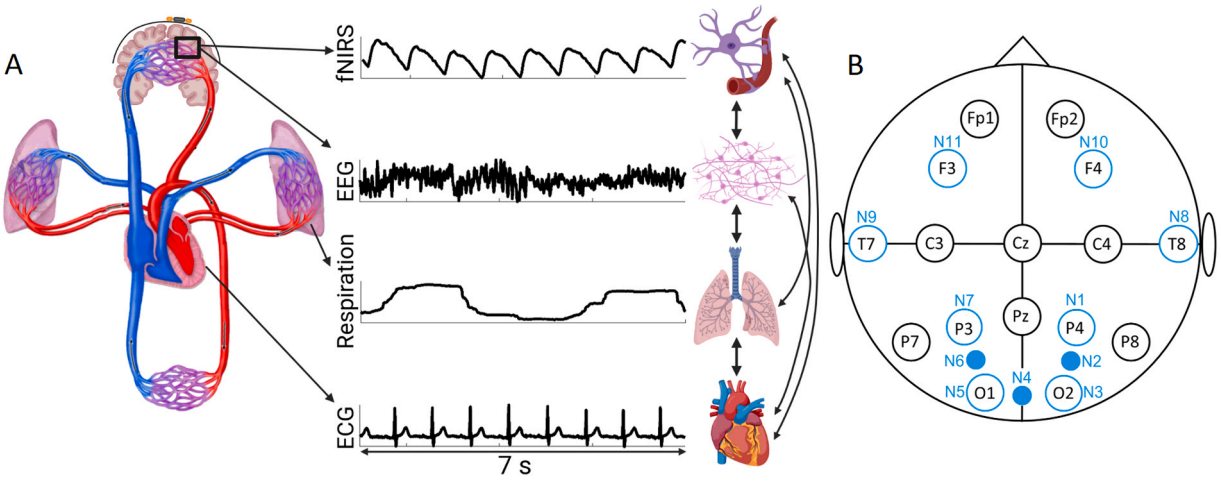

Fig. 1. A) The cardiovascular system and brain, illustrated schematically with a zoom to show the neurovascular unit (NVU), and examples of recorded signals: fNIRS to capture brain oxygenation, EEG to capture the electrical activity of the brain, and respiration and ECG to capture systemic effect of the blood circulation. The vertical arrows show the combinations for the phase coherences investigated. B) Sketch illustrating the 16 EEG electrode (black) and 11 fNIRS probe (light blue) placements. Note that 8 EEG and fNIRS probes (indicated with blue open circles) are co-located. Created using BioRender.com.

Table 2
Summary of the methods and parameters used in the analyses. IHR and IRR – instantaneous heart and respiratory rates (frequencies) respectively; γIF – instantaneous frequency of oscillations in gamma band; γIP – instantaneous power of oscillations in gamma band; WT – wavelet transform; WFT – windowed Fourier transform; f_0 – frequency resolution f_s – sampling frequency.

Analysis	Method	Parameters
Heart rate	Peak detection and ridge extraction	WT: $f_0 = 2$ $f \in [0.6,1.7]$ $fs = 100$ Hz
Respiration rate	Peak detection and ridge extraction	WT: $f_0 = 1$ $f \in [0.1,0.6]$ $fs = 100$ Hz
γ instantaneous frequency	Ridge extraction	WT: $f_0 = 5$ $f \in [20,30]$ $fs = 142$ Hz
γ instantaneous power	Ridge extraction	WT: $f_0 = 5$ $f \in [20,30]$ $fs = 142$ Hz
IHR and IRR power	Time-averaged WT	WT: $f_0 = 1$ $f \in [0.007,2]$ $fs = 20$ Hz
EEG wavelet power	Time-averaged WT	WT: $f_0 = 1$ $f \in [0.007,4]$ $fs = 31.25$ Hz
fNIRS wavelet power	Time-averaged WT	WT: $f_0 = 1$ $f \in [0.007,4]$ $fs = 31.25$ Hz
Power of γ instantaneous frequency and power	Time-averaged WT	WT: $f_0 = 1$ $f \in [0.007,4]$ $fs = 142$ Hz
fNIRS-EEG coherence	Wavelet phase coherence	WT: $f_0 = 1$ $f \in [0.007,4]$ $fs = 31.25$ Hz
fNIRS-fNIRS coherence	Wavelet phase coherence	WT: $f_0 = 1$ $f \in [0.007,4]$ $fs = 31.25$ Hz
EEG-EEG coherence	Wavelet phase coherence	WT: $f_0 = 1$ $f \in [0.007,4]$ $fs = 20$ Hz WFT:$f \in$ [4,48] $fs = 142$ Hz
IHR-fNIRS, IRR-fNIRS, Respiration-fNIRS, IHR-EEG, IRR-EEG and Respiration-EEG coherence	Wavelet phase coherence	WT: $f_0 = 1$ $f \in [0.007,2]$ $fs = 20$ Hz
γIF-fNIRS and γIP-fNIRS coherence	Wavelet phase coherence	WT: $f_0 = 1$ $f \in [0.007,4]$ $fs = 31.25$ Hz

were each downsampled using a moving average. The resultant frequencies are listed in Table 2. The artefact in the EEG signals due to cross-talk between brain electrical activity and the electrical activity of the heart was extracted using nonlinear mode decomposition (Iatsenko et al., 2015b).

As we do not have individual 3D head geometry data, such as MRI scans, and as we use a relatively low-density EEG set-up, we chose to do the analysis on the sensor level rather than the source level. This is because a lack of geometrical data coupled with a low-density of EEG sensors is known to result in a low accuracy of source localisation (Brodbeck et al., 2011; Michel and Brunet, 2019). Increasing the number of electrodes would have improved spatial localisation to some extent, but would also have increased the set-up time for the experiment, constituting a limiting factor in clinical applications.

2.4. Time-frequency analysis

Time-frequency analysis provides information on how the frequency of an oscillation changes through time. We used the continuous wavelet transform (WT) and, at each discrete time t_n and frequency ω_k, obtained a complex number $X_{k,n} = a_{k,n} + ib_{k,n}$. From this a phase Φ and amplitude A were found:

$$\Phi_{k,n} = \arctan\left(\frac{b_{k,n}}{a_{k,n}}\right),$$

$$A_{k,n} = \left|X_{k,n}\right|.$$

Power was found by squaring the amplitude. The WT has a logarithmic frequency scale. When analysing low frequency oscillations, the WT therefore provides better frequency resolution than, for example, the windowed Fourier transform. After taking the transforms, the time-averaged WT power spectra were calculated for each of the 11 fNIRS signals, and for the instantaneous heart/respiration rates. The Morlet wavelet was used for the WT. An overview of the parameters used, including the frequency resolution and sampling frequencies, is provided in Table 2.

2.5. Wavelet phase coherence

Wavelet phase coherence (WPC), introduced by Bandrivskyy et al. (2004), is used to evaluate how consistent the phase difference between two oscillations remains over time. The phase coherence is evaluated at

each frequency, and the values of coherence and phase difference are originally evaluated at each time.

The WPC does not assume stationarity of the time-series and is particularly suitable when the non-stationarity comes from a time-variation of the characteristic frequencies. The logarithmic frequency resolution of WPC is particularly suitable for signals with a large span of characteristic frequencies. It provides a model-free approach that does not assume the existence of an underlying stochastic process. Taken together with wavelet analysis, it provides information about potential oscillatory modes contributing to the measured signal, and their degree of coordination and interaction. However, it does not provide information about direction of interaction, nor about couplings between oscillatory modes. For the evaluation of directional couplings one may use dynamical Bayesian inference, Granger causality, or similar information- or permutation-based methods Clemson et al. (2016), Stankovski et al. (2017, 2019).

The phase coherence is evaluated at each frequency and takes a value between 0 and 1. If the phase difference remained constant throughout the whole length of the signals at a certain frequency, the phase coherence value would be 1 at that frequency. As the measure only depends on the phase difference, it is independent of the amplitudes of the oscillations. The phase difference between signals 1 and 2 at time t_n and frequency ω_k is

$$\Delta\Phi_{k,n} = \Phi^{(2)}_{k,n} - \Phi^{(1)}_{k,n}.$$

The wavelet phase coherence is then defined as

$$C_\Phi(\omega_k) = \sqrt{\langle \cos\Delta\Phi_{k,n}\rangle^2 + \langle \sin\Delta\Phi_{k,n}\rangle^2},$$

where $\langle \cos\Delta\Phi_{k,n}\rangle$ and $\langle \sin\Delta\Phi_{k,n}\rangle$ are averaged in time.

We assessed the fNIRS–fNIRS pairwise coherence (for all permutations of the 11 fNIRS probes), as well as the EEG–fNIRS, instantaneous heart rate (IHR)–respiration, IHR–EEG, IHR–fNIRS, respiration–fNIRS, respiration–EEG, instantaneous respiration rate (IRR)–fNIRS, and IRR–EEG coherences.

2.6. Frequency bands

The sampling frequency of the fNIRS is 31.25 Hz, and so the Nyquist frequency would be $\sim$ 15 Hz. If the oscillations had constant frequencies, and there were no harmonics, then 15 Hz would have been the upper limit for investigation of oscillatory modes and their interactions in the fNIRS signal. Furthermore, fNIRS is known not to contain oscillations faster than the cardiac oscillation ($\sim$ 1 Hz). Consistent with this, we did not see any significant power above the cardiac frequency. So, we selected the upper frequency limit to be 4 Hz for the fNIRS and fNIRS-EEG interactions. The EEG signal was sampled at 1000 Hz, but we analysed it only up to 48 Hz, which allowed for investigation of the slow γ oscillatory modes. The other reason for our 48 Hz limit was to avoid the effect of the 50 Hz notch filter used by the monitoring system. For both the EEG and fNIRS, the lower frequency limit was set to 0.007 Hz.

Table 3
Frequency ranges used in the analysis (Stefanovska, 2007). The cardiac and δ ranges are slightly changed from past studies (see text).

Name	Frequency range (Hz)
Endothelial (V)	0.007–0.021
Neurogenic (IV)	0.021–0.052
Myogenic (III)	0.052–0.145
Respiratory (II)	0.145–0.6
Cardiac (I)	0.6–1.7
Delta (δ)	1.7–4
Theta (θ)	4–7.5
Alpha (α)	7.5–14
Beta (β)	14–22
Gamma (γ)	22–48

The power and coherence values were divided into the conventional frequency bands (Table 3) (Stefanovska, 2007), within each of which an average value was calculated. The first five bands, representing the characteristic frequency intervals of the cardiovascular system (Stefanovska, 2007), strongly overlap the slow oscillations in EEG (Buzsáki and Draguhn, 2004). The last five bands are the traditional EEG frequency bands. After obtaining single power/coherence values in each band for each subject, the two groups were compared.

In previous studies of cardiovascular dynamics, the cardiac band was defined as 0.6–2 Hz (Stefanovska, 2007). In the present case, however, we also need to take account of EEG dynamics which potentially overlap the cardiac band. To separate the cardiac and δ bands, we therefore defined the cardiac band as 0.6–1.7 Hz and the δ band as 1.7–4 Hz. With the upper limit set to 1.7 Hz, the variation in heart rate is still accommodated.

The respiratory oscillations are manifested in the frequency interval 0.145–0.6 Hz. They can be detected even in the smaller vessels such as capillaries, as they generate pressure waves that propagate throughout the entire cardiovascular system (Stefanovska and Hožič, 2000).

The 0.052–0.145 Hz frequency interval is referred to as myogenic, and the neurogenic band is defined as 0.021–0.052 Hz. The origins of these two bands are still debated, with perceptions depending on whether interest is being focused on the vascular or cardiac regulation mechanisms (see discussion section). The neurogenic response is similar to the myogenic response in that it also depends on pressure changes, but additionally involves neuronal pathways.

The frequency intervals 0.007–0.021 Hz is called the NO-dependent endothelial frequency band, in view of evidence that NO-dependent endothelial activity manifests itself within this range (Kvandal et al., 2006; Stefanovska, 2007; Shiogai et al., 2010).

2.7. Heart and respiration rates

Time-series of instantaneous heart and respiration rates were obtained in two ways: by peak detection and by the ridge extraction method. Peak detection was performed in the time domain with a customised program in MATLAB that searched for R-peaks in the ECG signals or maxima in the respiration signal. The instantaneous frequencies were extracted in the time-frequency domain by the ridge extraction method (Iatsenko et al., 2016) using the toolbox MODA (Newman et al., 2018). Note that “instantaneous heart rate” (IHR) is a time-series of heart frequency values. It is traditionally referred to as heart rate variability when derived in the time domain from the intervals between heart beats. Similarly, “instantaneous respiration rate” (IRR) is a time-series of respiration frequency values, and is usually called respiration rate variability when derived from the time intervals between maxima. The instantaneous heart and respiration rate time series were in close agreement whether obtained either by the peak detection method or by the ridge extraction method, as shown in Fig. 2 for the IHR. The average heart and respiration rates were obtained from their respective time-series.

Because the time-series obtained with the ridge extraction method

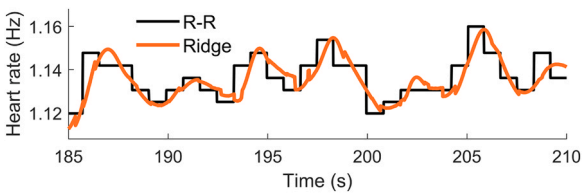

Fig. 2. Comparison of the IHR found by R-R peak detection with that found by ridge extraction. We use the lognormal wavelet (Iatsenko et al., 2015a) with a frequency resolution of 2 Hz. It has a better trade-off between time and frequency resolution than the Morlet wavelet.

are smooth functions, ready to use in time-series analysis, they were used in the wavelet and phase coherence analyses. Furthermore, the ridge extraction method is more appropriate for extracting IHR than the peak-detection method, as ridge extraction takes into account the whole ECG signal and not just the R-peaks, thus also capturing the effect of T-waves.

For the IHR, ridge extraction was applied to the WTs of ECG signals in the 0.6–1.7 Hz frequency range. The lognormal wavelet and a frequency resolution of 2 Hz were used for the WT. The sampling frequency of the IHR was the same as that of the ECG, and no interpolation was needed (Iatsenko et al., 2013). For the IRR, ridge extraction was applied to the WTs of respiration signals in the 0.1–0.6 Hz frequency range and with a frequency resolution of 1 Hz.

The standard deviation of the instantaneous rates (sd IHR and sd IRR), resulting in a single number in each case, was used to obtain a measure of their variability.

2.8. Frequency and amplitude modulation of the γ–band by low-frequency oscillations

From the EEG signals, the instantaneous frequency and power in the 20–30 Hz interval were obtained by ridge extraction (Iatsenko et al., 2016), and are referred to as a γ–instantaneous frequency and γ–instantaneous power time-series. Fig. 3 illustrates the procedure. The frequency resolution parameter was 5 Hz.

For the 8 locations where fNIRS and EEG sensors are co-located, the WPC was calculated between the γ–instantaneous frequency time-series and the fNIRS signal, to evaluate the effect of low frequency modulation on the oscillations in the γ–band. The WPC was also calculated between the γ–instantaneous power time-series and the fNIRS signal to evaluate the effect of low frequency modulation on the γ–band amplitude and the corresponding power.

2.9. Intersubject surrogates

To ensure that apparent coherence is statistically significant, we used intersubject surrogates (Lancaster et al., 2018). In addition to calculating coherence between the signals from one person, we calculated the apparent coherence between signals from different participants. This measure of coherence could not signify any underlying link between the signals, and was thus random. Inter-subject surrogates have previously been found suitable in the context of cardiorespiratory interactions Iatsenko et al. (2013). They are model-free and do not require stationary data.

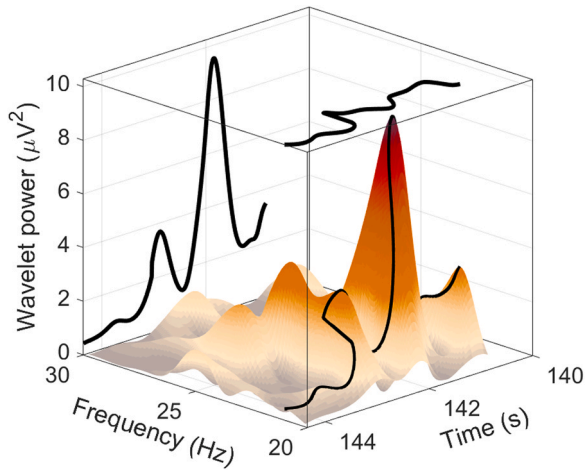

Fig. 3. γ–instantaneous frequency (projected onto the Frequency-Time plane) and γ–instantaneous power time-series (projected onto the Wavelet power-Time plane) as obtained by ridge extraction.

Based on 154 intersubject surrogates a surrogate threshold was set as the 95th percentile of all these coherences at each frequency. In the plots throughout the paper, only the effective coherence (i.e. coherence after subtracting the surrogate threshold) is shown, and it was the effective coherence that we used in testing for differences between the groups. Each subject and signal pair had an individual significance threshold to account for different spectral biases in the signals. Due to the lower number of complete oscillations at low frequencies, the likelihood of apparent coherence is increased. Hence, the surrogate threshold is high for low frequencies and, correspondingly, the measurement time is not long enough for a reliable study of oscillations in the endothelial band in the case of fNIRS–EEG coherence.

2.10. Group statistics

To assess population differences, the non-parametric two-sided Wilcoxon rank-sum test was applied, and differences are considered significant for $p < 0.05$. The data are presented as median values and violin plots (Hintze and Nelson, 1998). Additionally, for the fNIRS, EEG and fNIRS-EEG analyses, a Monte-Carlo permutation test (Maris and Oostenveld, 2007) was applied to check the reliability of the significance. From the total of 45 participants, 21 were randomly placed in one group and 24 in the other. The Wilcoxon rank-sum test was applied to test for differences between the permutated groups. After 16587 permutations the original p-value was compared with the values obtained with permutation. If the initial p-value was smaller than 95 % of the p-values obtained by permutations its significance was considered confirmed. Additional details are provided in Sec. 7 of the SM.

In time-frequency analysis, cluster-based permutation is a common method to correct for multiple comparisons (Maris and Oostenveld, 2007). As we averaged in both time and frequency before applying statistical tests, we would only see differences in power/coherence that were present over many time-points and frequencies. For the spatial aspect of multiple comparisons, the expected false discovery rate, quantifying how many null-hypotheses would be incorrectly rejected with $\alpha = 0.05$ *assuming all null-hypotheses were true*, was 0.8 for the EEG power analysis, 0.55 for the fNIRS power analysis, 6 for the EEG coherence analysis, 2.75 for the fNIRS coherence analysis and 8.8 for the fNIRS–EEG coherence analysis. From N trials, and assuming that there were no true differences, the probability of obtaining X or more positive findings was calculated from the binomial probability. This was used to assess the reliability of the results, keeping the multiple comparison problem in mind, as done in the literature (Montez et al., 2009; Nikulin et al., 2014).

2.11. Correlations

The correlations were found from the Spearman's rank-order correlation, which is a non-parametric alternative to the Pearson linear correlation. It tests for a monotonic relationship between two variables. The p-value was found from permutation distributions.

3. Results

Here we present the results of the analyses summarised in Table 2. These include the *central* oscillations of the cardiovascular system (evaluated from the instantaneous heart and respiration frequencies), and the *local* vascular and neural oscillations in the brain (from fNIRS and EEG). The analyses relate to the transport of nutrients to the NVU, quantifying its efficiency and the impact of ageing.

3.1. Central oscillations: heart and respiration rates

We first present the cardio-respiratory characteristics. This enables a consistency check with earlier results, and provides insight into systemic changes relevant to neurovascular interactions,

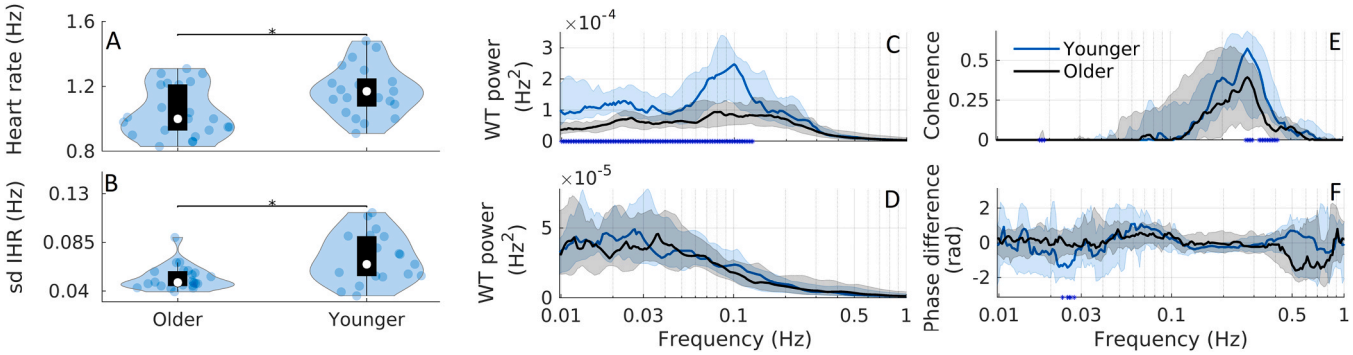

Fig. 4. Violin plots for A) heart rate, and B) its variability as quantified by the standard deviation (sd) of the IHR for the older and younger groups. The black stars indicate significant differences, $p < 0.05$, between groups. The white circles indicate the group medians. C) Time-averaged wavelet transform power of the IHR. D) Time-averaged wavelet transform power of the IRR. E) IHR–respiration coherence. F) Average phase differences between IHR and respiration, given in radians. A negative phase difference indicates that respiration is the leading signal. The blue and black lines are the median group power/coherence/phase difference, while the shaded areas show the 25–75th percentiles. Significant differences ($p < 0.05$) between the groups at particular frequencies are indicated by blue stars on the *x*-axis (causing effective thickenings of the axis).

Heart rates (older: 1.04 ± 0.16 Hz; younger: 1.17 ± 0.15 Hz) and sd IHR (older: 0.052 ± 0.011 Hz; younger: 0.070 ± 0.022 Hz) are significantly different between the groups ($p = 0.014$, $p = 0.005$), as shown in Fig. 4A,B. No significant difference is seen in the respiration rate (older: 0.23 ± 0.08 Hz; younger: 0.24 ± 0.05 Hz, $p = 0.300$), or sd IRR (older: 0.039 ± 0.009 Hz; younger: 0.045 ± 0.019 Hz, $p = 0.26$). The corresponding plots are shown in the SM Sec. 3.

IHR power is reduced in the older group in the 0.01–0.11 Hz range (see Fig. 4C). The IRR power is not significantly different between the groups (Fig. 4D).

Each group has significant IHR–respiration coherence in the respiratory band (see Fig. 4E; for the frequency band ranges, see Table 3). The younger group has significantly higher coherence around 0.3 Hz, compared to the older group. For both groups the IHR power and IHR–respiration coherence were shown not to differ significantly between males and females (see SM Sec. 6), consistent with earlier results (Iatsenko et al., 2013).

3.2. Interactions between instantaneous heart/respiration rates and brain oxygenation

The results presented here illustrate how the modulation of the heart and respiration rates is linked to the oxygenation of the brain. Fig. 5 shows the wavelet phase coherence between IHR and oxygenation, between IRR and oxygenation, and between the respiration signal and oxygenation, all at N5. For data from the other fNIRS probes see SM Sec. 3. The SM also includes the IHR–EEG, respiration–EEG and IRR–EEG coherence.

There are systematic differences in coherence, with the older group tending to have lower coherence. This difference is statistically significant for coherence between IHR and oxygenation (Fig. 5A), and is particularly pronounced in the myogenic and respiratory bands. The same significant reduction of coherence with age is observed in coherence between the IHR and all other oxygenation signals apart from the two temporal ones, where the coherence is reduced only in the respiratory band. Interestingly, the phase difference between oxygenation and IRR/respiration/IHR is found to be negative in the respiratory band, meaning that brain oxygenation is the leading signal. This result is consistent for both age groups. In contrast, the phase difference in the myogenic region is slightly positive, indicating that the brain oxygenation lags.

3.3. Brain oxygenation oscillations

Here we present the power calculated for all 11 fNIRS signals, and coherence between all possible signal combinations. The positions of the probes are shown in Fig. 1B.

The myogenic power (0.052–0.145 Hz frequency interval) in 8 of the 11 channels is significantly lower in the older group (Fig. 6A,B). A lower power is also found in the endothelial, neurogenic and respiratory bands (Fig. 6B), but the differences are statistically significant for fewer probes. In the endothelial band there are 3 fNIRS probes with a significant difference between the groups, while this number is 4 in the respiratory band, and 1 in the neurogenic and cardiac bands. The chance of obtaining 3 positive outcomes out of 11 is 1.5 % when there were no true differences, while the chance of obtaining 1 positive outcome out of 11 is

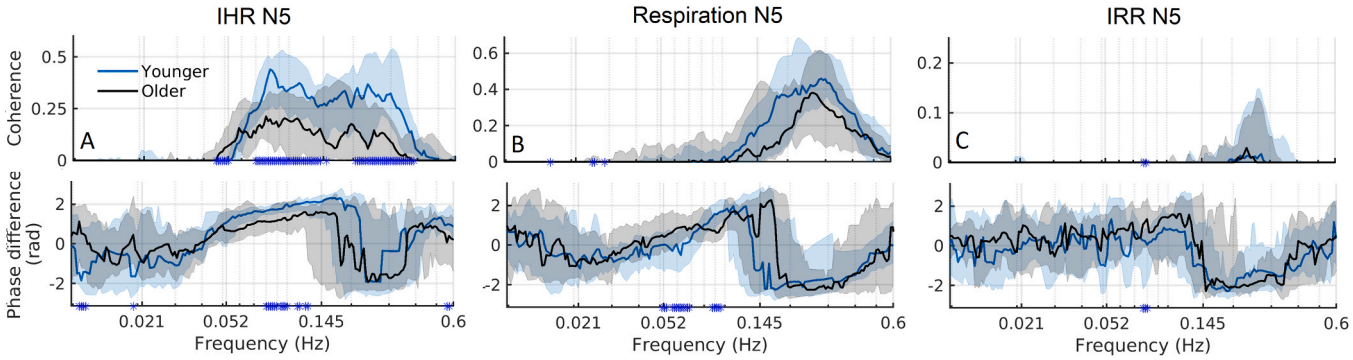

Fig. 5. Coherence (upper panels) and phase difference (lower panels) between A) IHR and N5, B) respiration rate and N5, C) IRR and N5. Note that the *y*-axes differ. See Fig. 1 for the locations of the EEG electrodes and fNIRS probes. The blue and black lines represent the younger and older group medians, respectively, while the shaded areas show the 25–75th percentiles. Significant group differences at particular frequencies are indicated by blue stars on the *x*-axis. Phase differences are given in radians, and a negative value indicates that N5 is the leading signal.

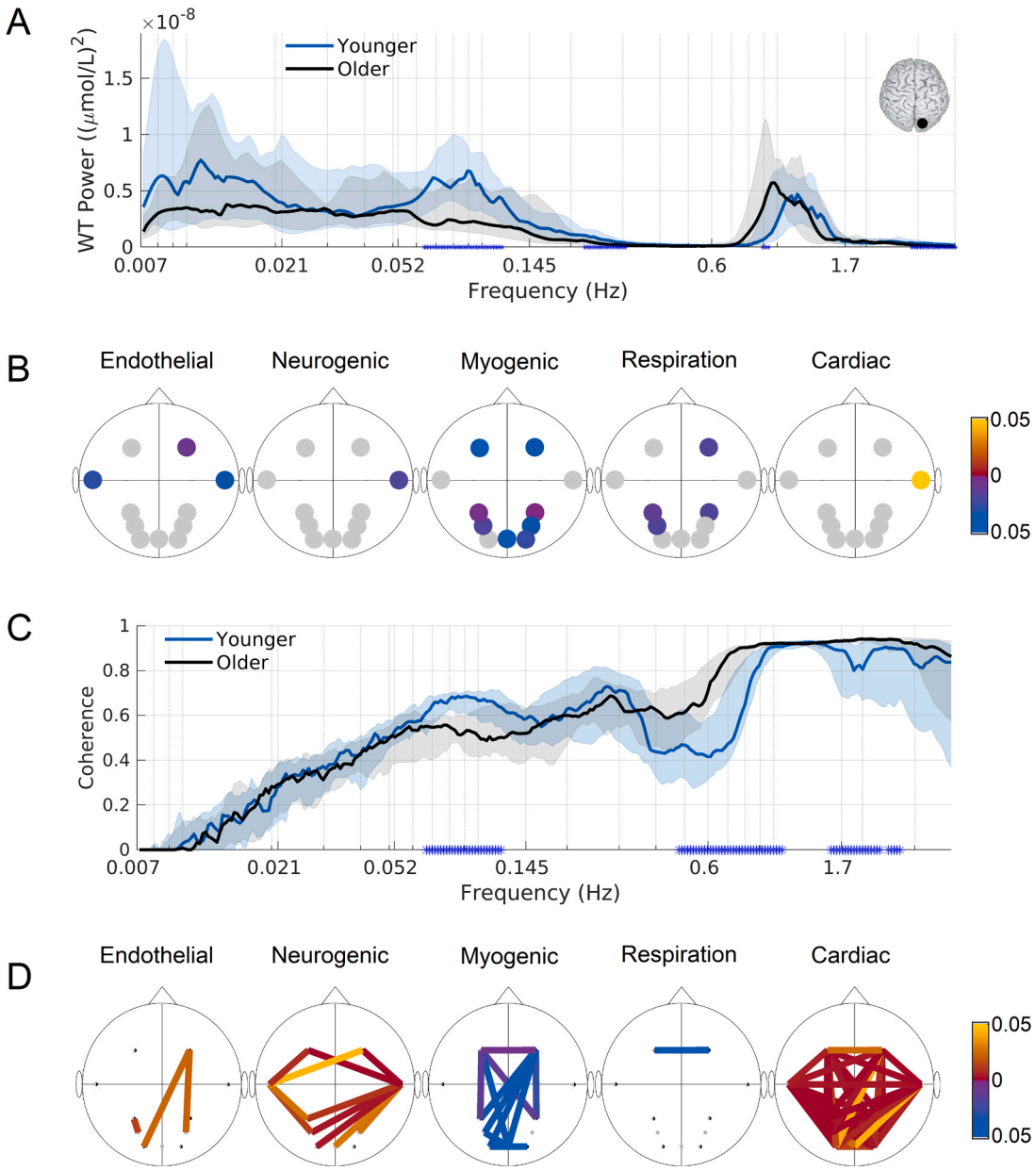

Fig. 6. fNIRS power and coherence. A) Time-averaged power spectra for N3. B) *p*-values indicating significant group differences between the powers in the frequency bands. Blue (yellow) indicates that the power is higher in the younger (older) group. C) Coherence between N11 and N7 (see Fig. 1 for locations). The blue and black lines are the median group coherences, while the shaded areas show the 25–75th percentiles. Significant differences between the groups at particular frequencies are indicated by blue stars on the *x*-axis. D) *p*-values indicating a significant group difference between the coherence in the frequency bands. Blue (yellow) indicates that the coherence is higher in the younger (older) group. For the frequency intervals see Table 3, and for the probe lay-out see Fig. 1.

43 % when there were no true differences.

Significantly lower myogenic coherence in the older participants is found in 12 fNIRS signal combinations: across the frontal-parietal signals, the frontal signals and the occipital signals (Fig. 6C,D). In the neurogenic band significantly higher coherence in 12 fNIRS combinations (mainly from the temporal probes) is observed in the older group. In the cardiac band in 50 of 55 combinations coherence is also significantly higher in the older group. The differences are found between the frontal-parietal, frontal-occipital and temporal signals. In the endothelial band coherence in 3 combinations is significantly higher in the older group, while in the respiratory band coherence in only one combination is significantly higher in the younger group. The chance of obtaining 12 positive outcomes out of 55 is 0.0014 % when there were no true differences, while the chance of obtaining 3 positive outcomes out of 55 is 52 %.

Brain oxygenation for males and females is summarised in Sec. 6 of the SM. The older male group has higher myogenic power at probes 1 and 9 compared to the older female group, while the older female group has higher myogenic coherence than the older male group in 7 signal combinations.

3.4. Brain neuronal activity evaluated by EEG

The EEG power and coherence are consistent with previous results (Meghdadi et al., 2021; Vysata et al., 2014; Scally et al., 2018; Moezzi et al., 2019; Richard Clark et al., 2004), and are summarised in the SM Sec. 4.

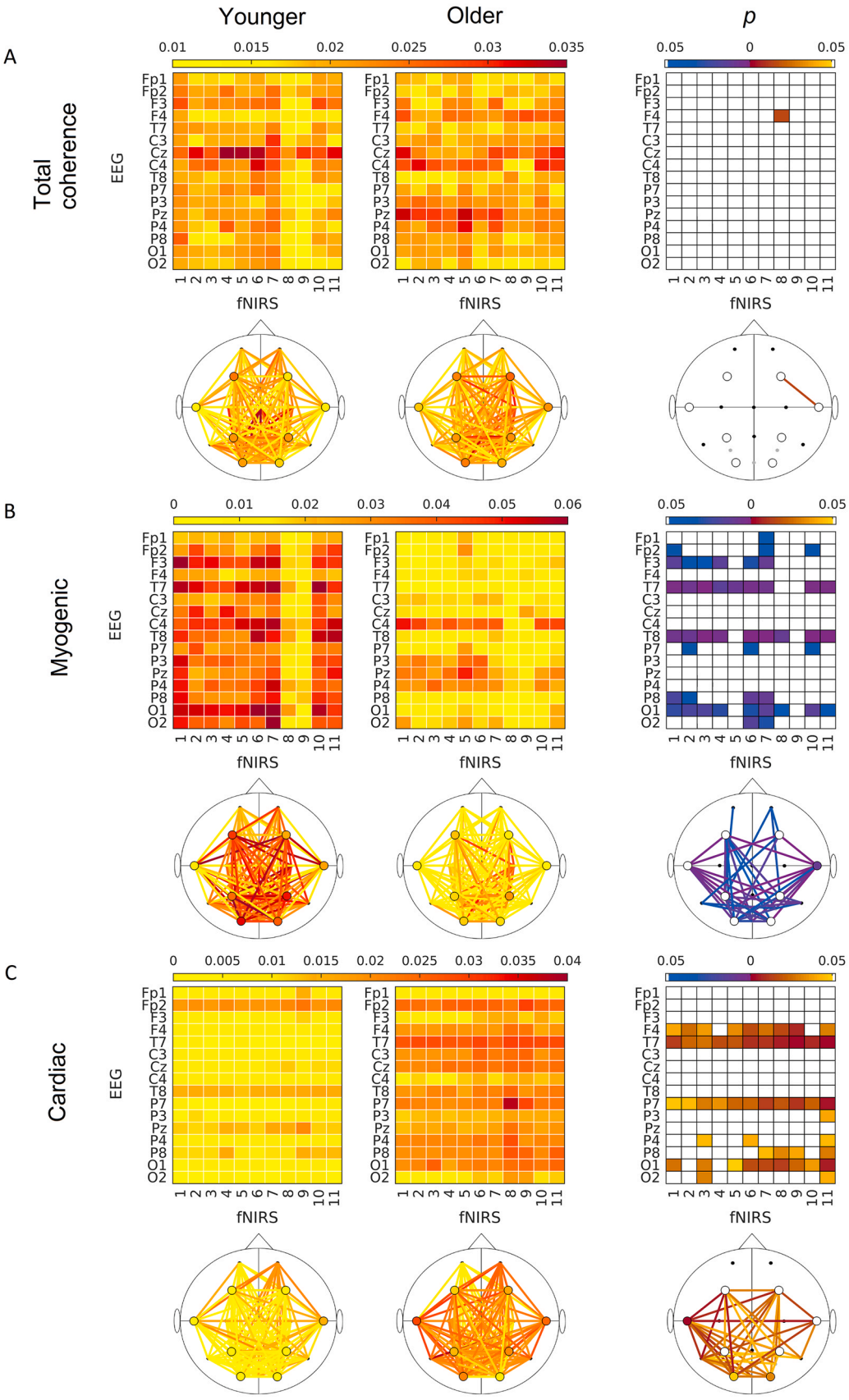

Fig. 7. A) Group median fNIRS–EEG coherence averaged over the frequency band 0.021–1.7 Hz. The results for the younger group (left) are compared with those for older group (middle) and *p*-values indicating a significant difference between the groups are shown on the right. Blue (yellow) coding indicate that coherence is higher in the younger (older) group. B) Same as for A but for the myogenic band. C) Same as for A but for the cardiac band. For the frequency intervals see Table 3, and for the probe lay-out see Fig. 1.

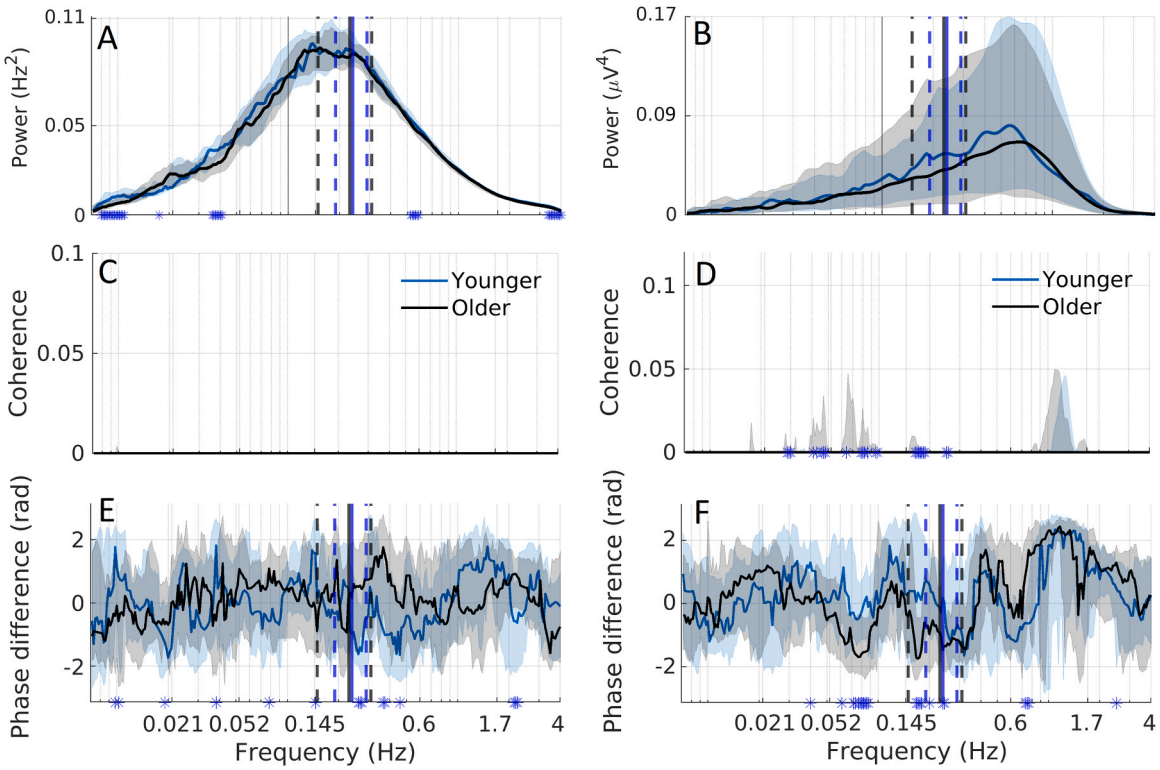

Fig. 8. Comparisons between the older and younger groups related to frequency and amplitude modulation in the EEG γ-interval. Median power of the A) γ–instantaneous frequency time-series and B) γ–instantaneous power time-series. C) Median coherence between fNIRS and the γ–instantaneous frequency time-series. D) Median coherence between fNIRS and γ–instantaneous power time-series. E) Phase difference between fNIRS and the γ–instantaneous frequency time-series. F) Phase difference between fNIRS and the γ–instantaneous power time-series. The blue and black lines are the median group coherences, while the shaded areas show the 25–75th percentiles. Significant differences between the groups at particular frequencies are indicated by blue stars on the *x*-axis. The blue and black solid vertical lines indicate the average respiration rates for the younger and older group, while the dashed lines indicate the standard deviations. Both fNIRS and EEG signals are from location O1.

3.5. Coherence between neuronal activity and brain oxygenation

The coherence between neuronal activity, as evaluated by EEG, and brain oxygenation, as evaluated by fNIRS, differs significantly between the groups, in both the myogenic and cardiac bands (Fig. 7B,C). In the myogenic band, the coherence is lower in the older group in 46/176 probe combinations and the decrease does not seem confined to any specific areas. However, both groups have low myogenic coherence in the two temporal fNIRS probes (N8 and N9). In contrast, the coherence in the cardiac band is higher in the older group in 50/176 probe combinations. The chance of having 46 or more positive findings out of 176 is 1.2×10^{-18} % assuming there were no true differences. Further information is provided in the SM. It consists of neurogenic and respiratory coherence (Fig. 23), the coherence plots of all 176 fNIRS-EEG combinations (Sec. 10), and the results divided by sex (Sec. 6).

3.6. Frequency and amplitude modulation of the γ–band by low-frequency oscillations

Here we show analysis of possible amplitude and phase modulation of γ–band oscillations by low-frequency oscillations. There is non-zero power for both the γ–instantaneous frequency and γ–instantaneous power time-series between 0.007 and 4 Hz (Fig. 8A, B) for both groups indicating the existence of modulation. The coherence between oxygenation and these time-series, and the phase shifts for both instances, are shown in Fig. 8C–F for the signals measured at location O1. For the remaining locations, see the SM Sec. 11. For the γ–instantaneous frequency time-series the coherence is zero for all frequencies in the interval 0.007–4 Hz. For the γ–instantaneous power time-series the median coherence is zero, but there is evidence of some significant effective coherence (Fig. 8D). For the oxygenation–power there is a negative phase shift for the older group around 0.06–0.08 Hz (Fig. 8F),

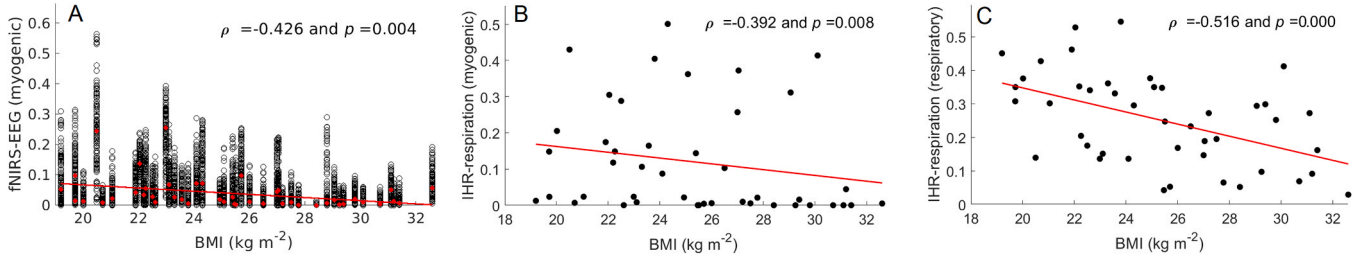

Fig. 9. Spearman correlations between A) BMI and fNIRS–EEG coherence in the myogenic band, B) BMI and IHR–respiration coherence in the myogenic band, and C) BMI and IHR–respiration coherence in the respiratory band. In A) the black circles show the coherence values between fNIRS–EEG combinations (176 combinations per participant), while the red crosses show the median coherence for each participant. The correlation is found between the median coherence values and BMI.

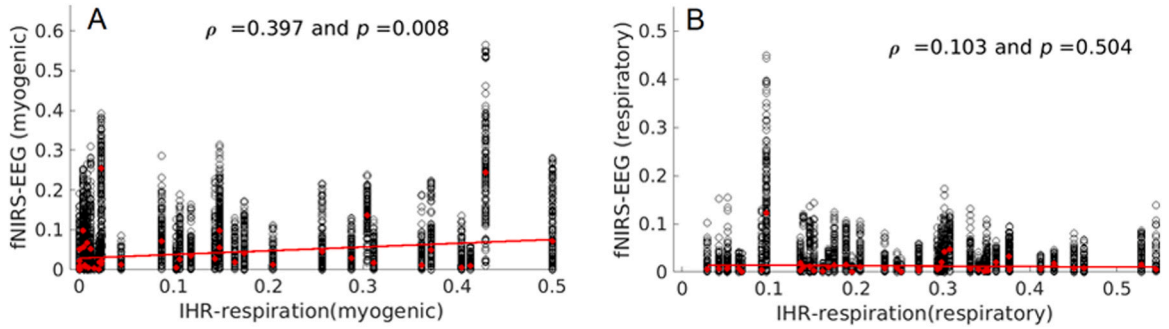

Fig. 10. Spearman correlations between A) IHR–respiration coherence in the myogenic band and fNIRS–EEG coherence in the myogenic band, B) IHR–respiration coherence in the respiratory band and fNIRS–EEG coherence in the respiratory band. The black circles show the coherence values between fNIRS–EEG combinations (176 combinations per participant), while the red crosses show the median coherence for each participant. The correlation is found between the median coherence values and IHR–respiration coherence.

which is significantly different between the groups in 5/8 probe combinations. A negative phase difference indicates that the oxygenation is lagging.

3.7. Correlations

BMI is negatively correlated with neurovascular coherence in the myogenic band, IHR–respiration coherence in the respiratory band and IHR–respiration coherence in the myogenic band (Fig. 9A,B,C). The systolic blood pressure is also negatively correlated with neurovascular coherence in the myogenic band ($\rho = -0.435$, $p = 0.004$) and IHR–respiration coherence in the respiratory band ($\rho = -0.356$, $p = 0.022$) (SM Sec. 8).

As shown in Fig. 10 the neurovascular coherence in the myogenic band is correlated with the IHR–respiration coherence in the myogenic band ($\rho = 0.397$, $p = 0.008$), while this is not the case for the neurovascular coherence and the IHR–respiration coherence in the respiratory band ($\rho = 0.103$, $p = 0.504$).

4. Discussion

Based on 25-minutes signals recorded in participants in resting state and novel time-frequency analysis methods, our investigation of cardiovascular and neurovascular interactions reveals clear changes with aging. These are manifested through:

- Weakened 0.052–0.145 Hz coherence between the neural activity and brain oxygenation, reflecting reduced neurovascular interactions;
- Reduced coherence between instantaneous heart rate and brain oxygenation oscillations in the myogenic and respiratory frequency bands;
- Changes in the heart and respiration rates, and their coordination through respiratory sinus arrhythmia; and
- Altered brain oxygenation resting state networks in the brain.

We now discuss these changes in more detail.

4.1. Central oscillations: heart and respiration activity

Consistent with previous studies (Iatsenko et al., 2013), we found a decrease in the variability of the cardiac frequency with age, as quantified by the sd IHR. Additionally, the average resting cardiac frequency (heart rate) is higher in the younger group. We did not find a significant reduction with age in the respiratory frequency band of the IHR (in studies with linear frequency resolution and shorter recordings often referred to as the high frequency band, 0.15–0.4 Hz, linked to parasympathetic nervous activity (Agelink et al., 2001). The IHR power decreases with age in the myogenic frequency band, 0.052–0.145 Hz. We note here that when evaluated with linear frequency resolution, and based on shorter, usually 5-min recordings, this frequency interval is also referred to as the low frequency band, 0.04–0.15 Hz, and is linked to sympathetic nervous activity (Agelink et al., 2001).

Note that the low/high frequency bands strongly overlap the myogenic/respiratory frequency bands. Low heart rate and insignificantly different respiratory band power in elderly participants could reflect relatively preserved parasympathetic tone. However, the changed parasympathetic/sympathetic activity is not sufficient to account for the variability in heart rate, which is generated by a complex interplay of nervous activity, respiration, smooth muscle cells and other factors (Billman, 2011; Clemson et al., 2022). Reduced variability with aging has previously been demonstrated (Agelink et al., 2001; Geovanini et al., 2020; Shiogai et al., 2010), also with wavelet-based methods (Iatsenko et al., 2013).

A tendency for the IHR–respiration coherence to be lower in the older group reaches significance at around 0.3 Hz. We did not, however, find a significant change in the respiration rate or its variability, as evaluated by the sd IRR, so this is an unlikely explanation for the reduced coherence. The significant IHR–respiration coherence reflects respiratory sinus arrhythmia (RSA), which is modulation of the heart frequency by the amplitude of respiration (Yasuma and Hayano, 2004; Stefanovska and Bračič, 1999). Wavelet based methods have previously been applied to investigate RSA (Keissar et al., 2009; Iatsenko et al., 2013), and Iatsenko et al. (2013) found the peak coherence in the respiratory band to decrease with age, suggesting that RSA is more time-variable and weaker in elderly subjects.

Consistent with the previous studies the present results show that the two central pumps of the cardiovascular system, heart and lungs, and their coordination, mainly through RSA, are affected by aging.

4.2. Propagation of the central oscillations: instantaneous heart/respiration rates and oxygenation

Next we investigated the effect of aging on the propagation of cardiovascular oscillations to the brain. Systemic cardiovascular oscillations naturally impact brain oxygenation (Katura et al., 2006), and their propagation may be affected by age-related structural changes in blood vessels. We investigated this latter possibility by evaluating the phase coherence between the cerebral blood oxygenation and the time-series of instantaneous heart or respiration rates.

The IHR–oxygenation coherence is significantly reduced in the older group in the myogenic and the respiratory frequency bands, across all non-temporal sites (Fig. 5A). These changes in coherence are consistent across combinations, indicating that the changes are systemic. The elastic properties of the vessels are known to change with aging (Desjardins et al., 2014), which could affect the propagation of pressure

waves and therefore impact the myogenic response, causing reduced IHR–oxygenation coherence. This reduced coherence is attributable to the way in which smooth muscle cells respond to pressure changes. In mice, the myogenic response to pulsatile pressure in the middle cerebral arteries has been shown to decrease with age (Springo et al., 2015).

Systemic cardiovascular oscillations have been shown to affect the ~ 0.1 Hz oscillations in cerebral oxygenation: Katura et al. (2006) estimated that such effects could only account for less than half of the observed changes. Note, however, that the study investigated heart rate and arterial blood pressure, but did not consider respiration. Furthermore, it has been shown that the Granger causality from heart rate to oxyHb during head-up tilt (Song et al., 2015) at 45° decreased with age, which is in line with our findings of reduced coherence in the older group.

In the myogenic frequency band the phase difference between the oscillations in the time-series of IHR and fNIRS is positive, implying that in this frequency interval the oscillations in the IHR are preceeding the oscillations recorded by the fNIRS signal. This furthermore confirms that the myogenic oscillations are propagating to the brain. The shift is significantly reduced with ageing, suggesting that the pulse propagates with less resistance to the small vasculature of the brain, as discussed in more detail below in Sec. 4.3.

The phase difference between the same signals in the respiratory band is negative (see Fig. 5A), suggesting that oxygenation is the leading signal. The reduction in phase coherence might, therefore, reflect decreasing efficacy of brain oxygenation with age. However, the phase difference between the two signals in the respiratory band is not altered by ageing.

There is a tendency for the respiration–oxygenation coherence to decrease with age in the respiratory band (at location N5 ~ 0.3 Hz $p < 0.1$, in several locations $p < 0.05$): see Fig. 5B and Fig. 6 in the SM). The phase difference is negative and similar for both groups, suggesting that oxygenation is the leading signal. The high coherence between respiration and each of the oxygenation signals implies a systemic orchestration of cortical oxygenation in rhythm with breathing, an effect that is reduced in the older group. The phase difference, indicating which signal leads or lags the other, can be explained as follows:

1. *The oxygenation signal is leading.* Respiration is controlled by the brain stem, and voluntary respiration can also be controlled by the motor cortex. The brain then controls the respiration signal.
2. *The respiration signal is leading.* The period of an oscillation at 0.2 Hz is 5 s, and the period of an oscillation at 0.3 Hz is 3.3 s. This means that if the lag is longer than these times the phase difference might appear to be negative when, in reality, it is not. Zhang et al. (2019) found in mice that breathing rate is a key modulator of cerebral oxygenation, and that oxygenation was correlated with both the respiration rate and the phase of the respiration cycle, which was true across the brain. They found a time lag of around 1–3 s between respiration and PtO2 consistent with the transit time of blood from the lungs to the brain, which was similar for blood oxygenation too. What a similar lag would be in humans is not known, and the corresponding phase difference is therefore also not known. However, it might be the case that, although the respiration is actually leading the oxygenation, the latter is delayed by more than the time for one complete respiration cycle.

4.3. Brain oxygenation oscillations and their spatial coherence

The reduced myogenic power and reduced myogenic coherence between the frontal probes, between the frontal-parietal probes and between the occipital probes seen in the older participants (see Fig. 6A,B,C) indicate altered vascular resting state networks.

There is increased coherence in the cardiac band in the older group, in 50/55 fNIRS combinations (see Fig. 6C), and between fNIRS and EEG signals (see Fig. 7C). This could be explained by several factors, such as the increased radii of vessels in the microvasculature of older participants (Cox et al., 2016) and decreased microvascular density in older participants (Desjardins et al., 2014). While the total cerebral blood flow decreases with age, the pulsatile flow increases (Xu et al., 2017). It propagates through vessels that are fewer and larger, with reduced surface area per unit volume, resulting in less oxygenation. The older group also has decreased vessel elasticity (Desjardins et al., 2014) and increased blood pressure (Table 1), and we note that if the cardiac pulse is stronger throughout the smaller vessels, this can cause increased cardiac coherence. These findings are consistent with earlier fNIRS studies as reported in the review by Yeung and Chan (2021).

These results illustrate that, in the brain vasculature, both the oscillations, and their coordination are altered in the older group, suggesting decreased oxygenation of the brain with aging. The myogenic vascular resting state network is weaker in the older group. We note that our definition of resting state networks is mainly operational in nature, as participants were recorded while not performing any task. However, it is interesting to note that, in addition to low coherence for the lateral sensors, we observe strong frontal-parietal coherence. This is consistent with earlier work (e.g. Sadaghiani et al., 2012), and shows that our results also relate to the placement of the sensors.

4.4. Neurovascular coherence

Our key findings are: that there is significant neurovascular phase coherence in the 0.052–0.145 Hz (myogenic) frequency range; that this coherence is greatly reduced in older participants, as compared to the younger group; and that there is higher neurovascular coherence in the cardiac band in the older group (Fig. 7). As can be seen by comparing Figs. 6B,C and 7B, the coherence is also reduced in some locations without a decrease in power, so that the reduction in coherence cannot be accounted for by reduced power. To our knowledge, this is the first report of such effects.

In both the myogenic and cardiac bands there was widely distributed coherence across the cortex, as seen in Fig. 7B,C. In comparison, the neurogenic and respiratory bands showed little or no significant coherence in either age group, so that little change in coherence with age could be detected (see SM Fig. 23). The altered neurovascular coherence in the older group reflects less effective neurovascular interaction. Magnitude squared coherence (which has linear frequency resolution) between fNIRS and EEG signals near 0.1 Hz was found in a previous study of healthy participants aged around 30 years (Nikulin et al., 2014). This is in agreement with the coherence found in the younger group of the present study.

Grooms et al. (2017) studied slow oscillations in EEG and blood oxygen level dependent (BOLD) signals in the default mode network. The authors concluded that there was evidence of a relationship between infra-slow (< 0.1 Hz) EEG and BOLD oscillations at the same frequencies, which was also found by Hiltunen et al. (2014) and Keinänen et al. (2018). These correlations were shown to span several brain regions and to be time-varying. Both fNIRS and BOLD signals reflect changes in oxygenation, and the BOLD signal has been shown to correlate with both oxyHb and deoxyHb (Strangman et al., 2002; Schroeter et al., 2006). These studies investigated linear correlation between BOLD signals and infraslow EEG time-series, whereas the wavelet phase coherence used in our present study has logarithmic frequency resolution and evaluates coherence at each frequency step. The earlier studies did not consider frequencies above 0.1 Hz, while our present results show coherence centred around approximately 0.1 Hz. Although the studies are not directly comparable, they all provide evidence of a significant relationship between electrical neural activity and oxygenation oscillations in the brain at low frequencies. Mitra et al. (2018) found a similar relationship in mice, using laminar electrophysiology and hemoglobin imaging. Such invasive recordings have the advantage of measuring activity that is more local but, given that our goal was in-vivo, non-invasive measurements in humans, we chose to

use EEG and fNIRS.

In fMRI studies it is found that typically, only 10 % of the variability in the hemodynamic signal can be explained by neural activity (Drew et al., 2020). Similarly, we show low, but significant, coherence between the EEG and fNIRS signals. BOLD signals are often thought of as a convolution of the neural activity with what is known as the hemodynamic response function (HRF) (Rangaprakash et al., 2018). The HRF contains vascular factors, such as vasomotion, which is also present in the fNIRS signals. The difference in coherence between the younger and older groups illustrates that care should be taken in studies estimating the HRF, as the response is age-dependent.

4.5. Neurovascular coupling

In the awake resting state the brain consumes around 11 % of the cardiac output and 20 % of the body's total metabolic energy, despite only making up about 2 % of the body's weight (Gusnard et al., 2001). Resting state functional networks are consistently observed both with fMRI (Biswal et al., 1995; Hiltunen et al., 2014) and fNIRS (Sasai et al., 2012), in addition to EEG (Babiloni et al., 2006), indicating that the resting state activity is not random. Neurovascular coupling, mediating the adjustment of local cerebral blood flow to match the energy demand of neurons, is maintained continuously by the diverse cells constituting the NVU (Iadecola, 2017).

Studies of neurovascular coupling usually consider information flow from neurons to the vasculature. However, Kim et al. (2016) introduced the term vasculo-neuronal coupling to describe information flow from vessel to astrocyte to neuron. From experiments on mice, both in vivo and in vitro, the authors concluded that neurons adjust their resting state activity based on brain perfusion changes in flow and pressure (Kim et al., 2015, 2016), probably to match the energy supply and demand. Changes in the blood flow and perfusion are characterised by oscillatory processes, and so is energy metabolism (Iotti et al., 2010). Hence, the energy exchange to the brain is also likely to occur in an oscillatory manner. To be efficient, this is coordinated between the cardiovascular system and the brain, leading to coherent oscillations. It therefore seems likely that the degree of myogenic phase coherence is a proxy for neurovascular efficiency, and that the neurovascular interaction can be considered as arising through the cardiovascular system and brain behaving as interacting oscillators.

Myogenic coherence is reduced in the older group of participants, indicating that the interaction between the oscillators has decreased. From the current results we cannot be certain of the direction of the interaction, but it could be bi-directional. The neurovascular coherence in the myogenic frequency band is negatively correlated with BMI (Fig. 9), an observation that could be further investigated in future studies.

In the present work we focused on quantifying the functioning of the neurovascular unit. Our reasoning is that the efficiency of coordination between neuronal and vascular activities can be evaluated by their phase coherence. It provides a measure of neurovascular coupling. Establishment of the directionality and strength of the coupling between the vascular and neuronal oscillatory modes, as identified in this work, will be the next step in the investigation. The efficiency of the neurovascular unit, and the neurovascular coupling, are of particular interest in relation to the older population, as decreased neurovascular coupling has been linked to cognitive decline and dementia (Tarantini et al., 2017; Csipo et al., 2019). Especially promising is the recent report of a treatment that can improve neurovascular coupling in mice (Tarantini et al., 2019). Evaluation of neurovascular phase coherence therefore has potential as a biomarker for the efficiency of the NVU, and could be used to evaluate the effects of treatment and lifestyle changes in humans.

4.6. Origins of 0.1 Hz oscillations

Having established that oxygenation and neural activity are coherent around 0.1 Hz, reflecting neurovascular interactions, the next question is: what are the mechanisms underlying the coherence? There are several possible origins of 0.1 Hz oscillations in the brain and cardiovascular system, which we now consider.

Systemic cardiovascular fluctuations. IHR is coherent with oxygenation at ~ 0.1 Hz (see Sec. 3.2), and, to a much lesser degree respiration is also coherent with oxygenation at ~ 0.1 Hz. However, the systemic cardiovascular fluctuations cannot fully explain the oscillations in oxygenation (Katura et al., 2006), indicating that the 0.1 Hz oscillations could have additional origins. Most EEG probes have low but non-zero coherence with the ~ 0.1 Hz IHR signal, but the IHR–EEG coherence is generally lower than the neurovascular coherence evaluated from the EEG and fNIRS time-series: see SM Fig. 5 and SM Sec. 10.

Vascular origin. In 1902 Bayliss (1902) considered how smooth muscle cells respond to changes in intravascular pressure. This myogenic hypothesis was later studied by Folkow (1949) who found it was important for blood autoregulation. Myogenic oscillations tend to manifest between 0.052 and 0.145 Hz (Mayhew et al., 1996; Stefanovska, 2007; Söderström et al., 2003; Landsverk et al., 2007). Local 0.1 Hz oscillations consistent with myogenic activity have been observed in vivo in the human cortex (Rayshubskiy et al., 2014; Noordmans et al., 2018). These oscillations are believed to contribute to the clearance of substances like amyloid-beta proteins from the brain (Aldea et al., 2019).

Vascular neural origin. The hemodynamic bases of Meyer waves are oscillations of the sympathetic vasomotor tone of arterial blood vessels (Julien, 2006). Note that this would contribute to systemic cardiovascular fluctuations by impacting the heart rate and arterial blood pressure. In studies on blood flow with neural blockers, however, it was shown that 0.1 Hz activity continues, suggesting at least a contribution from the myogenic activity (Kastrup et al., 1989; Söderström et al., 2003). Rayshubskiy et al. (2014) found that 0.1 Hz oscillations in the human cortex were spatially localised, and correlated with the diameter of local vessels, suggesting that the 0.1 Hz hemodynamic oscillation in the human cortex are primarily myogenic in nature.

Electrophysiological origin in the brain. Oscillations around or below 0.1 Hz detected with EEG in the brain are not traditionally referred to as myogenic, but rather as infra-slow (<0.1 Hz) or slow oscillations (Buzsáki and Draguhn, 2004). Such studies usually do not include measurements of cardiovascular activity, and rather focus on metabolic processes. The origin of these oscillations is still debated (Nita et al., 2004; Voipio et al., 2003; Nikulin et al., 2014; Watson, 2018; Kropotov, 2022). Mitra et al. (2018) have shown that, in mice, the infra-slow oscillations have unique dynamics when compared to higher frequencies, and should be considered as a separate physiological process. There is evidence for both a neuronal and a non-neuronal generator of these oscillations, and possibly both of them contribute.

One feature of the infra-slow oscillations is that their phases were found to be correlated with the amplitude of faster oscillations and with performance (Monto et al., 2008; De Goede and Van Putten, 2019). It has been suggested that infra-slow oscillations are related to gross cortical excitability (Palva and Palva, 2012) and to arousal (Raut et al., 2021; Sihn and Kim, 2022). Changes in arousal level would be reflected in the heart rate, which could explain why we observe IHR–EEG coherence. Non-neuronal infra-slow oscillations in EEG could stem from a potential difference across the blood-brain barrier (BBB) (Nita et al., 2004; Voipio et al., 2003; Revest et al., 1993; Tschirgi and Taylor, 1958; Vanhatalo et al., 2003). This difference is sensitive to pH (Tschirgi and Taylor, 1958), and can be manipulated by hypoventilation, hyperventilation (Voipio et al., 2003) or postural changes that affect intracranial hemodynamics (Vanhatalo et al., 2003). The BBB, consisting of endothelial cells, is known to be affected by aging (Shiogai et al., 2010), Further, electrical coupling through the endothelium is a mechanism for neurons to modulate smooth muscle cell activity and therefore arteriole diameter (Drew et al., 2020). At the molecular level, another component that could affect the slow EEG oscillations might be neural

mitochondrial calcium signalling, which is known to be altered in aging (Sanganahalli et al., 2013). Neuron-glia interactions are also thought to contribute to the slow oscillations (Lőrincz et al., 2009; Buzsáki et al., 2012), as are extracellular ion fluxes which have been shown to contribute to the coupling of brain activity and blood flow (Mathiesen et al., 1998).

Other origins. Another potential origin of infra-slow fluctuations is movement artifacts from fidgeting, which has been observed in both animal and human studies. It has been shown in mice that both flow in arterioles and also brain electrical activity can be impacted by these artifacts (Drew et al., 2020), however in humans it is hardly likely that such movement artefacts would be oscillatory.

We find widely-distributed ~ 0.1 Hz coherence across the cortex, which does not in itself represent evidence of a single generator. Neurovascular coherence in the myogenic band is correlated with the IHR–respiration coherence in the myogenic band, while the neurovascular coherence in the respiratory band is not correlated with the IHR–respiration coherence in the respiratory band. This result suggests that the myogenic frequency band and the 0.1 Hz oscillation are key to understanding aging from both the neural and vascular perspectives.

4.7. Frequency and amplitude modulation of the γ–band by low-frequency oscillations

An interesting question to explore is whether the amplitude and/or frequency of γ oscillations in the EEG is modulated by the slower oxygenation/vascular oscillations. Murta et al. (2015) have reported evidence for amplitude modulation from combined fMRI and EEG studies. There is also some evidence from previous fNIRS studies that β oscillations are modulated by brain oxygenation (Pfurtscheller et al., 2012). The ~ 0.1 Hz variations in the oxygenation level of brain blood are generally used as an fMRI-based surrogate of "resting-state" neuronal activity, implying that it is the γ band which is most closely correlated with BOLD signals (Drew et al., 2020).

To investigate possible amplitude and frequency modulation of neuronal activity by low-frequency oxygenation oscillations, we focused on the higher β / lower γ band (20–30 Hz). Our results revealed that the spatial coherence between EEG signals has a peak in this frequency range. They also showed non-zero power for γ–instantaneous frequency and γ–instantaneous power time-series between 0.007 and 4 Hz, as shown in Fig. 8A, B).

We therefore calculated the WPC of the γ–instantaneous frequency time-series with fNIRS (frequency modulation), and of the γ–instantaneous power time-series with fNIRS (amplitude modulation) for the 8 locations where the fNIRS and EEG are co-located. However, we found little to no coherence in the frequency band considered here (Fig. 8C) indicating that there was no significant frequency modulation. We comment however, that a single γ instantaneous frequency provides only a rough measure of the collective neuronal activity in the γ band.

On the other hand, a non-zero coherence was observed for amplitude modulation, as shown in Fig. 8D), though not for all participants. What is more interesting is that we observed a negative phase shift for the older group around 0.06–0.08 Hz. This frequency range is often linked to periodic breathing, which appears in hypoxia (Lancaster et al., 2020). This may indicate that some effects of hypoxia appear with aging, even in the resting state. These results suggest an exciting direction for future research through more detailed investigations of how fast neural activity measured by EEG is modulated by slow hemodynamic oscillations measured by fNIRS. Further investigation of the coherence between the band power and oxygenation should also include a broader γ frequency band, and could explore other frequency bands too. This may elucidate additional information about neurovascular interactions.

In addition, neuro–respiratory interactions with the γ-band may be investigated using the IRR and respiration signals. Our results show that both the instantaneous γ–frequency and instantaneous γ–power are modulated by respiration (Fig. 8A and B). Earlier studies in both humans and animals (Chang and Glover, 2009; Tu and Zhang, 2022; Folschweiller and Sauer, 2022) have provided evidence of respiration-related oscillations in several brain regions. Distinct from respiration-related artefacts in fMRI, respiration-related networks have been shown to be linked with the γ-band power (Tu and Zhang, 2022). Respiration-related oscillations might aid coordination between different brain regions (Folschweiller and Sauer, 2022). In humans, the phase of respiration has an impact on memory encoding and perception, further indicating the importance of respiration for cognitive function. The close relationship of neural activity to both hemodynamics and respiration illustrates the importance of simultaneous measurements to investigate interactions between the underlying systems, e.g. as done in systemic physiology augmented fNIRS (Scholkmann et al., 2022).

4.8. Effect of increased BMI and BP

The two age groups differ in BMI and sBP (Table 3). From Fig. 9A it is clear that BMI is correlated with neurovascular coherence in the myogenic band.

To separate these effects, we created a smaller data-set, matching the BMI and BP values between the younger and older groups. This modified data-sets consisted of 13 younger and 13 older participants with comparable BMI ($p = 0.80$,) and sBP ($p = 0.86$). We then compared the subgroups' power/coherence values. The results and subgroup details are shown in the SM Sec. 9. We conclude that, while it is difficult to disentangle the influence of aging from that of the increased BMI/BP, there is evidence for an effect of ageing on the parameters considered, independent of the BMI/BP differences.

It is likely that BMI/BP differences also contribute, but some of the loss of significance can be attributed to loss of statistical power due to having smaller groups.

Further investigation of the impact of increased BP and BMI could be useful given that raised BMI is associated with increased risk of cardiovascular diseases such as coronary heart disease (Lassale et al., 2018), and increased mid-life BMI is associated with the development of dementia in later life (Pedditzi et al., 2016).

5. Conclusions

We have investigated the function of the neurovascular unit at macroscopic level, evaluating the coherence between the oscillations in the cardiovascular system (simultaneously monitored centrally via ECG and respiration effort, and locally by whole-brain fNIRS) and oscillations in neuronal activity (monitored locally by EEG), thereby gaining insight into the mechanisms of ageing in the NVU.

Most notably, the neurovascular coherence near 0.1 Hz is significantly reduced by ageing. This presumably reflects progressively impaired control of cerebral blood flow. The changes in cardio-respiratory coherence with blood oxygenation confirm that age affects significantly brain vascular function and oxygenation. It seems that this then impacts neuronal activity.

The methods described here, combined with state-of-the-art time-frequency analysis focusing on phase dynamics, have yielded new insights into the neurovascular dynamics of the aging brain. In particular, they have provided a quantitative measure of the neurovascular efficiency and health of the NVU, information that cannot be obtained in other ways. The approach could thus be used for non-invasive evaluation of the decline of neurovascular function in normal aging, as well as for monitoring the efficacy of treatment or lifestyle changes in a wide range of neurodegenerative disorders.

Funding

The research reported in this paper was funded by the Engineering and Physical Sciences Research Council (UK) under Grant No. EP/M006298/1, the Sir John Fisher Foundation, and the Slovenian

Research Agency (ARRS) (Program No. P20232). The development of the toolbox MODA used for analysis was also supported by the Engineering and Physical Sciences Research Council (UK) Grant No. EP/100999X1, the EU projects BRACCIA [517133] and COSMOS [642563] and the Action Medical Research (UK) MASDA Project [GN1963].

Author contributions

GL did the measurements and preliminary analysis of the data. JK and BM organised all clinical aspects of the study. JB analysed the data completely, prepared the figures and a draft of the text. PVEMcC contributed to writing the funding proposal. TJC supervised JB and advised on writing the manuscript. AS conceived the study, wrote the funding proposal, provided the theoretical framework for the time-series analysis methods, selected and discussed the analysis methods, supervised GL and JB and closely discussed the results. She was also involved in structuring the manuscript. All authors contributed to editing the manuscript, and accepted the final version.

Declaration of Competing Interest

The authors have no conflict of interest.

Data availability

Data are being available on Lancaster University PURE system.

Acknowledgements

We are grateful to all the participants for taking part in the study. We would like to thank Franci Benko, research nurse at the Department of Neurology, University Medical Centre Ljubljana, for his help in organising and carrying out the measurements, and Fajko Bajrović for his support with the clinical part of the study. In addition, we would like to thank Boštjan Dolenc for the automated analysis used for initial checks, and Cheryl Hawkes and Christopher Gaffney for helpful comments on the manuscript. JB is grateful to Benediktas Valys, Joe Rowland Adams and Charlie Mpetha for useful discussions, and to Sam McCormack for help with programming. JB is funded by a PhD scholarship grant awarded to TJC by the Sir John Fisher Foundation. The High End Computing facility at Lancaster University was used for data analysis.

Code availability

MODA is a numerical toolbox developed by the Lancaster University Nonlinear Dynamics group (available at http://doi.org/10.5281/zenodo.3470856).

The code for the permutation test was based on: Cardillo G. (2008) Rndttest: An alternative to Student t-test assessing difference in means. http://www.mathworks.com/matlabcentral/fileexchange/20928.

In addition, these MATLAB functions were used for plotting: Rob Campbell (2021), https://github.com/raacampbell/sigstar, Bastian Bechtold (2016), Violin Plots for MATLAB, Github Project, https://github.com/bastibe/Violinplot-Matlab.

Appendix A. Supporting information

Supplementary data associated with this article can be found in the online version at doi:10.1016/j.brainresbull.2023.110704.

References

Agelink, M.W., Malessa, R., Baumann, B., Majewski, T., Akila, F., Zeit, T., Ziegler, D., 2001. Standardized tests of heart rate variability: Normal ranges obtained from 309 healthy humans, and effects of age, gender, and heart rate. Clin. Auton. Res. 11, 99–108.

Al Zoubi, O., Ki Wong, C., Kuplicki, R.T., Yeh, H.w., Mayeli, A., Refai, H., Paulus, M., Bodurka, J., 2018. Predicting age from brain EEG signals—a machine learning approach. Front. Aging Neurosci. 10, 184.

Aldea, R., Weller, R.O., Wilcock, D.M., Carare, R.O., Richardson, G., 2019. Cerebrovascular smooth muscle cells as the drivers of intramural periarterial drainage of the brain. Front. Aging Neurosci. 11.

Babiloni, C., Binetti, G., Cassarino, A., DalForno, G., DelPercio, C., Ferreri, F., Ferri, R., Frisoni, G., Galderisi, S., Hirata, K., Lanuzza, B., Miniussi, C., Mucci, A., Nobili, F., Rodriguez, G., LucaRomani, G., Rossini, P.M., 2006. Sources of cortical rhythms in adults during physiological aging: a multicentric EEG study. Hum. Brain Mapp. 27, 162–172.

Bandrivskyy, A., Bernjak, A., McClintock, P.V.E., Stefanovska, A., 2004. Wavelet phase coherence analysis: application to skin temperature and blood flow. Cardiovasc. Eng. 4, 89–93.

Bayliss, W.M., 1902. On the local reactions of the arterial wall to changes of internal pressure. J. Physiol. 28, 220–231.

Billman, G., 2011. Heart rate variability - a historical perspective. Front. Physiol. 2.

Biswal, B., Yetkin, F.Z., Haughton, V.M., Hyde, J.S., 1995. Functional connectivity in the motor cortex of resting human brain using echo-planar MRI. Magn. Reson. Med. 34, 537–541.

Brodbeck, V., Spinelli, L., Lascano, A.M., Wissmeier, M., Vargas, M.I., Vulliemoz, S., Pollo, C., Schaller, K., Michel, C.M., Seeck, M., 2011. Electroencephalographic source imaging: a prospective study of 152 operated epileptic patients. Brain 134, 2887–2897.

Buzsáki, G., Draguhn, A., 2004. Neuronal oscillations in cortical networks. Science 304, 1926–1929.

Buzsáki, G., Anastassiou, C.A., Koch, C., 2012. The origin of extracellular fields and currents — EEG, ECoG, LFP and spikes. Nat. Rev. Neurosci. 13, 407–420.

Chang, C., Glover, G.H., 2009. Relationship between respiration, end-tidal CO_2, and BOLD signals in resting-state fMRI. NeuroImage 47, 1381–1393.

Clemson, P., Lancaster, G., Stefanovska, A., 2016. Reconstructing time-dependent dynamics. Proc. IEEE 104, 223–241.

Clemson, P.T., Hoag, J.B., Cooke, W.H., Eckberg, D.L., Stefanovska, A., 2022. Beyond the baroreflex: a new measure of autonomic regulation based on the time-frequency assessment of varifront. physiol.ability, phase coherence and couplings. Front. Net. Physiol. 2, 891604.

Cohen, J., 1988. Statistical Power Analysis for the Behavioral Sciences, 2nd ed.,. Lawrence Erlbaum Associates,.

Cox, S.R., Ritchie, S.J., Tucker-Drob, E.M., Liewald, D.C., Hagenaars, S.P., Davies, G., Wardlaw, J.M., Gale, C.R., Bastin, M.E., Deary, I.J., et al., 2016. Ageing and brain white matter structure in 3,513 UK Biobank participants. Nat. Commun. 7, 13629.

Csipo, T., Mukli, P., Lipecz, A., Tarantini, S., Bahadli, D., Abdulhussein, O., Owens, C., Kiss, T., Balasubramanian, P., Nyúl-Tóth, A., Hand, R.A., Yabluchanska, V., Sorond, F.A., Csiszar, A., Ungvari, Z., Yabluchanskiy, A., 2019. Assessment of age-related decline of neurovascular coupling responses by functional near-infrared spectroscopy (fNIRS) in humans. Geroscience 41 (5), 495–509.

Custo, A., Van De Ville, D., Wells, W.M., Tomescu, M.I., Brunet, D., Michel, C.M., 2017. Electroencephalographic resting-state networks: source localization of microstates. Brain Connect 7, 671–682.

De Goede, A.A., Van Putten, M.J.A.M., 2019. Infraslow activity as a potential modulator of corticomotor excitability. J. Neurophysiol. 122, 325–335.

Desjardins, M., Berti, R., Lefebvre, J., Dubeau, S., Lesage, F., 2014. Aging-related differences in cerebral capillary blood flow in anesthetized rats. Neurobiol. Aging 35, 1947–1955.

Drew, P.J., Mateo, C., Turner, K.L., Yu, X., Kleinfeld, D., 2020. Ultra-slow oscillations in fMRI and resting-state connectivity: neuronal and vascular contributions and technical confounds. Neuron 107, 782–804.

Dustman, R., Shearer, D., Emmerson, R., 1999. Life-span changes in EEG spectral amplitude, amplitude variability and mean frequency. Clin. Neurophysiol. 110, 1399–1409.

Faul, F., Erdfelder, E., Lang, A.G., Buchner, A., 2007. G*power 3: a flexible statistical power analysis program for the social, behavioral, and biomedical sciences. Behav. Res. Methods 39, 175–191.

Fjell, A.M., Walhovd, K.B., 2010. Structural brain changes in aging: courses, causes and cognitive consequences. Rev. Neurosci. 21, 187–221.

Folkow, B., 1949. Intravascular pressure as a factor regulating the tone of the small vessels. Acta Physiol. Scand. 17, 289–310.

Folschweiller, S., Sauer, J.F., 2022. Controlling neuronal assemblies: a fundamental function of respiration-related brain oscillations in neuronal networks. Pflug. Arch. 475, 13–21.

Geovanini, G.R., Vasques, E.R., De Oliveira Alvim, R., Mill, J.G., Andreão, R.V., Vasques, B.K., Pereira, A.C., Krieger, J.E., 2020. Age and sex differences in heart rate variability and vagal specific patterns - Baependi heart study. Glob. Heart 15, 71.

Gonneaud, J., Baria, A.T., Pichet Binette, A., Gordon, B.A., Chhatwal, J.P., Cruchaga, C., Jucker, M., Levin, J., Salloway, S., Farlow, M., et al., 2021. Accelerated functional brain aging in pre-clinical familial Alzheimer's disease. Nat. Commun. 12, 5346.

Grooms, J.K., Thompson, G.J., Pan, W.J., Billings, J., Schumacher, E.H., Epstein, C.M., Keilholz, S.D., 2017. Infraslow electroencephalographic and dynamic resting state network activity. Brain Connect 7, 265–280.

Gusnard, D.A., Raichle, M.E., Raichle, M.E., 2001. Searching for a baseline: functional imaging and the resting human brain. Nat. Rev. Neurosci. 2, 685–694.

Hashemi, A., Pino, L.J., Moffat, G., Mathewson, K.J., Aimone, C., Bennett, P.J., Schmidt, L.A., Sekuler, A.B., 2016. Characterizing population EEG dynamics throughout adulthood. eNeuro 3, 0275–16.2016.

Hiltunen, T., Kantola, J., Abou Elseoud, A., Lepola, P., Suominen, K., Starck, T., Nikkinen, J., Remes, J., Tervonen, O., Palva, S., Kiviniemi, V., Palva, J.M., 2014.

Infra-slow EEG fluctuations are correlated with resting-state network dynamics in fMRI. J. Neurosci. 34, 356–362.
Hintze, J.L., Nelson, R.D., 1998. Violin plots: a box plot-density trace synergism. Am. Stat. 52, 181–184.
Hoshi, H., Shigihara, Y., 2020. Age- and gender-specific characteristics of the resting-state brain activity: a magnetoencephalography study. Aging 12, 21613–21637.
Iadecola, C., 2017. The neurovascular unit coming of age: a journey through neurovascular coupling in health and disease. Neuron 96, 17–42.
Iatsenko, D., Bernjak, A., Stankovski, T., Shiogai, Y., Owen-Lynch, P.J., Clarkson, P.B.M., Mcclintock, P.V.E., Stefanovska, A., 2013. Evolution of cardiorespiratory interactions with age. Philos. Trans. R. Soc. 371, 20110622.
Iatsenko, D., McClintock, P.V.E., Stefanovska, A., 2015a. Linear and synchrosqueezed time-frequency representations revisited: overview, standards of use, resolution, reconstruction, concentration, and algorithms. Digit. Signal Process. 42, 1–26.
Iatsenko, D., McClintock, P.V.E., Stefanovska, A., 2015b. Nonlinear mode decomposition: a noise-robust, adaptive decomposition method. Phys. Rev. E 92, 032916.
Iatsenko, D., McClintock, P.V.E., Stefanovska, A., 2016. Extraction of instantaneous frequencies from ridges in time-frequency representations of signals. Signal Process. 125, 290–303.
Intaglietta, M., 1990. Vasomotion and flowmotion: physiological mechanisms and clinical evidence. Vasc. Med. Rev. 1, 101–112.
Iotti, S., Borsari, M., Bendahan, D., 2010. Oscillations in energy metabolism. Biochim. Biophys. Acta Bioenergy 1797, 1353–1361.
Julien, C., 2006. The enigma of Mayer waves: facts and models. Cardiovasc. Res. 70, 12–21.
Kastrup, J., Bülow, J., Lassen, N.A., 1989. Vasomotion in human skin before and after local heating recorded with laser Doppler flowmetry. A method for induction of vasomotion. Int. J. Microcirc. Clin. Exp. 8, 205–215.
Katura, T., Tanaka, N., Obata, A., Sato, H., Maki, A., 2006. Quantitative evaluation of interrelations between spontaneous low-frequency oscillations in cerebral hemodynamics and systemic cardiovascular dynamics. Neuroimage 31, 1592–1600.
Keinänen, T., Rytky, S., Korhonen, V., Huotari, N., Nikkinen, J., Tervonen, O., Palva, J. M., Kiviniemi, V., 2018. Fluctuations of the EEG-fMRI correlation reflect intrinsic strength of functional connectivity in default mode network. J. Neurosci. Res. 96, 1689–1698.
Keissar, K., Davrath, L.R., Akselrod, S., 2009. Coherence analysis between respiration and heart rate variability using continuous wavelet transform. Philos. Trans. R. Soc. 367, 1393–1406.
Kim, K.J., Iddings, J.A., Stern, J.E., Blanco, V.M., Croom, D., Kirov, S.A., Filosa, J.A., 2015. Astrocyte contributions to flow/pressure-evoked parenchymal arteriole vasoconstriction. J. Neurosci. 35, 8245–8257.
Kim, K.J., RamiroDiaz, J., Iddings, J.A., Filosa, J.A., 2016. Vasculo-neuronal coupling: retrograde vascular communication to brain neurons. J. Neurosci. 36, 12624–12639.
Kropotov, J.D., 2022. The enigma of infra-slow fluctuations in the human EEG. Front. Hum. Neurosci. 16, 928410.
Kvandal, P., Landsverk, S.A., Bernjak, A., Stefanovska, A., Kvernmo, H.D., Kirkebøen, K. A., 2006. Low frequency oscillations of the laser Doppler perfusion signal in human skin. Microvasc. Res. 72, 120–127.
Lancaster, G., Iatsenko, D., Pidde, A., Ticcinelli, V., Stefanovska, A., 2018. Surrogate data for hypothesis testing of physical systems. Phys. Rep. 748, 1–60.
Lancaster, G., Debevec, T., Millet, G.P., Poussel, M., Willis, S.J., Mramor, M., Goričar, K., Osredkar, D., Dolžan, V., Stefanovska, A., et al., 2020. Relationship between cardiorespiratory phase coherence during hypoxia and genetic polymorphism in humans. J. Physiol. 598, 2001–2019.
Landsverk, S.A., Kvandal, P., Bernjak, A., Stefanovska, A., Kirkeboen, K.A., 2007. The effects of general anesthesia on human skin microcirculation evaluated by wavelet transform. Anesth. Analg. 105, 1012–1019.
Lassale, C., Tzoulaki, I., Moons, K.G.M., Sweeting, M., Boer, J., Johnson, L., Huerta, J.M., Agnoli, C., Freisling, H., Weiderpass, E., Wennberg, P., van der A, D.L., Arriola, L., Benetou, V., Boeing, H., Bonnet, F., Colorado-Yohar, S.M., m, G., Eriksen, A.K., Ferrari, P., Grioni, S., Johansson, M., Kaaks, R., Katsoulis, M., Katzke, V., Key, T.J., Matullo, G., Melander, O., Molina-Portillo, E., Moreno-Iribas, C., Norberg, M., Overvad, K., Panico, S., s, J.R., Saieva, C., Skeie, G., Steffen, A., Stepien, M., nneland, A., Trichopoulou, A., Tumino, R., van der Schouw, Y.T., Verschuren, W.M. M., Langenberg, C., Di Angelantonio, E., Riboli, E., Wareham, N.J., Danesh, J., Butterworth, A.S., 2018. Separate and combined associations of obesity and metabolic health with coronary heart disease: a pan-European case-cohort analysis. Eur. Heart J. 39, 397–406.
Li, Y., Xie, L., Huang, T., Zhang, Y., Zhou, J., Qi, B., Wang, X., Chen, Z., Li, P., 2019. Aging neurovascular unit and potential role of DNA damage and repair in combating vascular and neurodegenerative disorders. Front. Neurosci. 13, 778.
Li, Z., Zhang, M., Xin, Q., Luo, S., Cui, R., Zhou, W., Lu, L., 2013. Age-related changes in spontaneous oscillations assessed by wavelet transform of cerebral oxygenation and arterial blood pressure signals. J. Cereb. Blood Flow. Metab. 33, 692–699.
Lőrincz, M.L., Geall, F., Ying, B., Crunelli, V., Hughes, S.W., 2009. ATP-dependent infra-slow (< 0.1 Hz) oscillations in thalamic networks. PLOS ONE 4, e4447.
Maris, E., Oostenveld, R., 2007. Nonparametric statistical testing of EEG- and MEG-data. J. Neurosci. Methods 164, 177–190.
Mathiesen, C., Caesar, K., Akgören, N., Lauritzen, M., 1998. Modification of activity-dependent increases of cerebral blood flow by excitatory synaptic activity and spikes in rat cerebellar cortex. J. Physiol. 512, 555–566.
Mayhew, J.E., Askew, S., Zheng, Y., Porrill, J., Westby, G.W., Redgrave, P., Rector, D.M., Harper, R.M., 1996. Cerebral vasomotion: a 0.1-Hz oscillation in reflected light imaging of neural activity. NeuroImage 4, 183–193.
Meghdadi, A.H., StevanovićKarić, M., McConnell, M., Rupp, G., Richard, C., Hamilton, J., Salat, D., Berka, C., 2021. Resting state EEG biomarkers of cognitive decline associated with Alzheimer's disease and mild cognitive impairment. PLOS ONE 16, 1–31.
Mesquita, R.C., Franceschini, M.A., Boas, D.A., 2010. Resting state functional connectivity of the whole head with near-infrared spectroscopy. Biomed. Opt. Express 1 (1), 324–336.
Michel, C.M., Brunet, D., 2019. EEG source imaging: a practical review of the analysis steps. Front. Neurol. 10, 325.
Mitra, A., Kraft, A., Wright, P., Acland, B., Snyder, A.Z., Rosenthal, Z., Czerniewksi, L., Bauer, A., Snyder, L., Culver, J., Lee, J., Raichle, M.E., 2018. Spontaneous infra-slow brain activity has unique spatiotemporal dynamics and laminar structure. Neuron 98 (2), 297–305.e6.
Moezzi, B., Pratti, L.M., Hordacre, B., Graetz, L., Berryman, C., Lavrencic, L.M., Ridding, M.C., Keage, H.A., McDonnell, M.D., Goldsworthy, M.R., 2019. Characterization of young and old adult brains: an EEG functional connectivity analysis. Neuroscience 422, 230–239.
Montez, T., Poil, S.S., Jones, B.F., Manshanden, I., Verbunt, J.P.A., Van Dijk, B.W., Brussaard, A.B., Van Ooyen, A., Stam, C.J., Scheltens, P., et al., 2009. Altered temporal correlations in parietal alpha and prefrontal theta oscillations in early-stage Alzheimer disease. Proc. Natl. Acad. Sci. U.S.A. 106, 1614–1619.
Monto, S., Palva, S., Voipio, J., Palva, J.M., 2008. Very slow EEG fluctuations predict the dynamics of stimulus detection and oscillation amplitudes in humans. J. Neurosci. 28, 8268–8272.
Murta, T., Leite, M., Carmichael, D.W., Figueiredo, P., Lemieux, L., 2015. Electrophysiological correlates of the BOLD signal for EEG-informed fMRI. Hum. Brain Mapp. 36, 391–414.
Newman, J., Lancaster, G., Stefanovska, A., 2018. Multiscale Oscillatory Dynamics Analysis User Manual v1.01. Department of Physics, Lancaster University.
Nikulin, V.V., Fedele, T., Mehnert, J., Lipp, A., Noack, C., Steinbrink, J., Curio, G., 2014. Monochromatic ultra-slow (~ 0.1 Hz) oscillations in the human electroencephalogram and their relation to hemodynamics. NeuroImage 97, 71–80.
Nita, D., Vanhatalo, S., Lafortune, F., Voipio, J., Kaila, K., Amzica, F., 2004. Nonneuronal origin of CO_2-related DC EEG shifts: An in vivo study in the cat. J. Neurophysiol. 92, 1011–1022.
Noordmans, H.J., van Blooijs, D., Siero, J.C.W., Zwanenburg, J.J.M., Klaessens, J.H.G.M., Ramsey, N.F., 2018. Detailed view on slow sinusoidal, hemodynamic oscillations on the human brain cortex by Fourier transforming oxy/deoxy hyperspectral images. Hum. Brain Mapp. 39, 3558–3573.
Palva, J.M., Palva, S., 2012. Infra-slow fluctuations in electrophysiological recordings, blood-oxygenation-level-dependent signals, and psychophysical time series. NeuroImage 62, 2201–2211.
Pedditzi, E., Peters, R., Beckett, N., 2016. The risk of overweight/obesity in mid-life and late life for the development of dementia: a systematic review and meta-analysis of longitudinal studies. Age Ageing 45, 14–21.
Peters, M.J., Joehanes, R., Pilling, L.C., Schurmann, C., Conneely, K.N., Powell, J., Reinmaa, E., Sutphin, G.L., Zhernakova, A., Schramm, K., et al., 2015. The transcriptional landscape of age in human peripheral blood. Nat. Commun. 6, 8570.
Pfurtscheller, G., Daly, I., Bauernfeind, G., Müller-Putz, G.R., 2012. Coupling between intrinsic prefrontal HbO2 and central EEG beta power oscillations in the resting brain. PLOS ONE 7, e43640.
Pinto, E., 2007. Blood pressure and ageing. Postgrad. Med. J. 83, 109–114.
Rangaprakash, D., Wu, G.R., Marinazzo, D., Hu, X., Deshpande, G., 2018. Hemodynamic response function (HRF) variability confounds resting-state fMRI functional connectivity. Magn. Reson. Med. 80, 1697–1713.
Raut, R.V., Snyder, A.Z., Mitra, A., Yellin, D., Fujii, N., Malach, R., Raichle, M.E., 2021. Global waves synchronize the brainas functional systems with fluctuating arousal. Sci. Adv. 7.
Rayshubskiy, A., Wojtasiewicz, T.J., Mikell, C.B., Bouchard, M.B., Timerman, D., Youngerman, B.E., McGovern, R.A., Otten, M.L., Canoll, P., McKhann, G.M., Hillman, E.M., 2014. Direct, intraoperative observation of 0.1 Hz hemodynamic oscillations in awake human cortex: implications for fMRI. NeuroImage 87, 323–331.
Revest, P.A., Jones, H.C., Abbott, N.J., 1993. The transendothelial DC potential of rat blood-brain barrier vessels in situ. In: Drewes, L.R., Betz, A.L. (Eds.), Frontiers in Cerebral Vascular Biology: Transport and Its Regulation. Springer, US, Boston, MA, pp. 71–74.
Richard Clark, C., Veltmeyer, M.D., Hamilton, R.J., Simms, E., Paul, R., Hermens, D., Gordon, E., 2004. Spontaneous alpha peak frequency predicts working memory performance across the age span. Int. J. Psychophysiol. 53, 1–9.
Sadaghiani, S., Scheeringa, R., Lehongre, K., Morillon, B., Giraud, A.L., D'Esposito, M., Kleinschmidt, A., 2012. Alpha-band phase synchrony is related to activity in the fronto-parietal adaptive control network. J. Neurosci. 32 (41), 14305–14310.
Salerud, E.G., Tenland, T., Nilsson, G.E., Oberg, P.A., 1983. Rhythmical variations in human skin blood flow. Int. J. Microcirc. Clin. Exp. 2, 91–102.
Sanganahalli, B.G., Herman, P., Hyder, F., Kannurpatti, S.S., 2013. Mitochondrial functional state impacts spontaneous neocortical activity and resting state fMRI. PLOS ONE 8, e63317.
Sasai, S., Homae, F., Watanabe, H., Sasaki, A.T., Tanabe, H.C., Sadato, N., Taga, G., 2012. A NIRS-fMRI study of resting state network. NeuroImage 63, 179–193.
Scally, B., Burke, M.R., Bunce, D., Delvenne, J.F., 2018. Resting-state EEG power and connectivity are associated with alpha peak frequency slowing in healthy aging. Neurobiol. Aging 71, 149–155.
Scholkmann, F., Tachtsidis, I., Wolf, M., Wolf, U., 2022. Systemic physiology augmented functional near-infrared spectroscopy: a powerful approach to study the embodied human brain. Neurophotonics 9, 030801.

Schroeter, M.L., Kupka, T., Mildner, T., Uludağ, K., vonCramon, D.Y., 2006. Investigating the post-stimulus undershoot of the BOLD signal – a simultaneous fMRI and fNIRS study. NeuroImage 30, 349–358.
Shiogai, Y., Stefanovska, A., McClintock, P.V.E., 2010. Nonlinear dynamics of cardiovascular ageing. Phys. Rep. 488, 51–110.
Sihn, D., Kim, S.P., 2022. Brain infraslow activity correlates with arousal levels. Front. Neurosci. 16, 765585.
Söderström, T., Stefanovska, A., Veber, M., Svensson, H., 2003. Involvement of sympathetic nerve activity in skin blood flow oscillations in humans. Am. J. Physiol. Heart Circ. Physiol. 284, H1638–1646.
Song, S., Kim, D., Jang, D.P., Lee, J., Lee, H., Lee, K.M., Kim, I.Y., 2015. Low-frequency oscillations in cerebrovascular and cardiovascular hemodynamics: their interrelationships and the effect of age. Microvasc. Res. 102, 46–53.
Springo, Z., Toth, P., Tarantini, S., Ashpole, N.M., Tucsek, Z., Sonntag, W.E., Csiszar, A., Koller, A., Ungvari, Z.I., 2015. Aging impairs myogenic adaptation to pulsatile pressure in mouse cerebral arteries. J. Cereb. Blood Flow. Metab. 35 (4), 527–530.
Stankovski, T., Pereira, T., McClintock, P.V.E., Stefanovska, A., 2017. Coupling functions: universal insights into dynamical interaction mechanisms. Rev. Mod. Phys. 89, 045001.
Stankovski, T., Pereira, T., McClintock, P.V.E., Stefanovska, A., 2019. Introduction. Coupling functions: dynamical interaction mechanisms in the physical, biological and social sciences. Philos. Trans. R. Soc. Lond. A 377, 20190039.
Stefanovska, A., 2007. Coupled oscillators: complex but not complicated cardiovascular and brain interactions. IEEE Eng. Med. Biol. Mag. 26, 25–29.
Stefanovska, A., Bračič, M., 1999. Physics of the human cardiovascular system. Contemp. Phys. 40, 31–55.
Stefanovska, A., Hožič, M., 2000. Spatial synchronization in the human cardiovascular system. Prog. Theor. Phys. Suppl. 139, 270–282.
Strangman, G., Culver, J.P., Thompson, J.H., Boas, D.A., 2002. A quantitative comparison of simultaneous BOLD fMRI and NIRS recordings during functional brain activation. NeuroImage 17, 719–731.
Tarantini, S., Tran, C.H.T., Gordon, G.R., Ungvari, Z., Csiszar, A., 2017. Impaired neurovascular coupling in aging and Alzheimer's disease: contribution of astrocyte dysfunction and endothelial impairment to cognitive decline. Exp. Gerontol. 94, 52–58.
Tarantini, S., Yabluchanskiy, A., Csipo, T., Fulop, G., Kiss, T., Balasubramanian, P., Delfavero, J., Ahire, C., Ungvari, A., Nyúl-Tóth, A., Farkas, E., Benyo, Z., Tóth, A., Csiszar, A., Ungvari, Z., 2019. Treatment with the poly(ADP-ribose) polymerase inhibitor PJ-34 improves cerebromicrovascular endothelial function, neurovascular coupling responses and cognitive performance in aged mice, supporting the NAD. depletion hypothesis of neurovascular aging. GeroScience 41 (5), 533–542.
Tschirgi, R.D., Taylor, J.L., 1958. Slowly changing bioelectric potentials associated with the blood-brain barrier. Am. J. Physiol. 195, 7–22.
Tu, W., Zhang, N., 2022. Neural underpinning of a respiration-associated resting-state fMRI network. eLife 11, e81555.
Vanhatalo, S., Tallgren, P., Becker, C., Holmes, M.D., Miller, J.W., Kaila, K., Voipio, J., 2003. Scalp-recorded slow EEG responses generated in response to hemodynamic changes in the human brain. Clin. Neurophysiol. 114, 1744–1754.
Veldsman, M., Tai, X.Y., Nichols, T., Smith, S., Peixoto, J., Manohar, S., Husain, M., 2020. Cerebrovascular risk factors impact frontoparietal network integrity and executive function in healthy ageing. Nat. Commun. 11, 4340.
Voipio, J., Tallgren, P., Heinonen, E., Vanhatalo, S., Kaila, K., 2003. Millivolt-scale DC shifts in the human scalp EEG: Evidence for a nonneuronal generator. J. Neurophysiol. 89, 2208–2214.
Vysata, O., Kukal, J., Prochazka, A., Pazdera, L., Simko, J., Valis, M., 2014. Age-related changes in EEG coherence. Neurol. Neurochir. Pol. 48, 35–38.
Wang, B., Zhang, M., Bu, L., Xu, L., Wang, W., Li, Z., 2016. Posture-related changes in brain functional connectivity as assessed by wavelet phase coherence of NIRS signals in elderly subjects. Behav. Brain Res. 312, 238–245.
Watson, B.O., 2018. Cognitive and physiologic impacts of the infraslow oscillation. Front. Syst. Neurosci. 12, 44.
Xu, X., Wang, B., Ren, C., Hu, J., Greenberg, D.A., Chen, T., Xie, L., Jin, K., 2017. Age-related impairment of vascular structure and functions. Aging Dis. 8, 590–610.
Yasuma, F., Hayano, J., 2004. Respiratory sinus arrhythmia: why does the heartbeat synchronize with respiratory rhythm? Chest 125, 683–690.
Yeung, M.K., Chan, A.S., 2021. A systematic review of the application of functional near-infrared spectroscopy to the study of cerebral hemodynamics in healthy aging. Neuropsychol. Rev. 31, 139–166.
Zhang, Q., Roche, M., Gheres, K.W., Chaigneau, E., Kedarasetti, R.T., Haselden, W.D., Charpak, S., Drew, P.J., 2019. Cerebral oxygenation during locomotion is modulated by respiration. Nat. Commun. 10, 5515.

Chapter 4

Neurovascular phase coherence is altered in Alzheimer's disease

This research is published in Brain Communications.

Bjerkan, J., Meglič, B., Lancaster, G., Kobal, J., McClintock, P. V. E., Crawford, T. J. & Stefanovska, A. Neurovascular phase coherence is altered in Alzheimer's disease. *Brain Commun.* **7,** fcaf007 (2025)

https://doi.org/10.1093/braincomms/fcaf007 BRAIN COMMUNICATIONS 2025: fcaf007 | 1

BRAIN COMMUNICATIONS

Neurovascular phase coherence is altered in Alzheimer's disease

Juliane Bjerkan,[1] Bernard Meglič,[2] Gemma Lancaster,[1] Jan Kobal,[2] Peter V. E. McClintock,[1] Trevor J. Crawford[3] and Aneta Stefanovska[1]

Alzheimer's disease is the commonest form of dementia, but its cause still remains elusive. It is characterized by neurodegeneration, with amyloid-beta and tau aggregation. Recently, however, the roles of the vasculature and the neurovascular unit are being highlighted as important for disease progression. In particular, there is reduced microvascular density, and altered gene expression in vascular and glial cells. Structural changes naturally impact the functioning of the neurovascular unit, and the goal of the study was to quantify the corresponding changes *in vivo*, non-invasively. Our assessment is based on recordings of brain oxygenation, neuronal and cardiorespiratory activities, captured by functional near-infrared spectroscopy, electroencephalogram, electrocardiogram and respiration effort, respectively. Two groups were compared: an Alzheimer's disease group (N = 19) and a control group (N = 20) of similar age. The time-series were analysed using methods that can capture multi-scale and time-varying oscillations such as the wavelet transform power and wavelet phase coherence. The Alzheimer's disease group shows a significant decrease in the power of brain oxygenation oscillations compared to the control group. There is also a significant global reduction in the phase coherence between brain oxygenation time-series. The neurovascular phase coherence around 0.1 Hz is also significantly reduced in the Alzheimer's disease group. In addition, the average respiration rate is increased in the Alzheimer's disease group compared to the control group. We show that the phase coherence between vascular and neuronal activities is reduced in Alzheimer's disease compared to the control group, indicating altered functioning of the neurovascular unit. The brain oxygenation dynamics reveals reduced power and coordination of oscillations, especially in frequency ranges that are associated with vasomotion. This could lead to reduced oxygen delivery to the brain, which could affect ATP production, and potentially reduce amyloid-beta clearance. These changes in neurovascular dynamics have potential for early diagnosis, as a marker of disease progression, and for evaluating the effect of interventions.

1 Department of Physics, Lancaster University, LA1 4YB Lancaster, UK
2 Department of Neurology, University Medical Centre, 1525 Ljubljana, Slovenia
3 Department of Psychology, Lancaster University, LA1 4YF Lancaster, UK

Correspondence to: Aneta Stefanovska
Department of Physics, Lancaster University, C507
C - Floor, Physics Building, LA1 4YB Lancaster, UK
E-mail: aneta@lancaster.ac.uk

Keywords: neurovascular unit; time-frequency analysis; multi-scale oscillatory analysis; phase coherence; brain oxygenation

Received August 15, 2024. Revised November 01, 2024. Accepted January 08, 2025. Advance access publication February 3, 2025

Graphical Abstract

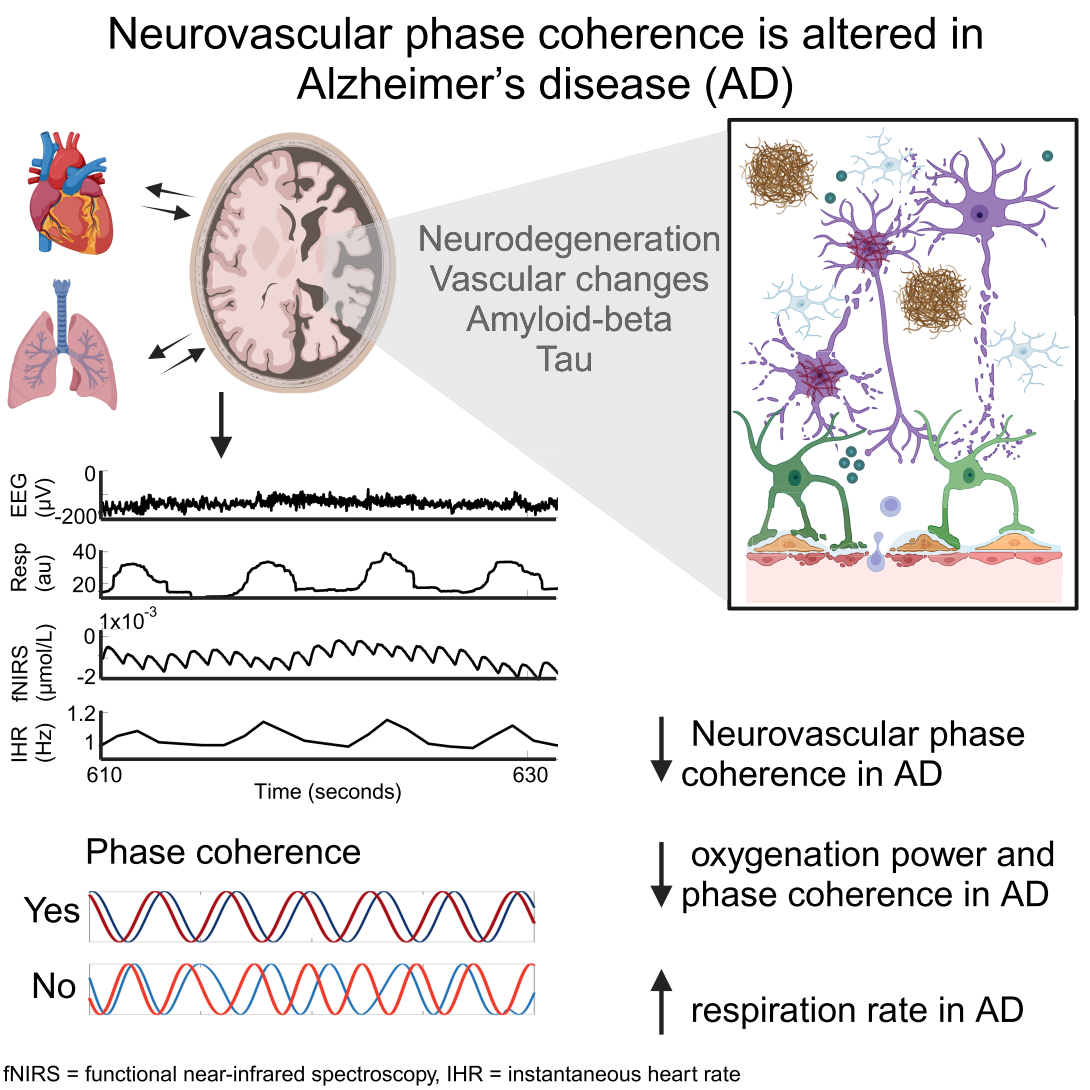

Introduction

Alzheimer's disease is a neurodegenerative disease leading to memory problems and a decline in cognitive function. It is the commonest form of dementia, and is especially prevalent in the older population. The mechanisms leading to Alzheimer's disease are not fully elucidated, but Alzheimer's disease is associated with amyloid-beta deposits,[1,2] tau protein tangles,[3] brain atrophy[4] and vascular changes.[5] Vascular and neurovascular pathways to neurodegeneration are increasingly being recognized as important for both the onset and progression of the disease.[6,7] The two-hit vascular hypothesis singles out vascular factors, such as hypertension and diabetes, and genetic factors, such as APOE4, to initiate vascular damage (hit one).[8] This then leads to reduced amyloid-beta clearance leading to amyloid-beta accumulation (hit two). According to the hypothesis the two hits, both independently and synergistically, cause synaptic dysfunction and neurodegeneration, which can be seen as disrupted structural and functional connectivity in the brain. This has a major effect on brain function, and leads to the symptoms of dementia.[8]

The brain consumes around 20% of the body's energy usage, and works together with the cardiovascular system to maintain a balance between local energy demand and supply. This is ensured through neurovascular coupling, controlled by the neurovascular unit (NVU).[9] The NVU consists of many cell types, such as astrocytes, vascular smooth muscle cells (VSMC), neurons and endothelial cells. There is evidence of neurovascular de-coupling in

Alzheimer's disease, such as dysregulation of cerebral blood flow, potentially caused by alterations in VSMCs and astrocytes.[8,10] Interestingly, neurovascular de-coupling is implicated in cognitive decline in both ageing and Alzheimer's disease,[11] and several vascular and glial cells have genes that are expressed differently in Alzheimer's disease compared to healthy controls.[12] Hence, evaluating neurovascular interactions non-invasively in Alzheimer's disease participants could provide useful insights into the disease progression and mechanisms, potentially aiding in diagnosis and the assessment of future treatments.

Earlier research found that electrical activity (measured by electroencephalography (EEG) or neuropixels probes) is correlated with hemodynamic activity (measured with functional near-infrared spectroscopy (fNIRS) or fMRI) at the same slow frequencies (around 0.1 Hz), both in the healthy human and mouse brains.[13-17] We have reported previously that this correlation decreases with ageing,[17] but no study has yet investigated such a relationship in participants with Alzheimer's disease. We hypothesise that, due to neurovascular de-coupling, the neurovascular coherence will be reduced. To test this, we employed fNIRS and EEG. Both techniques have good temporal resolution,[18-20] and are therefore well-suited to studies of time-varying phase dynamics. In addition, the methods are non-invasive and relatively inexpensive, making them an attractive option compared to methods such as fMRI and positron emission tomography (PET).

We treat the cardiovascular system and the brain as systems of interacting oscillators,[21] recognizing that living systems, being thermodynamically open systems and far-from-equilibrium, exhibit oscillations with time-varying frequencies.[22,23] In view of the latter, methods able to capture multi-scale time-localized dynamics with logarithmic frequency resolution need to be used.[24] Time-frequency analysis methods such as the wavelet transform (WT) and wavelet phase coherence (WPC)[25-27] were accordingly applied to the measured time-series as illustrated in Fig. 1.

The brain does not work in isolation from the cardiovascular and respiratory systems, and hence we also recorded simultaneously the heart rate (from ECG) and respiration effort (from a respiration belt). Systemic cardiovascular oscillations naturally impact brain oxygenation, and so it is especially important to understand the oscillations in fNIRS.

The overall aim of the study was to evaluate quantitatively, we believe for the first time, how the cardiovascular and neurovascular phase interactions change in participants with Alzheimer's disease. According to the two-hit vascular hypothesis either or both could play a role in the development of the disease. There is growing recognition that Alzheimer's disease is a multi-system disorder and should be regarded as a non-linear dynamical disorder.[28] Consideration of dynamics in health and disease calls for studies of oscillations.[29] We therefore combine non-invasive measurements of cardiovascular and neurovascular dynamics, with state-of-the-art time-frequency analysis methods, in order to obtain a more integrated picture of Alzheimer's disease.

Materials and methods

Participants

The study was conducted according to the Declaration of Helsinki. Study protocols were approved by the Commission of the Republic of Slovenia for Medical Ethics or by the Faculty of Science and Technology Research Ethics Committee (FSTREC) at Lancaster University. Written informed consent was given by all participants.

Measurements were conducted on 29 Alzheimer's disease participants (18 F, 11 M). Out of these, six were excluded as they were older than the control participants, and therefore it was not possible to match the groups; two were excluded due to not completing the full recordings; one was excluded due to the participant touching the wires and cap multiple times, causing poor signal quality; one was excluded due to being an outlier (a combination of tachypnoea, atrial fibrillation and obesity). Data of included Alzheimer's disease patients can be found in Table 1.

Alzheimer's disease was diagnosed by clinical evaluation, and the presence of abnormal tau and/or amyloid-beta 1–42 concentrations in the cerebrospinal fluid[30,31] (CSF) (Table 1). Four people in the Alzheimer's disease group were mild cognitive impairment (MCI) patients, and had CSF amyloid-beta or tau levels which strongly suggested Alzheimer's disease.

Twenty control participants of similar ages to the Alzheimer's disease participants were also included. Exclusion criteria for the control group were not completing the full recordings, movement artefacts causing poor signal quality or having a BMI ≥ 40. Participants with Class 3 obesity were excluded to better align the BMI of the control and Alzheimer's disease groups.

Data were analysed from a total of 39 participants: an Alzheimer's disease group ($N = 19$) and a control group ($N = 20$). All participants were from Slovenia, apart from seven of the control participants who were from England.

In analyses involving respiration, six control participants were excluded. For five of them, the respiration belt had not been placed correctly, and therefore failed to measure the respiration. For the sixth participant, respiration was not measured.

In analyses involving instantaneous heart rate (IHR), six participants (two control and four Alzheimer's disease) were excluded. Four participants (one control and three Alzheimer's disease) were excluded due to abnormal ECGs, and one further Alzheimer's disease participant was excluded due to a noisy ECG signal. For the sixth participant, ECG was not measured. The four abnormal ECGs are shown in the Supplementary Material section 2.

Based on the group sizes, a power of 0.8 and an alpha of 0.05, the effect size sensitivity analysis performed in

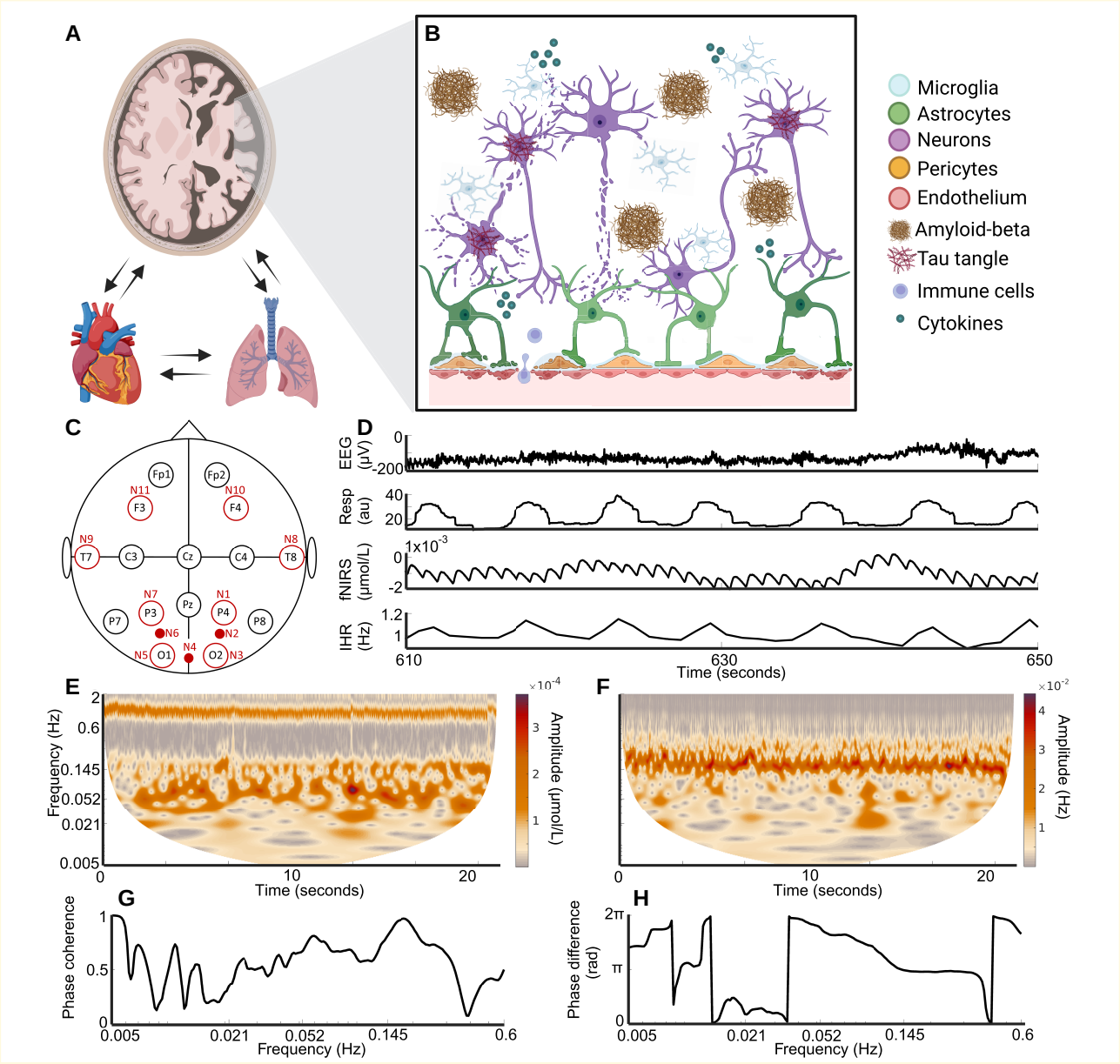

Figure 1 Overview figure. (**A**) Diagram of the brain, heart and lungs. Notice that the right side of the brain illustrates the atrophy associated with Alzheimer's disease. The arrows indicate interactions between the systems. (**B**) Illustration of the NVU, showing how astrocytes link the blood vessels and neurons. Alzheimer's disease is associated with a leaky blood–brain-barrier, inflammation, neurodegeneration, amyloid-beta plaques and tau tangles. (**C**) The probe layout for fNIRS and electroencephalogram (EEG). The open black circles indicate EEG probes, the open red circles indicate both an EEG and a fNIRS probe, while the small red circles indicate only fNIRS probes. (**D**) Example time-series measured from a control participant, shown for 30 s. IHR, instantaneous heart rate; Resp, respiration. (**E**) The WT of the fNIRS time-series from one participant. (**F**) The WT of the IHR time-series from the same participant. The *y*-axis is the same as in (**E**). (**G**) The WPC between the fNIRS and IHR time-series. (**H**) The phase difference between the fNIRS and IHR time-series. Rad, radians. Created in BioRender. Bjerkan, J. (2025) https://BioRender.com/z13u692.

G*Power reveal that an effect size of 1.0 or more can reliably be detected in this study.

Data acquisition

During the measurement, each participant was sitting in a comfortable chair in a quiet room at the Neurology Clinic, University Medical Center Ljubljana, Ljubljana, Slovenia or in the Nonlinear and Biomedical Physics Lab, Lancaster University, Lancaster, UK. The same measurement system and procedure were used in both locations. During the measurement intervals, which lasted ~30 min, the participants were asked to keep their eyes open, without a fixation point.

Table 1 Participant data and patient data

Participant data							
	N	Age (years)	Sex	BMI (kgm^{-2})	sBP (mmHg)	dBP (mmHg)	MMSE
AD	19	70.9 ± 6.7	12F/7M	25.2 ± 3.9	135 ± 23	79 ± 12	21.8 ± 4.9
C	20	67.8 ± 6.9	11F/9M	27.5 ± 3.0	139 ± 16	85 ± 11	
P		0.125		0.0543	0.173	0.140	

Patient data							
			CSF				
NN	Age (years)	Sex	P tau (pg/ml)	Tau (pg/ml)	Amyloid-beta 1–42 (pg/ml)	MMSE	Stage
1	56	F	107	704	580	24	1
2	68	M	63	398	417	NA	1
3	73	F	203	1568	397	19	1
4	77	F	382	67	557	24	1
5	68	M	146	29	431	28	0
6	60	F	1150	130	512	15	2
7	60	M	520	63	531	11	1
8	77	M	862	152	442	22	1
9	78	M	1403	134	545	18	2
10	76	F	885	108	572	17	2
11	69	F	2068	200	494	20	2
12	77	F	328	46	314	18	2
13	73	F	500	68	533	28	0
14	73	M	1347	221	373	25	1
15	63	F	1080	133	735	20	1
16	73	F	315	55	455	29	0
17	76	F	464	63	536	27	0
18	75	F	647	93	526	24	1
19	76	M	530	77	515	23	2

AD, Alzheimer's disease group; C, control group; N, number (of participants); *P*, *P*-value from the Wilcoxon rank-sum test comparing the groups; BMI, body mass index; sBP, systolic blood pressure; dBP, diastolic blood pressure; NN, participant number; CSF, cerebral spinal fluid; M, male; F, female; P tau, phosphorylated tau; MMSE, mini mental state exam. All MMSE scores were obtained within 1.5 months of the recording, apart from the scores of Patients 3, 4, 7 and 15 (obtained within 3 months). Stage 0 corresponds to MCI, Stage 1 to mild disease and Stage 2 to moderate disease. The cut-off for normal levels are approximately[30,31]: P tau <400 pg/ml, tau <60 pg/ml and amyloid 1–42 > 570 pg/ml.

A 16-channel system (V-Amp, Brain Products, Germany) was used to record the EEG at 1 kHz. An 8 source/8 detector LED system (NIRScout, NIRx, Germany) was used to record the fNIRS at 31.25 Hz. Locations of the resulting 16 EEG electrodes and 11 fNIRS sensors are shown in Fig. 1C. In addition, the EEG reference electrode was placed at FCz and the ground electrode at AFz. fNIRS measured relative changes in both oxygenated haemoglobin (oxyHb) and deoxygenated haemoglobin (deoxyHb) concentrations, and the oxyHb signal was used for this analysis: for the rest of the paper, it is the oxyHb signal that we are referring to when saying fNIRS signal or brain oxygenation time-series. Hence, oxygenation power refers to the power of the fNIRS time-series. An electrocardiogram (ECG) recorded the heart rate with bipolar precordial lead and a sampling frequency of 1.2 kHz, enabling sharp R-peaks to be reliably detected. The electrodes were placed on each shoulder and over the lower left rib, in a similar position as the D2 lead electrodes. A respiration belt wrapped around the participant's chest measured the respiration effort (Biopac TSD201 Respiratory Effort Transducer, Biopac Systems Inc., CA, USA), also with a sampling frequency of 1.2 kHz. Both ECG and respiration effort were measured with a signal conditioning system with 24-bit A/D conversion (CardioSignal, Institute Jožef Stefan, Slovenia). Figure 1D shows examples of time-series measured from a member of the control group.

Data preparation

All analysis was done using MATLAB, and the toolbox MODA was employed for the time-frequency analysis.[32] First, continuous 25 min time-series were extracted from the data. For each participant, the same 25 min interval was used for the different types of time-series, as simultaneous recordings were needed for the coherence analysis. For the different time-series, before power and coherence analysis, the data were detrended by subtracting a best-fit third-order polynomial. The data were also bandpass filtered between 0.005 and 2 Hz with a zero-phase Butterworth bandpass filter. Respiration and ECG time-series were resampled to 100 Hz for peak detection analysis. The EEG was resampled to 31.25 Hz to match the fNIRS sampling frequency for fNIRS-EEG coherence analysis. The IHR, instantaneous respiration rate (IRR) and fNIRS time-series were resampled to 20 Hz for coherence analysis.

Table 2 Summary of analysis methods and parameters

Analysis	Method	Parameter	N
Heart rate	Peak detection and ridge extraction	WT: $f_0 = 2$ $f \in [0.6,2]$ $f_s = 100$ Hz	15 AD, 18 C
Respiration rate	Peak detection and ridge extraction	WT: $f_0 = 1$ $f \in [0.1,0.6]$ $f_s = 100$ Hz	19 AD, 14 C
IHR power	Time-averaged WT	WT: $f_0 = 1$ $f \in [0.005,2]$ $f_s = 20$ Hz	15 AD, 18 C
IRR power	Time-averaged WT	WT: $f_0 = 1$ $f \in [0.005,2]$ $f_s = 20$ Hz	19 AD, 14 C
fNIRS power and coherence	Time-averaged WT and WPC	WT: $f_0 = 1$ $f \in [0.005,4]$ $f_s = 31.25$ Hz	19 AD, 20 C
IHR-respiration coherence	WPC	WT: $f_0 = 1$ $f \in [0.005,2]$ $f_s = 20$ Hz	15 AD, 14 C
IHR-fNIRS coherence	WPC	WT: $f_0 = 1$ $f \in [0.005,4]$ $f_s = 20$ Hz	15 AD, 18 C
Respiration-fNIRS coherence	WPC	WT: $f_0 = 1$ $f \in [0.005,4]$ $f_s = 20$ Hz	19 AD, 14 C
fNIRS-EEG coherence	WPC	WT: $f_0 = 1$ $f \in [0.005,4]$ $f_s = 31.25$ Hz	19 AD, 20 C
EEG power and coherence	Time-averaged WT and WPC	WT: $f_0 = 1$ $f \in [0.005,4]$ $f_s = 31.25$ Hz WFT: $f \in [4,48]$ $f_s = 142$ Hz	19 AD, 20 C

N, number (of participants); AD, Alzheimer's disease group; C, control group; WT, wavelet transform; WFT, windowed Fourier transform; WPC, wavelet phase coherence; IHR, instantaneous heart rate; IRR, instantaneous respiration rate; f_s, sampling frequency; f_0, frequency resolution parameter.

An overview of the analysis methods and parameters can be found in Table 2. Non-linear mode decomposition was used to remove the cardiac artefact in EEG caused by cross-talk between brain electrical activity and heart electrical activity.[33]

Peak detection

To detect the IHR and IRR, peak detection was used and then checked using ridge extraction.[34] A custom MATLAB script identified the R-peaks in the ECG or the maxima in the respiration effort signal. At the mid-point between two peaks the IHR or IRR was set to the inverse of the time between the peaks. Linear interpolation was then used to find the values between each of these points and produce equidistantly sampled time-series. The resulting time-series of IRR or IHR had a sampling frequency of 100 Hz. However, by construction, these time-series cannot contain information on frequencies higher than half of the heart rate or respiration rate frequencies. Hence, they were downsampled to 20 Hz before further analysis. The average heart/respiration rate was found as the average of the IHR/IRR. To measure the variability in the heart and respiration rates, the standard deviations (SDs) of the IHR and IRR were found. When we refer to the respiration signal throughout the manuscript, we refer to the respiration effort, i.e. the raw respiration time-series as seen in Fig. 1D.

Physiological oscillations: frequency bands

Previous time-frequency analysis of time-series such as blood flow and cardiac function has shown that cardiovascular oscillations are manifested in specific frequency intervals, corresponding to different physiological processes.[21] These frequency intervals and their physiological origins are summarized in Table 3, and range from 0.005 to 2 Hz. The cardiovascular oscillations overlap with slow oscillations in the EEG,[35] whose origin is still debated.

The lowest frequency of interest was therefore 0.005 Hz. We analysed fNIRS and EEG up to 4 Hz to include the δ band in EEG. fNIRS is not thought to contain oscillatory modes faster than the cardiac activity.

Power and coherence, which are explained below, were averaged within the frequency bands to obtain a single value per person per probe or probe combination.

Table 3 Frequency bands

	Frequency (Hz)	Period (s)	Physiological process
Endothelial	0.005–0.0095	105–200	Endothelial activity that modulates the activity of SMCs by the release of substances other than NO.
Endothelial NO	0.0095–0.021	48–105	Endothelial activity that modulates the activity of SMCs by the release of NO.
Neurogenic	0.021–0.052	19–48	Neurogenic activity by the autonomous nervous system that modulates the activity of SMCs by the release of substances.
Myogenic	0.052–0.145	7–19	SMCs alter their activity in response to intravascular pressure changes, and thus contract or relax.
Respiration	0.145–0.6	1.7–7	Respiration activity.
Cardiac	0.6–1.7	1.7–0.6	Heart activity.

Cardiovascular frequency bands with frequency ranges, the corresponding periods in seconds and the underlying physiological process.[21]

Strength of oscillations: wavelet transform

We are interested in the presence and strength of the cardiovascular oscillations, and in whether there are differences between the Alzheimer's disease and control groups. Previous time-frequency analysis of cardiovascular oscillations has shown that these oscillations are time-varying.[21] This is likely due to biological systems being open systems, with interacting sub-systems (e.g. cardiorespiratory interactions) that are also interacting with the environment (e.g. through breathing, the body inhales oxygen from the environment and exhales carbon dioxide). This time-variability is why time-frequency analysis can be more appropriate than frequency-domain analysis when studying cardiovascular oscillations. In addition, cardiovascular oscillations are manifested in the frequency interval 0.005–2 Hz, meaning that the oscillations have periods from around 0.5 to 200 s. To capture such multi-scale dynamics, a logarithmic frequency resolution is desirable. The WT is therefore an excellent choice for the analysis,[36] and can be thought of as a convolution of the time-series with a mother wavelet. The wavelet is finite and centred on one time, so to achieve time resolution the wavelet is moved across the time-series. In order to investigate various frequencies, the wavelet is stretched and squeezed. The Morlet wavelet was used in this analysis, with a frequency resolution parameter of 1.

From the transform, an instantaneous amplitude and an instantaneous phase for each frequency are obtained. We average the amplitude over time, and square it, to find the time-averaged WT power. This is similar to the use of a Fourier spectrum, but has the advantages discussed above.

Coordination of oscillations: wavelet phase coherence

In order to quantify potential interactions between subsystems of the body, we treat the cardiovascular system and the brain as interacting phase oscillators.[21] If the phase difference between two oscillations is constant throughout time, it indicates an underlying interaction, and we quantify the consistency of the phase difference using WPC.[25-27] The instantaneous phase obtained from the WT, at a time t and frequency k for oscillator 1 is $\theta^1_{t,k}$ The phase difference between oscillator 1 and 2 is given by:

$$\Delta\theta_{t,k} = \theta^1_{t,k} - \theta^2_{t,k}.$$

The time-averaged WPC is then found as:

$$\mathrm{WPC}_k = \sqrt{\langle\cos(\Delta\theta_k)\rangle^2 + \langle\sin(\Delta\theta_k)\rangle^2}.$$

The brackets indicate that the cosine and sine terms are averaged over all times. WPC_k takes values from 0 to 1, where 1 indicates a constant phase difference throughout the length of the time-series. There is one coherence value per frequency and, due to the properties of the WT discussed above, the WPC is suitable to investigate coherence in time-series that contain several oscillations of different frequencies. It is model-free, and completely independent of amplitude information. The WPC was calculated between fNIRS-fNIRS, fNIRS-IHR, fNIRS-respiration, fNIRS-EEG and IHR-respiration time-series.

We define the global coherence as the average coherence of all unique probe combinations in a frequency band, because the WPC between oscillator 1 and 2 is the same as the WPC between oscillator 2 and 1. For example, oxyHb global myogenic coherence is the average coherence in the myogenic band of 55 fNIRS probe combinations.

Effect size

Effect size was calculated to quantify how different the groups are, when a significant difference was found. The effect size was calculated *post hoc* with a non-parametric adjustment to the Cohen's d.[37,38] Starting with the standard score z, found from ranks, r was calculated as

$$r = \frac{z}{N},$$

where N was the total sample size.[39] Cohen's d was then calculated as:

$$d = \frac{2r}{\sqrt{1-r^2}}.$$

An effect size between 0.5 and 0.8 is considered medium, while above 0.8 is considered large.

Statistical analysis

The WPC computed between two randomly generated time-series is not necessarily 0, and so a method is needed for the

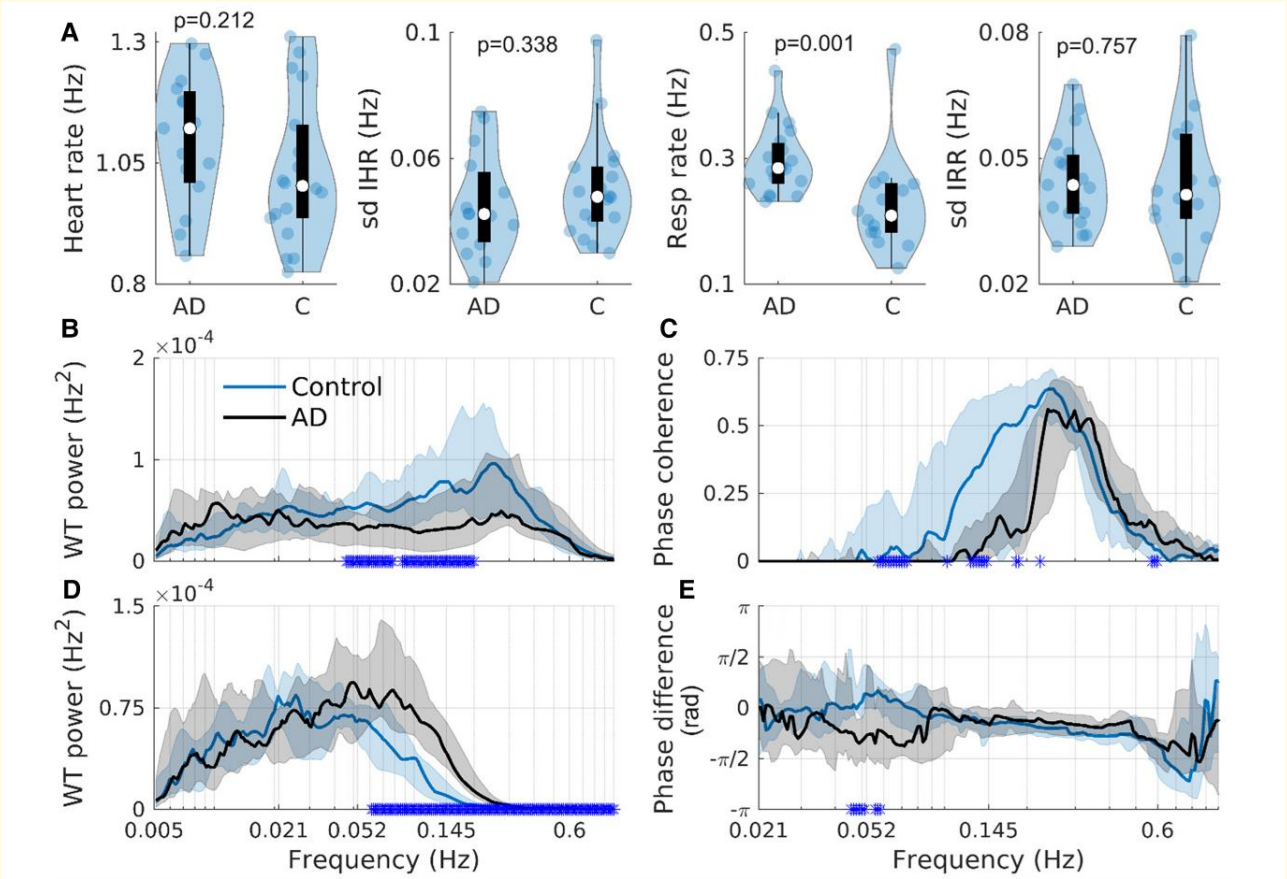

Figure 2 Cardiorespiratory oscillations. (**A**) Violin plots showing the average heart rate, SD IHR (N = 18 for controls, N = 15 for AD), average respiration rate and the SD IRR (N = 14 for controls, N = 19 for AD). Each point in the plots corresponds to one participant's data. (**B**) The IHR WT power (N = 18 for controls, N = 15 for AD). (**C**) The WPC between the IHR and respiration time-series (N = 14 for controls, N = 15 for AD). (**D**) The IRR WT power (N = 14 for controls, N = 19 for AD). (**E**) The phase difference between the IHR and respiration time-series (N = 14 for controls, N = 19 for AD). A negative value indicates that respiration was preceding the IHR. The black and blue solid lines show the group medians, while the shaded areas show the 25–75th percentiles. A blue star on the *x*-axis indicates a significant difference ($P \leq 0.05$) between the groups at that frequency. All *P*-values were calculated using the Wilcoxon rank-sum test. AD, Alzheimer's disease; C, controls.

detection of significant coherence. For this, inter-subject surrogates were used.[40] This tests what coherence level can be obtained when calculating WPC between time-series from two different participants. This coherence can only be random, and cannot signify a coupling or interaction between the oscillations. So, for each participant, the significance threshold was chosen as the 95th percentile of the 166 inter-subject coherences at each frequency. The effective coherence was then found by subtracting this threshold from the original coherence, and only effective coherence is shown throughout the paper.

When testing for significant differences in power or effective coherence between the two groups the non-parametric two-sided Wilcoxon rank-sum test was used. *P*-values below 0.05 were considered as significant. Performing many significance tests increases the chance of false positives, known as the multiple comparison problem. In this analysis, coherence and power were averaged in time and frequency, and so only the number of sensor combinations contributes to the multiple comparison problem. Assuming all null-hypotheses were true (i.e. no difference between the groups), and $\alpha = 0.05$, the number of expected null-hypotheses being incorrectly rejected was 2.75 for the fNIRS coherence analysis and 8.8 for the fNIRS-EEG coherence analysis. The probability of obtaining *X* or more positive findings from a total of *N* tries can be found from the binomial probability.[41] The probability of a positive finding was set to 0.05, and the total number of tries was 55 for the NIRS coherence analysis and 176 for the NIRS-EEG coherence analysis. If the binomial probability of obtaining *X* positive findings was over 5%, the results were corrected for multiple comparison using the Benjamini–Hochberg (BH) correction.[42]

Results

Here, we present results that were obtained from 25 min continuous recordings of fNIRS, EEG, ECG and respiration

effort from the 39 participants (19 Alzheimer's disease participants and 20 control participants), whose details are provided in Table 1. As reported in the previous section on participants, in some cases, the signals were not of sufficient quality for inclusion. The number of participants in each comparison is indicated in Table 2.

Cardiorespiratory oscillations

There are no significant differences in the average heart rate ($P = 0.21$) or SD of the IHR ($P = 0.34$) between the two groups (Fig. 2A). The average respiration rate is significantly different between the groups ($P = 0.001$), with an effect size of 1.45 (Table 4). The median rate is 0.21 Hz (~13 breaths/min) for the control group, and 0.28 Hz (~17 breaths/min) for the Alzheimer's disease group (Fig. 2). The SD IRR is not significantly different ($P = 0.76$), see Fig. 2A. The control group has higher IHR power in the range 0.05–0.2 Hz (Fig. 2B), while the Alzheimer's disease group has higher IRR power in the range 0.06–1 Hz (Fig. 2D).

The IHR-respiration effective phase coherence is significantly different between the two groups in the range 0.06–0.07 and ~1.4 Hz (Fig. 2C), and the control group has higher coherence. In both groups, the phase difference is negative in the 0.145–0.5 Hz range, indicating that respiration is leading. The Supplementary Material section 2 contains additional IHR results. Analysis of 25 min-recordings for all participants for which ECG was recorded (19 Alzheimer's disease and 18 control) and 5 min-recordings from the originally included participants (15 Alzheimer's disease and 18 control), where artefacts were avoided, show that the length of recording does not weaken the significant findings, but including the participants with abnormal ECGs does.

Brain oxygenation oscillations

Next, phase coherence between respiration/IHR and fNIRS signals was found. In Fig. 3A and B, this is shown at location N11 (see Fig. 1C for sensor locations). The coherence with the remaining fNIRS sensors is shown in the Supplementary Material, sections 3 and 4. For both groups, IHR-fNIRS effective phase coherence was seen in the 0.052–0.6 Hz frequency range. Respiration-fNIRS effective phase coherence is mostly found in the 0.145–0.6 Hz range. The phase difference increases steadily from ~0.06 to ~0.3 Hz, suggesting a consistent time lag between the two oscillators of around 2.5 s. In Fig. 3A, one can see that the IHR-fNIRS coherence is reduced in the Alzheimer's disease group, which is consistent across all fNIRS channels. The phase difference is also significantly different between the two groups around 0.2 Hz, a result that is consistent in 9/11 fNIRS channels. The respiration-fNIRS coherence is lower in the control group in the 0.3–0.4 Hz range, which is consistent in 4/11 fNIRS channels. On the other hand, the coherence is lower in the Alzheimer's disease group around 0.145 Hz, which is consistent in 7/11 fNIRS channels.

The Alzheimer's disease group has reduced brain oxygenation power compared to the control group in the neurogenic and myogenic frequency bands, both at N10 and N11 (Fig. 3C). In the myogenic band reduced power is also seen at N1 and N7. In addition, the Alzheimer's disease group has reduced power at N11 in the endothelial band. The probability of 1 or more positive findings, assuming all null hypothesis are true, is 45%, while for 2 or more it is 10%, and for 4 or more findings the probability is 0.16%. Further multiple comparison corrections are therefore not needed for the myogenic band, but have been applied to the neurogenic and endothelial bands. The significant difference in the endothelial band does not survive BH correction (original P-value 0.029, corrected P-value 0.21). The significant differences in the neurogenic band survive BH correction (original P-values 0.0035 and 0.0042, corrected P-values 0.0139 and 0.0139).

The global coherence in all frequency bands is significantly reduced in the Alzheimer's disease group (Fig. 3D). Effect size calculations are shown in Table 4, and generally show large differences between the groups.

Neuronal oscillations

For completeness, the results and discussion on neuronal oscillations extracted from the EEG are presented in the Supplementary Material, section 6.

Neurovascular oscillations

In the cardiac, myogenic and neurogenic frequency bands the Alzheimer's disease group has reduced neurovascular coherence in 14/176, 18/176 and 18/178 of the fNIRS-EEG combinations, respectively (Fig. 4A–C). In the control group, the coherence in the myogenic frequency band is highest in the parietal and central electrodes, while in the Alzheimer's disease group, it has more or less vanished (Fig. 4B). Coherence in the neurogenic band is generally low in both groups, but the control group has higher median values in the Fp1, Fp2 and central electrodes (Fig. 4C). The surrogate threshold at low frequencies is so high that the endothelial frequency band was not considered for the fNIRS-EEG coherence analysis. The probability of 14 or more positive findings, assuming all null hypothesis are true, is 5.9%, and therefore further multiple comparison corrections were needed in the cardiac band. None of the 14 combinations survives BH correction. The average effect size of the 18 significant combinations in the myogenic band is 0.76, while the average effect size in the neurogenic band is 0.84 (Table 4).

Discussion

We analysed time-series of cardiovascular and neural origin, from Alzheimer's disease patients and control participants in the resting-state, in an attempt to develop a non-invasive methodology for assessing the functioning of the NVU

Table 4 Effect size

	Cohen's *d*
Average respiration rate	1.45
fNIRS power in neurogenic band	N10: 1.13, N11: 1.11
fNIRS power in myogenic band	N1: 0.89, N7: 0.85, N10: 1.16, N11: 1.19
fNIRS coherence in endothelial band	0.85
fNIRS coherence in neurogenic band	1.12
fNIRS coherence in myogenic band	1.22
fNIRS coherence in respiration band	0.88
fNIRS coherence in cardiac band	0.87
fNIRS-EEG coherence in myogenic band	0.76 ± 0.05
fNIRS-EEG coherence in neurogenic band	0.84 ± 0.16

The effect size calculations for various significant differences between the groups. The fNIRS power effect size is shown for each probe where a significant difference was found. For the fNIRS-EEG coherence in the myogenic band, the effect size is shown as mean ± SD of the 18 combinations with a significant difference.

in vivo. We find that data from Alzheimer's disease patients exhibit the following three main features:

- Decreased oxygenation power and decreased global oxygenation phase coherence compared to controls,
- Increased respiration rate compared to controls,
- Decreased neurovascular phase coherence compared to controls.

The following sections will discuss these findings and their implications.

Vascular and neurovascular alterations in Alzheimer's disease

We find stark changes in the oxygenation dynamics in the Alzheimer's disease group compared to the control group, when considering either the power or the coordination of oscillations (Fig. 3C and D). The Alzheimer's disease group has reduced fNIRS power at N10 and N11 in the myogenic and neurogenic frequency bands. The myogenic frequency band is linked to vasomotion caused by myogenic activity (i.e. SMCs activity),[21,43-45] which has also been observed *in vivo* in the human cortex.[46] The neurogenic frequency band is associated with vasomotion caused by nervous activity.[44,45]

The production of ATP requires oxygen, and so the brain relies on a sufficient supply of oxygen to meet its metabolic demand. ATP is essential for maintaining cellular pumps, which, in turn, facilitate vasomotion, thereby controlling blood flow and oxygen supply.[47] Dysfunction in vasomotion is implicated in Alzheimer's disease,[47] such as hypercontractility.[48] Disrupted vasomotion might contribute to cerebral hypoperfusion, which is observed in Alzheimer's disease.[8] Mild cerebral hypoperfusion can negatively affect neuronal function, through disrupted neuronal protein synthesis, which is important for synaptic plasticity.[49] Hypoperfusion can also disrupt the ability of neurons to generate action potentials through decreased ATP production.

Another aspect of vasomotion especially relevant to Alzheimer's disease is that vasomotion is thought to contribute to clearance of amyloid-beta from the brain.[50] The reduced power might be a sign of reduced vasomotion and therefore reduced clearance in the Alzheimer's disease brain. The reduced clearance might further affect the vasomotion, as amyloid-beta has a negative effect on endothelial cells.[51] The need for additional energy in response to increased neuronal activity is signalled to the local microvasculature by neurons and astrocytes. This signal propagates further up the vascular tree, to the arteries, due to the electrical coupling between endothelial cells.[9] The endothelial cells are also in electrical contact with SMCs[52] and therefore reduced functioning of endothelial cells can impact vasomotion causing a vicious circle. The control of cerebral blood flow is orchestrated by the NVU.[9] Information flow is needed between the various cell types, such as neurons, astrocytes, pericytes, SMCs and endothelial cells. By calculating the phase coherence between oxygenation and neural signals, we aim to quantify this information flow, and thereby find a marker of the efficiency of the NVU.[17] We found previously that neurovascular phase coherence decreases with age and with Huntington's disease,[17,53] and we now show that this coherence is also reduced in Alzheimer's disease. This indicates reduced cooperation between cells in the NVU or, correspondingly, reduced neurovascular coupling.

Patients with Alzheimer's disease have reduced microvascular density compared to controls.[6] Further, morphological changes like kinking and focal constriction of the microvasculature have been seen in the Alzheimer's disease brain,[51] as well as a thickening of the basement membrane in Alzheimer's disease participants.[51] The morphological changes and thickening of the basement membrane could indicate that the cardiac pulse is not propagated to the microvasculature as efficiently as in control participants. These differences might explain why the cardiac coherence, and the coherence in the other frequency bands, are lower in the Alzheimer's disease group. In addition, loss of neurons and altered functional connectivity could also cause the brain oxygenation to be less coherent.

Altered oxygen dynamics in the brain might also be linked to systemic cardiovascular oscillations,[54] as the blood is oxygenated in the lungs and pumped by the heart. We find that the Alzheimer's disease group has a higher average respiration rate compared to the control group. Respiratory dysfunction is observed in Alzheimer's disease, such as decreased respiratory muscle strength compared to healthy controls.[55] A previous study found that a higher respiration rate was linked to cognitive impairment.[56] Another study found that both Alzheimer's disease and controls had similar breathing rates of around 18 breaths/min.[57] Further investigations are needed to confirm whether or not a higher respiration rate is common in Alzheimer's disease patients.

The reduced IHR-oxygenation coherence in the lower respiratory band (~0.145–0.2 Hz) seen in the Alzheimer's disease group (Fig. 3; Supplementary Material section 3) is likely due to their increased respiration rate. Across frontal, parietal and occipital locations the Alzheimer's disease group has reduced coherence in the myogenic frequency range,

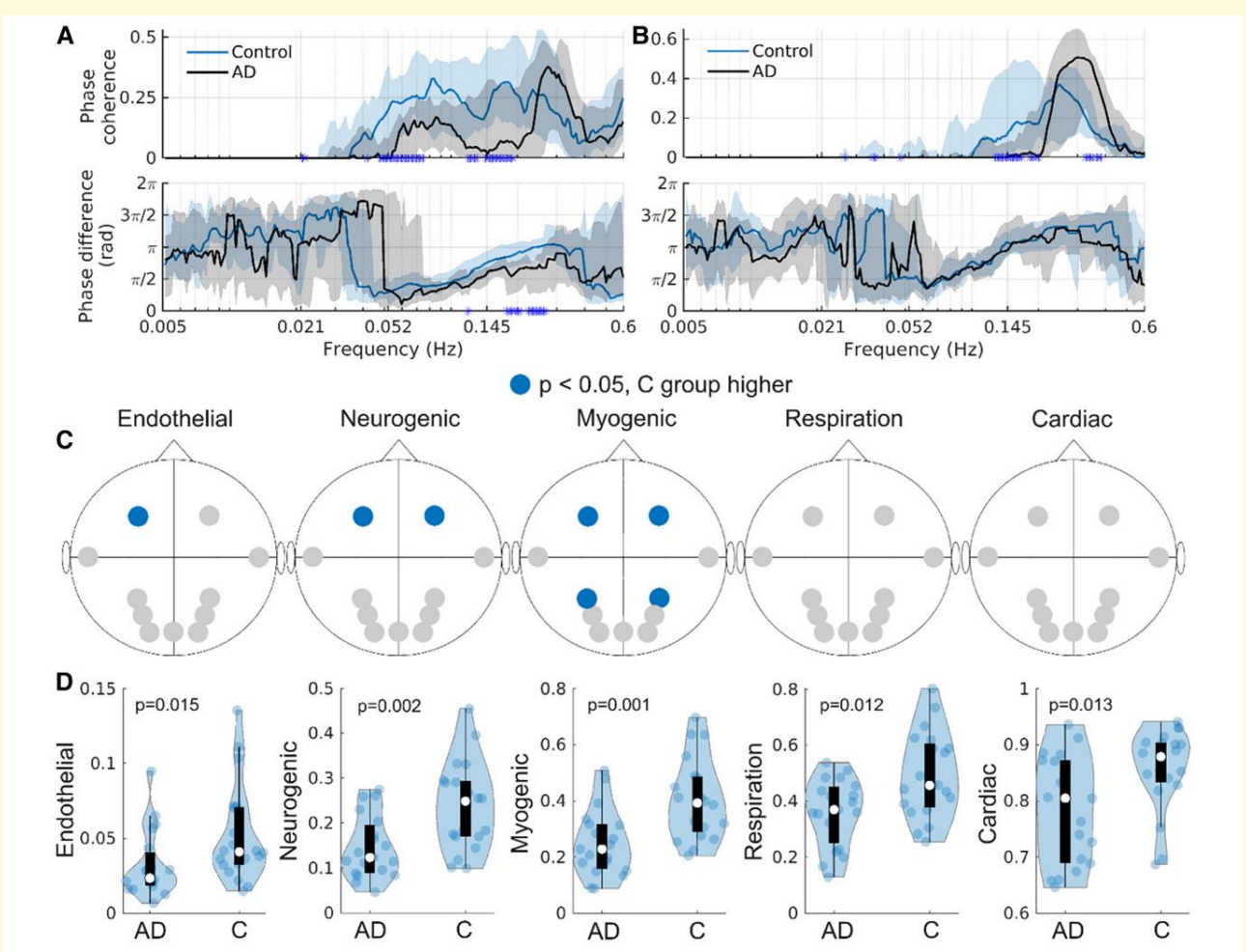

Figure 3 Brain oxygenation oscillations. (**A**) The WPC and phase difference between the IHR and brain oxygenation time-series at N11. N = 18 controls, N = 15 AD. (**B**) The WPC and phase difference between respiration and brain oxygenation time-series at N11. N = 14 controls, N = 19 AD. The black and blue solid lines show the group medians, while the shaded areas show the 25–75th percentiles. A blue star on the *x*-axis indicates a significant difference ($P \leq 0.05$) between the groups at that frequency. (**C**) Significant differences ($P \leq 0.05$) between the two groups in brain oxygenation power at specific probes, and in specific frequency bands, are indicated in blue. N = 20 controls, N = 19 AD. (**D**) Violin plots showing the brain oxygenation global coherence in the five cardiovascular frequency bands. N = 20 controls, N = 19 AD. All *P*-values were calculated using the Wilcoxon rank-sum test. AD, Alzheimer's disease; C, controls. Each point in the plots corresponds to one participant's data.

indicating a systemic origin. The reduction could be linked to disrupted vasomotion and the non-efficient propagation of the cardiac pulse discussed above. In both the control and Alzheimer's disease groups the IHR is leading the respiration oscillation in the myogenic band, indicating that the myogenic oscillation is propagated to the brain, as the SMCs responds to pressure changes caused by the cardiac pulse.

Concurrent EEG, fNIRS, ECG and respiration combined with state-of-the-art time-frequency analysis as a potential biomarker

In addition to contributing to the understanding of physiological changes in Alzheimer's disease, a secondary goal of the analysis was to consider the potential of these methods to create a biomarker. In the research setting, Alzheimer's disease can be defined using the National Institute on Aging and Alzheimer's Association Research framework.[58] This is a purely biological definition (i.e. not dependent on clinical symptoms), in which Alzheimer's disease is identified through Amyloid-beta, Tau and Neurodegeneration (A, T and N). These can be assessed by employing CSF, PET and MRI.[58] Functional MRI resting-state networks and blood-based tests also have potential as biomarkers.[59] Most of the mentioned biomarkers are expensive and some are invasive. As Alzheimer's disease is a global disease, having access to less-expensive, non-invasive and also portable techniques is desirable. In this respect, EEG and fNIRS are potential candidates.[60,61] If either EEG or fNIRS is taken in isolation, one obtains only an incomplete picture as neuronal activity and

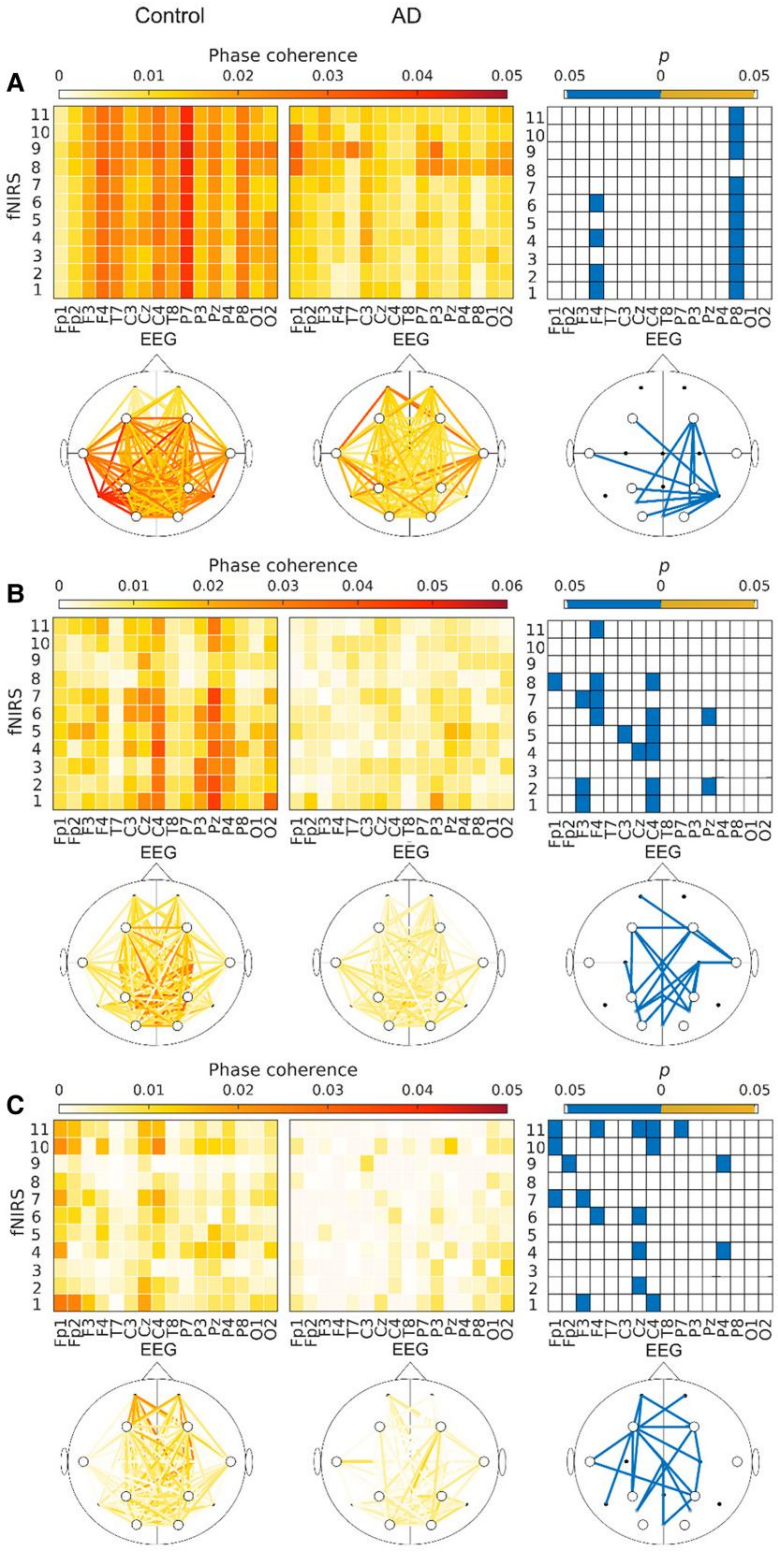

Figure 4 Neurovascular oscillations. (**A**) The WPC in the cardiac frequency band between fNIRS and electroencephalogram time-series, for all possible combinations. The left column shows the control group median, while the middle column shows the Alzheimer's disease group median. The right column shows significant differences ($P \leq 0.05$) between the groups. The square plots and head plots depict the same information. (**B**) As in (**A**), but for the myogenic band. (**C**) As in (**A**), but for the neurogenic band. All *P*-values were calculated using the Wilcoxon rank-sum test. AD, Alzheimer's disease; C, controls. N = 20 controls, N = 19 AD.

oxygenation are interlinked, and dependent on cardiorespiratory function. Fortunately, as is done in the present study and many others,[62] EEG and fNIRS can be combined in a single scan. Previous work related to Alzheimer's disease has been performed by Perpetuini *et al.*[63] and Chiarelli *et al.*,[64] where differences between the Alzheimer's disease group and control group were found in both studies. We now show that the inclusion of simultaneous measurements of ECG and respiration enables metabolic aspects to be taken into account.

Previous studies employing fNIRS to study oxygenation dynamics in dementia have generally focused on absolute values, Pearson correlation and entropy.[61,65] In contrast, in the present work, we have used a non-autonomous oscillatory dynamics approach.[66] Combining non-invasive measurements of neurovascular function with time-frequency analysis methods—specifically selected to study oscillations with time-varying frequencies—we have revealed clear differences between the Alzheimer's disease and control groups. Also focusing on time-dependence, Cruzat *et al.*[67] showed that the temporal irreversibility of brain activity measured by fMRI and EEG is reduced in Alzheimer's disease patients. They argue that this indicates that the unhealthy brain has activity closer to equilibrium dynamics. This might mean that the brain is less able to respond to environmental demands, or that intrinsic couplings are reduced. Non-autonomous dynamical systems[68] (i.e. systems with explicit time-dependence of their characteristic frequencies and couplings) have inherent time-irreversibility. While both approaches consider time-dependence, a strength of focusing specifically on oscillations is the clearer link to physiology.[69,70] Thus, our finding of reduced myogenic neurovascular coherence can be linked to decreased efficiency of the NVU. As such, our results provide a potential avenue for *in vivo* assessment of the efficiency of the NVU in the human brain.

Limitations and strengths

This study has several limitations, such as a relatively small sample size. A strength of the study is that the Alzheimer's disease patients were confirmed by standard biomarkers. The long recordings contain more information than shorter recordings and mean that sporadic or random changes in the investigated parameters would average out over time, making the significant differences between groups robust. However, it can be challenging for the participants to remain still during the recording. While some fidgeting can have impacted the measurements, it is very unlikely that this behaviour was oscillatory or that it can explain the group differences. This is illustrated by considering shorter time-series to repeat the analysis in Supplementary Figs. S3 and S6. To maintain alertness, the participants were asked to keep their eyes open during the measurement. However, we did not record electrooculography (EOG) signals or use EOG artefact rejection for the EEG time-series. Such an approach would not in fact have been feasible because time-series must be continuous for the coherence analysis of slow oscillations. This artefact affects only the EEG time-series by introducing large amplitude changes. As the WPC is independent of amplitude information, the artefact is unlikely to have affected the fNIRS-EEG coherence.

fNIRS measures only the relative changes in oxygenated and deoxygenated haemoglobin concentrations, and the exact locations of these changes are often unclear. This uncertainty complicates the quantification of absolute changes in these concentrations.[71] We use wavelengths of 760 and 850 nm, thus avoiding wavelengths in the 770–800 nm range previously discussed as giving less accurate measurements.[71] Haemodynamic changes in the scalp likely affect the amplitude of the signal more than the phase. However, amplitude-based measures are prone to cross-talk, movement artefacts, and other noise sources. For this reason, our approach emphasizes phase, as phase coherence has been shown to be more resilient to various types of noise.[27] Additionally, fNIRS is a relatively inexpensive, portable and non-invasive method,[72] making it a promising tool for monitoring haemodynamics in dementia.

Nested data is common in neuroscience and requires particular attention in their statistical evaluation.[73] Here, we aggregate data so that for each statistical test only one value per participant is considered. We check for group differences at the probe level for spectral power and at the global level for fNIRS coherence. We also apply inter-subject surrogates to ensure that coherence is statistically significant.

Concluding remarks

This work shows clear evidence of changes in brain oxygenation dynamics in Alzheimer's disease, thereby supporting suggestions that vascular changes contribute to neurodegeneration. We detected reduced oxygenation power in the neurogenic and myogenic frequency bands, which are both associated with vasomotion. Reduced vasomotion can contribute to insufficient delivery of oxygen and nutrients and to reduced clearance of amyloid-beta which is known to aggregate in Alzheimer's disease. Not surprisingly, we see direct evidence of reduced efficiency of the NVU in Alzheimer's disease, investigated by phase coherence between EEG and fNIRS. Another important discovery is the significant increase in the frequency of respiration in participants with Alzheimer's disease, suggesting the presence of inflammation.

The present work stands on two pillars. First, we consider both the neuronal and the cardiovascular aspects of brain function to understand changes in Alzheimer's disease. Second, we apply multi-scale oscillatory dynamics analysis to gain neurophysiological insight into these changes.

After further validation, such a method could be used for the evaluation of treatments and routine follow-ups. With disappointing results from protein-focused drug trials, the vasculature and NVU are promising targets for future treatments of Alzheimer's disease.

Supplementary material

Supplementary material is available at *Brain Communications* online.

Acknowledgements

We thank all the participants for partaking in this study, and Franci Benko, research nurse at the Department of Neurology, University Medical Centre Ljubljana, for his assistance in organising and performing the measurements. In addition, we would like to thank Fajko Bajrović for support with the clinical aspects of the study and Boštjan Dolenc for the automated initial checks of the data. The High End Computing facility at Lancaster University was used for data analysis. Figure 1 and the Graphical Abstract were created in https://BioRender.com. Graphical Abstract: Bjerkan, J. (2025) https://BioRender.com/z11w988.

Funding

The Engineering and Physical Sciences Research Council (UK) under Grant No. EP/M006298/1 and the Slovenian Research Agency (ARRS) (Program No. P20232) funded this research. J.B. is funded by the Sir John Fisher Foundation. The Engineering and Physical Sciences Research Council (UK) Grant Nos. EP/100999X1 and EP/M006298/1, the EU projects Brain, Respiration and Cardiac Causalities in Anaesthesia (BRACCIA) [517133] and Complex Oscillatory Systems: Modelling and Analysis (COSMOS) [642563], the Action Medical Research (UK) Marker for Autism Spectrum Disorder based on EEG Analysis (MASDA) Project [GN1963] and the Slovenian Research Agency (ARRS) (Program No. P20232) supported the development of the toolbox MODA.

Competing interests

The authors report no competing interests.

Data availability

The data will be made available on Lancaster University PURE depository, accessible for researchers that share their re-use intention (10.17635/lancaster/researchdata/692). The toolbox MODA is freely available on GitHub: https://github.com/luphysics/MODA. It was developed by the Nonlinear & Biomedical Physics Group at Lancaster University and the Nonlinear Dynamics and Synergetic Group at the University of Ljubljana.

References

1. Masters CL, Simms G, Weinman NA, Multhaup G, McDonald BL, Beyreuther K. Amyloid plaque core protein in Alzheimer disease and down syndrome. *Proc Natl Acad Sci U S A*. 1985;82(12):4245-4249.
2. Hardy J, Allsop D. Amyloid deposition as the central event in the aetiology of Alzheimer's disease. *Trends Pharmacol Sci*. 1991;12(10):383-388.
3. Iqbal K, Liu F, Gong CX, Grundke-Iqbal I. Tau in Alzheimer disease and related tauopathies. *Curr Alzheimer Res*. 2010;7(8):656-664.
4. Pini L, Pievani M, Bocchetta M, *et al*. Brain atrophy in Alzheimer's disease and aging. *Ageing Res Rev*. 2016;30:25-48.
5. Klohs J. An integrated view on vascular dysfunction in Alzheimer's disease. *Neurodegener Dis*. 2019;19(3–4):109-127.
6. Zlokovic BV. Neurovascular pathways to neurodegeneration in Alzheimer's disease and other disorders. *Nat Rev Neurosci*. 2011;12(12):723-738.
7. Cortes-Canteli M, Iadecola C. Alzheimer's disease and vascular aging: JACC focus seminar. *J Am Coll Cardiol*. 2020;75(8):942-951.
8. Nelson AR, Sweeney MD, Sagare AP, Zlokovic BV. Neurovascular dysfunction and neurodegeneration in dementia and Alzheimer's disease. *Biochim Biophys Acta*. 2016;1862(5):887-900.
9. Iadecola C. The neurovascular unit coming of age: A journey through neurovascular coupling in health and disease. *Neuron*. 2017;96:17-42.
10. González-Reyes RE, Nava-Mesa MO, Vargas-Sánchez K, Ariza-Salamanca D, Mora-Muñoz L. Involvement of astrocytes in Alzheimer's disease from a neuroinflammatory and oxidative stress perspective. *Front Mol Neurosci*. 2017;10:427.
11. Tarantini S, Tran CHT, Gordon GR, Ungvari Z, Csiszar A. Impaired neurovascular coupling in aging and Alzheimer's disease: Contribution of astrocyte dysfunction and endothelial impairment to cognitive decline. *Exp Gerontol*. 2017;94:52-58.
12. Sun N, Akay LA, Murdock MH, *et al*. Single-nucleus multiregion transcriptomic analysis of brain vasculature in Alzheimer's disease. *Nat Neurosci*. 2023;26(6):970-982.
13. Nikulin VV, Fedele T, Mehnert J, *et al*. Monochromatic ultra-slow (\sim0.1 Hz) oscillations in the human electroencephalogram and their relation to hemodynamics. *Neuroimage*. 2014;97:71-80.
14. Hiltunen T, Kantola J, Abou Elseoud A, *et al*. Infra-slow EEG fluctuations are correlated with resting-state network dynamics in fMRI. *J Neurosci*. 2014;34(2):356-362.
15. Grooms JK, Thompson GJ, Pan WJ, *et al*. Infraslow electroencephalographic and dynamic resting state network activity. *Brain Connect*. 2017;7(5):265-280.
16. Nunez-Elizalde AO, Krumin M, Reddy CB, *et al*. Neural correlates of blood flow measured by ultrasound. *Neuron*. 2022;110(10):1631-1640.e4.
17. Bjerkan J, Lancaster G, Meglič B, *et al*. Aging affects the phase coherence between spontaneous oscillations in brain oxygenation and neural activity. *Brain Res Bull*. 2023;201:110704.
18. Scheeren TW, Schober P, Schwarte LA. Monitoring tissue oxygenation by near infrared spectroscopy (NIRS): Background and current applications. *J Clin Monit Comput*. 2012;26(4):279-287.
19. Wilcox T, Biondi M. fNIRS in the developmental sciences. *Wiley Interdiscip Rev Cogn Sci*. 2015;6(3):263-283.
20. Burle B, Spieser L, Roger C, Casini L, Hasbroucq T, Vidal F. Spatial and temporal resolutions of EEG: Is it really black and white? A scalp current density view. *Int J Psychophysiol*. 2015;97(3):210-220.
21. Stefanovska A. Coupled oscillators: Complex but not complicated cardiovascular and brain interactions. *IEEE Eng Med Biol Mag*. 2007;26(6):25-29.
22. Suprunenko YF, Clemson PT, Stefanovska A. Chronotaxic systems: A new class of self-sustained nonautonomous oscillators. *Phys Rev Lett*. 2013;111(2):024101.
23. Newman J, Scott JP, Adams JR, Stefanovska A. Intermittent phase dynamics of non-autonomous oscillators through time-varying phase. *Phys Nonlinear Phenom*. 2024;461:134108.
24. Adams JR, Newman J, Stefanovska A. Distinguishing between deterministic oscillations and noise. *Eur Phys J Spec Top*. 2023;232(20):3435-3457.
25. Bandrivskyy A, Bernjak A, McClintock PVE, Stefanovska A. Wavelet phase coherence analysis: Application to skin temperature and blood flow. *Cardiovasc Eng*. 2004;4(1):89-93.

26. Sheppard LW, Stefanovska A, McClintock PVE. Testing for time-localized coherence in bivariate data. *Phys Rev E*. 2012;85(4):046205.
27. Barnes SJK, Bjerkan J, Clemson PT, Newman J, Stefanovska A. Phase coherence—A time-localized approach to studying interactions. *Chaos*. 2024;34(7):073155.
28. Rollo J, Crawford J, Hardy J. A dynamical systems approach for multiscale synthesis of Alzheimer's pathogenesis. *Neuron*. 2023;111(14):2126-2139.
29. Xiong LI, Garfinkel A. Are physiological oscillations physiological? *J Physiol*. 2025. https://doi.org/10.1113/JP285015
30. Sjögren M, Vanderstichele H, Ågren H, *et al*. Tau and Aβ42 in cerebrospinal fluid from healthy adults 21–93 years of age: Establishment of reference values. *Clin Chem*. 2001;47(10):1776-1781.
31. Mulder C, Verwey NA, van der Flier WM, *et al*. Amyloid-β(1–42), total tau, and phosphorylated tau as cerebrospinal fluid biomarkers for the diagnosis of Alzheimer disease. *Clin Chem*. 2010;56(2):248-253.
32. Newman J, Lancaster G, Stefanovska A. Multiscale Oscillatory Dynamics Analysis User Manual v1.01, Lancaster University. Available at https://github.com/luphysics/MODA. 2018.
33. Iatsenko D, McClintock PVE, Stefanovska A. Nonlinear mode decomposition: A noise-robust, adaptive decomposition method. *Phys Rev E*. 2015;92(3):032916.
34. Iatsenko D, McClintock PVE, Stefanovska A. Extraction of instantaneous frequencies from ridges in time–frequency representations of signals. *Signal Process*. 2016;125:290-303.
35. Buzsáki G, Draguhn A. Neuronal oscillations in cortical networks. *Science*. 2004;304(5679):1926-1929.
36. Bračič M, Stefanovska A. Wavelet-based analysis of human blood-flow dynamics. *Bull Math Biol*. 1998;60(5):919-935.
37. Fritz CO, Morris PE, Richler JJ. Effect size estimates: Current use, calculations, and interpretation. *J Exp Psychol Gen*. 2012;141(1):2-18.
38. Ivarsson A, Andersen MB, Johnson U, Lindwall M. To adjust or not adjust: Nonparametric effect sizes, confidence intervals, and real-world meaning. *Psychol Sport Exerc*. 2013;14(1):97-102.
39. Coolican H. *Research methods and statistics in psychology*. 5th ed. Hodder Education; 2009.
40. Lancaster G, Iatsenko D, Pidde A, Ticcinelli V, Stefanovska A. Surrogate data for hypothesis testing of physical systems. *Phys Rep*. 2018;748:1-60.
41. Montez T, Poil SS, Jones BF, *et al*. Altered temporal correlations in parietal alpha and prefrontal theta oscillations in early-stage Alzheimer disease. *Proc Natl Acad Sci U S A*. 2009;106(5):1614-1619.
42. Benjamini Y, Hochberg Y. Controlling the false discovery rate: A practical and powerful approach to multiple testing. *J R Stat Soc Ser B Methodol*. 1995;57(1):289-300.
43. Mayhew JE, Askew S, Zheng Y, *et al*. Cerebral vasomotion: A 0.1-Hz oscillation in reflected light imaging of neural activity. *NeuroImage*. 1996;4(3 Pt 1):183-193.
44. Söderström T, Stefanovska A, Veber M, Svensson H. Involvement of sympathetic nerve activity in skin blood flow oscillations in humans. *Am J Physiol Heart Circ Physiol*. 2003;284(5):H1638-H1646.
45. Landsverk SA, Kvandal P, Bernjak A, Stefanovska A, Kirkeboen KA. The effects of general anesthesia on human skin microcirculation evaluated by wavelet transform. *Anesth Analg*. 2007;105(4):1012-1019.
46. Rayshubskiy A, Wojtasiewicz TJ, Mikell CB, *et al*. Direct, intraoperative observation of 0.1 Hz hemodynamic oscillations in awake human cortex: Implications for fMRI. *Neuroimage*. 2014;87:323-331.
47. Di Marco LY, Farkas E, Martin C, Venneri A, Frangi AF. Is vasomotion in cerebral arteries impaired in Alzheimer's disease? *J Alzheimers Dis*. 2015;46(1):35-53.
48. Chow N, Bell RD, Deane R, *et al*. Serum response factor and myocardin mediate arterial hypercontractility and cerebral blood flow dysregulation in Alzheimer's phenotype. *Proc Natl Acad Sci U S A*. 2007;104(3):823-828.
49. Iadecola C. Neurovascular regulation in the normal brain and in Alzheimer's disease. *Nat Rev Neurosci*. 2004;5(5):347-360.
50. Aldea R, Weller RO, Wilcock DM, Carare RO, Richardson G. Cerebrovascular smooth muscle cells as the drivers of intramural periarterial drainage of the brain. *Front Aging Neurosci*. 2019:11:1.
51. Kelleher RJ, Soiza RL. Evidence of endothelial dysfunction in the development of Alzheimer's disease: Is Alzheimer's a vascular disorder? *Am J Cardiovasc Dis*. 2013;3(4):197-226.
52. Drew PJ, Mateo C, Turner KL, Yu X, Kleinfeld D. Ultra-slow oscillations in fMRI and resting-ttate connectivity: Neuronal and vascular contributions and technical confounds. *Neuron*. 2020;107(5):782-804.
53. Bjerkan J, Kobal J, Lancaster G, *et al*. The phase coherence of the neurovascular unit is reduced in Huntington's disease. *Brain Commun*. 2024;6(3):fcae166.
54. Katura T, Tanaka N, Obata A, Sato H, Maki A. Quantitative evaluation of interrelations between spontaneous low-frequency oscillations in cerebral hemodynamics and systemic cardiovascular dynamics. *Neuroimage*. 2006;31(4):1592-1600.
55. Wrzesień A, Andrzejewski K, Jampolska M, Kaczyńska K. Respiratory dysfunction in Alzheimer's disease-consequence or underlying cause? Applying animal models to the study of respiratory malfunctions. *Int J Mol Sci*. 2024;25(4):2327.
56. Lucke JA, de Gelder J, Blomaard LC, *et al*. Vital signs and impaired cognition in older emergency department patients: The APOP study. *PLoS One*. 2019;14(6):e0218596.
57. Hibi S, Yamaguchi Y, Umeda-Kameyama Y, *et al*. Respiratory dysrhythmia in dementia with Lewy bodies: A cross-sectional study. *BMJ Open*. 2013;3(9):e002870.
58. Jack CR, Bennett DA, Blennow K, *et al*. NIA-AA Research framework: Toward a biological definition of Alzheimer's disease. *Alzheimers Dement*. 2018;14(4):535-562.
59. Dubois B, von Arnim CAF, Burnie N, Bozeat S, Cummings J. Biomarkers in Alzheimer's disease: Role in early and differential diagnosis and recognition of atypical variants. *Alzheimers Res Ther*. 2023;15(1):175.
60. Babiloni C, Arakaki X, Azami H, *et al*. Measures of resting state EEG rhythms for clinical trials in Alzheimer's disease: Recommendations of an expert panel. *Alzheimers Dement*. 2021;17(9):1528-1553.
61. Yeung MK, Chan AS. Functional near-infrared spectroscopy reveals decreased resting oxygenation levels and task-related oxygenation changes in mild cognitive impairment and dementia: A systematic review. *J Psychiatr Res*. 2020;124:58-76.
62. Li R, Yang D, Fang F, Hong KS, Reiss AL, Zhang Y. Concurrent fNIRS and EEG for brain function investigation: A systematic, methodology-focused review. *Sens Basel*. 2022;22(15):5865.
63. Perpetuini D, Chiarelli AM, Filippini C, *et al*. Working memory decline in Alzheimer's disease is detected by complexity analysis of multimodal EEG-fNIRS. *Entropy (Basel)*. 2020;22(12):1380.
64. Chiarelli AM, Perpetuini D, Croce P, *et al*. Evidence of neurovascular un-coupling in mild Alzheimer's disease through multimodal EEG-fNIRS and multivariate analysis of resting-state data. *Biomedicines*. 2021;9(4):337.
65. Butters E, Srinivasan S, O'Brien JT, Su L, Bale G. A promising tool to explore functional impairment in neurodegeneration: A systematic review of near-infrared spectroscopy in dementia. *Ageing Res Rev*. 2023;90:101992.
66. Stefanovska A, McClintock PVE. *Physics of biological oscillators. Understanding Complex Systems*. Springer; 2021.
67. Cruzat J, Herzog R, Prado P, *et al*. Temporal irreversibility of large-scale brain dynamics in Alzheimer's disease. *J Neurosci*. 2023;43(9):1643-1656.

68. Kloeden PE, Rasmussen M. *Nonautonomous dynamical systems*. American Mathematical Soc.; 2011.
69. Stefanovska A, Bračič M. Physics of the human cardiovascular system. *Contemp Phys*. 1999;40(1):31-55.
70. Shiogai Y, Stefanovska A, McClintock PVE. Nonlinear dynamics of cardiovascular ageing. *Phys Rep*. 2010;488(2–3):51-110.
71. Strangman G, Franceschini MA, Boas DA. Factors affecting the accuracy of near-infrared spectroscopy concentration calculations for focal changes in oxygenation parameters. *Neuroimage*. 2003;18(4):865-879.
72. Rathbone E, Fu D. Quantitative optical imaging of oxygen in brain vasculature. *J Phys Chem B*. 2024;128(29):6975-6989.
73. Aarts E, Verhage M, Veenvliet JV, Dolan CV, van der Sluis S. A solution to dependency: Using multilevel analysis to accommodate nested data. *Nat Neurosci*. 2014;17(4):491-496.

Chapter 5

The phase coherence of the neurovascular unit is reduced in Huntington's disease

This research is published in Brain Communications.

Bjerkan, J., Kobal, J., Lancaster, G., Šešok, S., Meglič, B., McClintock, P. V. E., Budohoski, K. P., Kirkpatrick, P. J. & Stefanovska, A. The phase coherence of the neurovascular unit is reduced in Huntington's disease. *Brain commun.* **6,** fcae166 (2024)

https://doi.org/10.1093/braincomms/fcae166 BRAIN COMMUNICATIONS 2024: fcae166 | 1

BRAIN COMMUNICATIONS

The phase coherence of the neurovascular unit is reduced in Huntington's disease

Juliane Bjerkan,[1] Jan Kobal,[2] Gemma Lancaster,[1] Sanja Šešok,[2] Bernard Meglič,[2] Peter V. E. McClintock,[1] Karol P. Budohoski,[3] Peter J. Kirkpatrick[3] and Aneta Stefanovska[1]

Huntington's disease is a neurodegenerative disorder in which neuronal death leads to chorea and cognitive decline. Individuals with ≥40 cytosine–adenine–guanine repeats on the interesting transcript 15 gene develop Huntington's disease due to a mutated huntingtin protein. While the associated structural and molecular changes are well characterized, the alterations in neurovascular function that lead to the symptoms are not yet fully understood. Recently, the neurovascular unit has gained attention as a key player in neurodegenerative diseases. The mutant huntingtin protein is known to be present in the major parts of the neurovascular unit in individuals with Huntington's disease. However, a non-invasive assessment of neurovascular unit function in Huntington's disease has not yet been performed. Here, we investigate neurovascular interactions in presymptomatic ($N = 13$) and symptomatic ($N = 15$) Huntington's disease participants compared to healthy controls ($N = 36$). To assess the dynamics of oxygen transport to the brain, functional near-infrared spectroscopy, ECG and respiration effort were recorded. Simultaneously, neuronal activity was assessed using EEG. The resultant time series were analysed using methods for discerning time-resolved multiscale dynamics, such as wavelet transform power and wavelet phase coherence. Neurovascular phase coherence in the interval around 0.1 Hz is significantly reduced in both Huntington's disease groups. The presymptomatic Huntington's disease group has a lower power of oxygenation oscillations compared to controls. The spatial coherence of the oxygenation oscillations is lower in the symptomatic Huntington's disease group compared to the controls. The EEG phase coherence, especially in the α band, is reduced in both Huntington's disease groups and, to a significantly greater extent, in the symptomatic group. Our results show a reduced efficiency of the neurovascular unit in Huntington's disease both in the presymptomatic and symptomatic stages of the disease. The vasculature is already significantly impaired in the presymptomatic stage of the disease, resulting in reduced cerebral blood flow control. The results indicate vascular remodelling, which is most likely a compensatory mechanism. In contrast, the declines in α and γ coherence indicate a gradual deterioration of neuronal activity. The results raise the question of whether functional changes in the vasculature precede the functional changes in neuronal activity, which requires further investigation. The observation of altered dynamics paves the way for a simple method to monitor the progression of Huntington's disease non-invasively and evaluate the efficacy of treatments.

1 Department of Physics, Lancaster University, Lancaster LA1 4YB, UK
2 Department of Neurology, University Medical Centre, 1525 Ljubljana, Slovenia
3 Division of Neurosurgery, Department of Clinical Neurosciences, Addenbrooke's Hospital, University of Cambridge, Cambridge CB2 0QQ, UK

Correspondence to: Aneta Stefanovska
Department of Physics, Lancaster University
C507, C—Floor, Physics Building,
Lancaster LA1 4YB, UK
E-mail: aneta@lancaster.ac.uk

Keywords: neurovascular unit; time–frequency analysis; multiscale oscillatory analysis; phase coherence; brain oxygenation

Received December 05, 2023. Revised March 07, 2024. Accepted May 09, 2024. Advance access publication June 10, 2024

Graphical Abstract

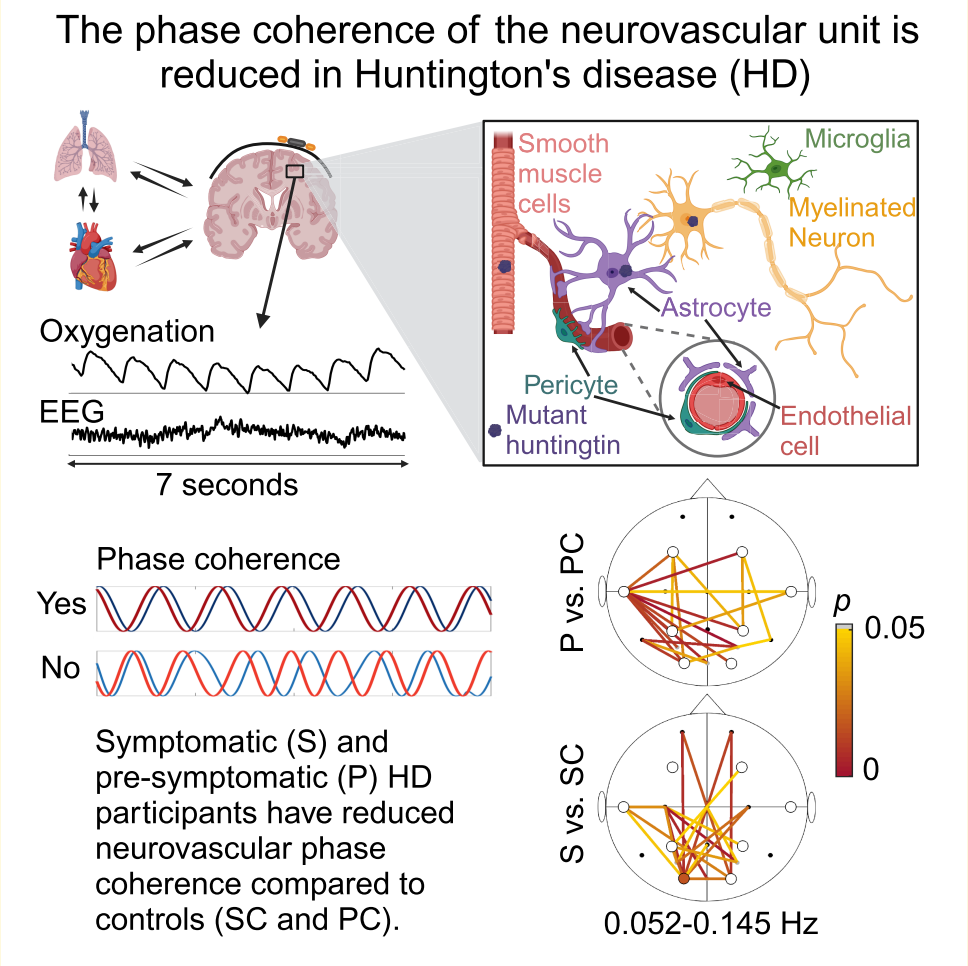

Introduction

Huntington's disease is a genetic neurodegenerative disease, causing disordered movement, altered cognition and behavioural changes. The disease is linked to a mutation in the interesting transcript 15 gene on chromosome 4, which codes for the protein huntingtin. The mutation involves additional cytosine–adenine–guanine (CAG) repeats compared to the normal (17–30). Possession of 40 or more CAG repeats almost guarantees development of Huntington's disease, while 36–39 repeats may lead to Huntington's disease (reduced penetrance).[1] The abnormal huntingtin protein damages the brain cells and gives rise to neuronal death.[2] By the time symptoms manifest, the striatum has decreased in volume by around 50%.[3] The corresponding structural and functional changes of the brain have been demonstrated using MRI and EEG.[2,4]

Recently, the role of vascular and neurovascular changes in neurodegenerative diseases has gained attention, often as a key early event important in disease progression.[5,6] The vasculature is not a bystander in the brain but, rather, actively supplies the brain with the energy it needs to function properly. The supply is regulated by the cells making up the neurovascular unit (NVU), including endothelial cells, astrocytes, neurons and smooth muscle cells (see Fig. 1C).[7,8] In people with Huntington's disease, the mutant huntingtin protein is found in the major components of the NVU.[9,10] Brain vascular changes observed post-mortem in human Huntington's disease include an increased number of small vessels, increased vessel density and increased blood–brain barrier (BBB) permeability.[9] Furthermore, Garcia *et al.*[11] have recently reported molecular changes in vascular and glial cells in Huntington's disease. They involve activation of immune signalling and a decrease in the levels of proteins important for BBB function. Based on the aforementioned changes to the vasculature and glial cells, we hypothesize that the functioning of the NVU is decreased in people with Huntington's disease. However, the efficiency

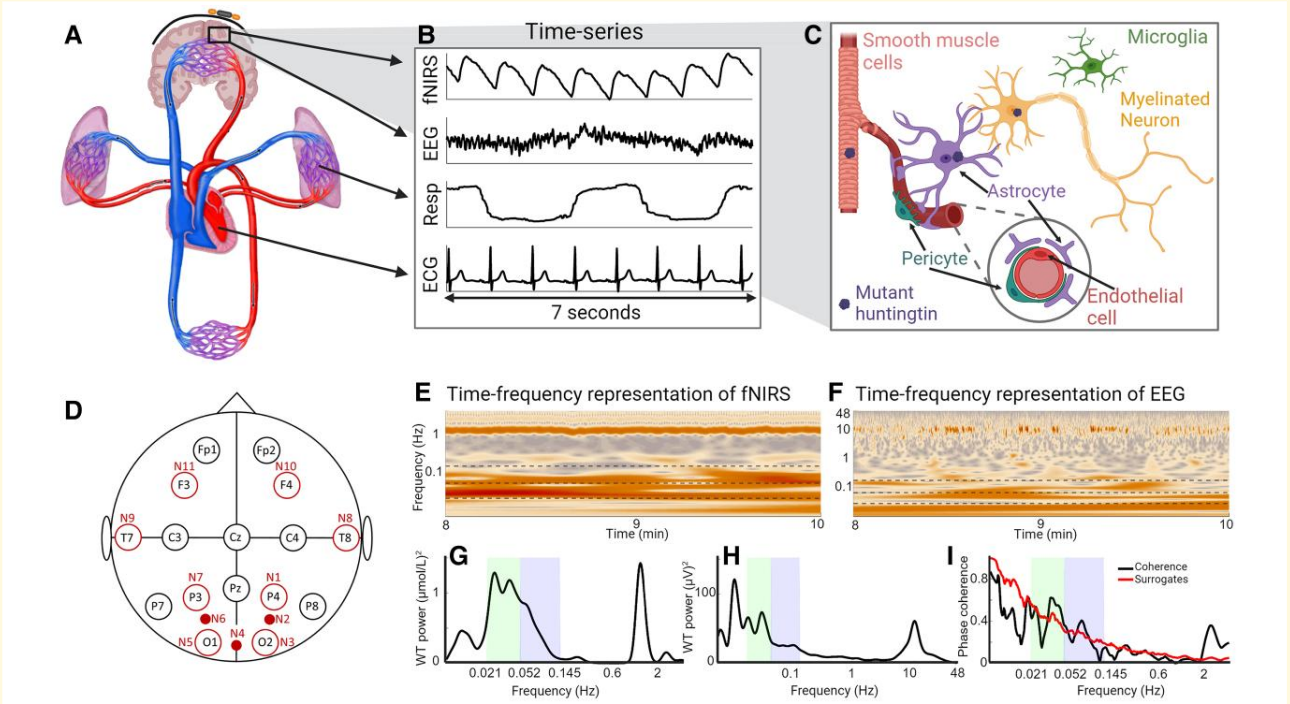

Figure 1 Overview figure. (**A**) A systemic view of the cardiovascular system and the brain. (**B**) Seven seconds of recorded time series from one participant. fNIRS captures brain oxygenation dynamics, EEG captures brain electrical activity, while the respiration and ECG time series capture cardio-respiratory dynamics. (**C**) Illustration of the NVU, consisting of smooth muscle cells, neurons, astrocytes, endothelial cells, pericytes and microglia. The mutant huntingtin protein has been found in all parts of the NVU. (**D**) Layout of fNIRS sensors and EEG electrodes. A black circle indicates that there is an EEG electrode at this position. A large unfilled red circle indicates that there are both an fNIRS sensor and an EEG electrode at this position. A small filled red circle indicates that there is an fNIRS sensor at this location. (**E**) The WT of an fNIRS time series showing the frequency content over time. (**F**) Same as **E**, but for an EEG time series. (**G**) The time-averaged WT power of the fNIRS time series as above. (**H**) Same as **G**, but for the EEG time series. (**I**) The black line is the WPC between the fNIRS and EEG time series, and the red line shows the surrogate threshold from the inter-subject surrogates. The green- and blue-shaded areas indicate the neurogenic and myogenic bands, respectively.

of the NVU *in vivo* in humans with Huntington's disease has not yet been assessed.

This study explores the hypothesis that simultaneous measurements of neuronal activity and haemodynamics in the resting state could be used to assess NVU efficiency[12] and that it might show reduced efficiency in Huntington's disease participants. Our study will thus provide functional correlates of the known structural[9] and molecular changes[11] in the vasculature and the NVU in people with Huntington's disease. To measure the local vascular and electrical oscillations, we use functional near-infrared spectroscopy (fNIRS) and EEG, respectively. Like fMRI, fNIRS is used to measure changes in oxygenation. However, fNIRS is simpler, is more portable and only requires probes placed on the scalp. fNIRS has been used in earlier studies of ageing and Alzheimer's disease,[13,14] but this is the first time fNIRS has been applied in the study of Huntington's disease. Blood is oxygenated in the lungs and transported by the pressure generated by the heart. Thus, the oxygenation of the brain is naturally affected by the rest of the cardiovascular system, including the properties of the vessels through which the oxygenated blood travels. We therefore measured the respiration and heart rates using respiration effort and ECG, respectively. Huntington's disease is known to affect the autonomic nervous system and blood vessels,[15,16] and the chosen measurement methods allow us to further investigate such effects.

The electrical activity measured using EEG is traditionally considered in terms of different frequency bands, which are attributed to particular functions and states of the brain.[17] A similar approach can be taken with the cardiovascular system, with distinct oscillations of varying frequency observed in recordings of blood flow and oxygenation.[18,19] Based on this, the cardiovascular system and the brain can naturally be considered as systems of oscillators acting on multiple time scales (i.e. multiple frequencies).[19-21] The time-varying oscillations of different frequencies can readily be captured due to the good temporal resolution of EEG and fNIRS.[22,23] Multiscale time–frequency analysis methods with logarithmic frequency resolution are employed to optimize resolution at lower frequencies.

The goal of this study was thus to investigate functional changes in the NVU related to Huntington's disease progression via application of non-invasive measurement techniques and powerful time–frequency analysis methods.

Materials and methods

Participants

This study was conducted in accordance with the Declaration of Helsinki, and written informed consent was obtained from all participants. The study protocols were approved by the Ethical Committee of the Slovenian National Ministry of Health (approval number 81-11-05).

Measurements were carried out on 47 [28 female (F), 19 male (M)] participants with a positive genetic test (CAG repeats ≥36) for Huntington's disease, of whom 1 F was excluded due to having particularly thick black hair, which resulted in fNIRS time series of poor quality. Of the other 46 participants, 18 (9 F, 9 M) exhibited severe chorea and were excluded from the initial investigation in order to minimize the effect of movement artefacts.

The remaining 28 (18 F, 10 M) Huntington's disease participants were split into 2 groups: 13 (10 F, 3 M) presymptomatic Huntington's disease (P) participants and 15 (8 F, 7 M) symptomatic Huntington's disease (S) participants. Symptomatic Huntington's disease was indicated by a Unified Huntington's Disease Rating Score–Total Motor Score (UHDRS–TMS) of 4 or higher. Presymptomatic Huntington's disease was defined by a UHDRS–TMS below 4. Two of the P participants had 39 CAG repeats, implying a high likelihood of developing the Huntington's disease phenotype.[1]

Measurements were also carried out on healthy controls of similar ages to the Huntington's disease groups. Exclusion criteria were diastolic blood pressure > 95 mmHg, body mass index (BMI) > 40 and having suffered a stroke in the past. The control group consisted of 36 (21 F, 15 M) participants that were assigned to 2 groups to match the ages of the Huntington's disease groups, as the P group were younger than the S group. These were denoted as control group for P (PC; 29—16 F, 13 M) and control group for S (SC; 33—21 F, 12 M), respectively. Some of the healthy participants were members of both groups.

Data for the P and S participants and the corresponding control groups are shown in Table 1. The data for the severe chorea (CS) participants are also included. Of the 36 participants in the control group, 5 (included in both PC and SC groups) have no data from the Pz electrode position, due to a faulty electrode. Calculations including the Pz electrode therefore have five fewer participants in both control groups.

Based on the sample sizes, a power of 0.8 and a significance level of 0.05, this study could reliably pick up differences between groups with effect sizes of 1.03 (P versus

Table 1 Participant details, shown as mean (minimum value–maximum value)

	P	PC	*P*	S	SC	*P*	CS	*P S*	*P SC*
Participant details									
N	13	29		15	33		18		
Age (years)	40.6 (30–57)	42.9 (28–57)	0.45	52.1 (33–69)	48.4 (35–72)	0.26	56.7 (36–79)	0.29	0.04
Sex	10 F/3 M	16 F/13 M		8 F/7 M	21 F/12 M		9 F/9 M		
BMI (kg/m^2)	24.5 (17.3–41.0)	24.3 (19.9–33.2)	0.51	25.3 (19.1–37.1)	24.4 (19.0–33.2)	0.37	23.1 (18.4–29.1)	0.12	0.38
sBP (mmHg)	121 (93–145)	119 (88–158)	0.71	131 (97–169)	121 (88–158)	0.22	110 (89–139)	0.01	0.12
dBP (mmHg)	85 (70–101)	77 (57–95)	0.055	86 (64–109)	78 (57–95)	0.057	71 (61–84)	0.002	0.04
CAG repeats	41.5 (39–46)			43.9 (40–53)			44.9 (36–52)		
DBS	238 (116–483)			414 (275–683)			496 (40–905)		
UHDRS test scores and education									
Education (years)	14.3 (12–17)			12.4 (8–16)			12.6 (6–16)	0.78	
Motor score	0.38 (0–2)			25.4 (4–63)			62.9 (18–95)	2×10^{-4}	
Verbal fluency	30.2 (12–58)			13.7 (3–26)			12.1 (5–22)	0.63	
Stroop W	92.2 (79–103)			49.5 (8–86)			37.1 (17–63)	0.12	
Stroop C	73.1 (61–80)			36.8 (19–49)			27.6 (17–43)	0.03	
Stroop WC	39.7 (20–50)			21 (7–48)			10.9 (5–21)	0.02	
Luria	0.17 (0–1)			1.47 (0–3)			3.1 (1–4)	5×10^{-5}	

BMI, body mass index; CS, symptomatic Huntington's disease with severe chorea; dBP, diastolic blood pressure; DBS, disease burden score [age*(CAG-35.5)]; *N*, number (of participants); P, presymptomatic Huntington's disease; *P*, *P*-value from the Wilcoxon rank-sum test comparing Huntington's disease groups with their control groups; *P* S, *P*-value from the Wilcoxon rank-sum test when comparing S and CS groups; *P* CS, *P*-value from the Wilcoxon rank-sum test when comparing SC and CC groups; PC, control group for P; S, symptomatic Huntington's disease; sBP, systolic blood pressure; SC, control group for S.

PC) and 0.89 (S versus SC). These are considered large effect sizes[24] (see Supplementary Fig. 2 for the calculations done in G*Power[25] and Supplementary Figs. 5 and 6 for a discussion on reproducibility).

Data acquisition

Data were recorded for participants in a comfortable, seated position, with eyes open and no fixation point, in a quiet room at around 25°C at the Neurological Clinic, Ljubljana, Slovenia. The EEG was recorded at 1 kHz using a 16-channel system (V-Amp, Brain Products, Germany) and fNIRS at 31.25 Hz with an 8-source/8-detector LED system (NIRScout, NIRx, Germany). The same system and methodology were also used in our recent study of ageing.[12]

Analyses of oxygenated haemoglobin data are presented below. Note that while fNIRS measures relative changes in haemoglobin concentration, not absolute values, we refer to these measures as brain oxygenation. An ECG with bipolar precordial lead similar to the D2 lead electrodes placed on each shoulder and the lower left rib was recorded. A belt fitted with a Biopac TSD201 Respiratory Effort Transducer (Biopac Systems Inc., CA, USA) wrapped around the participant's chest recorded respiratory effort. Both ECG and respiration were sampled at 1.2 kHz using a signal conditioning system with 24-bit A/D conversion (CardioSignal, Institute Jožef Stefan, Slovenia). Figure 1B shows examples of recorded time series, and the EEG/fNIRS probe layout is shown in Fig. 1D, and Supplementary Fig. 1. The EEG ground electrode was placed at AFz, and the reference electrode at FCz. The data were recorded simultaneously for ~30 min.

Time–frequency analysis

Preprocessing

MATLAB was used for all time series analyses. The time–frequency analyses were performed using algorithms in the MODA toolbox.[26] Continuous 20-min time series were extracted for all participants. To remove the effects of frequencies lower than those of interest, the time series were detrended by subtracting a best-fit third-order polynomial and bandpass filtered. The filtering range was 0.007–4 Hz, apart from for the EEG frequency bands above δ, when it was 4–48 Hz. Further details and discussion of the preprocessing are provided in Iatsenko *et al.*[27] To reduce the computational load, the time series were down-sampled by using a moving average before analysis. ECG and respiration time series were down-sampled to 100 Hz during the extraction of instantaneous rates. fNIRS was originally sampled at 31.25 Hz, so, for the fNIRS–EEG coherence analysis, the EEG was down-sampled to the same frequency. For EEG–EEG coherence in a frequency interval up to 4 Hz, fNIRS–instantaneous respiration rate (IRR) coherence, fNIRS– instantaneous heart rate (IHR) coherence and fNIRS–respiration coherence, the corresponding time series were down-sampled to 20 Hz. For EEG analysis above the δ band, the EEG time series were down-sampled to 142 Hz. Nonlinear mode decomposition[28] was used to remove the electrical signature of the heart beat when present in EEG.

Physiological meaning of the oscillations: frequency bands

Previous research on both the cardiovascular system and the brain has identified oscillations in specific frequency bands, corresponding to different physiological processes. The frequency bands, their names and processes generating the oscillations are shown in Table 2. Cardiovascular oscillations have been identified for frequencies from 0.005 to 2 Hz,[18,19] which overlap with slow oscillations found in EEG time series,[17] leading to the hypothesis that they may have a common origin.

Coherence and power values (explained below) were averaged over each frequency band. For example, we refer to the α band power, which is the time-averaged power in the 7.5–14 Hz frequency range.

We investigated frequencies up to 48 Hz in EEG, as this includes slow γ oscillations but avoids phase distortions due to the 50-Hz notch filter applied by the monitoring system. For the fNIRS and fNIRS–EEG analyses, we investigated frequencies up to 4 Hz, as there is no evidence of fNIRS containing oscillatory modes with frequencies higher than the cardiac oscillation (~1 Hz). In all cases, the minimum frequency was set to 0.007 Hz.

Determining the presence and strength of oscillations: the wavelet transform and windowed Fourier transform

We first investigated if the strength of the oscillations in oxygenation and neuronal activity was similar in both the Huntington's disease and the control participants. A natural way to investigate the presence and power of oscillations in a time series is to examine its frequency content, traditionally with the Fourier transform. However, biological oscillations are known to have time-varying frequencies. Therefore, to observe the frequency content and how it changes with time, we used the wavelet transform (WT; Morlet mother wavelet with frequency resolution of 1) for frequencies below 4 Hz (Fig. 1E for an example). The WT was used for this frequency interval on account on its logarithmic frequency resolution, as time and frequency are inversely related. For EEG power in the frequency range 4–48 Hz, the windowed Fourier transform (WFT) was used, as a linear frequency resolution is traditionally used for these frequency bands which make the results easily comparable. The time-averaged WT and WFT give power spectra similar to the Fourier power spectrum (see examples in Fig. 1G and H), abbreviated to WP. Total power was calculated as the double integral of the transform squared with respect to time and frequency.[47]

Determining the instantaneous frequency of an oscillation: ridge extraction

As mentioned, the oscillations investigated are known to have time-varying frequencies. Extracting the instantaneous

Table 2 Frequency bands

Frequency range (Hz)	Name	Process
Cardiovascular frequency bands[19]		
0.007–0.0095	Endothelial (V1)	Nitric oxide (NO)-independent endothelial activity. Modulation of the activity of smooth muscle cells by endothelial cells, mediated through the release of substances other than NO.[29,30]
0.0095–0.021	Endothelial (V)	NO-dependent endothelial activity. Modulation of the activity of smooth muscle cells by endothelial cells, mediated through the release of substances where NO is most important.[31-34] The release of NO is dependent on metabolic substances.
0.021–0.052	Neurogenic (IV)	Neurogenic activity. Modulation of vascular tone by nervous activity. Blood vessels are innervated by the autonomous nervous system, which can alter the vessel size by releasing substances that change the activity of smooth muscle cells.[30,35-37]
0.052–0.145	Myogenic (III)	Myogenic response. Vascular smooth muscle cells respond to changes in intravascular pressure by contracting or relaxing.[38,39]
0.145–0.6	Respiratory (II)	Respiration activity.[18]
0.6–2	Cardiac (I)	Heart activity.[18]
Brain oscillation frequency bands[17]		
0.025–1.5	Slow and ultraslow	The origin of these oscillations is still debated, and there is evidence for both neuronal and non-neuronal generators. Linked to excitability, the blood–brain barrier and neuron–glial interactions.[40,41]
0.5–4	Delta (δ)	Linked to sleep[42] but also observed during wakefulness.[43] Increased delta power during rest has been detected in Huntington's disease and Alzheimer's disease.[44,45]
4–7.5	Theta (θ)	Linked to REM sleep and to memory consolidation.[42]
7.5–14	Alpha (α)	The dominant oscillation during wakeful resting, especially during eyes closed.[46] Decreased alpha power is found in Huntington's disease and Alzheimer's disease.[44,45]
14–22	Beta (β)	Linked to sensory processing and motor preparation.[42]
22–48	Gamma (γ)	Linked to focused attention and efficient cognitive processing.[42]

frequency of an oscillation over time can be of interest, as in the case of the IHR. From the WT (lognormal mother wavelet, frequency resolution parameter of 2) of the ECG time series, we extracted a ridge largely following the highest amplitude in the 0.6–2-Hz frequency range.[48] For one participant's ECG, the frequency range was 0.8–3 Hz, as they were found to have an average heart rate of 2.2 Hz. The result is then a time series of the heart rate over the length of the recording. When derived in the time domain from the intervals between R-peaks, the similar time series is often referred to as heart rate variability, and a comparison of the time series derived from ridge extraction and R-peaks is shown in Supplementary Figs. 7–10. The ridge extraction method has the advantage of resulting in a time series with the same sampling frequency as the original time series, and no interpolation is needed. It also considers the whole ECG time series rather than just the R-peaks.

Determining the presence of coordinated oscillations: wavelet phase coherence

To investigate systemic connectivity between cardiovascular oscillations and brain waves, we calculated the wavelet phase coherence (WPC).[49] The WPC determines the presence or absence of coordination between different oscillations, which could indicate a form of interaction between their sources. The WPC is model free and is appropriate for time series containing several oscillations of different frequencies. The logarithmic frequency resolution of the WPC enables investigations spanning a wide frequency interval.

The WPC takes values between 0 and 1 and is calculated between two recorded time series at discrete frequencies (see Fig. 1I for an example). It evaluates how constant the phase difference at each frequency is over time (see Fig. 2). A value of 1 would indicate that the phase difference is constant at all times. When oscillations have strictly constant frequency, the value of 1 can be achieved, while if the characteristic frequencies are varying (like the heart beat), then even perfect coherence will yield values slightly less than 1.

The WPC was calculated between the following pairs of time series: EEG–EEG, fNIRS–fNIRS, fNIRS–EEG, IHR–fNIRS, IRR–fNIRS, respiration–fNIRS and respiration–IHR. Additionally, the EEG–EEG, fNIRS–fNIRS and fNIRS–EEG coherences were calculated for all possible probe combinations.

Statistical analysis

Testing for significant coherence

Even two random time series of non-infinite length will have non-zero apparent coherence, especially at lower frequencies. Inter-subject surrogates were therefore used to provide significance thresholds.[50] Coherence was calculated not only between time series from one participant but also between time series from different participants to provide examples of the level of apparent coherence in scenarios where there is no physical link between the time series. From the participants in the study, 176 inter-subject surrogates were created for each pair of time series. The significance threshold was set to be the 95th percentile of the surrogate coherence obtained at each frequency (see Fig. 1I for illustration). The 'effective coherence' was then obtained by subtracting the surrogate threshold from the original coherence. Coherence refers to this effective coherence throughout the paper unless clearly stated otherwise and was used to test the hypothesis that differences exist between the groups.

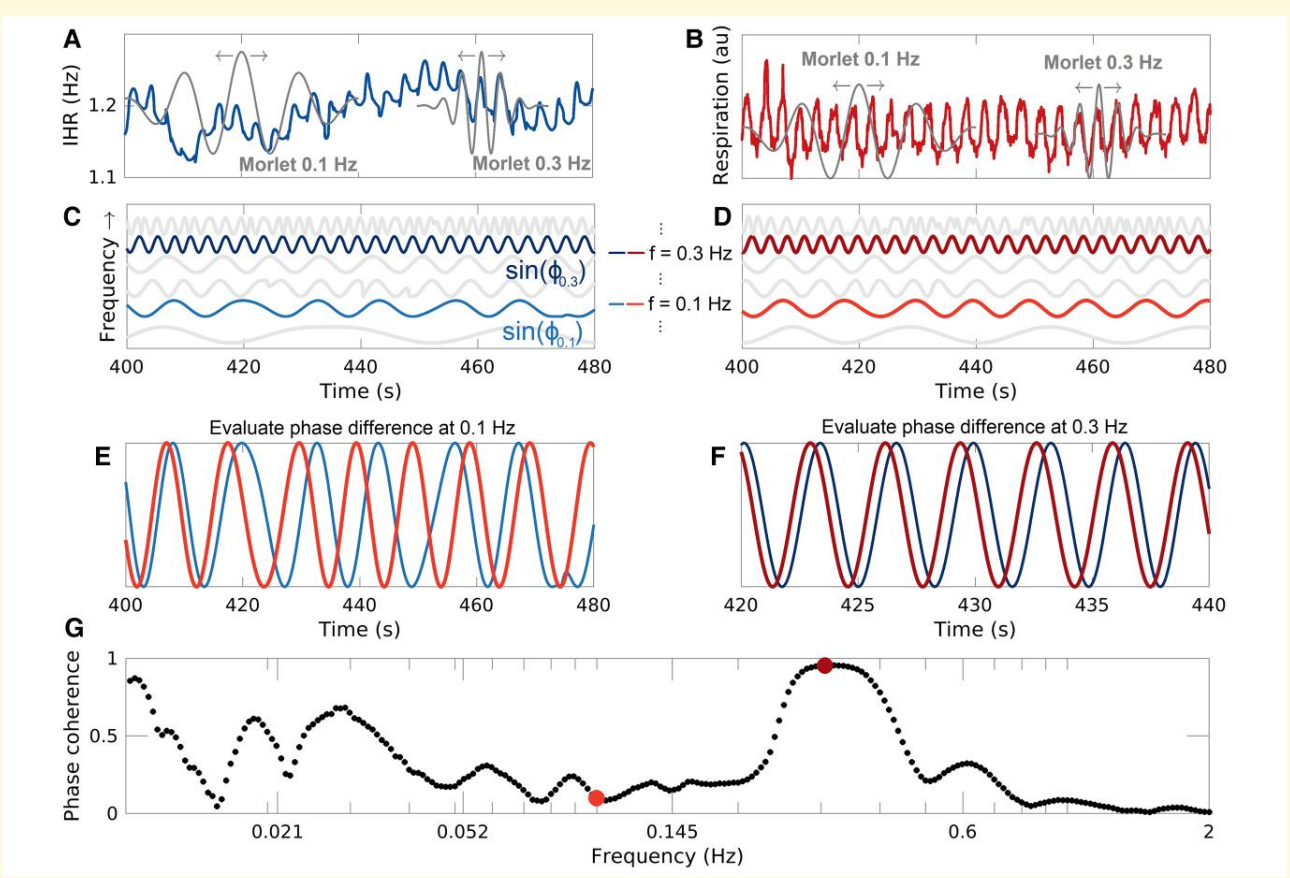

Figure 2 WPC. (**A**) IHR time series and examples of the Morlet wavelet at 0.3 and 0.1 Hz. The arrows indicate that the wavelet slides along the signal. (**B**) Respiration time series and examples of Morlet wavelets. (**C**) Sines of the instantaneous phases extracted from the WT of the IHR, at 0.1 Hz (light blue) and 0.3 Hz (dark blue). (**D**) Same as **C** but for the respiration time series and with the colour red. (**E**) Sines of the instantaneous phases at 0.1 Hz for both time series. Note the inconsistency in the phase difference. (**F**) Sines of the instantaneous phases at 0.3 Hz for both time series. Note the consistency in the phase difference. (**G**) The WPC between the two time series, where each dot corresponds to one of 273 different frequencies. 0.1 and 0.3 Hz are indicated by a light and dark red dots, respectively. au, arbitrary units.

Testing for group differences

Once single values had been obtained, for example of the WPC between the time series from two probes averaged over a frequency band, the populations were compared using the Wilcoxon rank-sum test. This is a non-parametric pair-wise test and does not assume a normal distribution of the data. Differences were considered significant if $P < 0.05$.

The significances of the group differences in fNIRS, EEG and fNIRS–EEG power or coherence were further assessed using a Monte Carlo permutation test. Participants from the P and PC groups were randomly assigned to groups of size 13 and 29, and participants from the S and SC groups were randomly assigned to groups of size 15 and 33. The Wilcoxon rank-sum test tested for differences between these permuted groups. After ~16 000 permutations, if a *P*-value had a value smaller than 95% of the new ones, its significance was considered confirmed. The results of the permutation test are further discussed Supplementary Figs. 3 and 4.

In the case of comparisons between data from different spatial locations (for EEG and fNIRS), the issue of multiple comparisons should be considered. The binomial probability was calculated to assess the probability of obtaining X or more positive outcomes from a total of N combinations.[51] The probability of a positive outcome was set to 0.05, and the total number of combinations was 55 for the fNIRS coherence analysis, 120 for the EEG coherence analysis and 176 for the fNIRS–EEG coherence analysis. If the probability was found to be <5%, the result is considered significant with respect to the multiple comparison problem.

Cognitive and motor tests

For the participants with Huntington's disease, cognitive and motor tests were conducted according to the UHDRS.[52] The results are summarized in Table 1. Three participants in the P group did not have cognitive scores. Only eight participants in the CS group had cognitive data, except in the case of the symbol digit test where the number was five. These data are not included in the calculations of the group mean, maximum and minimum.

Results

The results are presented in three sections: cardiovascular oscillations, neuronal oscillations and neurovascular oscillations. As mentioned above, data from the four groups initially analysed, i.e. the S ($N = 15$) and P ($N = 13$) groups and the two control groups, SC ($N = 33$) and PC ($N = 29$), are summarized in Table 1.

Cardiovascular oscillations

Cardio-respiratory oscillations

We start the investigations with the two main oscillators of the cardiovascular system: the heart and lungs. Average heart rate and total power of the IHR are shown in Table 3. The S group has higher heart and respiration rates when compared to the SC group (*P*-value 0.023 for heart rate and 0.006 for respiration). The IHR total power is not significantly different (Table 3), but the P group has higher power in the respiratory band (Fig. 3).

The N3 (right occipital—co-located with EEG O2)–IHR coherence is significant in the myogenic and respiratory bands (Fig. 3). For all groups, the phase difference is positive in the myogenic range and negative in the respiration range. A positive phase difference means that IHR is the leading oscillation. This is consistent across most fNIRS probes, apart from N8 and N9 (temporal—T7/T8; see Supplementary Figs. 11 and 12). The P group has significantly reduced coherence around 0.06–0.08 Hz between IHR and N3, N4, N5 and N6 in comparison to the PC group (see Supplementary Figs. 13–16 for fNIRS coherence with respiration and IRR).

Brain oxygenation

We investigated oscillations in the brain oxygenation by calculating the WP of fNIRS time series and the coordination of the oscillations using the WPC between fNIRS time series. Results for oxygenated haemoglobin are shown in Fig. 3, with the myogenic total power shown in Table 3.

In Fig. 3I, only the significant *P*-values are shown, indicating a difference in power between the Huntington's disease and control groups. The results show that the P group has lower power in 5/11 fNIRS probes in the neurogenic and myogenic frequency bands, respectively. In contrast, the S group has higher power in 5/11 fNIRS probes in the respiratory band. The probability of 5 or more positive findings if all 11 null hypotheses are true is 0.16%.

In the cardiac frequency band, the coherence is relatively high between all probe combinations in all groups. However, the cardiac coherence is significantly lower in the S group compared to the SC group in 36 probe combinations (Fig. 3J). The probability of 36 or more positive findings if all 55 null hypotheses are true is 1.58×10^{-31}%. The coherence and power values for all frequency bands are summarized in Supplementary Fig. 17. In addition, effect size was calculated *post hoc* and is shown Supplementary Table 1. Most values of the effect size were medium to large.

Neuronal oscillations

We investigated the electrical activity in the brain, obtaining both the WP and the WPC from the EEG time series. The WPC gives information on the coordination of neuronal activity from different brain regions, often referred to as functional connectivity.

The comparisons of EEG power with their respective controls for the P and S groups are shown in Fig. 4A, while total EEG power is shown in Table 3 and Supplementary Table 2. There are no statistically significant differences between the P and PC groups, although there is a tendency for the α band power to be reduced in the P group compared to the PC group in the occipital and parietal areas, with *P*-values of between 0.05 and 0.12 (Fig. 4A). In the parietal and occipital areas, the P group's α power lies in-between the S group and the control groups (Table 3). In the θ, α, β and γ bands, the S group has lower power than the SC group in many time series recorded from different electrodes. Most prominent is the α band, where the difference is statistically significant at all electrodes apart from Fp1 and Fp2. The probability of 6 or more positive findings if all 16 null hypotheses are true is 0.008%, while the probability of 2 or more positive findings if all 16 null hypotheses are true is 19%.

Significant differences in the WPC for different electrode positions are shown in Fig. 4B (for all frequency bands, see Supplementary Fig. 18). The α band WPC is clearly reduced in both the S (18/120 combinations) and P (14/120 combinations) groups compared to their control groups. In the γ band, the S group has lower WPC in 28/120 combinations, while the P group has lower WPC in 9/120 probe combinations, compared to their respective control groups. The probability of 14 or more positive findings if all 120 null hypotheses are true is 0.28% (significant), while the probability of 9 or more positive findings if all 120 null hypotheses are true is 15% (not significant). Effect size calculations can be found in Supplementary Table 1 and generally show medium to large differences.

Here, the β band is defined as 14–22 Hz. A comparison of the β and γ results within this frequency range and when β is defined up to 30 Hz can be seen in Supplementary Fig. 19. Some γ WPC differences can be attributed to 22–30-Hz range, which is often assigned to β.

Neurovascular oscillations

To investigate the coordination of slow electrical and oxygenation oscillations, the WPC was calculated between fNIRS and EEG time series. Figure 4C shows the group coherence for all fNIRS–EEG combinations in the myogenic band. Figure 4D illustrates the significant differences between the Huntington's disease groups and their control groups for all fNIRS–EEG combinations in the neurogenic and myogenic bands (for the remaining frequency bands, see Supplementary Fig. 20). From Fig. 4D, one can see that there is a significant difference between S and SC at electrode O1 with the blood oxygenation time series measured from

Table 3 Averages and group median total power

	P	S	PC	SC
Heart rate (Hz)	1.21	1.23*	1.19	1.13
Respiration rate (Hz)	0.24	0.28*	0.24	0.23
TP IHR $\times 10^{-5}$ (Hz^2)	5.71	5.07	3.29	2.94
TP IRR $\times 10^{-5}$ (Hz^2)	7.88	7.81	8.83	9.24
TP EEG (μV^2)				
Fp1	62.4	34.8	35.7	38.3
Fp2	63.4	27.9	34.6	36.6
F3	9.80	6.13	9.79	9.87
F4	11.7	6.42	10.2	10.5
T7	26.7	18.4	32.6	35.3
C3	9.34	6.28	9.93	8.75
Cz	1.97	1.49*	2.75	2.75
C4	8.78	6.37	10.1	9.86
T8	29.8	18.2	30.2	30.2
P7	25.3	18.3*	31.6	33.5
P3	14.4	9.75*	18.9	18.9
Pz	12.1	6.95*	17.3	16.7
P4	16.8	8.89*	18.8	18.9
P8	26.2	19.7*	34.0	34.9
O1	28.2	22.1*	36.1	35.9
O2	36.6	20.3*	35.7	35.7
EEG α (μV^2)				
Fp1	6.73	4.73	5.27	7.54
Fp2	7.03	3.99	6.20	6.38
F3	1.78	0.83*	1.68	1.87
F4	1.76	0.89*	1.64	1.82
T7	6.13	4.45*	7.04	9.09
C3	2.22	0.96*	2.73	2.73
Cz	0.41	0.24*	0.82	0.83
C4	3.15	1.22*	3.51	3.22
T8	6.34	3.80*	6.29	7.29
P7	6.38	4.53*	9.81	11.3
P3	4.31	2.29*	7.73	7.93
Pz	3.53	1.55*	9.22	8.76
P4	6.20	2.17*	8.93	8.49
P8	8.70	4.03*	14.0	14.4
O1	7.93	3.66*	14.5	16.6
O2	8.53	3.50*	14.0	14.4
TP fNIRS $\times 10^{-8}$ ((μmol/mL)^2)				
N1	1.17	1.12	1.29	1.05
N2	0.10	0.16	0.18	0.15
N3	0.56	0.55	0.53	0.51
N4	0.17	0.19	0.18	0.18
N5	0.40	0.34	0.49	0.43
N6	0.13	0.13	0.14	0.14
N7	1.12	1.09	1.30	1.26
N8	1.01	1.18	1.25	1.17
N9	1.43	1.79*	1.07	1.07
N10	0.90	0.89	0.75	0.76
N11	1.11	1.21	1.20	1.11
fNIRS III $\times 10^{-10}$ ((μmol/mL)^2)				
N1	4.47*	6.23	9.76	8.67
N2	0.53	1.02	1.06	0.98
N3	2.40*	3.13	5.18	4.47
N4	0.76	1.34	1.73	1.46
N5	1.58*	2.78	4.10	3.31
N6	0.45*	0.76	0.96	0.85
N7	4.17*	5.98	10.3	8.77
N8	4.31	6.48	5.86	4.89
N9	4.53	12.4*	7.59	5.77
N10	2.99	2.65	5.07	3.22
N11	4.51	4.10	5.57	4.69

P = presymptomatic Huntington's disease, S = symptomatic Huntington's disease, PC = control group for P, SC = control group for S, TP = total power, IHR = instantaneous heart rate, IRR = instantaneous respiration rate, EEG = electroencephalogram, fNIRS = functional near infra-red spectroscopy, * = $p<0.05$ for the P vs PC, or S vs. SC comparison, using the Wilcoxon rank-sum test. The EEG θ,β,γ total power is summarised in SM, supplementary table 2.

the same location in the myogenic frequency range. There are also significant differences in other fNIRS–EEG combinations, including frontal to occipital probes and central (C3, Cz, and C4) to parietal probes. In the P group, the most significant differences are seen in the myogenic band and are associated with the T7 electrode. In the S group, 23 combinations decreased significantly in the myogenic band. In the P case, 21 and 19 combinations are decreased in the myogenic and neurogenic bands, respectively, while 1 combination is increased in the P group in the neurogenic band. In the neurogenic band, the S group has higher WPC than the P group 21 combinations. The S and P groups are significantly different in 14 combinations in the myogenic band. The probability of 14 or more positive findings if all 176 null hypotheses are true is 5.9% (not significant). The probability of 20 or more positive findings if all 176 null hypotheses are true is 0.06% (significant).

Neurovascular oscillations in choreatic participants

The fNIRS–EEG WPC was also investigated in the 18 severely choreatic participants (56.7 ± 13.9 years, 9 F/9 M). This group is slightly older than the S group, but not significantly so ($P = 0.29$; see Table 1). They are significantly older than the SC group ($P = 0.04$). The neurovascular coherence in the myogenic band is decreased in 38/176 combinations for the CS group compared to the SC group (Fig. 5E), which is significant. The choreatic symptomatic group's neurovascular coherence is not significantly different from the S group (differences in 5/176 combinations).

Discussion

In this study, the hypothesis of disrupted neurovascular dynamics in Huntington's disease was confirmed for the first time, suggesting reduced efficiency of the NVU. Our findings, supporting the hypothesis, are as follows:

- Reduced neurovascular phase coherence indicating reduced efficiency of the NVU.
- Decreased oxygenation power in the P group and decreased coherence in the S group, indicating vascular changes in both the P and S groups.

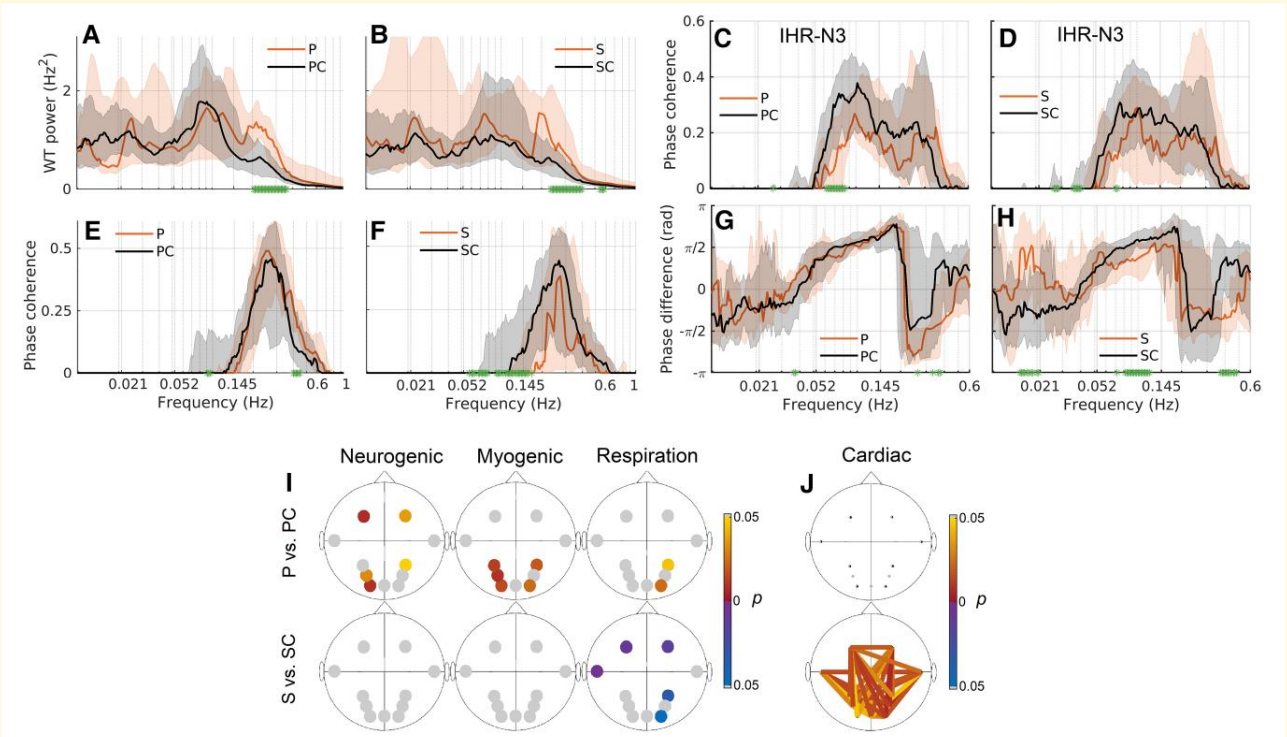

Figure 3 Cardiovascular and brain oxygenation results. (**A, B**) Time-averaged WT power of the IHR. (**C, D**) WPC between N3 and IHR. (**E, F**) WPC between the IHR and respiration time series. (**G, H**) Phase difference in radians (rad) between N3 and IHR. For all plots, the Huntington's disease groups are in orange, and the control groups are in black. The solid lines show the group median, and the shaded area shows the 25–75th percentiles. Significant differences ($P < 0.05$) are shown as green stars on the *x*-axis. (**I**) Significant *P*-values for oxygenated haemoglobin wavelet power. The first row is between the P and PC groups, while the second row is between the S and SC groups. Yellow/red (blue/purple) circles indicate that the power is higher in the controls (Huntington's disease). (**J**) Significant *P*-values for fNIRS WPC in the cardiac band. Yellow/red (blue/purple) lines indicate that the WPC is higher in the controls (Huntington's disease). All *P*-values calculated using the Wilcoxon rank-sum test.
P, presymptomatic Huntington's disease; S, symptomatic Huntington's disease; PC, control group for P; SC, control group for S.

- Decreased EEG power in the S group and decreased coherence in the P and S groups, reflecting altered neuronal brain activity in both the P and S groups and its gradual deterioration.
- Increased IHR power in the respiratory band in the P and S groups, indicating early autonomic changes in Huntington's disease.

The results obtained therefore confirm our initial hypothesis that neurovascular dynamics and the functioning of the NVU, in particular, are changed in Huntington's disease.

Neurovascular, vascular, cardio-respiratory and neuronal oscillations in Huntington's disease

Restructuring of the vasculature in symptomatic Huntington's disease does not restore NVU efficiency

Here, we demonstrate neurovascular phase coherence in healthy adults (mean ages for the control groups were 40 and 48 years old), and we show that it occurs to a significantly lesser degree in participants with Huntington's disease (Fig. 4C and D). This reduction could mean a dysfunction in neurovascular coupling in Huntington's disease participants, noticeable already at the presymptomatic stage. We have previously demonstrated that neurovascular phase coherence decreases with age[12] (for a thorough discussion about the origin of ~0.1-Hz oscillations in brain electrical activity and oxygenation dynamics, please see Bjerkan *et al.*[12]). A possible explanation for the reduction in coherence relates to the compromised BBB, a key part of the NVU, in the Huntington's disease participants.[6] Evidence of BBB leakage in symptomatic Huntington's disease participants has been detected, as well as evidence of mutant huntingtin in all major parts of the NVU, including in astrocytes,[9,53,54] which are thought to be key for communication between neurons and vessels.[55-57] This then results in a decrease in neurovascular coherence, as inferred in the case of ageing.

It is known that the mutant huntingtin disrupts the function of mitochondria, decreasing ATP production.[58] The neurogenic/myogenic oxygenation power reductions in P (Fig. 3I) could be in response to a change of metabolism in the cortex,[59] with the vessels adapting to the altered metabolic state as the disease progresses. Altered neuronal

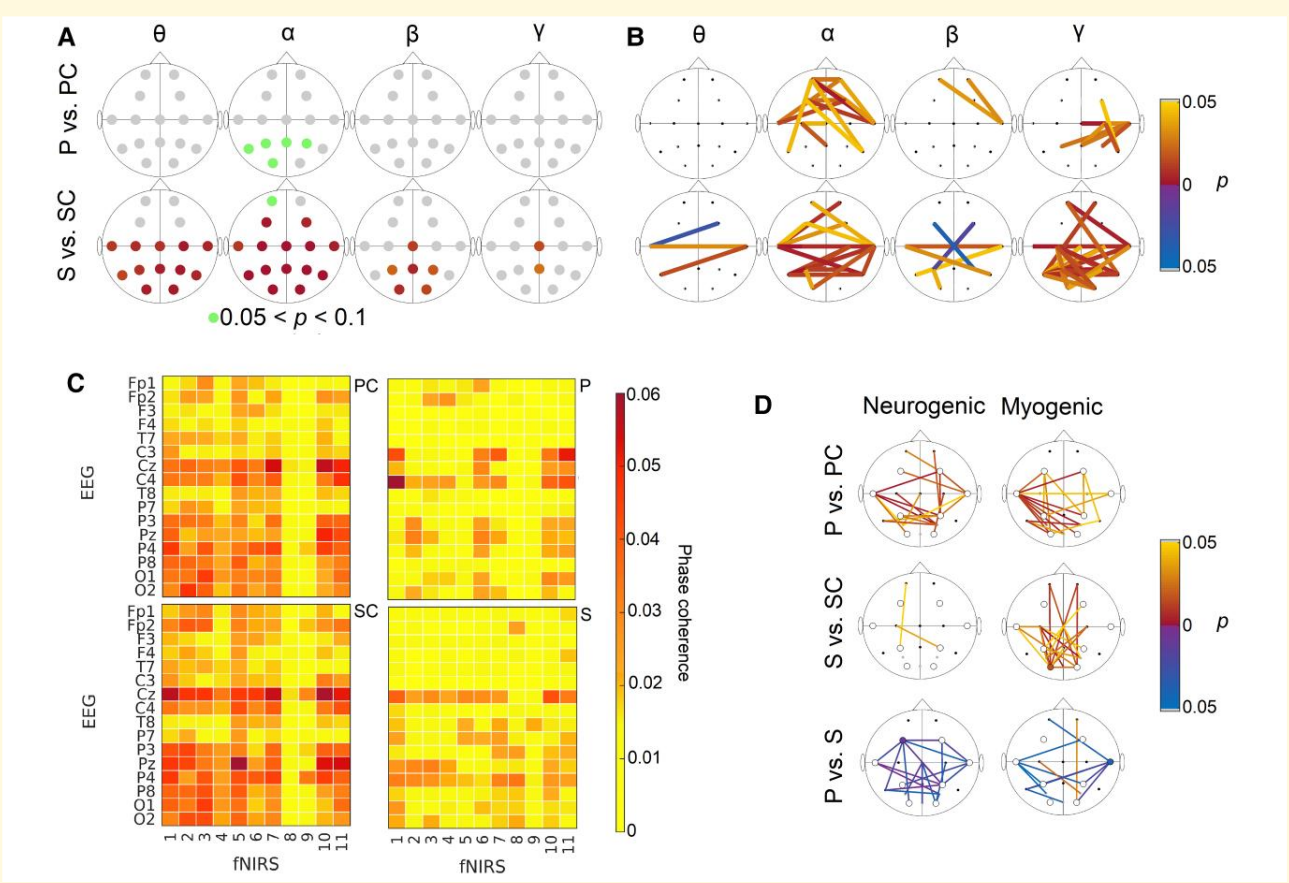

Figure 4 Neuronal and neurovascular results. (**A**) *P*-values for the EEG time-averaged wavelet power. Yellow/red (blue/purple) circles indicate that the power is significantly higher in the controls (Huntington's disease). The first row is the *P*-values between the P and PC groups, while the second row is the *P*-values for the S and SC groups. In the α band, $P > 0.05$ but <0.1 are highlighted in green. (**B**) Significant differences in EEG WPC. The *top* row shows differences between the P and PC groups, while the *bottom* row is between S and SC. Yellow/red (blue/purple) lines indicate higher WPC in the controls (Huntington's disease). (**C**) Median WPC between fNIRS and EEG pairs in the myogenic frequency band. The first row shows the P and PC groups, while the second row shows the S and SC groups. (**D**) Significant differences in fNIRS–EEG WPC. Yellow/red (blue/purple) lines indicate higher WPC in the controls (Huntington's disease) or in P (Ss). All *P*-values calculated using the Wilcoxon rank-sum test. P, presymptomatic Huntington's disease; S, symptomatic Huntington's disease; PC, control group for P; SC, control group for S.

activity could also result in a different metabolic state. The power reductions could also reflect a vascular pathology occurring before the onset of reduced metabolic demand, resulting in an insufficient energy supply to the brain cells. Both possibilities can be linked to NVU dysfunction.

The clear oxygenation power differences in the P group (Fig. 3I), and the lack of significant EEG power differences (Fig. 4A) could suggest that changes in oxygenation occur before changes in neuronal activity and show that fNIRS can offer prognostic information additional to EEG in the presymptomatic stages of the disease. Evidence suggests that in Huntington's disease, alterations in white matter are independent of alterations in grey matter, and possibly occur earlier,[60] and that reduced blood flow to the striatum is an early event in Huntington's disease,[61] which is in line with our findings of reduced oxygenation power in the P group. Studies in mice show extensive changes to the vasculature early in Huntington's disease without clear corresponding neuronal losses or detectable motor symptoms.[9,62] The healthy elderly and the presymptomatic participants have in common that their arteries are stiffer,[16,63] which could affect the myogenic response. However, smooth muscle cells in Huntington's disease are not well characterized,[64] and our results warrant further investigation.

The S group has lower cardiac coherence than the SC group (Fig. 3J). This might be explained by the increased microvascular density[9,62] in Huntington's disease leading to a reduced ability to participate in oscillations. This reshaping of the vasculature could be a compensatory reaction to inadequate oxygen delivery across a non-optimal vascular network, as more oxygen can be provided locally via capillaries, but without restoration of appropriate timing. Increased microvascular density might explain why power at low frequencies is not reduced during the symptomatic stage. Another possible explanation could be that movement artefacts, caused by mild chorea, mask the myogenic and neurogenic power decreases in the S group. Still, the vascular reshaping did not restore neurovascular phase coherence and

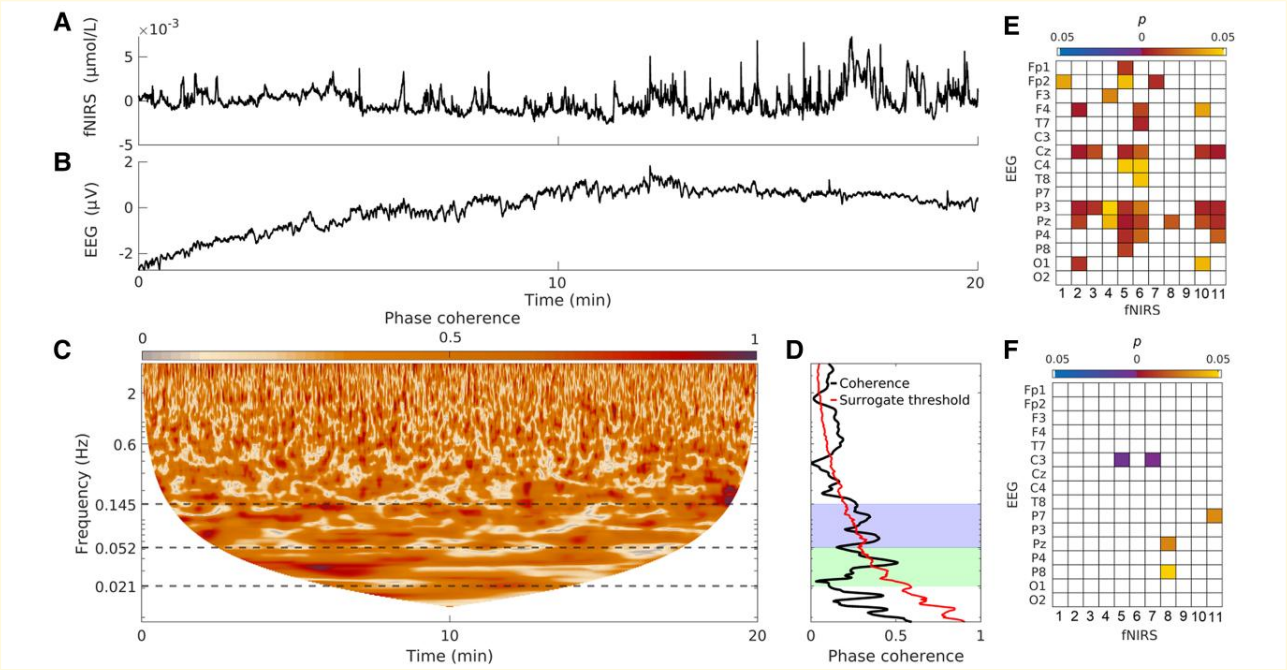

Figure 5 Neurovascular results for participants with severe chorea. (**A**) Recorded fNIRS time series from N5, from one participant with severe chorea. The mean is subtracted before plotting. (**B**) Recorded EEG time series from location O1 (co-located with N5), from the same participant. The mean is subtracted before plotting. (**C**) Time-localized WPC between the time series shown in **A** and **B**. (**D**) Time-averaged WPC for the time series shown in **A** and **B**. The shaded area shows the neurogenic and myogenic frequency bands. (**E**) Significant differences in the fNIRS–EEG WPC, between the SC group and the CS group. (**F**) Significant differences in the fNIRS–EEG WPC, between the S group and the CS group. Yellow/red (blue/purple) lines indicate higher WPC in the controls (Huntington's disease) or in S (CSs). All *P*-values calculated using the Wilcoxon rank-sum test. S, symptomatic Huntington's disease; SC, control group for S; CS, symptomatic Huntington's disease with severe chorea.

therefore did not seem to improve the efficiency of the NVU. The results presented can be considered as functional correlates of the molecular mechanisms revealed by Garcia *et al.*[11] They have shown that genes associated with the growth of vessels are expressed differently in Huntington's disease compared to healthy controls, leading to the previously reported increased microvascular density.[9,62] This can be linked to our finding of decreased coherence in blood oxygenation in the cardiac frequency interval, probably caused by the increased microvascular density. Garcia *et al.* also show that genes associated with BBB permeability are expressed differently. This likely manifests as functional changes in the NVU efficiency, as observed in our study.

Huntington's disease leads to a gradual deterioration of neuronal function

We found reduced α power in the S group and a tendency for reduced α power in the P group (Table 3 and Fig. 4). This suggests that the occipital areas may have functional changes before symptoms manifest, in addition to the known structural changes, such as cortical atrophy, found in presymptomatic patients.[2] We note that we also found clear differences in oxygenation in the parietal and occipital areas. While it is well known that the mutant huntingtin can alter neural connections by impairing neurotransmitters and altering protein homeostasis,[58] it is also worth considering that changes to the vasculature and neurovascular interactions could contribute to disrupted neuronal function by reducing nutrient availability. The current data cannot pinpoint whether the vascular or neuronal changes occurred first. However, the methods described, combined with longitudinal data, could potentially elucidate this. Reduced α power was found in several previous studies[4,65-70] and is one of the characteristics of the EEG in Huntington's disease. Oscillations with α frequencies are modulated by corticothalamic circuits and thalamic nuclei which are affected by the disease.[71] However, this reduction in power is not limited to Huntington's disease—several studies have found reduced α power in Alzheimer's disease.[72] In both diseases, a slowing of the EEG power is reported (decrease in higher-frequency bands, increase in lower-frequency bands).[44]

We also find that phase coherence between time series from different EEG electrodes is altered in both Huntington's disease groups, especially in the α band. Decreased α coherence in P patients in the absence of a power decrease might be the first electrophysiological sign of changes in brain network interactions. The power and coherence changes in EEG are more pronounced in S (Table 3 and Fig. 4). An intermediate electrophysiological phenotype for presymptomatic Huntington's disease has also been suggested by a previous study.[73] This implies a gradual deterioration of neuronal activity, starting with the coordination of

the oscillations and then with the power of the oscillations. We do not see a compensatory mechanism like vascular remodelling. Our results indicate that EEG coherence could be used to evaluate and monitor the disease non-invasively, including in the presymptomatic phase.

Autonomic changes in presymptomatic and symptomatic Huntington's disease

We show increased IHR power in the respiratory band, in both the P and S groups (Fig. 3A and B). The IHR power in the respiratory band likely reflects respiratory sinus arrhythmia, which is a modulation of cardiac frequency by the respiration cycle.[74] However, despite the increase in power, the symptomatic group has lower coherence between IHR and respiration (Fig. 3F), indicating that respiratory sinus arrhythmia is disrupted in symptomatic Huntington's disease patients. These changes could be linked to neuronal degeneration or to changes in cardiovascular interactions or respiratory function.[75] The changes in the P group are evidence of early autonomic dysfunction in Huntington's disease before symptoms manifest, in line with the previous studies.[15,76] Simultaneous measurements of heart rate and respiration therefore offer a promising avenue for non-invasive testing of disease progression. Previous heart rate variability studies in Huntington's disease have not recorded respiration,[15,77-79] but the benefit of its inclusion is that respiratory sinus arrhythmia can be investigated directly and more thoroughly while adding minimal extra set-up time for the experiment.

Summary

Taken together, the results from our study show that the consequences of Huntington's disease are complex: the vasculature, neuronal activity and autonomic nervous system are all affected. Particularly interestingly, our results show that changes to the vasculature occur in the presymptomatic stages of the disease. Thus, the vasculature and the NVU are potential therapeutic targets in Huntington's disease,[80] either with medication or through lifestyle changes.[81]

Biomarker

With this research, we aimed to get a better understanding of the neurovascular correlates of Huntington's disease. A secondary goal was to investigate if non-invasive measurement techniques in combination with our algorithms for time-resolved coherence have potential as biomarkers for Huntington's disease. This would be advantageous, as other possible biomarkers such as MRI are much more expensive and mostly suitable for patients that can remain still—i.e. not choreatic. The clear differences between the Huntington's disease and control groups suggest that this is indeed the case. Future investigations may benefit from the following considerations. Many of the differences between the Huntington's disease groups and controls are observed in the parietal and occipital areas. Both areas are known to be affected by atrophy, even in the presymptomatic stages of the disease.[2] This opens the possibility of conducting experiments with fewer electrodes and probes, which would reduce the set-up and analysis times. To explore the early changes in the disease and, potentially, to establish whether the vascular or the neuronal changes occur first, a longitudinal study of presymptomatic and early-stage Huntington's disease is required, where imaging techniques could also be included.

Limitations and strengths

As we are interested in slow oscillations, it is necessary that the measurement time be sufficiently long. The 20–30 min of sitting still can be challenging, especially for participants with Huntington's disease. The long measurement time means that movement artefacts in the time series are more likely to appear. We did not use a movement–artefact–removal algorithm. The mild chorea present in most of the S participants might have masked the power in low-frequency intervals in both fNIRS and EEG time series. Hence, the power in frequency intervals below the cardiac frequency should be interpreted with caution for the S group. In addition, we did not record electrooculography (EOG) signals. As the time series must be continuous for the analysis, robust rejection of EOG artefacts would be challenging, but future studies might benefit from including an EOG recording. However, this artefact is only relevant for the EEG and therefore would not impact the EEG–fNIRS phase coherence. Furthermore, the EOG artefact has a large amplitude, but the phase coherence measure applied here is independent of amplitude.

Another limitation is that coherence analysis does not imply causality or provide the direction of the interaction, if present. From the phase shift, it can be inferred which of the two physiological processes under study is leading. However, for the evaluation of directional couplings, one should perform additional investigations, using dynamical Bayesian inference, Granger causality or similar information- or permutation-based methods.[82-84]

The number of participants, especially those with Huntington's disease after being divided into the P and S (with mild chorea only) groups, is relatively small, because recruiting participants with Huntington's disease is problematic. Cognitive tests were not performed on the control participants which is also a limitation of the study. Further, some of the participants were obese (BMI $\geq$ 30). Obesity can impact neuronal and vascular functions. However, we found no correlation between BMI and the average myogenic neurovascular coherence across the brain (Supplementary Fig. 21). As there are no significant differences in BMI between groups, the differences in neuronal and vascular functions presented here can be attributed to Huntington's disease.

In this study, we focused on functional changes. However, the next step would be to combine such studies with imaging techniques to explore the correlation between structural and functional changes and to see if atrophy occurs before functional changes.

For the purpose of understanding the neurovascular correlates of Huntington's disease, the initial analysis was with

data from participants with little to mild chorea. This was technically motivated, as EEG and fNIRS are known to be affected by movement artefacts. However, phase coherence evaluates the consistency in phase difference between two time series. We hypothesized that the phase consistency of two oscillations would not be severely impacted by movement artefacts (unlike their amplitudes), as the random movements caused by chorea would not affect the phases significantly. Therefore, we also calculated the fNIRS–EEG WPC in the group of participants with relatively severe chorea, who were initially excluded. Despite the severe chorea, we see evidence of significant phase coherence (Fig. 5D), confirming that the phase-based methods are less affected by chorea than amplitude-based methods. The fNIRS–EEG WPC in the myogenic band is reduced in the chorea group when compared to the SC group, to a larger extent than was the case for the S group, which suggests that this functional test is also suitable for choreatic patients. This could be attributed to disease progression, as the CS group is more advanced than the S group. Some of the changes may also be attributed to the increased age in the CS group, as we have shown previously that age decreases WPC in the myogenic band.[12] The neurovascular correlates of various intensities of chorea will be investigated separately.

Conclusion

Our results support the hypothesis that the functioning of the NVU is affected in Huntington's disease, as we found altered neurovascular dynamics in patients with Huntington's disease compared to control participants. The simultaneous recordings of cardiovascular and neuronal activities, combined with algorithms for extracting time-localized dynamics, provide a non-invasive evaluation of Huntington's disease. We also add to the discussion about the neuron-centric view of neurodegenerative diseases,[85] by highlighting the importance of the vasculature and NVU in Huntington's disease.

A clear result of this study is that cerebral oxygenation is affected even in the P group, demonstrating an early disruption of normal vascular function in the disease. Blood flow oscillations at low frequencies are likely influenced by local factors such as brain metabolism. The decrease in power of these oscillations might reflect either disturbed brain cortical metabolism in the P group or decreased control of cerebral blood flow. In the S group, we see reduced coherence, which might be a consequence of the higher microvascular density in this group. Still, in both Huntington's disease groups, coherence between neuronal activity and blood oxygenation around 0.1 Hz is reduced. This could reflect reduced efficiency in the functioning of the NVU in participants with Huntington's disease, where the mutant huntingtin protein has been found in all major parts. Whether this is part of the accelerating disease progression is an important question, and it calls for research to address cerebral nutrient delivery in participants with a positive genetic test for Huntington's disease. It is well known that the brain requires ~20% of the body's total energy usage. This leads to the question of whether incoherent delivery of nutrients to the brain cells could also contribute to neuronal death in Huntington's disease, and whether reducing cardiovascular risk factors may improve outcomes. Studies on exercise in Huntington's disease patients have shown improved cardiovascular function,[86] but longer studies with more participants are needed to draw stronger conclusions.

It is evident that the analysis of time-varying oscillatory dynamics in data acquired by non-invasive measurements, even in the presence of movement artefacts due to chorea, provides a promising method for evaluating the effects of Huntington's disease treatment. It demonstrates clear links between physiology and parameters such as reduced α power and reduced neurovascular coherence around 0.1 Hz and helps to evaluate the physiological effect of the disease. The advantages of this approach should now be tested on larger cohorts. It can readily be extended to include coherence and couplings between time series measured by other non-invasive methods, not just the particular time series included in this study.

Supplementary material

Supplementary material is available at *Brain Communications* online.

Acknowledgements

We would like to thank all patients and control participants for their participation—without them, this study would not have been possible. We are grateful to Franci Benko, research nurse at the Department of Neurology, University Medical Centre Ljubljana, for his invaluable help in organizing and carrying out the measurements. We also thank Fajko Bajrović for his support with the clinical part of the study and Boštjan Dolenc for the automated analysis which was used for initial checks. J.B. would like to thank Trevor Crawford, Benediktas Valys, Joe Rowland Adams and Charlie Mpetha for helpful discussions and Sam McCormack for guidance with programming. The High-End Computing facility at Lancaster University was used for data analysis. Figure 1 and the graphical abstract were created using BioRender.com.

Funding

The research was funded by the Engineering and Physical Sciences Research Council (UK) under grant no. EP/M006298/1, the Slovenian Research Agency (ARRS; programme no. P20232) and the Sir John Fisher Foundation. The development of the toolbox MODA was supported by the Engineering and Physical Sciences Research Council (UK) grant nos. EP/100999X1 and EP/M006298/1, the EU projects BRACCIA (517133) and COSMOS (642563), the Action Medical Research (UK) MASDA Project (GN1963) and the Slovenian Research Agency (ARRS; programme no. P20232).

Competing interests

The authors report no competing interests.

Data availability

The data used for this study are available in Lancaster University's Pure database: https://doi.org/10.17635/lancaster/researchdata/416. The toolbox MODA, including algorithms developed by the Nonlinear and Biomedical Physics Group at Lancaster University and the Nonlinear Dynamics and Synergetic Group at the University of Ljubljana, is available on GitHub: https://github.com/luphysics/MODA.

References

1. Tabrizi SJ, Schobel S, Gantman EC, *et al*. A biological classification of Huntington's disease: The integrated staging system. *Lancet Neurol*. 2022;21(7):632-644.
2. Rosas HD, Salat DH, Lee SY, *et al*. Cerebral cortex and the clinical expression of Huntington's disease: Complexity and heterogeneity. *Brain*. 2008;131(Pt 4):1057-1068.
3. Steven M, Hersch H, Rosas D, Ferrante RJ. Chapter 34. Neuropathology and pathophysiology of Huntington's disease. In: Watts RL, Standaert DG, Obeso JA, eds. *Movement disorders*. 3rd ed. McGraw Hill; 2012:683-711.
4. Painold A, Anderer P, Holl AK, *et al*. EEG low-resolution brain electromagnetic tomography (LORETA) in Huntington's disease. *J Neurol*. 2011;258(5):840-854.
5. Zlokovic BV. Neurovascular pathways to neurodegeneration in Alzheimer's disease and other disorders. *Nat Rev Neurosci*. 2011;12(12):723-738.
6. Sweeney MD, Sagare AP, Zlokovic BV. Blood–brain barrier breakdown in Alzheimer disease and other neurodegenerative disorders. *Nat Rev Neurol*. 2018;14(3):133-150.
7. Muoio V, Persson PB, Sendeski MM. The neurovascular unit—Concept review. *Acta Physiol*. 2014;210(4):790-798.
8. Iadecola C. The neurovascular unit coming of age: A journey through neurovascular coupling in health and disease. *Neuron*. 2017;96:17-42.
9. Drouin-Ouellet J, Sawiak SJ, Cisbani G, *et al*. Cerebrovascular and blood-brain barrier impairments in Huntington's disease: Potential implications for its pathophysiology. *Ann Neurol*. 2015;78(2):160-177.
10. Jansen AH, van Hal M, Op den Kelder IC, *et al*. Frequency of nuclear mutant huntingtin inclusion formation in neurons and glia is cell-type-specific. *Glia*. 2017;65(1):50-61.
11. Garcia FJ, Sun N, Lee H, *et al*. Single-cell dissection of the human brain vasculature. *Nature*. 2022;603(7903):893-899.
12. Bjerkan J, Lancaster G, Meglič B, *et al*. Aging affects the phase coherence between spontaneous oscillations in brain oxygenation and neural activity. *Brain Res Bull*. 2023;201:110704.
13. Yeung MK, Chan AS. Functional near-infrared spectroscopy reveals decreased resting oxygenation levels and task-related oxygenation changes in mild cognitive impairment and dementia: A systematic review. *J Psychiatr Res*. 2020;124:58-76.
14. Yeung MK, Chan AS. A systematic review of the application of functional near-infrared spectroscopy to the study of cerebral hemodynamics in healthy aging. *Neuropsychol Rev*. 2021;31:139-166.
15. Kobal J, Melik Z, Cankar K, *et al*. Autonomic dysfunction in presymptomatic and early symptomatic Huntington's disease. *Acta Neurol Scand*. 2010;121(6):392-399.
16. Kobal J, Cankar K, Pretnar J, *et al*. Functional impairment of precerebral arteries in Huntington disease. *J Neurol Sci*. 2017;372:363-368.
17. Buzsáki G, Draguhn A. Neuronal oscillations in cortical networks. *Science*. 2004;304(5679):1926-1929.
18. Stefanovska A, Bračič M. Physics of the human cardiovascular system. *Contemp Phys*. 1999;40(1):31-55.
19. Stefanovska A. Coupled oscillators: Complex but not complicated cardiovascular and brain interactions. *IEEE Eng Med Biol Mag*. 2007;26(6):25-29.
20. Musizza B, Stefanovska A, McClintock PVE, *et al*. Interactions between cardiac, respiratory and EEG-δ oscillations in rats during anaesthesia. *J Physiol*. 2007;580(1):315-326.
21. Stankovski T, Petkoski S, Raeder J, Smith AF, McClintock PVE, Stefanovska A. Alterations in the coupling functions between cortical and cardio-respiratory oscillations due to anaesthesia with propofol and sevoflurane. *Phil Trans R Soc*. 2016;374(2067):20150186.
22. Burle B, Spieser L, Roger C, Casini L, Hasbroucq T, Vidal F. Spatial and temporal resolutions of EEG: Is it really black and white? A scalp current density view. *Int J Psychophysiol*. 2015;97(3):210-220.
23. Wilcox T, Biondi M. fNIRS in the developmental sciences. *Wiley Interdiscip Rev Cogn Sci*. 2015;6(3):263-283.
24. Cohen J. *Statistical power analysis for the behavioral sciences (2nd ed.)*. Lawrence Erlbaum Associates; 1988.
25. Faul F, Erdfelder E, Lang AG, Buchner A. G*Power 3: A flexible statistical power analysis program for the social, behavioral, and biomedical sciences. *Behav Res Methods*. 2007;39(2):175-191.
26. Newman J, Lancaster G, Stefanovska A. *Multiscale oscillatory dynamics analysis user manual v1.01*. Lancaster University; 2018. https://github.com/luphysics/MODA
27. Iatsenko D, McClintock PVE, Stefanovska A. Linear and synchrosqueezed time–frequency representations revisited: Overview, standards of use, resolution, reconstruction, concentration, and algorithms. *Digit Signal Process*. 2015;42:1-26.
28. Iatsenko D, McClintock PVE, Stefanovska A. Nonlinear mode decomposition: A noise-robust, adaptive decomposition method. *Phys Rev E*. 2015;92(3):032916.
29. Kvandal P, Landsverk SA, Bernjak A, Stefanovska A, Kvernmo HD, Kirkebøen KA. Low-frequency oscillations of the laser Doppler perfusion signal in human skin. *Microvasc Res*. 2006;72(3):120-127.
30. Shiogai Y, Stefanovska A, McClintock PVE. Nonlinear dynamics of cardiovascular ageing. *Phys Rep*. 2010;488(2-3):51-110.
31. Kvernmo HD, Stefanovska A, Kirkeboen KA, Kvernebo K. Oscillations in the human cutaneous blood perfusion signal modified by endothelium-dependent and endothelium-independent vasodilators. *Microvasc Res*. 1999;57(3):298-309.
32. Stefanovska A, Bračič M, Kvernmo HD. Wavelet analysis of oscillations in the peripheral blood circulation measured by laser Doppler technique. *IEEE Trans Biomed Eng*. 1999;46(10):1230-1239.
33. Kvernmo HD, Stefanovska A, Kirkebøen KA, Osterud B, Kvernebo K. Enhanced endothelium-dependent vasodilatation in human skin vasculature induced by physical conditioning. *Eur J Appl Physiol Occup Physiol*. 1998;79(1):30-36.
34. Stewart JM, Taneja I, Goligorsky MS, Medow MS. Noninvasive measure of microvascular nitric oxide function in humans using very low-frequency cutaneous laser Doppler flow spectra. *Microcirculation*. 2007;14(3):169-180.
35. Söderström T, Stefanovska A, Veber M, Svensson H. Involvement of sympathetic nerve activity in skin blood flow oscillations in humans. *Am J Physiol Heart Circ Physiol*. 2003;284(5):H1638-H1646.
36. Landsverk SA, Kvandal P, Bernjak A, Stefanovska A, Kirkeboen KA. The effects of general anesthesia on human skin microcirculation evaluated by wavelet transform. *Anesth Analg*. 2007;105(4):1012-1019.
37. Kastrup J, Bülow J, Lassen NA. Vasomotion in human skin before and after local heating recorded with laser Doppler flowmetry. A

method for induction of vasomotion. *Int J Microcirc Clin Exp*. 1989;8(2):205-215.
38. Folkow B. Intravascular pressure as a factor regulating the tone of the small vessels. *Acta Physiol Scand*. 1949;17(4):289-310.
39. Schroeter ML, Schmiedel O, von Cramon DY. Spontaneous low-frequency oscillations decline in the aging brain. *J Cereb Blood Flow Metab*. 2004;24(10):1183-1191.
40. Vanhatalo S, Palva JM, Holmes MD, Miller JW, Voipio J, Kaila K. Infraslow oscillations modulate excitability and interictal epileptic activity in the human cortex during sleep. *Proc Natl Acad Sci U A S*. 2004;101(14):5053-5057.
41. Buzsáki G, Anastassiou CA, Koch C. The origin of extracellular fields and currents—EEG, ECoG, LFP and spikes. *Nat Rev Neurosci*. 2012;13(6):407-420.
42. Buskila Y, Bellot-Saez A, Morley JW. Generating brain waves, the power of astrocytes. *Front Neurosci*. 2019;13:1125.
43. Sachdev RN, Gaspard N, Gerrard JL, Hirsch LJ, Spencer DD, Zaveri HP. Delta rhythm in wakefulness: Evidence from intracranial recordings in human beings. *J Neurophysiol*. 2015;114(2):1248-1254.
44. Cassani R, Estarellas M, San-Martin R, Fraga FJ, Falk TH. Systematic review on resting-state EEG for Alzheimer's disease diagnosis and progression assessment. *Dis Markers*. 2018;2018:5174815.
45. Odish OFF, Johnsen K, van Someren P, Roos RAC, van Dijk JG. EEG may serve as a biomarker in Huntington's disease using machine learning automatic classification. *Sci Rep*. 2018;8(1):16090.
46. Stankovski T, Ticcinelli V, McClintock PVE, Stefanovska A. Neural cross-frequency coupling functions. *Front Syst Neurosci*. 2017;11:33.
47. Bračič M, Stefanovska A. Wavelet-based analysis of human blood-flow dynamics. *Bull Math Biol*. 1998;60(5):919-935.
48. Iatsenko D, McClintock PVE, Stefanovska A. Extraction of instantaneous frequencies from ridges in time–frequency representations of signals. *Signal Process*. 2016;125:290-303.
49. Bandrivskyy A, Bernjak A, McClintock PVE, Stefanovska A. Wavelet phase coherence analysis: Application to skin temperature and blood flow. *Cardiovasc Eng*. 2004;4(1):89-93.
50. Lancaster G, Iatsenko D, Pidde A, Ticcinelli V, Stefanovska A. Surrogate data for hypothesis testing of physical systems. *Phys Rep*. 2018;748:1-60.
51. Montez T, Poil SS, Jones BF, *et al*. Altered temporal correlations in parietal alpha and prefrontal theta oscillations in early-stage Alzheimer disease. *Proc Natl Acad Sci U S A*. 2009;106(5):1614-1619.
52. Kieburtz K, Penney JB, Como P, *et al*. Unified Huntington's disease rating scale: Reliability and consistency. *Mov Disord*. 1996;11(2):136-142.
53. Shin JY, Fang ZH, Yu ZX, Wang CE, Li SH, Li XJ. Expression of mutant huntingtin in glial cells contributes to neuronal excitotoxicity. *J Cell Biol*. 2005;171(6):1001-1012.
54. Chan CS, Surmeier DJ. Astrocytes go awry in Huntington's disease. *Nat Neurosci*. 2014;17(5):641-642.
55. Kugler EC, Greenwood J, MacDonald RB. The "neuro-glial-vascular" unit: The role of glia in neurovascular unit formation and dysfunction. *Front Cell Dev Biol*. 2021;9:732820.
56. Kim KJ, Iddings JA, Stern JE, *et al*. Astrocyte contributions to flow/pressure-evoked parenchymal arteriole vasoconstriction. *J Neurosci*. 2015;35(21):8245-8257.
57. Kim KJ, Ramiro Diaz J, Iddings JA, Filosa JA. Vasculo-neuronal coupling: Retrograde vascular communication to brain neurons. *J Neurosci*. 2016;36(50):12624-12639.
58. Labbadia J, Morimoto RI. Huntington's disease: Underlying molecular mechanisms and emerging concepts. *Trends Biochem Sci*. 2013;38(8):378-385.
59. Tang CC, Feigin A, Ma Y, *et al*. Metabolic network as a progression biomarker of premanifest Huntington's disease. *J Clin Invest*. 2013;123(9):4076-4088.
60. Casella C, Lipp I, Rosser A, Jones DK, Metzler-Baddeley C. A critical review of white matter changes in Huntington's disease. *Mov Disord*. 2020;35(8):1302-1311.
61. Furr-Stimming E, Rocha NP, Latham L, *et al*. Decreased cerebral blood flow in the striatum is an early event in Huntington's disease pathology (P1.8-044). *Neurology*. 2019;92(15 Supplement):P1.8-044.
62. Lin CY, Hsu YH, Lin MH, *et al*. Neurovascular abnormalities in humans and mice with Huntington's disease. *Exp Neurol*. 2013;250:20-30.
63. Pinto E. Blood pressure and ageing. *Postgrad Med J*. 2007;83(976):109-114.
64. Hayes G, Pinto J, Sparks SN, Wang C, Suri S, Bulte DP. Vascular smooth muscle cell dysfunction in neurodegeneration. *Front Neurosci*. 2022;16:1010164.
65. Streletz LJ, Reyes PF, Zalewska M, Katz L, Fariello RG. Computer analysis of EEG activity in dementia of the Alzheimer's type and Huntington's disease. *Neurobiol Aging*. 1990;11(1):15-20.
66. Bylsma FW, Peyser CE, Folstein SE, Folstein MF, Ross C, Brandt J. EEG power spectra in Huntington's disease: Clinical and neuropsychological correlates. *Neuropsychologia*. 1994;32(2):137-150.
67. de Tommaso M, Carlo FD, Difruscolo O, Massafra R, Sciruicchio V, Bellotti R. Detection of subclinical brain electrical activity changes in Huntington's disease using artificial neural networks. *Clin Neurophysiol*. 2003;114(7):1237-1245.
68. van der Hiele K, Jurgens CK, Vein AA, *et al*. Memory activation reveals abnormal EEG in preclinical Huntington's disease. *Mov Disord*. 2007;22(5):690-695.
69. Hunter A, Bordelon Y, Cook I, Leuchter A. QEEG measures in Huntington's disease: A pilot study. *PLoS Curr*. 2010;2:RRN1192.
70. Ponomareva N, Klyushnikov S, Abramycheva N, *et al*. Alpha-theta border EEG abnormalities in preclinical Huntington's disease. *J Neurol Sci*. 2014;344(1-2):114-120.
71. Leuchter MK, Donzis EJ, Cepeda C, *et al*. Quantitative electroencephalographic biomarkers in preclinical and human studies of Huntington's disease: Are they fit-for-purpose for treatment development? *Front Neurol*. 2017;8:91-91.
72. Moretti DV, Babiloni C, Binetti G, *et al*. Individual analysis of EEG frequency and band power in mild Alzheimer's disease. *Clin Neurophysiol*. 2004;115(2):299-308.
73. Delussi M, Nazzaro V, Ricci K, De Tommaso M. EEG functional connectivity and cognitive variables in premanifest and manifest Huntington's disease: EEG low-resolution brain electromagnetic tomography (LORETA) study. *Front Physiol*. 2020;11:612325.
74. Lotrič MB, Stefanovska A. Synchronization and modulation in the human cardiorespiratory system. *Phys Stat Mech Appl*. 2000;283(3):451-461.
75. Jones U, Busse M, Enright S, Rosser AE. Respiratory decline is integral to disease progression in Huntington's disease. *Eur Respir J*. 2016;48(2):585-588.
76. Schultz JL, Harshman LA, Kamholz JA, Nopoulos PC. Autonomic dysregulation as an early pathologic feature of Huntington disease. *Auton Neurosci*. 2021;231:102775.
77. Kobal J, Meglic B, Mesec A, Peterlin B. Early sympathetic hyperactivity in Huntington's disease. *Eur J Neurol*. 2004;11(12):842-848.
78. Andrich J. Autonomic nervous system function in Huntington's disease. *J Neurol Neurosurg Psychiatry*. 2002;72(6):726-731.
79. Schultz JL, Heinzerling AE, Brinker AN, *et al*. Autonomic changes in Huntington's disease correlate with altered central autonomic network connectivity. *Brain Commun*. 2022;4(5):fcac253.
80. VanGilder RL, Rosen CL, Barr TL, Huber JD. Targeting the neurovascular unit for treatment of neurological disorders. *Pharmacol Ther*. 2011;130(3):239-247.
81. Trembath MK, Horton ZA, Tippett L, *et al*. A retrospective study of the impact of lifestyle on age at onset of Huntington disease. *Mov Disord*. 2010;25(10):1444-1450.

82. Clemson P, Lancaster G, Stefanovska A. Reconstructing time-dependent dynamics. *Proc IEEE*. 2016;104(2):223-241.
83. Stankovski T, Pereira T, McClintock PVE, Stefanovska A. Coupling functions: Universal insights into dynamical interaction mechanisms. *Rev Mod Phys*. 2017;89(4):045001.
84. Stankovski T, Pereira T, McClintock PVE, Stefanovska A. Coupling functions: Dynamical interaction mechanisms in the physical, biological and social sciences. *Philos Trans A Math Phys Eng Sci*. 2019;377(2160):20190039.
85. Liddelow SA, Sofroniew MV. Astrocytes usurp neurons as a disease focus. *Nat Neurosci*. 2019;22(4):512-513.
86. Mueller SM, Petersen JA, Jung HH. Exercise in Huntington's disease: Current state and clinical significance. *Tremor Other Hyperkinet Mov (N Y)*. 2019;9:601.

Chapter 6

Concluding remarks

6.1 Summary and conclusions

This thesis has presented a quantitative assessment of neurovascular function using non-invasive measurements of brain oxygenation, brain electrical activity, and cardiorespiratory function, combined with time-frequency analysis methods within the time-dependent finite-time-dynamics framework. Neurovascular function was evaluated in younger and older adults, as well as in patients with Alzheimer's disease and Huntington's disease. By taking the phase coherence between brain oxygenation and electrical activity as an indicator of neurovascular unit efficiency, it was found that this efficiency decreases with age and further declines in Alzheimer's disease. Additionally, patients with pre-symptomatic and symptomatic Huntington's disease exhibited lower efficiency compared to age-matched controls. The changes in blood oxygenation dynamics varied between the groups (see figure 6.1). The affordability of these non-invasive measurement techniques makes them suitable for repeated use, and ideal for disease monitoring. Further, this could be positive for patients, as other techniques such as fMRI and MEG can be experienced as stressful or scary. As the neurovascular unit is affected by several diseases it would be highly beneficial to monitor its efficiency in a clinical setting.

Chapter 1 introduced the cardiovascular system, the brain, and the neurovascular unit, summarising changes associated with ageing, Alzheimer's disease, and Huntington's disease. The close collaboration between the cardiovascular system and the brain was highlighted. Four non-invasive measurement techniques were presented: the electroencephalogram, functional near-infrared spectroscopy, the electrocardiogram, and the respiration belt. These methods form the basis for the analyses in subsequent chapters. The chapter also covers the physics of living systems to provide context for the data-driven approach to dynamical systems, with an emphasis on oscillations and how to detect them. A strength of the thesis is the focus on several systems and their interactions. For complex systems such as living systems this approach can offer additional insights compared to when

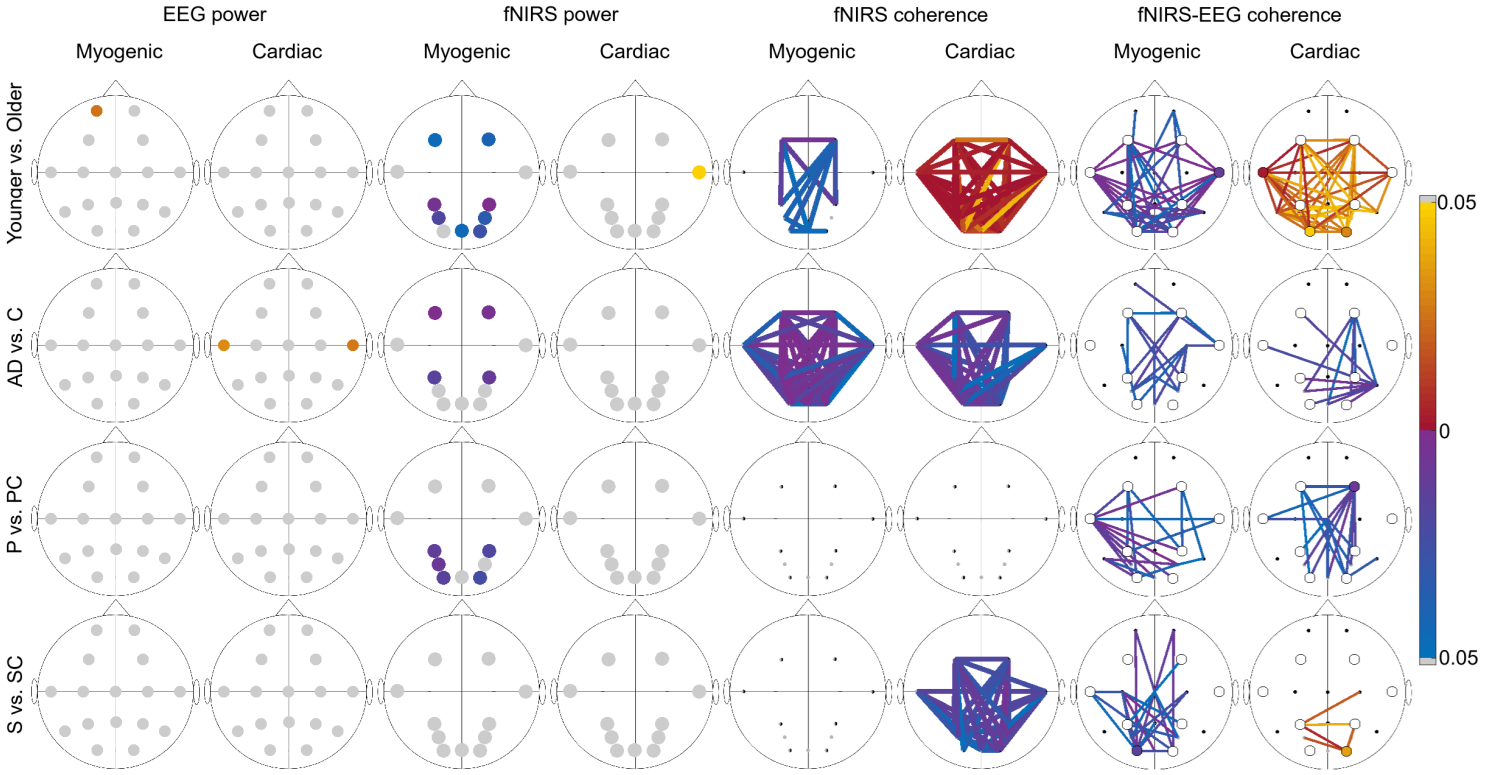

Figure 6.1: Summary of EEG and fNIRS power, fNIRS coherence and fNIRS–EEG coherence results in the myogenic and cardiac bands for all groups considered in the thesis. Blue/purple (yellow/red) indicates that the power or coherence was higher in the younger/control (older/AD/P/S) group. The neurovascular phase coherence was decreased for the older group and the disease groups compared to their control groups. However, the changes in the blood oxygenation dynamics differ between the groups.

only considering one aspect. This line of thinking could have a big impact on research on living systems in general, and on research on the brain specifically. For example, the field of systems biology aim to study interactions and emergent behaviour within living systems [163]. Within this context, Ishii *et al.* [164] measured the transcriptome, proteome and metabolome from Escherichia coli (E. coli) cells in order to study the response to genetic and environmental perturbations. They concluded E. coli cells maintained a stable metabolic network robust against perturbations. In terms of brain research, both the gut-brain axis and brain-heart interactions are gaining popularity. To consider several systems, by for example measuring functional brain activity and heart rate, can elucidate how they influence

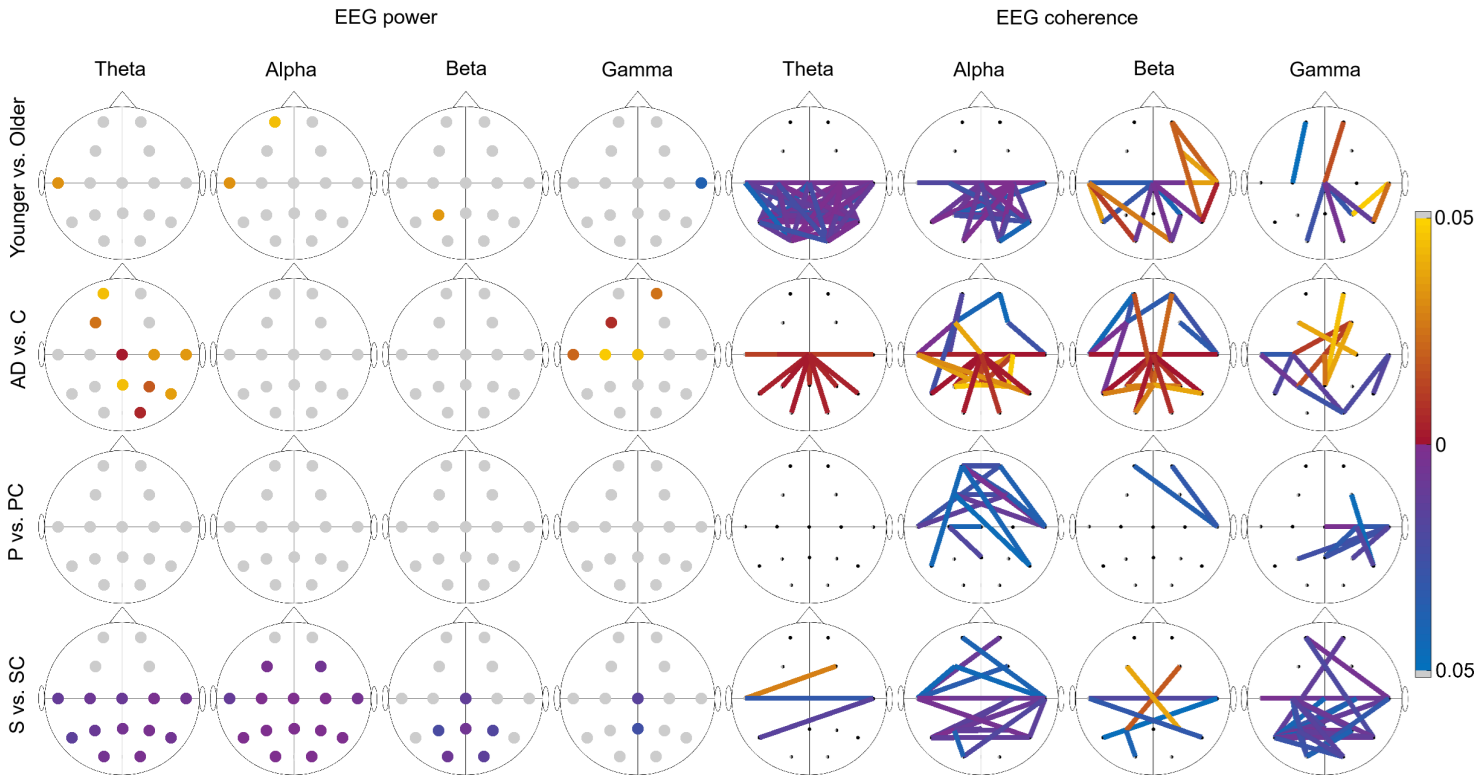

Figure 6.2: Summary of EEG power and coherence in the theta, alpha, beta and gamma bands for all groups considered in the thesis. Blue/purple (yellow/red) indicates that the power or coherence was higher in the younger/control (older/AD/P/S) group.

eachother [165].

In chapter 2 coherence was discussed in detail, and it was illustrated that using phase-only phase coherence rather than amplitude-weighted phase coherence was more robust to noise. The strengths of the wavelet transform were highlighted. For the analysis of the measured data in chapters 3, 4 and 5, the methods must be suitable for finite-time analysis from out-of-equilibrium, thermodynamically open systems. As such, two lines of analysis were pursued: quantifying the presence and strength of oscillations via the wavelet transform, and quantifying the coordination of oscillations via wavelet phase coherence.

In chapter 3 we learnt that neurovascular phase coherence in the myogenic frequency range decreased with age, reflecting reduced efficiency of the neurovascular unit. Further, the phase coherence between the instantaneous heart rate and brain

oxygenation was reduced in the myogenic and respiration frequency ranges. With age, there was reduced power in the myogenic brain oxygenation oscillations and reduced phase coherence. However, in the cardiac band, there was increased phase coherence between brain oxygenation oscillation with age. This likely reflects the increased radii of vessels and increased blood pressure in the older participants. The results also indicate reduced function of the smooth muscle cells lining the blood vessels.

In chapter 4 we discovered that the neurovascular phase coherence is reduced in Alzheimer's disease participants compared to age-matched controls. We also found decreased power in oxygenation oscillations in the myogenic and neurogenic bands, and decreased coherence in all the cardiovascular frequency bands in the Alzheimer's patients. Combined these results indicate reduced vasomotion and thereby reduced local control of blood flow in Alzheimer's disease, coupled with reduced efficiency of the neurovascular unit. The decrease in vasomotion might contribute to reduced clearance of amyloid-beta from the brain. Lastly, Alzheimer's patients have an increased respiration rate compared to controls, which warrants further investigation.

In chapter 5 we found that the presymptomatic Huntington's disease participants have reduced power of oxygenation oscillations in the neurogenic and myogenic frequency bands, indicating reduced vasomotion. On the other hand, the symptomatic participants have reduced phase coherence in the cardiac band between oxygenation oscillations. These results might be explained by vascular remodelling, which has been observed in Huntington's disease and might be a compensatory response to reduced efficiency of the vascular network. However, in both groups, we found decreased neurovascular phase coherence compared to controls, so vascular remodelling does not restore the efficiency of the neurovascular unit. The results from the brain electrical activity indicate a gradual deterioration of neuronal activity, starting with the coherence and then the power of oscillations.

Considering the combined results from chapters 3, 4 and 5 (figure 6.1) it is clear

that the methods can capture disease-specific changes. The figure shows EEG power, fNIRS power, fNIRS coherence and fNIRS-EEG coherence in the myogenic and cardiac frequency bands, for all groups considered. The EEG power differences are not significant when considering the multiple comparisons in any of the comparisons. The older group, the Alzheimer's group and the presymptomatic Huntington's group all have decreased myogenic fNIRS power compared to the younger/control groups. Unlike in symptomatic Huntington's disease, we do not find evidence of vascular remodelling in Alzheimer's disease. The vascular remodelling is indicated by the reduced fNIRS cardiac coherence in tandem with no power differences and no decrease in myogenic fNIRS coherence. Interestingly, molecules that contribute to vessel growth have been found in the vasculature of people with Alzheimer's disease, which might indicate that vascular repair and/or remodelling is unsuccessful rather than non-existent [166]. The neurovascular phase coherence (fNIRS-EEG coherence) is reduced in the older group and the disease groups in the myogenic frequency band, indicating reduced efficiency of the neurovascular unit with age and disease.

For the sake of completeness, figure 6.2 shows the combined EEG results, in the theta, alpha, beta and gamma bands. The younger group does not have significant changes in EEG power when considering the multiple comparisons. The Alzheimer's group have increased theta power compared to their control group, while the symptomatic Huntington's group have decreased power in the theta, alpha and beta bands compared to their control group. The older group, and both Huntington's groups have decreased alpha coherence. On the other hand, the Alzheimer's group has significantly higher alpha coherence in 21 EEG combinations (11 of which includes the Cz electrode), while the control group has higher coherence in 8 EEG combinations. In conclusion, the groups have different patterns of neuronal changes.

In conclusion, this work provides valuable physiological insights into ageing, Alzheimer's disease, and Huntington's disease through non-invasive measurement techniques combined with powerful finite-time analysis, focusing on oscillations and their coordination.

6.2 Original contributions

- Amplitude-weighted phase coherence and phase coherence were compared using both numerically generated and real time-series, which provided insights to how the two methods are affected by noise and phase perturbations and movement artifacts.

- It was demonstrated that wavelet phase coherence can be used to calculate neurovascular coherence based on EEG and fNIRS recordings, providing a non-invasive method to quantify the efficiency of the neurovascular unit.

- Neurovascular coherence around 0.052–0.145 Hz was shown to decrease with age, and further with Alzheimer's disease. Patients with presymptomatic and symptomatic Huntington's disease have lower coherence than controls of similar ages.

- fNIRS was used to study Huntington's disease for the first time, showing a decrease in the power of oscillations in the 0.021–0.052 Hz and 0.052–0.145 Hz frequency ranges in the presymptomatic participants.

- Wavelet phase coherence was demonstrated between oxygenation and instantaneous heart rate signals, and shown to decrease with age and Alzheimer's disease.

6.3 Future work

- Validate the results obtained in chapters 3, 4 and 5 in larger groups.

- Evaluate the potential for classification of Alzheimer's disease and Huntington's disease using machine learning. For example, the datasets used in this study could be used to train classification algorithms, such as decision trees or K-nearest neighbours. Another similar dataset could be used as a testing

dataset, to evaluate the model performance. Alternatively, leave-one-out cross validation could be used if a new dataset cannot be obtained.

- Investigate other patient groups where changes in neurovascular function is implicated: for examples, participants with vascular dementia, frontotemporal dementia, dementia with Lewy bodies or Parkinson's disease.
- Explore potential influences of sex and race on the results.
- Longitudinal research to examine if neurovascular coherence can be altered by lifestyle changes or medication, and if this would correlate with disease progression.
- Correlate neurovascular coherence and other parameters with behavioural data.
- Develop a device and algorithm for non-invasive monitoring of the neurovascular unit.
- Use effective connectivity measures, such as coupling functions [45], to reason about the direction of influence of the interactions. This could help elucidate the mechanisms of interaction within the NVU.

Chapter A

Appendices

SUPPLEMENTARY MATERIAL

Phase coherence – A time-localised approach to studying interactions

S. J. K. Barnes[1] J. Bjerkan [1] P. T. Clemson[1] J. Newman[2] A. Stefanovska[1*]

[1]Lancaster University Physics Department, Lancaster, LA1 4YB, England
[2]Department of Mathematics and Statistics, University of Exeter, Exeter, UK
*Corresponding author: aneta@lancaster.ac.uk

Here we present an alternative to figure 1 in the main manuscript. Namely, to facilitate the comparison of both representations, the Fourier transform is now shown in logarithmic scale in figures 1C,D,G,H. By comparing figure 1 in the main text and supplementary figure 1, it is clear that the logarithmic scale is disadvantageous to the short-time Fourier transform, which is obtained with linear frequency resolution.

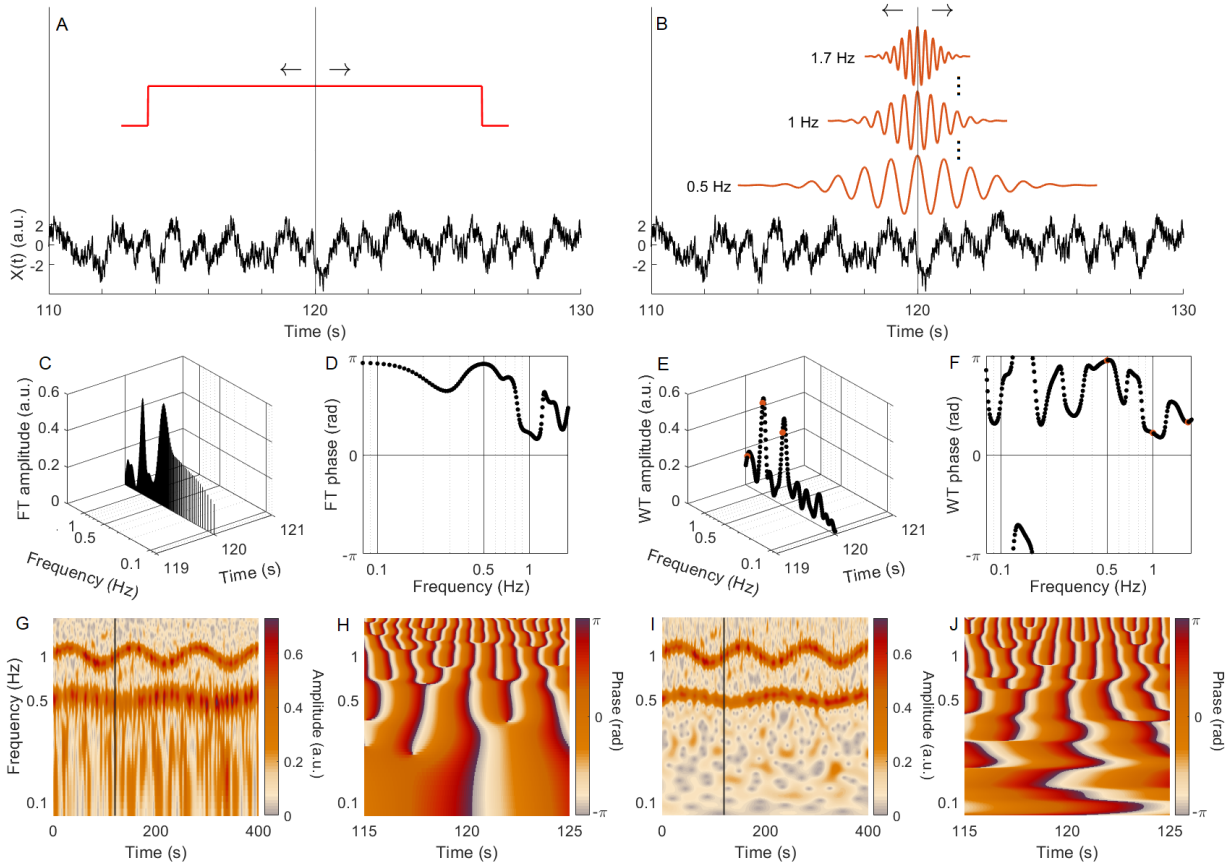

Supplementary Figure 1: Time-frequency analysis illustrated for time-localised versus fixed-window approaches. (A) Generated time-series of Poincaré oscillators as defined by Eq. (5) in the main manuscript, with additive $1/f$ noise and $\xi_r = 0.005$. A window of size 12.6 s centred at 120 s is drawn above the time-series. The arrows above the window illustrate that the window slides across the time-series when the short-time Fourier transform (STFT) is applied. (B) The same time-series as in A, with three wavelets with frequency resolution $f_0 = 2$ at different frequencies (0.5 Hz, 1 Hz and 1.7 Hz) drawn above the time-series. The wavelets slide across the time-series when the WT is applied. The dots between the wavelets illustrates that there is one wavelet for each frequency, in our case 288 wavelets. (C) The STFT amplitude found at 120 s. Note the logarithmic frequency scale. (D) The STFT phase found at 120s projected onto the frequency-phase plane. (E) The WT amplitude found at 120s. The orange dots correspond to the frequencies of the three wavelets in B. Note the logarithmic frequency resolution of the WT. (F) The WT phase found at 120s projected onto the frequency-phase plane. (G) The STFT amplitude for the whole 400s time-series. A line is drawn at 120s. Note the logarithmic frequency scale. (H) The STFT phase for 10s of the time-series. (I) the WT amplitude for the whole 400s time-series. (J) The WT phase for 10s of the time-series.

SUPPLEMENTARY MATERIAL

for

Aging affects the phase coherence between spontaneous oscillations in brain oxygenation and neural activity

Juliane Bjerkan[a], Gemma Lancaster[a], Bernard Meglič[b], Jan Kobal[b], Trevor J. Crawford[c]
Peter V. E. McClintock[a], Aneta Stefanovska[a*]

[a]Department of Physics, Lancaster University, LA1 4YB, Lancaster, UK
[b] Department of Neurology, University Medical Centre, 1525 Ljubljana, Slovenia
[c]Department of Psychology, Lancaster University, LA1 4YF, Lancaster, UK
[*]Corresponding author, aneta@lancaster.ac.uk

Contents

1 Introduction

This document contain material supplementary to the paper "Aging affects the phase coherence between spontaneous oscillations in brain oxygenation and neural activity". In section 2, the effect size is calculated for the main findings in the paper. In section 3, the average respiration rate and instantaneous respiration rate, and their statistical evaluation for both groups, are presented. In addition, the coherence between instantaneous heart/respiration rate with fNIRS and EEG signals are shown for all fNIRS and EEG locations. In section 4, the EEG power and EEG inter-electrode coherence are shown. In section 5, the influence of sex on aging is explored. In section 6 the permutation test is explained in more detail than in the main paper. In section 7 we show the fNIRS–EEG coherence as a function of frequency, for all fNIRS–EEG combinations. Lastly, in section 8 we show correlations that were not included in the main paper.

Throughout this document black solid and blue dashed lines in graphs are median values, while shaded areas show the 25–75th percentiles. Blue stars on the x-axis indicate a significant difference between the two groups at that frequency.

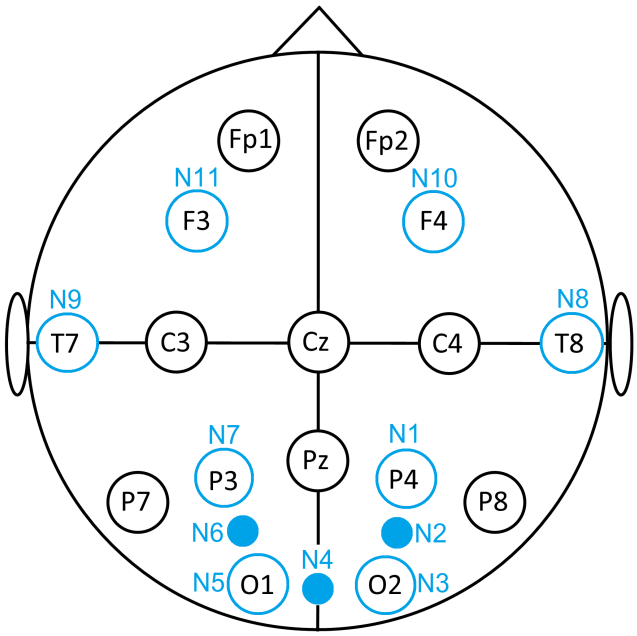

Figure 1: Placement of EEG and fNIRS sensors. Note that in 8 locations there is both an EEG and an fNIRS sensor.

2 Effect size

Cohen's d was used for the effect size. It provides the number of standard deviations by which two groups differ [1] and is calculated from

$$d = \frac{m_1 - m_2}{sd}, \tag{1}$$

where m_1 and m_2 are the means of groups 1 and 2, and sd is the pooled standard deviation of the two groups, which is given by

$$sd = \sqrt{\frac{(n_1 - 1)SD_1^2 + (n_2 - 1)SD_2^2}{n_1 + n_2 - 2}}. \tag{2}$$

Here n_1 and n_2 are the numbers of people in groups 1 and 2, respectively, and SD_1 and SD_2 are the standard deviations of the two groups.

2.1 Sensitivity of study

Based on a significance level of 0.05, a power of 0.8 and the sample sizes (21 younger subjects and 24 older subjects) we tested what effect sizes could reliably be picked up by the study. The effect size found, using G*Power [2], was 0.92, which means the study can reliably find large differences between the two groups. See figure 2 for the calculation in G*Power.

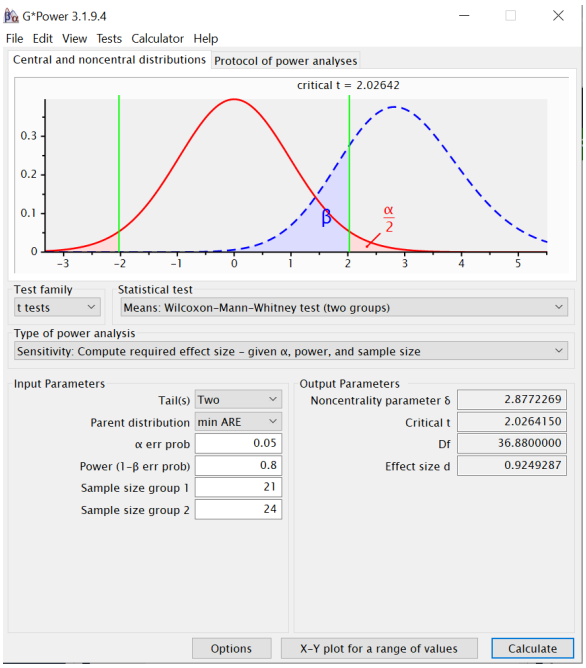

Figure 2: Screenshot from G*Power.

2.2 oxyHb fNIRS myogenic effect sizes

8/11 fNIRS sensors are significantly different between the groups in the myogenic band, with the older group having lower power. The Cohen's d values are 1.027, 0.5966, 0.4535, 0.5962, 0.7412, 0.8774, 0.6635, 0.6239. These are considered to be medium ($d = 0.5$) and large ($d = 0.8$) effect sizes. The mean effect size is therefore 0.697.

2.3 fNIRS–EEG coherence in the myogenic band effect sizes

Forty six fNIRS–EEG probe combinations are significantly different between the groups, with the older group having lower coherence. The maximum, minimum and mean Cohen's d values are 0.9636, 0.4349 and 0.6841, respectively.

2.4 EEG coherence in the alpha band effect sizes

Thirty EEG-EEG electrode combinations are significantly different between the groups, with the older group having lower coherence. The maximum, minimum and mean Cohen's d values are 1.5038, 0.4594 and 0.9802, respectively.

3 Heart and respiration rates, coherence with EEG and fNIRS

The heart and lungs are the flow and pressure pumps of the cardiovascular system. In the main text average heart rate, heart rate variability and instantaneous heart rate power is presented. Here, in figure 3 the average respiration rate and respiration rate variability is shown. We calculated the wavelet phase coherence between the instantaneous heart rate (IHR) and fNIRS/EEG, between the instantaneous respiration rate (IRR) and fNIRS/EEG, and between the respiration signal and fNIRS/EEG.

The fNIRS signals are coherent with the IHR, IRR and respiration signals. For the IHR–oxygenation coherence, the older group has reduced coherence around 0.1Hz, and in the respiratory band in all fNIRS sensors apart from 7 and 8. In these two sensors the coherence is still reduced in the respiration band. fNIRS is coherent with respiration and, to a smaller extent, IRR in the respiratory band. The respiration–fNIRS coherence is reduced in the older group compared to the younger group in the range around $0.3 - 0.6$Hz.

The EEG signals are coherent with IHR around 0.1Hz, but show little to no coherence with the respiration and IRR signals (median 0, and low non-zero percentiles). The IHR–EEG coherence is especially high in electrodes O1, O2, P3, P7, C4 and T7.

The plots. Solid lines show median values, and shaded areas show 25–75th percentiles. Blue stars on the x-axis indicate a p-value below 0.05 at that frequency. A positive phase difference means that either IHR, or IRR or respiration is the leading signal. The phase difference is given in radians.

3.1 Average respiration rate and instantaneous respiration rate

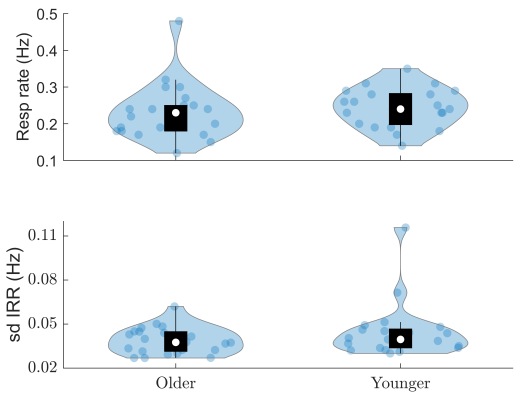

Figure 3: Average respiration rate (older: 0.23 ± 0.08 Hz; younger: 0.24 ± 0.05 Hz, $p = 0.300$), and standard deviation of the IRR (sd IRR) (older: 0.039 ± 0.009 Hz; younger: 0.045 ± 0.019 Hz, $p = 0.26$).

3.2 Instantaneous heart rate–fNIRS coherence

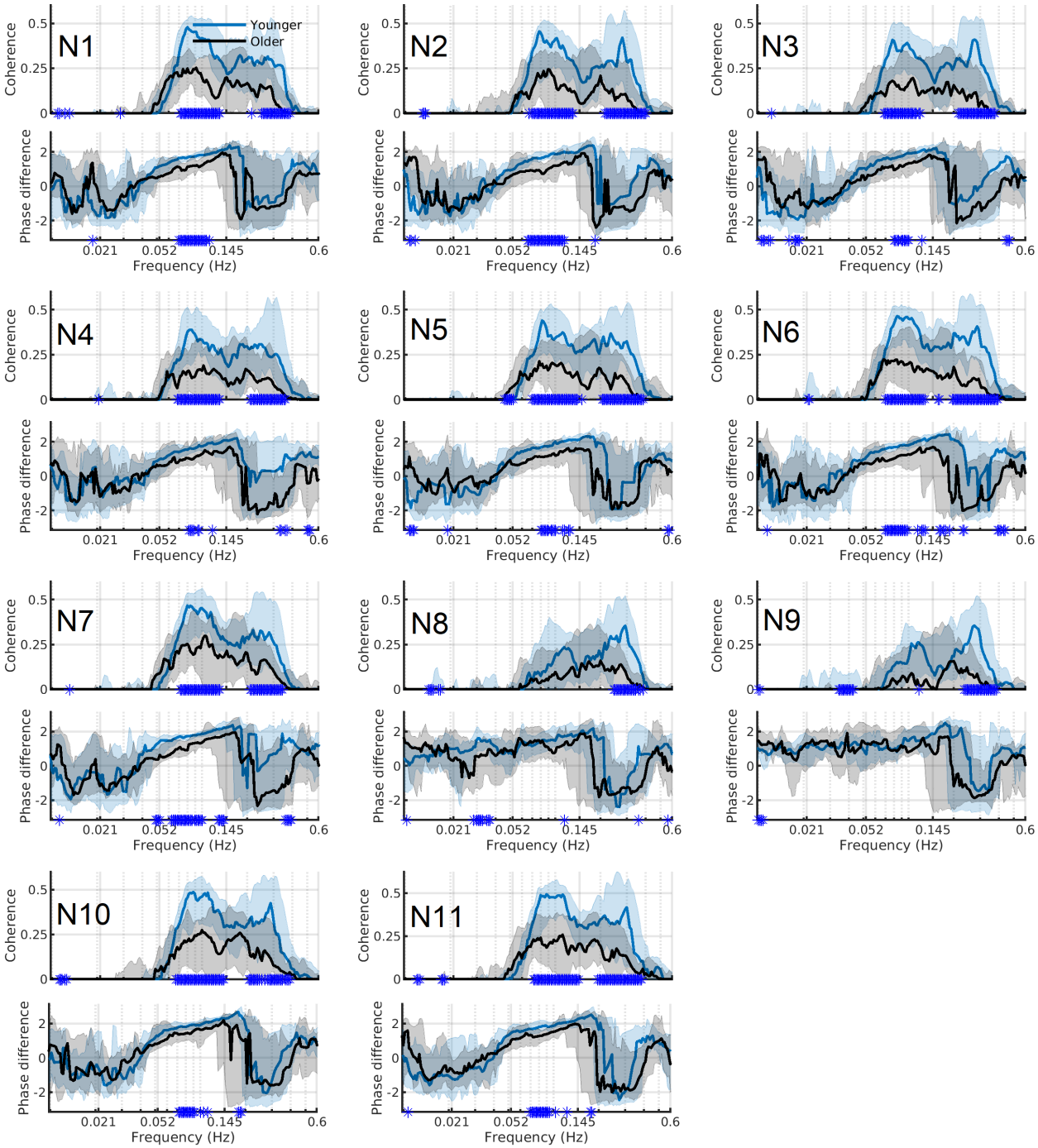

Figure 4: IHR–fNIRS coherence and phase difference for the 11 locations.

3.3 Instantaneous heart rate–EEG coherence

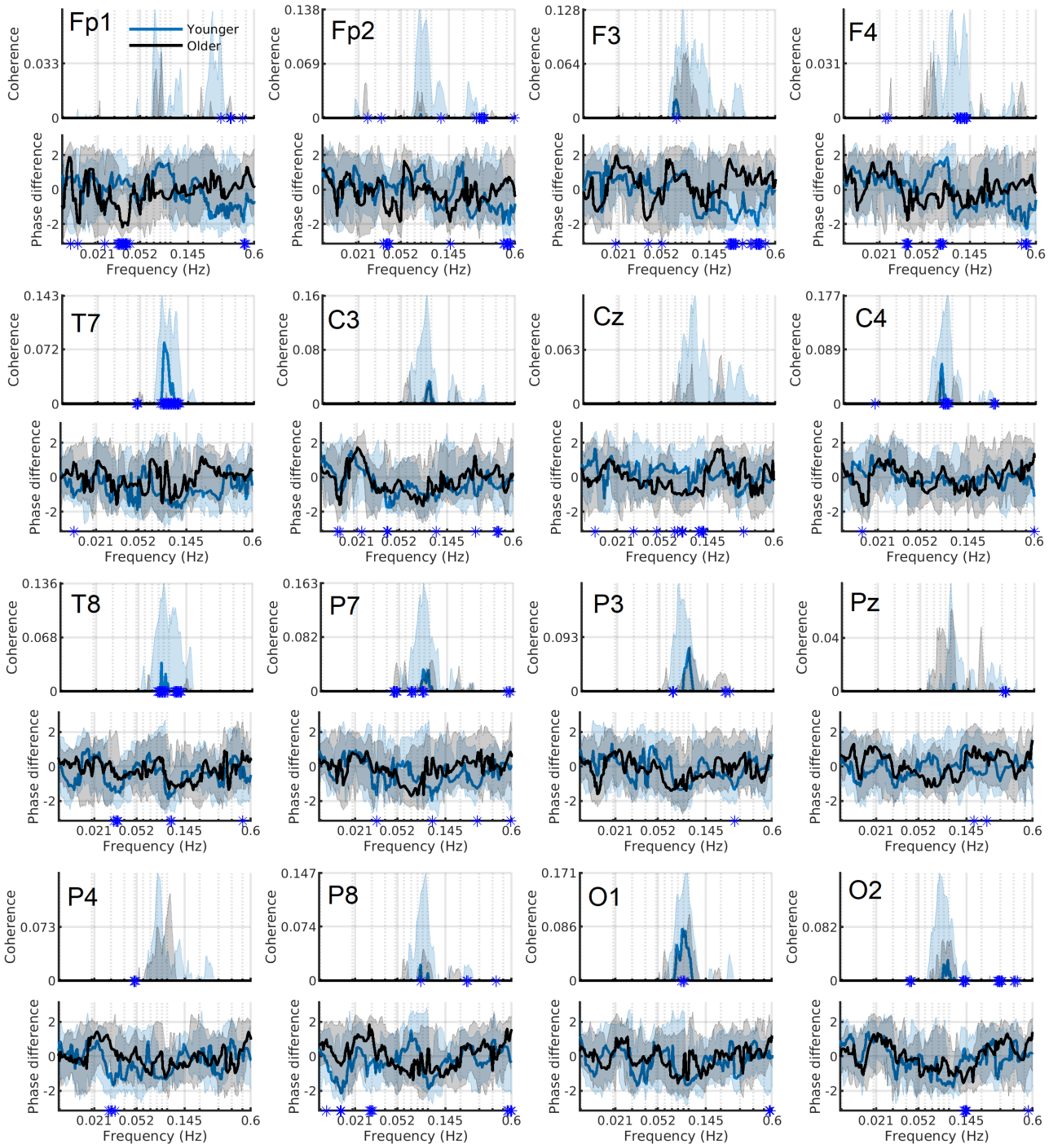

Figure 5: IHR–EEG coherence and phase difference for the 16 locations.

3.4 Respiration–fNIRS coherence

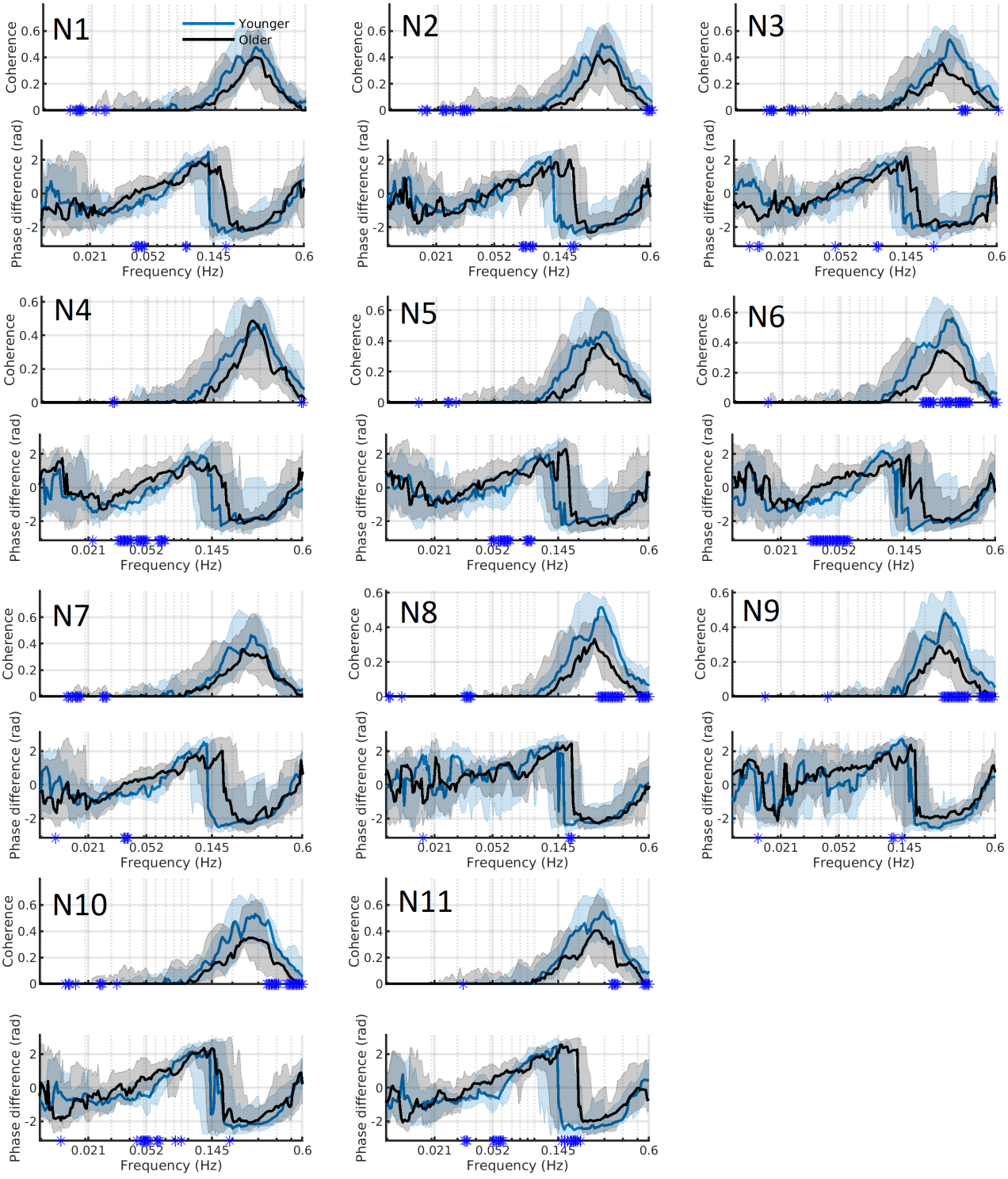

Figure 6: Resp–fNIRS coherence and phase difference for the 11 locations.

3.5 Respiration–EEG coherence

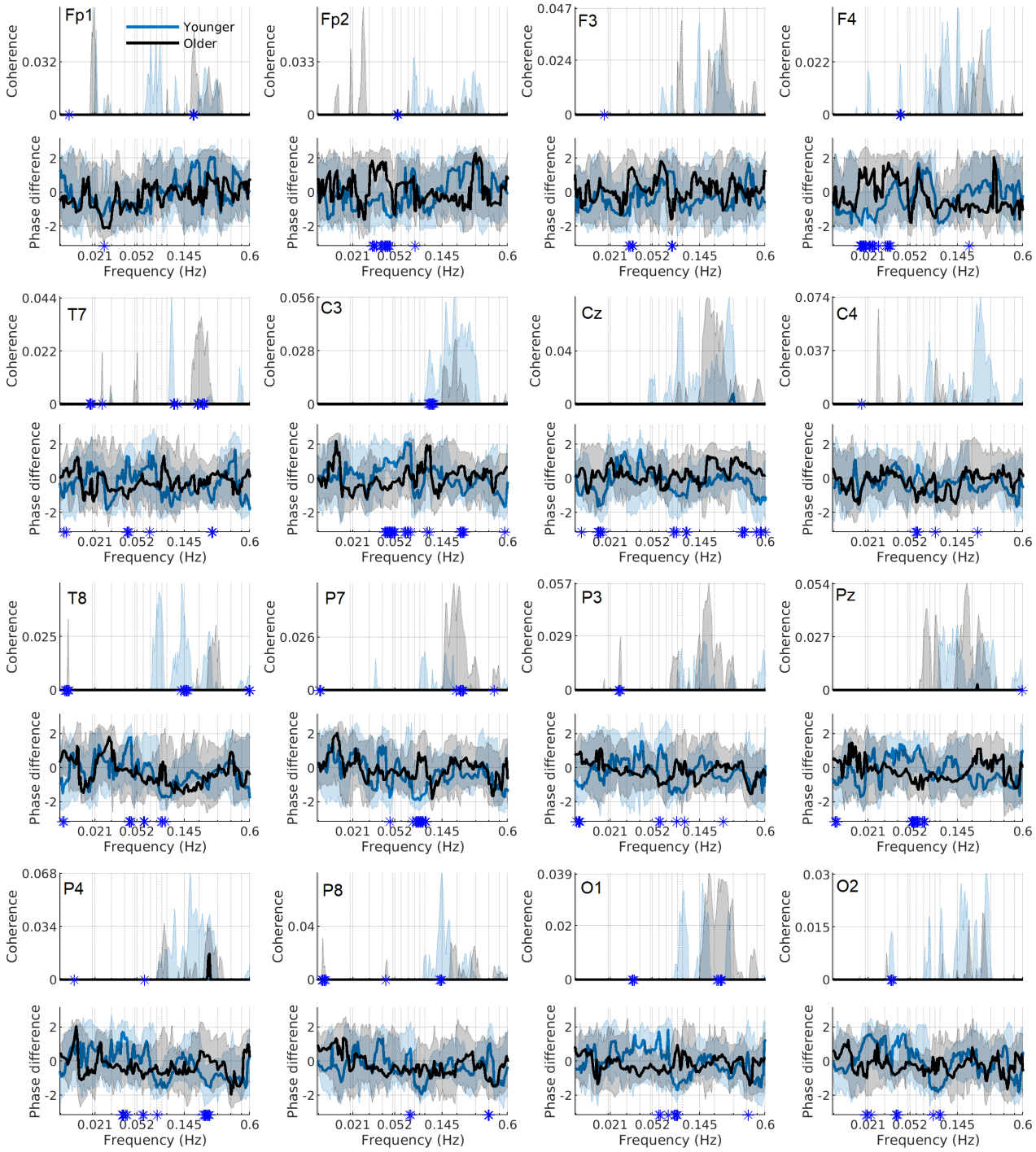

Figure 7: Resp–EEG coherence and phase difference for the 16 locations.

3.6 Instantaneous respiration rate–fNIRS coherence

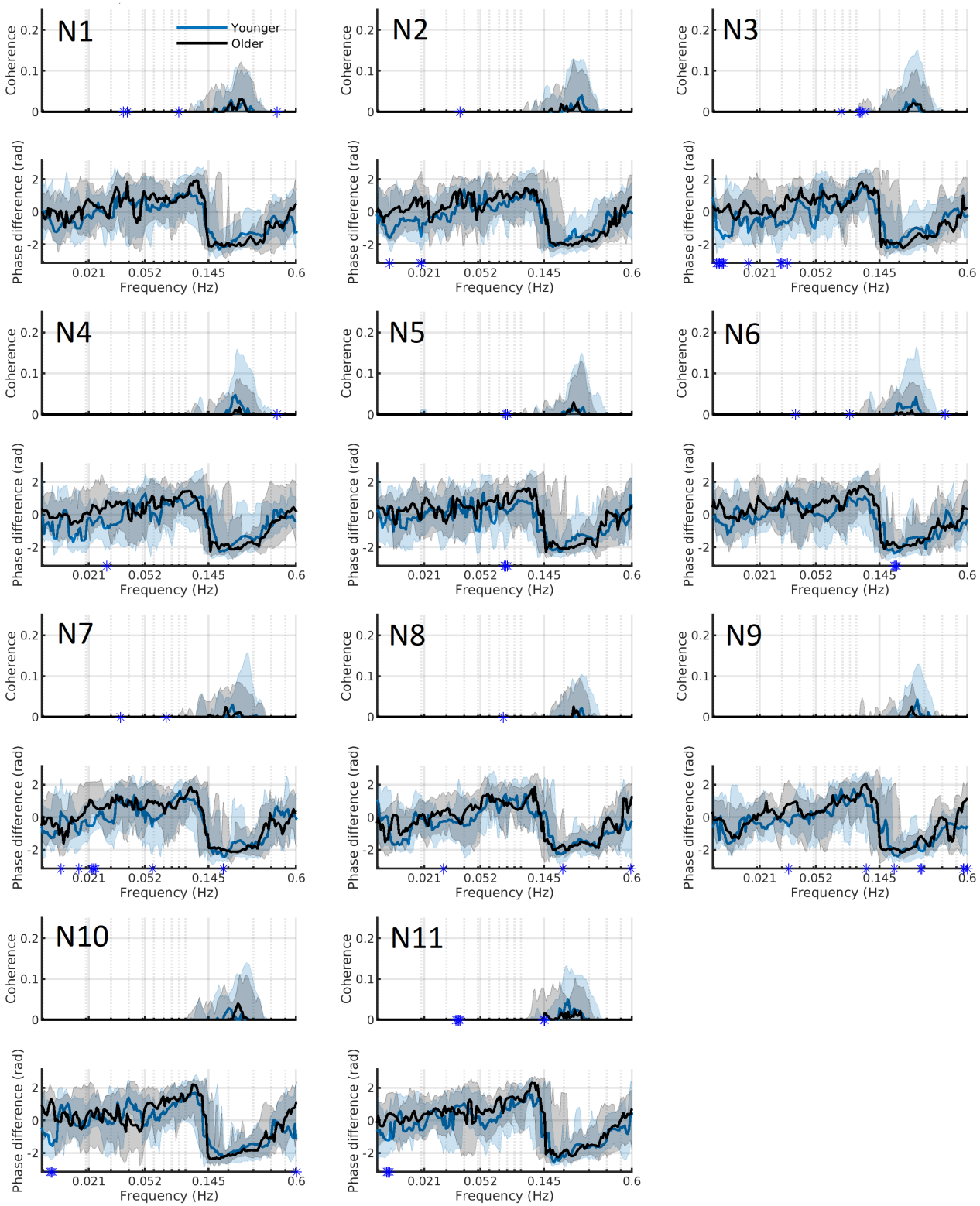

Figure 8: IRR–fNIRS coherence and phase difference for the 11 locations.

3.7 Instantaneous respiration rate–EEG coherence

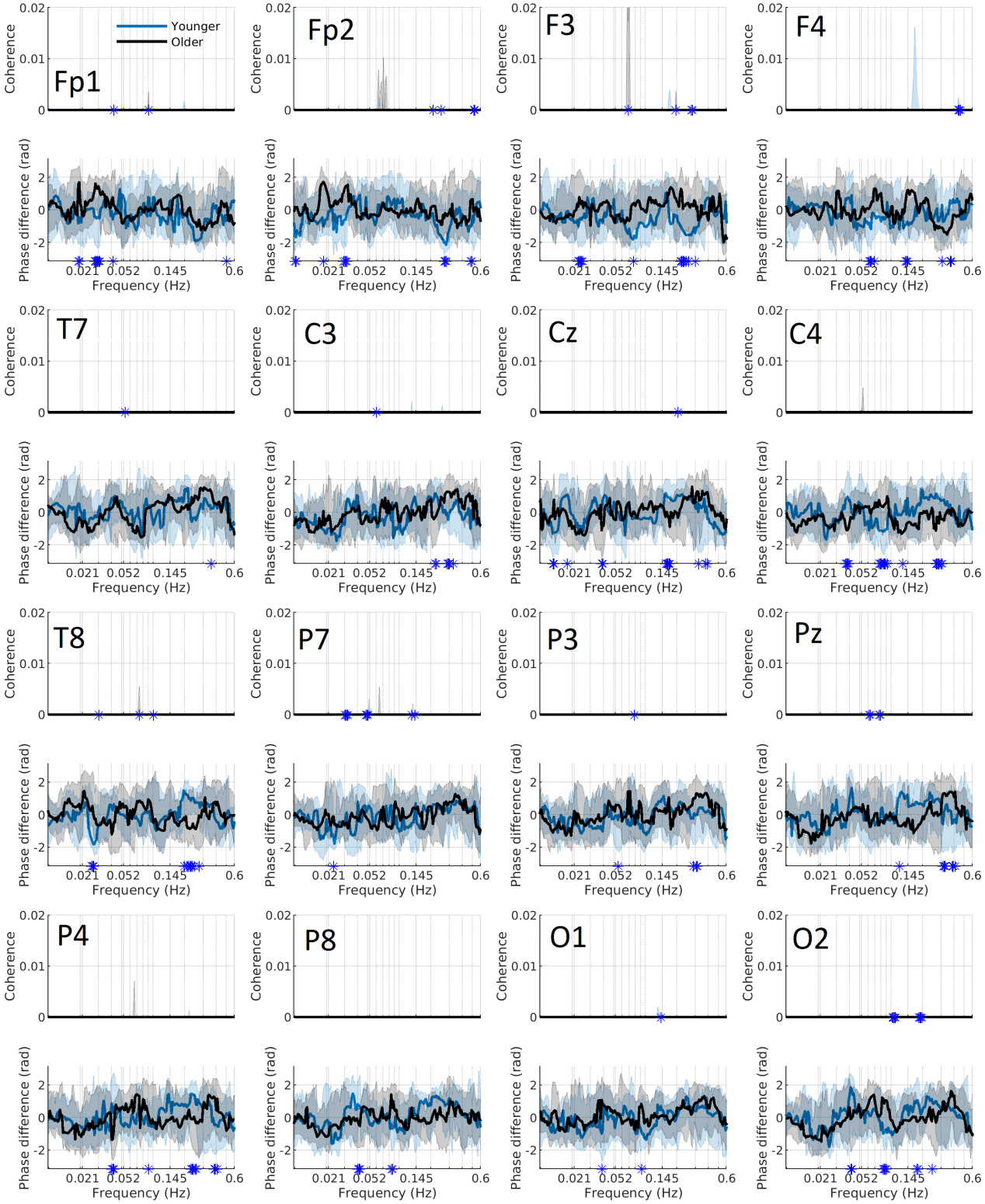

Figure 9: IRR–EEG coherence and phase difference for the 16 locations.

4 EEG results

The low frequency EEG analysis (0.007–4 Hz) were analysed using the Wavelet transform (WT) with the Morlet wavelet and f0=1 Hz. For frequencies above 4 Hz (4–48 Hz) the windowed Fourier transform (WFT) was used, with a Gaussian window and f0=1 Hz. Similarly to the WT, one can obtain a phase from the WFT which was used for the wavelet phase coherence. The preprocessing for this was as described in the manuscripts, but the filtering range was 4–48 Hz.

Across all frequency bands and electrodes, there are only 6 significant power differences. At electrode Fp1 the older group has higher myogenic and alpha power; at electrode T7 the older group has higher theta and alpha power; at electrode T8 the younger group has higher gamma power; and, lastly, at electrode P4 the younger group has higher beta power (figure 10A).

We identified the frequency within the alpha band which had the highest power for each individual, referred to as the alpha peak frequency. Previous research has shown this peak frequency to be altered in aging. At electrodes O1, O2, P7, P3, Pz, P4, P8, T8 and T7 the older group has a significantly lower peak frequency compared to the younger group (see figure 11).

The largest coherence differences are in the theta and alpha bands, where the younger group has higher coherence in the posterior leads (figure 10D). In addition there are significant differences in the beta band, where the younger group has higher coherence in EEG pairs including Cz, and the older group has higher coherence in some electrodes including electrodes T7 and T8. There are few differences in the myogenic and cardiac bands. Across most electrodes there is a dip in coherence at around 31.25 Hz. This was the sampling frequency of the fNIRS detector, and represented an artifact affecting all the signals. It stems from the fact that active electrodes can pick up small amounts of signal from powered optodes if the wires from the LEDs or detectors overlap the electrode.

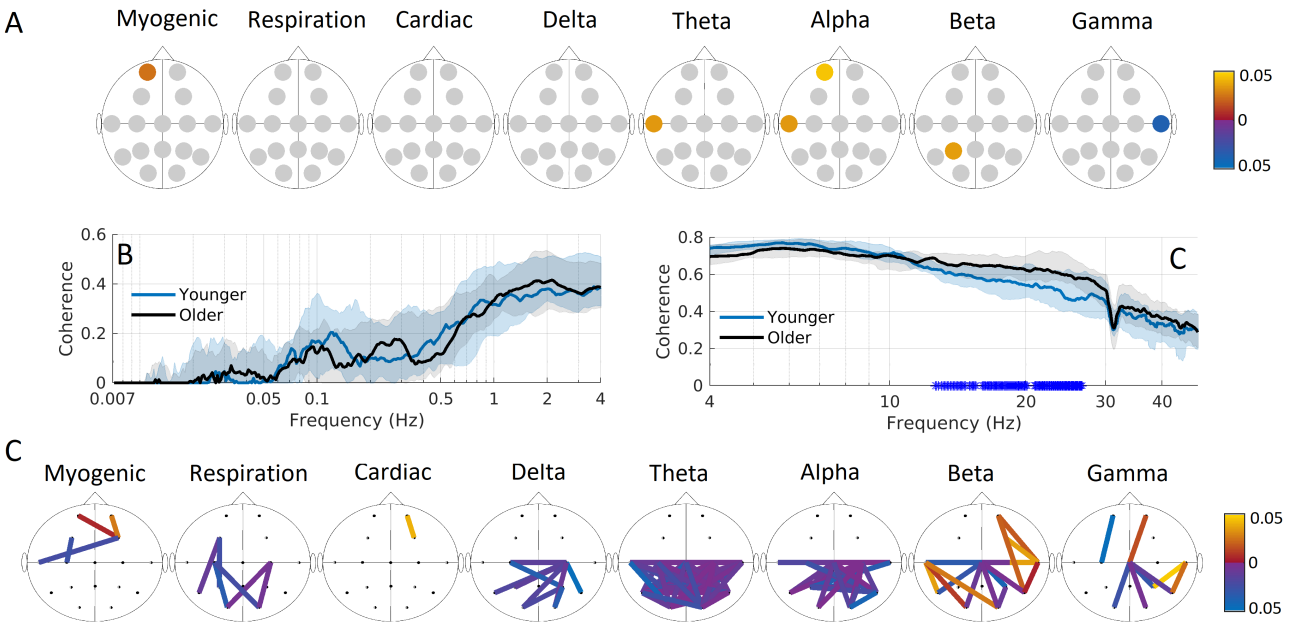

Figure 10: EEG power and coherence. A) Colour-coded p-values indicate significant group differences between the power in the frequency bands. Blue (yellow) indicates that the power is higher in the younger (older) group. Significant coherence between B) F3 and F4 and C) P7 and T7 (see figure 1 in Methods for their locations). The dashed blue and full black lines represent the median group coherence, while the shaded areas show the 25–75th percentiles. Significant differences between the groups at particular frequencies are indicated by blue stars on the x-axis. D) p-values indicating significant group differences between the coherence in the various frequency bands. Blue (yellow) indicates that the coherence is higher in the younger (older) group.

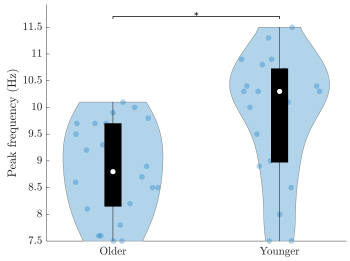

Figure 11: Violin plot showing alpha peak frequencies at electrode O1 for the older and younger groups. The star signifies a significant difference ($p < 0.05$). The white circles indicate the group medians.

4.1 Relationship to previous results

Significant differences in power between groups are observed only in four EEG electrodes (Fp1, T7, P4 and T8), with differences detected across the myogenic, theta, alpha, beta and gamma frequency bands. We observed significantly reduced phase coherence in the older group in EEG pairs involving electrode Cz, and significantly increased coherence in EEG pairs involving temporal electrodes (T7 and T8) across the same frequency bands. The few differences in power suggest that phase coherence measures, especially in the alpha, theta and beta bands, are either more sensitive to the effects of healthy aging or are a more appropriate method to detect the effects. Several earlier studies have, as here, found coherence in the alpha band to decrease with age [3, 4, 5]. A decrease in alpha power has also often been reported in aging [6], and is more apparent where there is a larger difference in mean age between the groups [7]. A recent study found that alpha power decreased with age only until around 40 years [8]. The age gap in our study was moderate, with several participants in the younger group close to 40 years old, so our finding of little change in the alpha power is not surprising. However, we did replicate the findings of reduced alpha peak frequency in the older group reported previously [9, 4], indicating that this measure is also more sensitive to aging. Decreased theta connectivity in older participants has previously been reported [5, 10], with one study detecting increased coherence in the theta band until around 40 years and then a subsequent decrease after 60 years [8]. Our present findings are in line with these earlier results.

5 Influence of site

The subjects were measured at two sites, Lancaster and Ljubljana, and there were no site effects that we can detect; hence they were grouped together. As shown in Figure 12A, in the younger group there are 9 (4M/5F) participants from Lancaster (age=24.8±4.6 years) and 12 (6M/6F) from Ljubljana (age=35.8±3.8 years), while in the older group there are 14 (5M/9F) participants from Lancaster (age=67.7±6.5 years) and 10 (4M/6F) from Ljubljana (age=61.0±5.5 years). The younger Lancaster participants tend to be younger than the Ljubljana ones (p=0.0006), while the older Lancaster participants tend to be older than the Ljubljana ones (p=0.02). The groups in Ljubljana and Lancaster were primarily collected to create control groups for different clinical studies, whence the slight difference in average ages. Furthermore, the same equipment was used in both places, and the measurements were done by the same researcher within the same year.

For example, the average heart rate (Fig. 12B,C) do not differ between the two sites; old: Lancaster 1.06±0.16 Hz, Ljubljana 1.03±0.15 Hz, p=0.6; young: Lancaster 1.11±0.15 Hz, Ljubljana 1.22±0.14 Hz, p=0.08. Comparably, the average respiration rate (Fig. 12D,E) do not differ significantly between the two sites; old: Lancaster 0.23±0.05 Hz, Ljubljana 0.23±0.10 Hz, p=0.3; young: Lancaster 0.24±0.05 Hz, Ljubljana 0.25±0.06 Hz, p=0.9. The p-values are calculated using the Wilcoxon rank-sum test.

Similarly, the BMI did not differ between the sites in either the younger ($p = 0.97$), or the older ($p = 0.23$) pairs of groups (old: Lancaster 27.5±2.6, Ljubljana 26.2±3.5, young: Lancaster 23.7±4.0, Ljubljana 23.5±3.4).

6 Influence of sex

The two groups can be divided by sex into 4 groups: a younger female group, a younger male group, an older female group and an older male group. The numbers of participants and their ages are summarised in table 1. The two younger groups were not significantly different age-wise ($p = 0.6$), and nor were the two older groups

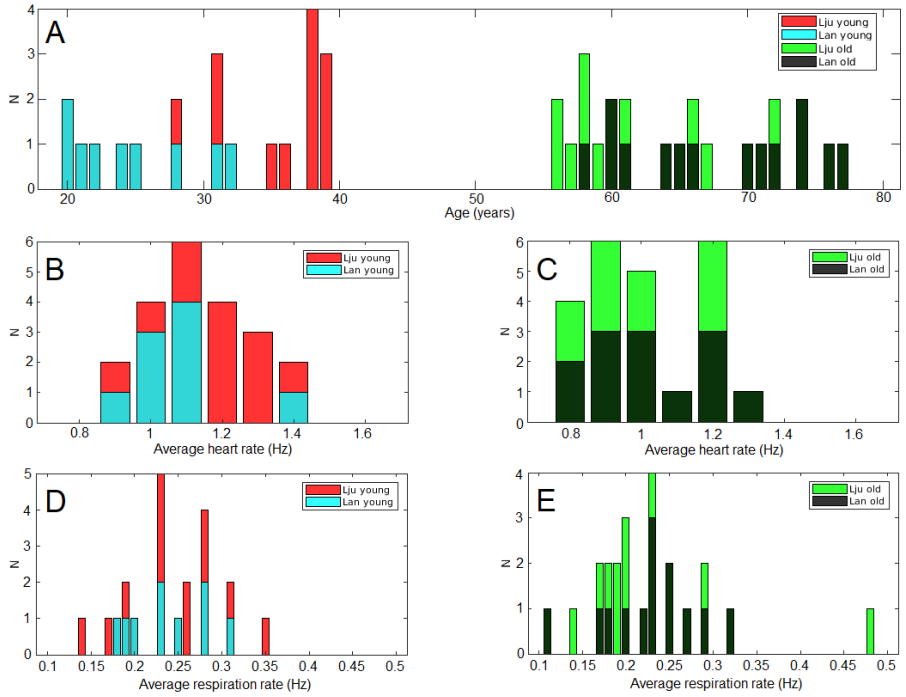

Figure 12: Histograms, divided by site for A) ages, B) average heart rate in the younger groups, C) average heart rate in the older groups, D) average respiration rate in the younger groups and E) average respiration rate in the older groups. The outlier in the older Ljubljana group in E) has a BMI of 28.4, which might explain why their respiration rate is high.

($p = 0.79$). We found that there are often differences between the groups of similar age but different sex. For example, fNIRS-EEG coherence in the myogenic band has 41/176 combinations differ between the two older groups, with the female group having higher coherence than the male group. For fNIRS myogenic power, the older male group had higher power in sensor 1 compared to the older female group. These findings suggest that age is not the only factor influencing the measured parameters, but that sex also plays a role. Future studies could explore this further.

	Younger F	Younger M	Older F	Older M
N	11	10	15	9
Age (yrs)	31.9 ± 7.1	30.2 ± 7.0	64.9 ± 6.3	65.0 ± 8.1

Table 1: Ages for the younger and older groups when divided by sex. F = female, M = male. Age is given as mean ± standard deviation. The p-values from the Wilcoxon Rank sum test between the two younger(older) groups are 0.60(0.79).

6.1 Heart rate variability

There are no differences in sd IHR between the groups of similar age but different sex. While the older male group has reduced sd IHR compared to the younger male group ($p = 0.0044$), this difference did not reach significance in the older female group compared to the younger female group ($p = 0.11$). The older female group has a larger spread of values compared to the older male group.

6.2 IHR–respiration coherence

There is little difference between the sexes in terms of instantaneous heart rate (IHR)–respiration coherence, apart from between the young groups ~ 0.03Hz where both medians were zero, and ~ 0.4Hz where the female group has higher coherence. The IHR power has some significant differences between the older female and

male groups, at low frequencies, with the male group having higher power. In the younger groups there was a tendency for the male group to have higher power ~ 0.1Hz, but this does not reach significance.

6.3 fNIRS myogenic power

- 2 sensor significantly different between the two older groups (sensor 1 and 9 - male higher power)
- 2 sensors significantly different between the two younger groups (sensor 8 and 9 - male higher power)
- 4 sensors significantly different between the two female groups (sensor 1,3,6,7 - younger higher power)
- 1 sensor significantly different between the two male groups (sensor 1 - younger higher power)

6.4 fNIRS coherence in the myogenic band

- 7 sensor combinations significantly different between the two older groups (1 to 9, 2 to 9, 5 to 9, 6 to 9, 7 to 9, 9 to 10, 9 to 11, female group higher coherence)
- 3 sensor combinations significantly different between the two younger groups (1 to 2, 1 to 3 and 2 to 3, male group higher coherence)
- 1 sensor combination significantly different between the younger and older female group (10 to 11, younger group higher coherence)
- 5 sensor combinations significantly different between the younger and older male group (5 to 1, 5 to 2, 5 to 11, 1 to 2, 1 to 10, younger group higher coherence)

6.5 fNIRS coherence in the cardiac band

- No differences between the two older groups.
- 3 sensors different between the younger groups, female group higher coherence
- 12 significant differences between younger and older female groups, older group higher coherence
- 44 sensor significantly different between the younger and older male groups, older group higher coherence

6.6 fNIRS–EEG coherence in the myogenic band

- 8 sensors significantly different between the younger and older female groups, younger group higher coherence in 3 sensors
- 52 sensors significantly different between younger and older male groups, younger group higher coherence
- No significant differences between the two younger groups.
- 41 significant differences between the two older groups, female group higher coherence

6.7 fNIRS–EEG coherence in the cardiac band

- 3 significant differences between the two older groups, female higher
- 2 significant differences between younger groups (female higher in one, male higher in one).
- 6 significant differences between male groups (T8 with various fNIRS signals, older group higher coherence)
- 36 significant differences between female groups (older group higher)

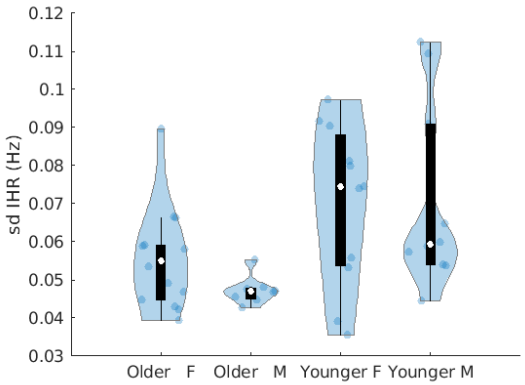

Figure 13: Violin plots showing standard deviation of IHR (sd IHR). The younger groups are not significantly different ($p = 1$), and nor are the older groups ($p = 0.16$). The male older group has reduced HRV compared to the younger male group ($p = 0.0044$); for the females, sd IHR is not significantly reduced in the older group ($p = 0.11$).

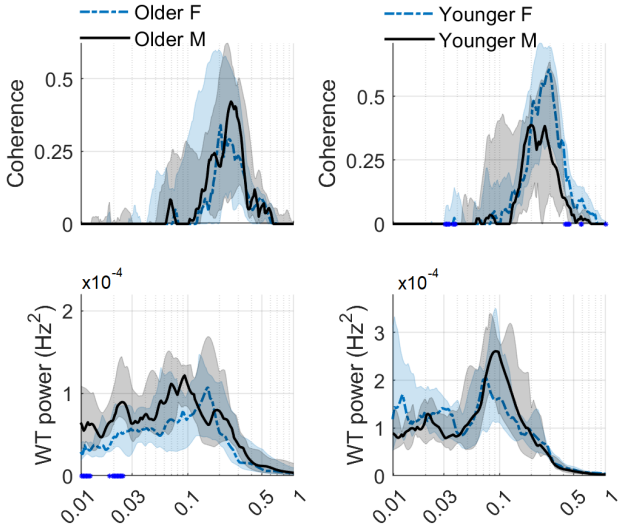

Figure 14: IHR–respiration coherence (top). Time-averaged wavelet transform power of the instantaneous heart rate (IHR) (bottom). The blue and black lines are the median group power/coherence, while the shaded areas show the 25–75th percentiles. Significant differences ($p < 0.05$) between the groups at particular frequencies are indicated by blue stars on the x-axis.

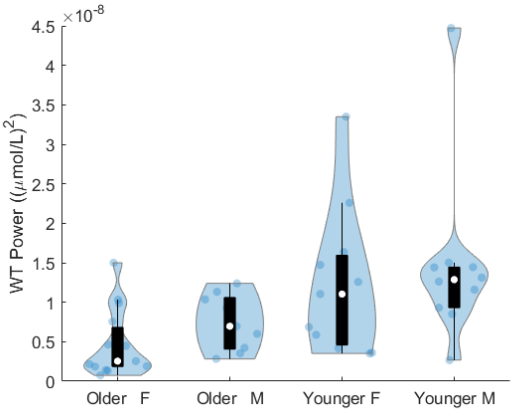

Figure 15: Violin plots showing the fNIRS myogenic power at sensor 1 for the 4 groups. The younger groups are not significantly different ($p = 0605$), but the older groups are significantly different ($p = 0.049$). Both older groups have reduced myogenic power compared to the younger group of the same sex ($p = 0.007$ for female and $p = 0.022$ for male).

7 Permutation test

For the fNIRS power and coherence, EEG power and coherence and fNIRS–EEG coherence, when the Wilcoxon Rank Sum test indicated a significant difference a permutation test was applied to test this significance. From the total of 45 participants, 21 were randomly put into one group and 24 into another. The power/coherence in the two random groups were compared with the Wilcoxon Rank Sum test. After 16587 permutations, the original p-value was compared with the randomly obtained p-values. The original p-value was considered still significant if it was smaller than 95% of the randomly found p-values. An example of this is shown in figure 16. The original p-value was smaller than 99.1% of the randomly found p-values. Another example of this is shown in figure 17. The original p-value was smaller than 99.95% of the randomly found p-values.

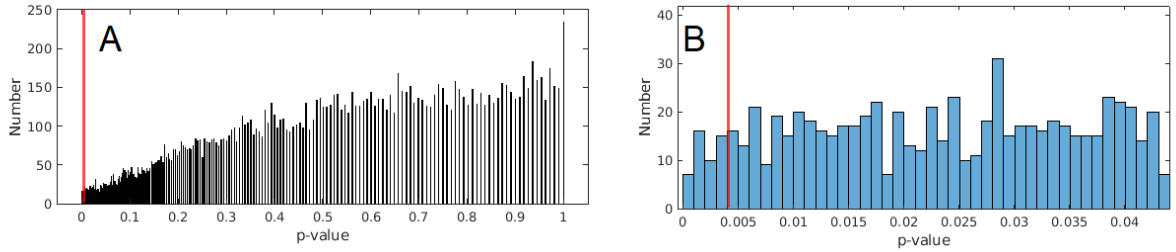

Figure 16: A) Histogram of the p-values obtained for fNIRS-EEG coherence in the cardiac band at EEG P7 and fNIRS 11. The red line is the original p-value. There are 1000 bins in the histogram. B) Zoom of A.

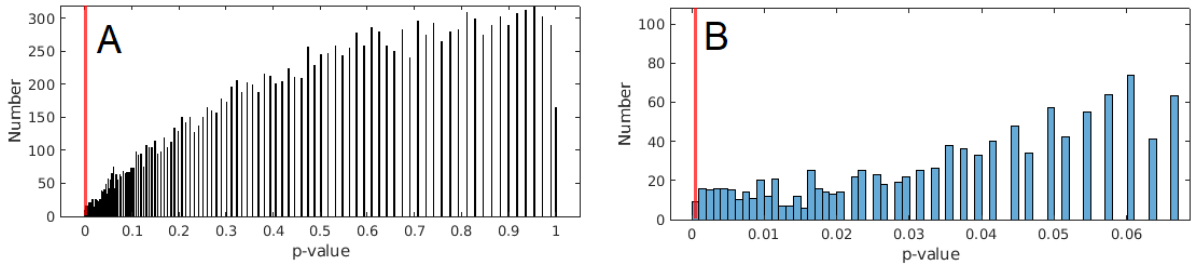

Figure 17: A) Histogram of the p-values obtained for fNIRS myogenic power at fNIRS 1. The red line is the original p-value. There are 1000 bins in the histogram. B) Zoom of A.

8 Correlations

The correlations was found from the Spearman's rank-order correlation, which is a non-parametric alternative to the Pearson linear correlation. It tests for a monotonic relationship between two variables. The p-value was found from permutation distributions.

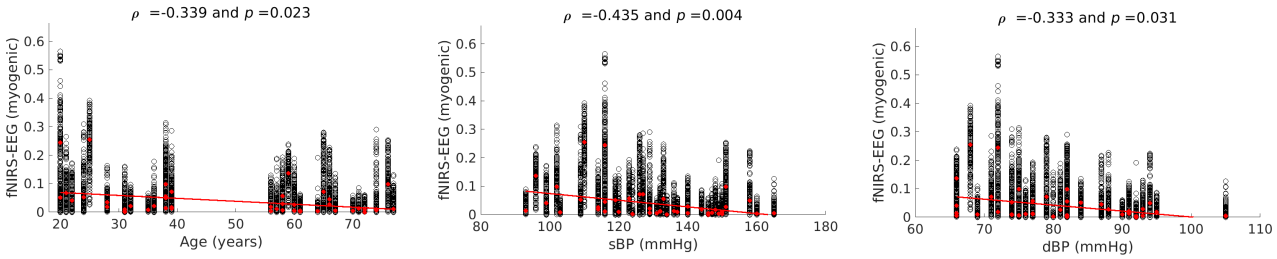

Figure 18: Correlation between fNIRS-EEG coherence in the myogenic band and age, sBP and dBP.

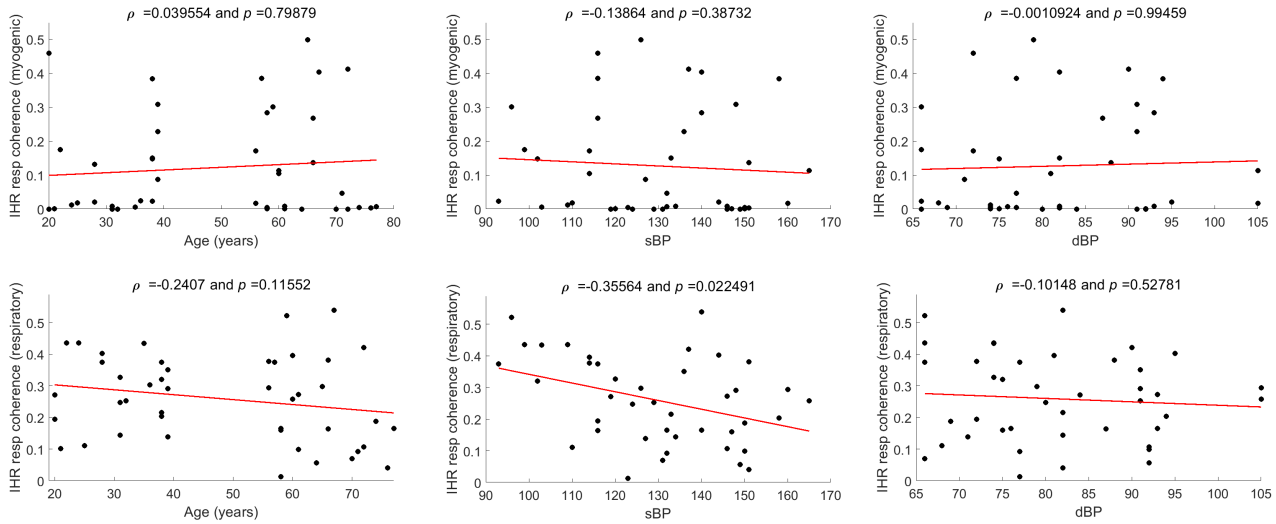

Figure 19: Correlation between IHR–respiration coherence in the myogenic band and age, sBP and dBP, and correlation between IHR–respiration coherence in the respiration band and age, sBP and dBP.

9 BMI and sBP groups

We wanted to find the differences caused by aging, but the two age groups also differed in their BMI and blood pressure. This was not unexpected as increased blood pressure and BMI are common in the older age group we investigated. It is therefore difficult to distinguish between the effect of just aging and the effect of increased blood pressure and BMI, as the variables are not independent. To investigate the effect of just aging we created two smaller groups (Younger = 13, Older = 13) that had similar BMI and blood pressure (BMI p=0.80, sBP p=0.86). Figure 20) shows the age, BMI and sBP violin plots.

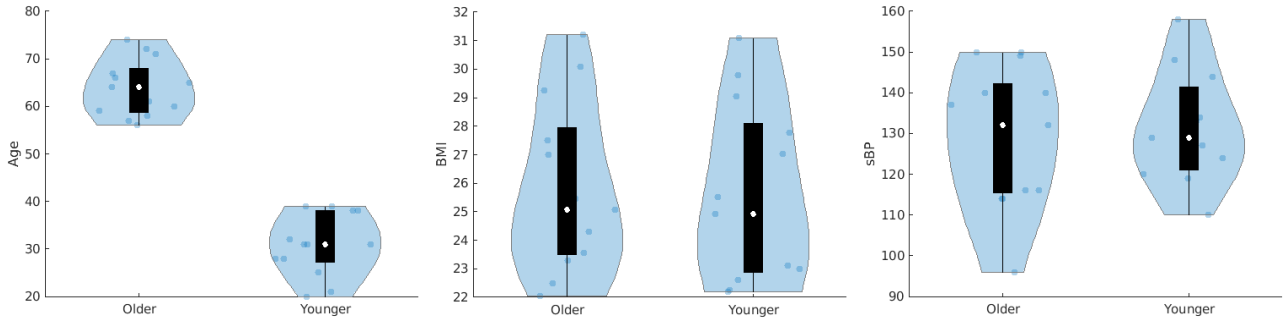

Figure 20: Violin plots showing age, BMI and sBP for the smaller younger and older groups.

9.1 fNIRS power and coherence

The power in the endothelial band was significantly different in N8, N9 and N10 between the original groups, but only in N8 and N9 when comparing the smaller groups at the 0.05 significance level. However, at the 0.1 signficance level N10 also differ between the smaller groups. Both the original groups and the smaller groups differ only at N8 in the neurogenic band power. The original groups had significantly different power in the myogenic band in 8/11 fNIRS probes, while the smaller groups only differ in 1 probes at the 0.05 significance level. Many significant differences are also lost when considering fNIRS coherence in the smaller groups, but when looking at the 0.1 significance level it is clear that the smaller groups follow similar trends to the original groups. The statistical power is naturally reduced when comparing groups of 13, which might also explain the loss of significant differences. It is of course possible that increased blood pressure and BMI contribute to the differences observed, but the current results indicate that there is an effect from aging that is independent of the BMI/BP.

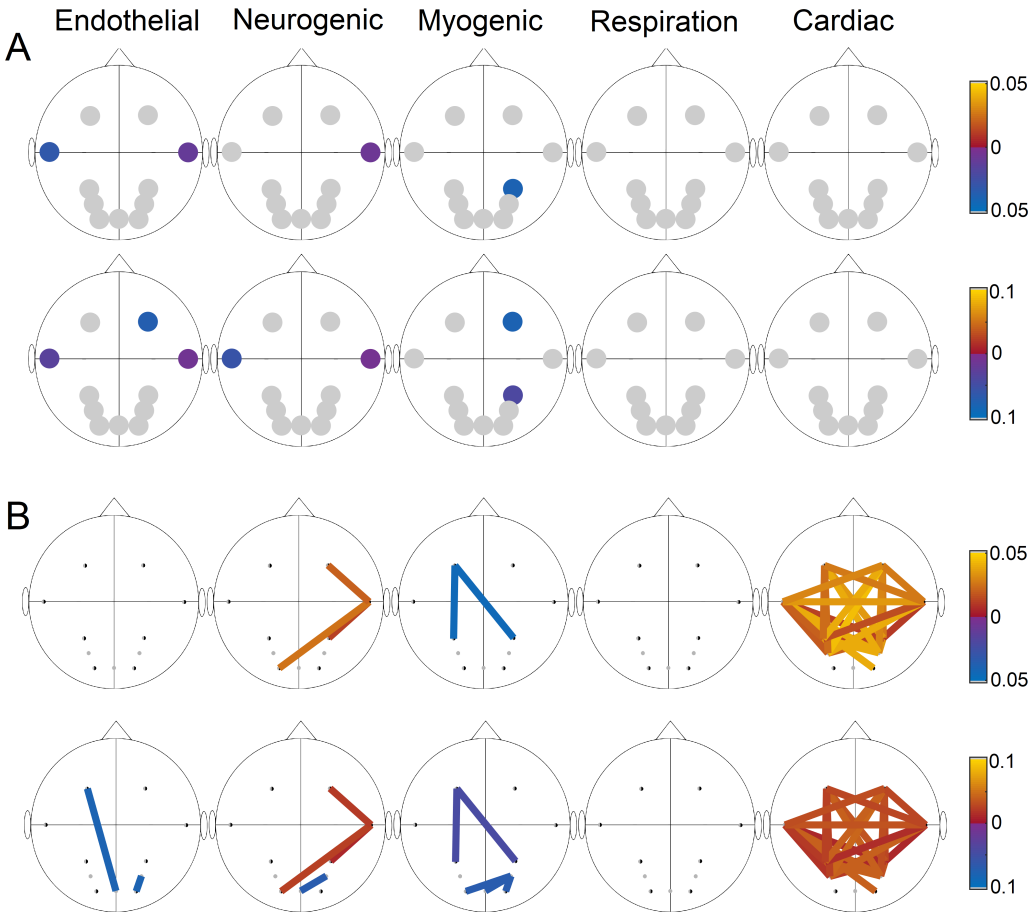

Figure 21: Significant differences between the two smaller age groups. The top rows only shows differences where the p-value is smaller than 0.05, while the bottom rows shows differences where the p-value is smaller than 0.1. A) fNIRS power, B) fNIRS coherence.

9.2 fNIRS-EEG coherence

The fNIRS–EEG myogenic coherence was significantly different in 46/176 probe combinations between the original groups, while for the cardiac coherence it was significantly different in 50/176 probe combinations. The smaller groups have significantly different myogenic coherence in 6/176 probe combinations and significantly different cardiac coherence in 23/176 probe combinations. The numbers increase when considering the 0.1 significance level. This suggests that the smaller groups follow a similar trend to the original groups, but that the smaller number reduces the statistical power. The results indicate that there is an effect on the coherence that is independent to the BMI and blood pressure differences between the original groups.

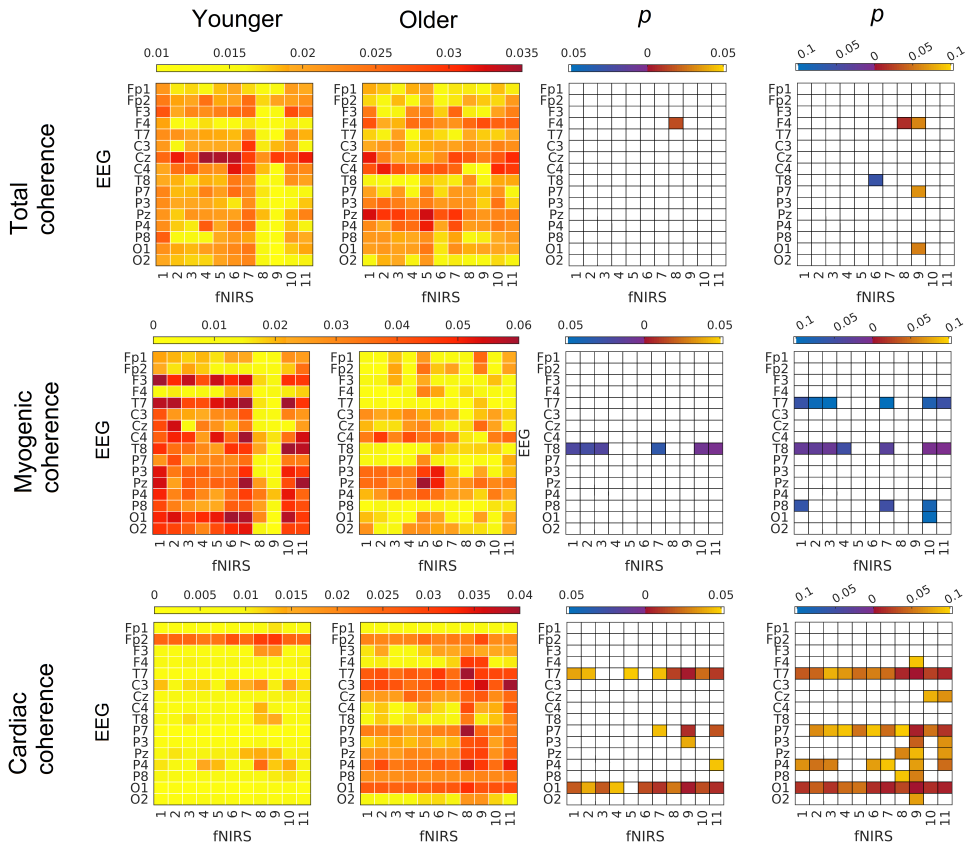

Figure 22: Group median fNIRS–EEG coherence for the younger group (left) and older group (middle); and p-values indicating a significant difference between the groups (right), either at a level of 0.05 or 0.1. Blue (yellow) values indicate that coherence is higher in the younger (older) group. The top row shows the total coherence averaged over the whole frequency band (0.021–1.7 Hz), the middle row shows the myogenic frequency band and the bottom row shows the cardiac frequency band.

10 oxyHb fNIRS–EEG coherence

We show phase coherence for all EEG fNIRS combinations. The sensor layout is shown in figure 1. There are in total $16 \times 11 = 176$ combinations, as there are 16 EEG electrodes and 11 fNIRS sensors. The method for obtaining the wavelet phase coherence, introduced by Bandrivskyy et al. (2004)[11], is described in detail in the main paper.

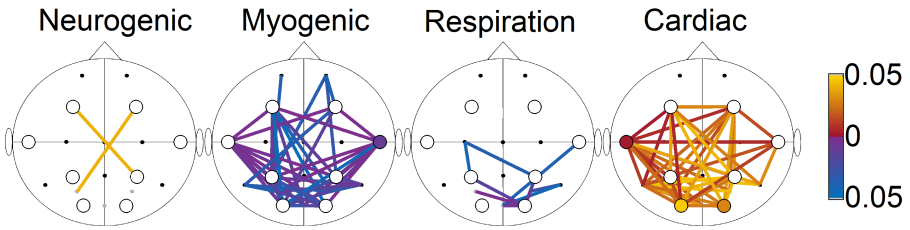

Figure 23: The coloured lines represent the significant p-values for the group differences in coherence in the frequency bands, while the circle is for co-located fNIRS and EEG probes. Blue (yellow) indicates that the coherence is higher in the younger (older) group.

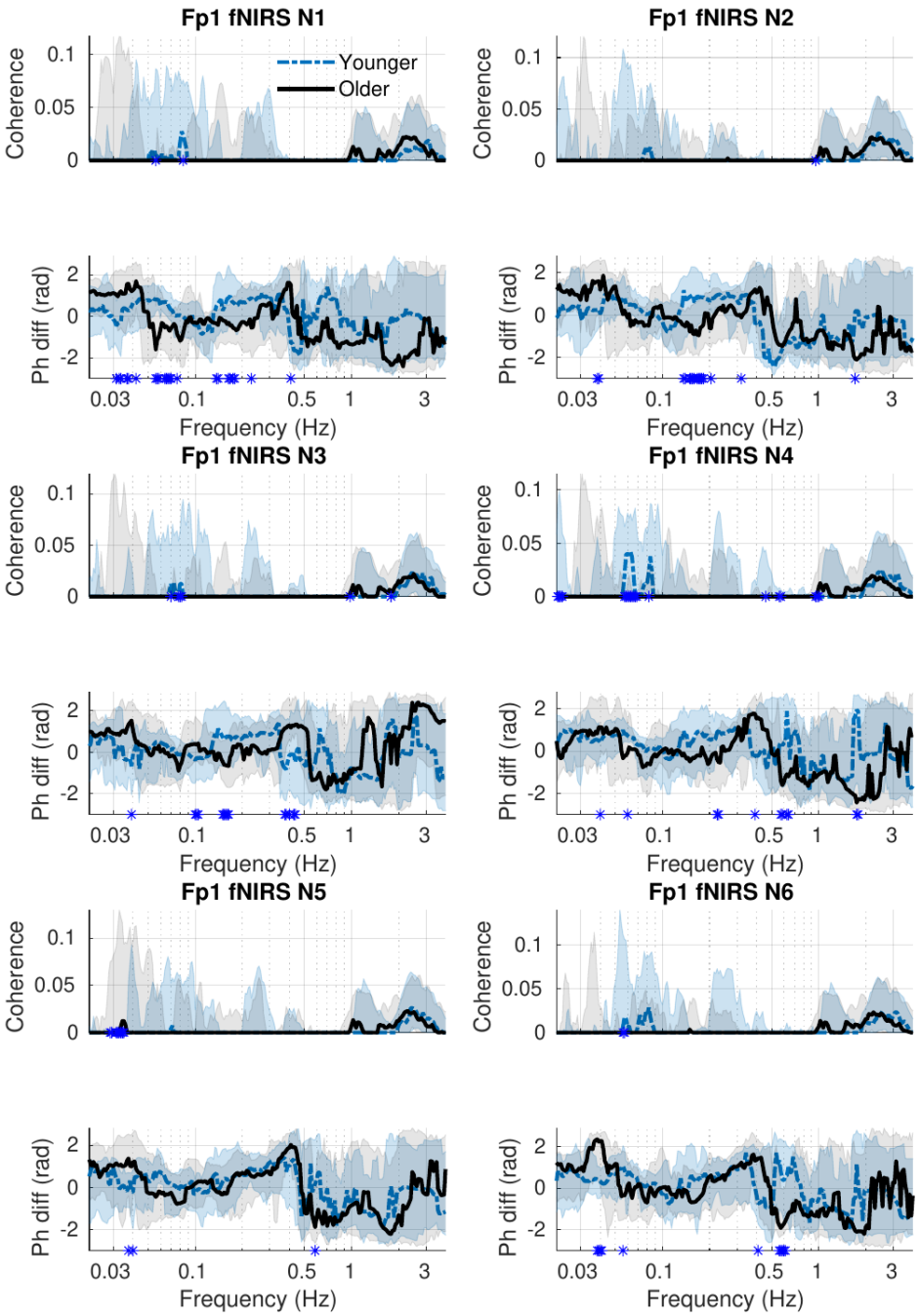

Figure 24: fNIRS–EEG coherence and phase difference for electrode Fp1 and 6 fNIRS sensors. The dashed blue and full black lines represent the median group coherence, while the shaded areas show the 25–75th percentiles. Significant differences between the groups at particular frequencies are indicated by blue stars on the x-axis. A negative phase difference means that fNIRS is the leading signal.

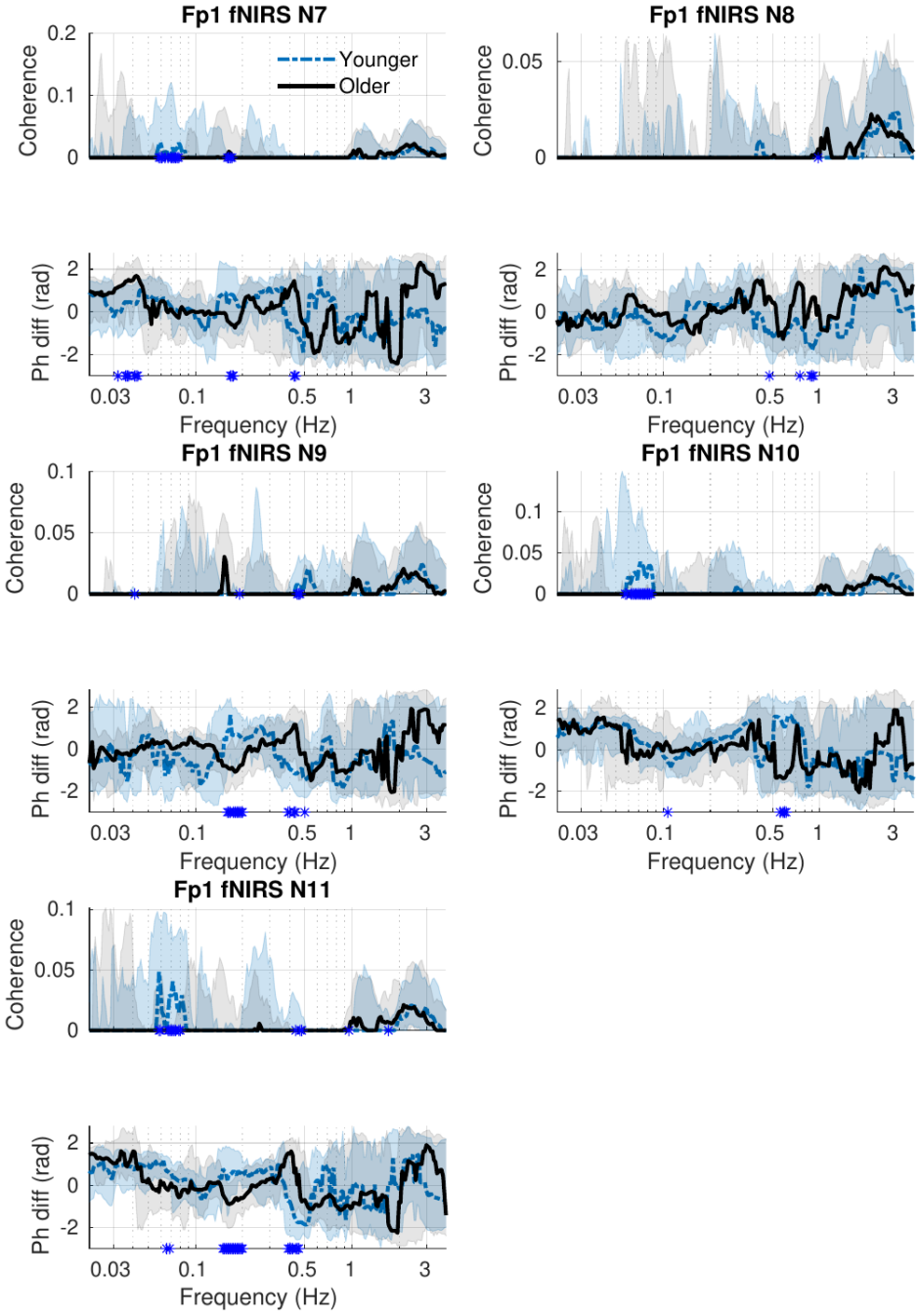

Figure 25: fNIRS–EEG coherence and phase difference for electrode Fp1 and 5 fNIRS sensors. The dashed blue and full black lines represent the median group coherence, while the shaded areas show the 25–75th percentiles. Significant differences between the groups at particular frequencies are indicated by blue stars on the x-axis. A negative phase difference means that fNIRS is the leading signal.

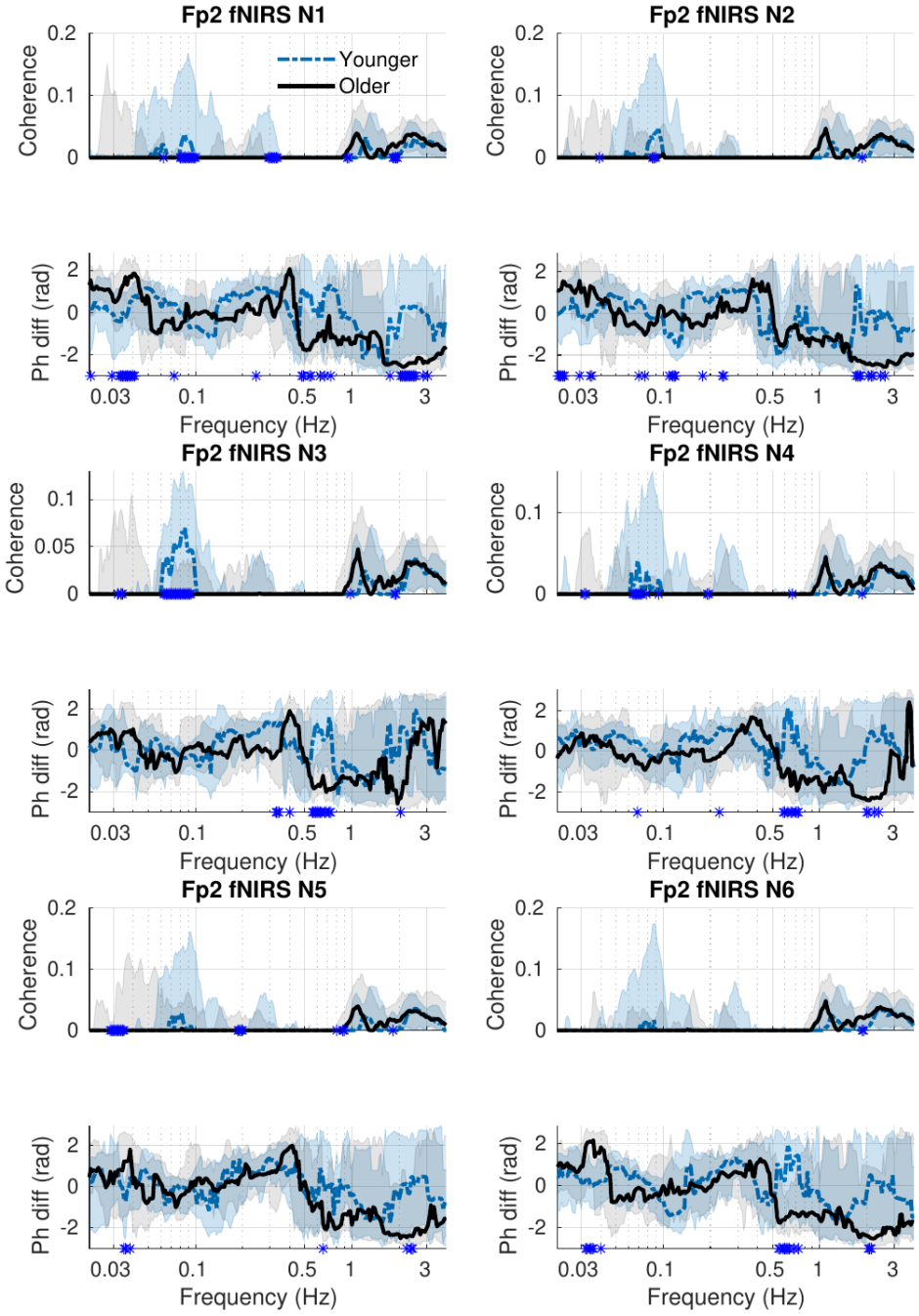

Figure 26: fNIRS–EEG coherence and phase difference for electrode Fp2 and 6 fNIRS sensors. The dashed blue and full black lines represent the median group coherence, while the shaded areas show the 25–75th percentiles. Significant differences between the groups at particular frequencies are indicated by blue stars on the x-axis. A negative phase difference means that fNIRS is the leading signal.

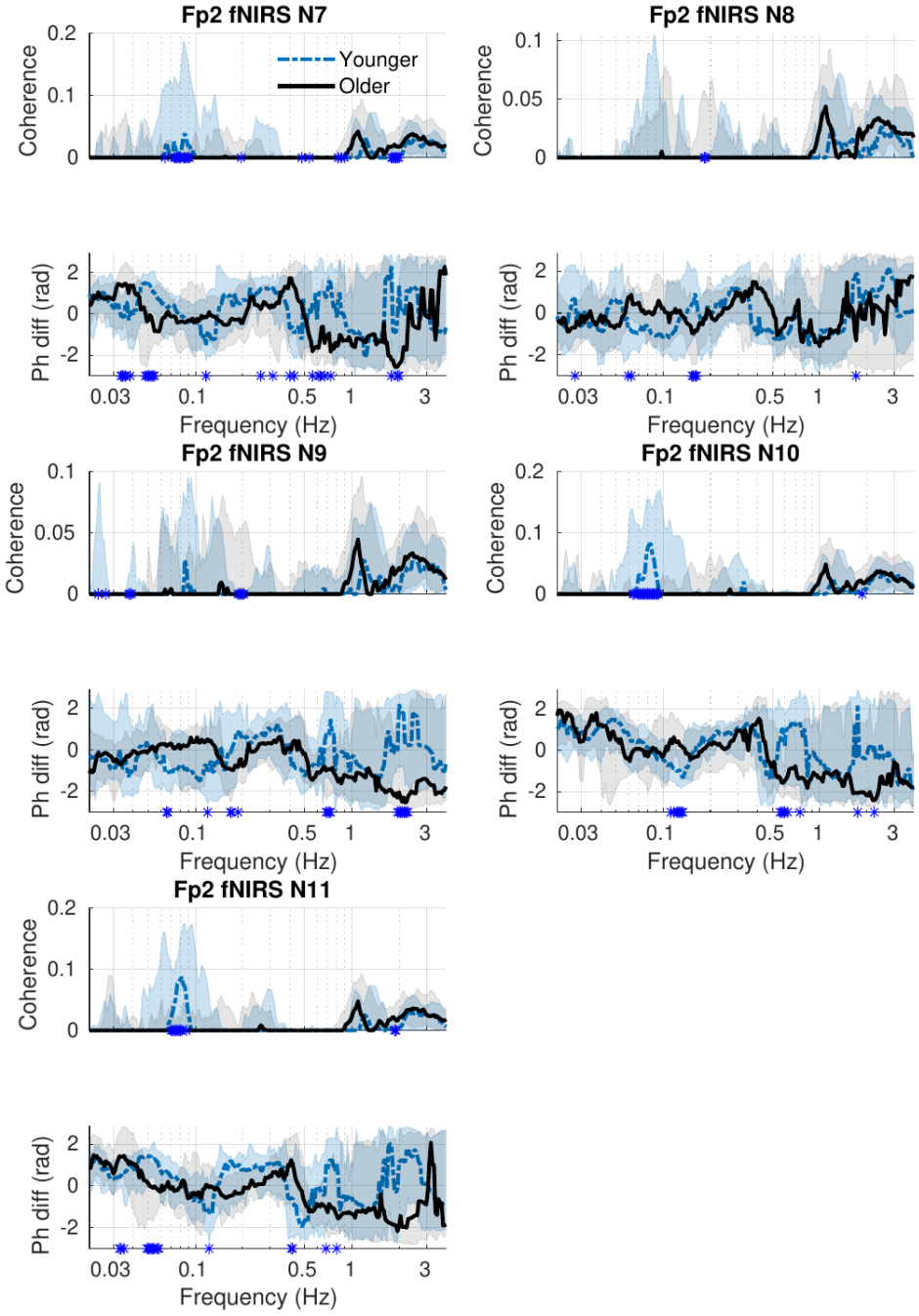

Figure 27: fNIRS–EEG coherence and phase difference for electrode Fp2 and 5 fNIRS sensors. The dashed blue and full black lines represent the median group coherence, while the shaded areas show the 25–75th percentiles. Significant differences between the groups at particular frequencies are indicated by blue stars on the x-axis. A negative phase difference means that fNIRS is the leading signal.

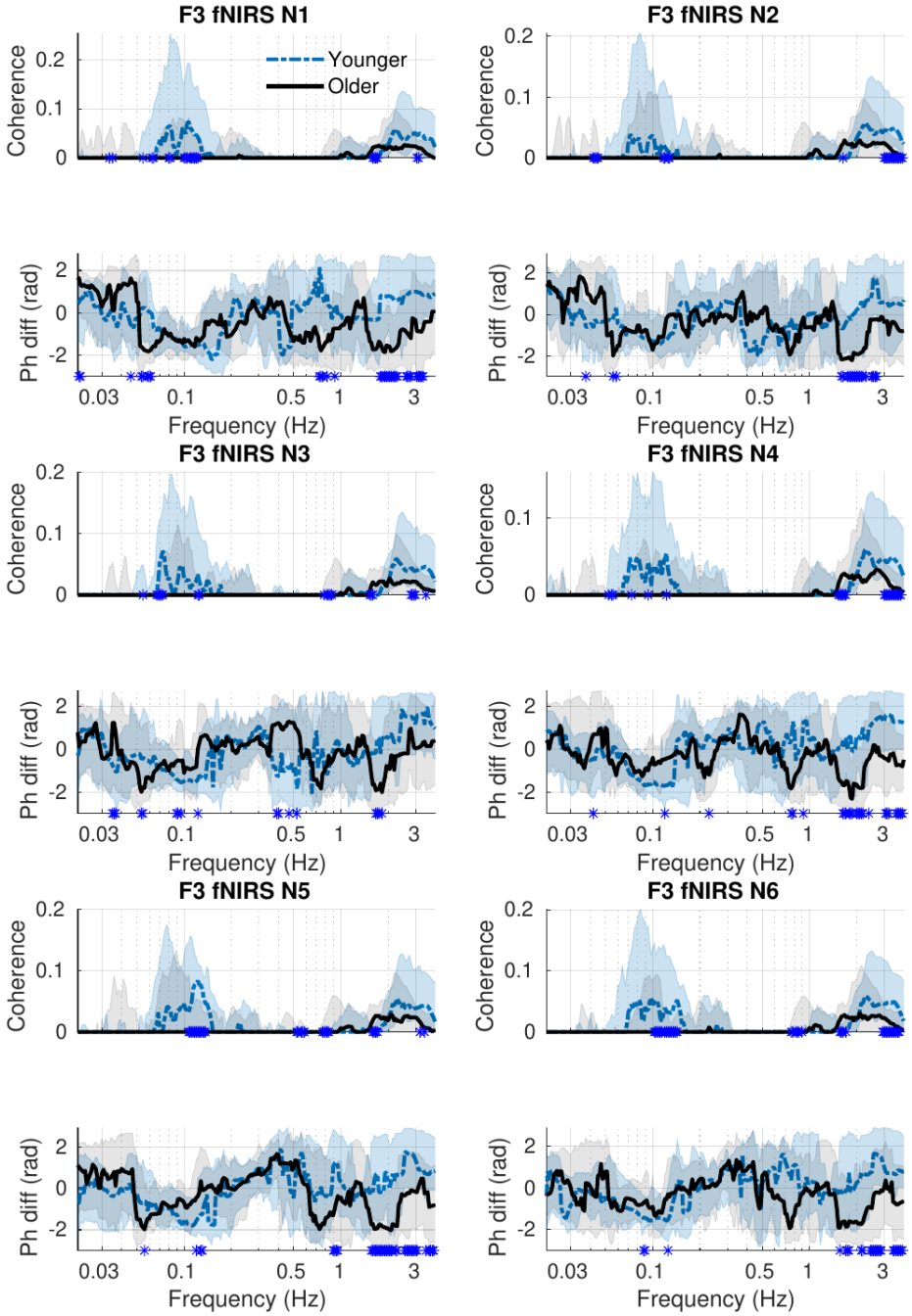

Figure 28: fNIRS–EEG coherence and phase difference for electrode F3 and 6 fNIRS sensors. The dashed blue and full black lines represent the median group coherence, while the shaded areas show the 25–75th percentiles. Significant differences between the groups at particular frequencies are indicated by blue stars on the x-axis. A negative phase difference means that fNIRS is the leading signal.

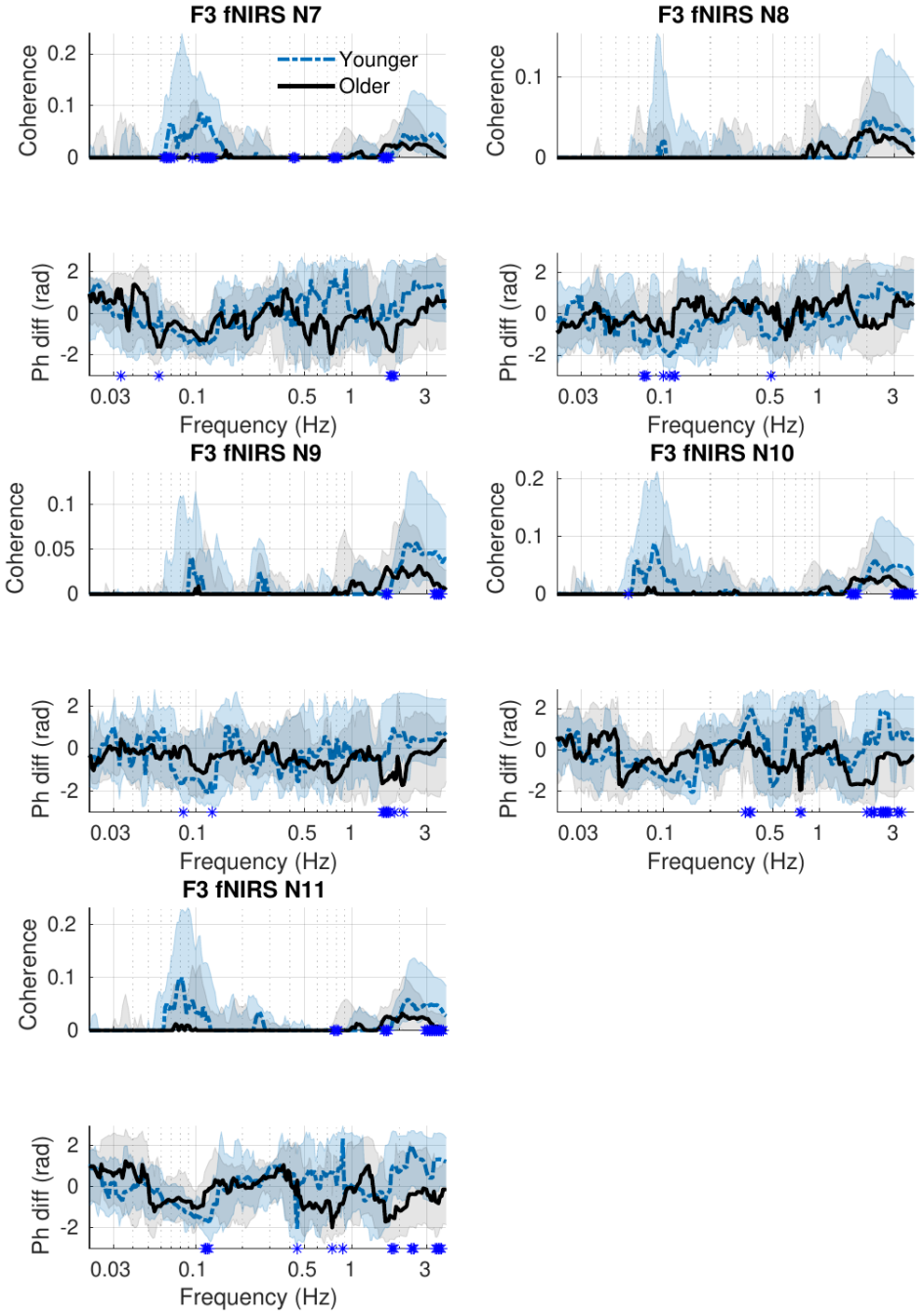

Figure 29: fNIRS–EEG coherence and phase difference for electrode F3 and 5 fNIRS sensors. The dashed blue and full black lines represent the median group coherence, while the shaded areas show the 25–75th percentiles. Significant differences between the groups at particular frequencies are indicated by blue stars on the x-axis. A negative phase difference means that fNIRS is the leading signal.

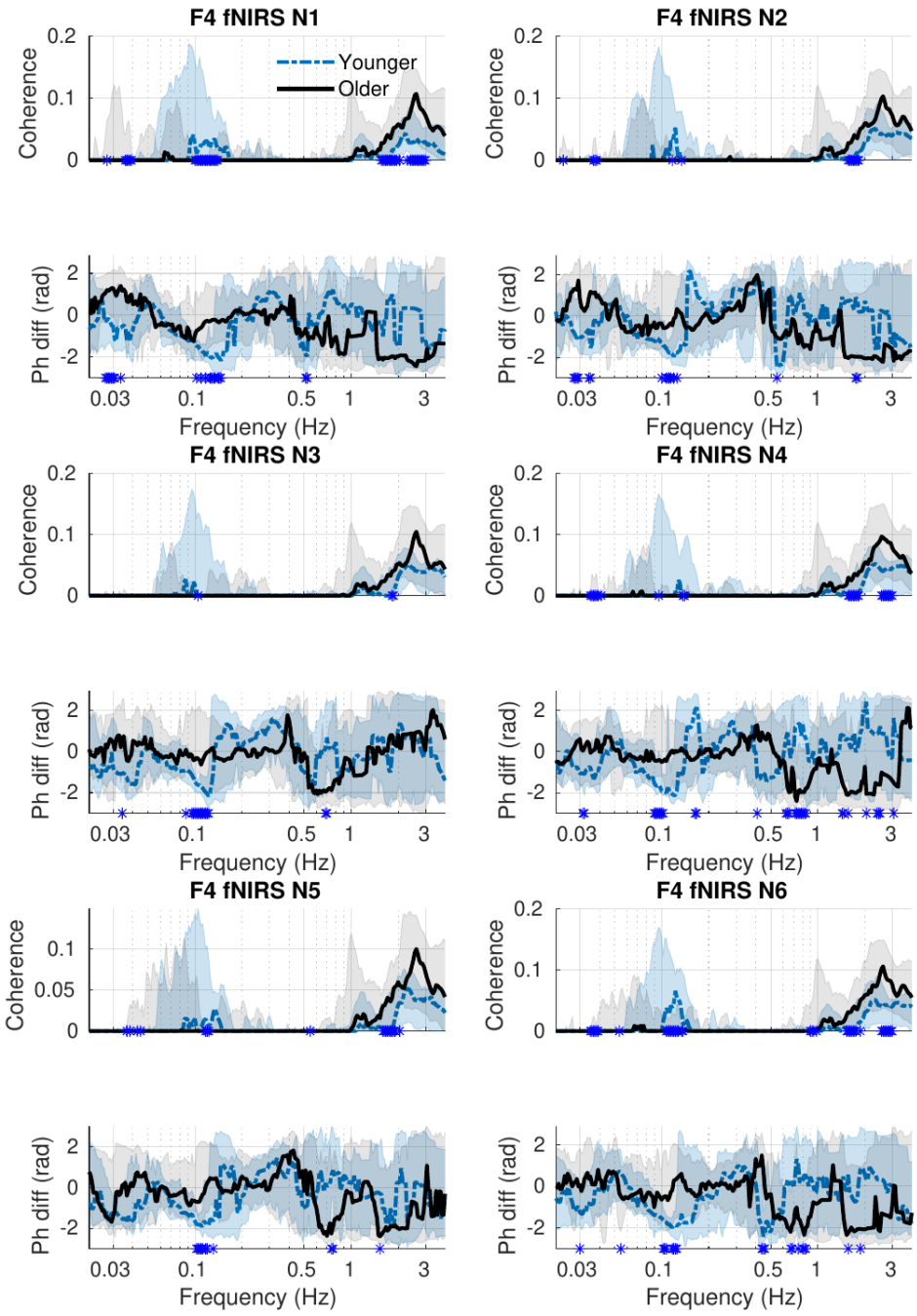

Figure 30: fNIRS–EEG coherence and phase difference for electrode F4 and 6 fNIRS sensors. The dashed blue and full black lines represent the median group coherence, while the shaded areas show the 25–75th percentiles. Significant differences between the groups at particular frequencies are indicated by blue stars on the x-axis. A negative phase difference means that fNIRS is the leading signal.

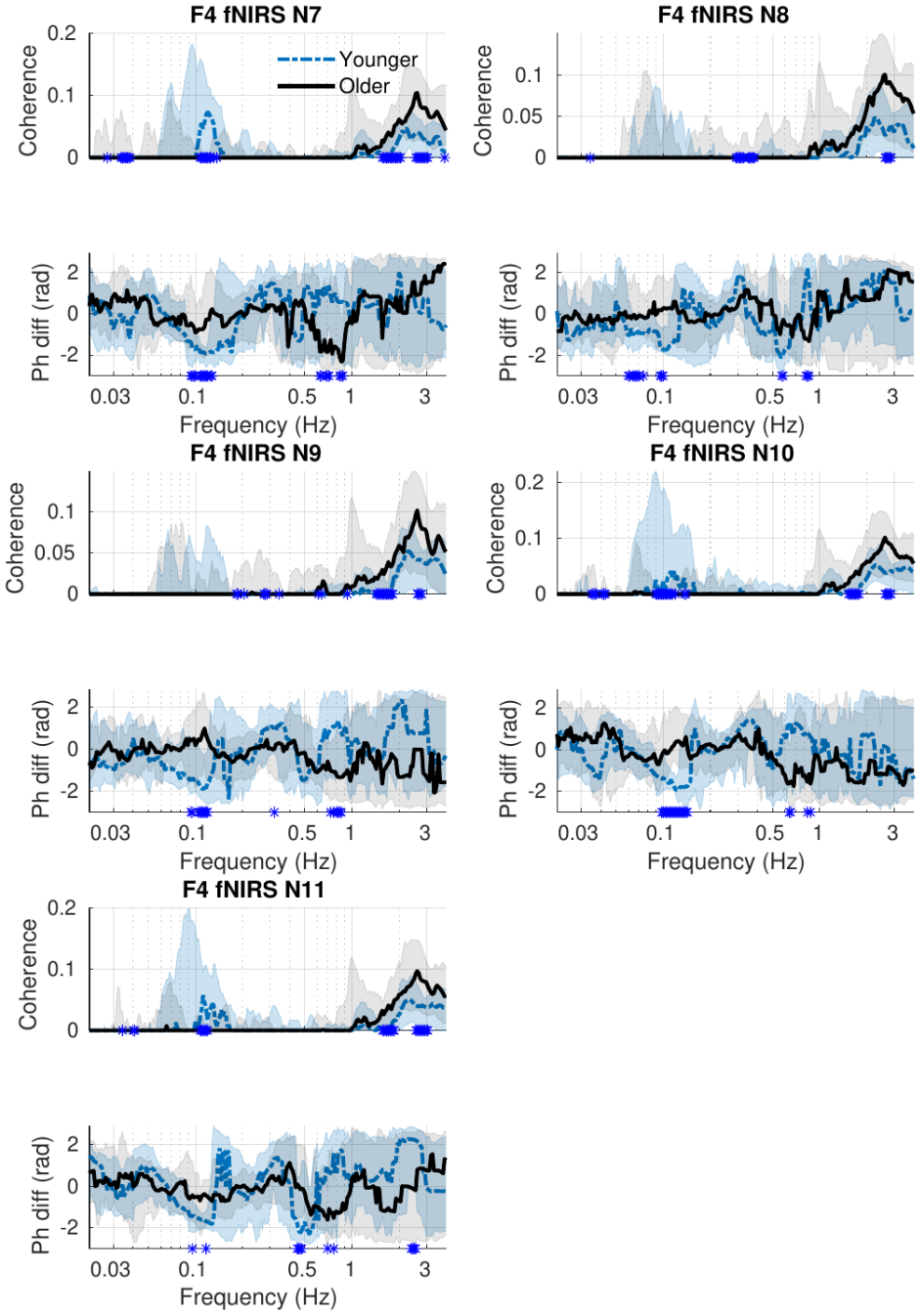

Figure 31: fNIRS–EEG coherence and phase difference for electrode F4 and 5 fNIRS sensors. The dashed blue and full black lines represent the median group coherence, while the shaded areas show the 25–75th percentiles. Significant differences between the groups at particular frequencies are indicated by blue stars on the x-axis. A negative phase difference means that fNIRS is the leading signal.

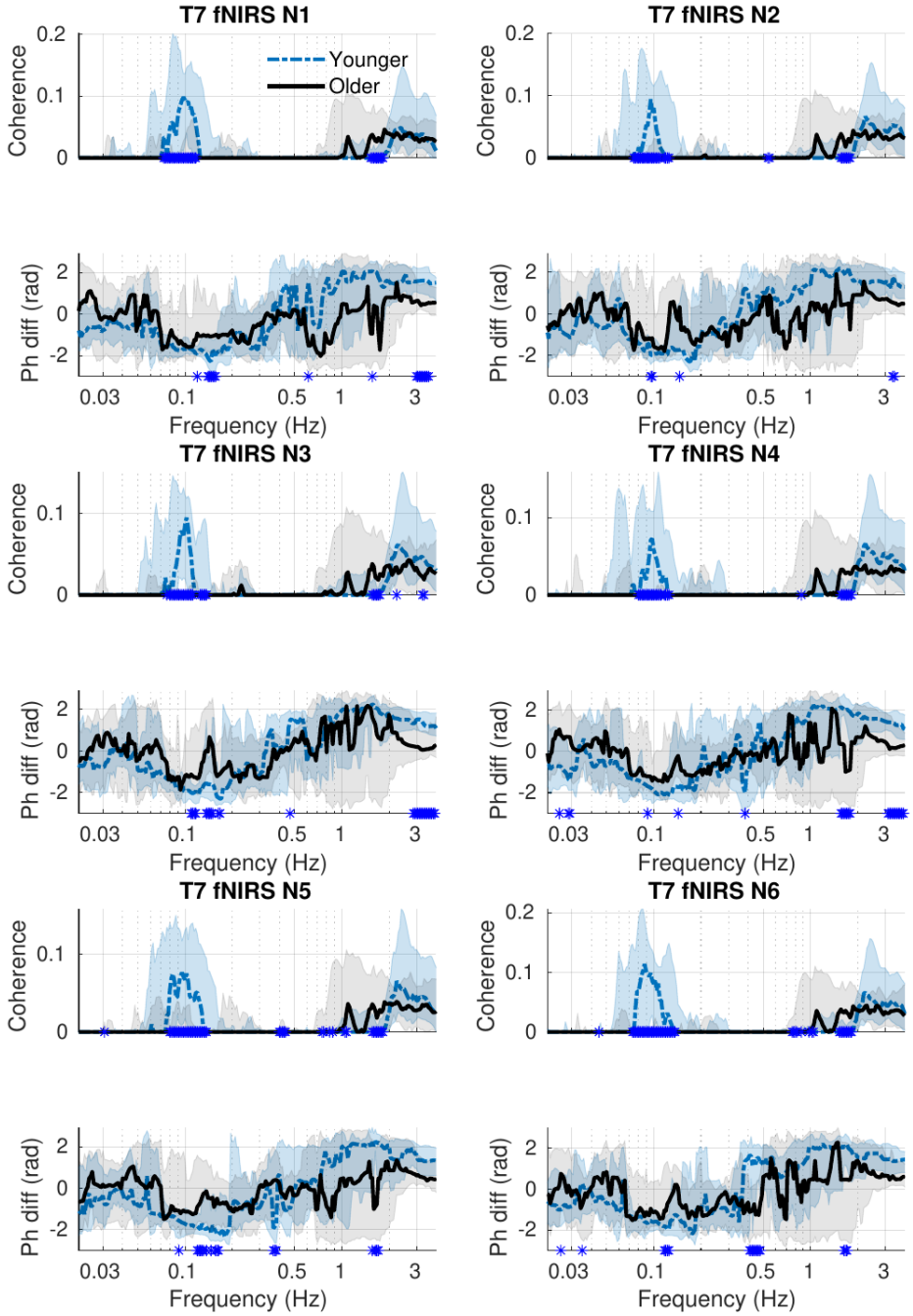

Figure 32: fNIRS–EEG coherence and phase difference for electrode T7 and 6 fNIRS sensors. The dashed blue and full black lines represent the median group coherence, while the shaded areas show the 25–75th percentiles. Significant differences between the groups at particular frequencies are indicated by blue stars on the x-axis. A negative phase difference means that fNIRS is the leading signal.

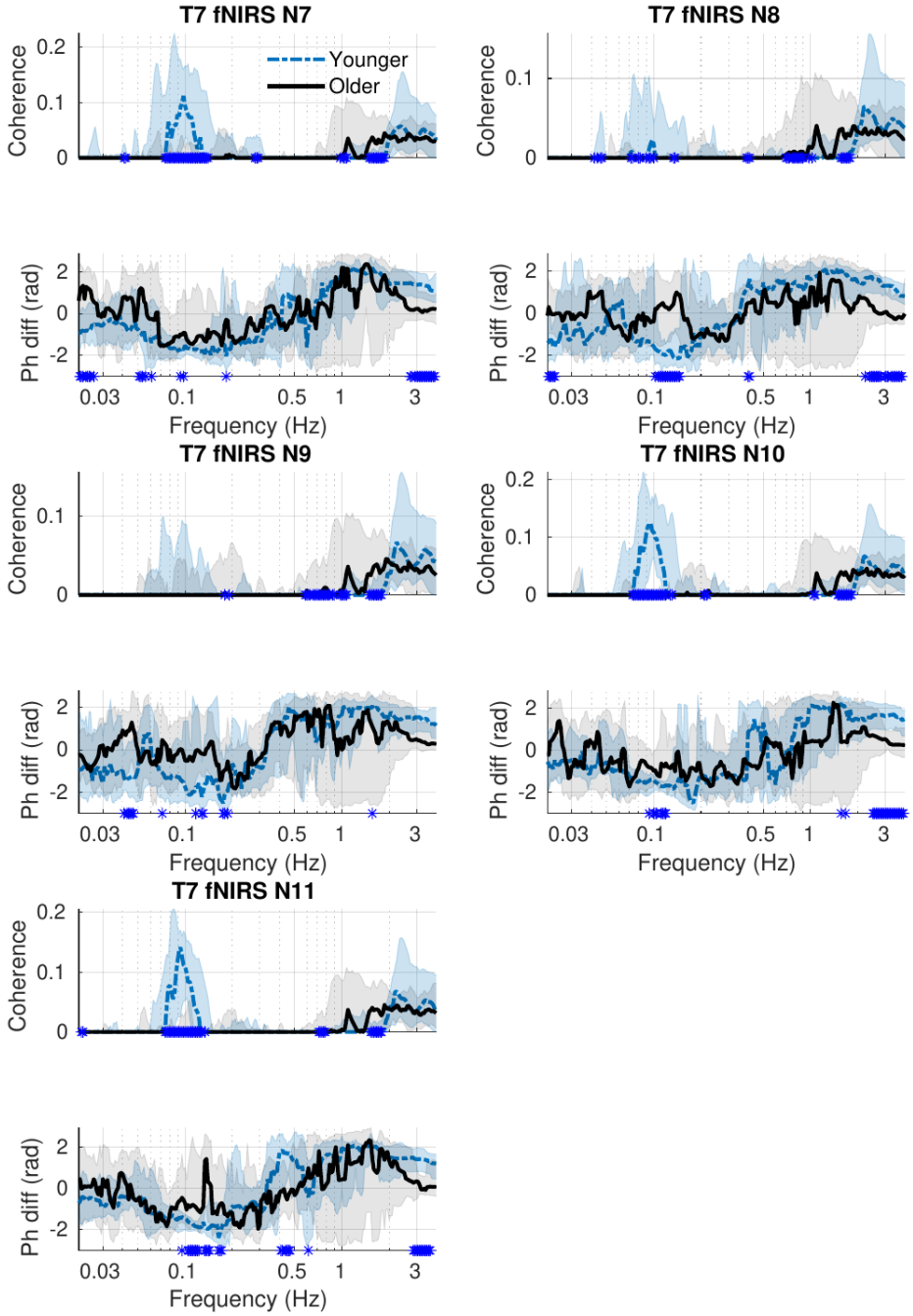

Figure 33: fNIRS–EEG coherence and phase difference for electrode T7 and 5 fNIRS sensors. The dashed blue and full black lines represent the median group coherence, while the shaded areas show the 25–75th percentiles. Significant differences between the groups at particular frequencies are indicated by blue stars on the x-axis. A negative phase difference means that fNIRS is the leading signal.

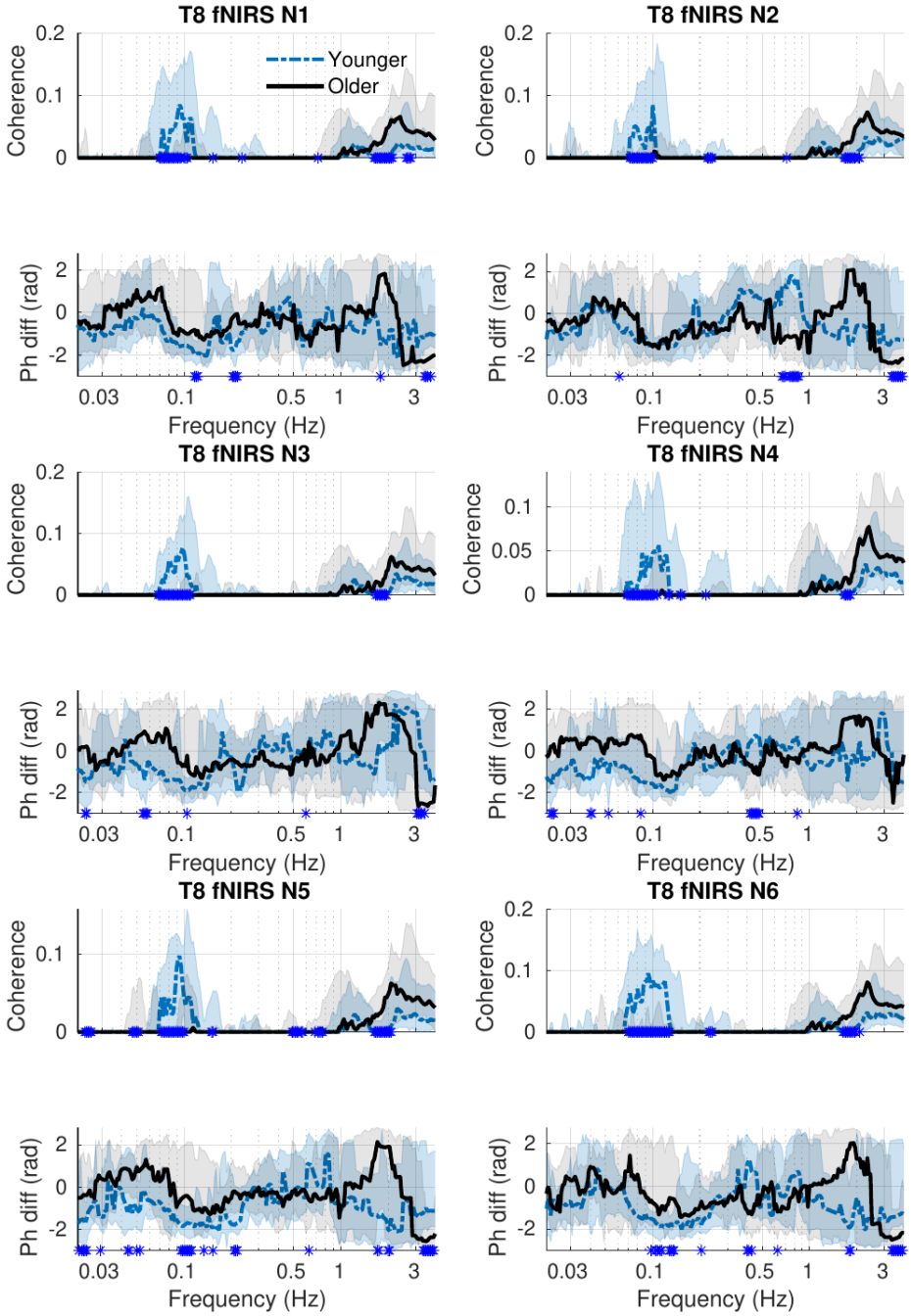

Figure 34: fNIRS–EEG coherence and phase difference for electrode T8 and 6 fNIRS sensors. The dashed blue and full black lines represent the median group coherence, while the shaded areas show the 25–75th percentiles. Significant differences between the groups at particular frequencies are indicated by blue stars on the x-axis. A negative phase difference means that fNIRS is the leading signal.

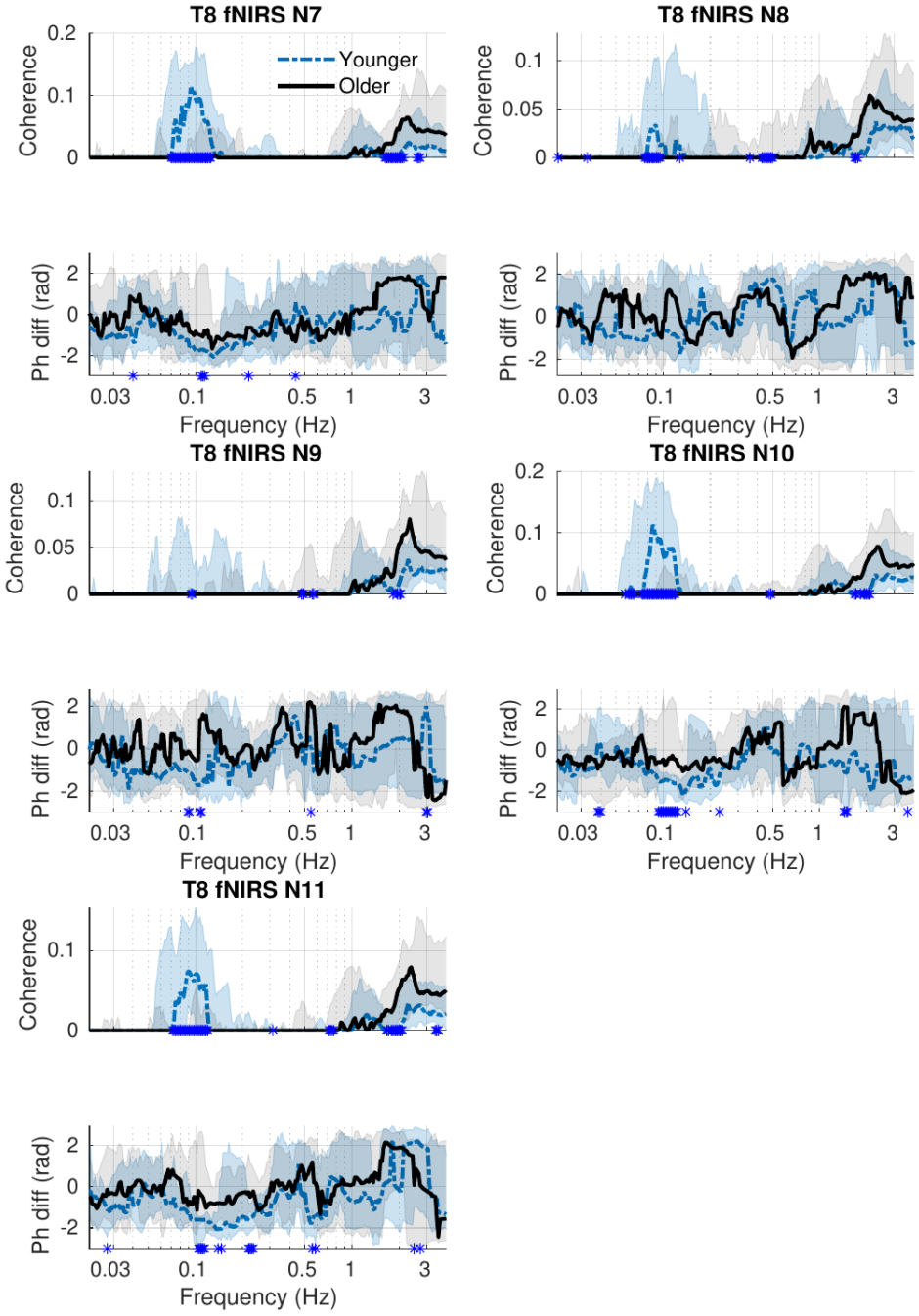

Figure 35: fNIRS–EEG coherence and phase difference for electrode T8 and 5 fNIRS sensors. The dashed blue and full black lines represent the median group coherence, while the shaded areas show the 25–75th percentiles. Significant differences between the groups at particular frequencies are indicated by blue stars on the x-axis. A negative phase difference means that fNIRS is the leading signal.

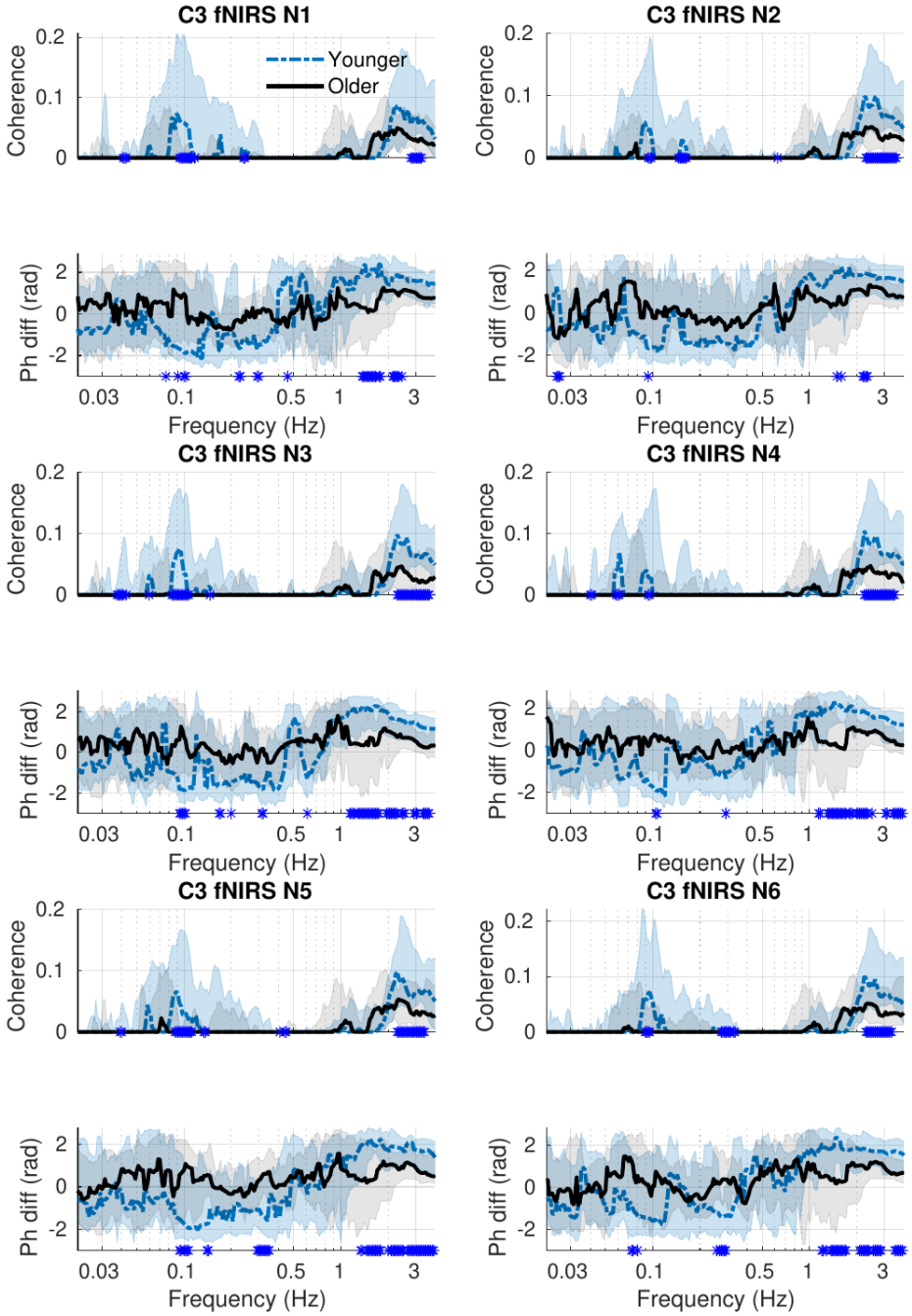

Figure 36: fNIRS–EEG coherence and phase difference for electrode C3 and 6 fNIRS sensors. The dashed blue and full black lines represent the median group coherence, while the shaded areas show the 25–75th percentiles. Significant differences between the groups at particular frequencies are indicated by blue stars on the x-axis. A negative phase difference means that fNIRS is the leading signal.

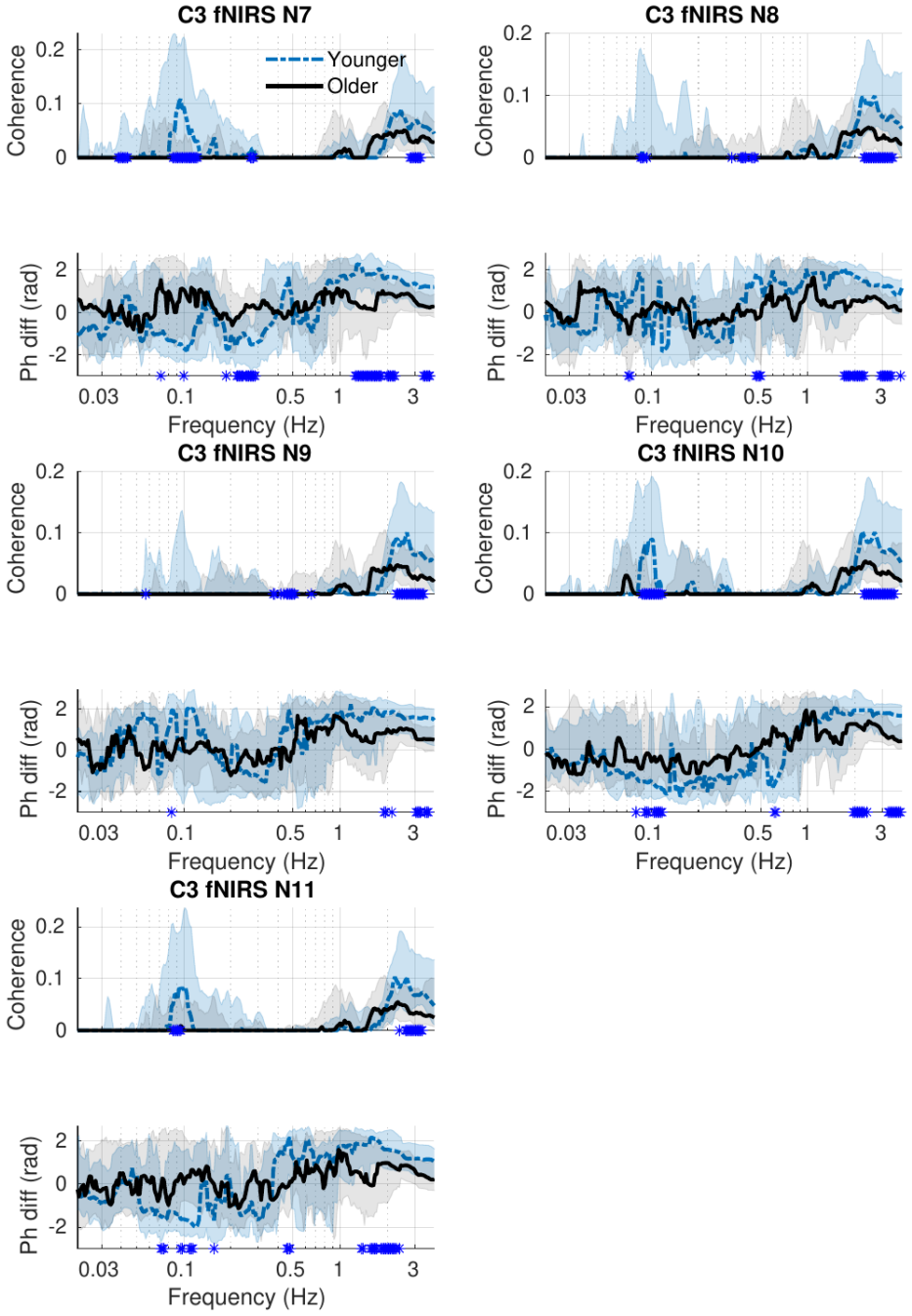

Figure 37: fNIRS–EEG coherence and phase difference for electrode C3 and 5 fNIRS sensors. The dashed blue and full black lines represent the median group coherence, while the shaded areas show the 25–75th percentiles. Significant differences between the groups at particular frequencies are indicated by blue stars on the x-axis. A negative phase difference means that fNIRS is the leading signal.

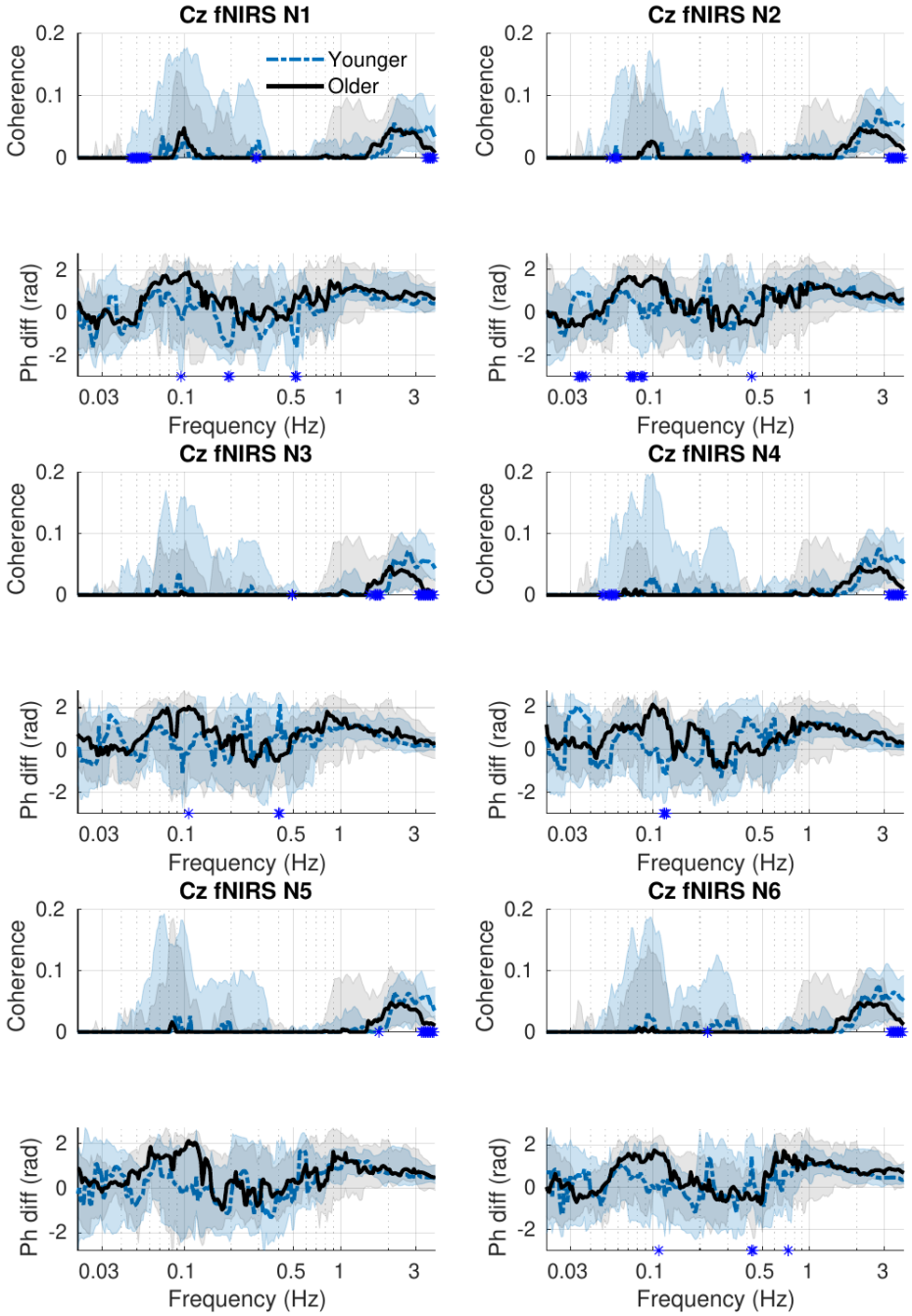

Figure 38: fNIRS–EEG coherence and phase difference for electrode Cz and 6 fNIRS sensors. The dashed blue and full black lines represent the median group coherence, while the shaded areas show the 25–75th percentiles. Significant differences between the groups at particular frequencies are indicated by blue stars on the x-axis. A negative phase difference means that fNIRS is the leading signal.

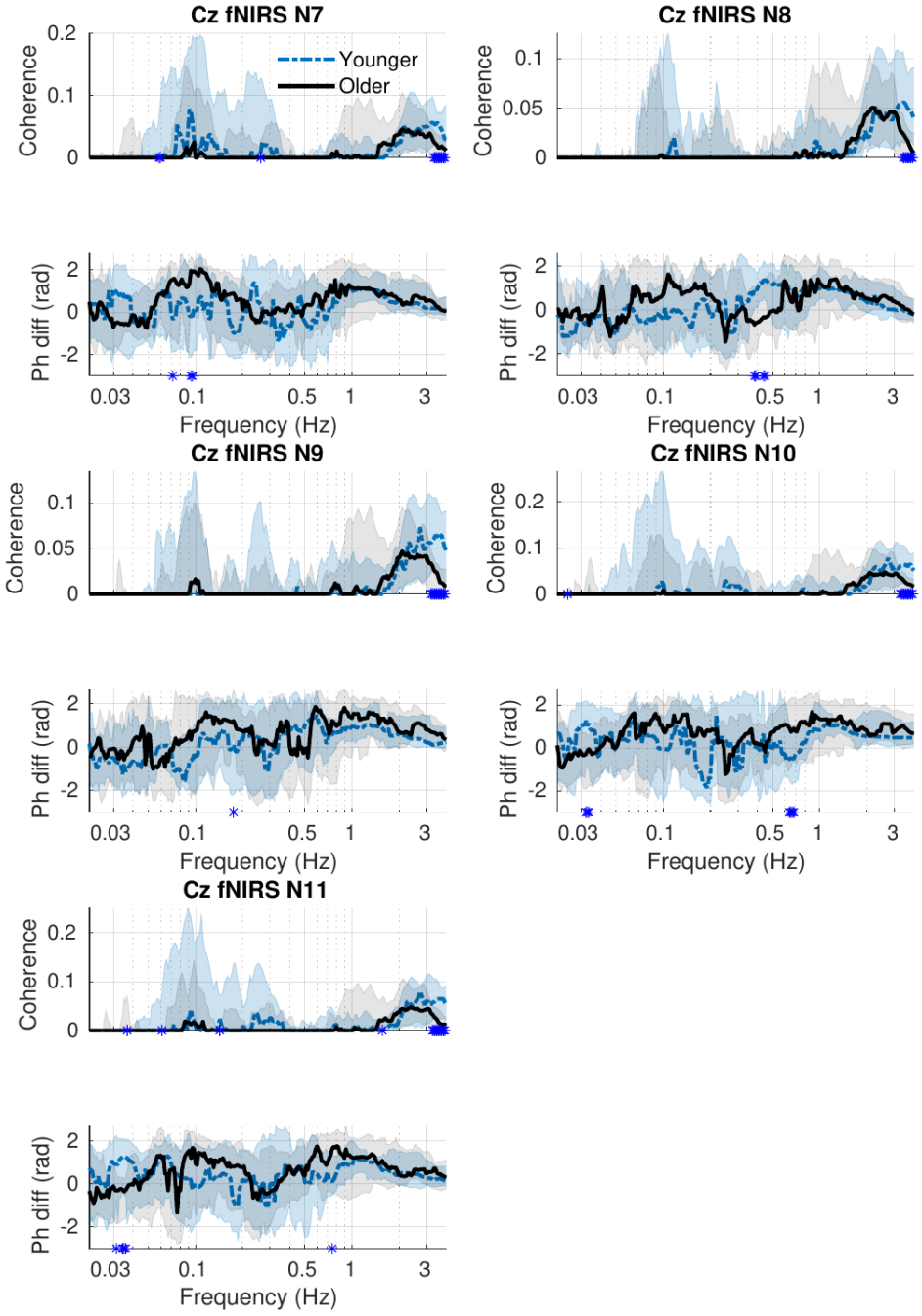

Figure 39: fNIRS–EEG coherence and phase difference for electrode Cz and 5 fNIRS sensors. The dashed blue and full black lines represent the median group coherence, while the shaded areas show the 25–75th percentiles. Significant differences between the groups at particular frequencies are indicated by blue stars on the x-axis. A negative phase difference means that fNIRS is the leading signal.

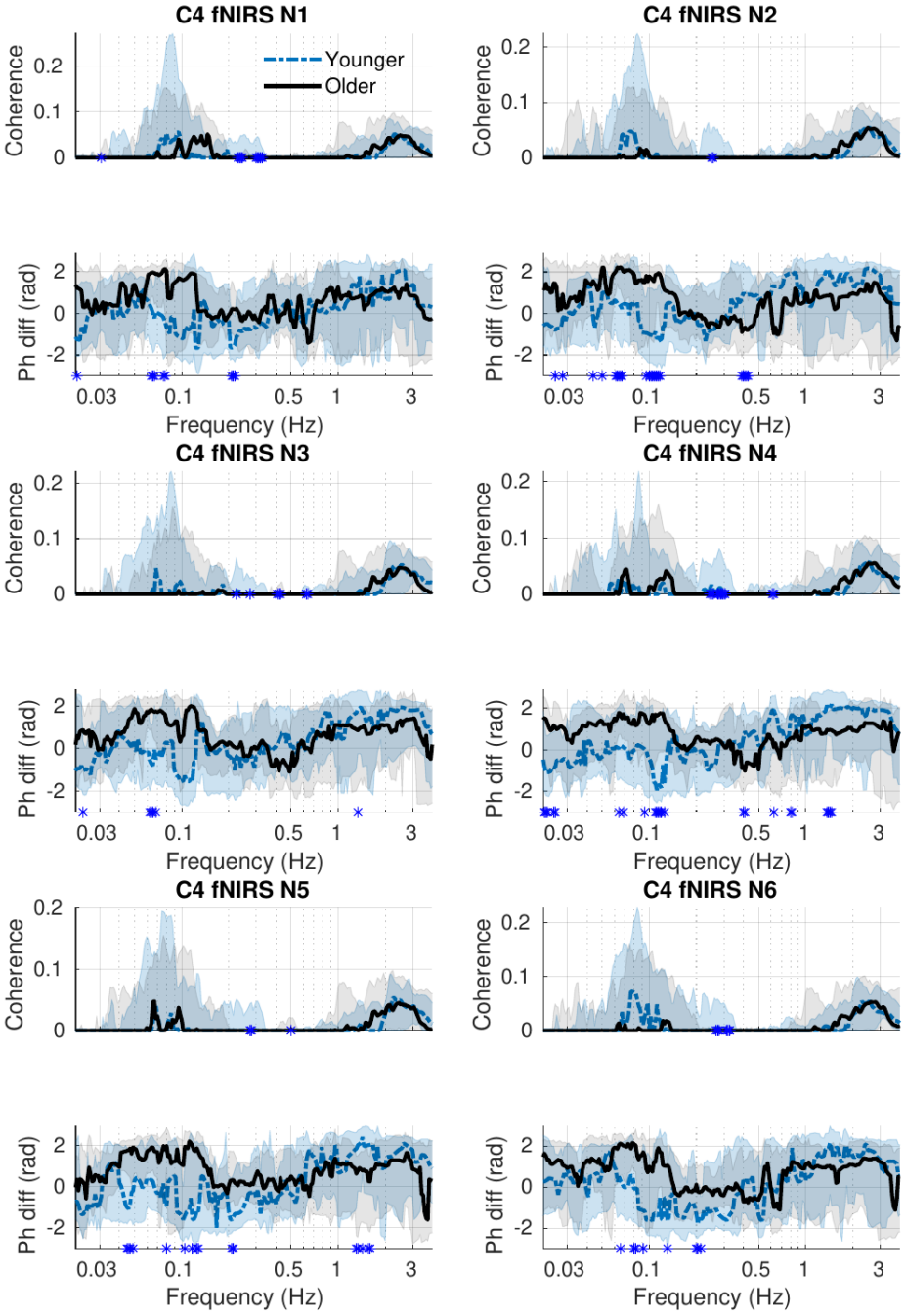

Figure 40: fNIRS–EEG coherence and phase difference for electrode C4 and 6 fNIRS sensors. The dashed blue and full black lines represent the median group coherence, while the shaded areas show the 25–75th percentiles. Significant differences between the groups at particular frequencies are indicated by blue stars on the x-axis. A negative phase difference means that fNIRS is the leading signal.

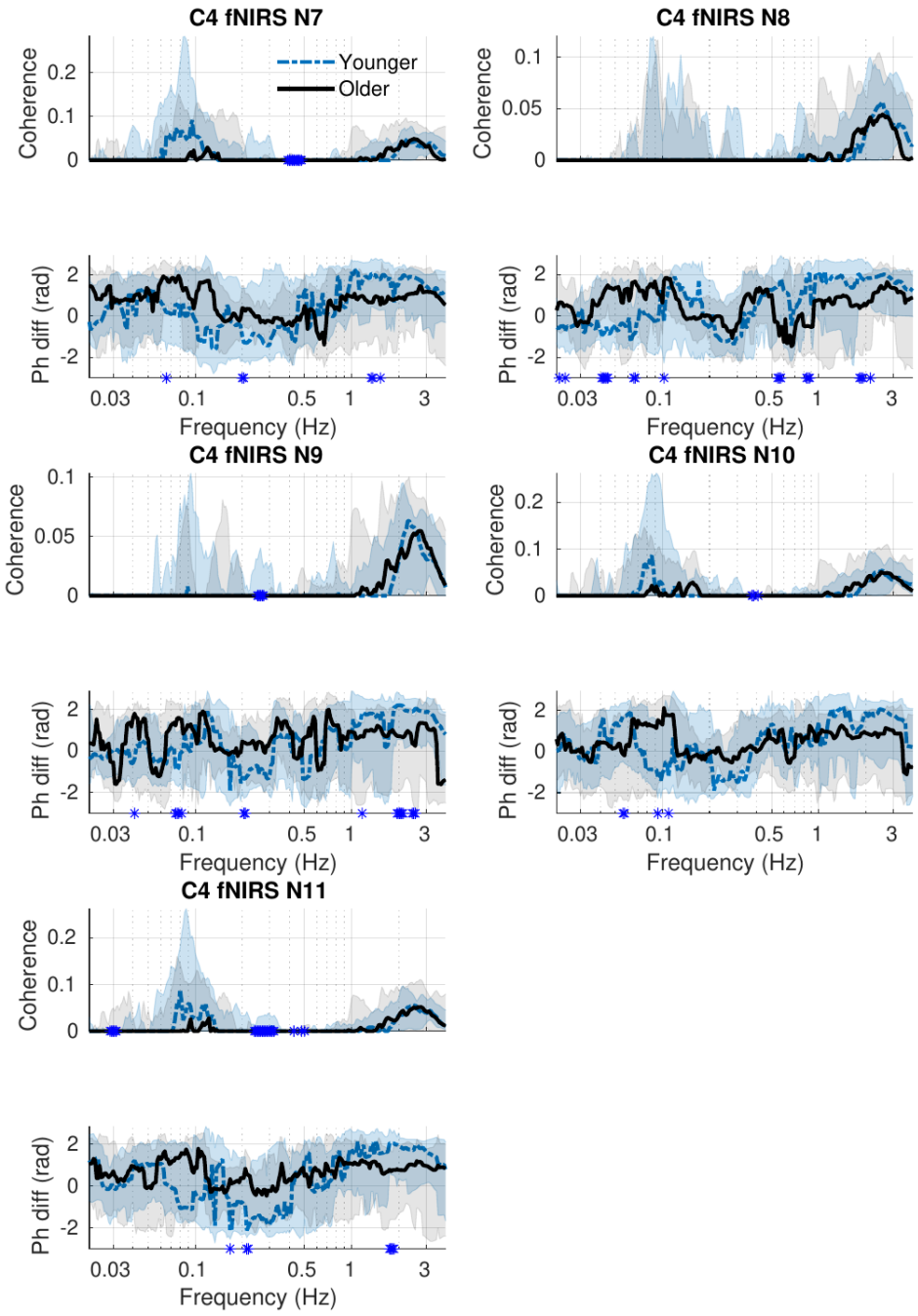

Figure 41: fNIRS–EEG coherence and phase difference for electrode C4 and 5 fNIRS sensors. The dashed blue and full black lines represent the median group coherence, while the shaded areas show the 25–75th percentiles. Significant differences between the groups at particular frequencies are indicated by blue stars on the x-axis.

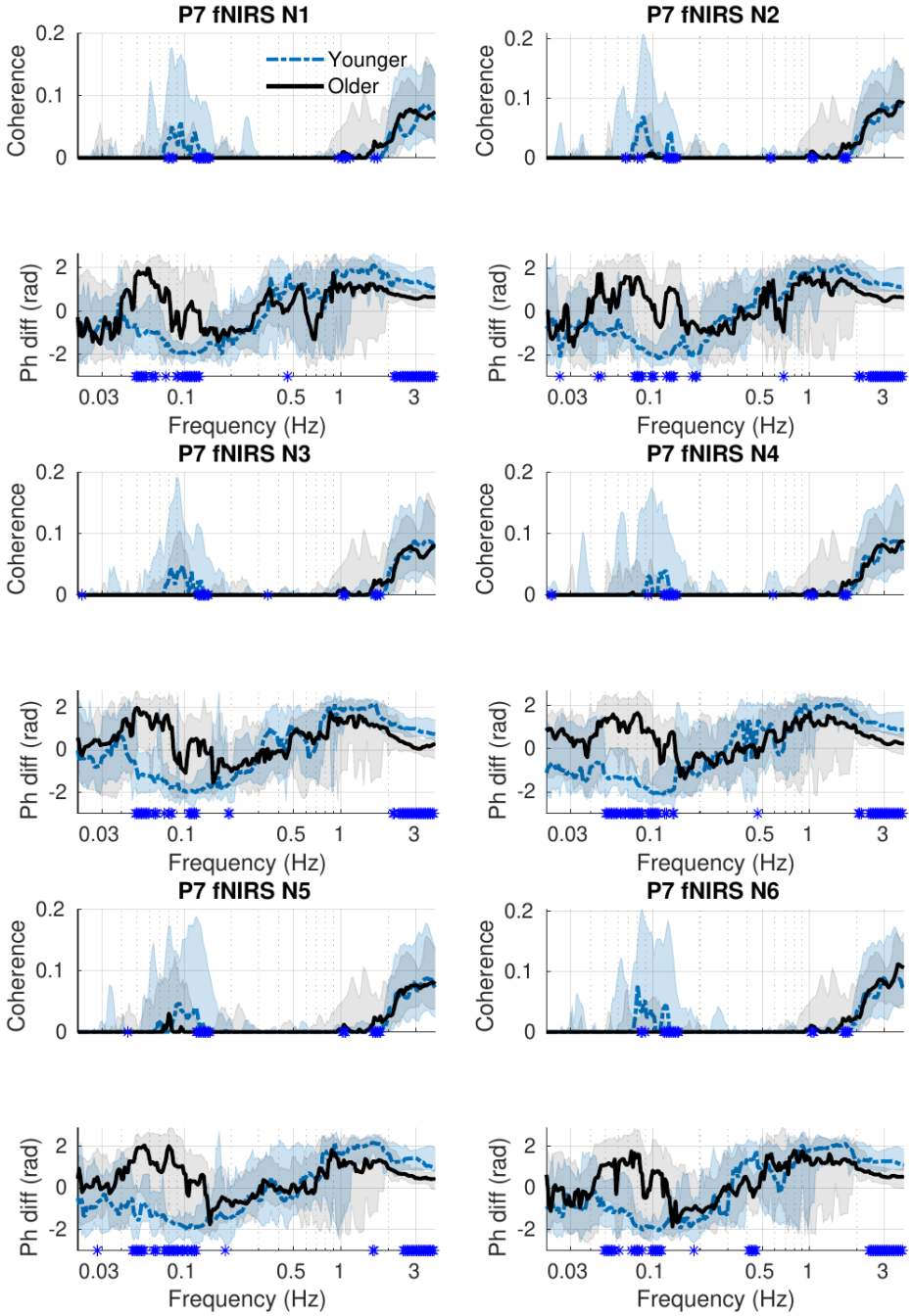

Figure 42: fNIRS–EEG coherence and phase difference for electrode P7 and 6 fNIRS sensors. The dashed blue and full black lines represent the median group coherence, while the shaded areas show the 25–75th percentiles. Significant differences between the groups at particular frequencies are indicated by blue stars on the x-axis. A negative phase difference means that fNIRS is the leading signal.

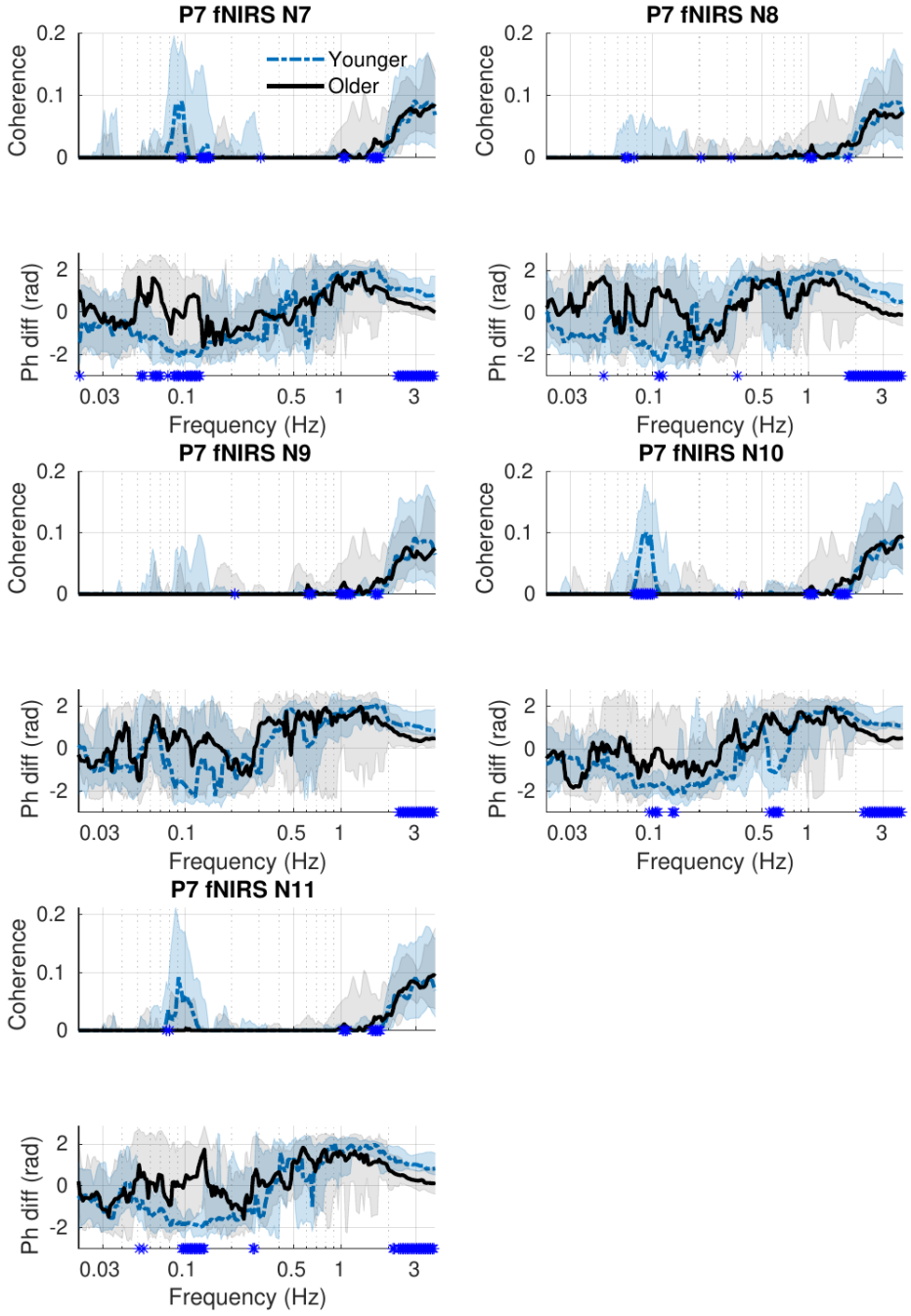

Figure 43: fNIRS–EEG coherence and phase difference for electrode P7 and 5 fNIRS sensors. The dashed blue and full black lines represent the median group coherence, while the shaded areas show the 25–75th percentiles. Significant differences between the groups at particular frequencies are indicated by blue stars on the x-axis. A negative phase difference means that fNIRS is the leading signal.

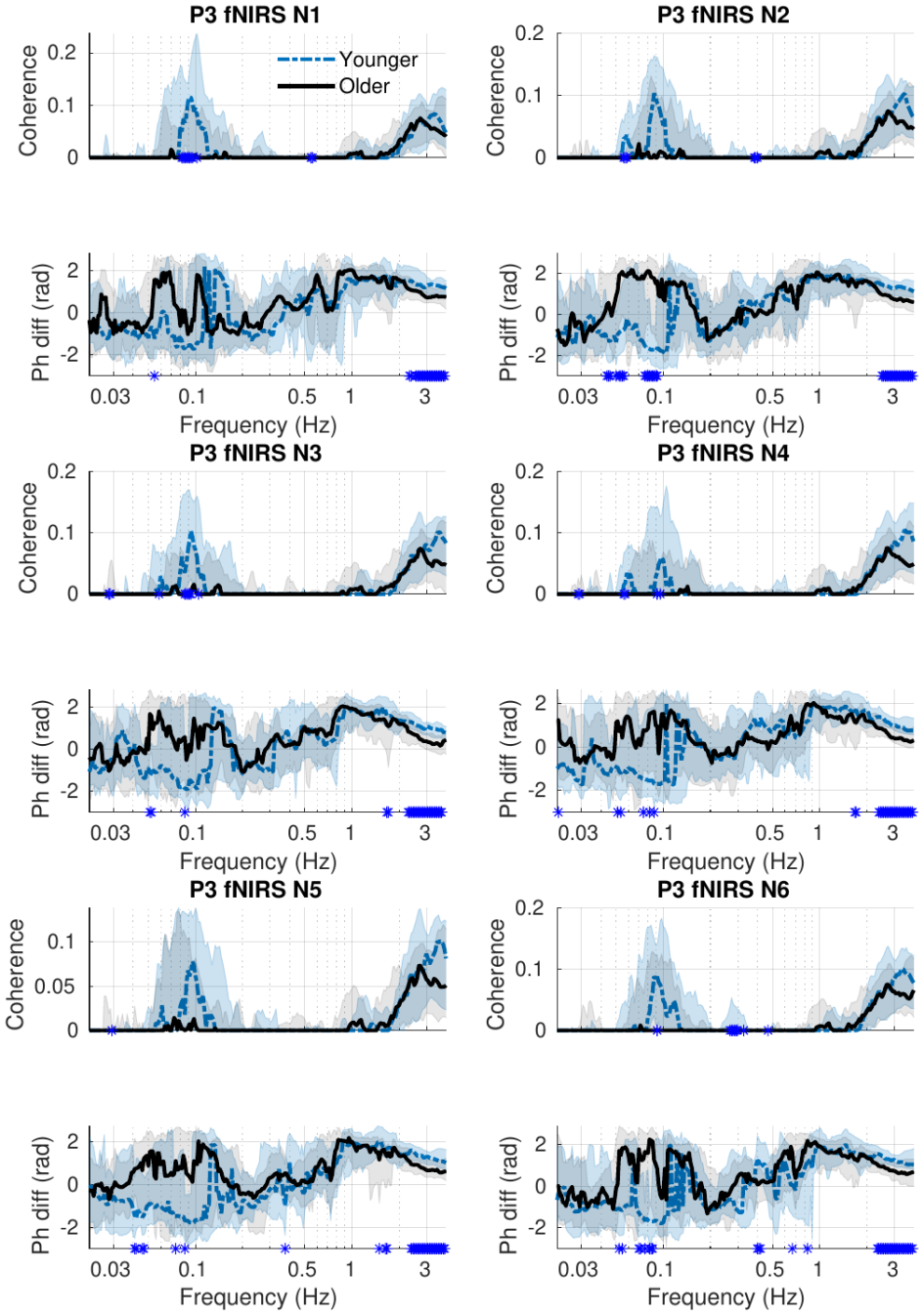

Figure 44: fNIRS–EEG coherence and phase difference for electrode P3 and 6 fNIRS sensors. The dashed blue and full black lines represent the median group coherence, while the shaded areas show the 25–75th percentiles. Significant differences between the groups at particular frequencies are indicated by blue stars on the x-axis. A negative phase difference means that fNIRS is the leading signal.

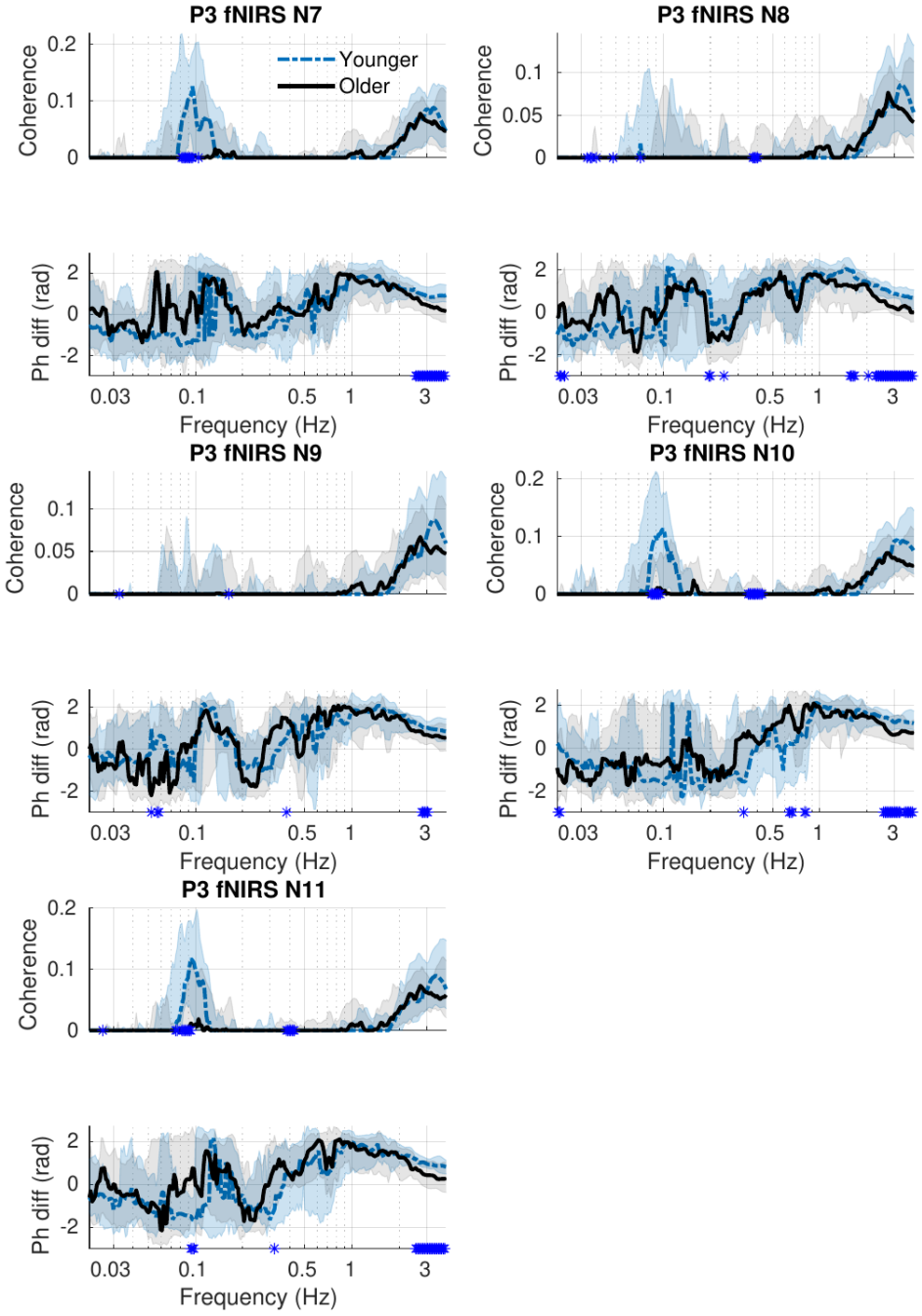

Figure 45: fNIRS–EEG coherence and phase difference for electrode P3 and 5 fNIRS sensors. The dashed blue and full black lines represent the median group coherence, while the shaded areas show the 25–75th percentiles. Significant differences between the groups at particular frequencies are indicated by blue stars on the x-axis. A negative phase difference means that fNIRS is the leading signal.

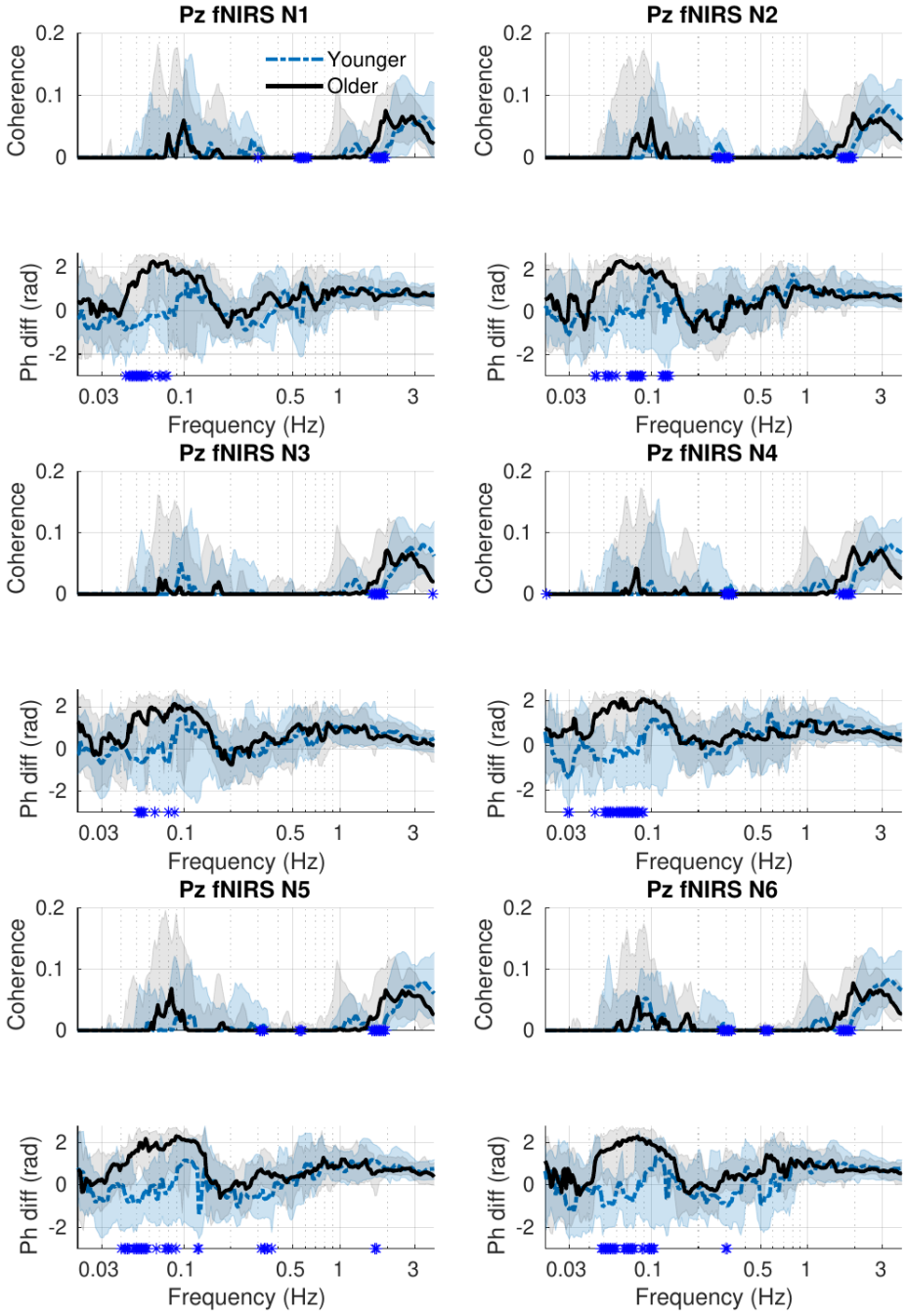

Figure 46: fNIRS–EEG coherence and phase difference for electrode Pz and 6 fNIRS sensors. The dashed blue and full black lines represent the median group coherence, while the shaded areas show the 25–75th percentiles. Significant differences between the groups at particular frequencies are indicated by blue stars on the x-axis. A negative phase difference means that fNIRS is the leading signal.

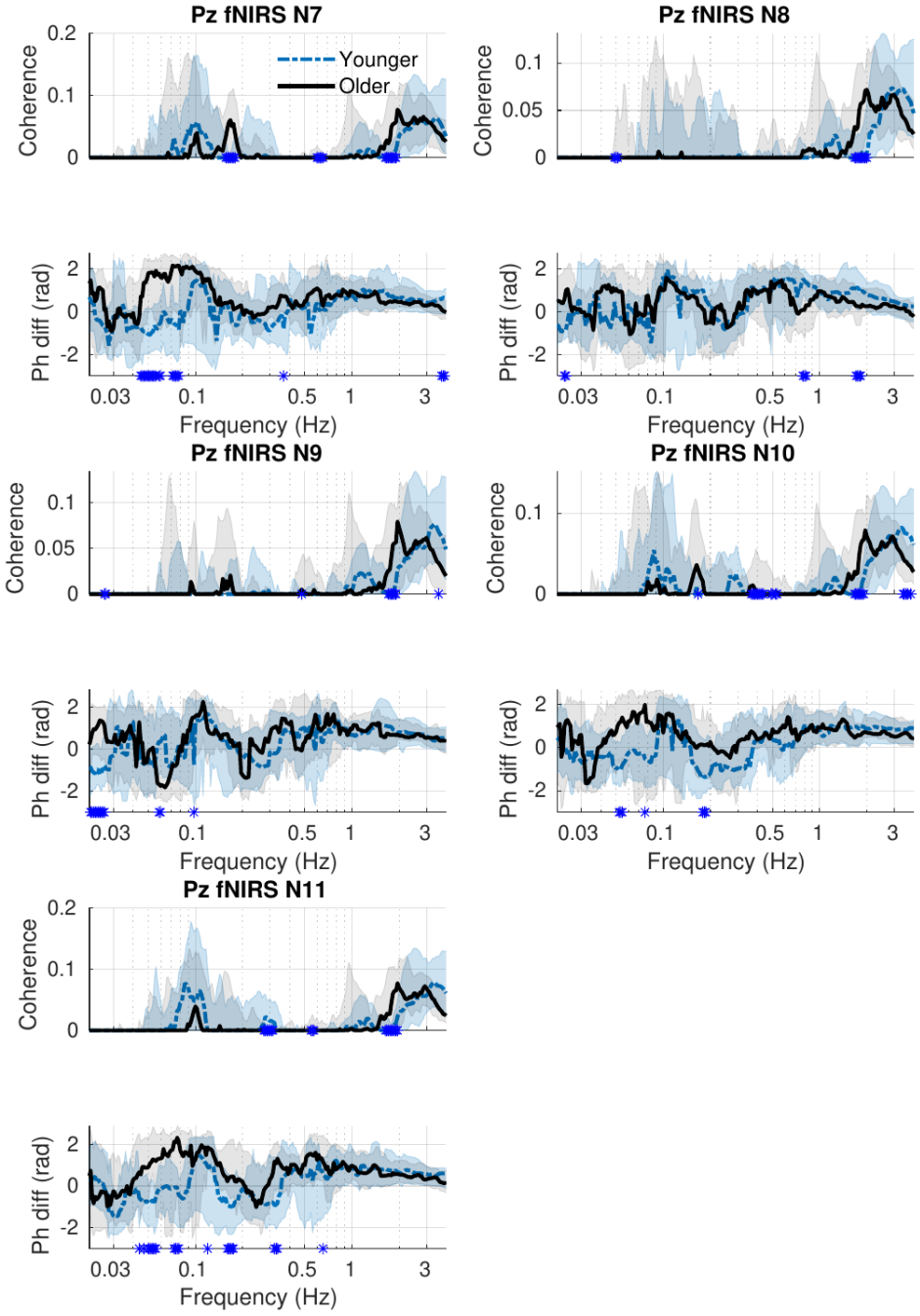

Figure 47: fNIRS–EEG coherence and phase difference for electrode Pz and 5 fNIRS sensors. The dashed blue and full black lines represent the median group coherence, while the shaded areas show the 25–75th percentiles. Significant differences between the groups at particular frequencies are indicated by blue stars on the x-axis. A negative phase difference means that fNIRS is the leading signal.

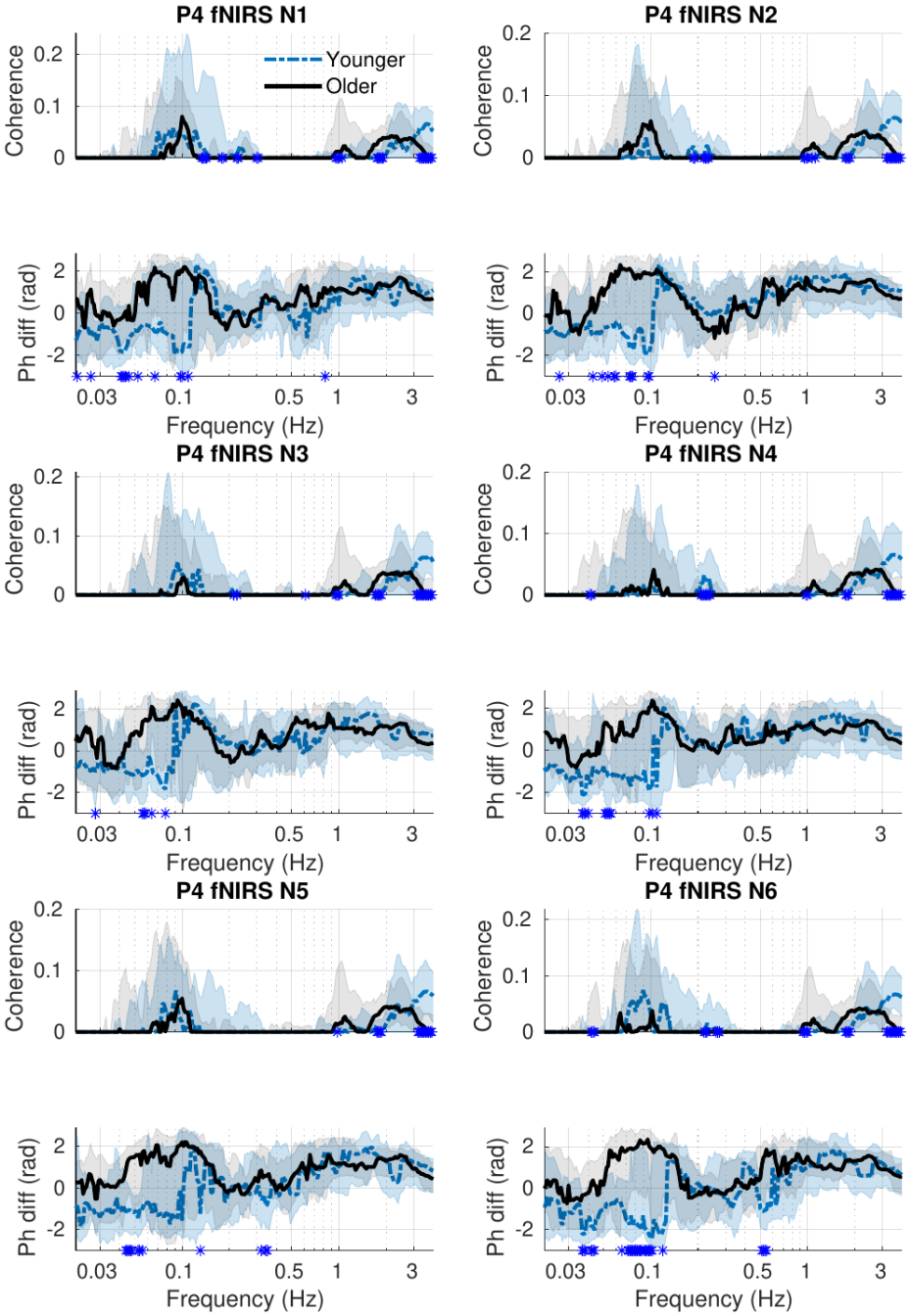

Figure 48: fNIRS–EEG coherence and phase difference for electrode P4 and 6 fNIRS sensors. The dashed blue and full black lines represent the median group coherence, while the shaded areas show the 25–75th percentiles. Significant differences between the groups at particular frequencies are indicated by blue stars on the x-axis. A negative phase difference means that fNIRS is the leading signal.

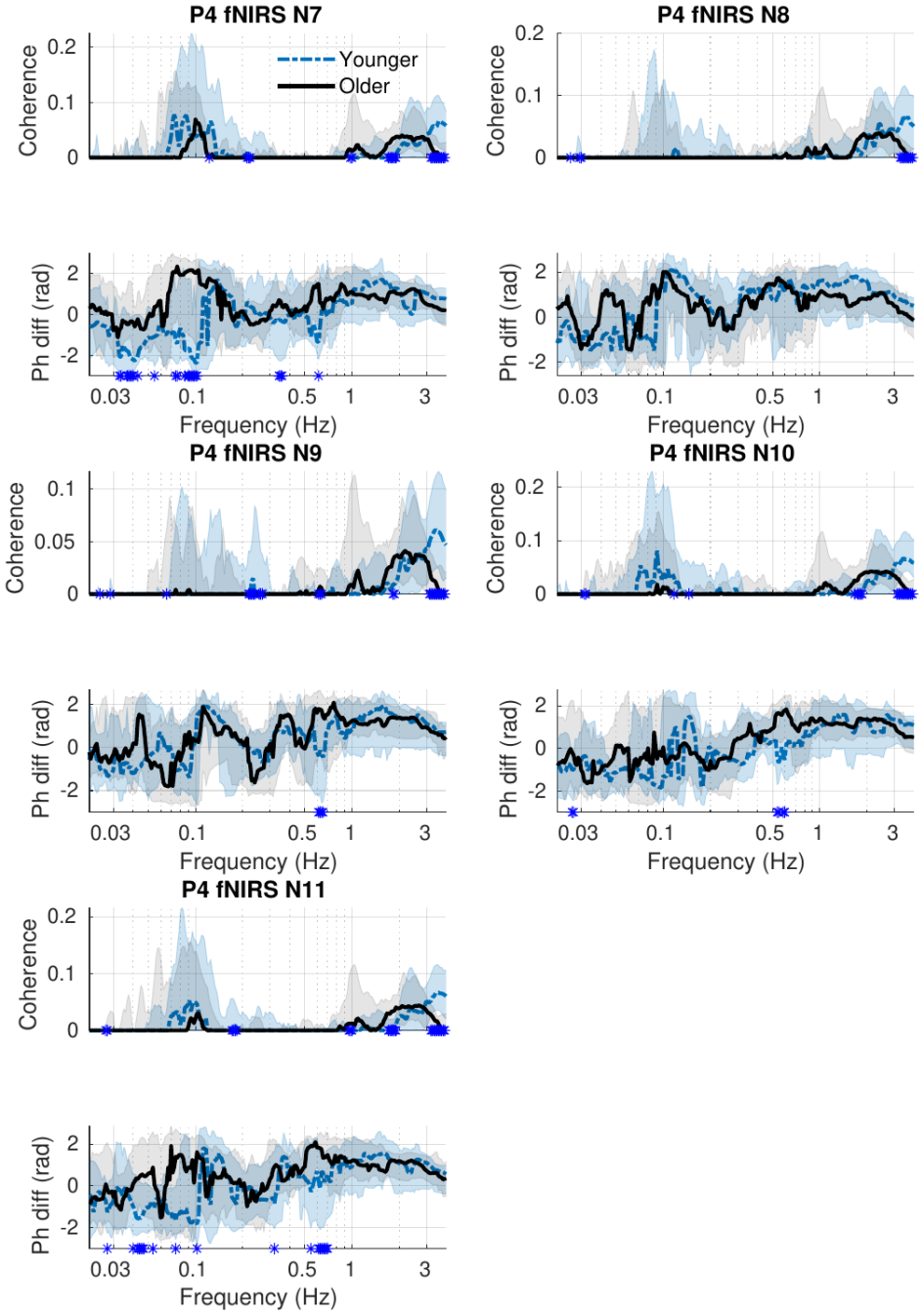

Figure 49: fNIRS–EEG coherence and phase difference for electrode P4 and 5 fNIRS sensors. The dashed blue and full black lines represent the median group coherence, while the shaded areas show the 25–75th percentiles. Significant differences between the groups at particular frequencies are indicated by blue stars on the x-axis. A negative phase difference means that fNIRS is the leading signal.

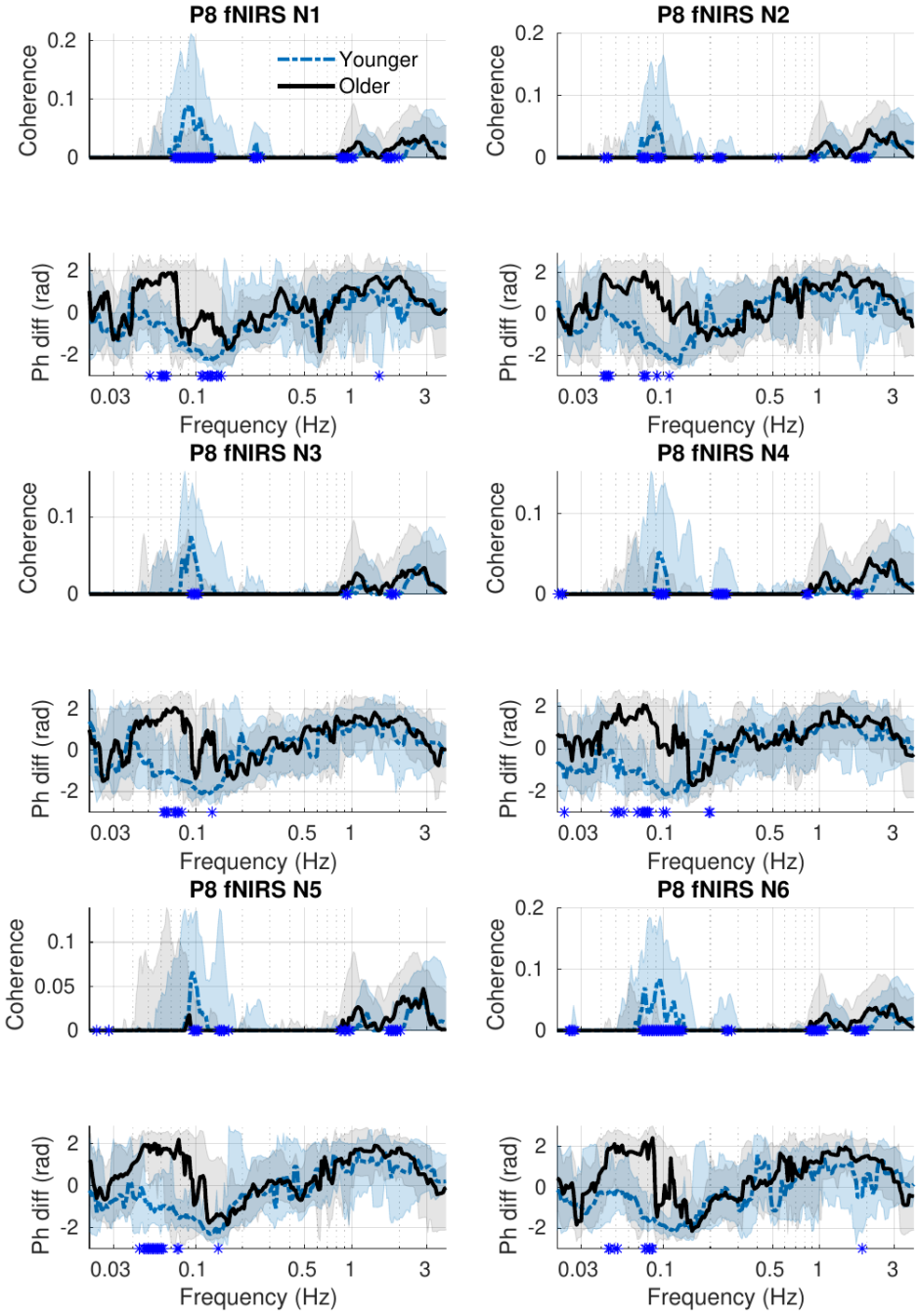

Figure 50: fNIRS–EEG coherence and phase difference for electrode P8 and 6 fNIRS sensors. The dashed blue and full black lines represent the median group coherence, while the shaded areas show the 25–75th percentiles. Significant differences between the groups at particular frequencies are indicated by blue stars on the x-axis. A negative phase difference means that fNIRS is the leading signal.

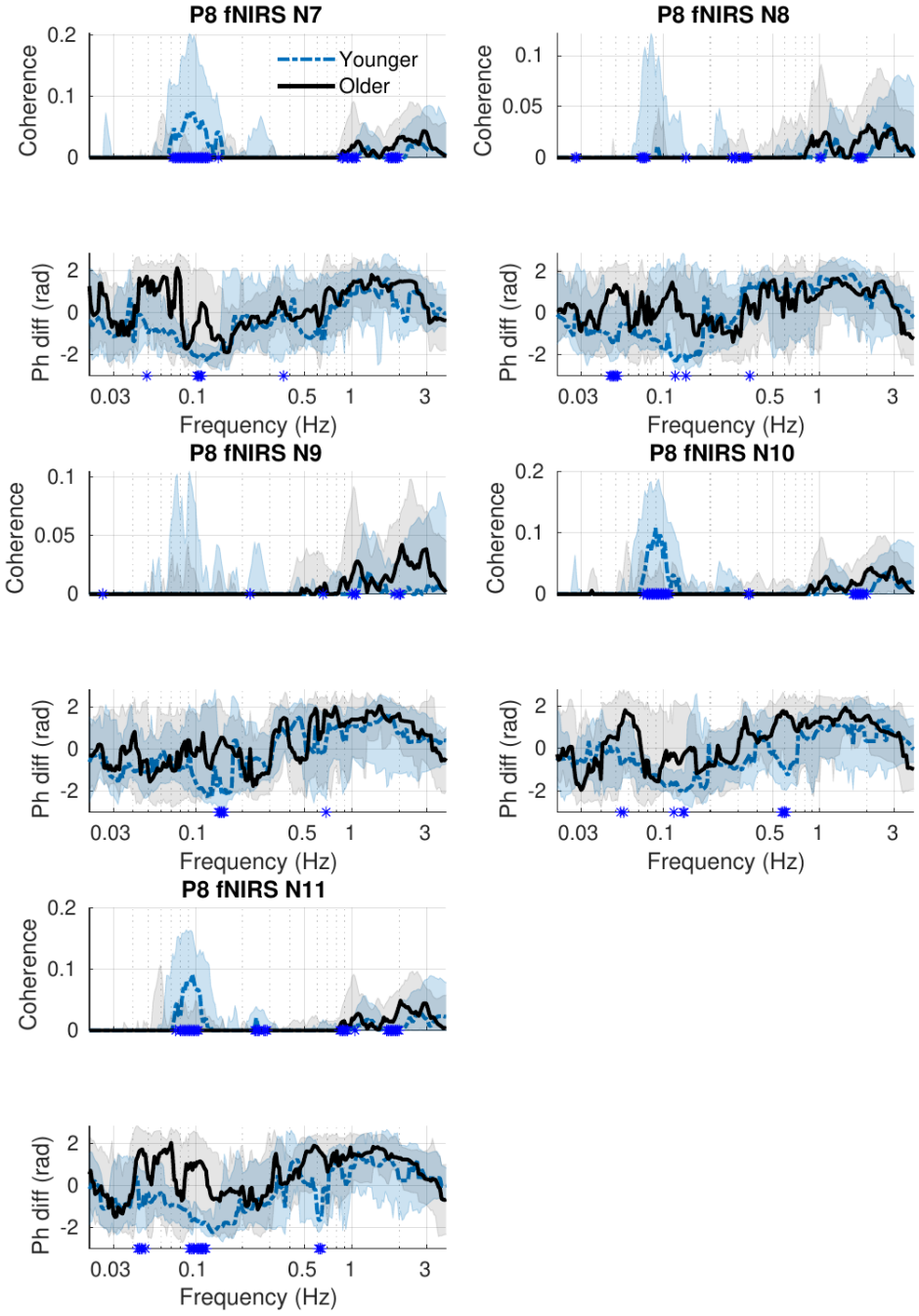

Figure 51: fNIRS–EEG coherence and phase difference for electrode P8 and 5 fNIRS sensors. The dashed blue and full black lines represent the median group coherence, while the shaded areas show the 25–75th percentiles. Significant differences between the groups at particular frequencies are indicated by blue stars on the x-axis. A negative phase difference means that fNIRS is the leading signal.

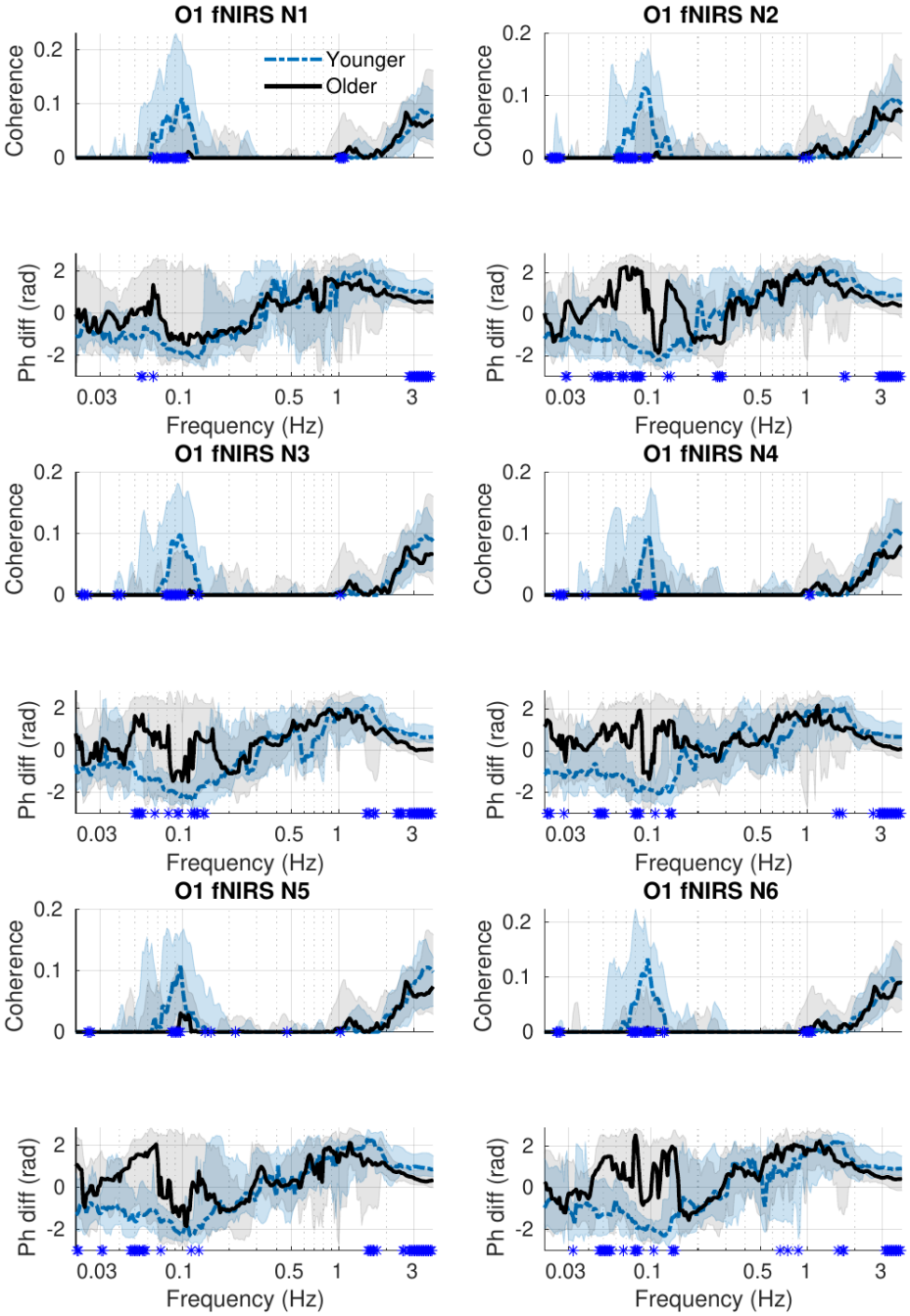

Figure 52: fNIRS–EEG coherence and phase difference for electrode O1 and 6 fNIRS sensors. The dashed blue and full black lines represent the median group coherence, while the shaded areas show the 25–75th percentiles. Significant differences between the groups at particular frequencies are indicated by blue stars on the x-axis. A negative phase difference means that fNIRS is the leading signal.

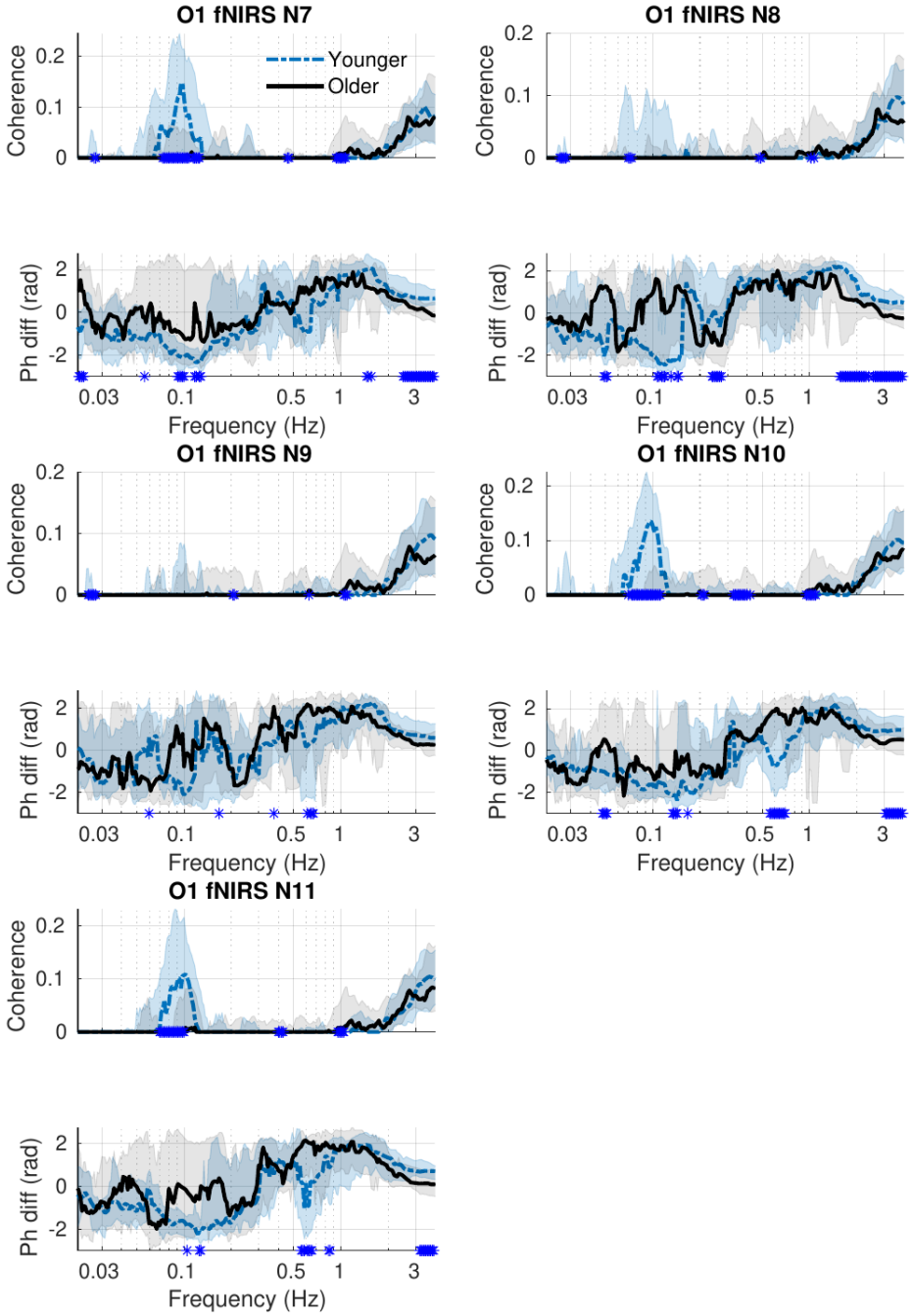

Figure 53: fNIRS–EEG coherence and phase difference for electrode O1 and 5 fNIRS sensors. The dashed blue and full black lines represent the median group coherence, while the shaded areas show the 25–75th percentiles. Significant differences between the groups at particular frequencies are indicated by blue stars on the x-axis. A negative phase difference means that fNIRS is the leading signal.

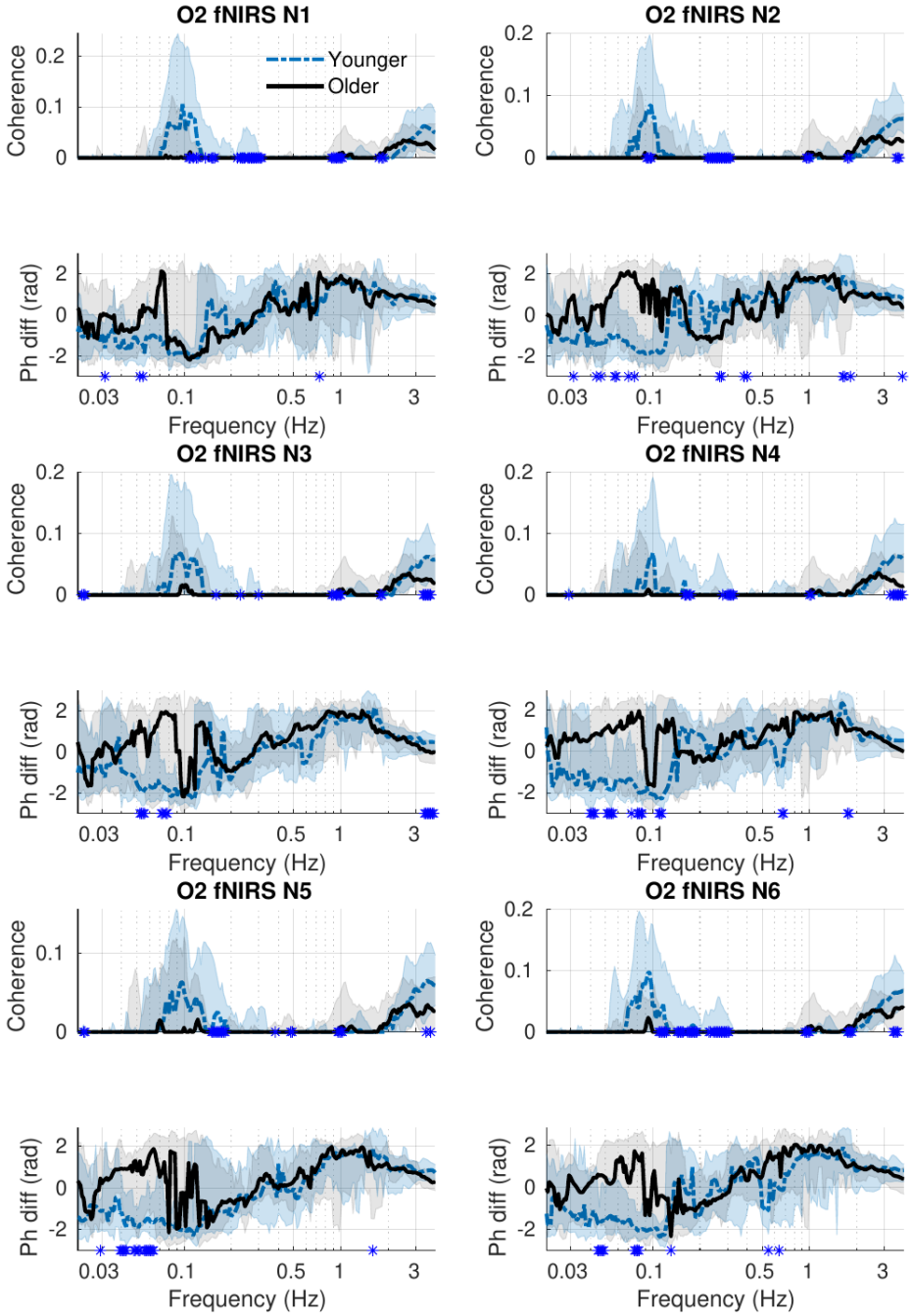

Figure 54: fNIRS–EEG coherence and phase difference for electrode O2 and 6 fNIRS sensors. The dashed blue and full black lines represent the median group coherence, while the shaded areas show the 25–75th percentiles. Significant differences between the groups at particular frequencies are indicated by blue stars on the x-axis. A negative phase difference means that fNIRS is the leading signal.

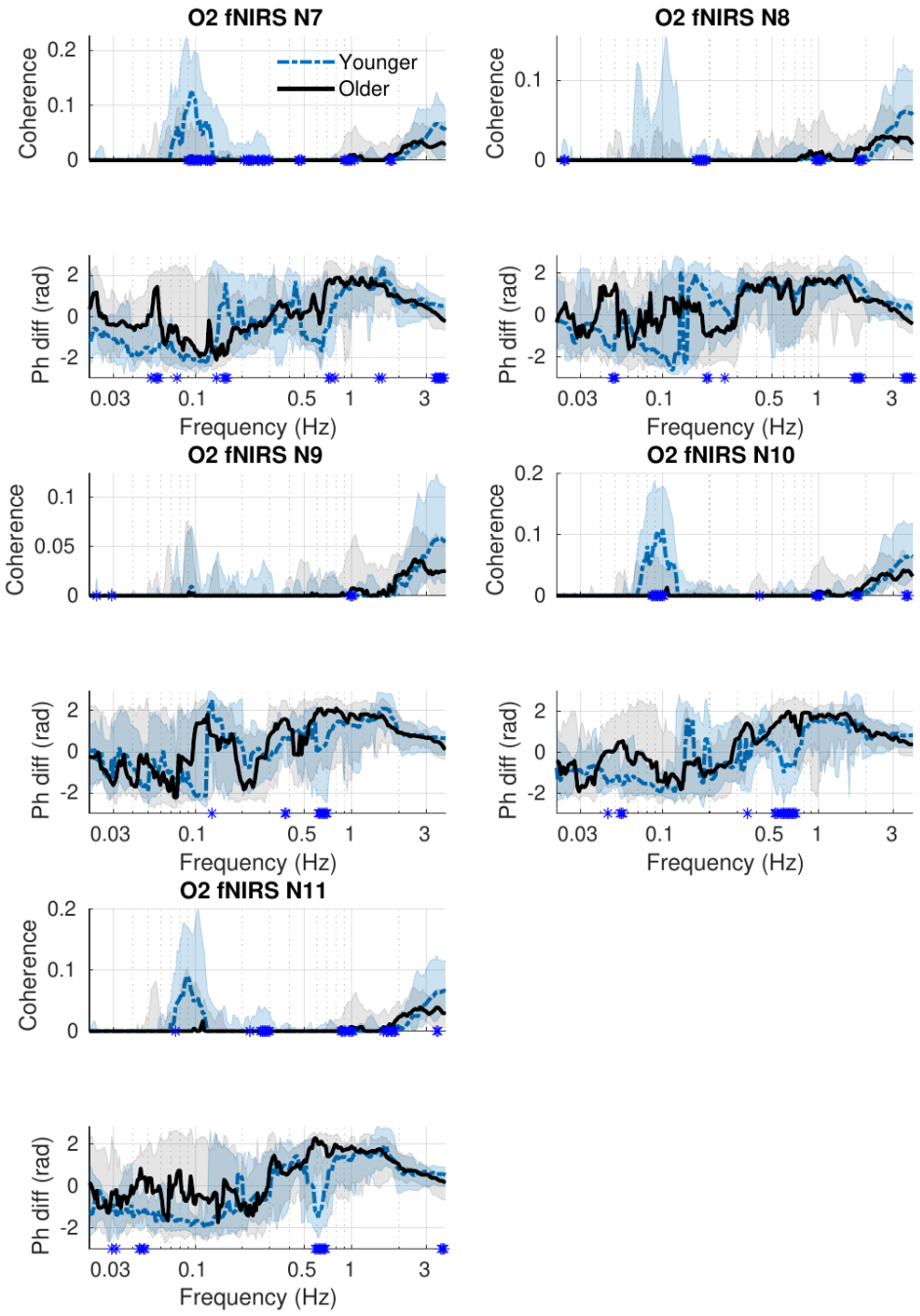

Figure 55: fNIRS–EEG coherence and phase difference for electrode O2 and 5 fNIRS sensors. The dashed blue and full black lines represent the median group coherence, while the shaded areas show the 25–75th percentiles. Significant differences between the groups at particular frequencies are indicated by blue stars on the x-axis.

11 Frequency and amplitude modulation

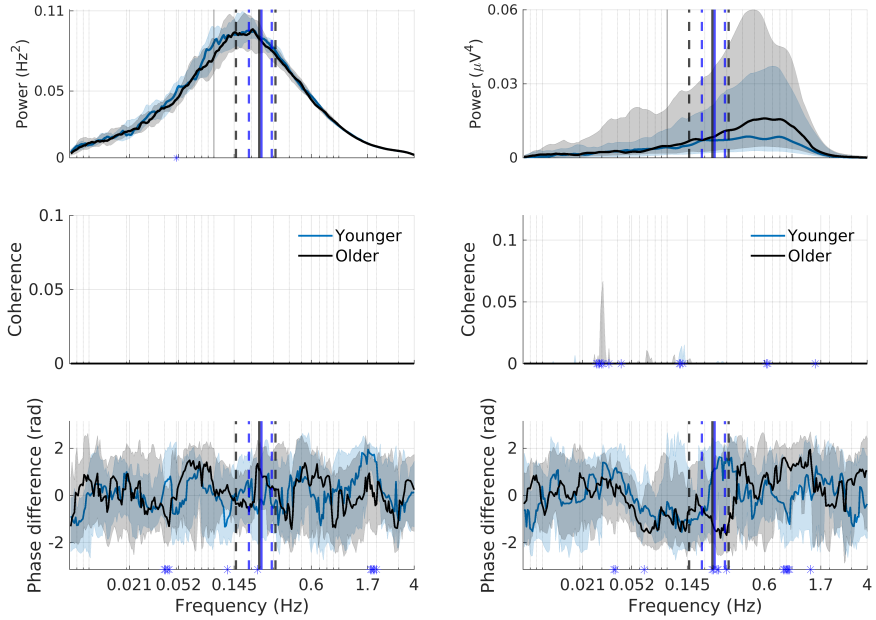

Figure 56: Comparisons between the older and younger groups related to frequency and amplitude modulation in the EEG γ-interval. Median power of the A) γ–instantaneous frequency time-series and B) γ–instantaneous power time-series. C) Median coherence between fNIRS and the γ-instantaneous frequency time-series. D) Median coherence between fNIRS and γ-instantaneous power time-series. E) Phase difference between fNIRS and the γ–instantaneous frequency time-series. F) Phase difference between fNIRS and the γ–instantaneous power time-series. The blue and black lines are the median group coherences, while the shaded areas show the 25–75th percentiles. Significant differences between the groups at particular frequencies are indicated by blue stars on the x-axis. The blue and black solid vertical lines indicate the average respiration rates for the younger and older group, while the dashed lines indicate the standard deviations. Both fNIRS and EEG signals are from location F3.

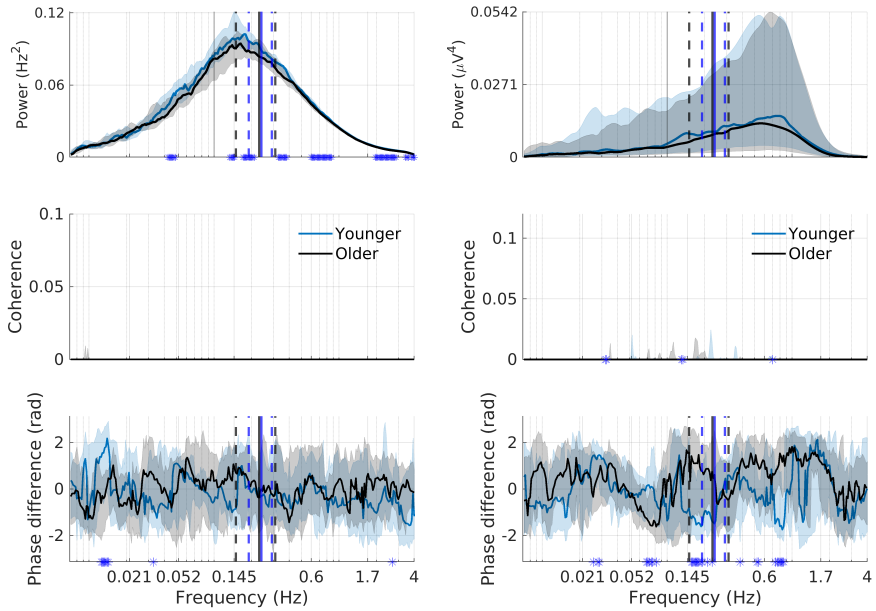

Figure 57: Comparisons between the older and younger groups related to frequency and amplitude modulation in the EEG γ-interval. Median power of the A) γ–instantaneous frequency time-series and B) γ–instantaneous power time-series. C) Median coherence between fNIRS and the γ-instantaneous frequency time-series. D) Median coherence between fNIRS and γ-instantaneous power time-series. E) Phase difference between fNIRS and the γ–instantaneous frequency time-series. F) Phase difference between fNIRS and the γ–instantaneous power time-series. The blue and black lines are the median group coherences, while the shaded areas show the 25–75th percentiles. Significant differences between the groups at particular frequencies are indicated by blue stars on the x-axis. The blue and black solid vertical lines indicate the average respiration rates for the younger and older group, while the dashed lines indicate the standard deviations. Both fNIRS and EEG signals are from location F4.

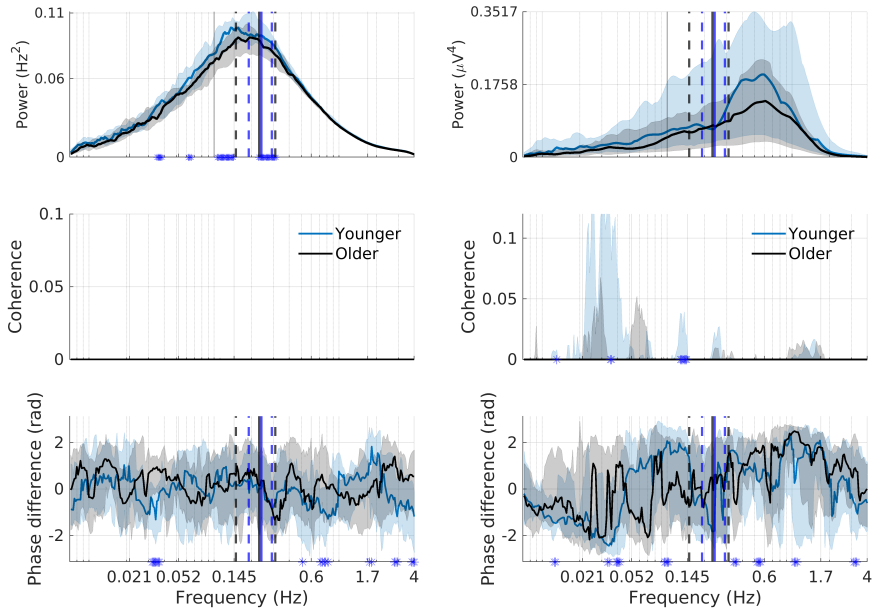

Figure 58: Comparisons between the older and younger groups related to frequency and amplitude modulation in the EEG γ-interval. Median power of the A) γ–instantaneous frequency time-series and B) γ–instantaneous power time-series. C) Median coherence between fNIRS and the γ-instantaneous frequency time-series. D) Median coherence between fNIRS and γ-instantaneous power time-series. E) Phase difference between fNIRS and the γ–instantaneous frequency time-series. F) Phase difference between fNIRS and the γ–instantaneous power time-series. The blue and black lines are the median group coherences, while the shaded areas show the 25–75th percentiles. Significant differences between the groups at particular frequencies are indicated by blue stars on the x-axis. The blue and black solid vertical lines indicate the average respiration rates for the younger and older group, while the dashed lines indicate the standard deviations. Both fNIRS and EEG signals are from location T7.

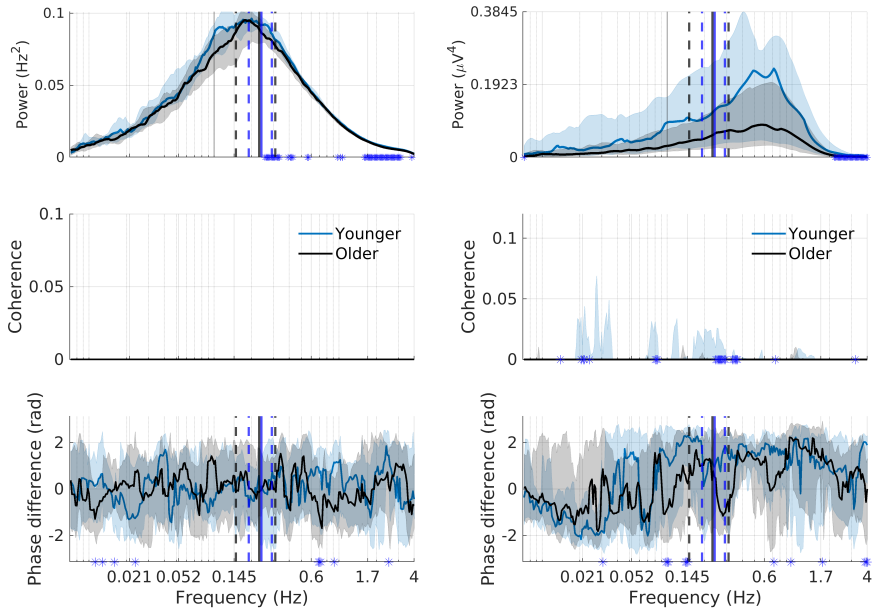

Figure 59: Comparisons between the older and younger groups related to frequency and amplitude modulation in the EEG γ-interval. Median power of the A) γ–instantaneous frequency time-series and B) γ–instantaneous power time-series. C) Median coherence between fNIRS and the γ-instantaneous frequency time-series. D) Median coherence between fNIRS and γ-instantaneous power time-series. E) Phase difference between fNIRS and the γ–instantaneous frequency time-series. F) Phase difference between fNIRS and the γ–instantaneous power time-series. The blue and black lines are the median group coherences, while the shaded areas show the 25–75th percentiles. Significant differences between the groups at particular frequencies are indicated by blue stars on the x-axis. The blue and black solid vertical lines indicate the average respiration rates for the younger and older group, while the dashed lines indicate the standard deviations. Both fNIRS and EEG signals are from location T8.

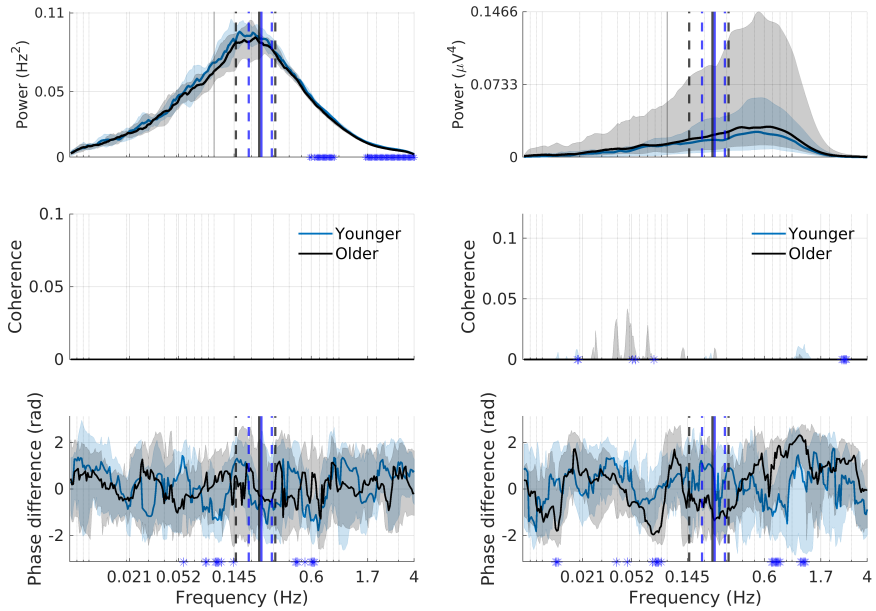

Figure 60: Comparisons between the older and younger groups related to frequency and amplitude modulation in the EEG γ-interval. Median power of the A) γ–instantaneous frequency time-series and B) γ–instantaneous power time-series. C) Median coherence between fNIRS and the γ-instantaneous frequency time-series. D) Median coherence between fNIRS and γ-instantaneous power time-series. E) Phase difference between fNIRS and the γ–instantaneous frequency time-series. F) Phase difference between fNIRS and the γ–instantaneous power time-series. The blue and black lines are the median group coherences, while the shaded areas show the 25–75th percentiles. Significant differences between the groups at particular frequencies are indicated by blue stars on the x-axis. The blue and black solid vertical lines indicate the average respiration rates for the younger and older group, while the dashed lines indicate the standard deviations. Both fNIRS and EEG signals are from location P3.

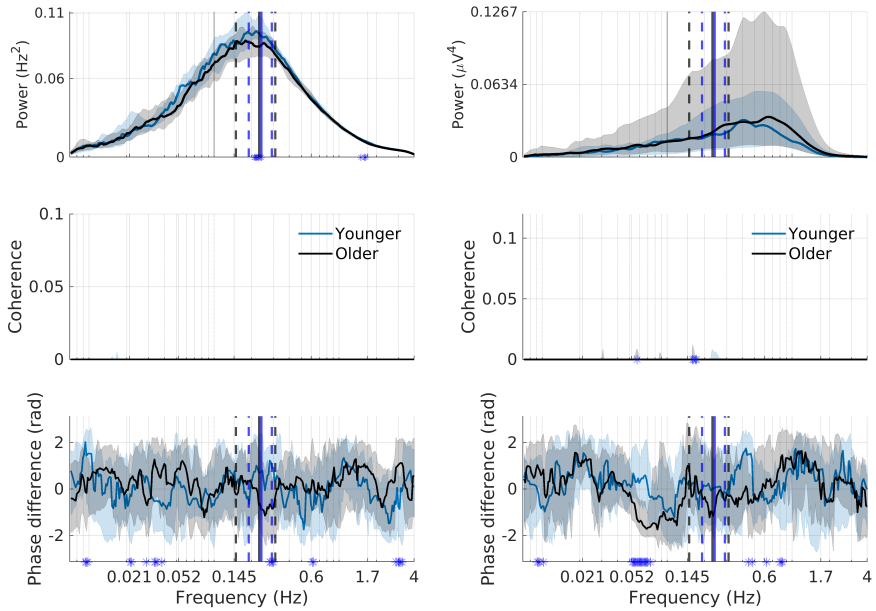

Figure 61: Comparisons between the older and younger groups related to frequency and amplitude modulation in the EEG γ-interval. Median power of the A) γ–instantaneous frequency time-series and B) γ–instantaneous power time-series. C) Median coherence between fNIRS and the γ-instantaneous frequency time-series. D) Median coherence between fNIRS and γ-instantaneous power time-series. E) Phase difference between fNIRS and the γ–instantaneous frequency time-series. F) Phase difference between fNIRS and the γ–instantaneous power time-series. The blue and black lines are the median group coherences, while the shaded areas show the 25–75th percentiles. Significant differences between the groups at particular frequencies are indicated by blue stars on the x-axis. The blue and black solid vertical lines indicate the average respiration rates for the younger and older group, while the dashed lines indicate the standard deviations. Both fNIRS and EEG signals are from location P4.

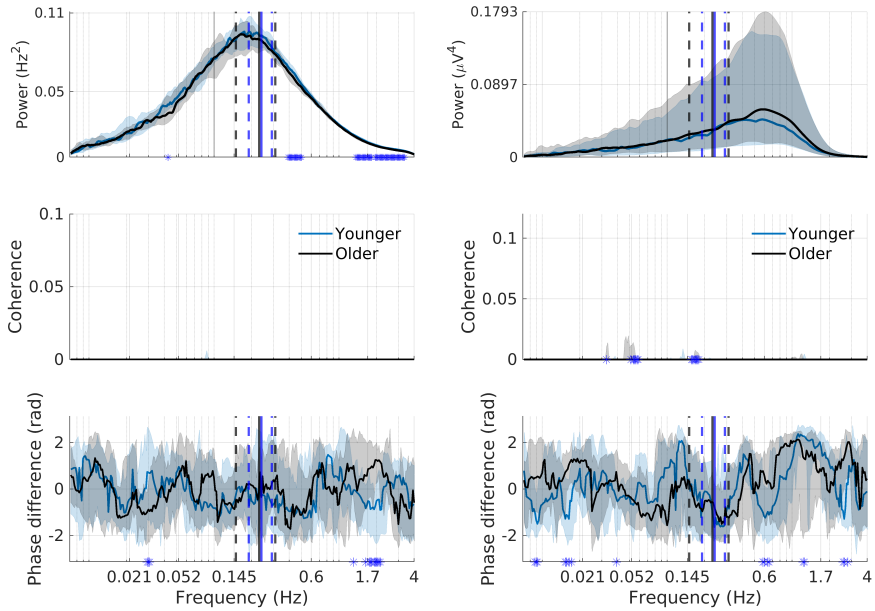

Figure 62: Comparisons between the older and younger groups related to frequency and amplitude modulation in the EEG γ-interval. Median power of the A) γ–instantaneous frequency time-series and B) γ–instantaneous power time-series. C) Median coherence between fNIRS and the γ-instantaneous frequency time-series. D) Median coherence between fNIRS and γ-instantaneous power time-series. E) Phase difference between fNIRS and the γ–instantaneous frequency time-series. F) Phase difference between fNIRS and the γ–instantaneous power time-series. The blue and black lines are the median group coherences, while the shaded areas show the 25–75th percentiles. Significant differences between the groups at particular frequencies are indicated by blue stars on the x-axis. The blue and black solid vertical lines indicate the average respiration rates for the younger and older group, while the dashed lines indicate the standard deviations. Both fNIRS and EEG signals are from location O2.

References

[1] Cohen, J. *Statistical Power Analysis for the Behavioral Sciences* (2nd ed.) (Lawrence Erlbaum Associates, 1988).

[2] Faul, F., Erdfelder, E., Lang, A.-G. & Buchner, A. G*power 3: A flexible statistical power analysis program for the social, behavioral, and biomedical sciences. *Behav. Res. Methods* **39**, 175–191 (2007).

[3] Vysata, O. *et al.* Age-related changes in EEG coherence. *Neurol. Neurochir. Pol.* **48**, 35–38 (2014).

[4] Scally, B., Burke, M. R., Bunce, D. & Delvenne, J.-F. Resting-state EEG power and connectivity are associated with alpha peak frequency slowing in healthy aging. *Neurobiol. Aging.* **71**, 149 – 155 (2018).

[5] Moezzi, B. *et al.* Characterization of young and old adult brains: An EEG functional connectivity analysis. *Neuroscience* **422**, 230–239 (2019).

[6] Babiloni, C. *et al.* Sources of cortical rhythms in adults during physiological aging: A multicentric EEG study. *Hum. Brain. Mapp.* **27**, 162–172 (2006).

[7] Dustman, R., Shearer, D. & Emmerson, R. Life-span changes in EEG spectral amplitude, amplitude variability and mean frequency. *Clin. Neurophysiol.* **110**, 1399–1409 (1999).

[8] Meghdadi, A. H. *et al.* Resting state EEG biomarkers of cognitive decline associated with Alzheimer's disease and mild cognitive impairment. *PLOS ONE* **16**, 1–31 (2021).

[9] Richard Clark, C. *et al.* Spontaneous alpha peak frequency predicts working memory performance across the age span. *Int. J. Psychophysiol.* **53**, 1–9 (2004).

[10] Smit, D. J. A. *et al.* The brain matures with stronger functional connectivity and decreased randomness of its network. *PLOS ONE* **7**, 1–11 (2012).

[11] Bandrivskyy, A., Bernjak, A., McClintock, P. V. E. & Stefanovska, A. Wavelet phase coherence analysis: Application to skin temperature and blood flow. *Cardiovasc. Eng.* **4**, 89–93 (2004).

Supplementary Material for "Neurovascular phase coherence is altered in Alzheimer's disease"

Juliane Bjerkan[1], Bernard Meglič[2], Gemma Lancaster[1], Jan Kobal[2], Peter V. E. McClintock[1], Trevor J. Crawford[3], Aneta Stefanovska[1,*]

[1]Department of Physics, Lancaster University, Lancaster, LA1 4YB, UK
[2] Department of Neurology, University Medical Centre, 1525 Ljubljana, Slovenia
[3] Department of Psychology, Lancaster University, Lancaster, LA1 4YF, UK
[*]Corresponding author

Contents

1 Introduction

This document contains supplementary material for the paper "Neurovascular phase coherence is altered in Alzheimer's disease". Section 2 discusses how some apparently healthy subjects were excluded on the basis of their abnormal ECG patterns. In sections 3 and 4 the coherence between instantaneous heart rate and oxygenation, and between respiration and oxygenation are shown for all fNIRS probes. The reproducibility of oxygenation power is discussed in Section 5. Section 6 contains additional information about the analysis, results and discussion for the EEG data.

2 ECG analysis

Despite not being diagnosed with heart problems, 4 of the participants had abnormal ECG traces, as can be seen in Supplementary Figure 1. The participants in Supplementary Figure 1A,B had many instances of ectopic heart beats throughout the entirety of the ∼30 minutes recordings. The participant in Supplementary Figure 1C might have persistent atrial fibrillation, and the participant in Supplementary Figure 1D might have hyperkalemia. The instantaneous heart rates (IHRs) of all 4 participants were clearly atypical, with very large variability. In all cases there was a problem with the conductance of the heart. These participants were therefore excluded from IHR analysis as stated in the main manuscript.

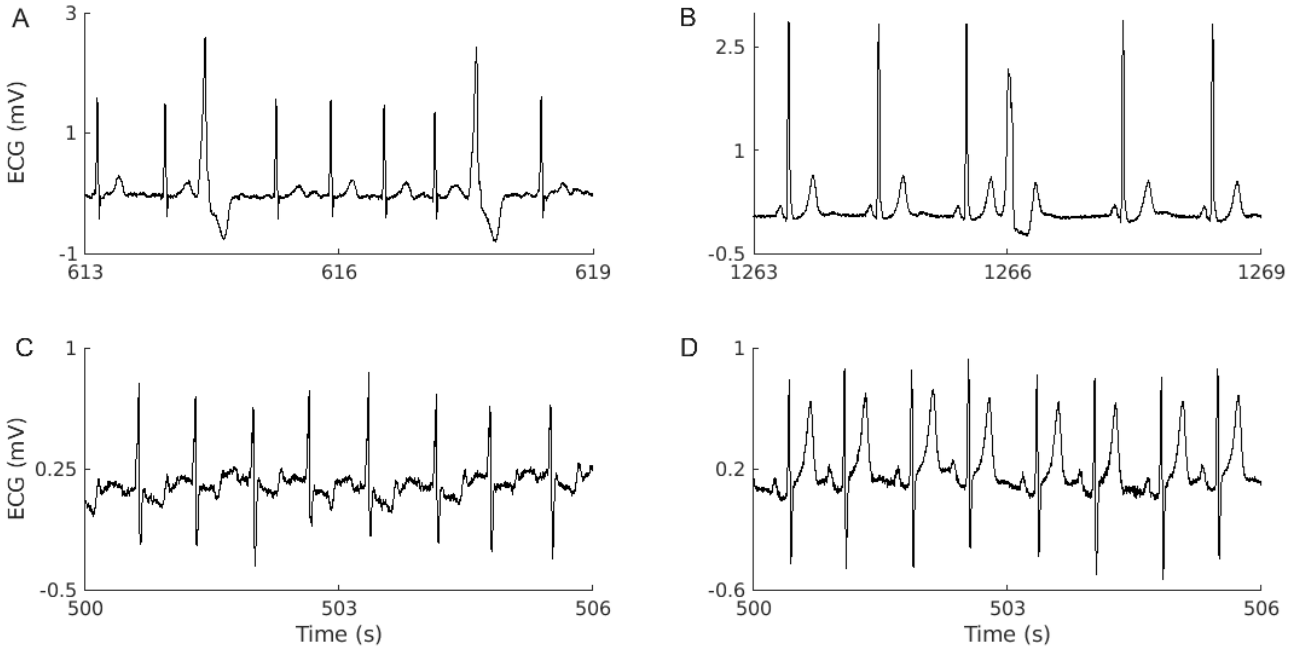

Supplementary Figure 1: Zoom-ins of the ECG recordings from (A) the control participant, and (B-D) AD participants that were excluded from the analysis due to abnormal ECGs. The recordings in (A) and (B) show ectopic heart beats, which were present throughout the length of the recordings. The recording in (C) does not have the characteristic ECG shape, potentially due to persistent atrial fibrillation. The recording in (D) have a large T-wave, in addition to a low S wave, potentially due to hyperkalemia. All 4 recordings resulted in abnormal instantaneous heart rates.

The results for IHR power and IHR–respiration coherence when these participants are included are shown in Supplementary Figures 2A and B respectively. The 75th percentile of IHR power is clearly affected by the additional 3 AD participants, and some of the significance in the 0.052-0.145 Hz range is now gone. On the other hand, the difference in IHR–respiration coherence is more significant, likely due to the increased statistical power when more people are included.

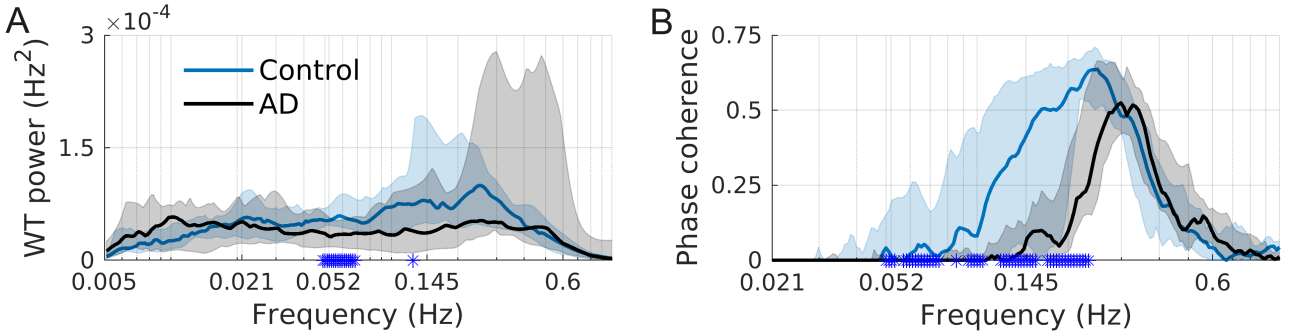

Supplementary Figure 2: (A) Instantaneous heart rate (IHR) power and (B) IHR–respiration coherence, with the excluded participants now included. The solid black and blue lines show the median group coherence, while the shaded areas show the 25–75th percentiles. Significant differences ($p \leq 0.05$) between the groups at particular frequencies, found using the Wilcoxon rank-sum test, are indicated by blue stars on the x-axis. AD = Alzheimer's disease, C = control group.) $N = 19$ for controls, $N = 18$ for AD.

Many studies of heart rate variability use 300 second recordings. We too calculated the IHR power for 300 seconds for the participants included in the main manuscript. Supplementary Figure 3 shows that the power is significantly reduced in the 0.052–0.2 Hz range, which is consistent with the results from the full recording. Shorter time-series limit the frequency interval which can be investigated at its lower end.

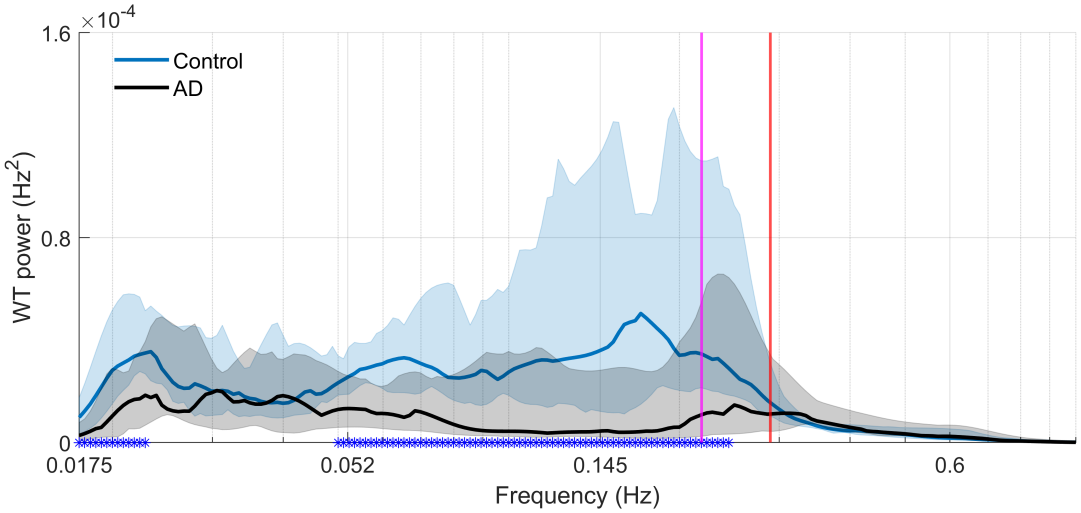

Supplementary Figure 3: Instantaneous heart rate power, calculated from 300 seconds time-series. The red vertical line shows the average respiration rate for the Alzheimer's disease group, while the green vertical line show the average respiration rate for the control group. The solid black and blue lines show the median group coherence, while the shaded areas show the 25–75th percentiles. Significant differences ($p \leq 0.05$) between the groups at particular frequencies, found using the Wilcoxon rank-sum test, are indicated by blue stars on the x-axis. AD = Alzheimer's disease, C = control group. $N = 18$ for controls, $N = 15$ for AD.

3 Instantaneous heart rate and oxygenation coherence

Supplementary Figure 4 plots the IHR-fNIRS coherence and phase difference for all 11 fNIRS channels.

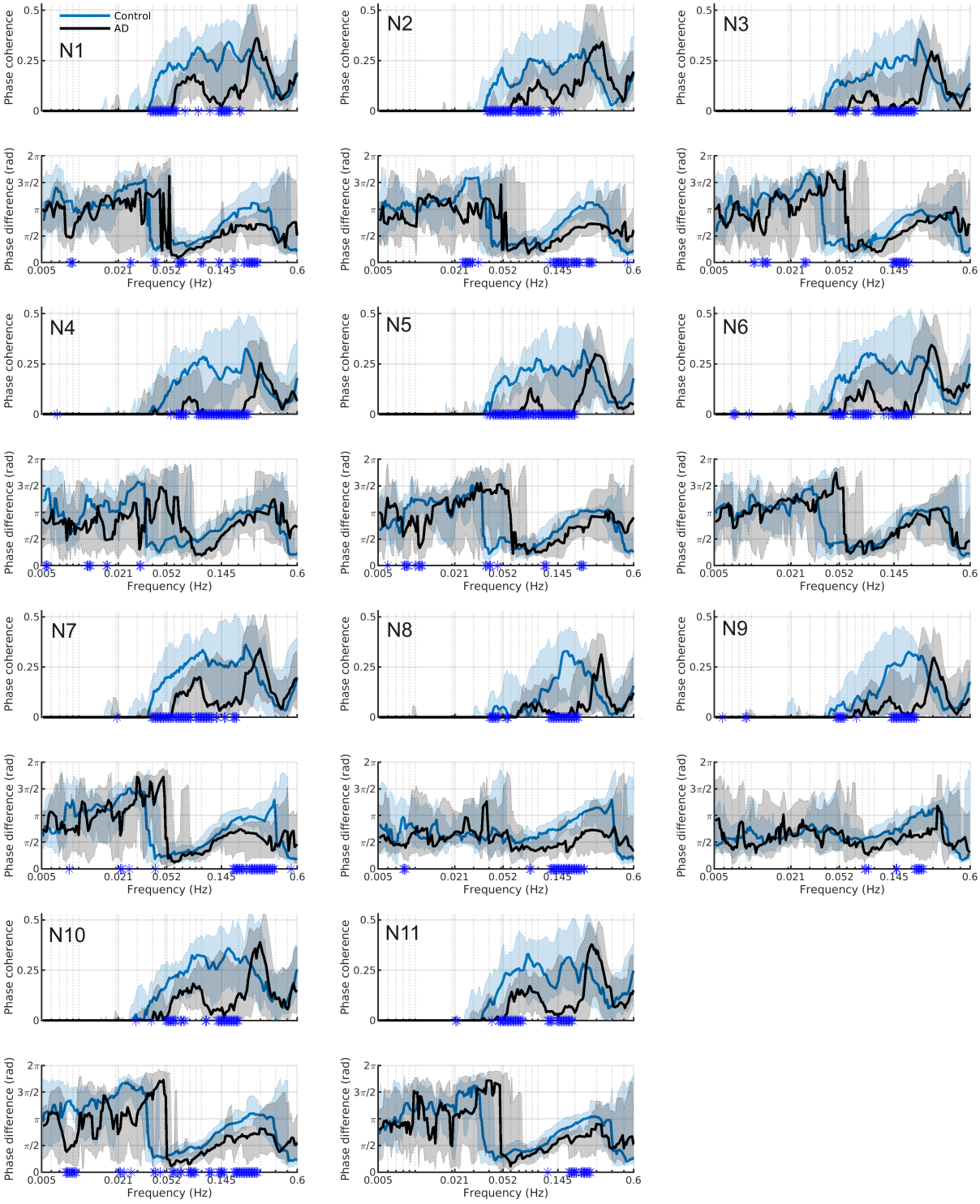

Supplementary Figure 4: Instantaneous heart rate (IHR)–fNIRS coherence and phase difference for all 11 fNIRS channels. The solid black and blue lines show the median group coherence, while the shaded areas show the 25–75th percentiles. Significant differences ($p \leq 0.05$), found using the Wilcoxon rank-sum test, between the groups at particular frequencies are indicated by blue stars on the x-axis. AD = Alzheimer's disease, C = control group. $N = 18$ for controls, $N = 15$ for AD.

4 Respiration and oxygenation coherence

Supplementary Figure 5 plots the Respiration–fNIRS coherence and phase difference for all 11 fNIRS channels.

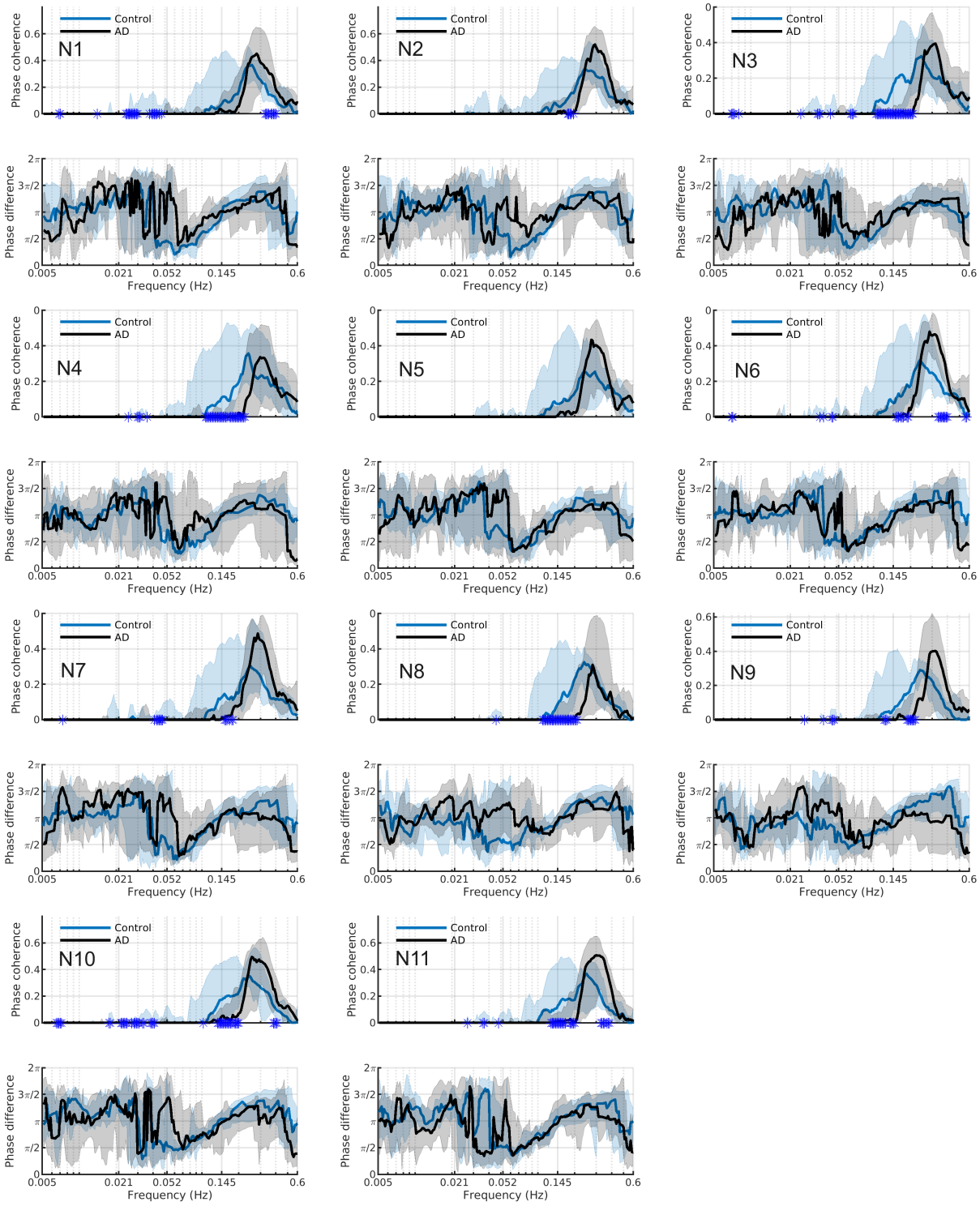

Supplementary Figure 5: Respiration–fNIRS coherence and phase difference for all 11 fNIRS channels. The solid black and blue lines show the median group coherence, while the shaded areas show the 25–75th percentiles. Significant differences ($p \leq 0.05$) between the groups at particular frequencies, found using the Wilcoxon rank-sum test, are indicated by blue stars on the x-axis. AD = Alzheimer's disease, C = control group. N = 14 for controls, N = 19 for AD.

5 Reproducibility of oxygenation power

To verify the reproducibility of our results, we have split the fNIRS time-series into two halves and calculated the wavelet power. The significant differences in power between the two groups for the two segments are shown in the figure below (Supplementary Figure 6). Combined with the IHR power calculated from 300 s (Supplementary Figure 3), this shows that the power results are consistent across segments.

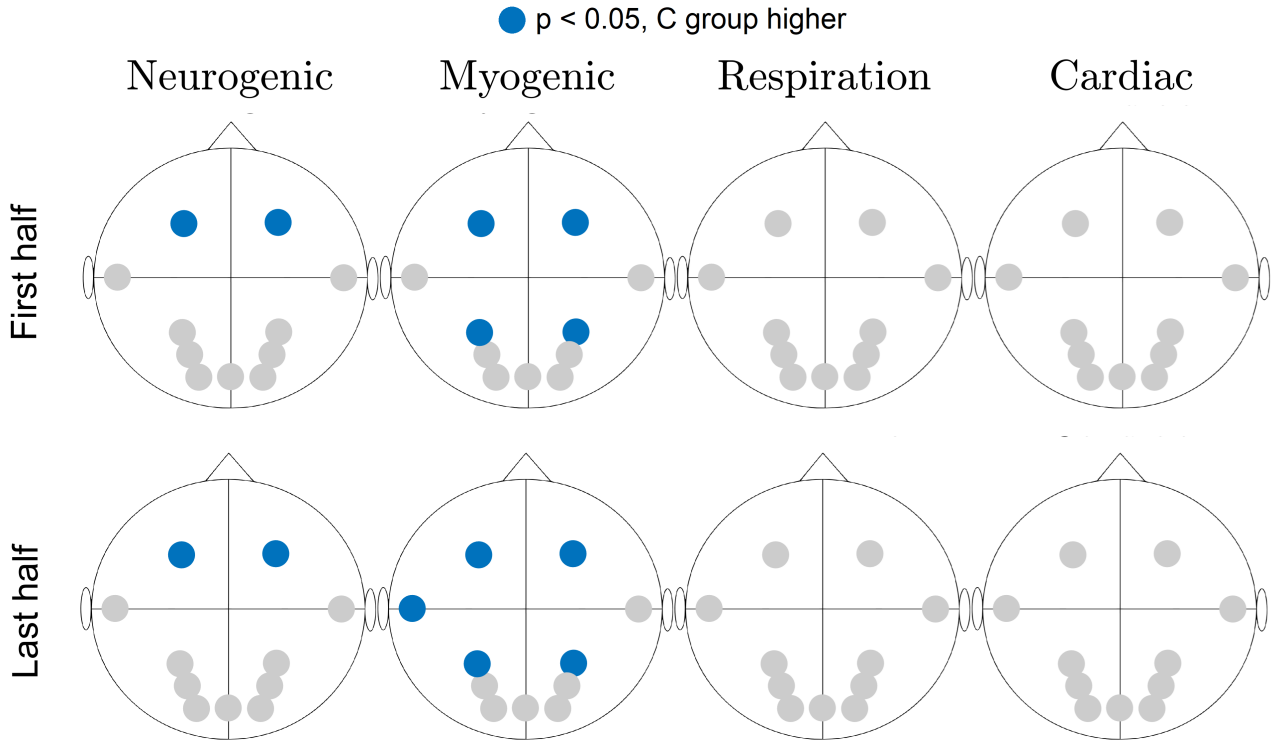

Supplementary Figure 6: Significant differences ($p \leq 0.05$) in fNIRS power between the Alzheimer's disease (AD) and control (C) groups, for fNIRS power calculated for the first and last 12.5 minutes. The Wilcoxon rank-sum test was used. It is evident that the results are consistent with those obtained from the whole-length (25 min) time-series as shown in the main part of the manuscript, Fig. 3. At location N9 there is an additional significant difference between the Alzheimer's disease and control groups in the last half of the recordings. The p-value is 0.35 for the first half and 0.07 for the whole-length. $N = 20$ for the C participants, $N = 19$ for AD patients.

6 EEG analysis, results and discussion

6.1 Analysis

The data acquisition and preparation is described in the main manuscript, as is the wavelet transform power, wavelet phase coherence and statistics. For frequencies up to the delta band the time-series were downsampled to 31.25 Hz, while for frequencies up to the gamma band the time-series were downsampled to 142 Hz. The wavelet transform was used to obtain power and phases for frequencies up to 4 Hz (delta band), while for frequencies up to the gamma band the windowed Fourier transform was used. The frequency bands used are myogenic (0.052-0.145 Hz), respiration (0.145-0.6 Hz), cardiac (0.6-1.7 Hz), delta (1.7-4 Hz), theta (4-7.5 Hz), alpha (7.5-14 Hz), beta (14-22 Hz) and gamma (22-48 Hz).

6.2 Results

The EEG power and phase coherence results are shown in Supplementary Figure 7. The AD group has higher power in the cardiac (2 channels), delta (3 channels), theta (9 channels) and gamma (5 channels) bands. The probability of 3 or more positive findings is 4%, and so the delta, theta and gamma results are significant. The

probability of 2 or more findings is 19%, and the cardiac result is therefore not significant.

For coherence significant differences are:

- AD group has significantly higher coherence in 11 combinations in the theta band, all of which includes the Cz electrode.
- The AD group has significantly higher coherence in 21 combinations (11 of which includes the Cz electrode) in the alpha band, while the control group has higher coherence in 8 combinations.
- The AD group has higher coherence in 15 combinations (8 of which includes the Cz electrode) in the beta, while the control group has higher coherence in 8 combinations.
- The AD group has higher coherence in 8 combinations in the gamma band, and the control group also has higher coherence in 7 combinations.

The probability of 11 significant findings is 3.8%, so the theta, alpha, beta and gamma results are significant. The myogenic and respiration results are not significant.

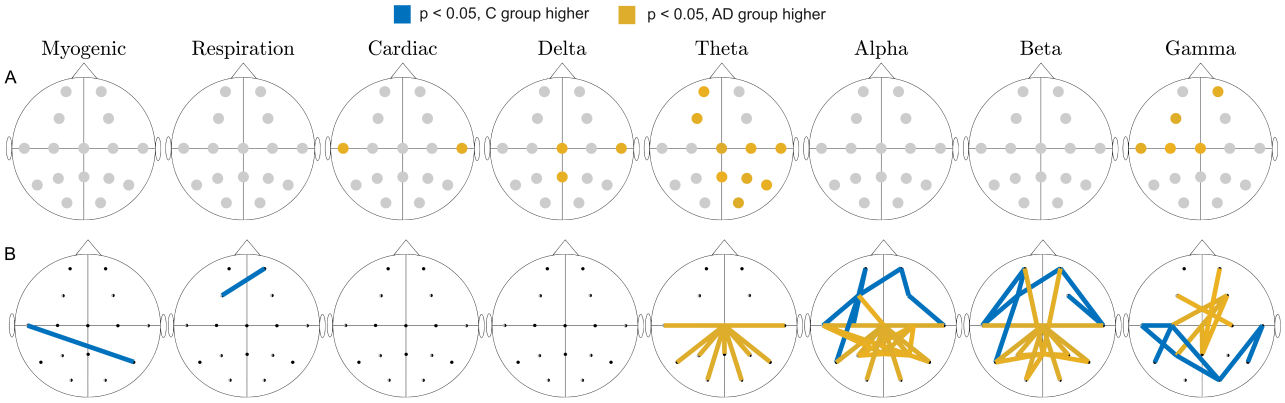

Supplementary Figure 7: (A) Significant differences ($p \leq 0.05$) in the EEG power in different frequency bands between the AD and C groups, found using the Wilcoxon rank-sum test. Orange (blue) circles indicate that the power was higher in the AD (control) group compared to the control (AD) group. Grey circles indicate there are no significant differences between the groups. (B) Significant differences ($p \leq 0.05$) in the EEG coherence in different frequency bands between the AD and C groups, found using the Wilcoxon rank-sum test. Orange (blue) lines indicate that the coherence was higher in the AD (control) group compared to the control (AD) group. AD = Alzheimer's disease, C = control. $N = 20$ for controls, $N = 19$ for AD.

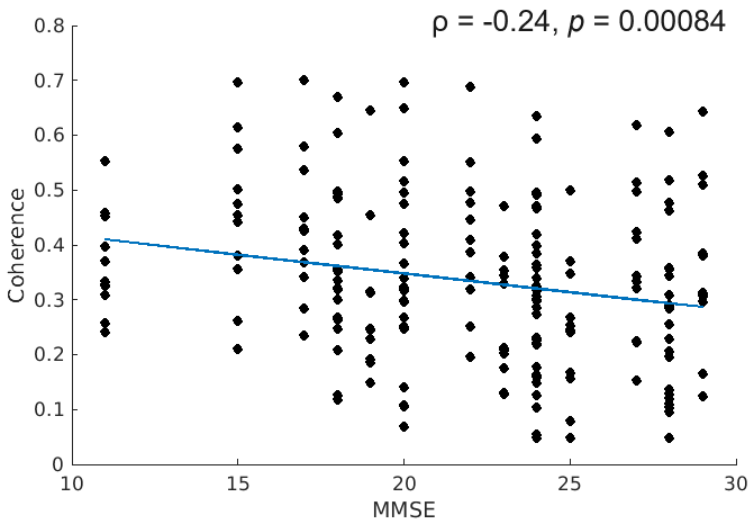

Supplementary Figure 8: Spearman's Rho between alpha coherence for the Cz probe with temporal, central, parietal and occipital probes (11 coherence values per person, shown as black dots) and the MMSE score, for participants with Alzheimer's disease. MMSE = mini mental state exam. The p-value is calculated from a permutation test. The blue line is the best fit linear function based on all data points.

6.3 Discussion

We show that both the power and coherence of EEG time-series are altered in AD, indicating altered neuronal activity. A slowing of the EEG is often found in AD, shown by increases in delta and theta power and decreases in alpha and beta power [1]. We find increases in delta and theta, but not decreases in alpha and beta power. However, our study was done with long, continuous recordings and eyes open, which is different to most EEG studies in AD. Alpha power is known to decrease in the eyes open condition, which might explain why we do not see a decrease [2, 3]. In addition, we see high variability in the alpha power in the AD group, which might also impact our ability to pick up the differences. With the sample sizes we can reliably pick up large effect sizes.

The increased alpha coherence in the central, temporal, parietal and occipital areas in the AD group is negatively correlated with disease stage as evaluated by the mini mental state exam score (Supplementary Figure 8). This could mean that increased coherence is associated with more atrophy, and that less synaptic connections could cause increased coherence. It would also mean that the volume conduction is more severe in the later stages of disease, and that causes increased coherence between EEG time-series from different probes.

Supplementary references

[1] Babiloni, C. *et al.* Abnormalities of cortical neural synchronization mechanisms in subjects with mild cognitive impairment due to Alzheimer's and Parkinson's diseases: An EEG study. *J. Alzheimer's. Dis.* **59**, 339–358 (2017).

[2] Kan, D. P. X., Croarkin, P. E., Phang, C. K. & Lee, P. F. EEG differences between eyes-closed and eyes-open conditions at the resting stage for euthymic participants. *Neurophysiology* **49**, 432–440 (2017).

[3] Stankovski, T., Ticcinelli, V., McClintock, P. V. E. & Stefanovska, A. Neural cross-frequency coupling functions. *Front. Syst. Neurosci.* **11**, 33 (2017).

Supplementary Material for "The phase coherence of the neurovascular unit is reduced in Huntington's disease"

Juliane Bjerkan[1], Jan Kobal[2], Gemma Lancaster[1], Bernard Meglič[2], Peter V. E. McClintock[1], Karol Budohoski[3], Peter Kirkpatrick[4], Aneta Stefanovska[1,*]

[1]Department of Physics, Lancaster University, Lancaster, UK
[2] University Medical Centre, Ljubljana, Slovenia
[3] Department of Neurosurgery, Cambridge University Hospitals NHS Trust, Cambridge, UK
[4] Addenbrooke's Hospital, University of Cambridge, Cambridge, UK
[*] Corresponding author

Contents

1 Introduction

This document contains supplementary material for the paper "The phase coherence of the neurovascular unit is reduced in Huntington's disease". The lay-out of the fNIRS and EEG probes used to record data discussed in the paper is shown in Supplementary Figure 1.

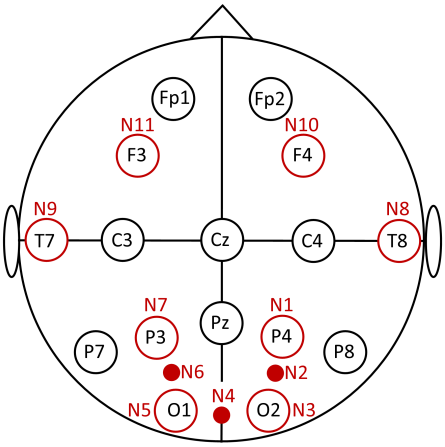

Supplementary Figure 1: EEG electrode and fNIRS channel placements. Note that in 8 locations EEG and fNIRS probes are co-located.

2 Effect sizes

2.1 The effect size that can be reliably detected

The data for this study were collected in April and May 2018. The effect size sensitivity was calculated based on a power of 0.8, a significance level of 0.05 and considering the existing sample sizes. We then found the effect size that the study can reliably pick up. It is 1.03 for the pre-symptomatic HD and 0.96 for the symptomatic HD, which means the study can reliably find large differences between the groups. The calculations were done using G*Power [3], and an example is shown in Supplementary Figure 2.

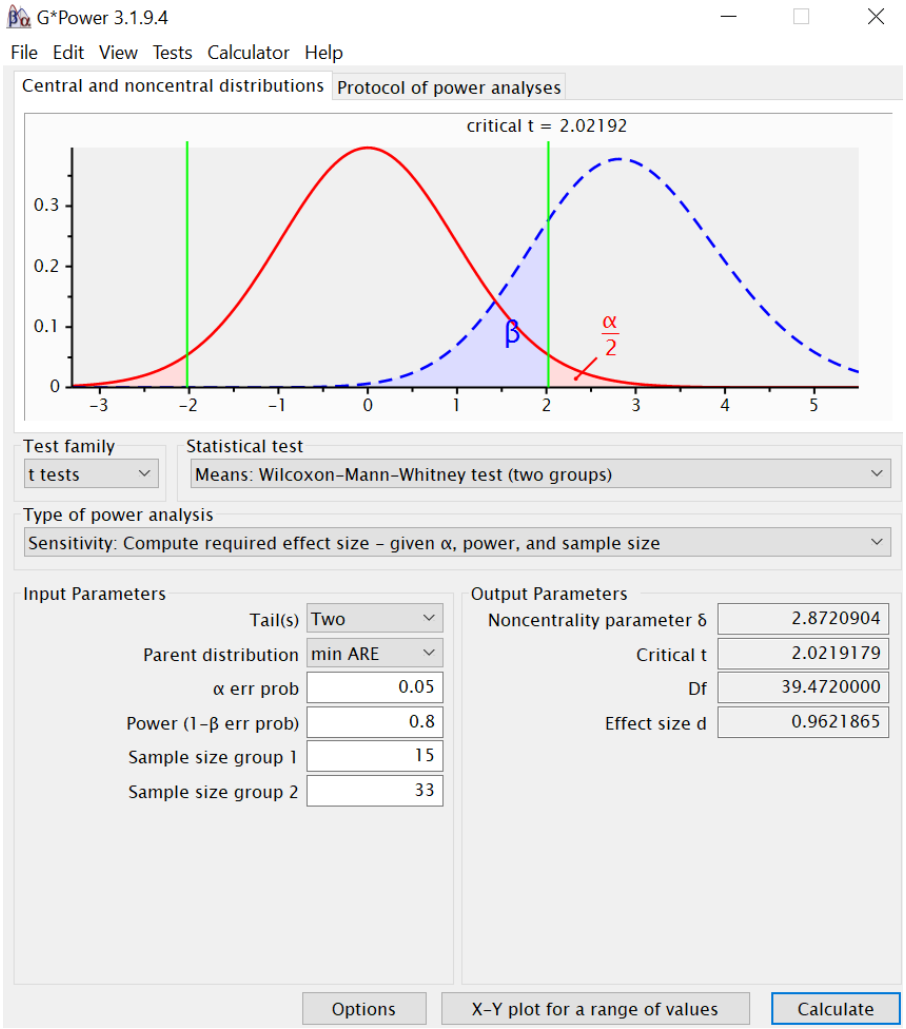

Supplementary Figure 2: Screenshot from G*Power, showing the calculation of the effect size that this study can reliably detect in the case of the S vs. SC comparisons. S = symptomatic HD, SC = control group for S.

2.2 Evaluation of the effect size

The effect size was calculated post-hoc using Cohen's d with a non-parametric adjustment [4, 5]. The z-value is the standard score, calculated from the ranks when applying the Wilcoxon rank-sum test [6]. Based on the z-value, r is calculated as

$$r = \frac{z}{\sqrt{N}}, \tag{1}$$

where N is the number of participants [6]. Cohen's d is found as

$$d = \frac{2 \times r}{\sqrt{1 - r^2}}. \tag{2}$$

A Cohen's d greater than 0.8 is considered large, while a value between 0.5 and 0.8 is considered medium. The results are summarised in Supplementary Table 1. The effect size is calculated for cases where $p \leq 0.05$ was obtained, so that the differences are statistically significant. For the coherence and alpha power, we show the minimum, maximum and mean effect size of all significant combinations. The results are summarised in Supplementary Table 1, and a large effect size obtained from the nonparametric Cohen's d is indicated in red, while a medium effect size is indicated in blue.

	Cohen's d	Nonparametric Cohen's d	r
Neurogenic fNIRS power (P vs. PC)	11: 0.7477 10: 0.6159 6: 0.6295 5: 0.6462 1: 0.6852	11: 0.9139 10: 0.6832 6: 0.7031 5: 0.8917 1: 0.6552	11: 0.4156 10: 0.3233 6: 0.3317 5: 0.4072 1: 0.3113
Myogenic fNIRS power (P vs. PC)	7: 0.8727 6: 0.7175 5: 0.5528 3: 0.6534 1: 0.5910	7: 0.8664 6: 0.8917 5: 0.8056 3: 0.7435 1: 0.8054	7: 0.3975 6: 0.4072 5: 0.3736 3: 0.3484 1:0.3736
Respiration fNIRS power (S vs. SC)	11: -0.8829 10: -0.7625 9: -0.3611 3: -0.9170 1: -0.6217	11: -0.8026 10: -0.7628 9: -0.8695 3: -0.6014 1: -0.6840	11: -0.3724 10: -0.3564 9: -0.3987 3: -0.2879 1: -0.3082
Cardiac fNIRS coherence (S vs. SC)	mean: 0.7472 min: 0.4294 max: 1.0601	mean: 0.7078 min: 0.5963 max: 0.8932	mean: 0.3331 min: 0.2857 max: 0.4078
Alpha EEGpower (S vs. SC)	mean: 0.3929 min: 0.1631 max: 0.6060	mean: 1.0876 min: 0.7945 max: 1.3436	mean: 0.4755 min: 0.3692 max: 0.5576
Alpha EEG coherence (P vs. PC)	mean: 0.4089 min: 0.0260 max: 1.2901	mean: 0.3502 min: -0.1431 max: 1.1026	mean: 0.1645 min: -0.0714 max: 0.4828
Alpha EEG coherence (S vs. SC)	mean: 0.9125 min: 0.6276 max: 1.5763	mean: 0.8018 min: 0.6036 max: 1.3697	mean: 0.3680 min: 0.2889 max: 0.5650
Gamma EEG coherence (S vs. SC)	mean: 0.5813 min: -0.1480 max: 1.0744	mean: 0.5933 min: -0.1158 max: 1.0153	mean: 0.2757 min: -0.0578 max: 0.4527
Neurogenic fNIRS-EEG coherence (P vs. PC)	mean: 0.5312 min: -0.4892 max: 0.9318	mean: 0.7368 min: -0.7535 max: 1.2932	mean: 0.3331 min: -0.3526 max: 0.5430
Myogenic fNIRS-EEG coherence (P vs. PC)	mean: 0.6225 min: 0.4273 max: 0.7684	mean: 0.8010 min: 0.6352 max: 1.1704	mean: 0.3698 min: 0.3027 max: 0.5051
Myogenic fNIRS-EEG coherence (S vs. SC)	mean: 0.6491 min: 0.4668 max: 0.7548	mean: 0.7136 min: 0.5900 max: 0.9560	mean: 0.3350 min: 0.2830 max: 0.4313

Supplementary Table 1: Effect size for the significant parameters, using the parametric Cohen's d (refered to as Cohen's d), nonparametric Cohen's d, and r. For the fNIRS power the effect size is calculated for each probe where a significant difference is found. The information is given as probe: effect size. For coherence and alpha power the effect size is calculated for the significant combinations/electrodes, and we show the mean, minimum and maximum values. Positive values mean that the control groups had higher values than the HD groups, while negative values mean the opposite. For the nonparametric Cohen's d, large effect sizes are indicated in red and medium effect sizes in blue. S = symptomatic HD, SC = control group for S, P = presymptomatic HD, PC = control group for P.

3 Permutation test

For the fNIRS, EEG and fNIRS–EEG power/coherence calculations, significant differences were assessed also using a Monte-Carlo permutation test. Participants from the P and CP groups were randomly placed into two groups of size 13 and 29, while participants from the S and SC groups were randomly placed into two groups of size 15 and 33. The Wilcoxon rank-sum test was then applied to test for differences between these groups. After $\sim$ 16000 permutations of the groups, the original p-value was compared to the new ones. Supplementary Figure 3 shows an example. 95.1% of the randomly found p-values were above 0.05, and the original p-value was smaller than 98.7% of them. Another example is shown in Supplementary Figure 4. 95.2% of the randomly found p-values were above 0.05, and the original p-value was smaller than 97.5% of them.

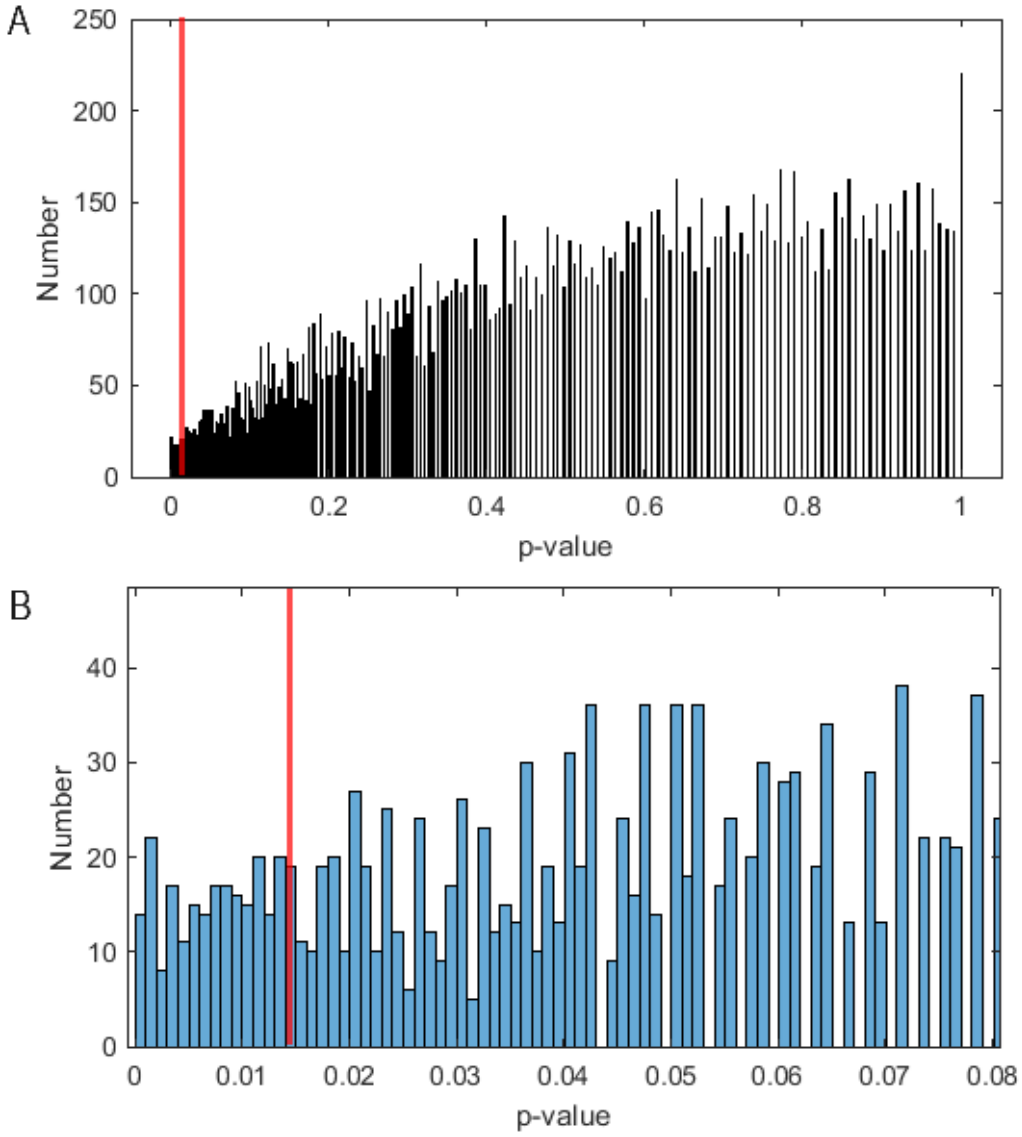

Supplementary Figure 3: (A) Histogram of the p-values obtained for fNIRS-EEG coherence in the myogenic band at EEG P8 and fNIRS 10, for the S and SC groups. The red line is the original p-value. There are 1000 bins in the histogram. (B) Zoom of the smaller p-values in (A).

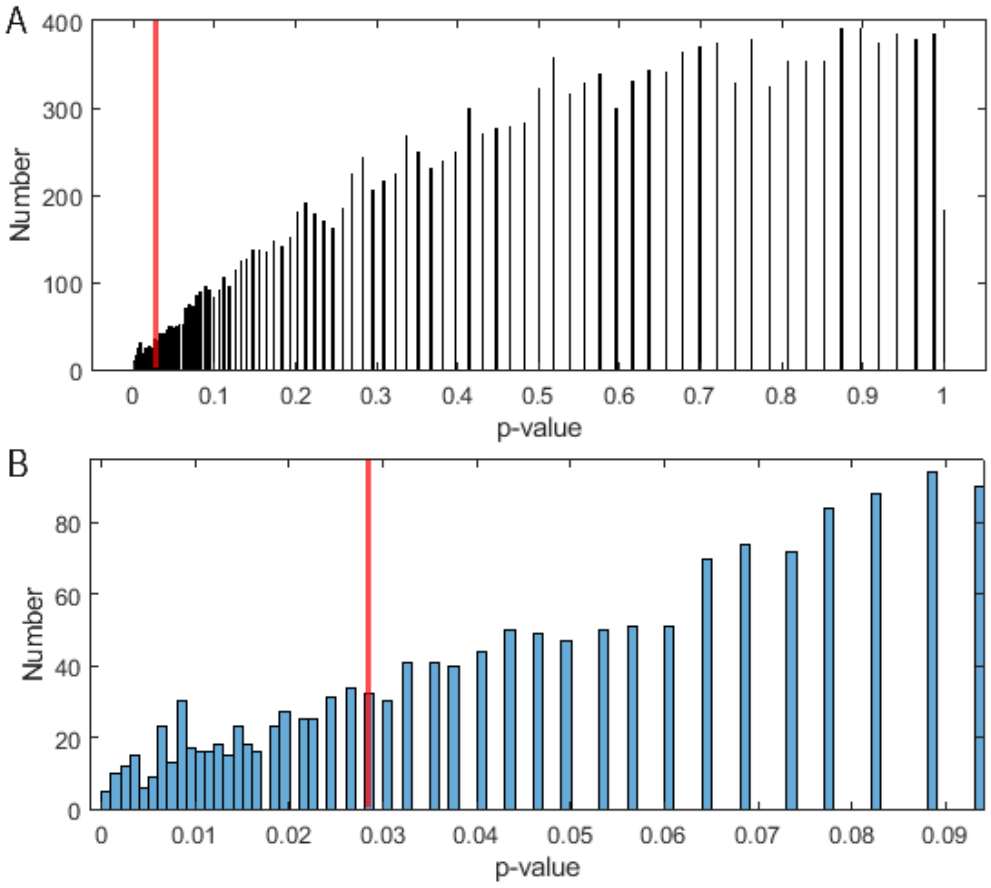

Supplementary Figure 4: (A) Histogram of the p-values obtained for fNIRS myogenic power at probe 1 for the P and PC groups. The red line is the original p-value. There are 1000 bins in the histogram. (B) A zoom of the smaller p-values shown in (A),

4 Reproducibility

The number of participants is a limiting factor in our study, which raises the important question of the reproducibility of the results obtained. Due to the intensive nature of the experimental protocol further measurements are not possible at this time. We have therefore addressed reproducibility in the following ways:

- Where appropriate we have compared the first and last 10 minutes of recordings, to assess the consistency of the differences between the groups throughout the session. We did this for the fNIRS and EEG power, but not for the coherence calculations as the latter comparisons require longer recordings. The results of the power comparisons can be seen in Supplementary Figures 5 and 6.
- When comparing the coherence between groups, only the effective coherence was considered. The effective coherence is found by subtracting the 95th percentile of the surrogate coherences found at each frequency, creating a high surrogate threshold [7, 8]. This ensures that the coherence is statistically significant.
- We have used long recordings (20 minutes). The properties analysed must be present over sufficient time for significant differences between groups to be detected: sporadic, random changes would average out over time in such long recordings.

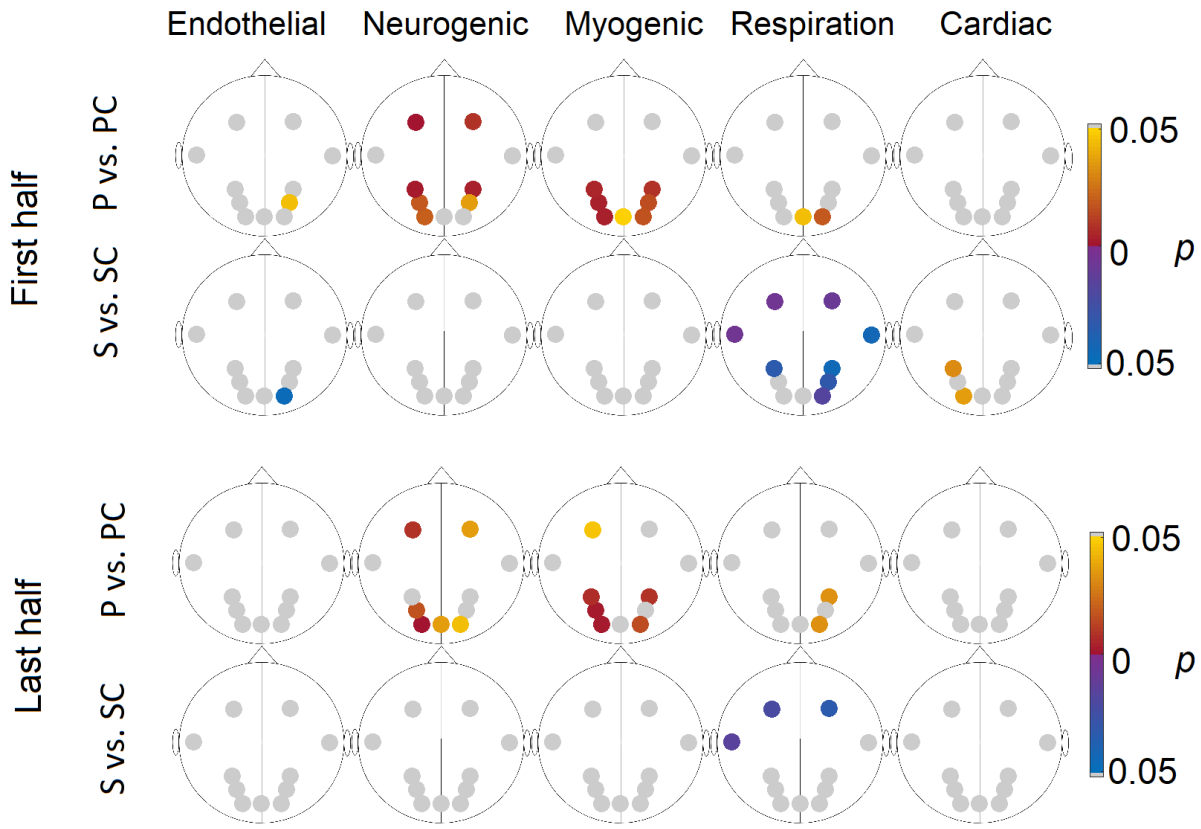

Supplementary Figure 5: Significant p-values, found using the Wilcoxon rank-sum test, for oxyHb power for the first 10 minutes of the signals and the last 10 minutes of the signals. The first rows are between the P and PC groups, while the second rows are between the S and SC groups. Yellow/red (blue/purple) circles indicate that the power is higher in the controls (HDs). P = presymptomatic Huntington's disease, S = symptomatic Huntington's disease, PC = control group for P, SC = control group for S.

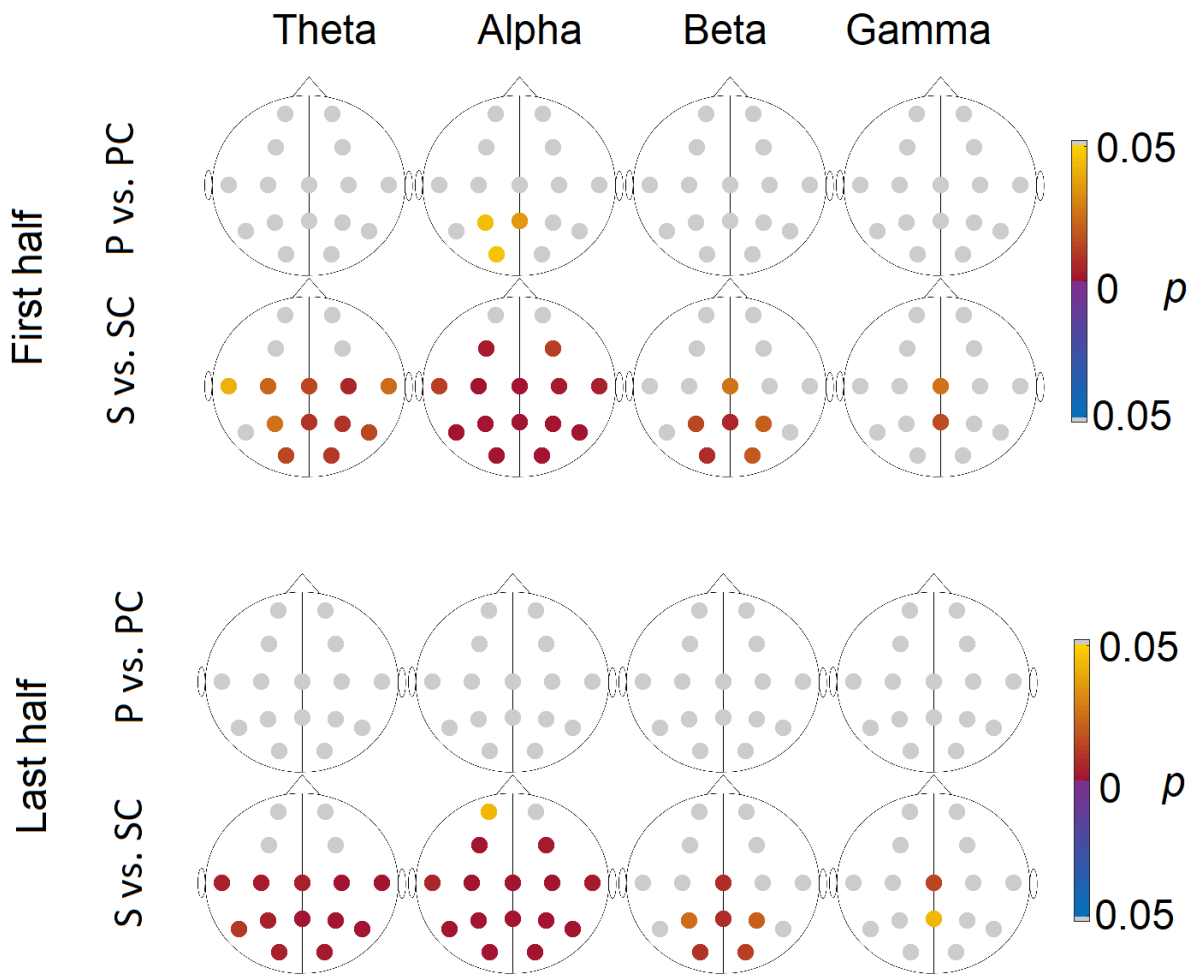

Supplementary Figure 6: Significant p-values, found using the Wilcoxon rank-sum test, for EEG power for the first 10 minutes of the signals and the last 10 minutes of the signals. The first rows are between the P and PC groups, while the second rows are between the S and SC groups. Yellow/red (blue/purple) circles indicate that the power is higher in the controls (HDs). P = presymptomatic Huntington's disease, S = symptomatic Huntington's disease, PC = control group for P, SC = control group for S.

5 Peak detection vs. ridge extraction

We compared the instantaneous heart rate (IHR) results obtained by ridge extraction to those obtained by peak detection. Two examples in the time-domain are shown in Supplementary Figure 7.

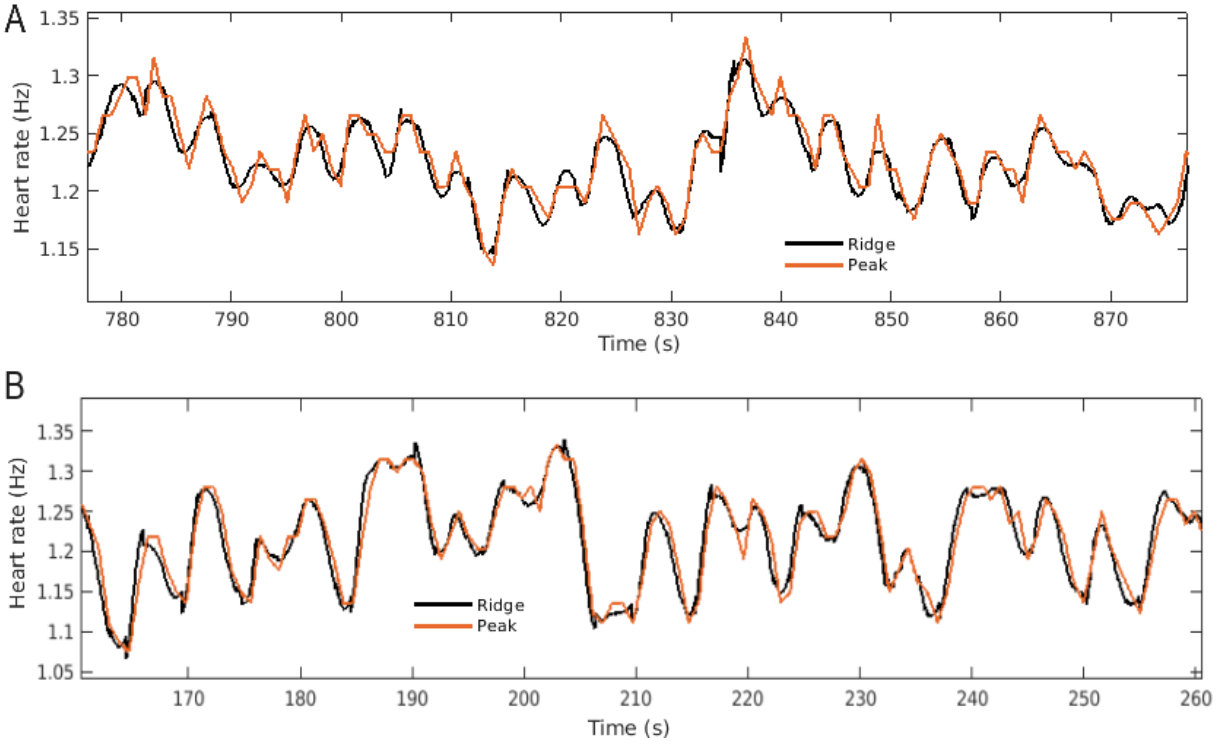

Supplementary Figure 7: Examples of heart rate found from ridge extraction and peak detection, for (A) one control participant and (B) one Huntington's disease participant.

For the coherence results we obtain similar results with both methods: lower respiration-IHR coherence for the S group (Supplementary Figure 8), lower fNIRS-IHR coherence between 0.052-0.1Hz in the P group for N2, N3, N4, N5 and N6 (Supplementary Figures 9 and 11) and a smaller fNIRS-IHR phase shift around 0.1Hz for the S group (Supplementary Figures 10 and 12). The phase difference is no longer negative in the respiration range, likely due to the discontinuity in phase difference at $\pm\pi$. The IHR power is increased, probably due to difficultly in detecting an R-peak when there is a movement artifact. For the reasons outlined in the main text the results in the paper are shown for the ridge extraction.

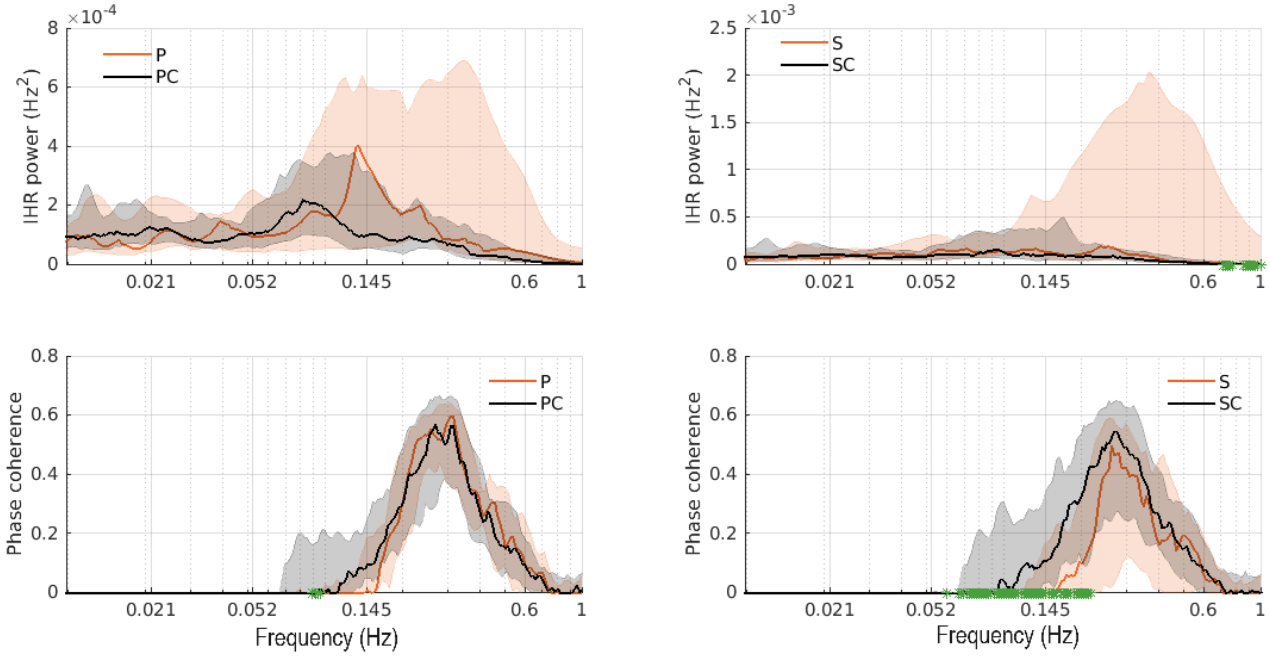

Supplementary Figure 8: The top row shows the instantaneous heart rate power (found with peak detection), for the P and PC groups (left), and for the S and SC groups (right). The instantaneous heart rate and respiration coherence are shown in the bottom row. The solid lines show the median group coherence, while the shaded areas show the 25–75th percentiles. Significant differences (p<0.05), found using the Wilcoxon rank-sum test, between the groups at particular frequencies are indicated by green stars on the x-axis. P = presymptomatic Huntington's disease, S = symptomatic Huntington's disease, PC = control group for P, SC = control group for S.

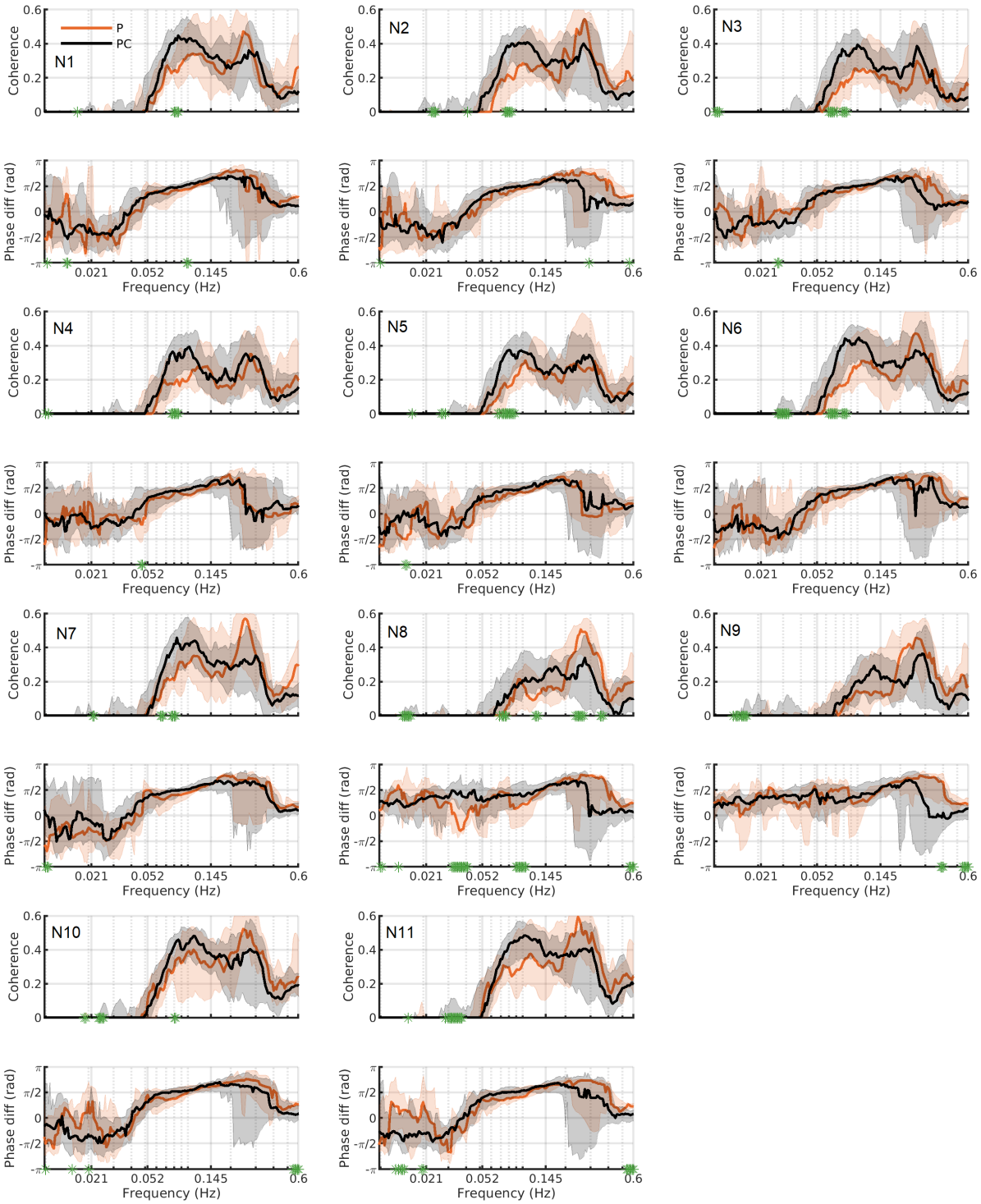

Supplementary Figure 9: Peak IHR–fNIRS coherence and phase difference for all 11 fNIRS channels (see Supplementary Figure 1 for locations). The solid lines show the median group coherence, while the shaded areas show the 25–75th percentiles. Significant differences ($p<0.05$), found using the Wilcoxon rank-sum test, between the groups at particular frequencies are indicated by green stars on the x-axis. P = presymptomatic Huntington's disease, S = symptomatic Huntington's disease, PC = control group for P, SC = control group for S.

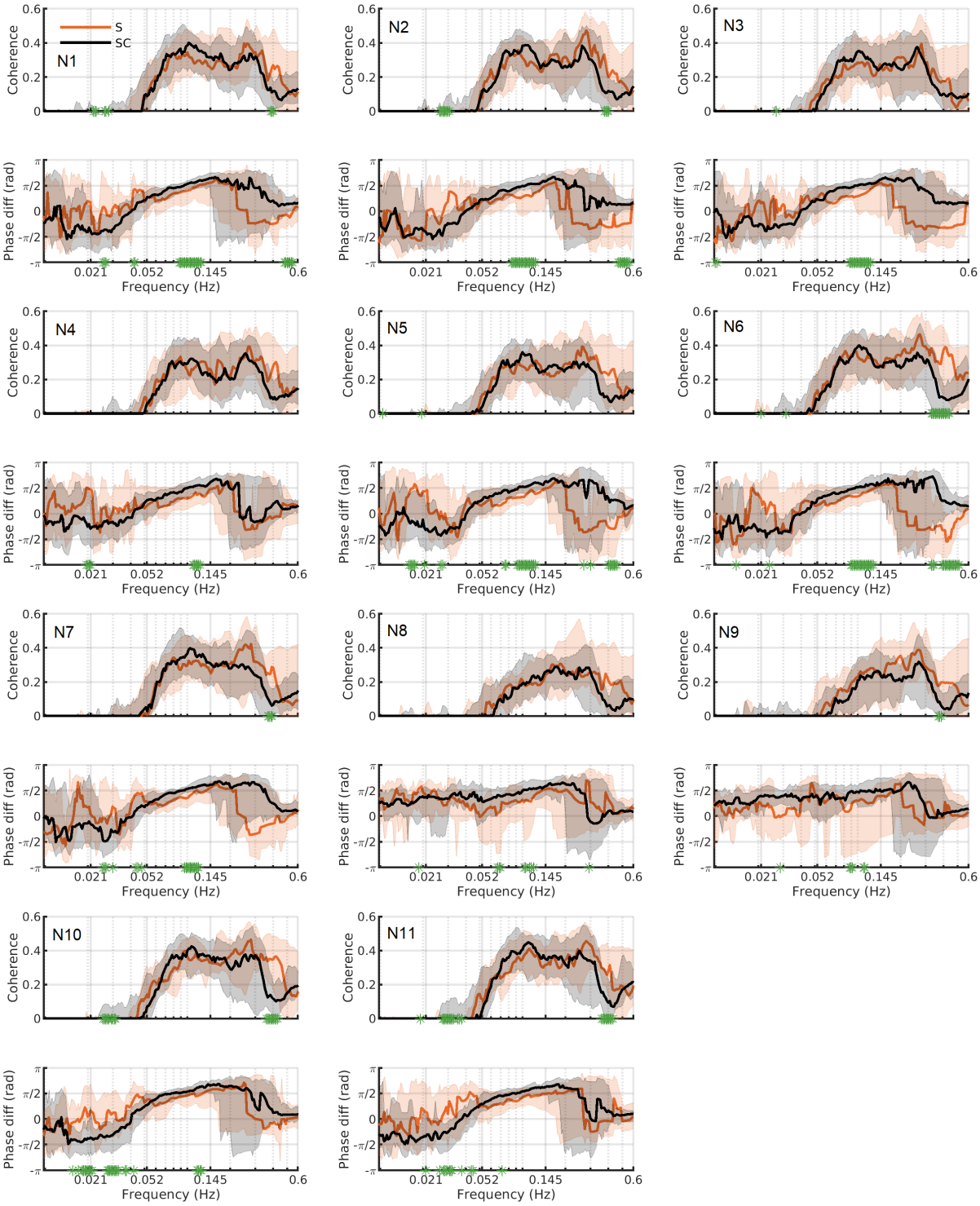

Supplementary Figure 10: Peak IHR–fNIRS coherence and phase difference for all 11 fNIRS channels (see Supplementary Figure 1 for locations). The solid lines show the median group coherence, while the shaded areas show the 25–75th percentiles. Significant differences ($p<0.05$), found using the Wilcoxon rank-sum test, between the groups at particular frequencies are indicated by green stars on the x-axis. P = presymptomatic Huntington's disease, S = symptomatic Huntington's disease, PC = control group for P, SC = control group for S.

6 Heart and respiration rates, coherence with fNIRS

6.1 IHR–fNIRS coherence

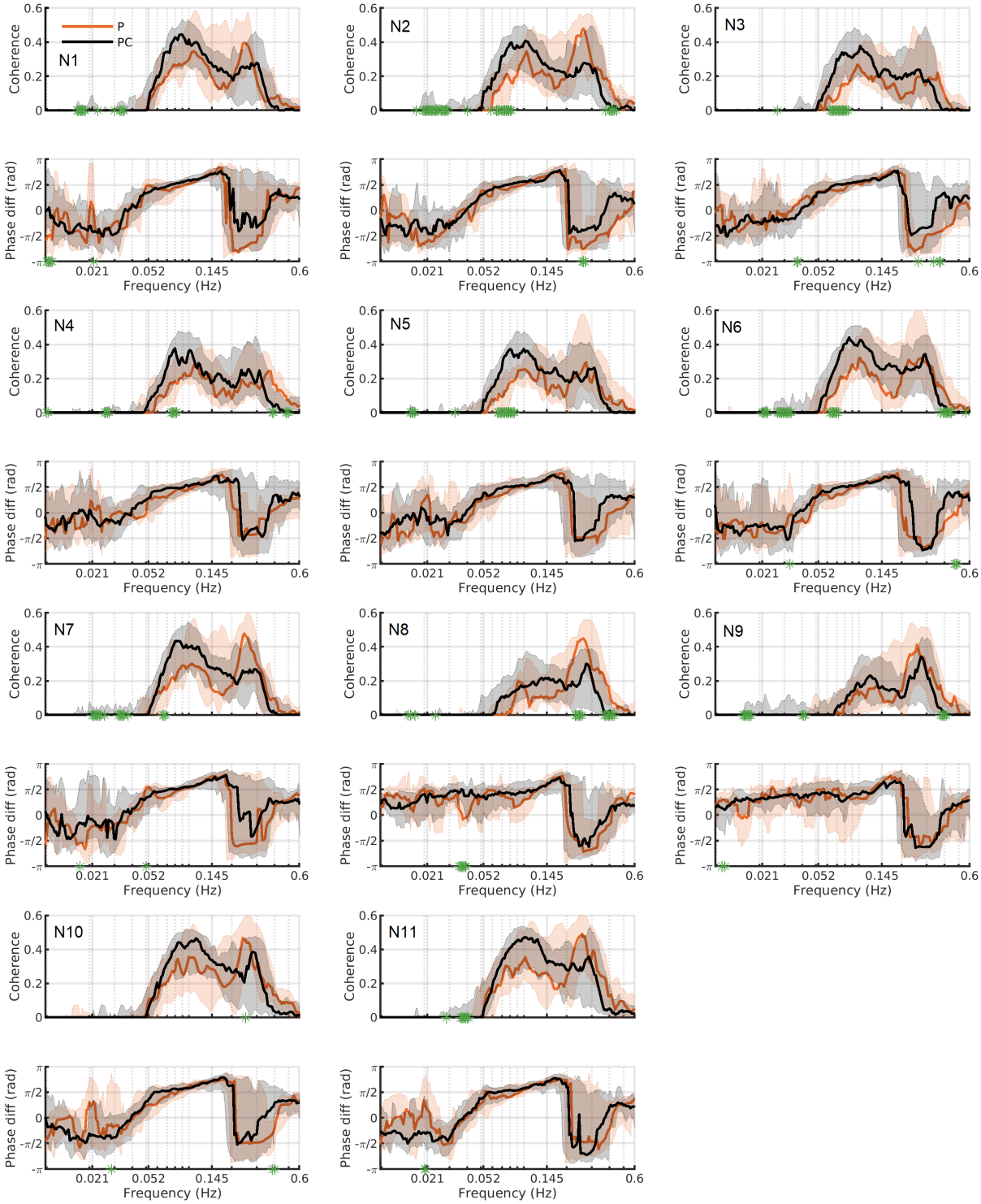

Supplementary Figure 11: IHR–fNIRS coherence and phase difference for all 11 fNIRS channels (see Supplementary Figure 1 for locations). The solid lines show the median group coherence, while the shaded areas show the 25–75th percentiles. Significant differences ($p<0.05$), found using the Wilcoxon rank-sum test, between the groups at particular frequencies are indicated by green stars on the x-axis. P = presymptomatic Huntington's disease, PC = control group for P.

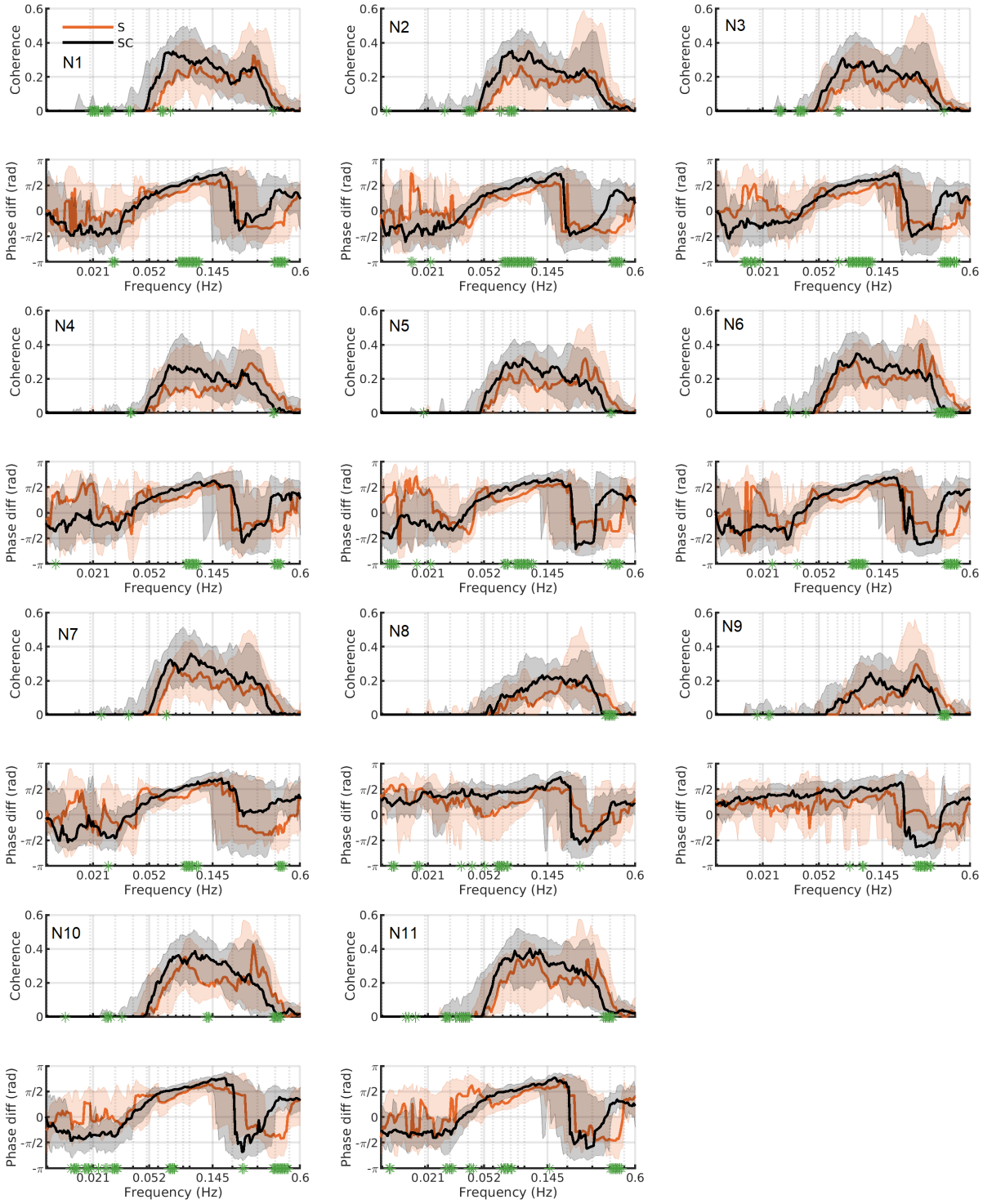

Supplementary Figure 12: IHR–fNIRS coherence and phase difference for all 11 fNIRS channels (see Supplementary Figure 1 for locations). The solid lines show the median group coherence, while the shaded areas show the 25–75th percentiles. Significant differences ($p<0.05$), found using the Wilcoxon rank-sum test, between the groups at particular frequencies are indicated by green stars on the x-axis. S = symptomatic Huntington's disease, SC = control group for S.

6.2 Respiration–fNIRS coherence

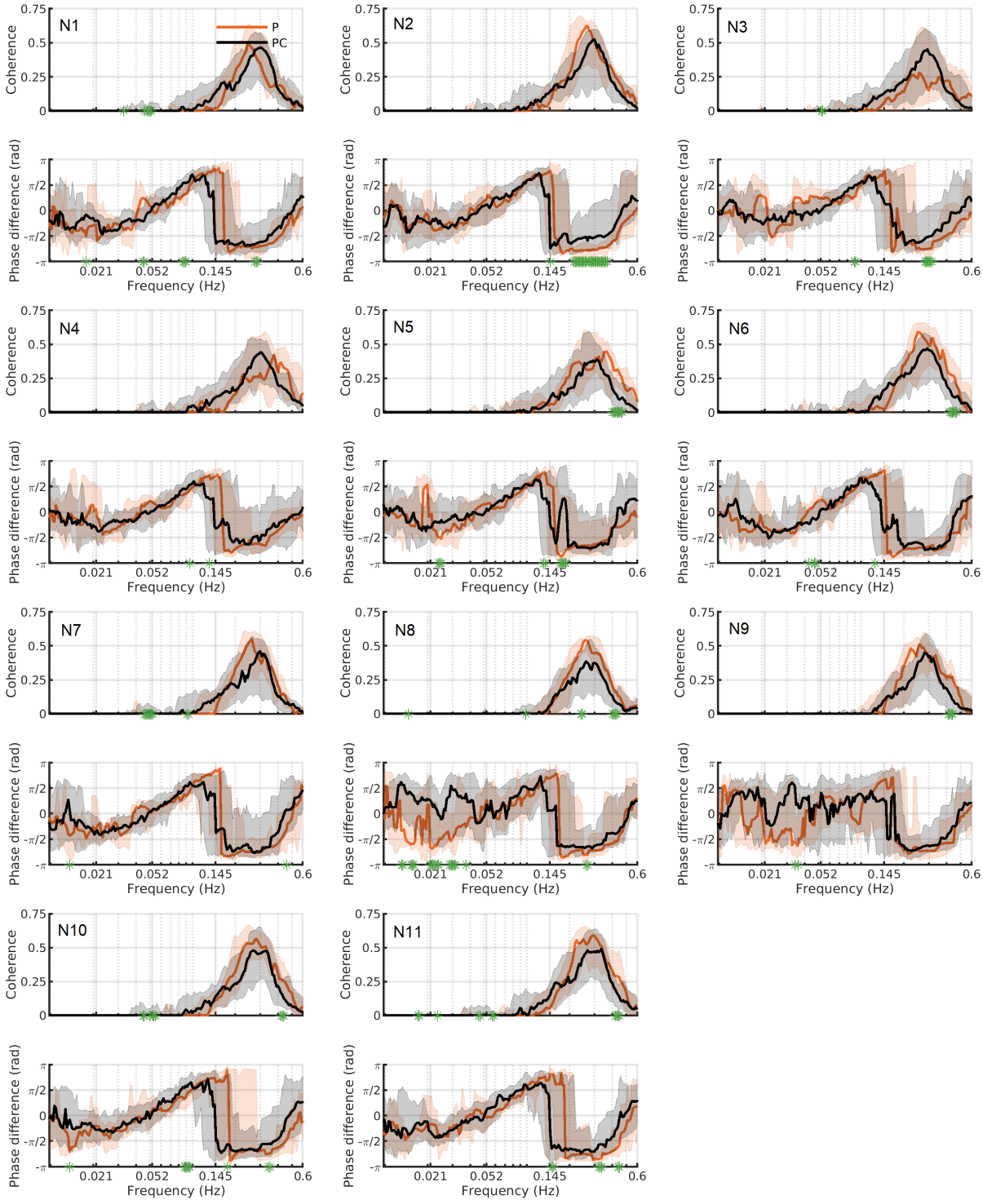

Supplementary Figure 13: Respiration–fNIRS coherence and phase difference for all 11 fNIRS channels (see Supplementary Figure 1 for locations). The solid lines show the median group coherence, while the shaded areas show the 25–75th percentiles. Significant differences ($p<0.05$), found using the Wilcoxon rank-sum test, between the groups at particular frequencies are indicated by green stars on the x-axis. P = presymptomatic Huntington's disease, PC = control group for P.

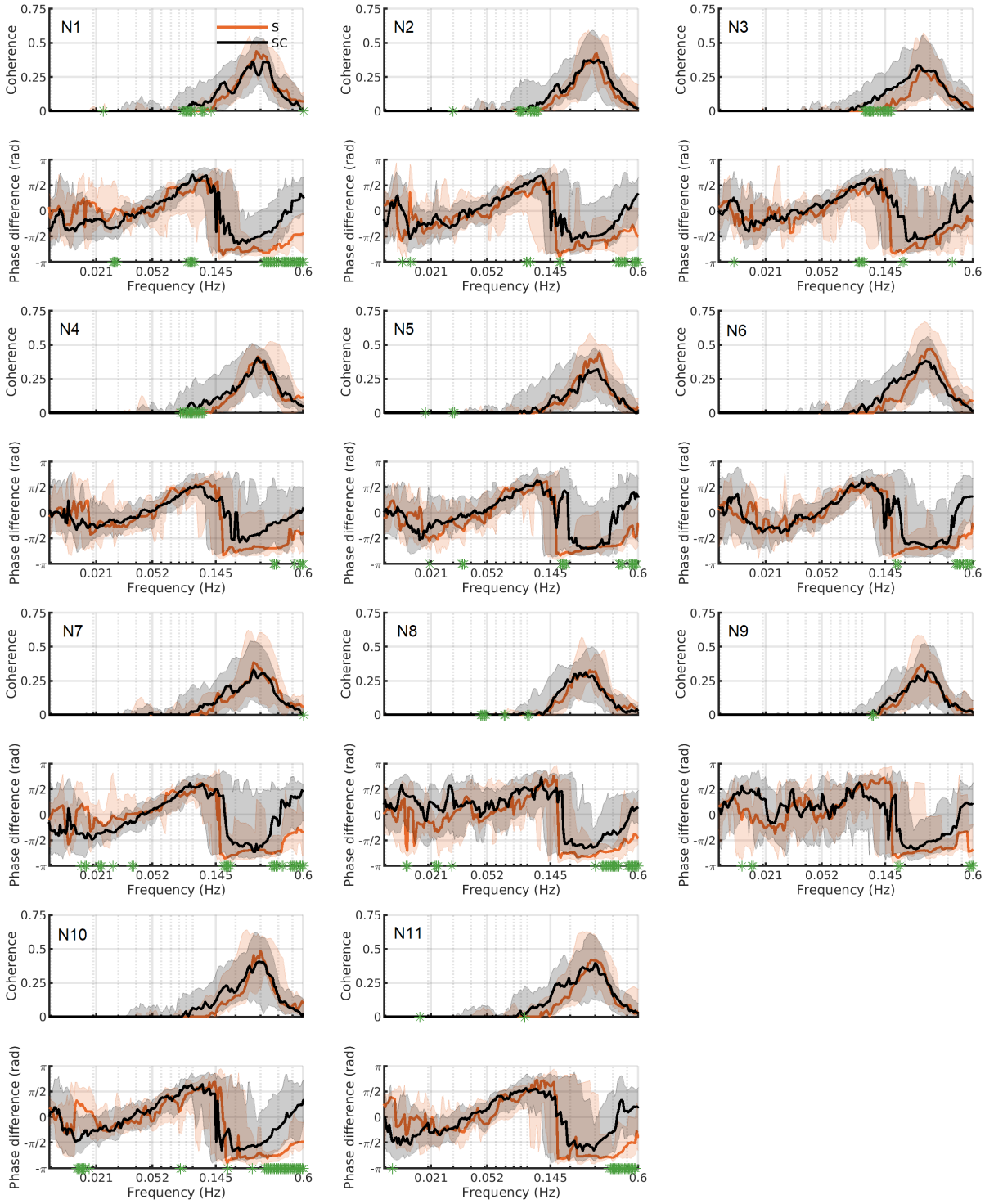

Supplementary Figure 14: Respiration–fNIRS coherence and phase difference for all 11 fNIRS channels (see Supplementary Figure 1 for locations). The solid lines show the median group coherence, while the shaded areas show the 25–75th percentiles. Significant differences ($p<0.05$), found using the Wilcoxon rank-sum test, between the groups at particular frequencies are indicated by green stars on the x-axis. S = symptomatic Huntington's disease, SC = control group for S.

6.3 IRR–fNIRS coherence

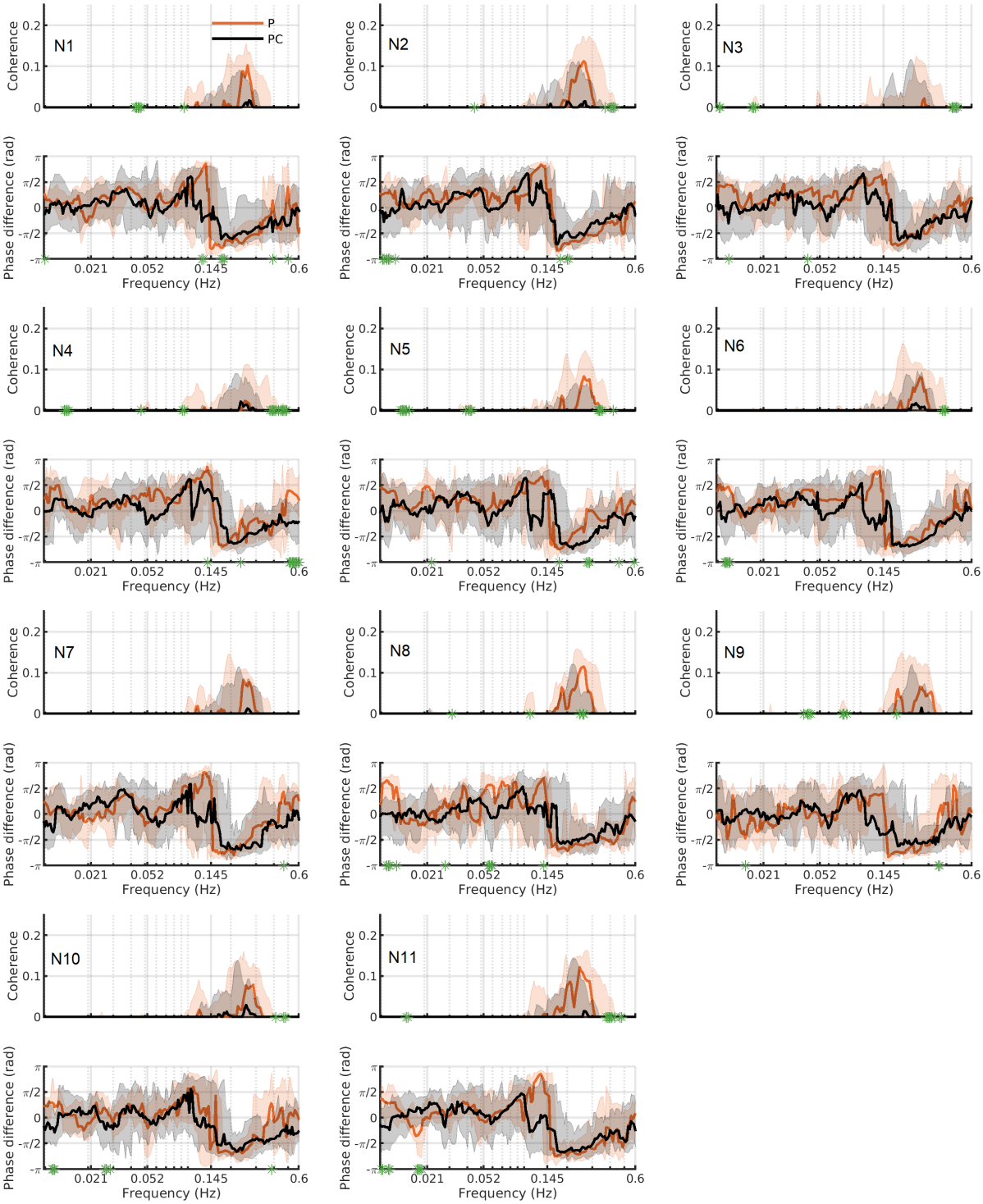

Supplementary Figure 15: IRR–fNIRS coherence and phase difference for all 11 fNIRS channels (see Supplementary Figure 1 for locations). The solid lines show the median group coherence, while the shaded areas show the 25–75th percentiles. Significant differences ($p<0.05$), found using the Wilcoxon rank-sum test, between the groups at particular frequencies are indicated by green stars on the x-axis. P = presymptomatic Huntington's disease, PC = control group for P.

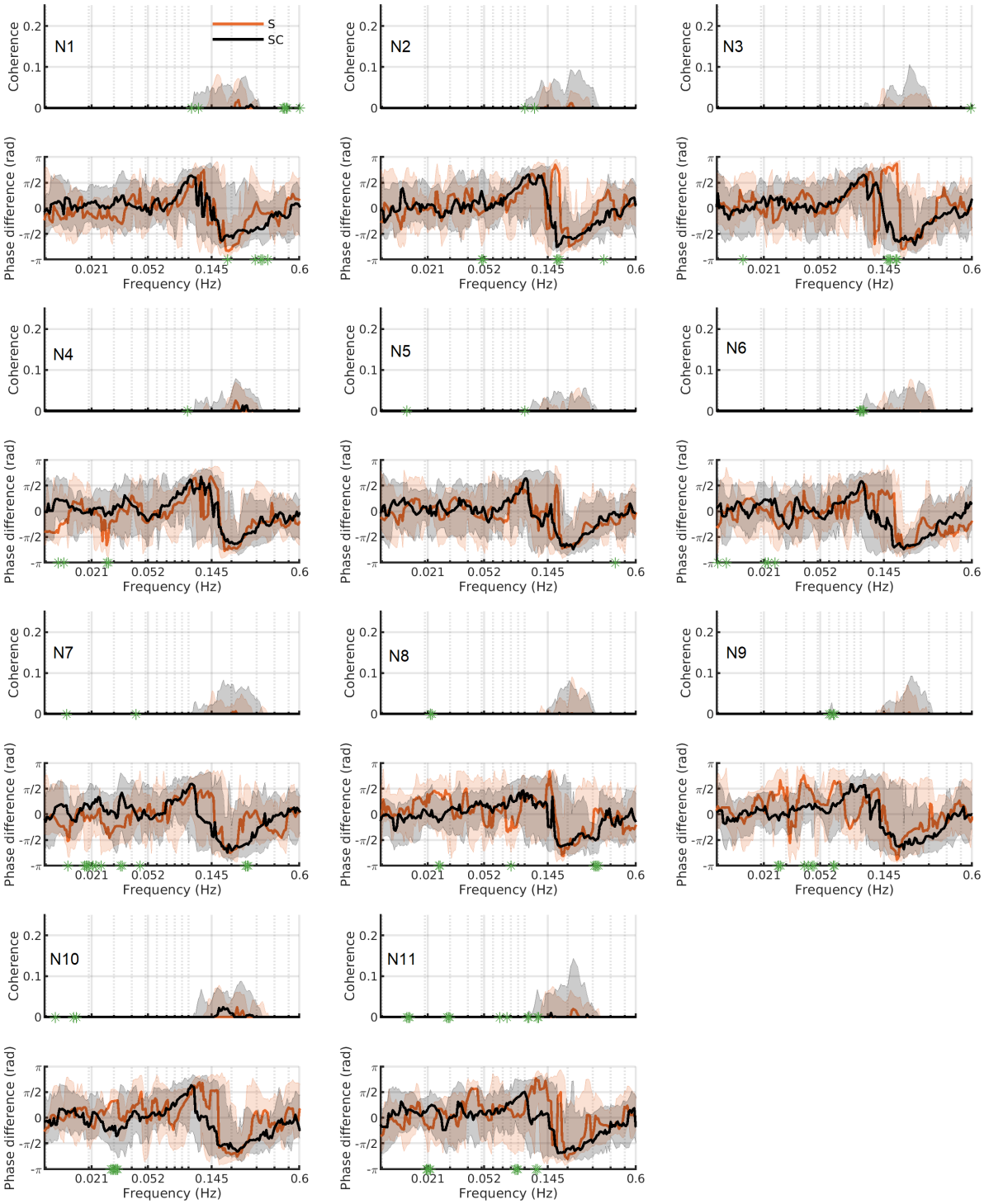

Supplementary Figure 16: IRR–fNIRS coherence and phase difference for all 11 fNIRS channels (see Supplementary Figure 1 for locations). The solid lines show the median group coherence, while the shaded areas show the 25–75th percentiles. Significant differences ($p<0.05$), found using the Wilcoxon rank-sum test, between the groups at particular frequencies are indicated by green stars on the x-axis. S = symptomatic Huntington's disease, SC = control group for S.

7 fNIRS power and coherence

Supplementary Figure 17 shows the fNIRS power (A) and coherence (B) results for the five cardiovascular frequency bands. Due to the high surrogate threshold we do not show the coherence in the endothelial band.

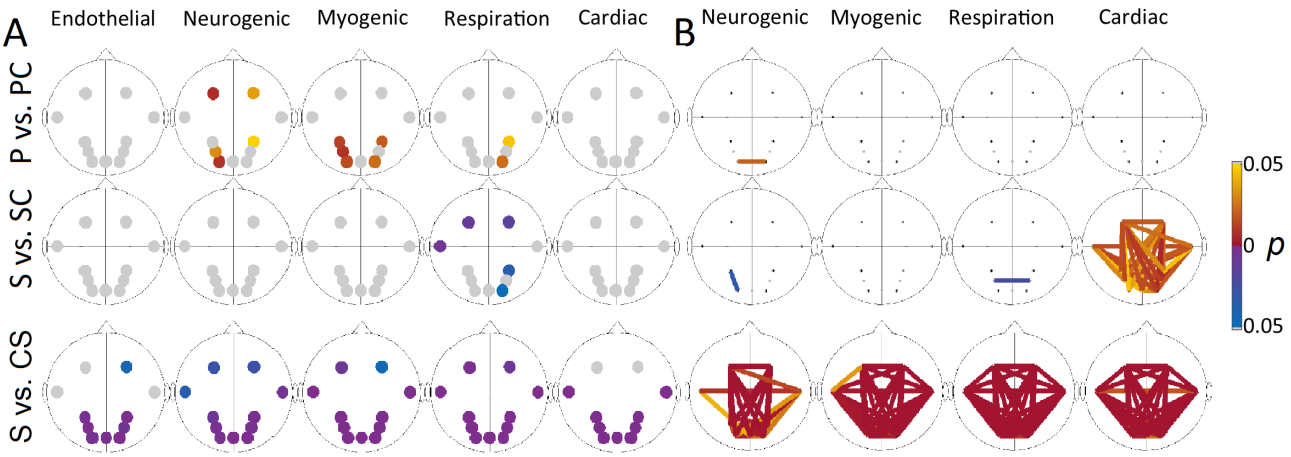

Supplementary Figure 17: (A) Significant p-values, found using the Wilcoxon rank-sum test, for oxyHb power. The first row is between the P and PC groups, while the second row is between the S and SC groups. The third row is between the S and the CS group. Yellow/red (blue/purple) circles indicate that the power is higher in the controls (HDs). (B) Significant p-values, found using the Wilcoxon rank-sum test, for fNIRS WPC in the cardiac band. Blue/purple lines indicate that the WPC was higher in the HD group compared to the control group, or in the S group compared to the CS group. P = presymptomatic Huntington's disease, S = symptomatic Huntington's disease, PC = control group for P, SC = control group for S, CS = symptomatic Huntington's disease with much chorea.

8 EEG power and coherence

Supplementary Figure 18 shows the EEG power (A) and coherence (B) results for all frequency bands starting from the myogenic range. Supplementary Table 2 shows the total power in the theta, beta and gamma bands. The alpha band is shown in the main manuscript.

Supplementary Figure 19 shows the EEG power and coherence results for two different ranges of β and γ. β is often defined up to 30 Hz, but in our study beta is defined as 14-22 Hz. The comparisons show that some of the γ results might be attributed to the 22-30 Hz range.

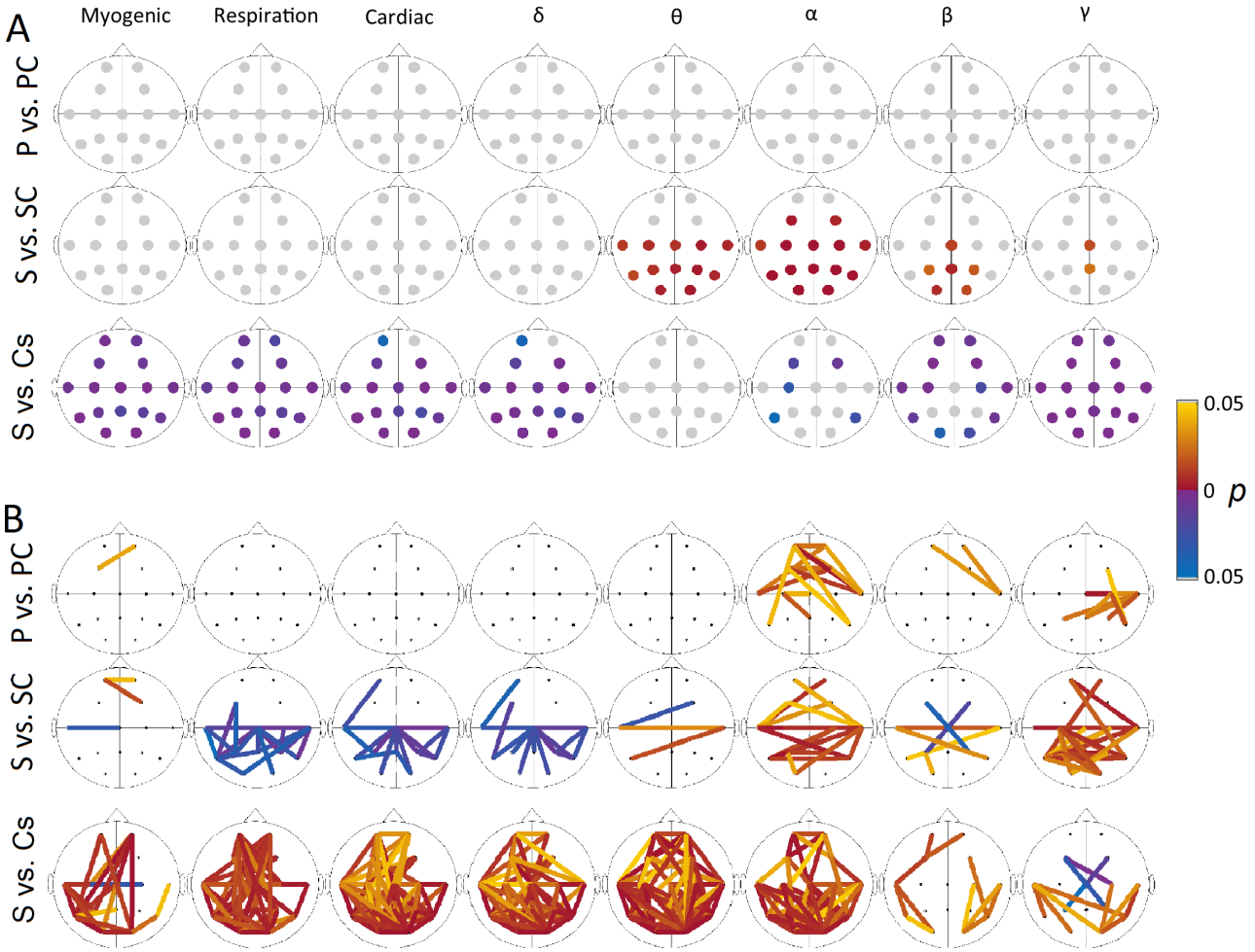

Supplementary Figure 18: (A) Significant p-values, found using the Wilcoxon rank-sum test, for the EEG time-averaged wavelet power. Yellow/red (blue/purple) circles indicate that the power is higher in the controls (HDs). The first row is the p-values between the P and PC groups, while the second row is the p-values for the S and SC groups (B) Significant differences, found using the Wilcoxon rank-sum test, in EEG WPC. The top row shows differences between the P and PC groups, while the middle row is between S and SC. The bottom row is between S and CS. Yellow/red (blue/purple) lines indicate higher WPC in the controls (HDs), or in the S group compared to the CS group. P = presymptomatic Huntington's disease, S = symptomatic Huntington's disease, PC = control group for P, SC = control group for S, CS = symptomatic Huntington's disease with much chorea.

Group median total power for EEG bands theta, beta and gamma.

	P	S	PC	SC
EEG θ (μV^2)				
Fp1	22.2	16.9	18.7	19.3
Fp2	21.2	13.6	17.8	17.9
F3	1.85	1.72	2.40	2.60
F4	2.31	1.82	2.04	2.14
T7	4.78	3.00*	5.33	5.67
C3	1.34	0.98*	1.68	1.68
Cz	0.61	0.34*	0.74	0.74
C4	1.55	1.06*	1.74	1.75
T8	4.53	3.71*	5.01	5.49
P7	5.35	3.94*	6.21	6.83
P3	3.49	2.70*	3.98	4.06
Pz	3.25	1.88*	3.68	3.69
P4	3.57	2.54*	4.11	4.20
P8	5.26	3.93*	6.69	7.01
O1	6.93	5.28*	7.29	7.34
O2	6.51	4.71*	7.01	7.45
EEG β (μV^2)				
Fp1	4.76	1.79	2.91	2.91
Fp2	3.80	3.37	3.66	3.66
F3	2.23	0.97	1.64	1.64
F4	1.70	1.30	1.63	1.60
T7	5.17	3.24	5.16	5.16
C3	2.15	1.02	1.72	1.63
Cz	0.52	0.18*	0.42	0.44
C4	2.17	1.20	1.87	1.79
T8	5.30	4.23	4.95	4.79
P7	5.88	3.48	5.42	5.45
P3	4.12	1.65*	3.50	3.53
Pz	2.92	1.20*	2.54	2.63
P4	4.27	1.77*	3.57	3.63
P8	5.08	3.52	5.39	5.39
O1	6.26	2.93*	6.01	6.01
O2	6.10	3.53*	5.62	5.62
EEG γ (μV^2)				
Fp1	6.13	4.48	4.75	4.96
Fp2	6.76	4.25	6.57	6.80
F3	4.71	2.47	2.76	2.77
F4	4.01	1.72	2.58	2.60
T7	7.72	7.58	9.71	8.19
C3	2.07	2.03	1.88	1.53
Cz	0.54	0.33*	0.49	0.50
C4	2.21	1.47	1.70	1.50
T8	13.3	5.42	7.83	6.70
P7	5.70	3.49	4.21	3.91
P3	2.74	1.71	2.57	2.39
Pz	1.98	1.22*	2.05	1.95
P4	2.85	1.78	2.69	2.44
P8	5.33	3.39	3.84	3.72
O1	4.54	3.64	4.45	4.39
O2	4.80	4.28	4.71	4.28

P = presymptomatic Huntington's disease, S = symptomatic Huntington's disease,
PC = control group for P, SC = control group for S, EEG = electroencephalogram,
* = $p<0.05$ for the P vs PC, or S vs. SC comparison, using the Wilcoxon rank-sum test.

Supplementary Table 2: Group median total power in the θ, β and γ bands.

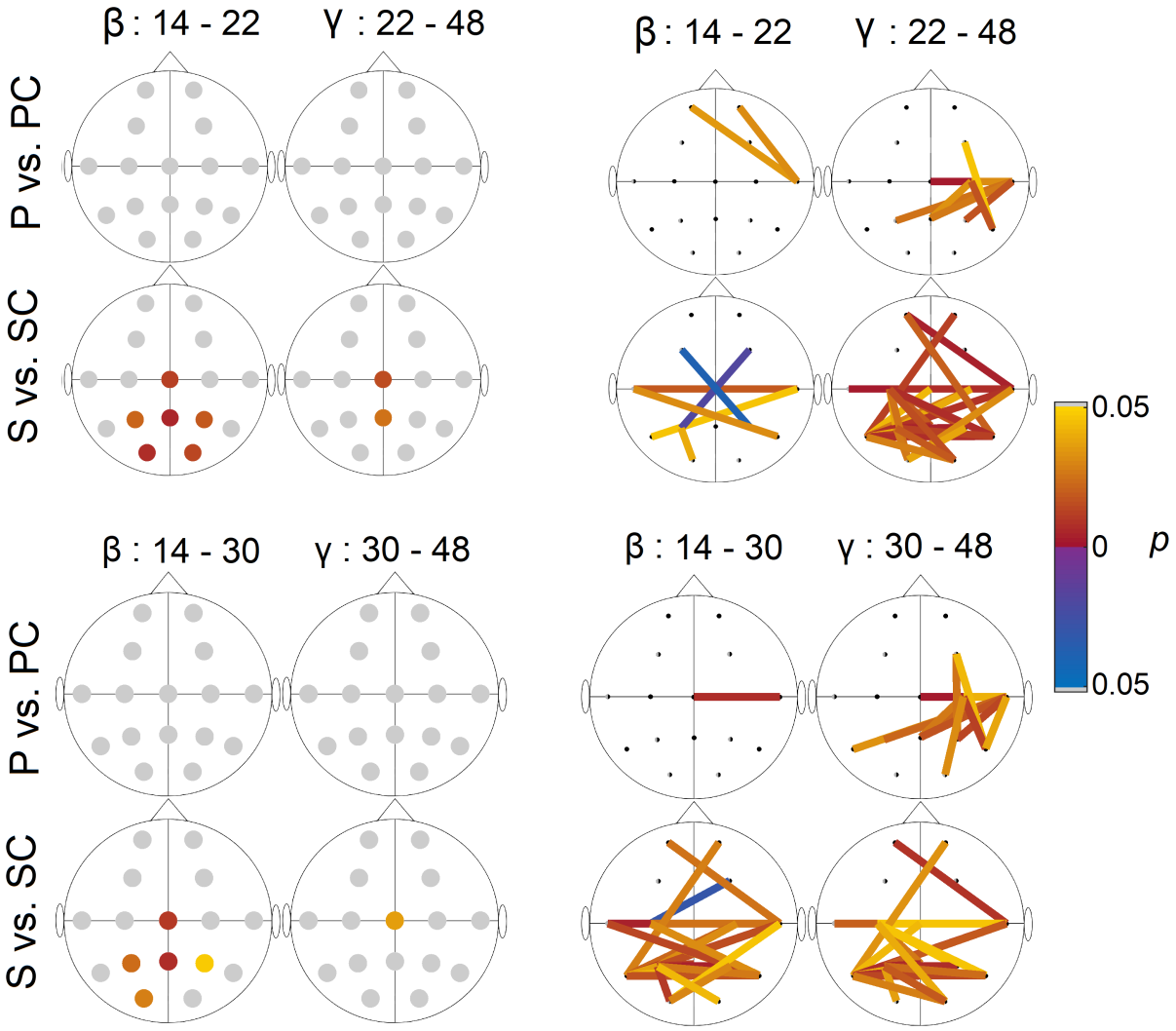

Supplementary Figure 19: Comparison of EEG results for two difference frequency ranges of beta and gamma. The left columns show EEG wavelet power, while the right columns show EEG wavelet phase coherence. P = presymptomatic Huntington's disease, S = symptomatic Huntington's disease, PC = control group for P, SC = control group for S.

9 fNIRS-EEG coherence

Supplementary Figure 20 shows the fNIRS–EEG coherence results for the cardiovascular frequency bands. Due to the high surrogate threshold at low frequencies, the endothelial band is not shown.

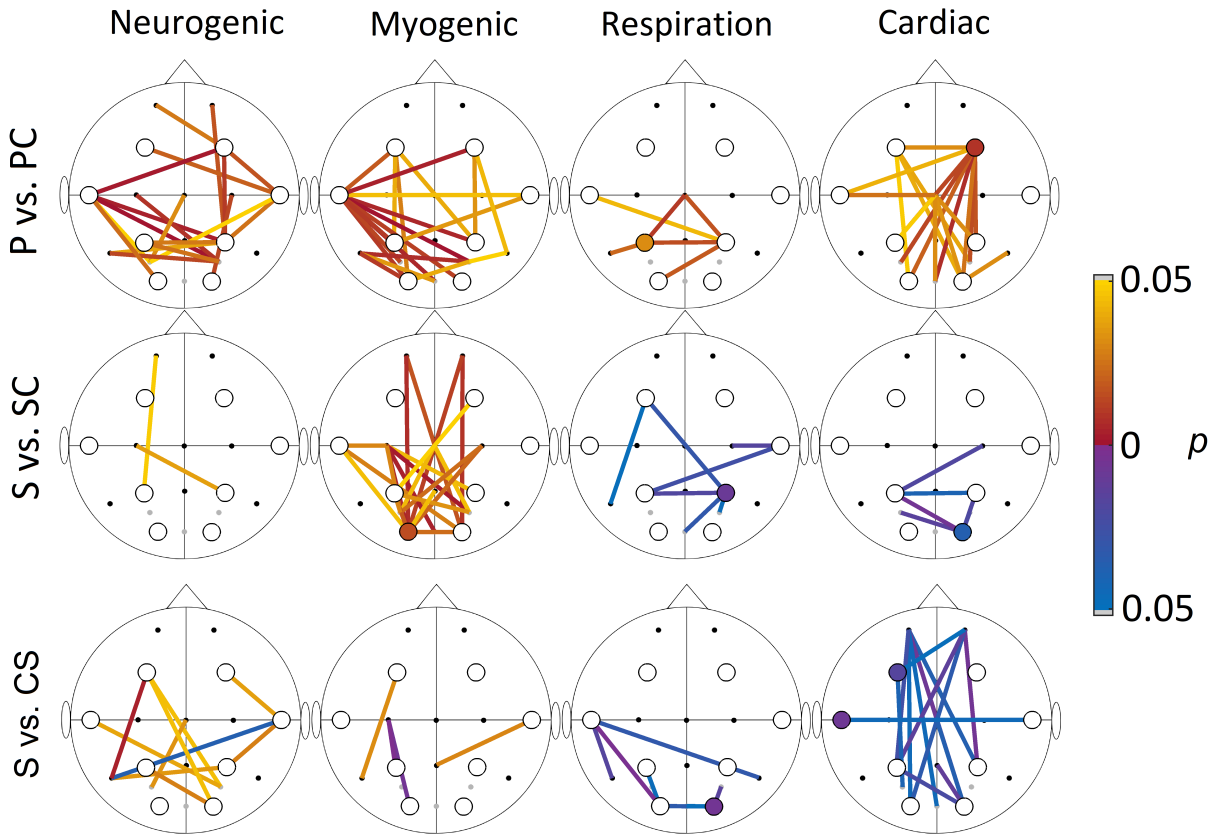

Supplementary Figure 20: Significant p-values, found using the Wilcoxon rank-sum test, for fNIRS-EEG WPC in the cardiac band. Blue/purple lines indicate that the WPC was higher in the HD group compared to the control group, or in the S group compared to the CS group. P = presymptomatic Huntington's disease, S = symptomatic Huntington's disease, PC = control group for P, SC = control group for S, CS = symptomatic Huntington's disease with much chorea.

10 BMI correlation

Supplementary Figure 21 shows the correlations between BMI and the average fNIRS-EEG myogenic coherence across all channel combinations. There were no significant correlations either for the pooled participants or for the different groups.

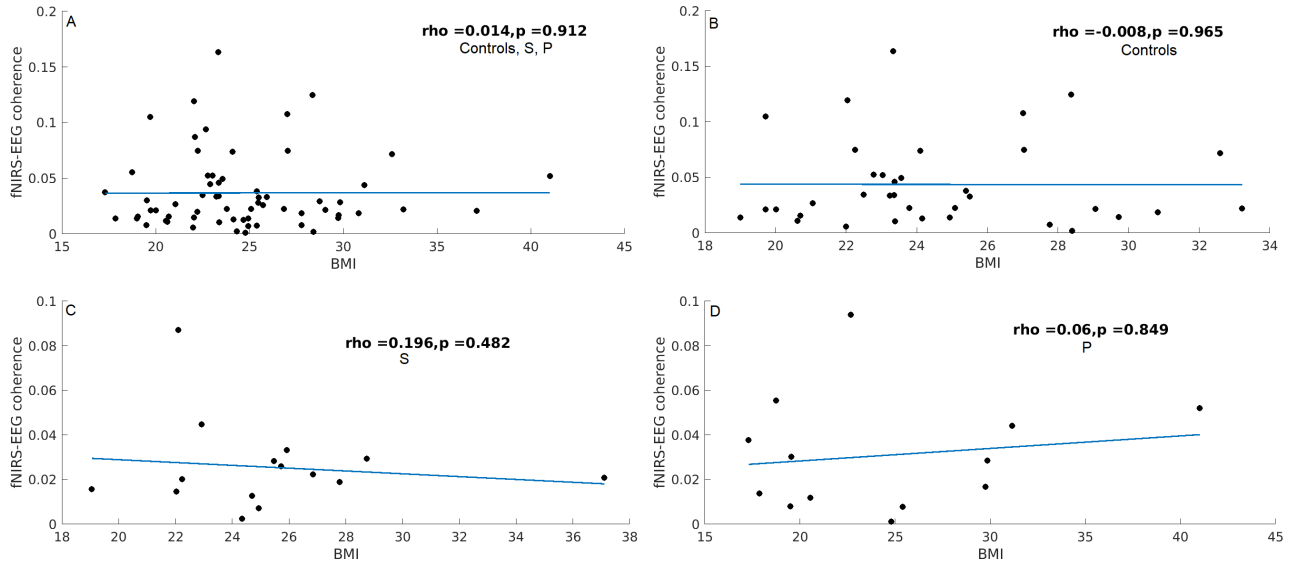

Supplementary Figure 21: Correlation between the average fNIRS-EEG myogenic coherence across the brain and BMI for (A) combined control, S and P groups, (B) only controls, (C) only S group and (D) only P group. P = presymptomatic Huntington's disease, S = symptomatic Huntington's disease.

Supplementary references

[1] Bandrivskyy, A., Bernjak, A., McClintock, P V. E. et al. Wavelet phase coherence analysis: Application to skin temperature and blood flow. *Cardiovasc. Engin.* **4**, 89–93 (2004).

[2] Cohen, J., & ProQuest. (1988). Statistical Power Analysis for the Behavioral Sciences (2nd ed.). Hillsdale, N.J.: L. Erlbaum Associates.

[3] Faul, F., Erdfelder, E., Lang, AG. et al. G*Power 3: A flexible statistical power analysis program for the social, behavioral, and biomedical sciences. *Behav. Res. Methods.* **39**, 175–191 (2007).

[4] Fritz, CO., Morris, PE., Richler, JJ. Effect size estimates: current use, calculations, and interpretation. *J. Exp. Psychol. Gen.*. **141**, 2-18 (2012).

[5] Ivarsson, A., Andersen, MB., Johnson, U. et al. To adjust or not adjust: Nonparametric effect sizes, confidence intervals, and real-world meaning. *Psychol Sport Exerc.* **14**, 97-102 (2013).

[6] Coolican, H. Research methods and statistics in psychology. (5th ed.) Hodder Education (2009).

[7] Lancaster, G., Iatsenko, D., Pidde, A. et al. Surrogate data for hypothesis testing of physical systems. *Phys. Rep.* **748**, 1-60 (2018).

[8] Barnes, S., Bjerkan, J., Clemson, P. et al. Phase coherence – A time-localised approach to studying interactions. In review for *Chaos*, invited review paper.

Glossary & Abbreviations

AD Alzheimer's disease. A neurodegenerative disease and the most common type of dementia.

HD Huntington's disease. A genetic neurodegenerative disease causing disordered movement and cognitive changes.

MCI Mild cognitive impairment. Greater decline in cognitive ability than is expected by normal ageing.

NVU Neurovascular unit. A functional unit consisting of neurons, microvasculature and glial cells. Orchestrates the control blood flow in the brain.

ECG Electrocardiogram. A monitoring technique that measures the electrical activity of the heart.

EEG Electroencephalogram. A monitoring technique that measures the electrical activity of the brain.

fNIRS Function near-infrared spectroscopy. A monitoring technique that measures the changes in oxygenated and deoxygenated hemoglobin concentrations in the brain.

fMRI Functional magnetic resonance imaging. A monitoring technique that measured blood flow associated changes in the brain.

MEG Magnetoencephalography. A monitoring technique that measures the magnetic fields caused by the electrical activity of the brain.

MS-OISI Multi-spectral optical intrinsic signal imaging. A monitoring technique that measures changes in light absorption caused by brain activity.

in vivo Studies performed on whole, living biological systems..

In vitro Studies performed on components of biological systems without their natural surroundings..

CO_2 Carbon dioxide.

ACh Acetylcholine. An endothelium-dependent vasodilator.

NO Nitric oxide. A soluble gas that can endothelial cells can produce, which modulate the activity of smooth muscle cells..

SNP Sodium nitroprusside. An endothelium-independent vasodilator.

PGs Prostaglandins. Can be produced by endothelial cells and contributes to vasodilation and vasoconstriction.

EDHF Endothelium-derived hyperpolarizing factor. A substance produced by endothelial cells contributing to vasodilation.

APOE4 An allele of the apolipoprotein E gene, which is a strong genetic risk factor for Alzheimer's disease.

EPSP Excitatory postsynaptic potentials.

IPSP Inhibitory postsynaptic potentials.

ATP Adenosine triphosphate. A molecule that provides energy to cells.

nonautonomous Explicitly dependent on time.

phase space A space where all possible states of a dynamical system are present, and each unique state corresponds to a point.

trajectory A path traced in phase space, showing which states a system occupies when evolved from an initial condition.

Fixed points Points in phase space where the derivatives of the system equals zero. Hence, a system will stay at the fixed point unless perturbed by external influences.

attractor A set of states in phase space that the systems evolves towards. If the trajectory is in the vicinity of the attractor it will converge to it or stay close forever, unless perturbed by an external force. Attractors can therefore lead to stable dynamics.

limit cycles Closed and isolated trajectories in phase space.

chronotaxic systems Dynamical systems described with nonautonomous point attractors moving along nonautonomous limit cycles.

References

1. Bjerkan, J. *et al.* Aging affects the phase coherence between spontaneous oscillations in brain oxygenation and neural activity. *Brain Res. Bull.* **201,** 110704 (2023).

2. Bjerkan, J. *et al.* The phase coherence of the neurovascular unit is reduced in Huntington's disease. *Brain commun.* **6,** fcae166 (2024).

3. Barnes, S. J. K., Bjerkan, J., Clemson, P. T., Newman, J. & Stefanovska, A. Phase coherence—A time–localized approach to studying interactions. *Chaos* **34,** 073155 (2024).

4. Bjerkan, J. *et al.* Neurovascular phase coherence is altered in Alzheimer's disease. *Brain Commun.* **7,** fcaf007 (2025).

5. Berger, H. Über das Elektrenkephalogramm des Menschen. *Archiv für Psychiatrie und Nervenkrankheiten* **94,** 16–60 (1931).

6. Sutton, P. *Cardiovascular system.* 4th ed. (Mosby Elsevier, Edinburgh, 2012).

7. Stefanovska, A. & Bračič, M. Physics of the human cardiovascular system. *Contemp. Phys.* **40,** 31–55 (1999).

8. Stefanovska, A. Coupled oscillatros: Complex but not complicated cardiovascular and brain interactions. *IEEE End. Med. Biol. Mag.* **26,** 25–29 (2007).

9. Söderström, T., Stefanovska, A., Veber, M. & Svensson, H. Involvement of sympathetic nerve activity in skin blood flow oscillations in humans. *Am. J. Physiol. Heart Circ. Physiol.* **284,** H1638–1646 (2003).

10. Bayliss, W. M. On the local reactions of the arterial wall to changes of internal pressure. *J. Physiol.* **28,** 220–231 (1902).

11. Davis, M. J. & Hill, M. A. Signaling mechanisms underlying the vascular myogenic response. *Physiol. Rev.* **79,** 387–423 (1999).

12. Folkow, B. Intravascular pressure as a factor regulating the tone of the small vessels. *Acta Physiol. Scand.* **17,** 289–310 (1949).

13. Folkow, B. Description of the myogenic hypothesis. eng. *Circ. Res.* **15,** SUPPL:279–SUPPL:287 (1964).

14. Folkow, B. Regulation of the peripheral circulation. *Br. Heart J.* **33,** 27–31 (1971).

15. Schubert, R. & Mulvany, M. J. The myogenic response: established facts and attractive hypotheses. *Clin. Sci. (Lond)* **96,** 313–326 (1999).

16. Koller, A. & Toth, P. Contribution of flow-dependent vasomotor mechanisms to the autoregulation of cerebral blood flow. *J. Vasc. Res.* **49,** 375–389 (2012).

17. Mayhew, J. E. *et al.* Cerebral vasomotion: A 0.1-Hz oscillation in reflected light imaging of neural activity. *NeuroImage* **4,** 183–193 (1996).

18. Landsverk, S. A., Kvandal, P., Bernjak, A., Stefanovska, A. & Kirkeboen, K. A. The effects of general anesthesia on human skin microcirculation evaluated by wavelet transform. *Anesth. Analg.* **105,** 1012–1019 (2007).

19. Kastrup, J., Bülow, J. & Lassen, N. A. Vasomotion in human skin before and after local heating recorded with laser Doppler flowmetry. A method for induction of vasomotion. *Int. J. Microcirc. Clin. Exp.* **8,** 205–215 (1989).

20. Hill, L. *The Physiology and Pathology of the Cerebral Circulation; an Experimental Research* (London, J. & A. Churchill, 1896).

21. Small, S. A. Quantifying cerebral blood flow: regional regulation with global implications. *J. Clin. Invest.* **114,** 1046–1048 (2004).

22. Kety, S. S. & Schmidt, C. F. The effects of altered arterial tensions of carbon dioxide and oxygen on cerebral blood flow and cerebral oxygen consumption of normal young men. *J. Clin. Invest.* **27,** 484–492 (1948).

23. Rayshubskiy, A. *et al.* Direct, intraoperative observation of 0.1 Hz hemodynamic oscillations in awake human cortex: implications for fMRI. *NeuroImage* **87,** 323–331 (2014).

24. Noordmans, H. J. *et al.* Detailed view on slow sinusoidal, hemodynamic oscillations on the human brain cortex by Fourier transforming oxy/deoxy hyperspectral images. *Hum. Brain. Mapp.* **39,** 3558–3573 (2018).

25. Roustit, M. & Cracowski, J.-L. Assessment of endothelial and neurovascular function in human skin microcirculation. *Trends Pharmacol. Sci.* **34,** 373–384 (2013).

26. Kvernmo, H. D., Stefanovska, A., Kirkebøen, K. A. & Kvernebo, K. Oscillations in the human cutaneous blood perfusion signal modified by endothelium-dependent and endothelium-independent vasodilators. *Microvasc. Res.* **57,** 298–309 (1999).

27. Kvandal, P., Stefanovska, A., Veber, M., Désirée Kvermmo, H. & Arvid Kirkebøen, K. Regulation of human cutaneous circulation evaluated by laser Doppler flowmetry, iontophoresis, and spectral analysis: importance of nitric oxide and prostaglandines. *Microvasc. Res.* **65,** 160–171 (2003).

28. Stewart, J. M., Taneja, I., Goligorsky, M. S. & Medow, M. S. Noninvasive measure of microvascular nitric oxide function in humans using very low-frequency cutaneous laser Doppler flow spectra. *Microcirculation* **14,** 169–180 (2007).

29. Bandrivskyy, A., Bernjak, A., McClintock, P. V. E. & Stefanovska, A. Wavelet phase coherence analysis: Application to skin temperature and blood flow. *Cardiovasc. Eng.* **4,** 89–93 (2004).

30. Bernjak, A., Clarkson, P. B., McClintock, P. V. & Stefanovska, A. Low-frequency blood flow oscillations in congestive heart failure and after beta1-blockade treatment. *Microvasc. Res.* **76,** 224–232 (2008).

31. P. Kvandal *et al.* Low frequency oscillations of the laser Doppler perfusion signal in human skin. *Microvasc. Res.* **72,** 120–127 (2006).

32. Shiogai, Y., Stefanovska, A. & McClintock, P. V. E. Nonlinear dynamics of cardiovascular ageing. *Phys. Rep.* **488,** 51–110 (2010).

33. Vanderah, T. W., Gould, D. J. & Nolte, J. *Nolte's the human brain: An introduction to its functional anatomy* 7th ed. (Elsevier, Philadelphia, PA, 2016).

34. Wang, J., Ma, S., Yu, P. & He, X. Evolution of human brain left–right asymmetry: Old genes with new functions. *Mol. Biol. Evol.* **40,** msad181 (2023).

35. Buzsáki, G. *Rhythms of the brain* (Oxford University Press, Oxford, 2006).

36. Raichle, M. E. Two views of brain function. *Trends. Cogn. Sci.* **14,** 180–190 (2010).

37. Sokoloff, L., Mangold, R., Wechsler, R. L., Kenney, C. & Kety, S. S. The effect of mental arithmetic on cerebral circulation and metabolism. *J. Clin. Invest.* **34,** 1101–1108 (1955).

38. Hebb, D. O. *The organization of behavior a neuropsychological theory* 1st ed. (L. Erlbaum Associates, Mahwah, N.J, 2002 - 1949).

39. Löwel, S. & Singer, W. Selection of intrinsic horizontal connections in the visual cortex by correlated neuronal activity. *Science* **255,** 209–212 (1992).

40. Buzsáki, G. Neural syntax: Cell assemblies, synapsembles, and readers. *Neuron* **68,** 362–385 (2010).

41. Buzsáki, G. & Draguhn, A. Neuronal oscillations in cortical networks. *Science* **304,** 1926–1929 (2004).

42. Buzsáki, G. & Watson, B. O. Brain rhythms and neural syntax: Implications for efficient coding of cognitive content and neuropsychiatric disease. *Dialogues. Clin. Neurosci.* **14,** 345–367 (2012).

43. Newson, J. J. & Thiagarajan, T. C. EEG Frequency Bands in Psychiatric Disorders: A Review of Resting State Studies. *Front. Hum. Neurosci.* **12** (2019).

44. Manasova, D. & Stankovski, T. Neural Cross-Frequency Coupling Functions in Sleep. *Neuroscience* **523,** 20–30 (2023).

45. Stankovski, T., Ticcinelli, V., McClintock, P. V. E. & Stefanovska, A. Neural Cross-Frequency Coupling Functions. *Front. Syst. Neurosci.* **11** (2017).

46. Sheppard, L. W., Hale, A. C., Petkoski, S., McClintock, P. V. E. & Stefanovska, A. Characterizing an ensemble of interacting oscillators: The mean-field variability index. *Phys. Rev. E.* **87,** 012905 (1 2013).

47. Brooks, H. *et al.* Theta–gamma coupling and ordering information: a stable brain–behavior relationship across cognitive tasks and clinical conditions. *Neuropsychopharmacol.* **45,** 2038–2047 (2020).

48. Girton, D., Benson, K. & Kamiya, J. Observation of very slow potential oscillations in human scalp recordings. *Electroencephalogr. Clin. Neurophysiol.* **35,** 561–568 (1973).

49. Nita, D. *et al.* Nonneuronal origin of CO_2-related DC EEG shifts: An in vivo study in the cat. *J. Neurophysiol.* **92,** 1011–1022 (2004).

50. Voipio, J., Tallgren, P., Heinonen, E., Vanhatalo, S. & Kaila, K. Millivolt-scale DC shifts in the human scalp EEG: Evidence for a nonneuronal generator. *J. Neurophysiol.* **89,** 2208–2214 (2003).

51. Revest, P. A., Jones, H. C. & Abbott, N. J. in *Frontiers in Cerebral Vascular Biology: Transport and Its Regulation* (eds Drewes, L. R. & Betz, A. L.) 71–74 (Springer US, Boston, MA, 1993).

52. Tschirgi, R. D. & Taylor, J. L. Slowly changing bioelectric potentials associated with the blood-brain barrier. *Am. J. Physiol.* **195,** 7–22 (1958).

53. Buzsáki, G., Anastassiou, C. A. & Koch, C. The origin of extracellular fields and currents — EEG, ECoG, LFP and spikes. *Nat. Rev. Neurosci.* **13,** 407–420 (2012).

54. De Goede, A. A. & Van Putten, M. J. A. M. Infraslow activity as a potential modulator of corticomotor excitability. *J. Neurophysiol.* **122,** 325–335 (2019).

55. Palva, J. M. & Palva, S. Infra-slow fluctuations in electrophysiological recordings, blood-oxygenation-level-dependent signals, and psychophysical time series. *NeuroImage* **62,** 2201–2211 (2012).

56. Raut, R. V. *et al.* Global waves synchronize the brain's functional systems with fluctuating arousal. *Sci. Adv.* **7** (2021).

57. Sihn, D. & Kim, S. P. Brain infraslow activity correlates with arousal levels. *Front. Neurosci.* **16,** 765585 (2022).

58. Vanhatalo, S. *et al.* Infraslow oscillations modulate excitability and interictal epileptic activity in the human cortex during sleep. *Proc. Natl. Acad. Sci. U.S.A.* **101,** 5053–5057 (2004).

59. Trimmel, M., Mikowitsch, A., Groll-Knapp, E. & Haider, M. Occurrence of infraslow potential oscillations in relation to task, ability to concentrate and intelligence. *Int. J. Psychophysiol.* **9,** 167–170 (1990).

60. Capilla, A. *et al.* The natural frequencies of the resting human brain: An MEG-based atlas. *NeuroImage* **258,** 119373 (2022).

61. Harmony, T. The functional significance of delta oscillations in cognitive processing. *Front. Integr. Neurosci.* **7** (2013).

62. Buzsáki, G. Theta oscillations in the hippocampus. *Neuron* **33,** 325–340 (2002).

63. Palva, S. & Palva, J. M. Functional roles of alpha-band phase synchronization in local and large-scale cortical networks. *Front. Psychol.* **2** (2011).

64. Engel, A. K. & Fries, P. Beta-band oscillations—signalling the status quo? *Curr. Opin. Neurobiol.* **20,** 156–165 (2010).

65. Pogosyan, A., Gaynor, L. D., Eusebio, A. & Brown, P. Boosting cortical activity at beta-band frequencies slows movement in humans. *Curr. Biol.* **19,** 1637–1641 (2009).

66. Lundqvist, M., Miller, E. K., Nordmark, J., Liljefors, J. & Herman, P. Beta: Bursts of cognition. *Trends. Cogn. Sci.* **28,** 662–676 (2024).

67. Jasper, H. H. & Andrews, H. L. Brain potentials and voluntary muscle activity in man. *J. Neurophysiol.* **1,** 87–100 (1938).

68. Pritchett, D. L., Siegle, J. H., Deister, C. A. & Moore, C. I. For things needing your attention: The role of neocortical gamma in sensory perception. *Curr. Opin. Neurobiol.* **31,** 254–263 (2015).

69. Iadecola, C. The neurovascular unit coming of age: A journey through neurovascular coupling in health and disease. *Neuron* **96,** 17–42 (2017).

70. Kugler, E. C., Greenwood, J. & MacDonald, R. B. The "neuro-glial-vascular" unit: The role of glia in neurovascular unit formation and dysfunction. *Front. Cell Dev. Biol.* **9** (2021).

71. Claassen, J. A. H. R., Thijssen, D. H. J., Panerai, R. B. & Faraci, F. M. Regulation of cerebral blood flow in humans: physiology and clinical implications of autoregulation. *Physiol. Rev.* **101,** 1487–1559 (2021).

72. Zlokovic, B. V. Neurovascular mechanisms of Alzheimer's neurodegeneration. *Trends. Neurosci.* **28,** 202–208 (2005).

73. Cai, W. *et al.* Dysfunction of the neurovascular unit in ischemic stroke and neurodegenerative diseases: An aging effect. *Ageing Res. Rev.* **34,** 77–87 (2017).

74. Farrall, A. J. & Wardlaw, J. M. Blood–brain barrier: Ageing and microvascular disease – systematic review and meta-analysis. *Neurobiol. Aging* **30,** 337–352 (2009).

75. Drouin-Ouellet, J. *et al.* Cerebrovascular and blood–brain barrier impairments in Huntington's disease: Potential implications for its pathophysiology. *Ann. Neurol.* **78,** 160–177 (2015).

76. Gil-Salcedo, A., Massart, R., de Langavant, L. C. & Bachoud-Levi, A.-C. Modifiable factors associated with Huntington's disease progression in presymptomatic participants. *Ann. Clin. Transl. Neurol.* **11,** 1930–1941 (2024).

77. Livingston, G. *et al.* Dementia prevention, intervention, and care: 2020 report of the Lancet Commission. *Lancet* **396,** 413–446 (2020).

78. Furr-Stimming, E. *et al.* Decreased cerebral blood flow in the striatum is an early event in Huntington's disease pathology. *Neurology* **92,** P1.8–044 (2019).

79. Garcia, F. J. *et al.* Single-cell dissection of the human brain vasculature. *Nature* **603,** 893–899 (2022).

80. Scholkmann, F. *et al.* A review on continuous wave functional near-infrared spectroscopy and imaging instrumentation and methodology. *NeuroImage* **85,** 6–27 (2014).

81. Wikimedia Commons. *Oxy and Deoxy Hemoglobin Near-Infrared absorption spectra.* Accessed on 14/08/24. Available at: `https://commons.wikimedia.org/wiki/File:Oxy_and_Deoxy_Hemoglobin_Near-Infrared_absorption_spectra.svg`.

82. Delpy, D. T. *et al.* Estimation of optical pathlength through tissue from direct time of flight measurement. *Phys. Med. Biol.* **33,** 1433 (1988).

83. Polimeni, J. R. & Lewis, L. D. Imaging faster neural dynamics with fast fMRI: A need for updated models of the hemodynamic response. *Prog. Neurobiol.* **207,** 102174 (2021).

84. Yeung, M. K. & Chan, A. S. A systematic review of the application of functional near-infrared spectroscopy to the study of cerebral hemodynamics in healthy aging. *Neuropsychol. Rev.* **31,** 139–166 (2021).

85. Biasiucci, A., Franceschiello, B. & Murray, M. M. Electroencephalography. *Curr. Biol.* **29,** R80–R85 (2019).

86. Butters, E., Srinivasan, S., O'Brien, J. T., Su, L. & Bale, G. A promising tool to explore functional impairment in neurodegeneration: A systematic review of near-infrared spectroscopy in dementia. *Ageing Res. Rev.* **90,** 101992 (2023).

87. Yeung, M. K. & Chan, A. S. Functional near-infrared spectroscopy reveals decreased resting oxygenation levels and task-related oxygenation changes in mild cognitive impairment and dementia: A systematic review. *J. Psychiatr. Res.* **124,** 58–76 (2020).

88. Gervain, J., Minagawa, Y., Emberson, L. & Lloyd-Fox, S. Using functional near-infrared spectroscopy to study the early developing brain: Future directions and new challenges. *Neurophotonics* **10,** 023519 (2023).

89. Hakim, U. *et al.* Quantification of inter-brain coupling: A review of current methods used in haemodynamic and electrophysiological hyperscanning studies. *Neuroimage* **280,** 120354 (2023).

90. Srinivasan, S. *et al.* Illuminating neurodegeneration: A future perspective on near-infrared spectroscopy in dementia research. *Neurophotonics* **10,** 023514 (2023).

91. Hock, C. *et al.* Near infrared spectroscopy in the diagnosis of Alzheimer's disease. *Ann. N. Y. Acad. Sci.* **777,** 22–29 (1996).

92. Marmarelis, V. Z., Shin, D. C., Tarumi, T. & Zhang, R. Comparison of model-based indices of cerebral autoregulation and vasomotor reactivity using transcranial Doppler versus near-infrared spectroscopy in patients with amnestic mild cognitive impairment. *J. Alzheimers Dis.* **56,** 89–105 (2017).

93. Viola, S., Viola, P., Buongarzone, M., Fiorelli, L. & Litterio, P. Tissue oxygen saturation and pulsatility index as markers for amnestic mild cognitive impairment: NIRS and TCD study. *Clin. Neurophysiol.* **124,** 851–856 (2013).

94. Liu, J. *et al.* Global brain hypoperfusion and oxygenation in amnestic mild cognitive impairment. *Alzheimers. Dement.* **10,** 162–170 (2014).

95. Keles, H. O., Karakulak, E. Z., Hanoglu, L. & Omurtag, A. Screening for Alzheimer's disease using prefrontal resting-state functional near-infrared spectroscopy. *Front. Hum. Neurosci.* **16,** 1061668 (2022).

96. Chiarelli, A. M. *et al.* Evidence of neurovascular un-coupling in mild Alzheimer's disease through multimodal EEG-fNIRS and multivariate analysis of resting-state data. *Biomedicines* **9** (2021).

97. Nguyen, T. *et al.* Investigation of brain functional connectivity in patients with mild cognitive impairment: A functional near-infrared spectroscopy (fNIRS) study. *J. Biophotonics.* **12,** e201800298 (2019).

98. Niu, H. *et al.* Abnormal dynamic functional connectivity and brain states in Alzheimer's diseases: Functional near-infrared spectroscopy study. *Neurophotonics* **6,** 025010 (2019).

99. Ferdinando, H. *et al.* Spectral entropy provides separation between Alzheimer's disease patients and controls: A study of fNIRS. *Eur. Phys. J. Spec. Top.* **232,** 655–662 (2023).

100. Fallgatter, A. *et al.* Loss of functional hemispheric asymmetry in Alzheimer's dementia assessed with near-infrared spectroscopy. *Cogn. Brain Res.* **6,** 67–72 (1997).

101. Li, X. *et al.* Decreased resting-state brain signal complexity in patients with mild cognitive impairment and Alzheimer's disease: A multiscale entropy analysis. *Biomed. Opt. Express* **9,** 1916–1929 (2018).

102. Bu, L. *et al.* Effective connectivity in subjects with mild cognitive impairment as assessed using functional near-infrared spectroscopy. *Am. J. Phys. Med. Rehabil.* **98,** 438–445 (2019).

103. Zeller, J. B. M. *et al.* Reduced spontaneous low frequency oscillations as measured with functional near-infrared spectroscopy in mild cognitive impairment. *Brain Imaging Behav.* **13,** 283–292 (2019).

104. Ho, T. K. K. *et al.* Deep learning-based multilevel classification of Alzheimer's disease using non-invasive functional near-infrared spectroscopy. *Front. Aging. Neurosci.* **14,** 810125 (2022).

105. Buzsáki, G., Traub, R. D. & Pedley, T. A. in *Current practice of clinical electroencephalography* (eds Ebersole, J. S. & Pedley, T. A.) 3rd ed., 1–11 (Lippincott Williams & Wilkins, Philadelphia, 2003).

106. Ebersole, J. S. in *Current practice of clinical electroencephalography* (eds Ebersole, J. S. & Pedley, T. A.) 3rd ed., 12–31 (Lippincott Williams & Wilkins, Philadelphia, 2003).

107. Specmann, E.-J., Elger, C. E. & Gorji, A. in *Niedermeyer's electroencephalography: Basic principles, clinical applications, and related fields* (eds Niedermeyer, E., Schomer, D. L. & Lopes da Silva, F. H.) 6th ed., 17–32 (Lippincott Williams & Wilkins, Philadelphia, 2011).

108. Jackson, A. F. & Bolger, D. J. The neurophysiological bases of EEG and EEG measurement: A review for the rest of us. *Psychophysiology* **51,** 1061–1071 (2014).

109. Connolly, M. B., Sharbrough, F. W. & Wong, P. K. H. in *Current practice of clinical electroencephalography* (eds Ebersole, J. S. & Pedley, T. A.) 3rd ed., 72–99 (Lippincott Williams & Wilkins, Philadelphia, 2003).

110. Beniczky, S. & Schomer, D. L. Electroencephalography: Basic biophysical and technological aspects important for clinical applications. *Epileptic Disord.* **22,** 697–715 (2020).

111. Wikimedia Commons. *EEG 10-10 system with additional information.* Accessed on 14/08/24. Available at: `https://commons.wikimedia.org/wiki/File:EEG_10-10_system_with_additional_information.svg`.

112. Babiloni, C. *et al.* Measures of resting state EEG rhythms for clinical trials in Alzheimer's disease: Recommendations of an expert panel. *Alzheimers. Dement.* **17,** 1528–1553 (2021).

113. Odish, O. F. F., Johnsen, K., van Someren, P., Roos, R. A. C. & van Dijk, J. G. EEG may serve as a biomarker in Huntington's disease using machine learning automatic classification. *Sci. Rep.* **8,** 16090 (2018).

114. Gordillo, D. *et al.* The EEG multiverse of schizophrenia. *Cereb. Cortex* **33,** 3816–3826 (2023).

115. Babiloni, C. *et al.* Sources of cortical rhythms in adults during physiological aging: A multicentric EEG study. *Hum. Brain Mapp.* **27,** 162–172 (2006).

116. de Aguiar Neto, F. S. & Rosa, J. L. G. Depression biomarkers using non-invasive EEG: A review. *Neurosci. Biobehav. Rev.* **105,** 83–93 (2019).

117. Li, R. *et al.* Concurrent fNIRS and EEG for brain function investigation: A systematic, methodology-focused review. *Sensors (Basel)* **22** (2022).

118. Keles, H. O., Barbour, R. L. & Omurtag, A. Hemodynamic correlates of spontaneous neural activity measured by human whole-head resting state EEG+fNIRS. *NeuroImage* **138,** 76–87 (2016).

119. Govindan, R. B., Massaro, A., Chang, T., Vezina, G. & du Plessis, A. A novel technique for quantitative bedside monitoring of neurovascular coupling. *J. Neurosci. Methods.* **259,** 135–142 (2016).

120. Chalak, L. F. *et al.* Novel wavelet real time analysis of neurovascular coupling in neonatal encephalopathy. *Sci. Rep.* **7,** 45958 (2017).

121. Vijayakrishnan Nair, V. *et al.* Monitoring anesthesia using simultaneous functional near infrared spectroscopy and electroencephalography. *Clin. Neurophysiol.* **132,** 1636–1646 (2021).

122. Perpetuini, D. *et al.* Working memory decline in Alzheimer's disease is detected by complexity analysis of multimodal EEG-fNIRS. *Entropy* **22** (2020).

123. Babiloni, C. *et al.* Hypercapnia affects the functional coupling of resting state electroencephalographic rhythms and cerebral haemodynamics in healthy elderly subjects and in patients with amnestic mild cognitive impairment. *Clin. Neurophysiol.* **125,** 685–693 (2014).

124. Cicalese, P. A. *et al.* An EEG-fNIRS hybridization technique in the four-class classification of Alzheimer's disease. *J. Neurosci. Methods* **336** (2020).

125. Li, R., Nguyen, T., Potter, T. & Zhang, Y. Dynamic cortical connectivity alterations associated with Alzheimer's disease: An EEG and fNIRS integration study. *NeuroImage: Clin.* **21,** 101622 (2019).

126. Strauss, D. G., Schocken, D. D. & Wagner, G. S. *Marriott's practical electrocardiography* 13th ed. (Wolters Kluwer, Philadelphia, 2021).

127. Paluch, E. K. Biophysics across time and space. *Nature Physics* **14,** 646–647 (2018).

128. Strogatz, S. H. *Nonlinear Dynamics and Chaos: With Applications to Physics, Biology, Chemistry and Engineering* 2nd ed. (Westview Press, 2000).

129. Winfree, A. T. Biological rhythms and the behavior of populations of coupled oscillators. *J. Theor. Biol.* **16,** 15–42 (1967).

130. Kuramoto, Y. *Self-entrainment of a population of coupled non-linear oscillators* in *International Symposium on Mathematical Problems in Theoretical Physics* (ed Araki, H.) (Springer, Berlin, Heidelberg, 1975), 420–422.

131. Kloeden, P. E. & Rasmussen, M. *Nonautonomous Dynamical Systems* (American Mathematical Soc., 2011).

132. Stefanovska, A., Clemson, P. T. & Suprunenko, Y. F. *Introduction to chronotaxic systems – systems far from thermodynamics equilibrium that adjust their clocks* in *Selforganization in complex systems: The past, present, and future of synergetics* (eds Wunner, G. & Pelster, A.) (Springer International Publishing, Cham, 2016), 227–246.

133. Wikimedia Commons. *Limit cycle and its Poincare map.* Accessed on 15/08/24. Available at: `https://commons.wikimedia.org/wiki/File:Limit_cycle_Poincare_map.svg`.

134. Suprunenko, Y. F., Clemson, P. T. & Stefanovska, A. Chronotaxic Systems: A New Class of Self-Sustained Nonautonomous Oscillators. *Phys. Rev. Lett.* **111,** 024101 (2 2013).

135. Kocarev, L. & Parlitz, U. Generalized Synchronization, Predictability, and Equivalence of Unidirectionally Coupled Dynamical Systems. *Phys. Rev. Lett.* **76,** 1816–1819 (11 1996).

136. Stefanovska, A. & McClintock, P. V. E. *Physics of Biological Oscillators. Understanding Complex Systems* (Springer, Cham, Switzerland, 2021).

137. Xiong, L. & Garfinkel, A. Are physiological oscillations physiological? *J. Physiol.* (2023).

138. Jacobsen, J. C. B. & Aalkjær, C. in *Physics of Biological Oscillators: New Insights into Non-Equilibrium and Non-Autonomous Systems* (eds Stefanovska, A. & McClintock, P. V. E.) 261–272 (Springer, 2021).

139. Moser, M., hwirth, M., Penter, R. & Winker, R. Why life oscillates–from a topographical towards a functional chronobiology. *Cancer Causes Control* **17,** 591–599 (2006).

140. Tu, B. P. & McKnight, S. L. Metabolic cycles as an underlying basis of biological oscillations. *Nat. Rev. Mol. Cell. Biol.* **7,** 696–701 (2006).

141. Penzel, T. *et al.* in *Physics of Biological Oscillators: New Insights into Non-Equilibrium and Non-Autonomous Systems* (eds Stefanovska, A. & McClintock, P. V. E.) 311–327 (Springer, 2021).

142. Stankovski, T. in *Physics of Biological Oscillators: New Insights into Non-Equilibrium and Non-Autonomous Systems* (eds Stefanovska, A. & McClintock, P. V. E.) 175–189 (Springer, 2021).

143. Sabia, S. *et al.* Association of sleep duration in middle and old age with incidence of dementia. *Nat. Commun.* **12,** 2289 (2021).

144. Box, G. E. P. *Time series analysis: forecasting and control* 5th ed. (Wiley, Hoboken, New Jersey, 2016).

145. Lee, Y. *Statistical Theory of Communication* (John Wiley & Sons Inc, 1960).

146. Fourier, J.-B.-J. *Théorie analytique de la chaleur* French (F. Didot, Paris, 1822).

147. Osgood, B. G. *Lectures on the Fourier Transform and Its Applications.* (American Mathematical Society, Providence, 2019).

148. Gabor, D. Theory of communication. Part 1: The analysis of information. *J. IEEE* **93,** 429–441 (1946).

149. Addison, P. S. *The Illustrated Wavelet Transform Handbook: Introductory Theory and Applications in Science, Engineering, Medicine and Finance* (IOP Publishing, Bristol, 2002).

150. Goupillaud, P., Grossmann, A. & Morlet, J. Cycle-octave and related transforms in seismic signal analysis. *Geoexploration* **23,** 85–102 (1984).

151. Rowland Adams, J., Newman, J. & Stefanovska, A. Distinguishing between deterministic oscillations and noise. *Eur. Phys. J. Spec. Top.* **232,** 3435–3457 (2023).

152. Kluger, D. S. *et al.* Modulatory dynamics of periodic and aperiodic activity in respiration-brain coupling. *Nat. Commun.* **14,** 4699 (2023).

153. Pikovsky, A., Rosenblum, M. & Kurths, J. *Synchronization a universal concept in nonlinear sciences* 362–369 (Cambridge University Press, Cambridge, 2001).

154. Rosenblum, M., Pikovsky, A., Kühn, A. A. & Busch, J. L. Real-time estimation of phase and amplitude with application to neural data. *Sci. Rep.* **11,** 18037 (2021).

155. Butterworth, S. On the theory of filter amplifiers. *Experimental Wireless & the Wireless Engineer* **7,** 536–541 (1930).

156. Iatsenko, D., McClintock, P. V. E. & Stefanovska, A. Extraction of instantaneous frequencies from ridges in time–frequency representations of signals. *Signal Process.* **125,** 290–303 (2016).

157. Iatsenko, D., McClintock, P. V. E. & Stefanovska, A. Nonlinear mode decomposition: A noise-robust, adaptive decomposition method. *Phys. Rev. E* **92,** 032916 (3 2015).

158. Horwitz, B. The elusive concept of brain connectivity. *NeuroImage* **19,** 466–470 (2003).

159. Friston, K. J. Functional and effective connectivity: a review. *Brain Connect.* **1,** 13–36 (2011).

160. Rodgers, J. L. & Nicewander, W. A. Thirteen Ways to Look at the Correlation Coefficient. *The American Statistician* **42,** 59–66 (1988).

161. Schreiber, T. Measuring Information Transfer. *Phys. Rev. Lett.* **85,** 461–464 (2 2000).

162. Granger, C. W. J. Investigating causal relations by econometric models and cross-spectral methods. *Econometrica* **37,** 424–438 (1969).

163. Sauer, U., Heinemann, M. & Zamboni, N. Getting Closer to the Whole Picture. *Science* **316,** 550–551 (2007).

164. Ishii, N. *et al.* Multiple High-Throughput Analyses Monitor the Response of *E. coli* to Perturbations. *Science* **316,** 593–597 (2007).

165. Taggart, P., Critchley, H. & Lambiase, P. D. Heart–brain interactions in cardiac arrhythmia. *Heart* **97,** 698–708 (2011).

166. Zlokovic, B. V. Neurovascular pathways to neurodegeneration in Alzheimer's disease and other disorders. *Nat. Rev. Neurosci.* **12,** 723–738 (2011).